DESIGN AND VALIDATION OF INNOVATIVE EARTHQUAKE RESILIENT FUSED STRUCTURES

by

Dorian Peng Tung

B.S., Queen's University, 2000
M.S., Queen's University, 2002

A THESIS SUBMITTED IN PARTIAL FULFILLMENT OF
THE REQUIREMENTS FOR THE DEGREE OF

DOCTOR OF PHILOSOPHY

in

THE FACULTY OF GRADUATE AND POSTDOCTORAL STUDIES

(Civil Engineering)

THE UNIVERSITY OF BRITISH COLUMBIA

(Vancouver)

April 2017

Abstract

Recent earthquakes worldwide have shown that even countries with modern building codes suffer significant structural damages after a strong earthquake shaking. The issue lies in the design philosophy that earthquake energy is absorbed through inelastic deformation of structural components. This creates unrecoverable structural damages and prolonged recovery time. These deficiencies can be minimized using earthquake resilient structures where earthquake energy is dissipated by specially designed structural fuses. The structural fuses are decoupled from the gravity system, and hence, they can be replaced efficiently without affecting the functionality of a structure after an earthquake. This dissertation aims to provide a consistent approach for researchers to develop and validate earthquake resilient fused structures and for engineers to design and implement such structures. It encompasses two major constituents: alternative design approach and advanced experimental technique. An equivalent energy design procedure (EEDP) is developed for fused structures. EEDP allows designers to select different performance objectives at different levels of earthquake shaking intensities. EEDP also allows engineers to select structural members to achieve the desired structural period, strength, and deformation without iterations. In addition to the design procedure, this dissertation also develops an innovative hybrid simulation testing technique where a switch-based hybrid simulation (SHS) method is proposed to validate the seismic performance of fused structures. SHS combines analytical and experimental sub-assemblies to examine the dynamic responses of a fused structure during an earthquake shaking. SHS switches between the displacement-based and force-based algorithms to control hydraulic servo actuators in displacement or force. It improves experimental accuracy and safety to test structural fuses that undergo drastic changes in stiffness. An innovative fused seismic force resisting system named fused truss moment frame (FTMF) is presented in this dissertation. The FTMF is designed using EEDP and validated using SHS. The SHS result shows that the FTMF can be easily designed using EEDP to achieve various target performance objectives under different earthquake shaking intensities. This dissertation has demonstrated that EEDP and SHS are efficient and effective procedures to design and validate innovative earthquake resilient fused structures.

Preface

Most of this dissertation has been published in conference proceedings as detailed below.

1. Chapters 2 and 3: Yang TY, **Tung DP**, Li Y. Seismic Design of Novel Steel Resilient Structures. *Proceedings of the 8th International Conference on Behavior of Steel Structures in Seismic Areas*, Shanghai, China, July 1-3, 2015.
2. Chapter 5: Yang TY, **Tung DP**, Li Y. Design and Validation of Fused Truss Moment Frames. *Proceedings of the 2nd Huixian International Forum on Earthquake Engineering for Young Researchers*, Beijing, China, August 19-21, 2016.

The author of this dissertation is responsible for the literature review, formulation development, structural design, model construction, computational analysis, data processing, and result presentation of the above manuscripts. The author of this dissertation has drafted the manuscripts and revised them based on the comments by Prof. T.Y. Yang.

1. Chapter 4: Yang TY, Xie X, Lin JY, Li Y, **Tung DP**. Theory and Application of Innovative Hierarchical Control Framework. *Proceedings of the 5th SECE*, Xian, China, July 28-30, 2016.

The author of this dissertation is responsible for the algorithm development and implementation of hybrid simulation in the above manuscript.

Table of Contents

List of Tables

List of Figures

List of Abbreviations

ACMR = adjusted collapse margin ratio

BRB = buckling restrained brace

CMR = collapse margin ratio

CP = collapse prevention

DBE = design based earthquake

DC = displacement-based control

DCR = demand capacity ratio

DDBD = direct displacement-based design

DHS = displacement-based hybrid simulation

DOF = degree-of-freedom

EEDP = equivalent energy design procedure

EFT = effective force testing

ELSDOF = equivalent linear single degree-of-freedom

ENLSDOF = equivalent nonlinear single degree-of-freedom

ESFP = equivalent static force procedure

FC = force-based control

FHS = force-based hybrid simulation

FTMF = fused truss moment frame

HS = hybrid simulation

IDA = incremental dynamic analysis

IO = immediate occupancy

LVDT = linear variable differential transformer

MC = moment connection

MCE = maximum considered earthquake

MYD = metallic yielding damper

OS = operator-splitting

PBPD = performance-based plastic design

PID = proportional-integral-derivative

PSBD = performance-spectra-based design

RDR = roof drift ratio

RR = rapid return

RTDHT = real-time dynamic hybrid testing

SC = switch control

SFRS = seismic force resisting system

SHS = switch-based hybrid simulation

SLE = service level earthquake

SSF = spectral shape factor

List of Symbols

A_i = area of coupled yielding plate at storey i

C_o = roof displacement modification factor

C'_{vi} = base shear distribution factor at storey i

d_i = depth of truss top chord at storey i

D = depth of truss in FTMF

E_a = strain energy

E_h = hysteresis energy

E_i = earthquake input energy

E_k = kinetic energy

E_s = elastic strain energy

E_ξ = damping energy

F = base shear

$F_{BRB,i}$ = design force of BRB at each storey i

F_{DBE} = base shear of the ELSDOF system at the DBE shaking intensity

F_e = base shear of the ELSDOF system

F_{MCE} = base shear of the ELSDOF system at the MCE shaking intensity

F_p = plastic base shear of the ENLSDOF system

F_{PR} = design base shear of the primary SFRS

$F_{PR,i}$ = storey shear of the primary SFRS

F_{SE} = design base shear of the secondary SFRS

$F_{SE,i}$ = storey shear of the secondary SFRS

$F_{SE,y}$ = strength of the secondary SFRS at Δ_y

F_{SLE} = base shear of the ELSDOF system at the SLE shaking intensity

F_y = yielding base shear of the ENLSDOF system or yielding strength of steel

h_j = height of level j measured from the ground level

H = height of roof measured from the ground level

J = numerical reduction coefficient for base overturning moment

L = length of end panel in FTMF

m = total seismic mass

$M_{MC,i}$ = design moment of MC at each storey i

M_v = factor to account for higher mode effect on base shear

R = force reduction factor

R_μ = ductility reduction factor

R_y = ratio of expected to specified yielding strength

S_a = pseudo acceleration

$(S_a)_{DBE}$ = pseudo acceleration of the ELSDOF system at the DBE shaking intensity

$(S_a)_{MCE}$ = pseudo acceleration of the ELSDOF system at the MCE shaking intensity

$(S_a)_{SLE}$ = pseudo acceleration of the ELSDOF system at the SLE shaking intensity

$(S_a)_p$ = pseudo acceleration of the ENLSDOF system at Δ_p

$(S_a)_y$ = pseudo acceleration of the ENLSDOF system at Δ_y

S_d = spectrum displacement

$(S_d)_{DBE}$ = spectral displacement of the ELSDOF system at the DBE shaking intensity

$(S_d)_{MCE}$ = spectral displacement of the ELSDOF system at the MCE shaking intensity

$(S_d)_{SLE}$ = spectral displacement of the ELSDOF system at the SLE shaking intensity

S_{MT} = earthquake shaking intensity at median MCE

$\hat{S}_{CT}$ = earthquake shaking intensity at 50% probability of collapse

T = structural fundamental period

$V_{s,30}$ = average shear wave velocity in the top 30 meters of soil

w_j = seismic weight of level j

W = total seismic weight

W_{ext} = external work

W_{int} = internal work

α = ratio of base frame stiffness over fused system initial stiffness or BRB angle to column

β_{DR} = uncertainly due to quality rating of design requirement

β_i = ratio of storey shear at storey i over that at roof

β_{MDL} = uncertainly due to quality rating of numerical model

β_{RTR} = uncertainly due to record-to-record variability in ground motions

β_{TD} = uncertainly due to quality rating of test data

β_{TOT} = total system collapse uncertainty

γ = energy modification factor used by PBPD

γ_a = energy modification factor from the SLE to DBE shaking intensity

γ_b = energy modification factor from the DBE to MCE shaking intensity

η = ratio of fused system yielding strength over maximum ground force

θ_p = plastic rotation

λ = ratio of F_p over F_y or force reduction factor

μ_{max} = ratio of base frame yielding displacement over fused system yielding displacement

μ_p = ratio of Δ_p over Δ_y or plastic ductility

μ_s = ductility factor

μ_T = period-based ductility

ω = natural vibration frequency

ΔE_{E1} = incremental energy of the ELSDOF system from the SLE to DBE shaking intensity

ΔE_{ND1} = incremental dynamic energy of the ENLSDOF system from the SLE to DBE shaking intensity

ΔE_{NM1} = incremental monotonic energy of the ENLSDOF system from the SLE to DBE shaking intensity

ΔE_{E2} = incremental energy of the ELSDOF system from the DBE to MCE shaking intensity

ΔE_{ND2} = incremental dynamic energy of the ENLSDOF system from the DBE to MCE shaking intensity

ΔE_{NM2} = incremental monotonic energy of the ENLSDOF system from the DBE to MCE shaking intensity

Δ = roof drift ratio

Δ_{DBE} = roof drift ratio of the ELSDOF system at the DBE shaking intensity

Δ_e = roof drift ratio of the ELSDOF system

Δ_{MCE} = roof drift ratio of the ELSDOF system at the MCE shaking intensity

Δ_p = plastic roof drift ratio

Δ_{SLE} = roof drift ratio of the ELSDOF system at the SLE shaking intensity

Δ_u = ultimate roof drift ratio

Δ_y = yielding roof drift ratio

Acknowledgements

First and foremost, I would like to express my sincere thanks to my research supervisor, Prof. Tony Yang. Without his selfless guidance and push for excellence, this research would not have been the quality it is. I also would like to express my appreciation to my supervisory committee, Prof. Ken Elwood and Prof. Kang Li, for their inspiration and moral support. For my fellow students, I would like to acknowledge YJ (Yuanjie Li) for his intelligence and time to assist me in coding and data processing. I also would like to thank Jason Lin for his expertise in control algorithms and Ryan Xie for his role in testing documentations. As much as we want to minimize our time in the laboratory, I truly treasure the hours the four of us have spent together to get the jobs done and the friendship we have built from it. In terms of funding, I am thankful of the financial supports from the University of British Columbia, Natural Sciences and Engineering Research Council of Canada, and Canadian Institute of Steel Construction. The following industry sponsors are much appreciated: George Third & Son Ltd., Custom Plate & Profiles (A division of Samuel, Son & Co., Ltd.), Pacific Bolt Manufacturing Ltd., and StarSeismic. The experimental program of this research would not be possible without the technical staff in the Civil Engineering Department. I thank each one of the following for working with me to setup the tests: Scott Jackson, Harald Schrempp, Doug Hudniuk, and David Roberts. Last but definitely not least is my family. They have always given me the freedom without doubting my actions and choices. I am grateful for their unconditional patience that allows me to follow through each one of my life changing decisions.

Dedication

To my lovely wife, Naomi, and my sweetest girl, Iris:

Without your understanding, support, and encouragement, this work will never be completed.

Chapter 1
Introduction

The recent earthquakes have raised the world's attention to earthquake risks and researchers' interests in earthquake resilience. The 2011 Christchurch earthquake in New Zealand incurs an estimated economic loss of over $15 billion US. It is possible that up to 50% of the buildings in the central business district will be demolished [Eguchi *et al.* 2012]. The 2011 Tohoku earthquake in Japan is the most expensive disaster of all time reporting an estimated economic loss of over $300 billion US. About 332,000 buildings, 2,100 roads, 56 bridges, and 26 railroads are damaged [Eguchi *et al.* 2012]. The reality shows that these modern cities are not earthquake resilient. Not only the recovery will take decades, but the social and economic constitutions will also change permanently. The socio-economic impacts have challenged many fields of professions and particularly, how the seismic performance of a structure is currently measured and typically incorporated in a design methodology.

Conventional structures are designed to provide life safety against earthquake loadings. In another word, a structure is allowed to be severely damaged during a strong earthquake shaking, as long as it does not collapse to cause casualties. This design approach does not consider post-earthquake performance states such as recovery and downtime. To address the deficiency, innovative earthquake resilient fused structures have been researched in recent years [Yang *et al.* 2015; Lopes *et al.* 2012; Erochko *et al.* 2013; Vargas and Bruneau 2009b; El-Bahey and Bruneau 2010]. Structural fuses analogous to electrical fuses are utilized to dissipate earthquake energy. These fuses are specially designed and detailed to be efficiently replaceable after a strong earthquake shaking to ensure resilience. Structural fuses have also been incorporated in moment resisting frames [Koetaka *et al.* 2005; Shen *et al.* 2011],

concentrically braced frames [Tremblay *et al.* 2011; Gray *et al.* 2014], eccentrically braced frames [Malakoutian 2012], rocking and self-centred structures [Ma *et al.* 2013], precast concrete walls [Kurama 2000], as well as based-isolated systems [Vargas and Bruneau 2009b]. Although extensive research has been conducted, a consistent approach to develop earthquake resilient fused structures has not yet been established. This motivates the current study to develop a design methodology that is suitable for fused structures as well as a validation technique that is accurate and cost-effective.

The followings are the merits of this study:

1. Equivalent energy design procedure (EEDP) is formulated to design fused structures.
2. A new earthquake resilient structural system named fused truss moment frame (FTMF) is proposed to demonstrate the simplicity to apply EEDP.
3. New finite element force-based hybrid simulation (FHS) is developed to test stiff specimens.
4. Switch-based hybrid simulation (SHS) is implemented to validate fused structures whose structural fuse changes its stiffness during a strong earthquake shaking.

1.1 Objective and methodology

This dissertation aims to establish a general approach to develop earthquake resilient fused structures. It encompasses two major constituents: alternative design approach and advanced experimental technique.

1.1.1 Alternative design approach

Researchers have developed fused structures in the past decades. They have successfully shown the ability of structural fuses to absorb energy and isolate damages through numerical modeling and laboratory testing. The design approach, however, is not uniform, and most of the time, tries to adapt to the current design philosophy. However, fused structures use structural fuses as the first line of defense and have a back-up system to provide secondary safety precaution during a severe ground shaking. This type of system is fundamentally different from conventional codified systems because it provides multiple performance levels.

The force-deformation relationship of fused structures is trilinear rather than bilinear. Directly using the current design philosophy is not the most efficient approach to maximize the full potential of fused structures.

Earthquakes release energy as ground moves. Naturally, an energy-based approach would be the most appropriate to solve this energy issue. Energy concepts have been well researched and developed over the last five decades. Housner [1956] introduced his energy-balanced design approach in the First World Conference on Earthquake Engineering. He explained that an earthquake feeds energy, E_i, into a structure. While some of this energy is dissipated through damping, E_ξ, the remaining energy is stored in the structure in the form of kinetic, E_k, and strain, E_a, energies. If the structure were designed to remain elastic, E_a will be stored as the elastic strain energy, E_s. In the case where the structure yields, E_a will be separated into elastic strain, E_s and hysteresis, E_h, energies. This concept was later elaborated by Uang and Bertero [1988] using the following energy-balanced equation.

$$E_i = E_k + E_\xi + E_a = E_k + E_\xi + E_s + E_h \qquad \text{Equation 1.1}$$

Akiyama [1985; 1988; 2000] explained that the same energy-balanced equation can be obtained by multiplying a displacement increment on both sides of the equation of motion and integrating the equation over the duration of a ground motion. He echoed Housner [1956] that E_i is a stable quantity dependent mainly on the total mass and fundamental period of a structure. It is irrespective to the distribution of mass, strength, and stiffness within a structure. He concluded that the energy concept initiated by Housner [1956] must be the soundest basis for earthquake design procedure.

Akiyama [Fischinger 2014] continued to explain that E_k tends to change into E_ξ and E_a. Since the essence of earthquake resilience is to design structures with predictable performance, it is necessary to know the real contents of E_a. A sound estimate of E_a can be obtained by neglecting E_ξ. Therefore, E_i can be approximately equal to E_a. For a nonlinear structure, E_a consists of E_s and E_h. In this dissertation, an energy-based design approach named equivalent energy design procedure (EEDP) is developed. EEDP decomposes E_h at

component level and calculates E_h as the sum of the product of force and deformation for each component. The former can be the yielding strength, while the latter can be the cumulative plastic deformation of a component.

As stated previously, a fused structure has a trilinear force-deformation relationship. The proposed EEDP aims to take advantages of this behaviour and formulate a design procedure to incorporate multiple performance objectives for various yielding points. The occurrence of each yielding depends on the intensity of seismic hazard. As a result, a fused structure has different performance expectations for different scale events. This multi-tier resilience goal and strategy are also documented in National Earthquake Resilience [NER 2011].

1.1.2 Advanced experimental technique

An innovative earthquake resilient fused structure designed using EEDP has to face real earthquake scenarios to validate its seismic performance prior to being implemented in practice. The most comprehensive method to understand nonlinear dynamic behaviour of a structure is to construct it in its entirety and test it full-scale on a shake table. However, it is expensive and dangerous to shake full-scaled structures. Only a handful of shake tables around the world, mostly in China, Japan, and the United States of America, are capable of testing structures in full-scale. Shake table testing of small-scaled models is more readily available. Results, on the other hand, do not always represent the behaviour of full-sized structures. Therefore, an alternative validation technique that is economical and safe must be explored.

It is often observed during a shake table testing that damages or nonlinearities occur at limited regions of a structure. For an earthquake resilient structure, these regions should be replaced by structural fuses. Laboratory testing should then focus on fuses rather than the remaining structure. Hybrid simulation (HS) is an advanced experimental technique which combines advanced finite element analysis with experimental testing to simulate the nonlinear dynamic responses of a structural system subjected to ground excitations. HS is well suited as an alternative to shake table testing because it is capable to partition a structure into analytical and experimental sub-assemblies. Only a portion of the structural system, such

as structural fuses that are designed to be damaged, needs to be constructed and tested, while the remainder can be modelled using a finite element software. As a result, HS can significantly reduce experimental costs. It also provides the option to conduct geographically distributed testing where resources such as lab space, testing equipment, and research personnel from different laboratories can be shared.

The idea of HS was contemplated in the late 1960s which led to its formal introduction by Takanashi in 1975. At the time, it was referred to as on-line testing that combined computer and actuator to study the nonlinear responses of structures. Majority of the HS conducted relies on displacement-based integration schemes to solve the nonlinear responses of structures [Nakashima *et al.* 1988; Shing and Mahin 1984; Dermitzakis and Mahin 1985; Nakashima *et al.* 1988; Vannan 1991; Combescure and Pegon 1997; Chang 2002; Pan *et al.* 2013]. However, when an experimental sub-assembly is stiff, displacement-based HS (DHS) causes force overestimations because it is challenging to precisely control a hydraulic servo actuator. A small control error in displacement results in a large fluctuation in force. To address this problem, this dissertation proposes a force-based HS (FHS) that calculates trial forces instead of trial displacements to be used in HS. Such a force-based algorithm allows stiff specimens to be tested using the sub-assembly technique in a non-real-time environment. Rather than checking force equilibrium alone, FHS checks dynamic equilibrium and compatibility condition simultaneously. However, FHS may be unstable or difficult to converge once the stiffness of a specimen reduces. To further improve the robustness and accuracy of HS, this dissertation also proposes switch-based HS (SHS). An algorithm has been developed to automatically switch between DHS and FHS depending on the tangent stiffness of an experimental sub-assembly.

1.2 Organization

This dissertation aims to establish a general approach for researchers to develop and validate earthquake resilient fused structures and for engineers to design and implement such structures. This dissertation is organized by the following chapters.

Chapter 2 explains in detail the proposed EEDP for innovative earthquake resilient fused structures. This procedure allows engineers together with owners to select performance objectives that correspond to different levels of seismic shaking intensities. It provides a common language among design professionals. One significant advantage of EEDP is its ability to allow engineers to easily select structural member sizes to achieve the desired structural period, strength, and deformation with only simple hand calculations and without iterations. Hence, it is practical to the engineering community.

Chapter 3 proposes an earthquake resilient structure named fused truss moment frames (FTMFs) to illustrate the robustness and simplicity of EEDP. In addition to the ability to span long distance for gravity loadings, a FTMF incorporates structural fuses such as buckling restrained braces (BRBs) at the truss end panels to enhance lateral stiffness and ductility. To provide additional strength after BRB yielding, the truss top chord is moment connected to the column. A numerical model of the FTMF designed using EEDP is constructed to perform nonlinear dynamic analysis and determine adjusted collapse marginal ratio.

Chapter 4 focuses on the development and validation of control algorithms for HS. In addition to the traditional displacement-based algorithm, a finite element force-based algorithm is formulated specifically to address stiff experimental sub-assembly in HS. Since a stiff specimen often yields and eventually softens, conducting a simulation with only force control mode would result in non-convergence and hydraulic instability. Therefore, switch control laws are proposed based on the tangent stiffness of a specimen to improve HS accuracy and robustness. DHS, FHS, and SHS are conducted using a simple structural system to illustrate the superiority of SHS.

Chapter 5 applies the developed SHS control algorithm from Chapter 4 to simulate the nonlinear dynamic behaviour of the proposed FTMF from Chapter 3 that has been designed using EEDP from Chapter 2. SHS is ideal to validate earthquake resilient structures because structural fuses can be designated as the experimental sub-assembly while the remaining is modelled in a computer. In this chapter, the BRB is tested in the Structural Laboratory at the

University of British Columbia using a hydraulic servo actuator with switching command signals between force and displacement.

Chapter 6 provides a summary of this dissertation. A future innovative earthquake resilient structure that uses structural fuses can be designed using the proposed EEDP and validated using the developed SHS.

Chapter 2
Equivalent Energy Design Procedure

Earthquake loads are resisted by seismic force resisting systems (SFRSs). The current code pre-qualified SFRSs, however, are not earthquake resilient because earthquake energy is designed to be absorbed through inelastic deformation of structural components. These components form a part of the gravity system. After a strong ground shaking, they are expected to be damaged. In order to repair or replace them, shoring is required to provide an alternative load path. This disrupts occupancy and causes business downtime. The situation can be resolved when using earthquake resilient fused structures to dissipate earthquake energy. A well designed earthquake resilient fused structure isolates damages to designated structural fuses that are decoupled from the gravity system. Such fuses can be repaired or replaced efficiently without affecting the functionality of the structure after an earthquake.

An earthquake resilient fused structure or fused SFRS has a tri-linear force-deformation relationship as shown in Figure 2.1. This relationship represents the system performance in three damage states. During service level earthquake (SLE) shakings, the system performance is targeted to be immediate occupancy (IO) where the structure is expected to be not damaged after an earthquake. Hence, no repair is required. During design based earthquake (DBE) shakings, the system performance is targeted to be rapid return (RR) where replaceable structural fuses are designed to yield to dissipate earthquake energy, while the remaining structure is protected from earthquake damages. After an earthquake, structural fuses can be repaired or replaced efficiently to allow the structure to be functional again. During maximum considered earthquake (MCE) shakings, the system performance is targeted to be collapse prevention (CP) where both structural fuses and the remaining

structure will yield to prevent the structure from collapse. These performance objectives are consistent with those specified in ASCE/SEI 41-06 [2006]. They can provide a common language among design professionals, owners, and other stakeholders.

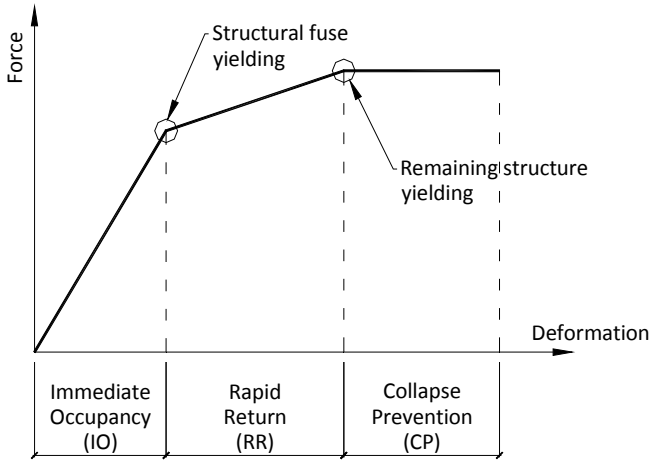

Figure 2.1 Performance objectives and force-deformation relationship of fused SFRSs

Innovative earthquake resilient fused structures cannot be routinely designed unless there is a simple and practical design procedure. In this chapter, an equivalent energy design procedure (EEDP) for fused SFRSs is presented. It uses the energy-balanced concept. Nonlinear responses of structural components are directly considered through plastic analysis. EEDP allows designers to select multiple performance objectives corresponding to different earthquake shaking intensities. EEDP also allows engineers to easily select structural member sizes to achieve the desired structural period, strength, and deformation with only simple hand calculations and without iterations. Hence, it is a very practical tool for the engineering community to design earthquake resilient fused structures.

In this chapter, Section 2.1 reviews the alternative design approaches recently developed by researchers. Section 2.2 explains the derivation of EEDP in detail. The purpose of EEDP is to design structural members that achieve the prescribed performances at different earthquake shaking intensities without design iterations. This is realized through the proper choices of energy modification factors. The determination of these factors is described in Section 2.3. Finally, nonlinear dynamic analysis is conduct in Section 2.4 to validate the proposed EEDP.

2.1 Alternative design approaches

Equivalent static force procedure (ESFP) is a common design approach adopted by many countries to design structures for seismic loads [NBCC 2005; ASCE/SEI 7-10 2010]. This design approach translates earthquake forces into “equivalent” static forces. Structural members are then selected to satisfy the strength requirements and drift limits through iterations. While ESFP quantifies seismic loads to be resisted by a structure, the design process relies on elastic analysis. Hence, the nonlinear responses of structural components are not explicitly accounted for. This results in severe and unexpected structural damages after a strong ground shaking. To improve, many alternative design approaches have been developed. Section 2.1.1 briefly reviews the displacement-based approach, while Section 2.1.2 and Section 2.1.3 review the energy-based and graph-based approaches, respectively.

2.1.1 Displacement-based design approach

Most of the building codes [NBCC 2005; ASCE/SEI 7-10 2010] treat earthquake inertia forces as equivalent static forces. This allows engineers to select structural members that satisfy the required loads. Since it is not economical to design structures to remain elastic, the building codes allow structures to be designed for a fraction of full earthquake inertia forces. This is achieved by dissipating the earthquake energy through the inelastic deformation of structural members. In North America, a force reduction factor, R, has been used to reduce earthquake loads [NBCC 2005; ASCE/SEI 7-10 2010]. The selection of R is based on the ductility and inherent over-strength of a SFRS. For a new SFRS, iterative experimental and numerical validations as outlined in FEMA-P695 [FEMA-P695 2009] can be used to define an appropriate force-based reduction factor. However, this validation process is very lengthy and costly. It is challenging to apply the process to new structural systems. In addition, the force-based design approach often underestimates the inelastic deformation demands of a structure because the approach only satisfies force demands to size structural members. To ensure a structure does not experience high inelastic deformation, the traditional force-based design approach typically requires a series of iterative checks to ensure that the final design will have sufficient strength and stiffness to resist strong earthquake shakings.

The direct displacement-based design (DDBD) method proposed by Priestley *et al.* [2007] focuses the seismic design of structures on displacement and ductility rather than force and strength. This method starts with an estimate of structural member sizes. The yield displacement is then calculated based on the yield strain, while the target displacement is calculated based on the ultimate strain of the flexural reinforcement. With these two displacements, the displacement ductility of the equivalent nonlinear single degree-of-freedom (ENLSDOF) system can be determined. The equivalent viscous damping including both elastic and hysteretic damping is then calculated using this ductility for a specific structural system or hysteretic rule. In DDBD, the design displacement spectrum for the calculated equivalent viscous damping needs to be available. From this spectrum, the effective structural period corresponding to the target displacement can be read off. It should be noted that the use of a displacement spectrum in DDBD is opposite to that of an acceleration spectrum in a force-based procedure. Once the period is obtained, the effective structural stiffness is calculated using the mass of the estimated member sizes. Finally, the design base shear is the product of the target displacement and effective structural stiffness. DDBD requires designers to provide a preliminary estimation of member sizes. The final structural stiffness needs to be verified at the end of DDBD to confirm that the initial stiffness assumption is correct. Hence, iterations might be required.

2.1.2 Energy-based design approach

Similar to DDBD, energy-balanced design concepts have been well researched and developed over the last five decades. Housner [1956] introduced the energy-based design approach in the First World Conference on Earthquake Engineering. He explained that an earthquake feeds energy, E_i, into a structure. While some of this energy is dissipated through damping, E_ξ, the remaining energy is stored in the structure in the form of kinetic, E_k, and strain, E_a, energies. If the structure were designed to remain elastic, E_a will be stored as the elastic strain energy, E_s. In the case where the structure yields, E_a will be separated into elastic strain, E_s and hysteresis, E_h, energies. This concept was later elaborated by Uang and Bertero [1988] using the following energy-balanced equation.

$$E_i = E_k + E_\xi + E_a = E_k + E_\xi + E_s + E_h \qquad \text{Equation 2.1}$$

Akiyama [1985; 1988; 2000] explained that the same energy-balanced equation can be obtained by multiplying a displacement increment on both sides of the equation of motion and integrating the equation over the duration of a ground motion. He echoed Housner [1956] that E_i is a stable quantity dependent mainly on the total mass and fundamental period of a structure. It is irrespective to the distribution of mass, strength, and stiffness within a structure. He concluded that the energy concept initiated by Housner [1956] must be the soundest basis for an earthquake design procedure.

Akiyama [Fischinger 2014] continued to explain that E_k tends to change into E_ξ and E_a. A sound estimate of E_a can be obtained by neglecting E_ξ. In other words, E_a can be approximately equal to E_i. The essence of earthquake resilience is to design structures with predictable performance. Therefore, it is necessary to know the real contents of E_a. For a nonlinear structure, E_a consists of E_s and E_h as discussed previously. It is E_h that an earthquake design procedure should be most interested in because E_h is an indication of structural damages and energy dissipation. E_h can be decomposed into component levels and calculated as the sum of the product of force and deformation for each component. The former can be the yielding strength, while the latter can be the cumulative plastic deformation of a component.

Although Equation 2.1 describes the relationship among the various energies during an earthquake excitation, it has been found cumbersome to implement in practice [Goel and Chao 2008]. Goel and Chao [2008] developed the performance-based plastic design (PBPD) method based on Housner's concept. This method is intended to provide a practical design procedure to obtain structural member sizes that satisfy both the strength and drift limits specified by designers. Figure 2.2 summarizes the concept of PBPD. At the target displacement, the energy to be stored by the equivalent linear single degree-of-freedom (ELSDOF) system is equal to E_a. The energy to be dissipated by an ENLSDOF is equal to the sum of E_s and E_h. PBPD recognizes these energies of ELSDOF and ENLSDOF are different and assumes them to be related by a factor, γ, as shown in Equation 2.2.

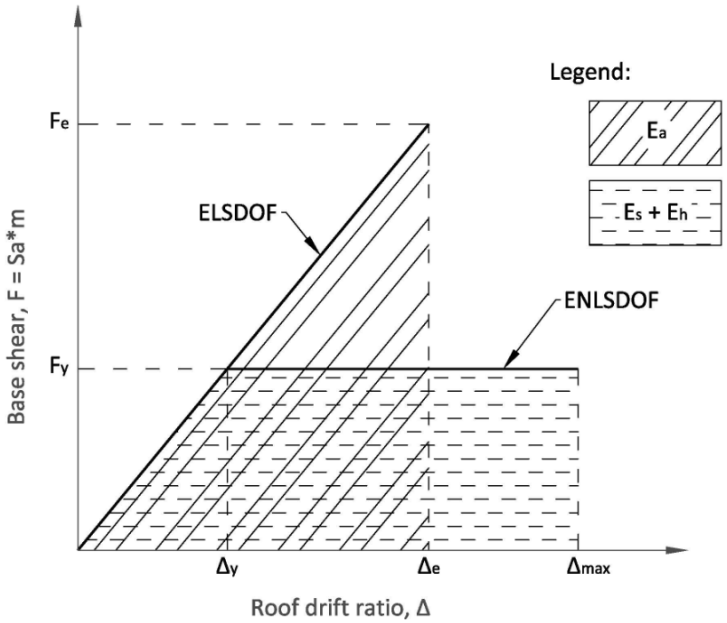

Figure 2.2 PBPD energy-balanced concept

$$E_s + E_h = \gamma E_a \qquad \text{Equation 2.2}$$

Figure 2.3 shows the values of γ derived by Goel and Chao [2008]. This derivation is based on an idealized inelastic spectrum published by Newmark and Hall [1982]. Other inelastic spectra such as the ones summarized by Miranda and Bertero [1994] can also be used. PBPD assumes that a portion of the strain energy is dissipated by a structure through a pre-selected yielding mechanism at the target roof drift. Using an energy-balanced concept, the strength and deformation of yielding components can be properly designed, while the remaining structural components can be protected through the capacity design principle. PBPD has been well applied to many code pre-qualified systems, such as steel moment resisting frames, steel concentrically braced frames, steel eccentrically braced frames, and steel special truss moment frames [Goel and Chao 2008]. The design method assumes that a system has a bi-linear force-deformation relationship. Though cyclic degradation can occur during the seismic responses of a SFRS, it is assumed that steel components can be properly detailed to have full energy dissipation after the components yield. In the case of concrete components where cyclic degradation is expected, factors such as C_2 in FEMA-440 [2006] can be used to modify a target roof drift [Liao and Goel 2014]. It should be noted that PBPD requires designers to make initial estimate of structural fundamental period. This period is then

checked at the end of PBPD to verify that the final member sizes can provide the stiffness needed to achieve the estimated period. Hence, iterations might be required.

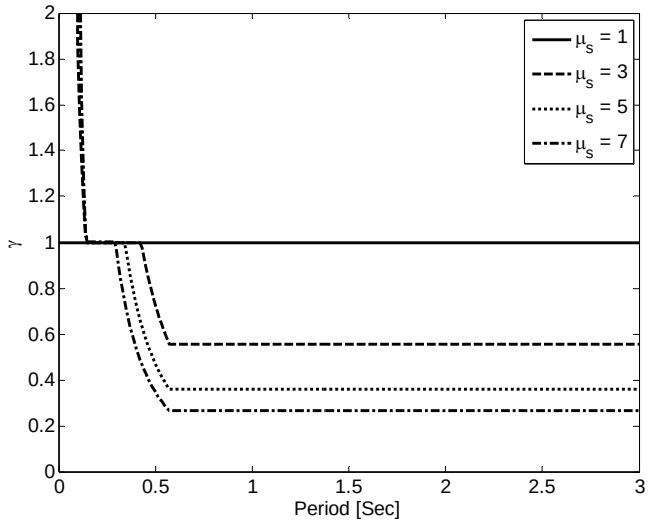

Figure 2.3 Relationship among γ, period, and ductility (μ_s) [Goel and Chao 2008]

2.1.3 Graph-based design approach

Performance-spectra-based design (PSBD) method has been proposed by Guo and Christopoulos [2013] to retrofit low- to medium-rise frame structures using supplemental dampers. The resulting force-deformation relationship of a retrofitted structure is tri-linear. The method considers multiple performance targets such as drift, base shear, acceleration, and residual drift. To use PSBD, it requires the construction of performance-spectra (P-spectra) of the original structure. This structure does not have supplemental dampers and is known as the base frame. P-spectra are graphic tools that relate the first mode responses of a base frame, mainly the peak displacement and acceleration, to structural and damping parameters that designers can control. To construct P-spectra, it is necessary to first obtain the base frame fundamental period from eigenvalue analysis and strength from pushover analysis. An ELSDOF system is then generated. In addition, multiple ENLSDOF systems are created by introducing various supplemental dampers to change the stiffness and ductility of the ENLSDOF systems. Time history analysis is conducted on both systems using a suite of ground motions. The maximum acceleration and displacement responses are then obtained. The inelastic responses are normalized by the elastic responses and plotted as P-spectra to

show the relationship between the ELSDOF and ENLSDOF systems. These spectra allow a direct comparison among different damper strategies that achieve similar performance targets prior to completing a damper design. In practice, designers can plot desired targets on P-spectra and then select damper stiffness and ductility that achieve these targets. It should be noted that P-spectra requires structural member sizes to generate the ENLSDOF system through pushover analysis. Hence, PSBD is ideal for retrofit projects, but can be difficult to apply for new projects.

Vargas and Bruneau [2009a] have proposed a design method for fused SFRSs. It is based on a parametric study of the nonlinear behaviour of a SDOF system that has a tri-linear force-deformation relationship. This study results in a dimensionless strength ratio chart (η-chart) that relates the following key parameters: 1) stiffness ratio, α, defined as the relationship between base frame stiffness and fused system initial stiffness, 2) maximum displacement ductility, μ_{max}, defined as the ratio of base frame yielding displacement over fused system yielding displacement, 3) strength ratio, η, defined as the relationship between fused system yielding strength and maximum ground force during an excitation, and 4) structural period, T. By selecting α, μ_{max}, and T, η can be read off the η-chart to calculate the design base shears for the base and fused frames. To control structural and non-structural damages, it is typical to limit storey drift. This can be achieved by selecting an appropriate structural period that results in an adequate structural stiffness. This selection, however, creates a potential conflict, because both T and α are related to the initial stiffness of a fused system. Selecting both T and α based on different criteria might result in design iterations. η-chart requires an engineer to determine and verify the actual values of the abovementioned key parameters via eigenvalue and pushover analyses after members are sized, and hence is an iterative process.

2.2 Equivalent energy design procedure

As reviewed in Section 2.1, an efficient design approach for fused SFRSs needs to directly take structural strength and ductility into consideration. The design parameters associated to force-deformation can be approximated using an equivalent SDOF system without nonlinear static or dynamic analysis. Designers should be able to select structural members to achieve the strength and stiffness requirements without iterations. More importantly, an ideal design

approach should also incorporate the concept of multiple performance objectives when a structural system is subjected to different levels of earthquake shaking intensities. To achieve all these objectives, the equivalent energy design procedure (EEDP) is developed. Table 2.1 summarizes the similarities and differences between the reviewed alternative design approaches.

Table 2.1 Comparison of EEDP with various alternative design approaches

Features & requirements	EEDP	DDBD	PBPD	P-spectra	η-chart
Incorporate multiple hazard levels	✓			✓	
Achieve multiple performance objectives	✓			✓	
Consider tri-linear force-deformation relationship	✓			✓	✓
Based on nonlinear SDOF responses	✓	✓	✓	✓	✓
Pre-select yielding mechanism & capacity design	✓	✓	✓	✓	✓
Require structural period estimation			✓	✓	✓
Require preliminary member sizes		✓		✓	
Require minimum iterations		✓	✓	✓	✓
Require nonlinear analyses				✓	✓

In general, both EEDP and P-spectra adopt the concept that structures shall be designed to achieve different performance objectives at different earthquake shaking intensities. EEDP, P-spectra, and η-chart are developed for systems with added energy dissipation where the overall fused systems behave with a tri-linear force-deformation relationship. All the alternative design approaches are based on the study of equivalent SDOF systems and allow users to pre-select a yielding mechanism and capacity. Some of the approaches (PBPD, P-spectra, and η-chart) require an initial estimate of structural period, while the others (DDBD and P-spectra) require an initial estimate of member sizes. All the approaches, except EEDP, need minimum iterations. Lastly, P-spectra and η-chart involve nonlinear analysis which might be less desirable for a typical engineering office due to time and budget constraints.

Figure 2.4 illustrates the concept of EEDP. In this figure, the force-deformation response of a fused SFRS is approximated by the ENLSDOF system. The energy to be dissipated by the ENLSDOF system is related to the energy of an ELSDOF system. In the case of a structural system where its higher mode participation is significant, higher mode modification factors

similar to M_v and J presented in NBCC [2005] can be introduced. The vertical axis represents the base shear, F, which is calculated using the pseudo acceleration, S_a, multiplied by the structural mass, m. The horizontal axis represents the roof drift ratio, Δ, which is the roof displacement normalized by the structural height, H. F_y $(= (S_a)_y m)$ and F_p $(= (S_a)_p m)$ are the yielding and plastic base shears of the ENLSDOF system, respectively. Δ_y and Δ_p are the yielding and plastic roof drift ratios of the ENLSDOF system that correspond to the base shears of F_y and F_p, respectively. Δ_u is the ultimate roof drift ratio of the ENLSDOF. Equation 2.3 is adopted from ASCE/SEI 41-06 [2006] to modify the spectrum displacement, S_d, of an ELSDOF system to the roof displacement of a multiple DOF system.

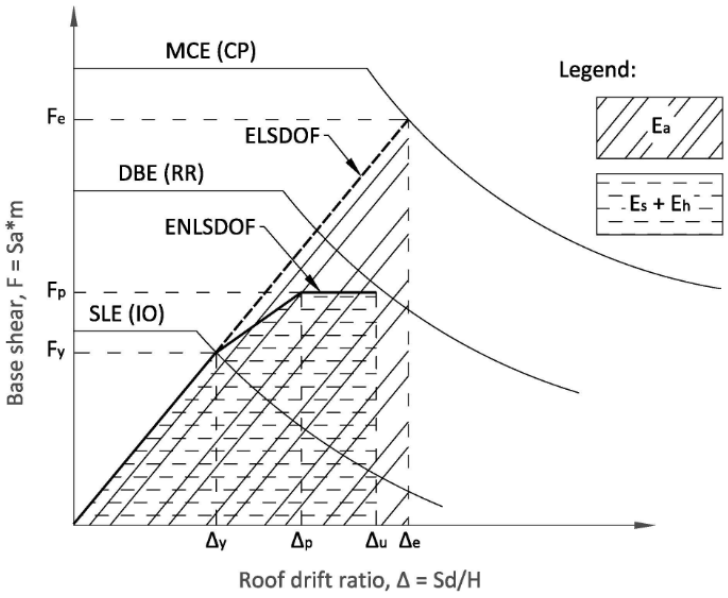

Figure 2.4 EEDP energy-balanced concept

$$\Delta_e = (C_0 S_d)/H \qquad \text{Equation 2.3}$$

where C_0 is the coefficient to modify the spectrum displacement, S_d, of an ELSDOF system to the roof displacement of a multiple DOF system.

EEDP is developed for fused SFRSs with a behaviour shown in Figure 2.1. The different performance objectives are related to three target seismic hazard levels as illustrated in Figure 2.4. For discussion purposes, the IO performance objective is achieved when a structure is subjected to a SLE hazard level. The RR and CP performance objectives are

achieved when a structure is subjected to DBE and MCE hazard levels, respectively. The selection of hazard levels at different performance objectives is completely arbitrary. Designers can select other hazard levels that suite their performance needs.

EEDP is not an iterative design procedure. The design parameters are logically determined as designers progressively choose performance objectives and design hazards. Without preliminary estimations, structural member sizes are selected using these parameters. The following sections detail the five key steps of EEDP. Section 2.2.1 thru Section 2.2.3 explains how the selection of hazard levels translates to system design backbone. Section 2.2.4 calculates design base shears. Section 2.2.5 discusses the vertical distribution of base shears as well as the design of yielding and non-yielding members.

2.2.1 Service level earthquake hazard level

At the SLE hazard level, a structure is designed to remain elastic. Hence, it is able to achieve the IO performance objective. As shown in Figure 2.5(a), the force-deformation relationship shall remain linear. The intersection of the system capacity and hazard demand curves can be defined using four parameters namely the elastic period (T), yielding base shear (F_y), shaking intensity at the SLE hazard level, and yielding roof drift ratio ($\Delta_y = \Delta_{SLE} = C_0(S_d)_{SLE}/H$). Because these parameters are not independent, only two of the four parameters can be selected by designers, and the other two have to be back calculated. Over selecting the parameters violate the principle of equal energies and result in unrealistic structures with unexpected performances.

It is recommended that designers start EEDP by selecting the SLE hazard level. This defines the largest earthquake shaking intensity where both structural and non-structural components shall remain elastic and hence undamaged. It should be noted that the SLE shaking intensity is directly related to the elastic performance of a structure. Selecting a high SLE shaking intensity will result in a strong structure which can withstand a large ground motion without damages. However, such a selection will increase material usages and lead to an expansive design. Once the SLE shaking intensity is selected, designers can proceed to select Δ_y to define the largest deformation where structural and non-structural components can deform

elastically. With Δ_y selected, F_y can be identified from the intersection of the SLE hazard curve and Δ_y on Figure 2.5(a). With Δ_y and F_y identified, the elastic period of the ENLSDOF system, T, which is the same as that of the ELSDOF system, can be calculated using Equation 2.4.

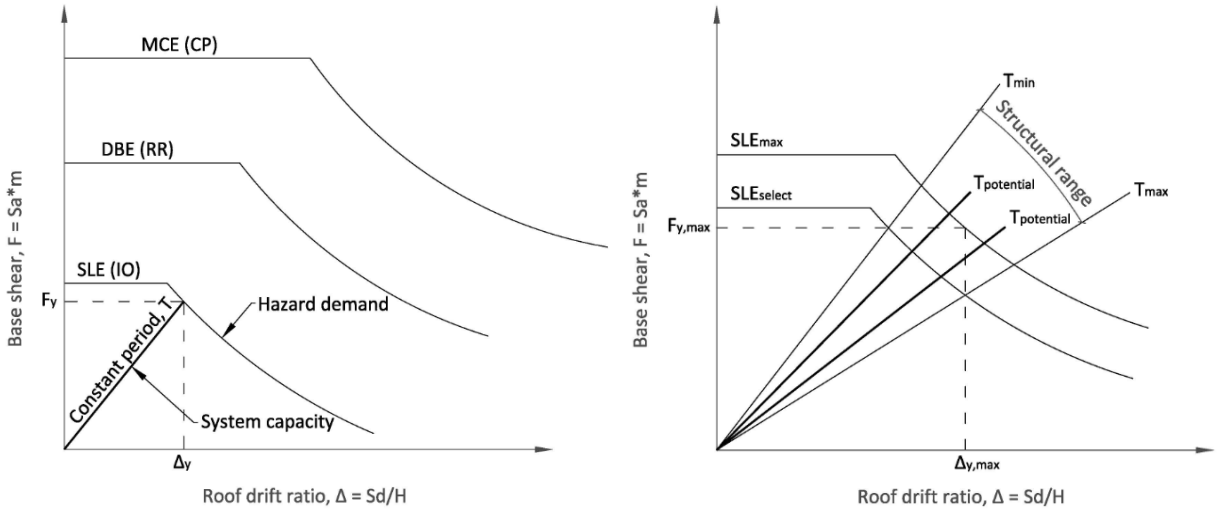

(a) Correlation of T, F_y, SLE, and Δ_y (b) Structural options with capped Δ_y and F_y

Figure 2.5 IO performance objective at SLE hazard level

$$T = \frac{2\pi}{\omega} = 2\pi\sqrt{\frac{1}{\omega^2}} = 2\pi\sqrt{\frac{S_a/\omega^2}{S_a}} = 2\pi\sqrt{\frac{S_d}{S_a}} = 2\pi\sqrt{\frac{(\Delta_y H)/C_o}{F_y/m}} \quad \text{Equation 2.4}$$

where ω is the natural frequency of vibration; $\Delta_y = \Delta_{SLE} = C_0(S_d)_{SLE}/H$ based on Equation 2.3; $F_y = F_{SLE} = (S_a)_{SLE}m$.

At the onset of a project, the intended usage and construction material are typically known. This provides sufficient input to estimate the overall structural mass. Often time, the architect together with the owner and design team select the location and type of the SFRS in a structure to satisfy the space requirements. The overall structural stiffness can then be approximated before individual structural member sizes are designed. With the mass and stiffness information, it is possible to obtain a rough approximation of the structural period. Instead of selecting Δ_y, it can now be identified from the intersection of the SLE hazard

curve and T on Figure 2.5(a). When the resulting Δ_y is not desirable, the SLE hazard level should be adjusted for the same structural period.

Structural and non-structural components are typically damaged due to excessive drifts. Designers can avoid these damages by limiting Δ_y. Construction costs can be measured by material weight which is proportional to base shear. Designers can control the costs by limiting F_y. At the onset of a project, designers can pre-determine these limiting Δ_y and F_y to define the maximum SLE hazard curve as shown in Figure 2.5(b). If the design SLE hazard curve is lower than the maximum SLE curve, the design SLE curve together with the limiting Δ_y and F_y defines a maximum structural period, T_{max}, and minimum structural period, T_{min}, respectively. As shown in the figure, a range of potential structural systems in between T_{max} and T_{min} can then be selected to satisfy both of the pre-determined damage and cost criteria. In this approach, two of the four parameters, namely the SLE hazard curve and elastic period, are selected, while the other two are back calculated. Therefore, the principle of equal energies is not violated.

2.2.2 Design based earthquake hazard level

After the structural parameters at the SLE hazard level have been defined, designers then select the DBE hazard level and plastic roof drift ratio, Δ_p. This defines the earthquake shaking intensity and roof drift ratio within which structural fuses are designed to yield and remain effective without fractures in order to protect the rest of a structure from damages. Figure 2.6 shows the expected performances of the ELSDOF and ENLSDOF systems when the shaking intensity increases from SLE to DBE.

The incremental energy of the ELSDOF system from an earthquake when the shaking intensity increases from SLE to DBE is defined as ΔE_{E1} which can be determined using Equation 2.5. This equation uses the area hatched as ΔE_{E1} on Figure 2.6. The incremental energy of the ENLSDOF system when pushed monotonically from the SLE to DBE shaking intensity is defined as ΔE_{NM1} which can be determined using Equation 2.6. This equation uses the area hatched as ΔE_{NM1} on Figure 2.6. The incremental energy of the ENLSDOF system when subjected to ground motions of increasing shaking intensity from SLE to DBE

is defined as ΔE_{ND1}. EEDP equates ΔE_{E1} to ΔE_{ND1} as shown in Equation 2.7. However, it is not possible to determine ΔE_{ND1} prior to knowing structural member sizes. To eliminate design iterations, it is practical to relate ΔE_{E1} to ΔE_{NM1} while preserving the energy equality. This is done by recognizing that when the ENLSDOF system is subjected to a cyclic dynamic load, energy is dissipated through all the cycles. This dissipation is greater than that through a simple monotonic pushover load. Therefore, an energy modification factor, γ_a, that is greater than unity is introduced. The derivation of γ_a will be provided in Section 2.3.1. Substituting Equation 2.7 into Equation 2.6 gives the plastic base shear, F_p, as shown in Equation 2.8.

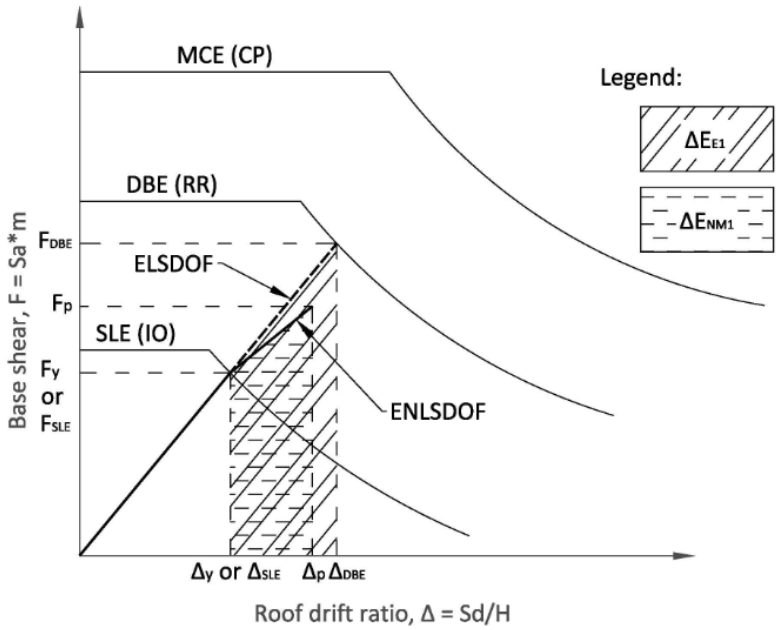

Figure 2.6 RR performance objective at DBE hazard level

$$\Delta E_{E1} = \frac{mC_o}{2}[(S_a)_{DBE} + (S_a)_{SLE}][(S_d)_{DBE} - (S_d)_{SLE}] \qquad \text{Equation 2.5}$$

where $(S_a)_{SLE}$ is the pseudo acceleration of the ELSDOF system at the SLE shaking intensity; $(S_a)_{DBE}$ is the pseudo acceleration of the ELSDOF system at the DBE shaking intensity; $(S_d)_{SLE}$ is the spectrum displacement of the ELSDOF system at the SLE shaking intensity; $(S_d)_{DBE}$ is the spectrum displacement of the ELSDOF system at the DBE shaking intensity.

$$\Delta E_{NM1} = \frac{mH}{2}\left[(S_a)_p + (S_a)_y\right](\Delta_p - \Delta_y) \quad \text{Equation 2.6}$$

where $(S_a)_y$ is the pseudo acceleration of the ENLSDOF system at Δ_y; $(S_a)_p$ is the pseudo acceleration of the ENLSDOF system at Δ_p.

$$\Delta E_{E1} = \Delta E_{ND1} = \gamma_a \Delta E_{NM1} \quad \text{Equation 2.7}$$

$$F_p = \frac{2\Delta E_{E1}}{\gamma_a H(\Delta_p - \Delta_y)} - F_y \quad \text{Equation 2.8}$$

2.2.3 Maximum considered earthquake hazard level

At this stage of EEDP, designers should define the MCE hazard level and ensure a fused SFRS can withstand this earthquake shaking intensity without collapse. It is achieved by designing structural fuses to maintain their yielding strength until the structure reaches the ultimate roof drift ratio, Δ_u. Meanwhile, the remaining structure is designed to dissipate the additional earthquake energy after the structure deforms beyond the plastic roof drift ratio, Δ_p. The combination of structural fuses (primary system) and remaining structure (secondary system) creates the tri-linear force-deformation response of a fused SFRS as shown in Figure 2.4. Figure 2.7 shows the expected performances of the ELSDOF and ENLSDOF systems when the shaking intensity increases from DBE to MCE.

The incremental energy of the ELSDOF system from an earthquake when the shaking intensity increases from DBE to MCE is defined as ΔE_{E2} which can be determined using Equation 2.9. This equation uses the area hatched as ΔE_{E2} on Figure 2.7. The incremental energy of the ENLSDOF system when pushed monotonically from the DBE to MCE shaking intensity is defined as ΔE_{NM2} which can be determined using Equation 2.10. This equation uses the area hatched as ΔE_{NM2} on Figure 2.7. The incremental energy of the ENLSDOF system when subjected to ground motions of increasing shaking intensity from DBE to MCE is defined as ΔE_{ND2}. EEDP equates ΔE_{E2} to ΔE_{ND2} as shown in Equation 2.11. Using a similar equal energy concept to γ_a, a modification factor, γ_b, that is greater than unity is introduced. The derivation of γ_b will be provided in Section 2.3.2. Substituting Equation 2.11 into Equation 2.10 gives Δ_u as shown in Equation 2.12.

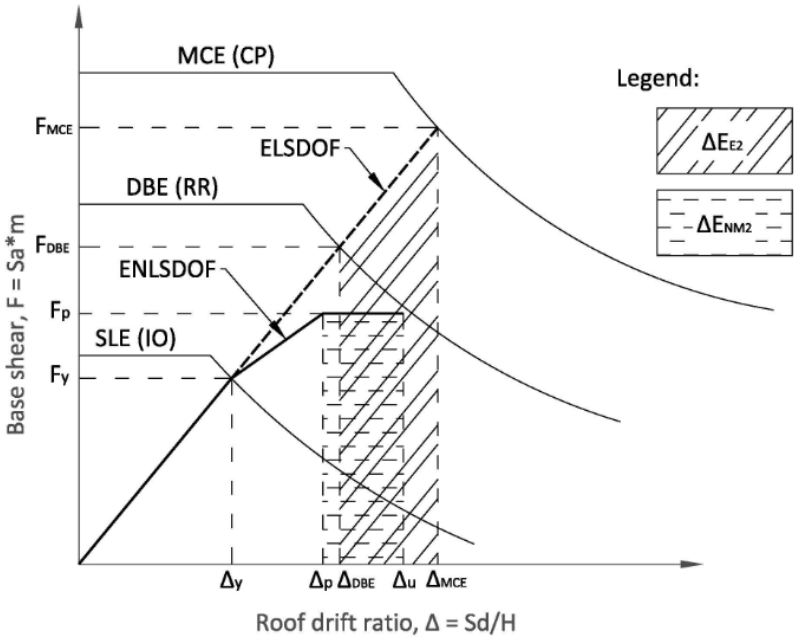

Figure 2.7 CP performance objective at MCE hazard level

$$\Delta E_{E2} = \frac{mC_o}{2}[(S_a)_{MCE} + (S_a)_{DBE}][(S_d)_{MCE} - (S_d)_{DBE}] \quad \text{Equation 2.9}$$

where $(S_a)_{MCE}$ is the pseudo acceleration of the ELSDOF system at the MCE shaking intensity; $(S_d)_{MCE}$ is the spectrum displacement of the ELSDOF system at the MCE shaking intensity.

$$\Delta E_{NM2} = (S_a)_p mH(\Delta_u - \Delta_p) = F_p H(\Delta_u - \Delta_p) \quad \text{Equation 2.10}$$

$$\Delta E_{E2} = \Delta E_{ND2} = \gamma_b \Delta E_{NM2} \quad \text{Equation 2.11}$$

$$\Delta_u = \frac{\Delta E_{E2}}{\gamma_b F_p H} + \Delta_p \quad \text{Equation 2.12}$$

2.2.4 Design base shear distribution

A fused SFRS consists of a primary (structural fuse) and secondary (remaining structure) SFRSs. Figure 2.8 shows the expected force-deformation responses of these systems. To design a fused SFRS, the tri-linear force-deformation response defined using EEDP thus far needs to be distributed between the sub-SFRSs.

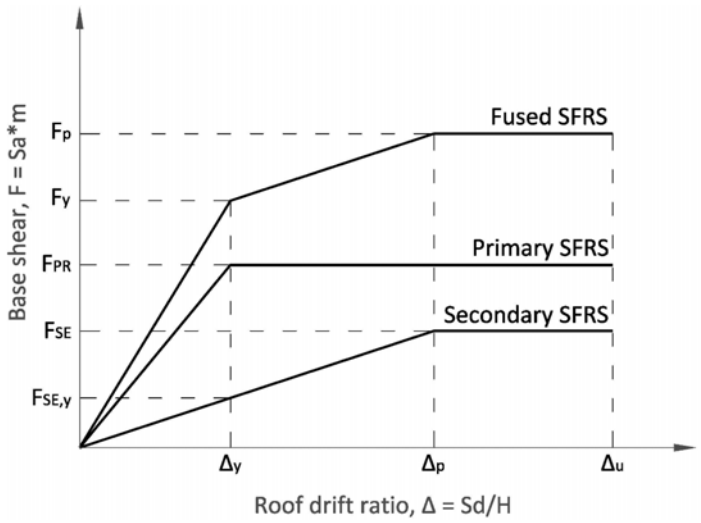

Figure 2.8 Distribution of design base shears to primary and secondary SFRSs

The yielding strength of the primary SFRS, F_{PR}, can be established based on the equilibrium relationship at Δ_y on Figure 2.8.

$$F_{PR} = F_y - F_{SE,y} \qquad \text{Equation 2.13}$$

where $F_{SE,y}$ is the strength of the secondary SFRS at Δ_y.

The yielding strength of the secondary SFRS, F_{SE}, can be expressed in terms of $F_{SE,y}$ since the system is assumed to be linear and elastic until Δ_p.

$$F_{SE} = \mu_p F_{SE,y} \qquad \text{Equation 2.14}$$

where μ_p is defined as the ratio of Δ_p over Δ_y.

With Equation 2.13 and Equation 2.14, the equilibrium relationship at Δ_p on Figure 2.8 can be expressed as follow.

$$F_p = F_{PR} + F_{SE} = F_y - F_{SE,y} + \mu_p F_{SE,y} \qquad \text{Equation 2.15}$$

Equation 2.15 can be re-arranged for $F_{SE,y}$.

$$\mu_p F_{SE,y} - F_{SE,y} = F_{SE,y}(\mu_p - 1) = F_p - F_y$$

$$\rightarrow F_{SE,y} = \frac{(F_p - F_y)}{(\mu_p - 1)} = \frac{\frac{F_y}{F_y}(F_p - F_y)}{(\mu_p - 1)} = \frac{\lambda F_y - F_y}{(\mu_p - 1)} = \frac{F_y(\lambda - 1)}{(\mu_p - 1)} \quad \text{Equation 2.16}$$

where λ is defined as the ratio of F_p over F_y.

Substitute Equation 2.16 into Equation 2.13 and Equation 2.14 to obtain F_{PR} and F_{SE}, respectively.

$$F_{PR} = F_y - \frac{F_y(\lambda - 1)}{(\mu_p - 1)} = \frac{F_y(\mu_p - 1) - F_y(\lambda - 1)}{(\mu_p - 1)} = F_y \frac{(\mu_p - \lambda)}{(\mu_p - 1)} \quad \text{Equation 2.17}$$

$$F_{SE} = \mu_p F_y \frac{(\lambda - 1)}{(\mu_p - 1)} \quad \text{Equation 2.18}$$

It should be noted that the primary SFRS is designed to yield prior to the secondary SFRS. On the other hand, the yielding strength of the primary can be either higher or lower than that of the secondary depending on designers' choices on the SLE and DBE shaking intensities. Figure 2.9(a) and Figure 2.9(b) use identical EEDP parameters except that the SLE shaking intensity is lower in Figure 2.9(b). As a result, the yielding strength of the primary SFRS is lower than that of the secondary.

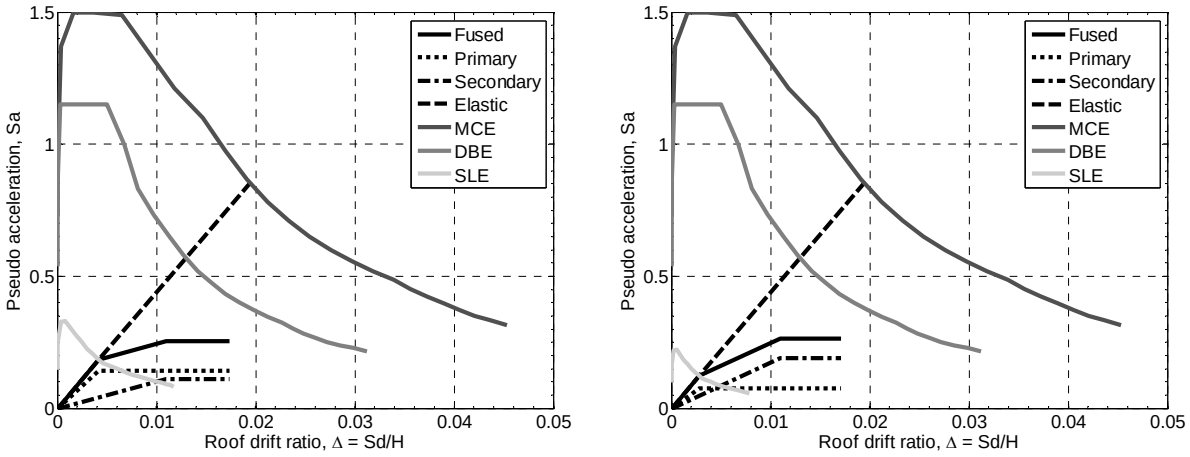

(a) $F_{PR} > F_{SE}$ (b) $F_{PR} < F_{SE}$

Figure 2.9 Comparison of design base shears in primary and secondary SFRSs

2.2.5 Plastic and capacity design

Once the yielding strength and deformation of the primary and secondary SFRSs have been established, designers can then select a yielding mechanism and associated yielding elements for each system. Because the yielding mechanism is defined for a multiple DOF system, the calculated design base shears by Equation 2.17 and Equation 2.18 need to be distributed over the structure height. Equation 2.19 shows the distribution proposed by Chao *et al.* [2007]. This distribution is not assuming the first mode shape. Rather, it is derived based on a range of nonlinear dynamic analysis and validated using the 21 ground motions obtained from the SAC (SEAOC, ATC, and CUREe) Los Angeles region study [FEMA-355C 2000]. It is intended to distribute the design base shears to match the demands observed in the nonlinear dynamic analysis, and hence, to promote simultaneous yielding or distributed damage of the yielding elements at all floors. With the yielding mechanism and vertical force distribution defined, the strength and ductility of the yielding elements can then be calculated using kinematic energy equilibrium method. Capacity design principle is employed to ensure that the non-yielding elements are protected. It should be noted that all loads including gravity need to be accounted for during the plastic and capacity design processes.

$$F_{PR,i} = C'_{vi} F_{PR} \text{ and } F_{SE,i} = C'_{vi} F_{SE} \qquad \text{Equation 2.19}$$

where $F_{PR,i}$ and $F_{SE,i}$ are the storey shear of the primary and secondary SFRSs, respectively; $C'_{vi} = (\beta_i - \beta_{i+1}) \left(\frac{w_n h_n}{\sum_{j=1}^{n} w_j h_j} \right)^{0.75T^{-0.2}}$; $\beta_i = \left(\frac{\sum_{j=i}^{n} w_j h_j}{w_n h_n} \right)^{0.75T^{-0.2}}$ $(when\ i = n, \beta_{i+1} = 0)$; w_j and w_n are the seismic weight of level j and roof, respectively; h_j and h_n are the height of level j and roof measured from the base, respectively.

2.3 Energy modification factors

Housner [1960] recognized that the energy dissipated by the ENLSDOF system is only a fraction of the energy stored by the ELSDOF system. However, he did not pursue the research to quantify the ratio between these two energies. Goel and Chao [2008] used the idealized inelastic spectra of elastic-plastic SDOF systems produced by Newmark and Hall [1982] to determine the ratio. This ratio is termed energy modification factor, γ, shown in Equation 2.20.

$$\gamma = \frac{2\mu_s - 1}{R_\mu{}^2} \qquad \text{Equation 2.20}$$

where μ_s is the ductility factor $\left(= \Delta_{max}/\Delta_y\right)$; R_μ is the ductility reduction factor $\left(= F_e/F_y\right)$; the definitions of the variables are shown in Figure 2.2.

The energy modification factor proposed by Goel and Chao [2008] is for a bi-linear system. In PBPD, a system is targeted to satisfy both the MCE and DBE shaking intensities. Because it is difficult to satisfy both intensities at the same time, the final design is typically governed by one of the intensities. EEDP, on the other hand, is designed to achieve three different performance objectives at three different shaking intensities. Therefore, two energy modification factors are required for an EEDP design. γ_a is used to modify the incremental energy when the shaking intensity increases from SLE to DBE, and γ_b is used when the intensity increases from DBE to MCE. Section 2.3.1 and Section 2.3.2 present the procedures to quantify the γ_a and γ_b factors, respectively, which are based on a large array of nonlinear dynamic time history analyses.

The first step to determine the energy modification factors in EEDP is to study the roof drift ratios of the ENLSDOF system subjected to ground motions. A suite of 20 ground motions from ten different earthquakes are selected from the PEER strong motion database [2010] and summarized in Table 2.2. Earthquake records are selected to have various fault mechanisms and an average shear wave velocity in the top 30 meters of soil within 180m/s and 360m/s. The target spectra are adopted from Yang *et al.* [2012]: 1) MCE hazard level having a 2% probability of exceedance in 50 years; 2) DBE hazard level having a 10% probability of exceedance in 50 years; 3) SLE hazard level having an 87% probability of exceedance in 50 years.

Table 2.2 Ground motions (GMs) used for energy modification factors

GM	Name	Year	Magnitude	NGA#	Mechanism	$V_{s,30}$ (m/s)	Record
1	Imperial Valley	1979	6.53	184	Strike-slip	202.3	H-EDA270
							H-EDA360
2	Superstition	1987	6.54	721	Strike-slip	192.1	B-ICC000
							B-ICC090

Table 2.2 Ground motions (GMs) used for energy modification factors

GM	Name	Year	Magnitude	NGA#	Mechanism	$V_{s,30}$ (m/s)	Record
3	Spitak, Armenia	1988	6.77	730	Reverse-oblique	274.5	GUK000
							GUK090
4	Loma Prieta	1989	6.93	733	Reverse-oblique	271.1	A2E000
							A2E090
5	Erzican, Turkey	1992	6.69	821	Strike-slip	274.5	ERZ-EW
							ERZ-NS
6	Big Bear	1992	6.46	902	Strike-slip	345.4	DHP090
							DHP360
7	Northridge	1994	6.69	949	Reverse	297.7	ARL090
							ARL360
8	Kobe, Japan	1995	6.90	1119	Strike-slip	312.0	TAZ000
							TAZ090
9	Chi-Chi, Taiwan	1999	7.62	1183	Reverse-oblique	210.7	CHY008-N
							CHY008-W
10	Duzce, Turkey	1999	7.14	1602	Strike-slip	326.0	BOL000
							BOL090

2.3.1 γ_a – Energy modification factor from SLE to DBE

γ_a relates the incremental monotonic and cyclic energies of the ENLSDOF system as the earthquake shaking intensity increases from the SLE to DBE hazard level. For a selected Δ_p, there are many possible post-yielding behaviour depending on the value of γ_a. As shown in Figure 2.10, $(\gamma_a)_{max}$ will result in an elastic-plastic behaviour, while $(\gamma_a)_{min}$ will result in an elastic-linear behaviour. A value of γ_a in between $(\gamma_a)_{max}$ and $(\gamma_a)_{min}$ will lead to a bi-linear behaviour shown as the dashed line in Figure 2.10. To determine the appropriate factor for the selected Δ_p, all possible values of γ_a are tried. For each trial, the force-deformation backbone curve defined by Equation 2.8 is assigned to the ENLSDOF system which is then excited by the 20 ground motions as presented in Table 2.2. The motions are amplitude scaled to match the DBE target spectrum. The medium of the maximum roof drift ratio is plotted against the trial γ_a as shown in Figure 2.11. EEDP only uses the converged γ_a such that the roof drift ratio due to ground motions at the DBE shaking intensity matches the selected Δ_p. This converged γ_a can be easily identified on the figure.

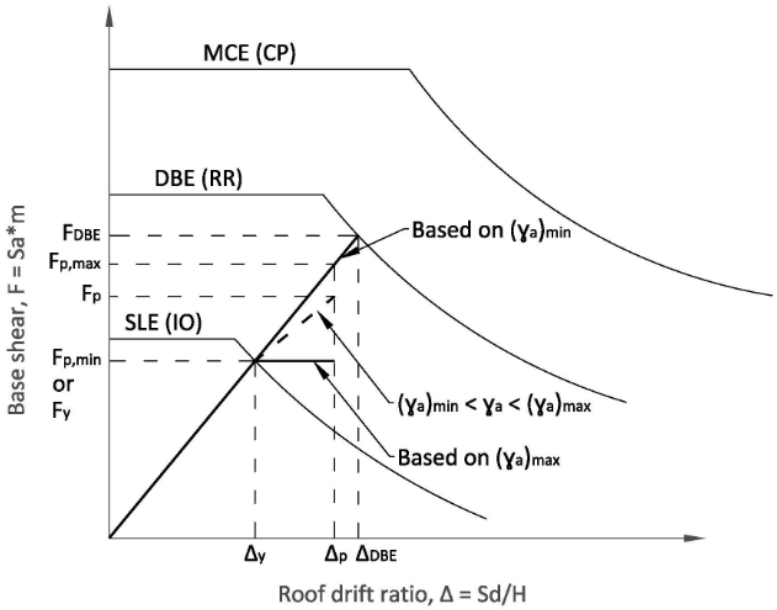

Figure 2.10 Effect of γ_a on F_p with constant Δ_p

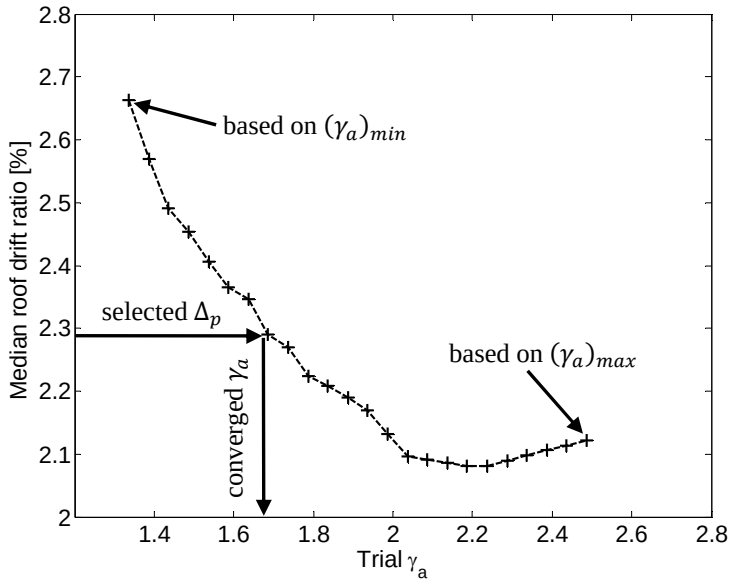

Figure 2.11 Effect of γ_a on roof drift ratio

The process is then repeated for different Δ_p and structural period, T. The detailed results are given in Appendix A. The converged γ_a is plotted against μ_p defined as the ratio of Δ_p over Δ_y and shown in Figure 2.12. It should be noted that Δ_p is bounded to ensure energies are balanced. If Δ_p is too small, there is insufficient displacement capacity in structural fuses to

dissipate earthquake energy. On the other hand, if Δ_p is too large, there is not enough earthquake energy to be dissipated by the fuses. Based on the findings indicated in Figure 2.12(a), Figure 2.12(b), and Figure 2.12(c), γ_a is relatively constant when T is less than 1.2 seconds. When T is more than 1.2 seconds, γ_a decreases linearly with increasing ductility as shown in Figure 2.12(d). To simplify the use of γ_a, the data are fitted by a linear trend line that has an applicable range of μ_p in between 2.5 and 3.2. For T in between 0.5 and 0.6 second, γ_a should be linearly interpolated and μ_p bound of Figure 2.12(a) should be used. For T in between 0.8 and 0.9 second, γ_a should be linearly interpolated and μ_p bound of Figure 2.12(b) should be used. For T in between 1.1 and 1.2 seconds, γ_a should be linearly interpolated and μ_p bound of Figure 2.12(c) should be used.

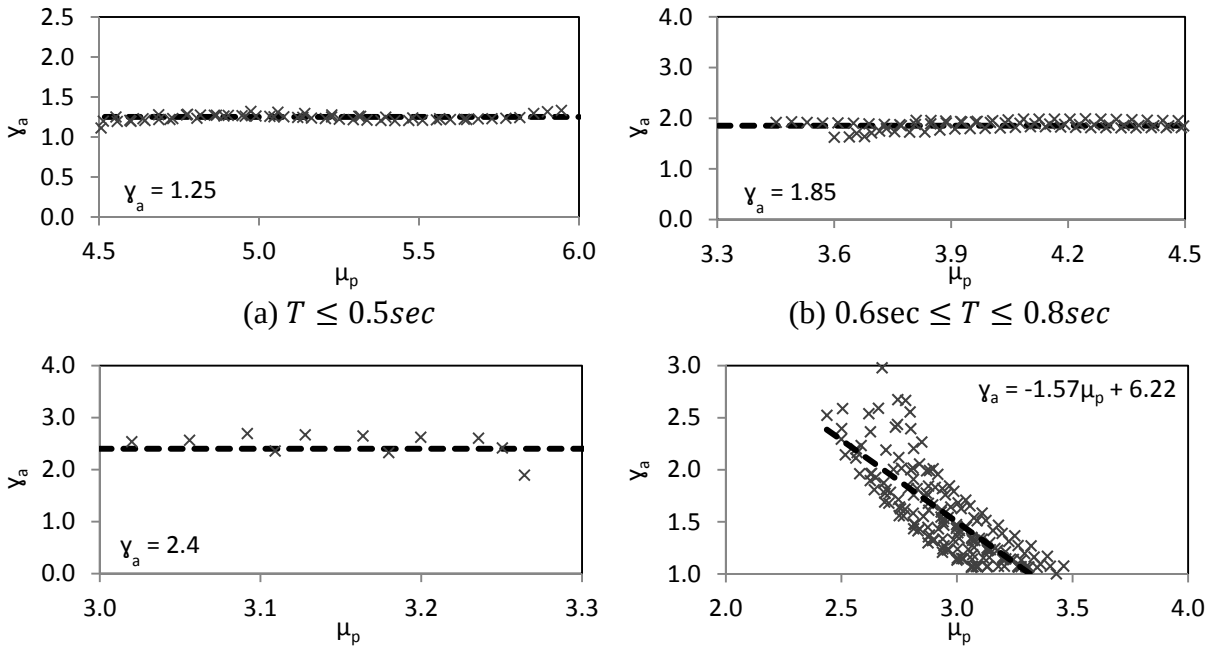

(a) $T \leq 0.5sec$ (b) $0.6\text{sec} \leq T \leq 0.8sec$

(c) $0.9\text{sec} \leq T \leq 1.1sec$ (d) $1.2\text{sec} \leq T \leq 3.0sec$

Figure 2.12 Incremental energy modification factor for SLE to DBE

2.3.2 γ_b – Energy modification factor from DBE to MCE

γ_b relates the incremental monotonic and cyclic energies of the ENLSDOF system as the earthquake shaking intensity increases from the DBE to MCE hazard level. γ_b can be calculated using Equation 2.12 where Δ_u is the median maximum roof drift ratio calculated using the ground motions presented in Table 2.2. The motions are amplitude scaled to match

the MCE target spectrum. The results are shown in Figure 2.13. Similar to γ_a, Figure 2.13(a), Figure 2.13(b), and Figure 2.13(c) show that γ_b is relatively constant when T is less than 1.2 seconds. When T is more than 1.2 seconds, γ_b decreases linearly with increasing ductility as shown in Figure 2.13(d). To simplify the use of γ_b, the data are fitted by a linear trend line that has an applicable range of μ_p in between 2.5 and 3.2. For T in between 0.5 and 0.6 second, 0.8 and 0.9 second, as well as 1.1 and 1.2 seconds, the same rules of linear interpolation and μ_p bound from γ_a should apply to γ_b.

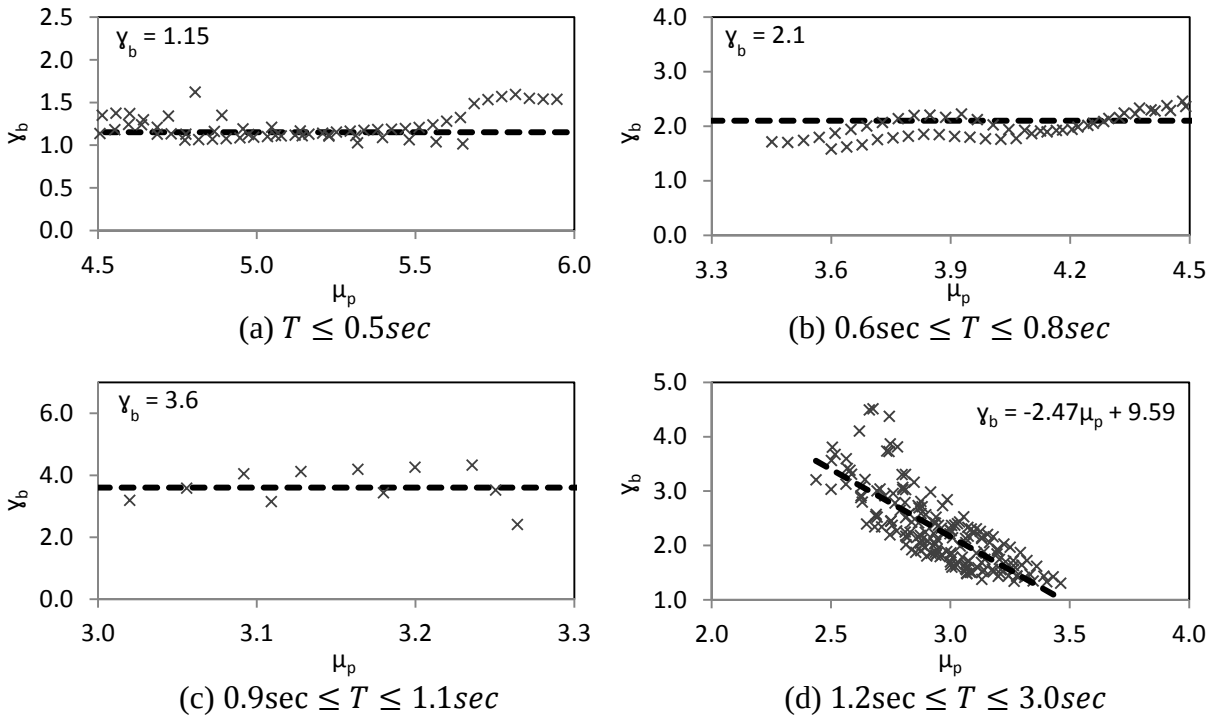

(a) $T \leq 0.5sec$ (b) $0.6\text{sec} \leq T \leq 0.8sec$

(c) $0.9\text{sec} \leq T \leq 1.1sec$ (d) $1.2\text{sec} \leq T \leq 3.0sec$

Figure 2.13 Incremental energy modification factor for DBE to MCE

2.4 Numerical validation

Figure 2.14 shows the prototype building used to validate EEDP. It is a simple one-storey one-bay fused truss moment frame (FTMF) which will be further elaborated in Chapter 3. The gravity system consists of long span truss and columns. The SFRS attributes to the primary system of axial braces and secondary system of moment connections. As the frame is displaced laterally, the primary SFRS dissipates earthquake energy thru axial yielding after Δ_y, and the secondary SFRS is activated after Δ_p.

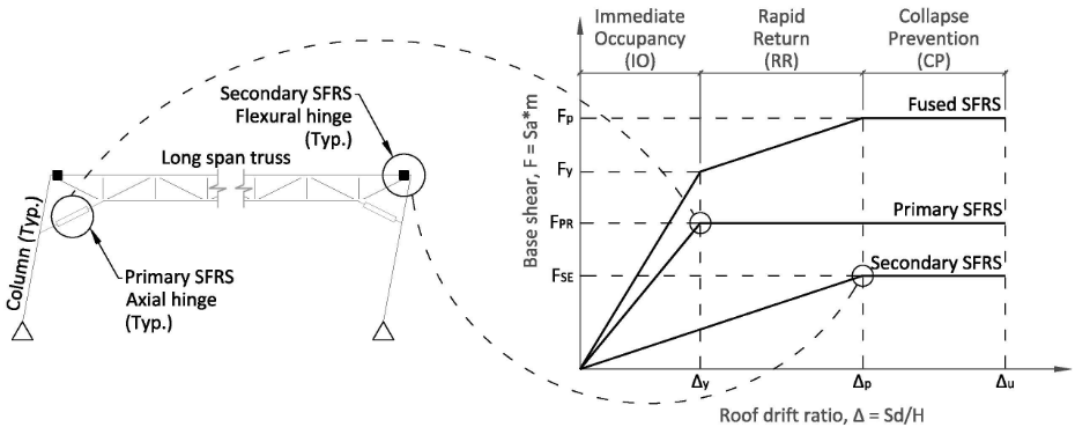

Figure 2.14 Prototype FTMF

To verify that γ_a and γ_b as presented in Figure 2.12 and Figure 2.13, respectively, are not site and hazard dependent, three sets of target spectra as shown in Figure 2.15 are used for validation. Figure 2.15(a) shows the hazard demand based on a site specific study in Berkeley, California. It represents a site with a high seismicity. Figure 2.15(b) and Figure 2.15(c) are the hazard demands based on Los Angeles in California and Seattle in Washington, respectively. These represent sites with a lower seismicity. Although the MCE shaking intensities in Figure 2.15(b) and Figure 2.15(c) are similar, these two sites are purposely selected because the SLE and DBE intensities are significantly different. This difference results in very different incremental energies at each site when the shaking increases from the SLE to DBE and DBE to MCE intensity. Varying incremental energy is an important parameter to validate the robustness of the energy modification factors presented in Figure 2.12 and Figure 2.13.

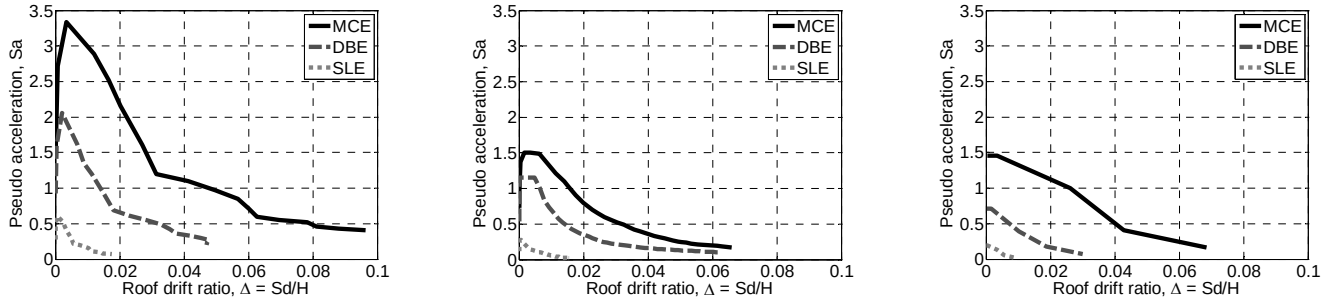

(a) UCB [2003] (b) Yang *et al.* [2012] (c) FEMA-355C [2000]

Figure 2.15 Target spectra

For each site, FTMFs with structural periods in between 0.4 and 2.6 seconds are studied. The maximum and minimum μ_p specified in Figure 2.12 and Figure 2.13 are used to obtain energy modification factors and EEDP design parameters. For each FTMF, the force-deformation design backbones of the primary and secondary SFRSs calculated by EEDP are assigned to the axial and flexural hinges, respectively, as shown in Figure 2.14. The non-yielding elements are assumed to be elastic. Each FTMF is subjected to the Table 2.2 ground motions amplitude scaled to the Figure 2.15 target spectra at the structural period. The results of the nonlinear dynamic analyses are shown in Figure 2.16, Figure 2.17, and Figure 2.18 for Berkeley, Los Angeles, and Seattle, respectively. The vertical axis of the figures shows the median maximum roof drift ratio of the frame. The horizontal axis indicates the target roof drift ratio. When the data points line up with the dashed lines in the figures, it implies that the median ratio matches the target ratio, i.e. predictable system behaviour. This is true under the SLE shaking intensity at all the sites. Although some data dispersion is observed as the earthquake shaking intensity increases, it is practical to conclude that an EEDP designed system exhibit predictable responses.

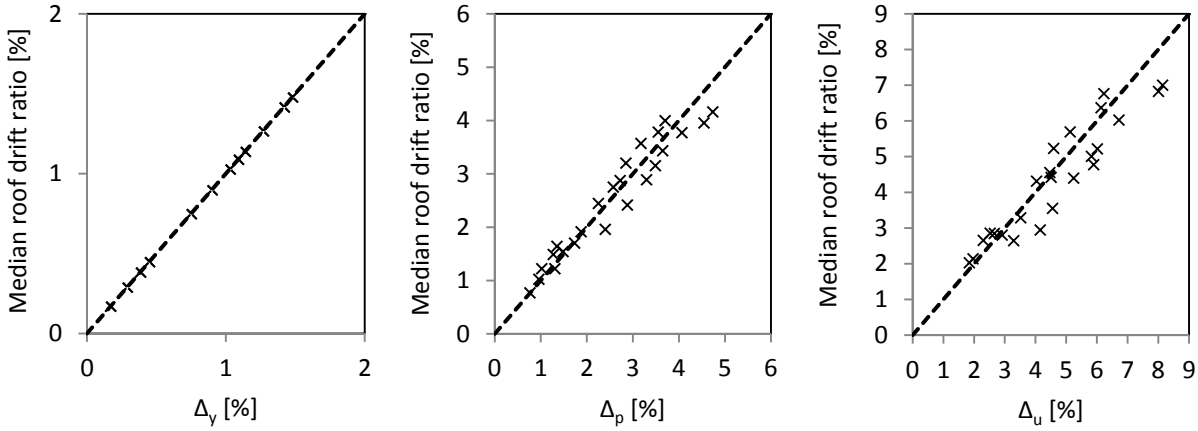

(a) SLE shaking intensity (b) DBE shaking intensity (c) MCE shaking intensity

Figure 2.16 Validation of EEDP with target spectra from UCB [2003]

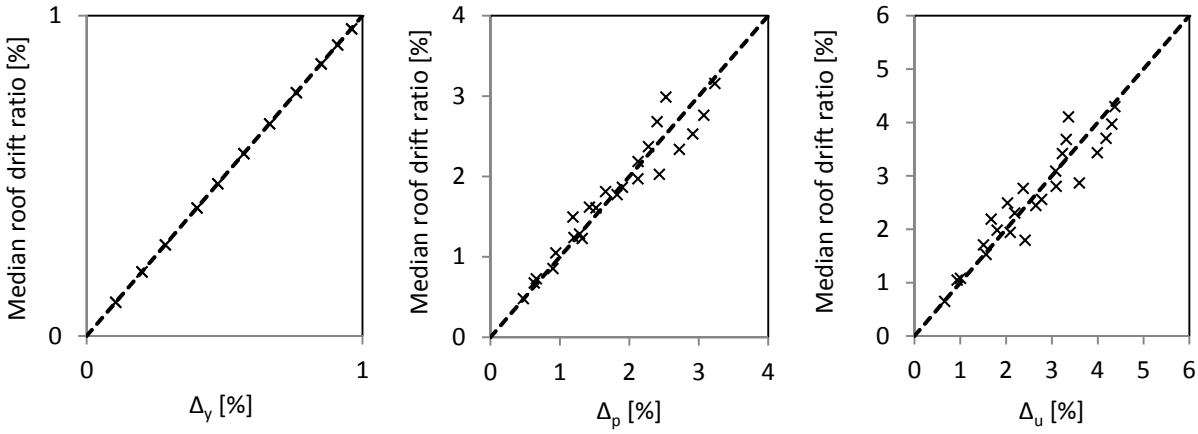

(a) SLE shaking intensity (b) DBE shaking intensity (c) MCE shaking intensity

Figure 2.17 Validation of EEDP with target spectra from Yang *et al.* [2012]

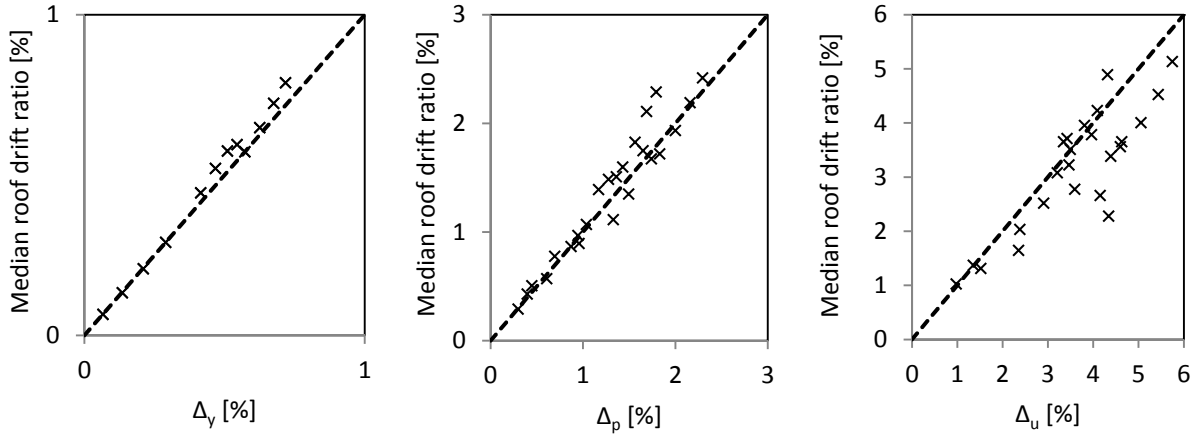

(a) SLE shaking intensity (b) DBE shaking intensity (c) MCE shaking intensity

Figure 2.18 Validation of EEDP with target spectra from FEMA-355C [2000]

2.5 Summary

With an increasing trend to build resilient communities towards future earthquakes, innovative resilient fused structures are being developed. These structures use structural fuses to dissipate earthquake energy. These fuses are decoupled from the gravity system and hence can be repaired or replaced efficiently to expedite recovery effort. The implementation of innovative earthquake resilient fused structures will not be possible unless there is a simple and practical design procedure. In this chapter, a novel energy design procedure called EEDP is presented to design fused SFRSs. This procedure directly takes structural strength and ductility into consideration. As compared to the other existing alternative

procedures, it does not require an estimation of member sizes nor design iterations. It allows designers to select multiple performance objectives at different earthquake shaking intensities. While the procedure is based on simple energy equivalence between inelastic and elastic systems, it recognizes the difference in energy dissipation between a system which is subjected to a monotonic pushover and that subjected to a cyclic dynamic load. This difference is addressed via energy modification factors developed using the responses of nonlinear SDOF systems through time history analysis. EEDP can be implemented through the following simple steps: 1) select performance objectives under different earthquake shaking intensities; 2) select yielding roof drift ratio; 3) select plastic roof drift ratio; 4) calculate ultimate roof drift ratio; 5) calculate strength requirements for the primary and secondary SFRSs; and 6) select yielding mechanisms to plastic design yielding members and capacity design non-yielding members. The concept of EEDP is validated using nonlinear dynamic analysis of a prototype fused SFRS. The result shows that the proposed EEDP can achieve the multiple performance objectives as selected by designers at different earthquake shaking intensities.

Chapter 3
Earthquake Resilient Fused Structure

The recent earthquakes in Japan and New Zealand have shown that even developed countries with modern building codes are not resilient. Severe damages are evident in structures. These damages are challenging to repair and cause prolonged downtime. In the case of New Zealand, it is possible that up to 50% of the buildings at the central business district of Christchurch will be demolished due to damages [Eguchi *et al.* 2012]. It is obvious that a large portion of the population will have to be displaced, and some might not return. The emigration further delays the recovery phase of earthquake resilience. Ultimately, it leads to de-urbanization and causes economic threats and social losses. The issue lies in the fundamental approach in structural design where earthquake energy is absorbed through inelastic deformation, i.e. through permanent damages, of structural components. Often times, these components form a part of the gravity system. They have not yet been designed to be easily inspected, repaired, or replaced. In another word, the notion of post-earthquake recovery has not yet been included in typical structural systems.

To improve post-disaster performances, earthquake resilient fused structural systems have been developed in the past [Yang *et al.* 2015; Lopes *et al.* 2012; Erochko *et al.* 2013; Vargas and Bruneau 2009b; El-Bahey and Bruneau 2010]. These systems are earthquake resilient because they are designed to be functional immediately or shortly after a strong earthquake shaking with no or minimum repair. It is achieved through the use of structural fuses. Fuses are designed to dissipate earthquake energy and to protect the main structural and non-structural components from damages. A well designed fused structural system shall have its structural fuses decoupled from the gravity system, which means that the fuses can be

inspected, repaired, or replaced efficiently after a strong earthquake shaking. This minimizes the repair costs and downtime, and ultimately, enhances the resilience of the structure against future earthquakes. A well designed fused structural system shall also be able to achieve different performance objectives at different earthquake shaking intensities. This can be accomplished by varying the fuse capacity as well as system stiffness and strength without significantly impacting the structural layout.

In this chapter, an innovative earthquake resilient fused structural system or fused seismic force resisting system (SFRS) is proposed. It is named the fused truss moment frame (FTMF). Section 3.1 first explains the structural mechanism. A prototype building of the FTMF is then designed using the equivalent energy design procedure (EEDP) as presented in Chapter 2. In Section 3.2, a detailed numerical model of the prototype is created using Open System for Earthquake Engineering Simulation (OpenSees) [PEER 2013]. The nonlinear force-deformation responses of the key structural components are calibrated against the available experimental data. The model is then subjected to a large array of nonlinear time history analyses to assess its structural performances. In Section 3.3, the adjusted collapse margin ratio of the system is determined via incremental dynamic analysis to confirm its seismic safety against strong earthquake shakings. This chapter intends to demonstrate that an earthquake resilient fused structure can be efficiently and safely designed using EEDP.

3.1 Fused truss moment frame

A fused truss moment frame (FTMF) is proposed. Such a frame utilizes conventional long-span trusses to resist gravity loads and at the same time, incorporates structural fuses to be its primary SFRS. In addition, a secondary SFRS is in place to mitigate structural collapse after fuse yielding. Section 3.1.1 and Section 3.1.2 explain the mechanism and design of a FTMF, respectively.

3.1.1 Mechanism of FTMF

Steel trusses are structurally efficient to span long distance and are commonly found in convention centres, lecture halls, auditoriums, airports, and other open space applications. They typically form a significant part of the gravity system within a structure. Their use for

earthquake loads has been limited due to the lack of lateral stiffness and ductility of the structural members. In this chapter, a fused truss moment frame (FTMF) as shown in Figure 3.1(a) is proposed for seismic applications. This configuration has been originally proposed by Wongpakdee *et al.* [2014] and Yang *et al.* [2014]. A FTMF preserves the architectural flexibility of a moment resisting frame, while introducing designated energy dissipation structural fuses to enhance structural resilience after a strong earthquake shaking.

Similar to conventional long-span trusses, a FTMF uses continuous top and bottom chords with vertical and diagonal web members to create open space. Out-of-plane braces at each truss panel point are provided for overall stability against lateral torsional buckling. To enhance in-plane truss lateral stiffness and ductility, a FTMF incorporates proprietarily designed buckling restrained braces (BRBs) by StarSeismic at the end panels of a truss as its structural fuses. These BRBs form the primary SFRS and are designed to dissipate earthquake energy. Such short-core BRBs have been found to be able to reduce storey and residual storey drifts in braced frames [Hoveidae *et al.* 2015]. The BRBs are pin connected via a gusset plate at one end to the truss bottom chord (Figure 3.1(b)) and the other end to the steel column (Figure 3.1(c)). Their locations are strategically selected to limit architectural interference. In addition, the BRBs are decoupled from the gravity system so that they can be inspected, repaired, and replaced efficiently after a severe ground shaking. Hence, a FTMF can be highly efficient and resilient against earthquakes.

To provide additional strength and stiffness after BRB yielding, the truss top chord is moment connected to the steel column in lieu of a typical shear tab connection. This connection is designed to form plastic hinge during strong earthquake shakings. Hence, it is considered as the secondary SFRS. Instead of welding, the bolted moment connection (MC) as proposed by Pryor and Murray [2012] shown in Figure 3.1(d) is utilized. This connection consists of a steel angle with two yielding plates. The steel angle provides the needed shear capacity, while the yielding plates above and below the top chord provide the needed moment capacity. Earthquake energy is dissipated by tension and compression yielding of these coupled plates via joint rotation. They are restrained from buckling and have a designated yielding zone as shown in Figure 3.1(e). When the plates are damaged and need

to be replaced, the steel angle is designed to support gravity loads. Therefore, shoring is not required, and occupancy can quickly return after a significant earthquake. In addition, the horizontally slotted holes at the top and bottom of the steel angle as well as the chamfer corner at the end of the top chord allow rotation. These details ensure that the angle transfers shear only and are not damaged in the case of a severe ground shaking.

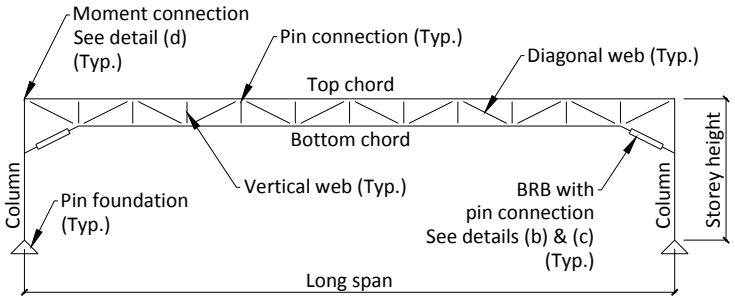

(a) Frame configuration

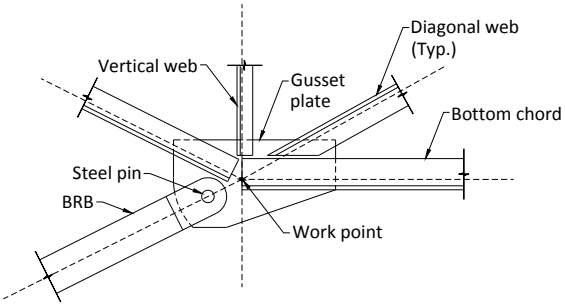

(b) BRB to bottom chord connection

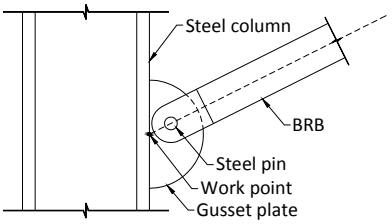

(c) BRB to column connection

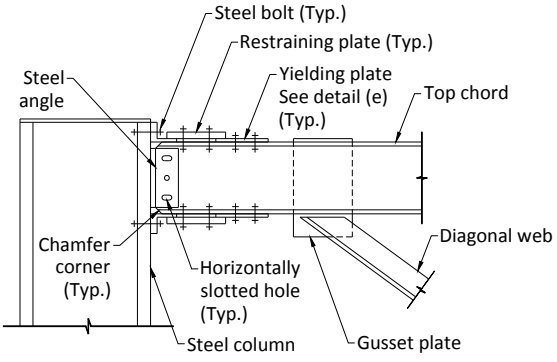

(d) Top chord to column connection

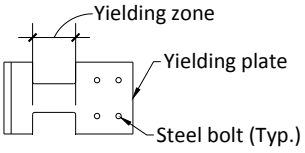

(e) Yielding plate

Figure 3.1 FTMF

In a FTMF, damages are controlled within the yielding elements such as the BRBs and MCs. The top and bottom chords, vertical and diagonal web members, as well as columns are

capacity designed not to yield under the worst loading condition. Hence, they will not need to be inspected nor repaired after a strong earthquake shaking. In addition, the base of the columns is pinned to the foundation. This detail eases column baseplate design and reduces construction costs. It also prevents plastic hinge from forming at the base of the column, and eliminates column repair costs after a strong earthquake shaking.

With the combination of the primary and secondary SFRSs, a FTMF has a tri-linear force-deformation relationship as shown in Figure 3.2. As the FTMF is displaced laterally, the force-deformation response increases linearly until the roof drift ratio reaches Δ_y and base shear reaches F_y. After that, the primary SFRS is designed to yield (BRB yielding through axial deformation), while the secondary SFRS is designed to remain elastic. The FTMF is expected to continue with the post-yielding stiffness primarily contributed by the secondary SFRS stiffness until the roof drift reaches Δ_p and base shear reaches F_p. After that, the secondary SFRS is designed to yield (MC yielding through flexural deformation), while the FTMF maintains its strength.

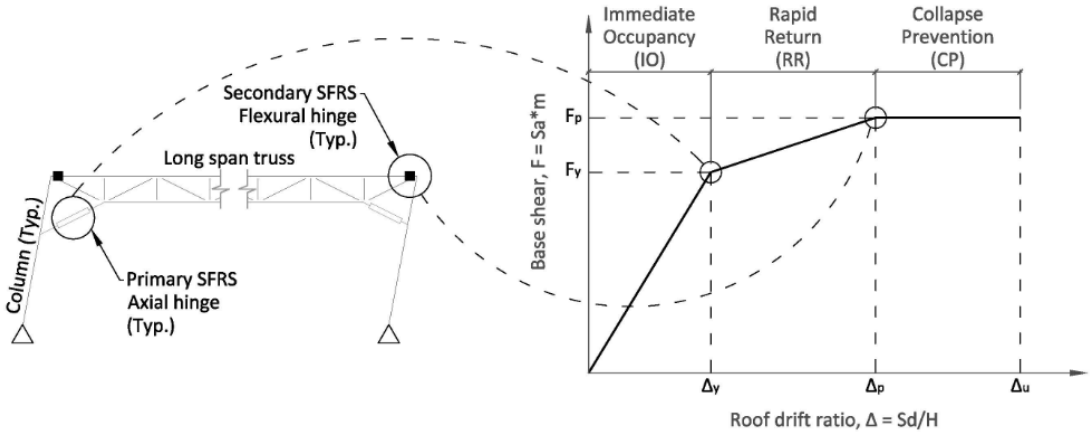

Figure 3.2 Force-deformation relationship and performance objectives of FTMF

The selection of Δ_y and Δ_p is such that the system can achieve three performance objectives at three earthquake shaking intensities. During a service level earthquake (SLE), the system performance is targeted to be immediate occupancy (IO), where the FTMF is expected to be damage-free after an earthquake. Hence, no repair is required. During a design based earthquake (DBE), the system performance is targeted to be rapid return (RR), where only

the BRBs are designed to yield to dissipate earthquake energy. The remaining FTMF shall be protected to exhibit no or minimum damages. To ensure the FTMF is resilient, the BRBs are designed to be easily inspected and efficiently repairable or replaceable immediately or shortly after an earthquake. Hence, the FTMF can achieve the RR performance objective. When earthquake intensity reaches the maximum considered earthquake (MCE), the system performance is targeted to be collapse prevention (CP), where both the BRBs and MCs are designed to dissipate earthquake energy to prevent the FTMF from collapse.

3.1.2 Design of FTMF

A FTMF can be practically and efficiently designed by structural engineers using EEDP as presented in Chapter 2. To illustrate this, a three-storey office prototype building located in Los Angeles, California, is designed using EEDP in this chapter. The building has the same geometry and gravity loading requirement as the three-storey template building presented in the SAC (SEAOC, ATC, and CUREe) joint venture [FEMA-355C 2000]. Figure 3.3 shows the structural layout. The joists span in the direction as shown in the figure and are supported by the girders. The columns are placed at the grid intersections. The FTMFs are located at the exterior bays of the building. The structural framing is strategically laid out to minimize gravity loading on the FTMF. As a result, the effects of gravity loading on the trusses can be practically neglected. This simplifies the truss design and reserves truss capacity for earthquake loading. It should be noted that the gravity loads on the columns are included based on tributary area.

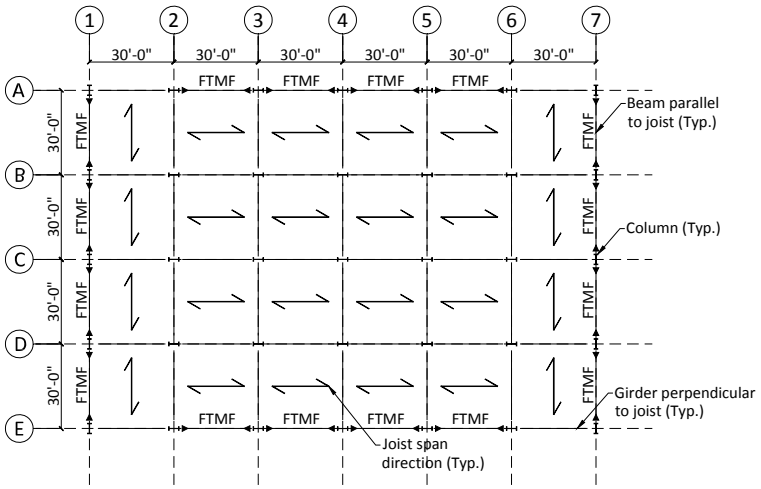

Figure 3.3 Plan view of prototype building

The following steps summarize the design of the FTMF using EEDP. The abbreviations and symbols used in EEDP are explained in Chapter 2. Please refer to Chapter 2 for the detailed derivations of the equations and energy modification factors.

Step 1: Select performance objectives under different earthquake shaking intensities

The first step of EEDP is to select the performance objectives for the building under different earthquake shaking intensities. For the prototype building, the performance objectives are selected as follows: 1) IO under the SLE shaking intensity, which represents the seismic hazard of 87% probability of exceedance in 50 years; 2) RR under the DBE shaking intensity, which represents the seismic hazard of 10% probability of exceedance in 50 years; 3) CP under the MCE shaking intensity, which represents the seismic hazard of 2% probability of exceedance in 50 years. These three seismic hazard levels are adopted from Yang *et al.* [2012] and shown in Figure 3.4(a). If needed, designers can select other hazard levels.

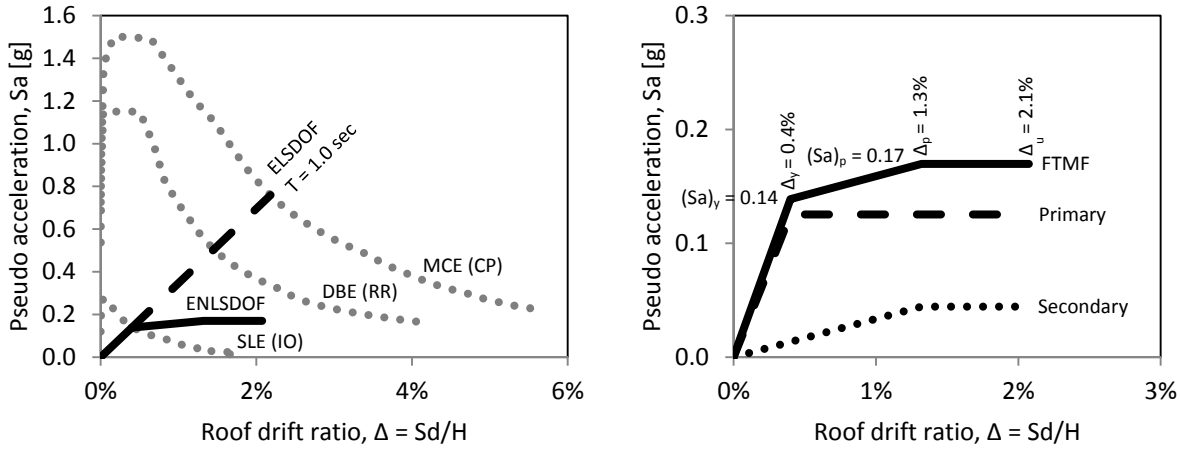

(a) Performance objectives and earthquake shaking intensities

(b) Design parameters

Figure 3.4 EEDP design parameters

Step 2: Select Δ_y to calculate F_y and T

Once the earthquake shaking intensities are selected, designers shall select Δ_y to represent the maximum roof displacement of the system where the building shall remain elastic. In this

example, Δ_y is selected as 0.4%. Because the system is designed to remain elastic under SLE, $(S_a)_y$ can be identified on Figure 3.4(a) as the intersection of the SLE hazard curve and Δ_y. In this case, $(S_a)_y$ is found to be approximately 0.14g which is better shown in Figure 3.4(b). F_y can be calculated as $0.14W$ where W is the seismic weight of the building. Using the equation as presented in Chapter 2, the structural period, T, can be calculated as follow.

$$T = 2\pi\sqrt{\frac{(\Delta_y H)/C_o}{F_y/m}} = 1.0\ second \qquad \text{from Equation 2.4}$$

where Δ_y= 0.4%; $H = 468in$; $C_o = 1.3$; $F_y/m = (S_a)_y = 0.14 \times 386.4in/sec^2$.

With T determined, the spectra demands for the ELSDOF system can be read from Figure 3.4(a). In this case, the values of $(S_a)_{SLE}$, $(S_a)_{DBE}$, $(S_a)_{MCE}$, $(S_d)_{SLE}$, $(S_d)_{DBE}$, and $(S_d)_{MCE}$ for T of 1.0 second are 0.14g, 0.51g, 0.76g, 0.004H, $0.015H$, and $0.022H$, respectively.

Then, the incremental energies, ΔE_{E1} and ΔE_{E2}, can be calculated using Equation 2.5 and Equation 2.9 as presented in Chapter 2, respectively. In this case, the values of ΔE_{E1} and ΔE_{E2} are $0.0034WH$ and $0.0046WH$, respectively.

Step 3: Select Δ_p to calculate F_p

The next step of EEDP is to select Δ_p. It defines the largest roof drift ratio within which the primary SFRS, which is the BRBs, should work without yielding the secondary SFRS, which is the MCs. In this study, Δ_p is selected to be 1.3%. It means that the system is selected to have a plastic ductility, μ_p, of 3.3. With the energy modification factors as provided in Figure 2.12 of Chapter 2, γ_a for this building is identified as 2.4. Hence, F_p is calculated using the following equation.

$$F_p = \frac{2\Delta E_{E1}}{\gamma_a H(\Delta_p - \Delta_y)} - F_y = 0.17W \qquad \text{from Equation 2.8}$$

where $\Delta E_{E1} = 0.0034WH$; $\gamma_a = 2.4$; Δ_y= 0.4%; Δ_p= 1.3%; $F_y = 0.14W$.

Step 4: Calculate Δ_u

With μ_p calculated in Step 3 and the energy modification factors as provided in Figure 2.13 of Chapter 2, γ_b for this building is identified as 3.6. Δ_u is then calculated using the following equation and shown in Figure 3.4(b).

$$\Delta_u = \frac{\Delta E_{E2}}{\gamma_b F_p H} + \Delta_p = 2.1\% \qquad \text{from Equation 2.12}$$

where $\Delta E_{E2} = 0.0046WH$; $\gamma_b = 3.6$; $F_p = 0.17W$; $\Delta_p = 1.3\%$.

Step 5: Calculate F_{PR} *and* F_{SE}

Once the base shear for the FTMF has been determined, the base shear for the primary and secondary systems can be calculated using the following equations. The distribution of the base shear between the primary and secondary SFRSs is shown in Figure 3.4(b).

$$F_{PR} = F_y \frac{(\mu_p - \lambda)}{(\mu_p - 1)} = 0.13W \qquad \text{from Equation 2.17}$$

$$F_{SE} = F_y \mu_p \frac{(\lambda - 1)}{(\mu_p - 1)} = 0.044W \qquad \text{from Equation 2.18}$$

where $F_y = 0.14W$; $\mu_p = 3.3$; $\lambda = 0.17W/0.14W$.

Step 6: Select yielding mechanism and plastic design yielding members

Once F_{PR} and F_{SE} have been identified, these base shears are distributed vertically over the height of the primary and secondary systems using the distribution as presented in Equation 2.19 of Chapter 2 which is adopted from Chao *et al.* [2007]. The vertically distributed base shears are then applied to a yielding mechanism. It should be note that the selection of a yielding mechanism is system dependent. Structural engineers shall choose a suitable mechanism for each fused SFRS. In this study, the desired yielding mechanism for the FTMF is shown in Figure 3.5(a). Based on this mechanism, the input energy, W_{ext}, to the primary or secondary system is calculated using Equation 3.1. Based on the kinematic method, W_{ext} needs to be dissipated by yielding the BRBs or MCs. Equation 3.2 shows the internal work, W_{int}, done by the BRBs. The expression for the BRB deformation is based on the linear

transformation as presented by Yang *et al.* [2016], and the parameters are defined in Figure 3.5(b).

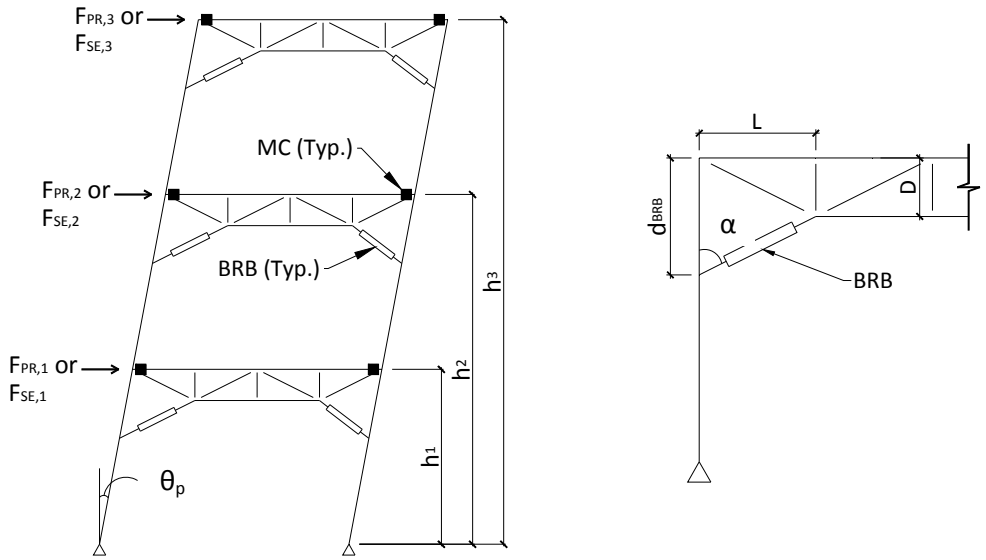

(a) Yielding mechanism (b) BRB geometry

Figure 3.5 Plastic design of yielding members

$$W_{ext} = \sum_{i=1}^{n} F_{PR,i} h_i \theta_p \ \ or \ \sum_{i=1}^{n} F_{SE,i} h_i \theta_p \qquad \text{Equation 3.1}$$

where $F_{PR,i}$ is the design storey force at level i of the primary SFRS; $F_{SE,i}$ is the design storey force at level i of the secondary SFRS; h_i is the height of level i measured from the ground level; θ_p is the plastic rotation of the FTMF.

$$W_{int} = 2 \sum_{i=1}^{n} \beta_i F_{BRB,roof} \, (D \sin \alpha + L \cos \alpha) \theta_p \qquad \text{Equation 3.2}$$

where $F_{BRB,roof}$ is the design force of the roof BRB.

To promote uniform yielding of the BRBs among all the stories, the strength capacity of the BRB at each storey is proportional to that at the roof by β_i proposed by Goel and Chao [2008].

Equating W_{ext} to W_{int}, the design force of the roof BRB can be calculated by Equation 3.3. Finally, the design force of the BRB at each storey, $F_{BRB,i}$, can be calculated by Equation 3.4.

$$F_{BRB,roof} = \frac{\sum_{i=1}^{n} F_{PR,i} h_i}{2(D \sin\alpha + L \cos\alpha) \sum_{i=1}^{n} \beta_i}$$ Equation 3.3

$$F_{BRB,i} = \beta_i F_{BRB,roof}$$ Equation 3.4

Similar to the BRBs, the design moment of the MCs is determined using the kinematic method. Equation 3.5 shows the internal work, W_{int}, done by the MCs. β_i is again utilized to proportion the strength capacity of the MC at each storey and to achieve distributed yielding.

$$W_{int} = 2 \sum_{i=1}^{n} \beta_i M_{MC,roof} \theta_p$$ Equation 3.5

where $M_{MC,roof}$ is the design moment of the roof MC.

Equating W_{ext} to W_{int}, the design moment of the roof MC can be calculated by Equation 3.6. Finally, the design moment of the MC at each storey, $M_{MC,i}$, can be calculated by Equation 3.7.

$$M_{MC,roof} = \frac{\sum_{i=1}^{n} F_{SE,i} h_i}{2 \sum_{i=1}^{n} \beta_i}$$ Equation 3.6

$$M_{MC,i} = \beta_i M_{MC,roof}$$ Equation 3.7

The MC capacity at each storey is provided by the coupled yielding plates shown in Figure 3.1(d). The area of each plate, A_i, can be determined by Equation 3.8. The depth of the truss top chord, d_i, is assumed to be 12 inches, and the specified yielding strength of the steel plate, F_y, is selected to be 50ksi. It should be noted that the ratio of the expected to specified yielding strength is defined as R_y.

$$A_i = \frac{M_{MC,i}}{(R_y F_y) d_i}$$ Equation 3.8

where $R_y = 1.1$ which is adopted from ESR-2802 [2013].

Step 7: Capacity design non-yielding members

After the yielding members are designed, the truss and columns of the FTMF need to be capacity designed to remain elastic under the probable forces created by the yielding members. Figure 3.6 shows the free body diagram for the design of the truss. The directions of the probable forces and moments are based on the lateral direction indicated in the figure. H_{TRUSS} and V_{TRUSS} at the support can be calculated using equilibrium. Gravity is negligible due to the chosen joist framing direction shown in Figure 3.3. This choice is intentional to simplify the truss design and reserve its capacity for seismic demands.

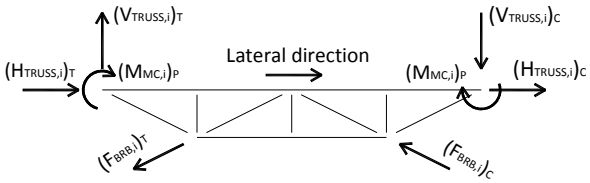

Legend:
$(M_{MC,i})_P$ = probable MC moment at level i
$(F_{BRB,i})_T$ = probable BRB tension force at level i
$(F_{BRB,i})_C$ = probable BRB compression force at level i
$(H_{TRUSS,i})_T$ = horizontal truss reaction at level i at the truss end with BRB under tension
$(V_{TRUSS,i})_T$ = vertical truss reaction at level i at the truss end with BRB under tension
$(H_{TRUSS,i})_C$ = horizontal truss reaction at level i at the truss end with BRB under compression
$(V_{TRUSS,i})_C$ = vertical truss reaction at level i at the truss end with BRB under compression

Figure 3.6 Free body diagram of truss

Figure 3.7 shows the free body diagram for the design of the columns. The gravity loading is considered based on the column tributary area. With the truss reactions as well as probable forces and moments from the yielding elements, the columns are not in equilibrium. To ensure equilibrium of the entire column, the column-tree design approach as proposed by Goel and Chao [2008] shall be followed. In their approach, a suite of unbalanced lateral forces defined by $a_i F$ over the building height shall be applied. a_i can be determined by Equation 3.9. All the forces in Figure 3.7 shall result in zero moment at the column base. By taking moments about the column base, F can be calculated by Equation 3.10, Equation 3.11, and Equation 3.12 for the exterior columns with the BRBs under tension, exterior columns with the BRBs under compression, and interior columns, respectively. It should be noted that the column moment amplification factors in accordance with ANSI/AISC 360-10 [2010] are utilized to consider P-delta effects.

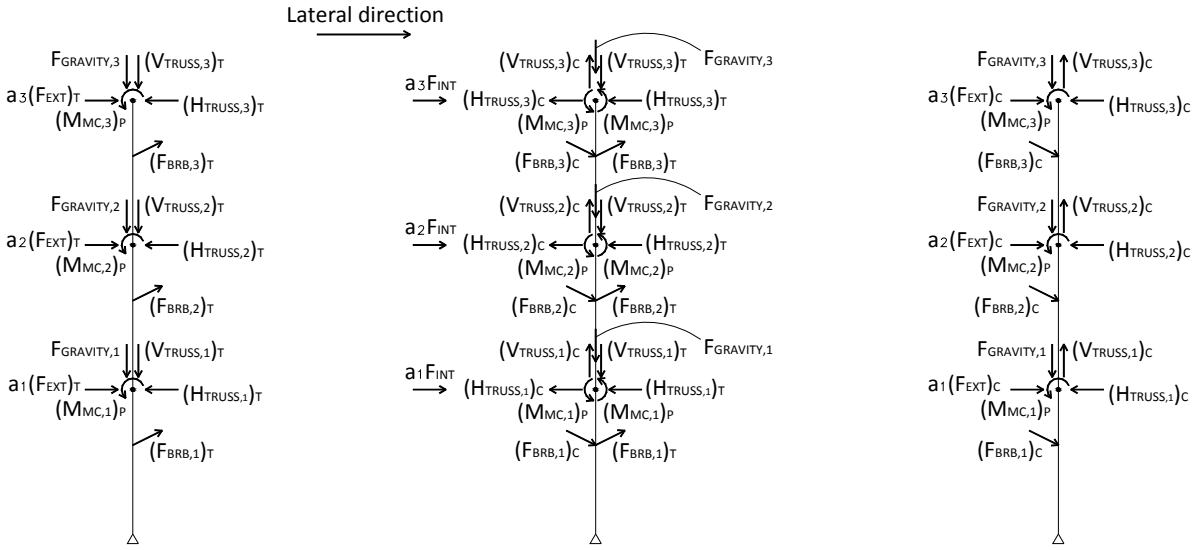

Legend:
$(M_{MC,i})_P$ = probable MC moment at level i
$(F_{BRB,i})_T$ = probable BRB tension force at level i
$(F_{BRB,i})_C$ = probable BRB compression force at level i
$(H_{TRUSS,i})_T$ = horizontal truss reaction at level i at the truss end with BRB under tension
$(V_{TRUSS,i})_T$ = vertical truss reaction at level i at the truss end with BRB under tension
$(H_{TRUSS,i})_C$ = horizontal truss reaction at level i at the truss end with BRB under compression
$(V_{TRUSS,i})_C$ = vertical truss reaction at level i at the truss end with BRB under compression
$F_{GRAVITY,i}$ = gravity load at level i
$(F_{EXT})_T$ = equilibrium lateral force at exterior column with BRB under tension
$(F_{EXT})_C$ = equilibrium lateral force at exterior column with BRB under compression
F_{INT} = equilibrium lateral force at interior column

Figure 3.7 Free body diagram of column

$$a_i = \frac{(\beta_i - \beta_{i+1})}{\sum_{i=1}^{n}(\beta_i - \beta_{i+1})} \quad \text{Equation 3.9}$$

$$(F_{EXT})_T = \frac{\sum_{i=1}^{n}(M_{MC,i})_P + \sum_{i=1}^{n}(H_{TRUSS,i})_T h_i - \sum_{i=1}^{n} \sin\alpha (F_{BRB,i})_T (h_i - d_{BRB})}{\sum_{i=1}^{n} a_i h_i} \quad \text{Equation 3.10}$$

$$(F_{EXT})_C = \frac{\sum_{i=1}^{n}(M_{MC,i})_P + \sum_{i=1}^{n}(H_{TRUSS,i})_C h_i - \sum_{i=1}^{n} \sin\alpha (F_{BRB,i})_C (h_i - d_{BRB})}{\sum_{i=1}^{n} a_i h_i} \quad \text{Equation 3.11}$$

$$F_{INT} = \frac{1}{\sum_{i=1}^{n} a_i h_i} \begin{Bmatrix} 2\sum_{i=1}^{n}(M_{MC,i})_P + \sum_{i=1}^{n}\left[(H_{TRUSS,i})_C + (H_{TRUSS,i})_T\right] h_i - \\ \sum_{i=1}^{n} \sin\alpha \left[(F_{BRB,i})_C + (F_{BRB,i})_T\right](h_i - d_{BRB}) \end{Bmatrix} \quad \text{Equation 3.12}$$

Figure 3.8 presents the final design of the FTMF. The truss has a depth of 2’-6” and typical panel width of 5’-0”. It should be noted that the truss diagonal web member at the last panel is moved 2 feet off the grid along the top chord to accommodate the moment connection depicted in Figure 3.1(d). A wide flange steel beam is selected as the top chord to provide adequate moment capacity and ease connection detailing. Double steel angles are used as the bottom chord to be structurally economical. The design of the truss top and bottom chords as well as columns includes the interaction of moment with compression or tension. Although P-delta effects are considered in the column design, they are not significant to affect the sizes. An Eigen analysis is conducted to identify the modal period and mode shape of the FTMF. The result shows that the modal period is 0.9 second, while the structural period estimated using EEDP is 1.0 second. In other words, the proposed EEDP is able to select the appropriate member sizes without iterations.

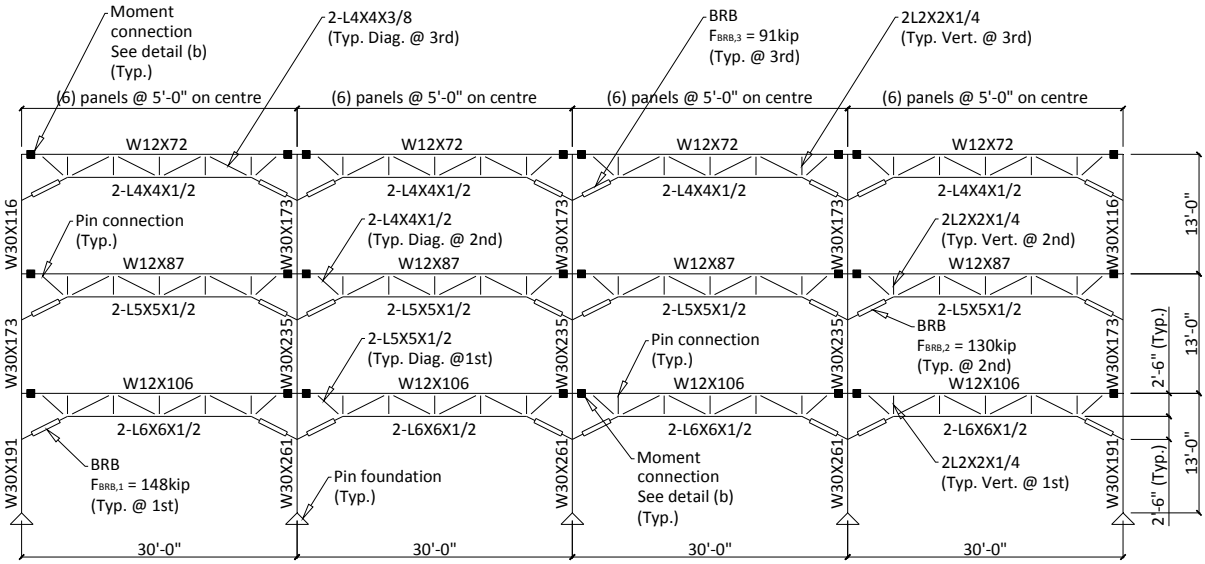

(a) Elevation view of FTMF

Figure 3.8 FTMF designed by EEDP

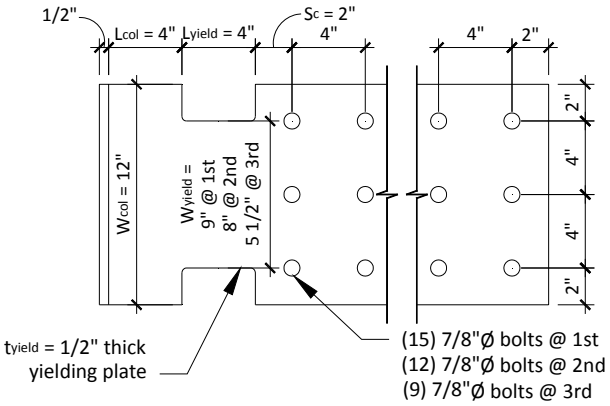

(b) Detail of yielding plate

Figure 3.8 FTMF designed by EEDP

3.2 Numerical model

The prototype building with FTMFs has been designed using EEDP. Each frame uses BRBs and MCs as its primary and secondary SFRSs, respectively, to dissipate earthquake energy. The other structural elements are capacity designed to remain elastic. To confirm that the structural performances of an EEDP designed FTMF are as intended, a detailed numerical model is constructed in Section 3.2.1 to conduct nonlinear time history analysis. Section 3.2.2 provides the analysis results.

3.2.1 Nonlinear model construction

A nonlinear finite element model of the FTMF shown in Figure 3.8 is constructed using Open System for Earthquake Engineering Simulation (OpenSees) [PEER 2013]. The model is subjected to a range of earthquake shaking intensities to verify the performance of the FTMF designed using EEDP. The mass is assigned to the model using lumped mass at each truss panel node. 5% Rayleigh mass and stiffness damping is calculated based on the first and third modes of the frame. The columns as well as truss top and bottom chords are modelled using beam-column elements because they experience moment with tension or compression. The truss web members are modelled as truss elements to capture tension or compression only. The columns and truss are non-yielding members and have been capacity designed to remain elastic. Therefore, they are modelled as elastic elements to save

computational efforts. To verify that these elements do not yield, the maximum forces in these elements are checked during post processing.

The BRBs are modelled using nonlinear truss elements with a yielding capacity at each storey as shown in Figure 3.8(a). The Giuffré-Menegotto-Pinto material developed by Filippou *et al.* [1983] is adopted to simulate the force-deformation response of the BRB material. The BRB modulus of elasticity, E_{BRB}, can be calculated by Equation 3.13. This material model has been calibrated against the experimental data obtained by StarSeismic [2011]. Figure 3.9(a) shows the calibration result. The vertical axis is the force in the BRB normalized by the yielding force of the BRB. The over-strength factors of 1.50 and 1.75 for tension and compression, respectively, have been used to obtain the probable forces of the BRBs. According to the figure, these factors are conservative approximations. Since the probable forces are used to capacity design the non-yielding members, it is appropriate to be conservative.

$$E_{BRB} = K_{BRB} \frac{L_{BRB}}{A_{BRB}} \qquad \text{Equation 3.13}$$

where K_{BRB} is the total elastic stiffness of the BRB which is the in-series sum of the core and connection stiffness [Black *et al.* 2004]; L_{BRB} is the length of the BRB; A_{BRB} is the area of the BRB.

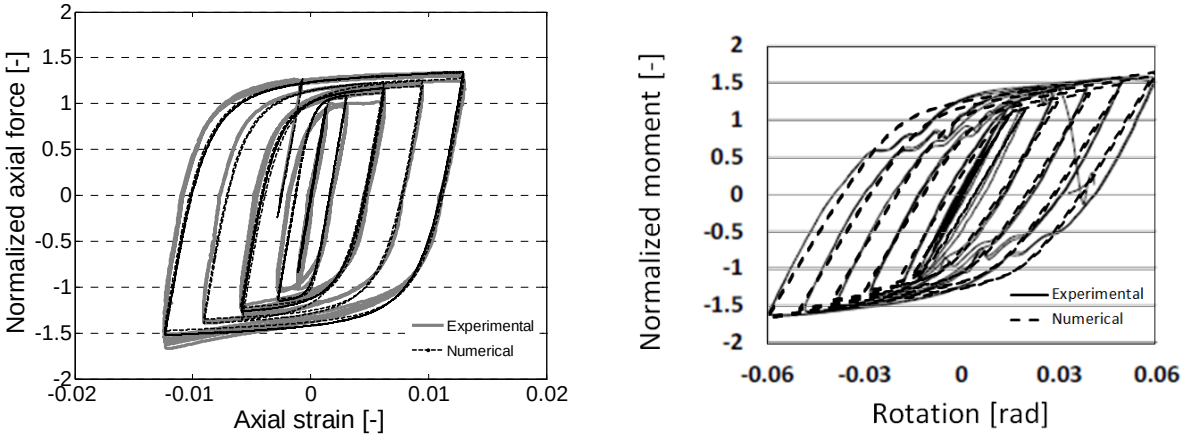

(a) BRB (b) MC

Figure 3.9 Material model calibrations

The MCs are modelled as hinges using zero-length elements to capture the flexural behaviour created by the coupled yielding steel plates shown in Figure 3.8(b). The Giuffré-Menegotto-Pinto [Filippou *et al.* 1983] is adopted to simulate the moment-rotation response of the flexural hinge. The hinge stiffness, E_{MC}, can be calculated by Equation 3.14.

$$E_{MC} = \frac{M_y}{\theta_y} \qquad \text{Equation 3.14}$$

where $M_y = P_y d = A\left(R_y F_y\right)d$; $\theta_y = \frac{P_y/K_{eff}}{d/2}$.

All the parameters in Equation 3.14 have been defined and determined previously in step 6 of EEDP. The only exception is the effective axial stiffness of the coupled plates, K_{eff}, which can be calculated by Equation 3.15 [ESR-2802 2013]. K_{eff} is a function of both the yielding and non-yielding portions of the plate. Most of the parameters used in the equation are defined in Figure 3.8(b). The hinge model has been calibrated against the experimental data obtained by Pryor and Murray [2012]. Figure 3.9(b) shows the calibration result. The vertical axis is the moment in the MC normalized by the yielding moment of the MC.

$$K_{eff} = \frac{K_1 K_2 K_3}{K_1 K_2 + K_2 K_3 + K_1 K_3} \qquad \text{Equation 3.15}$$

where $K_1 = 12 E_s W_{col}$; $K_2 = \frac{t_{yield} W_{col} E_s}{L_{col} + S_c + l_v}$; $K_3 = \frac{t_{yield} W_{yield} E_s}{L_{yield}}$; E_s is the modulus of elasticity of the plate; $l_v = 2$ for the design shown in Figure 3.8(b).

3.2.2 Nonlinear dynamic analysis

Nonlinear dynamic analysis is performed using the nonlinear finite element model presented in the previous section. A suite of ground motion records selected from the PEER strong motion database [2010] is used in this study. Table 3.1 shows the summary of the ground motions. The suite includes twenty-two pairs of far-field ground motions and contains a mixture of fault types. Only ground motions with a magnitude greater than 6.0 are included. In addition, only ground motions with an average shear wave velocity in the top 30 meters of soil in between 360m/s and 760m/s are selected. This is similar to very dense soil and soft rock as classified in ASCE/SEI 7-10 [2010].

Table 3.1 Ground motions (GMs) used for nonlinear dynamic analysis

GM	Name	Year	Magnitude	RSN#	Record
1	San Fernando	1971	6.61	57	SFERN_ORR021
					SFERN_ORR291
2	Imperial Valley	1979	6.53	164	IMPVALLH_H_CPE147
					IMPVALLH_H_CPE237
3	Irpinia, Italy	1980	6.90	289	ITALY_A_CTR000
					ITALY_A_CTR270
4	Corinth, Greece	1981	6.60	313	CORINTH_COR_L
					CORINTH_COR_T
5	Loma Prieta	1989	6.93	755	LOMAP_CYC195
					LOMAP_CYC285
6	Landers	1992	7.28	864	LANDERS_JOS000
					LANDERS_JOS090
7	Landers	1992	7.28	881	LANDERS_MVH045
					LANDERS_MVH135
8	Chi-Chi, Taiwan	1999	7.62	1184	CHICHI_CHY010_N
					CHICHI_CHY010_W
9	Chi-Chi, Taiwan	1999	7.62	1198	CHICHI_CHY029_E
					CHICHI_CHY029_N
10	Chi-Chi, Taiwan	1999	7.62	1484	CHICHI_TCU042_E
					CHICHI_TCU042_N
11	Chi-Chi, Taiwan	1999	7.62	1500	CHICHI_TCU061_E
					CHICHI_TCU061_N
12	Chi-Chi, Taiwan	1999	7.62	1533	CHICHI_TCU106_E
					CHICHI_TCU106_N
13	Chi-Chi, Taiwan	1999	7.62	1541	CHICHI_TCU116_E
					CHICHI_TCU116_N
14	Manjil, Iran	1990	7.37	1633	MANJIL_ABBAR_L
					MANJIL_ABBAR_T
15	Cape Mendocino	1992	7.01	3750	CAPEMEND_LFS270
					CAPEMEND_LFS360
16	Chuetsu-oki, Japan	2007	6.80	4841	CHUETSU_65004EW
					CHUETSU_65004NS
17	Chuetsu-oki, Japan	2007	6.80	4843	CHUETSU_65006EW
					CHUETSU_65006NS
18	Chuetsu-oki, Japan	2007	6.80	4850	CHUETSU_65013EW
					CHUETSU_65013NS
19	Iwate, Japan	2008	6.90	5664	IWATE_MYG005EW
					IWATE_MYG005NS
20	Iwate, Japan	2008	6.90	5783	IWATE_54026EW
					IWATE_54026NS
21	Iwate, Japan	2008	6.90	5806	IWATE_55461EW
					IWATE_55461NS

Table 3.1 Ground motions (GMs) used for nonlinear dynamic analysis

GM	Name	Year	Magnitude	RSN#	Record
22	Darfield, New Zealand	2010	7.00	6971	DARFIELD_SPFSN17E
					DARFIELD_SPFSN73W

The ground motions from Table 3.1 are amplitude scaled to match the three target spectra such that the median response spectrum of the motions (dashed line in Figure 3.10) is close to the target spectrum (solid line in Figure 3.10). To account for modal elongation and higher modes, the ground motions are scaled to match the target spectra in the period range between $0.2T$ and $1.5T$ where T is the fundamental period of the FTMF. To avoid over-scaling, the scale factor is limited to five.

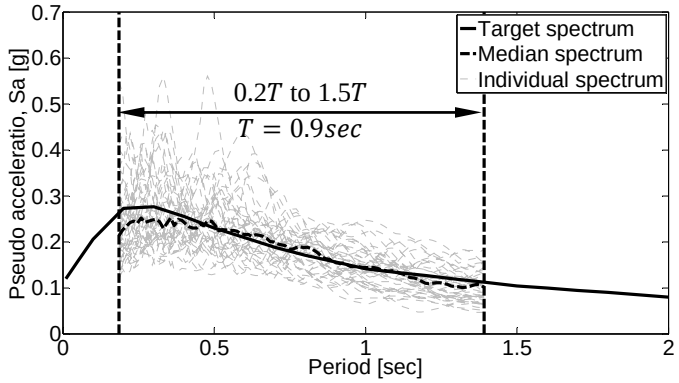

(a) SLE

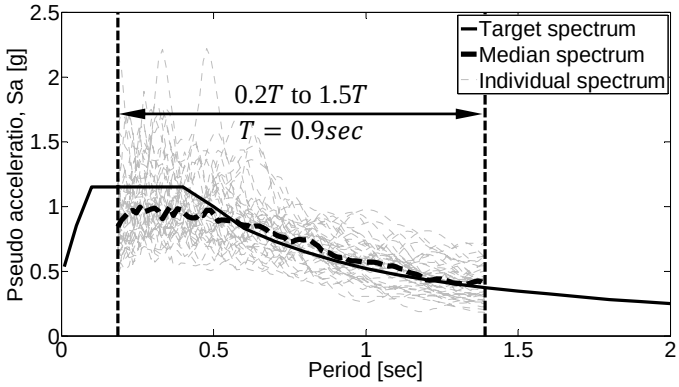

(b) DBE

Figure 3.10 Response spectra of scaled ground motions

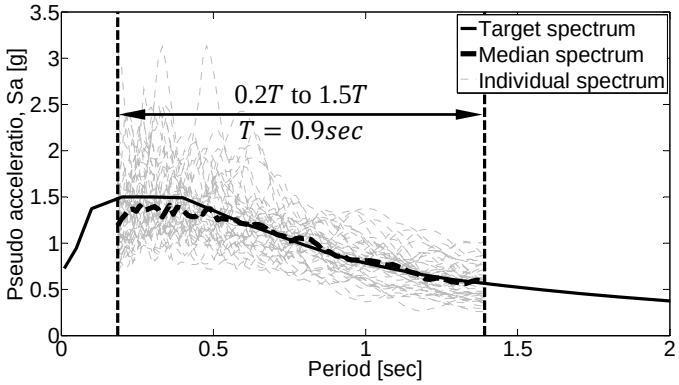

(c) MCE

Figure 3.10 Response spectra of scaled ground motions

Figure 3.11 shows the maximum roof drift ratios (RDRs) of the FTMF model when it is subjected to all the scaled ground motions shown in Table 3.1. For each earthquake shaking intensity, the solid line indicates the median of the maximum RDRs. The dashed line indicates the target roof displacement based on the EEDP design. The result shows that the median is close to the target. In other words, the FTMF designed using EEDP can achieve the target displacement as intended. For detailed RDR time histories, please refer to Appendix B.

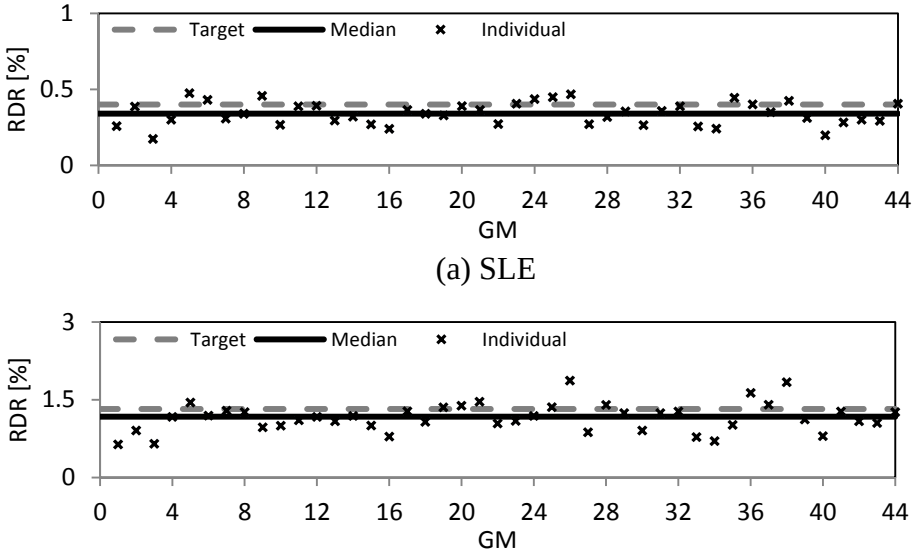

(a) SLE

(b) DBE

Figure 3.11 RDR of FTMF

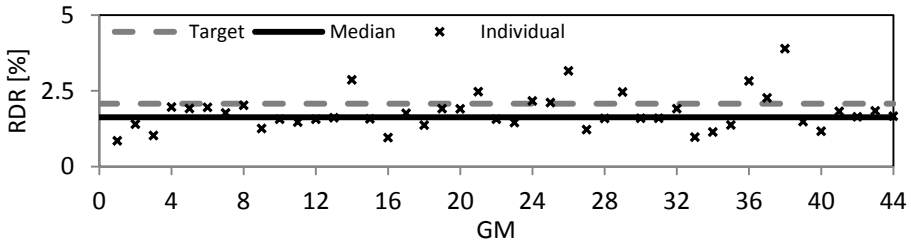

(c) MCE

Figure 3.11 RDR of FTMF

Figure 3.12 and Figure 3.13 show the median of the maximum BRB strain and MC rotation at each floor, respectively, when the prototype building is subjected to the scaled ground motions shown in Table 3.1. For detailed BRB strain and MC rotation time histories, please refer to Appendix C and Appendix D, respectively. In this study, the BRB yielding and ultimate strains are selected as 0.3% and 2.5%, respectively, based on the data as presented by Merritt *et al.* [2003]. The MC yielding and ultimate rotations are defined as 0.015 and 0.06, respectively, according to Figure 3.9(b). When the ground motions are scaled to the SLE shaking intensity, both the BRB and MC demands are under the yielding capacities. This means that the FTMF is damage-free and hence achieves the IO performance objective. When the ground motions are scaled to the DBE shaking intensity, Figure 3.12(b) shows that the BRB has yielded to protect the MC from yielding (Figure 3.13(b)). Because the BRB is designed to be easily inspected and efficiently replaced after an earthquake, this allows the FTMF to achieve the RR performance objective. When the FTMF is subjected to the MCE shaking intensity, Figure 3.12(c) shows increased strain in the BRB and Figure 3.13(c) shows yielding in the MC. At the same time, they are below the ultimate deformations to ensure that the FTMF can achieve the CP performance objective.

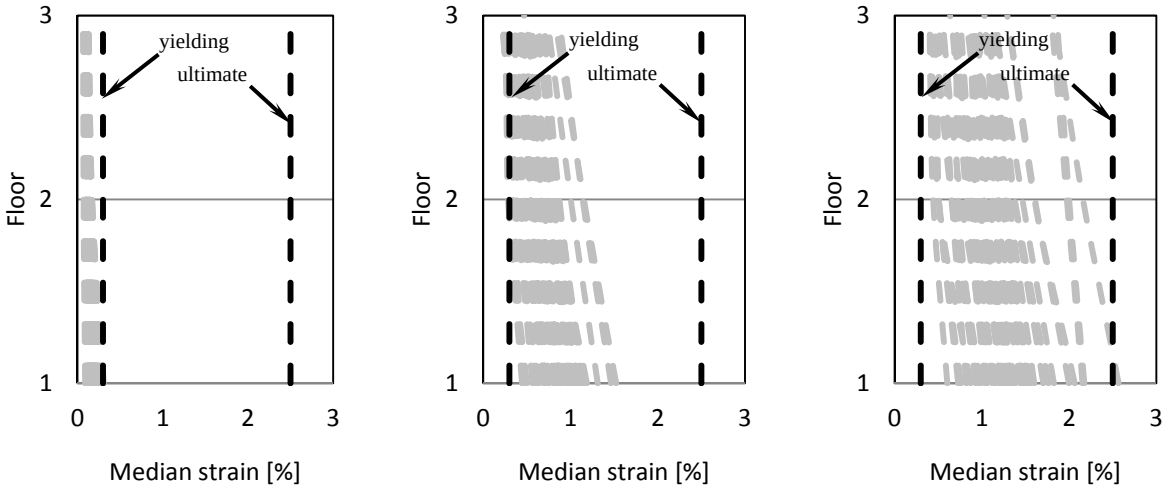

(a) SLE (b) DBE (c) MCE

Figure 3.12 BRB performance

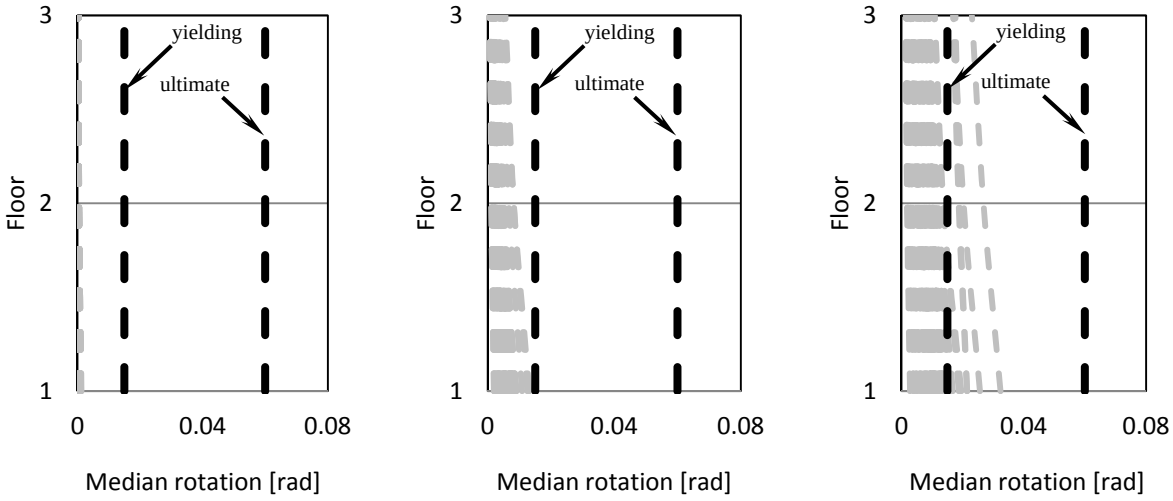

(a) SLE (b) DBE (c) MCE

Figure 3.13 MC performance

Figure 3.14 shows the maximum force demand capacity ratios (DCRs) of all the non-yielding members under the MCE shaking intensity. The capacity is defined by the nominal strength of the member per ANSI/AISC 360-10 [2010]. To be thorough, the DCRs are obtained at various locations. For the top and bottom chords of the truss, the ratios are determined at each panel point. For the web of the truss, each vertical and diagonal member is examined. For the columns, the ratios are calculated at the foundation, each floor, as well as above and

below the BRB connection. According to the figure, all the DCRs are less than unity. This suggests that the non-yielding members indeed remain elastic and hence can be modelled as elastic elements.

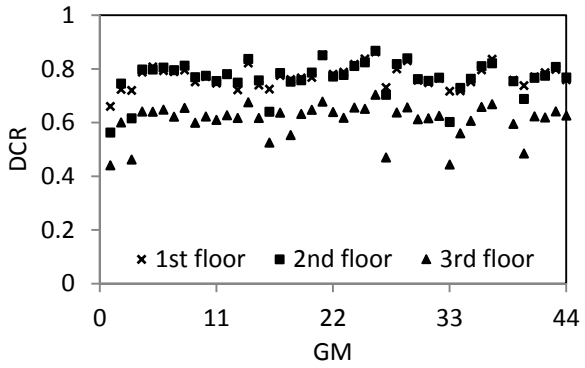

(a) Truss top chord

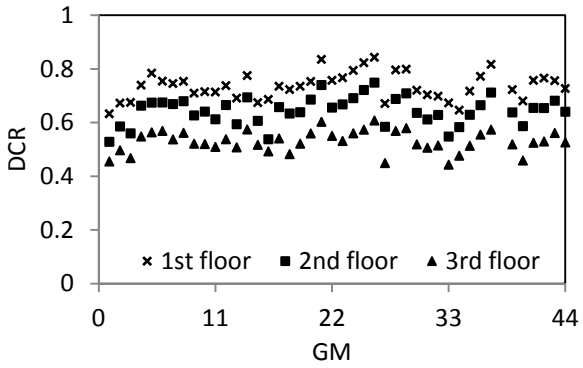

(b) Truss bottom chord

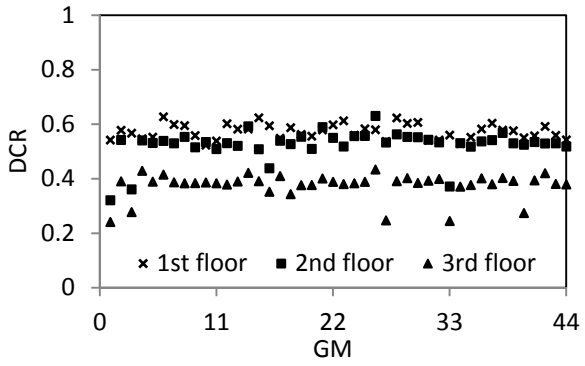

(c) Truss vertical web

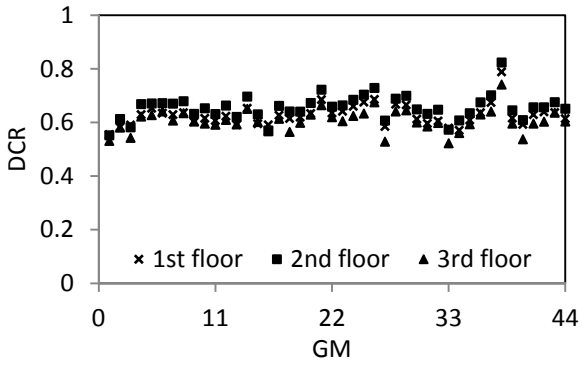

(d) Truss diagonal web

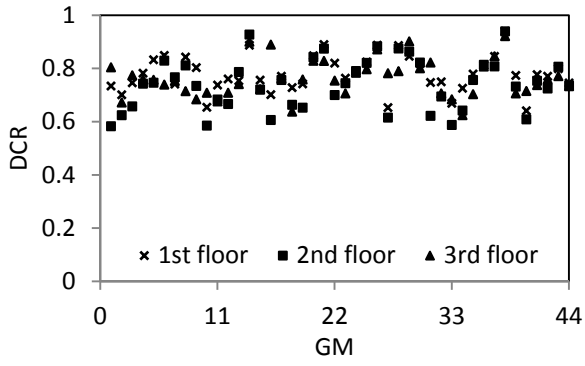

(e) Exterior column

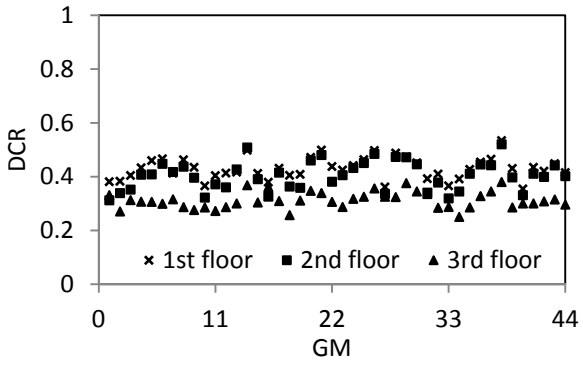

(f) Interior column

Figure 3.14 Maximum DCR of non-yielding members

3.3 Seismic safety

The results as presented in the previous section have shown that the proposed FTMF designed using EEDP can exhibit predictable structural behaviour under different selected earthquake shaking intensities. Meanwhile, it is crucial to demonstrate that the proposed FTMF designed using EEDP has adequate seismic safety against collapse. To quantify safety, the methodology described in FEMA-P695 [2009] is employed in this chapter.

The first step of the FEMA-P695 methodology is to perform nonlinear static analysis to quantify the backbone curve for the proposed FTMF. To properly model the force-deformation response of the prototype building, a BRB removal technique as presented in Yang *et al.* [2016] is implemented. This technique allows force redistribution within the frame after a BRB fractures. Figure 3.15 shows the pushover curve of the prototype building. As the FTMF displaces laterally, the frame yielding RDR, i.e. RDR_y, coincides with the RDR where the BRBs start to yield. The frame ultimate RDR, i.e. RDR_u, happens when the first floor BRB fractures. This causes a sudden drop in the force capacity of the frame. According to FEMA-P695, the period-based ductility, μ_T, is defined as the ratio of RDR_u to RDR_y, i.e. 6.6 for the FTMF. In this figure, the EEDP design backbone curve is also shown. Before yielding, the response of the prototype building is very comparable to the design target. After yielding, the pushover curve is higher than the idealized tri-linear curve from Figure 3.4(b). This is due to the inherent post-yielding stiffness of the BRBs and MCs which has not yet been accounted for in the EEDP design.

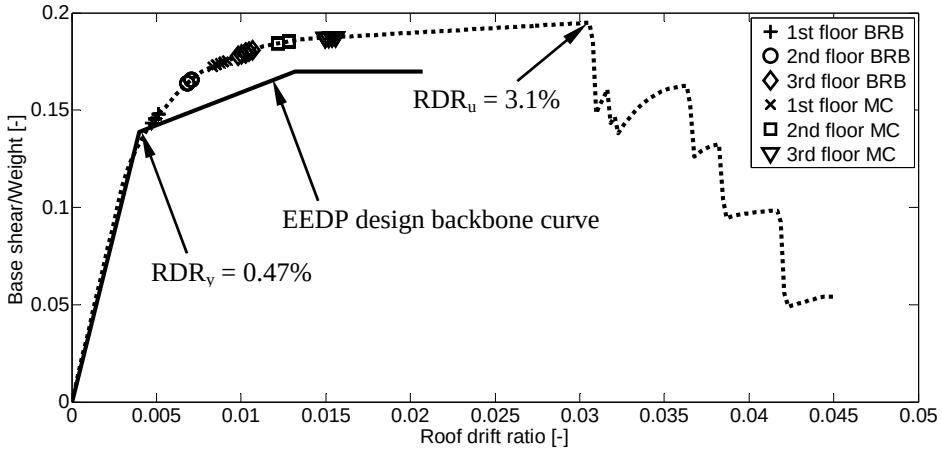

Figure 3.15 Pushover of FTMF

The second step of the FEMA-P695 methodology is to perform incremental dynamic analysis (IDA) [Vamvatsikos and Cornell 2002] using the suite of far-field ground motion records as presented in Table 3.1. The records are amplitude scaled incrementally while the RDR is monitored. When the RDR of 6% is reached, the FTMF is assumed to be globally collapsed because Figure 3.9(b) indicates that the MCs are effective up to 6%. The IDA curves of the individual ground motion as well as the median IDA curve of all the motions are given in Figure 3.16(a). The records are scaled as a suite such that their median (dashed line in Figure 3.10(c)) increases incrementally from 1% to 800%. This median spectrum acceleration at the structural fundamental period is plotted on the vertical axis of Figure 3.16(a). It is defined as the ground motion intensity measure. The corresponding RDR of the FTMF is plotted on the horizontal axis.

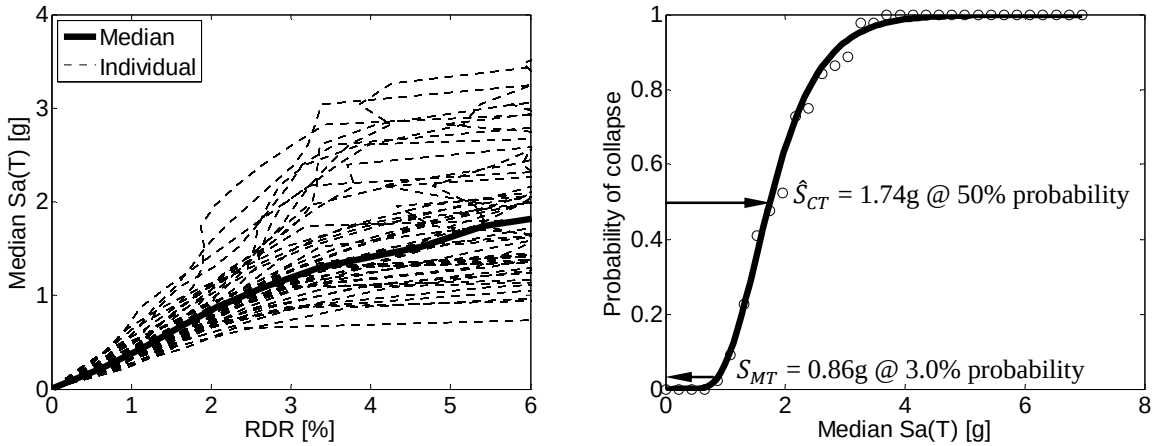

(a) IDA curves (b) Probability of collapse

Figure 3.16 IDA results

The third step of the FEMA-P695 methodology is to construct a collapse fragility curve from the IDA results. This fragility curve expresses the conditional probability of exceeding the 6% RDR limit state for a given ground motion intensity measure. The construction employs the curve fitting technique proposed by Ibarra and Krawinkler [2005]. For each individual IDA curve shown in Figure 3.16(a), the spectral acceleration at which RDR exceeds 6% is obtained. Assuming that the acceleration data of all the curves are lognormally distributed, the mean and standard deviation can be calculated to construct the collapse fragility curve shown in Figure 3.16(b). At the FTMF fundamental period, the median MCE intensity, S_{MT},

is about 0.86g. According to the figure, the probability of collapse corresponding to this intensity is approximately 3.0%. This is less than the 10% suggested by the methodology. At 50% probability of collapse, the corresponding intensity measure, $\hat{S}_{CT}$, can be read off the figure as 1.74g. Then, the collapse margin ratio (CMR) defined as the ratio of $\hat{S}_{CT}$ over S_{MT} can be approximated as 2.02. It should be noted that the counted probability of collapse as median seismic intensity increases is also plotted as the discrete points in Figure 3.16(b). The collapse fragility curve well fits the points.

The fourth step of the FEMA-P695 methodology is to determine the adjusted collapse margin ratio (ACMR) using a spectral shape factor (SSF). This factor recognizes that the calculated CMR can be significantly affected by the spectral shape of a ground motion. This factor is based on the FTMF fundamental period which is 0.9 second and period-based ductility which is 6.6 from Figure 3.15. Equation 3.16 indicates that the ACMR for the proposed FTMF is 2.81.

$$ACMR = SSF \times CMR = SSF \times \frac{\hat{S}_{CT}}{S_{MT}} = 2.81 \qquad \text{Equation 3.16}$$

where $SSF = 1.39$ [FEMA-P695 2009]; $\hat{S}_{CT} = 1.74\text{g}$; $S_{MT} = 0.86\text{g}$.

In order to determine the acceptable value of ACMR, the total system collapse uncertainty, β_{TOT}, of the FTMF is required. This uncertainly is due to the record-to-record variability in ground motions (β_{RTR}). It also addresses the quality ratings of design requirement (β_{DR}), test data (β_{TD}), and numerical model (β_{MDL}). If the fixed value of β_{RTR} were used and fair quality were assumed for all the ratings, Equation 3.17 calculates β_{TOT}.

$$\beta_{TOT} = \sqrt{{\beta_{RTR}}^2 + {\beta_{DR}}^2 + {\beta_{TD}}^2 + {\beta_{MDL}}^2} = 0.725 \qquad \text{Equation 3.17}$$

where $\beta_{RTR} = 0.40$ for period-based ductility greater than 3; $\beta_{DR} = \beta_{TD} = \beta_{MDL} = 0.35$ for fair quality rating [FEMA-P695 2009].

These assumptions result in 2.53 and 1.84 as the acceptable values of ACMR for a collapse probability of 10% and 20%, respectively [FEMA-P695 2009]. Since the proposed FTMF has an ACMR of 2.81 that exceeds the acceptable values, the FTMF designed using EEDP has adequate seismic safety against collapse.

3.4 Summary

Innovative earthquake resilient fused structures have gained popularity in recent years. They have the ability to be fully functional immediately or shortly after an earthquake with minimum downtime. They use sacrificial structural fuses to dissipate earthquake energy. For open space applications, a long-span FTMF is introduced in this chapter to the family of earthquake resilient fused structures. FTMF utilizes steel trusses and BRBs as structural fuses to form the primary SFRS. The BRBs are designed to be decoupled from the gravity system. Hence, they can be efficiently inspected, repaired or replaced after a strong earthquake shaking. To prevent a FTMF from losing all its lateral stiffness, the MCs between the truss top chords and columns are added to the system as the secondary SFRS. The innovative FTMF can be easily designed using EEDP proposed in Chapter 2 to achieve multi-level performance objectives at different earthquake shaking intensities. EEDP equates the input energy from an earthquake at different shaking intensities to the energy dissipated by the primary and secondary SFRSs. As shown by nonlinear dynamic analysis of the prototype building, the FTMF can control the location and degree of damages at the designated elements. At the low level shaking intensity, the FTMF is damage-free. At the design based earthquake shaking intensity, the BRBs start to yield while protecting the remaining system. During severe earthquake shakings, the secondary SFRS are then activated to prevent structural collapse. The analysis results indicate that the EEDP designed FTMF can achieve the target roof drift ratios and structural period without an iterative design process. This implies significant time and cost savings to the engineering community. This also allows designers to select appropriate non-structural components that are capable to withstand the anticipated system deformations. In addition, IDA is performed to obtain the collapse fragility curve for the FTMF. Based on the methodology described in FEMA-P695, the ACMR of the system is greater than the acceptable value. In other words, the proposed

FTMF designed using EEDP has adequate seismic safety against collapse during a strong earthquake shaking.

Chapter 4
Switch-based Hybrid Simulation

The knowledge of earthquake engineering is largely gained through experimental testing. The most direct method to recreate the loading experienced by a structure during an earthquake is via a shake table testing. To properly simulate the excitation experienced by a specimen, it shall be constructed in full or near to full scale. However, due to the limitation of a testing facility, it is usually time consuming, labour intensive, cost prohibitive, and technically difficult due to hydraulic control to conduct large scale shake table testing. Only a handful of testing facilities around the world, mostly in China, Japan, and the United States, are capable of conducting large scale testing. Most other shake table testing facilities require specimens to be tested at a significantly reduced scale. Because structural nonlinearity does not usually scale well when a specimen is drastically reduced, new and improved experimental testing techniques are needed.

With the advancement in finite element simulation and sub-structure testing, hybrid simulation (HS) is becoming a favorable alternative testing method to understand the behaviour of structures during earthquake shaking, particularly for the development of innovative structural fuses. HS combines analytical and experimental sub-assemblies through the equation of motion. Only the portion of a structure which is numerically difficult to model or new structural component with unknown structural responses is tested in a laboratory, while the remaining structure is modelled using finite element simulation. This testing method provides many significant advantages: 1) Experimental costs can be reduced as only a portion of the structure is constructed in the laboratory; 2) Large and complex structural systems can be tested as the analytical sub-assembly can be complex and multiple

experimental sub-assemblies can be tested at geographically distributed laboratories; 3) Structures can be safely evaluated at extreme states, such as collapse, which may be difficult or dangerous to do via shake table testing.

Traditionally, researchers conduct displacement-based HS (DHS). The algorithm calculates trial displacements and applies these displacements to both analytical and experimental sub-assemblies. Element resisting forces are then obtained and checked against global dynamic equilibrium. This approach has been widely used in many earthquake engineering research projects. However, DHS is not suitable for specimens with a high stiffness because it is difficult to precisely control a hydraulic servo actuator in small displacement. A small control error in displacement may result to large force response fluctuations in stiff specimens. This challenge can be resolved by using force-based HS (FHS) where the algorithm calculates trial forces instead of trial displacements. Such an algorithm allows stiff specimens to be tested using sub-assembly testing technique in a non-real-time environment. Rather than checking for force equilibrium alone, FHS checks dynamic equilibrium and compatibility conditions simultaneously. However, a stiff specimen typically softens after yielding. Conducting a simulation with only a force control algorithm would result in non-convergence and hydraulic instability. Therefore, the ideal HS should switch (SHS) based on the state of a specimen to use either trial displacements or trial forces. Such an approach provides the robustness to improve HS.

In this chapter, Section 4.1 reviews the development of HS. Section 4.2 provides a detailed derivation of DHS and proposes a new finite element based approach for FHS. In Section 4.3, a switching law is developed for SHS to examine the nonlinear dynamic responses of a structural system when the specimen is expected to have drastic changes in stiffness. In Section 4.4, DHS, FHS, and SHS are conducted for a one-storey one-bay concentrically braced moment frame to prove that SHS has superior performance over DHS and FHS.

4.1 Simulation development

It is often observed during a shake table testing that damages or nonlinearities occur at limited regions of a structure. This observation indicates that only structural components or

sub-structures need to be tested. Therefore, HS is well suited as an alternative to shake table testing to save time and costs. The idea of HS was contemplated in the late 1960s and early 1970s which led to its formal introduction by Takanashi in 1975 [Takanashi 1975]. At that time, it was referred to as on-line testing to combine computer and actuator in nonlinear analysis of structures. He studied structural systems as discrete spring-mass systems within the time domain and eliminated the need of real-time loading. As a result, typical quasi-static hydraulic loading systems could be used to perform HS. The term “on-line testing” has evolved over time to become “pseudodynamic testing” in the 1980s and 1990s. In recent literature and research, the term “hybrid simulation” has frequently been used. To conduct efficient, accurate, and stable HS, the fundamental issue related to damping as well as numerical issue associated to time-step integration should be addressed [Nakashima *et al.* 1988]. The former could be solved by carefully define and model the portion of damping that was in addition to the hysteretic damping of the tested structural component or sub-structure. This issue was less of a concern since such hysteretic damping was anticipated to be captured during HS. The latter was unavoidable due to the numerical approach to solve the equation of motion and has been researched intensively since the 1980s.

Shing and Mahin [1984] studied various stable explicit numerical integration schemes including the explicit Newmark method. Such a method did not require iterations which meant it was efficient and less likely to prematurely damage a specimen. As a result, it remained to be the widely used method today to perform HS. However, its stability was conditional upon the degree-of-freedom (DOF) in a finite element model. In the true spirit of HS, it was desired to have high DOF in a model and hence to limit the complexity of experimental sub-assembly. Dermitzakis and Mahin [1985] proposed a mixed implicit-explicit scheme to address the stability issue. The experimental sub-assembly of HS was solved using an explicit method, while the analytical sub-assembly used an implicit method. Nakashima *et al.* [1988] found the operator-splitting (OS), another type of implicit-explicit scheme, could effectively increase stability. In their OS, restoring force was split into linear and nonlinear parts with the former solved using an implicit method and latter using an explicit method.

Vannan [1991] proposed an unconditionally stable implicit direct time integration scheme. He investigated the error propagation characteristics of the scheme and established practical convergence criteria within the typical capabilities of experimental hardware. Combescure and Pegon [1997] investigated the non-iterative and implicit α-OS scheme due to its unconditional stability and implementation simplicity. They found that the damping associated with the α factor was crucial to the success of the scheme. Chang [2002] proposed an unconditionally stable explicit scheme which was ideal for HS. It did not require iterations and could be implemented without hardware modifications of experimental setup traditionally utilized by researchers. The scheme was similar to the central difference method and Newmark explicit method, but had less error propagation and was second-order accurate. In 2007, Chang further improved the scheme to show better error propagation properties. Investigation and development of numerical integration schemes for HS have been mostly documented in journal articles. In a book by Pan *et al.* [2013], they examined various notable schemes and offered comparisons and contrasts.

After more than a decade of development, Takanashi and Nakashima [1987] summarized the Japanese activities in HS. In addition to list the simulations to date by the Japanese researchers, they classified error sources. Intrinsic error sources were those associated to the formulation of HS algorithms. Examples were the approximation of a continuum system by a discrete system, numerical integration of the equation of motion, and assumption of constant damping ratios. Experimental error sources arose from the imperfect nature of experimental hardware. Examples were the conversion of digital to analog displacement comments sent to a hydraulic servo controller as well as accuracy of displacement and load cell sensors. Yi [1991] studied the effects of experimental error propagation. He performed error analysis for the implicit integration scheme and designed algorithm to minimize the effects of control error. Mosqueda *et al.* [2005] discussed errors based on numerical modelling, implementation techniques, and experimental setup. Among the various error sources, experimental error sources could be the most unknown and significant. They were classified as either random with no distinguishable pattern or systematic with a regular pattern of occurrence. Mosqueda *et al.* [2005] developed a method to estimate the reliability of HS

based on energy errors accumulated in an experimental sub-assembly. They also proposed several error indicators to assess the accuracy and efficiency of HS.

While the topics of numerical integration and experimental error remained the core of research in HS to produce efficient, accurate, and stable tests, the desire to perform real-time HS added complexities to these topics. Takanashi and Nakashima [1987] conducted the first fast HS and identified challenges that needed to be addressed. In a fast HS, the force readings taken by a load cell were often contaminated by the inertia of the load cell itself. Also, the force readings may include velocity-proportional damping typically modelled in a traditional HS. Researchers have been overcoming the challenges with the advancement in experimental hardware such as digital-analog signal converters, electro-servo controllers, and microcomputers. Sophisticated and advanced control algorithms are also being developed to compensate experimental delays. As HS becomes a common experimental practice around the world, attempts have been made to standardize the procedure [Schellenberg *et al.* 2009]. Facilities such as the George E. Brown, Jr. Network for Earthquake Engineering Simulation, i.e. NEES, are available to provide HS as a research tool to users without intimate knowledge of HS.

Most of the past advancement in HS has relied on a displacement-based integration scheme to control hydraulic servo actuators in displacement. Although DHS has demonstrated many significant successes, it is difficult to use DHS to test highly stiff specimens such as short braces and shear walls because it is challenging to accurately control an actuator in small displacements. Small control errors in displacement will result to large fluctuations in resisting force, and hence, cause convergence issue. More importantly, control errors in displacement can potentially damage a stiff specimen prematurely. To address these problems, schemes resulted in force commands for actuators must be developed. Shield *et al.* [2001] developed and implemented the effective force testing (EFT) method. EFT recreates an earthquake excitation as dynamic forces at all DOFs. To simulate the dynamic responses of a structure, the entire structure must be constructed in a laboratory and tested in real time. This creates many construction challenges and control issues. Chen [2007] developed the virtual mass method to improve EFT. In this method, the total mass of a structure is partially

removed from the experimental setup and simulated in computer software. The experiment, however, still needs the remaining portion of the mass, damping, and stiffness of the structure constructed and tested in real time. Reinhorn *et al.* [2004] proposed the real-time dynamic hybrid testing (RTDHT) method for structural systems. RTDHT uses actuators and finite element simulation to examine the seismic behaviour of structures. To achieve RTDHT, a mechanical spring is installed in between an actuator and a specimen. The spring is selected to remain linear under the maximum applied force. Hence, all applied forces can be approximated using the stiffness of the spring and its deformation. In RTDHT, the traditional displacement-based integration scheme can be used. Because mechanical springs are added to experimental setup, additional DOFs are introduced. Special compensation techniques are required to apply appropriate forces to a specimen.

Pan *et al.* [2005] performed HS of an eight-story two-span steel moment frame isolated by high damping rubber bearings (HDRBs). The moment frame is the analytical sub-assembly, while the HDRB is the experimental sub-assembly. The vertical actuator controls the vertical DOF of the HDRB with force when the bearing is being pushed down and with displacement when the bearing is being pulled up. This is because the HDRB is known to have high stiffness in compression and low stiffness in tension. In their test, the applied compressive force is calculated using the predicted displacement multiplied by the elastic axial stiffness of the HDRB. This is achievable since the bearing remains elastic with known axial stiffness. Elkhoraibi and Mosalam [2007] used secant stiffness to compute trial forces for HS. In their approach, the DOFs are assumed to be uncoupled so that the secant stiffness matrix only contains diagonal terms. They also performed switch-based HS using pre-defined thresholds in terms of restoring force and secant stiffness.

4.2 Simulation algorithms

HS is an advanced experimental method where structural responses are determined using both analytical and experimental sub-assemblies. Equation 4.1 shows the generalized equation of motion for a multiple DOF system subjected to a dynamic load.

$$[M]\{\ddot{U}\} + [C]\{\dot{U}\} + \{RF\} = \{P\} \quad \text{Equation 4.1}$$

where $[M]$ and $[C]$ are the mass and damping matrices of the multiple DOF system, respectively; $\{\ddot{U}\}$ and $\{\dot{U}\}$ are the acceleration and velocity vectors at the free DOFs, respectively; $\{RF\}$ and $\{P\}$ are the resisting and applied forces at the free DOFs, respectively.

As presented in Equation 4.1, $\{RF\}$ is assumed to be a rate independent nonlinear function. For sub-assemblies that are rate dependent, the formulation is presented in Yang [2006]. Figure 4.1 shows the hybrid combination of the analytical and experimental sub-assemblies of a sample structure. In this combination, it is assumed that the inertia, damping, and applied forces can be simulated numerically, while the resisting force can be obtained from a combination of analytical and experimental sub-assemblies. It should be noted that only the component which is numerically difficult to model or new structural component whose force-deformation response is unknown is tested in a laboratory, while the remaining structure is modelled analytically. The dynamic responses of a structure as presented in Equation 4.1 can be solved using both the displacement-based and force-based algorithms as detailed in Section 4.2.1 and Section 4.2.2, respectively. Section 4.2.3 derives the compatibility equation specifically needed in the force-based algorithm.

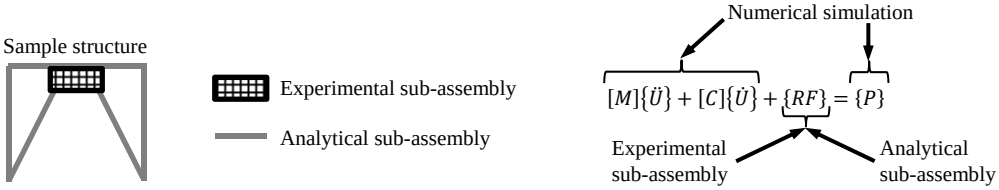

Figure 4.1 Diagrammatic illustration of HS

4.2.1 Displacement-based algorithm

The displacement-based algorithm for DHS uses a trial displacement at the global DOFs to check the dynamic equilibrium of a system as shown in Equation 4.1. This displacement at the global DOFs is transformed to the local DOFs using Equation 4.2 before it is applied to the analytical and experimental sub-assemblies.

$$\{v\} = [A_f]\{U\} \quad \text{Equation 4.2}$$

where $\{v\}$ is the element displacement vector at the local DOFs; $[A_f]$ is the compatibility matrix to transform the displacement from the global to local DOFs; $\{U\}$ is the nodal displacement vector at the global DOFs.

Equation 4.3 shows the constitutive relationship of the elements.

$$\{q\} = f_1(\{v\}) \quad \text{Equation 4.3}$$

where $\{q\}$ is the element force vector at the local DOFs; $f_1(\,)$ can be any linear or nonlinear function that relates the displacement to force of the element at the local DOFs.

Equation 4.4 shows the static force equilibrium from the local to global DOFs.

$$\{RF\} = [B_f]\{q\} \quad \text{Equation 4.4}$$

where $[B_f] = [A_f]^T$ = the equilibrium matrix of the system.

Equation 4.5 and Equation 4.6 show the Newmark integration algorithms [Newmark 1959] to solve the dynamic response of a system as presented in Equation 4.1.

$$\{\ddot{U}_{n+1}\} = \frac{1}{\beta h^2}(\{U_{n+1}\} - \{U_n\} - h\{\dot{U}_n\}) - \left(\frac{1}{2\beta} - 1\right)\{\ddot{U}_n\} \quad \text{Equation 4.5}$$

$$\{\dot{U}_{n+1}\} = \frac{\gamma}{\beta h}(\{U_{n+1}\} - \{U_n\}) + \left(1 - \frac{\gamma}{\beta}\right)\{\dot{U}_n\} + \left(1 - \frac{\gamma}{2\beta}\right)h\{\ddot{U}_n\} \quad \text{Equation 4.6}$$

where $\{\ddot{U}_n\}$, $\{\dot{U}_n\}$, and $\{U_n\}$ are the acceleration, velocity, and displacement vectors at the global DOFs at time step n; $\{\ddot{U}_{n+1}\}$, $\{\dot{U}_{n+1}\}$, and $\{U_{n+1}\}$ are the acceleration, velocity, and displacement vector at the global DOFs at time step n+1; h is the time step of the integration algorithm; γ and β are the dimensionless constant coefficients.

When $\gamma = 1/2$ and $\beta = 1/4$, Equation 4.5 and Equation 4.6 are known as the Newmark constant acceleration algorithm. When $\gamma = 1/2$ and $\beta = 1/6$, these equations are known as the Newmark linear acceleration algorithm.

The displacement-based algorithm starts the calculation by using a trial displacement vector at the global DOFs, $\{U_{n+1}\}$, which can be estimated using the previously converged displacement vector. Substituting $\{U_{n+1}\}$ into Equation 4.2, the element displacement vector at the local DOFs, $\{v_{n+1}\}$, at time step n+1 can be determined. The displacement-based algorithm sends $\{v_{n+1}\}$ to both the analytical and experimental sub-assemblies. The analytical sub-assembly calculates the local element force, ${q_{n+1}}^{i}$, at time step n+1 at the ith local element DOF, while the experimental sub-assembly measures ${q_{n+1}}^{j}$ at time step n+1 at the jth local element DOF. These element forces are then assembled to the element force vector at the local DOFs, $\{q_{n+1}\}$. Once $\{q_{n+1}\}$ is obtained, the resisting force, $\{RF_{n+1}\}$, at time step n+1 can be calculated by Equation 4.4. Using Equation 4.5 and Equation 4.6, $\{\ddot{U}_{n+1}\}$ and $\{\dot{U}_{n+1}\}$ can be determined. The inertial force, $[M]\{\ddot{U}_{n+1}\}$, and damping force, $[C]\{\dot{U}_{n+1}\}$, at time step n+1 can then be calculated. Equation 4.7 shows the dynamic equilibrium equation as presented in Equation 4.1 expressed as a function of $\{U_{n+1}\}$. In this equation, $\{U_{n+1}\}$ is the only unknown, and hence can be solved using any nonlinear solver such as Newton iteration [Burden and Faires 2001].

$$F_1(\{U_{n+1}\}) = [M]\left(\frac{1}{\beta h^2}\left(\{U_{n+1}\} - \{U_n\} - h\{\dot{U}_n\}\right) - \left(\frac{1}{2\beta} - 1\right)\{\ddot{U}_n\}\right)$$
$$+[C]\left(\frac{\gamma}{\beta h}(\{U_{n+1}\} - \{U_n\}) + \left(1 - \frac{\gamma}{\beta}\right)\{\dot{U}_n\} + \left(1 - \frac{\gamma}{2\beta}\right)h\{\ddot{U}_n\}\right)$$
$$+[B_f]f_1\left([A_f]\{U_{n+1}\}\right) - \{P_{n+1}\} = \{0\} \qquad \text{Equation 4.7}$$

Equation 4.8 shows the solution of Equation 4.7 using Newton iteration.

$$\{U_{n+1}^{k+1}\} = \{U_{n+1}^{k}\} - \left[{F_1}'\left(\{U_{n+1}^{k}\}\right)\right]^{-1} F_1\left(\{U_{n+1}^{k}\}\right) \qquad \text{Equation 4.8}$$

where $\{U_{n+1}^{k}\}$ and $\{U_{n+1}^{k+1}\}$ are the solutions of Newton iteration at the kth and (k+1)th iterations, respectively; $\left[{F_1}'\left(\{U_{n+1}^{k}\}\right)\right]$ is the derivative of F_1 with respect to $\{U_{n+1}^{k}\}$ as shown in Equation 4.9.

$$[F_1'(\{U_{n+1}\})] = \frac{1}{\beta h^2}[M] + \frac{\gamma}{\beta h}[C] + [B_f] f_1'([A_f]\{U_{n+1}\}) \quad \text{Equation 4.9}$$

where $f_1'([A_f]\{U_{n+1}\})$ is the stiffness of the elements which can be calculated from the analytical sub-assemblies or measured from the experimental sub-assemblies.

Below shows the steps to implement the displacement-based algorithm for DHS:

1. Form equilibrium using Equation 4.1 at time step n+1 by assuming a trial displacement vector at the global DOFs, $\{U_{n+1}\}$.
2. Calculate the displacement vector at the local DOFs, $\{v_{n+1}\}$, using Equation 4.2.
3. Calculate or measure the element force at the local DOFs, q_{n+1}, using constitutive relationship of Equation 4.3 or laboratory force feedback.
4. Assemble the element force vector at the local DOFs, $\{q_{n+1}\}$.
5. Calculate the system resisting force, $\{RF_{n+1}\}$, using Equation 4.4.
6. Calculate the acceleration, $\{\ddot{U}_{n+1}\}$, and velocity, $\{\dot{U}_{n+1}\}$, at the global DOFs using Equation 4.5 and Equation 4.6, respectively.
7. Assemble the equation of motion using Equation 4.7.
8. Check error norm to see if the trial $\{U_{n+1}\}$ is valid.
9. If the error norm is less than tolerance, the trail $\{U_{n+1}\}$ is valid. Go to Step (10). Otherwise, repeat from Step (1) using the Newton iteration as presented in Equation 4.8.
10. Update $\{U_{n+1}\}$ by the solution, and then move to the next time step.

4.2.2 Force-based algorithm

Similar to the displacement-based algorithm, a finite element force-based algorithm for FHS is presented in this section. The proposed FHS follows the traditional DHS, where experimental sub-assemblies are tested using sub-structure testing technique. More importantly, FHS can be conducted in a non-real-time environment provided that a specimen is not rate dependent. If the specimen were rate dependent, the presented force-based algorithm can be modified similar to the procedure as presented in Yang [2006]. In addition, the control algorithm of the hydraulic system in a laboratory should be updated to ensure the experimental sub-assembly can be tested in a real-time environment. In short, the proposed

FHS is directly comparable to the traditional DHS. It does not require the entire structure to be tested as a whole nor the use of mechanical springs in experimental sub-assemblies. The proposed FHS checks the dynamic equilibrium and compatibility conditions of the analytical and experimental sub-assemblies simultaneously. For a stiff experimental sub-assembly, FHS eliminates the need to control small trial displacements and hence minimizes any force fluctuations. In critical cases where a specimen has a low yielding displacement, FHS prevents premature damages to the specimen.

Equation 4.10 shows the static equilibrium equations of a statically indeterminate system.

$$\{q\} = [B_i]\{P\} + [B_x]\{q_x\} \qquad \text{Equation 4.10}$$

where $\{q_x\}$ represents the redundant forces in a statically indeterminate system, and the size of $\{q_x\}$ depends on the static indeterminacy of the system.

When $\{q_x\}$ is known or is removed from the structure, the equilibrium equation as presented in Equation 4.10 is reduced to a statically determinate system, sometimes called a primary structure. It should be noted that the selected statically determinate system must be stable in order to be called the primary structure. In other words, the selection of $\{q_x\}$ is important to ensure the remaining structure is statically determinate and stable. ($[B_i]\{P\}$) represents the equilibrium equation between the element force vector and applied load, $\{P\}$, on the primary structure. $[B_i]$ is known as the equilibrium matrix of the primary structure. Each column vector of $[B_i]$ represents the ratio of the element forces in the primary structure with respect to the applied force at each global DOF with the redundant forces set to zero. ($[B_x]\{q_x\}$) represents the portion of the element force vector as a function of the redundant force, $\{q_x\}$, on the primary structure. $[B_x]$ is known as the force influence matrix that relates $\{q_x\}$ to $\{q\}$. Each column vector of $[B_x]$ represents the ratio of the element forces in the primary structure with respect to the ith redundant force, ${q_x}^i$, with all the other redundant forces, ${q_x}^{j\neq i}$, set to zero.

Contrary to DHS that uses a trial displacement vector at the global DOFs, $\{U\}$, the proposed FHS algorithm starts the calculation by using a trial force vector at the local DOFs, $\{q\}$,

which can be estimated using the previously converged force vector. The force-based algorithm sends $\{q\}$ to both the analytical and experimental sub-assemblies. These sub-assemblies calculate or measure the local element displacement, v^i, at the ith local element DOF. These element displacements are then assembled to the element displacement vector at the local DOFs, $\{v\}$. Equation 4.11 shows the transformation from the local element force to local element displacement. $f_2(\,)$ can be any linear or nonlinear function that relates the force to displacement of the element at the local DOFs.

$$\{v\} = f_2(\{q\}) \qquad \text{Equation 4.11}$$

Equation 4.12 shows the compatibility equation for the displacement from the local to global DOFs. The detailed derivation is given in Section 4.2.3.

$$\{U\} = [B_i]^T\{v\} \qquad \text{Equation 4.12}$$

Substitute Equation 4.11 into Equation 4.12. The global displacement, $\{U_{n+1}\}$, at time step n+1 can be expressed in terms of the trial element force vector, $\{q_{n+1}\}$, at time step n+1.

$$\{U_{n+1}\} = [B_i]^T f_2(\{q_{n+1}\}) \qquad \text{Equation 4.13}$$

The Newmark equations [1959] as shown in Equation 4.5 and Equation 4.6 remain the same. $\{\ddot{U}_{n+1}\}$ and $\{\dot{U}_{n+1}\}$ can be expressed in terms of $\{U_{n+1}\}$ and hence, in term of $\{q_{n+1}\}$. Equation 4.14 and Equation 4.15 shows the acceleration and velocity of the system at the global DOFs.

$$\{\ddot{U}_{n+1}\} = \frac{1}{\beta h^2}\left(\{[B_i]^T f_2(\{q_{n+1}\})\} - \{U_n\} - h\{\dot{U}_n\}\right) - \left(\frac{1}{2\beta} - 1\right)\{\ddot{U}_n\} \qquad \text{Equation 4.14}$$

$$\{\dot{U}_{n+1}\} = \frac{\gamma}{\beta h}\left(\{[B_i]^T f_2(\{q_{n+1}\})\} - \{U_n\}\right) + \left(1 - \frac{\gamma}{\beta}\right)\{\dot{U}_n\} + \left(1 - \frac{\gamma}{2\beta}\right)h\{\ddot{U}_n\} \qquad \text{Equation 4.15}$$

In a structure, one can define n as the number of independent element forces in the local DOFs, and m as the number of free global DOFs. When n is greater than m, the structure is

statically indeterminate, i.e. there are more unknown element forces than available equilibrium equations. To determine the element forces in such a structure using the force method, the n-component element force vector, i.e. $\{q\}$, must satisfy m equilibrium equations along with $(n-m)$ displacement constraints. These constraints are called compatibility conditions and can be expressed by the following equation [Raju and Nagabhushanam 2000].

$$[B_x]^T\{v\} = \{0\} \qquad \text{Equation 4.16}$$

Equation 4.16 can be expressed in terms of the element forces when substituting Equation 4.10 into Equation 4.11.

$$[B_x]^T\{v\} = [B_x]^T f_2(\{q\}) = [B_x]^T f_2([B_i]\{P\}) + [B_x]^T f_2([B_x]\{q_x\}) = \{0\} \qquad \text{Equation 4.17}$$

$\left([B_x]^T f_2([B_i]\{P\})\right)$ represents the element displacement vector due to the applied loads on the primary structure, and $\left([B_x]^T f_2([B_x]\{q_x\})\right)$ represents the element displacement vector due to the redundant forces on the primary structure.

Similar to the displacement-based algorithm, the proposed force-based algorithm must satisfy the dynamic equilibrium as presented in Equation 4.1. In addition, the compatibility conditions as presented in Equation 4.17 need to be maintained. To satisfy these requirements simultaneously, Equation 4.1 and Equation 4.17 are combined with Equation 4.4, Equation 4.14, and Equation 4.15 concurrently. The result can be expressed in matrix form as shown in Equation 4.18.

$$F_2(\{q_{n+1}\}) = \begin{bmatrix}[M]\\ [0]\end{bmatrix}\begin{bmatrix}\frac{1}{\beta h^2}\left(\{[B_i]^T f_2(\{q_{n+1}\})\} - \{U_n\} - h\{\dot{U}_n\}\right) - \left(\frac{1}{2\beta} - 1\right)\{\ddot{U}_n\}\\ [0]\end{bmatrix}$$
$$+ \begin{bmatrix}[C]\\ [0]\end{bmatrix}\begin{bmatrix}\frac{\gamma}{\beta h}\left(\{[B_i]^T f_2(\{q_{n+1}\})\} - \{U_n\}\right) + \left(1 - \frac{\gamma}{\beta}\right)\{\dot{U}_n\} + \left(1 - \frac{\gamma}{2\beta}\right)h\{\ddot{U}_n\}\\ [0]\end{bmatrix}$$
$$+ \begin{bmatrix}[B_f]\{q_{n+1}\}\\ [B_x]^T f_2(\{q_{n+1}\})\end{bmatrix} - \begin{bmatrix}\{P_{n+1}\}\\ \{0\}\end{bmatrix} = \{0\} \qquad \text{Equation 4.18}$$

Note that $\{q_{n+1}\}$ is the only unknown. Hence, this nonlinear function can be solved using Newton iteration [Burden and Faires 2001]. Equation 4.19 shows the solution of Newton iteration.

$$\{q_{n+1}^{k+1}\} = \{q_{n+1}^{k}\} - \left[F_2{}'\left(\{q_{n+1}^{k}\}\right)\right]^{-1} F_2\left(\{q_{n+1}^{k}\}\right) \qquad \text{Equation 4.19}$$

where $\{q_{n+1}^{k}\}$ and $\{q_{n+1}^{k+1}\}$ are the solutions of Newton iteration at the kth and (k+1)th iterations, respectively; $\left[F_2{}'\left(\{q_{n+1}^{k}\}\right)\right]$ is the derivative of F_2 with respect to $\{q_{n+1}^{k}\}$ as shown in Equation 4.20.

$$[F_2{}'(\{q_{n+1}\})] = \begin{bmatrix} \frac{1}{\beta h^2}([M]\{[B_i]^T f_2{}'(\{q_{n+1}\})\}) + \frac{\gamma}{\beta h}([C]\{[B_i]^T f_2{}'(\{q_{n+1}\})\}) + [B_f] \\ [B_x]^T f_2{}'(\{q_{n+1}\}) \end{bmatrix} \qquad \text{Equation 4.20}$$

where $f_2{}'(\{q_{n+1}\})$ is the flexibility of the elements which can be calculated from the analytical sub-assembly or measured from the experimental sub-assembly.

Below shows the steps to implement the force-based algorithm for FHS:

1. Form equilibrium using Equation 4.1 at time step n+1 by assuming a trial force vector at the local DOFs, $\{q_{n+1}\}$.
2. Calculate or measure the element displacement at the local DOFs, v_{n+1}, using constitutive relationship of Equation 4.11 or laboratory displacement feedback.
3. Assemble the element displacement vector at the local DOFs, $\{v_{n+1}\}$.
4. Calculate the displacement vector at the global DOFs, $\{U_{n+1}\}$, using Equation 4.12.
5. Calculate the acceleration, $\{\ddot{U}_{n+1}\}$, and velocity, $\{\dot{U}_{n+1}\}$, at the global DOFs using Equation 4.14 and Equation 4.15, respectively.
6. Assemble the equation of motion using Equation 4.18.
7. Check error norm to see if the trial $\{q_{n+1}\}$ is valid.
8. If the error norm is less than tolerance, the trail $\{q_{n+1}\}$ is valid. Go to Step (8). Otherwise, repeat from Step (1) using the Newton iteration as presented in Equation 4.19.
9. Update $\{q_{n+1}\}$ by the solution, and then move to the next time step.

4.2.3 Compatibility equation

Equation 4.12 shows that the displacement vector at the global DOFs, $\{U\}$, can be calculated using only the equilibrium matrix of the primary structure, $[B_i]$, and the element displacement vector at the local DOFs, $\{v\}$. This equation can be derived using the principle of virtual work. By definition, the work done by internal forces shall equal to the work done by external forces on any stable system. In this case, the primary structure is selected as the stable and virtual system. Hence, the relationship between the virtual applied loads at the global DOFs, $\{P^*\}$, and the corresponding virtual element forces, $\{q^*\}$, can be established as follow.

$$\{q^*\}^T\{v\} = \{P^*\}^T\{U\} \quad \text{Equation 4.21}$$

Similar to Equation 4.10, $\{q^*\}$ can be expressed as a combination of $\{P^*\}$ and $\{q_x^*\}$.

$$\{q^*\} = [B_i]\{P^*\} + [B_x]\{q_x^*\} \quad \text{Equation 4.22}$$

where $\{q_x^*\}$ is the redundant force in the virtual system which is also the primary system.

Since a primary structure does not have redundant forces, $\{q_x^*\}$ is equal to $\{0\}$. Then, substitute the resulting Equation 4.22 into Equation 4.21 and expand.

$$\left[[B_i]\{P^*\}\right]^T\{v\} = \{P^*\}^T[B_i]^T\{v\} = \{P^*\}^T\{U\} \rightarrow \{P^*\}^T([B_i]^T\{v\} - \{U\}) = \{0\} \quad \text{Equation 4.23}$$

Since $\{P^*\}^T \neq \{0\}^T$, the following can be concluded.

$$[B_i]^T\{v\} - \{U\} = \{0\} \quad \text{Equation 4.24}$$

4.3 Switch control law

As presented previously, both the displacement-based and force-based algorithms are applicable to conduct HS with multiple analytical and experimental sub-assemblies. DHS is suitable for soft specimens, while FHS is developed for stiff specimens. When a specimen is

expected to experience significant changes in stiffness, a combination of DHS and FHS would be ideal. In this section, a switch-based hybrid simulation (SHS) is proposed for such test.

Figure 4.2(a) shows the force-displacement relationships of two sub-assemblies: the solid line denotes the specimen with a higher stiffness, and the dashed line denotes the specimen with a lower stiffness. As it is very difficult to perfectly control a hydraulic servo actuator, it is unavoidable to have a small control error in displacement, Δv. For the softer specimen, Δv only results in a small force error, $\Delta q1$. However, the same Δv leads to a large force error, $\Delta q2$, for the stiffer specimen. Therefore, it is not suitable to conduct DHS for stiff specimens.

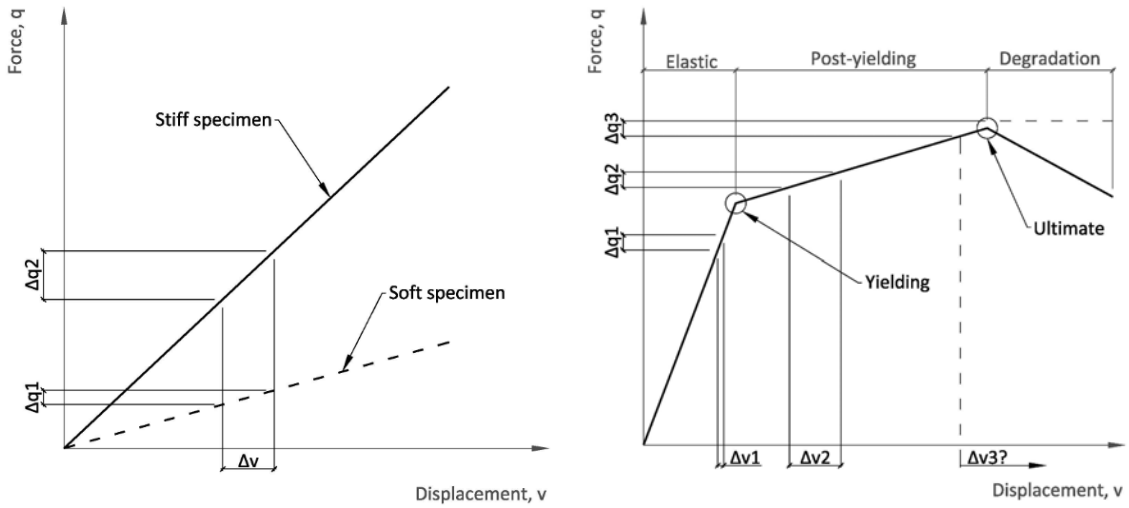

(a) Issue with DHS (b) Issue with FHS

Figure 4.2 Stiffness effect on DHS and FHS

Figure 4.2(b) shows the force-displacement relationship of an experimental sub-assembly that experiences yielding and finally degradation. In this example, it is assumed that a hydraulic servo actuator has small control errors in force, such as $\Delta q1$, $\Delta q2$, and $\Delta q3$. Assuming the magnitude of these control errors are the same, i.e. $|\Delta q1| = |\Delta q2| = |\Delta q3|$, the resulting errors in displacement are quite different. During the elastic stage, the force control error, $\Delta q1$, results in small displacement error, $\Delta v1$. This supports the argument to use FHS to test stiff specimens. However, after yielding, the small force control error, $\Delta q2$, can result to a large displacement error, $\Delta v2$. This could cause excessive damages to the

specimen and incorrect hysteresis loop. During degradation phase, an actuator simply cannot track increasing force signals. Hence, it is physically not possible to control via force. Therefore, FHS is not suitable for specimens with drastic changes in stiffness.

The ideal HS should take advantages of both DHS and FHS. A new SHS algorithm is proposed as presented in Figure 4.3. SHS starts a HS test using the force-based control (FC) algorithm when the specimen is elastic. After yielding, SHS switches to the displacement-based control (DC) algorithm. During load reversals, SHS will switch back to the FC algorithm if the unloading stiffness is similar to the initial stiffness. Otherwise, the DC algorithm will continue. The proposed switch control (SC) law improves the robustness of HS by combining the advantages of both the DC and FC algorithms.

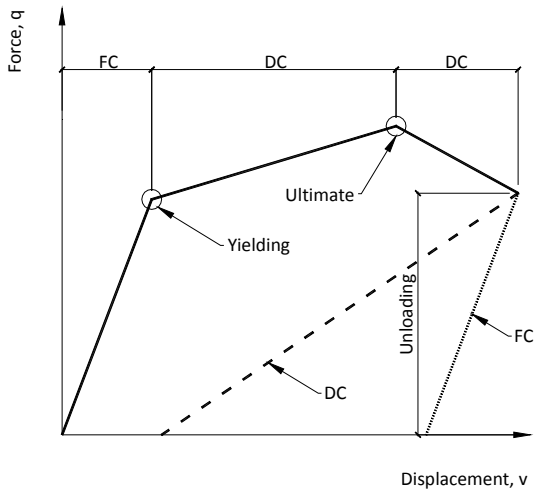

Figure 4.3 Switch control law

The effectiveness of SHS depends on the algorithm's ability to detect stiffness changes in an experimental sub-assembly. To achieve this, a second-order Langrage polynomial [Burden and Faires 2001] is used to fit the three previously converged data. Then, the tangent stiffness of the experimental sub-assembly is estimated as the derivative of the Langrage polynomial evaluated at the last converged data. This process is illustrated in Figure 4.4(a). If this tangent stiffness were less than a portion of the initial stiffness (i.e. 80% of the initial stiffness), SHS will automatically switch to use the DC algorithm. Within the same time step of integration, the experimental sub-assembly can also undergo changes in stiffness. SHS

uses the same technique to determine and monitor the change in tangent stiffness. The only difference is that instead of using previously converged data, the three previously tried data within the same time step are used. This is illustrated in Figure 4.4(b). This switch law avoids a hydraulic actuator controller to implement force commands which could potentially damage or degrade the experimental sub-assembly. SHS not only improves numerical convergence, but also increases the stability and safety of HS tests.

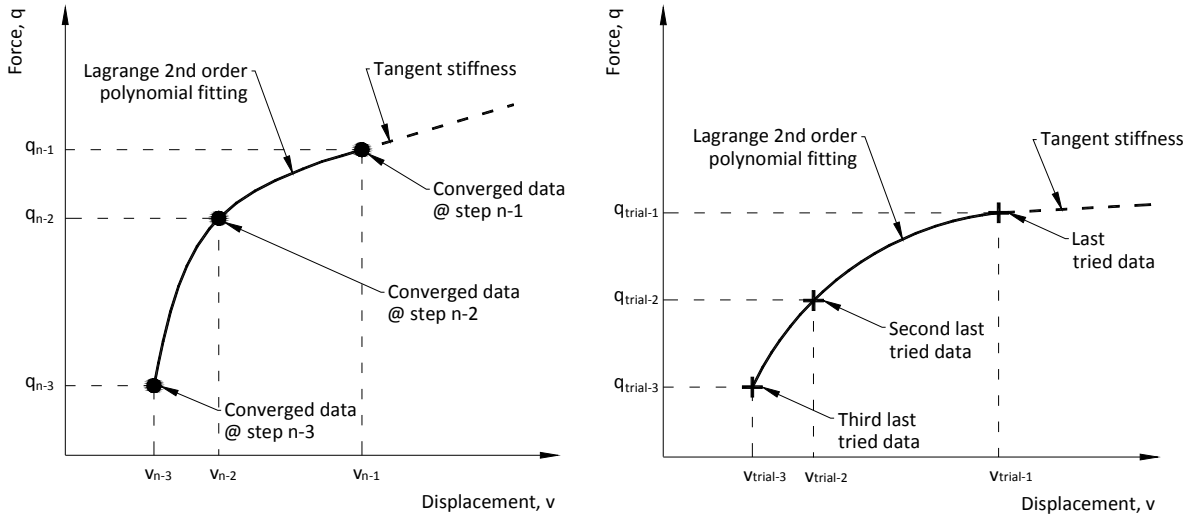

(a) Before entering a time step (b) After entering a time step

Figure 4.4 Stiffness detection

4.4 Experimental validation

A simple one-storey one-bay prototype model as shown in Figure 4.5(a) is used to validate the proposed SHS. This model consists of a metallic yielding damper (MYD) to dissipate earthquake energy, as well as an elastic moment frame to prevent collapse in the case of MYD failure. The prototype model is assumed to have pinned foundation and lumped masses on the nodes. DHS, FHS, and SHS are conducted at the University of British Columbia using the ground motion record from the 1994 Northridge earthquake as presented in Figure 4.5(b).

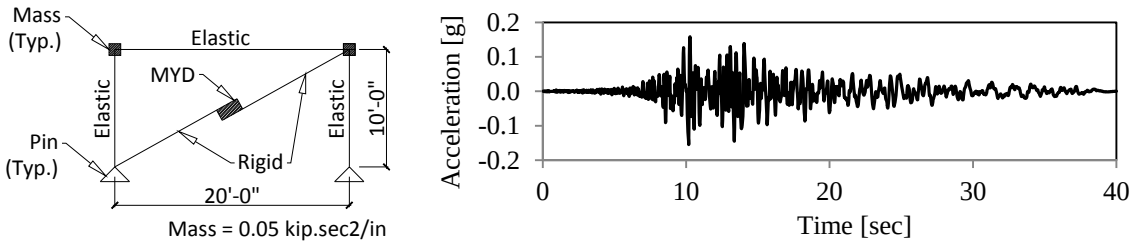

(a) Concentrically braced moment frame

(b) Northridge earthquake ground motion record (NGA #968)

Figure 4.5 Hybrid simulation parameter

For the various types of HS, the beam and columns are the analytical sub-assembly, while the force-deformation response of the MYD is measured experimentally using the setup shown in Figure 4.6. This setup uses a hydraulic servo actuator which can be controlled using either displacement or force commands. The actuator moves the loading beam which is supported on smooth rollers. The displacement and force feedbacks of the MYD are measured using the linear variable differential transformer (LVDT) and load cell mounted on the actuator, respectively.

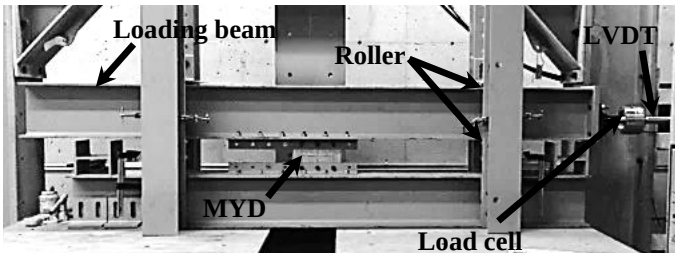

Figure 4.6 Experimental sub-assembly

Figure 4.7(a) and Figure 4.7(b) show zoom-in plots of the MYD displacement and force response histories recorded during the earthquake excitation, respectively. In the early stage of the excitation up to approximately 6 seconds, the responses are small and the MYD remains elastic. Up to this loading stage, the DHS overestimates the displacement and force responses when compared to the numerical simulation, as well as to the FHS and SHS. This shows that the DHS is not suitable to test experimental sub-assemblies with high stiffness. On the other hand, the FHS and SHS are very comparable to the numerical simulation up to this loading stage. However, at approximately 6 seconds into the excitation, the MYD starts

to yield. In FHS, the trial force exceeds the resistance of the MYD. Hence, it fractures the MYD. Figure 4.7(c) shows the MYD tested using FHS. The fracture of the MYD causes numerical non-convergence that terminates the FHS test. On the other hand, at around this time of the excitation, SHS switches to the DC algorithm and continues to perform well after the MYD has yielded. Figure 4.7(d) shows the MYD tested using SHS. This investigation proves that the proposed SHS is more ideal to test an experimental sub-assembly with large stiffness changes. SHS utilizes the FC algorithm during the elastic state of an experimental sub-assembly and switches to the DC algorithm after yielding. It should be noted that although SHS utilizes the DC algorithm after yielding, the MYD response time histories after 6 seconds are very different from those by DHS. The reason is that DHS has caused incorrect hysteresis loops during the elastic state and softened the MYD. Consequently, it affects the post-yielding behaviour of the MYD.

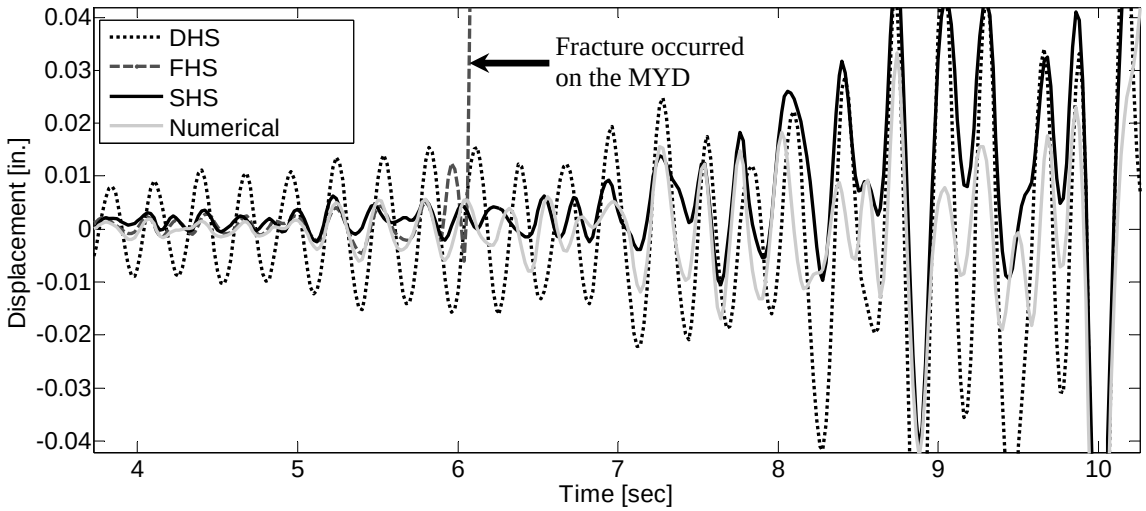

(a) Displacement time history

Figure 4.7 Experimental study of DHS, FHS, and SHS

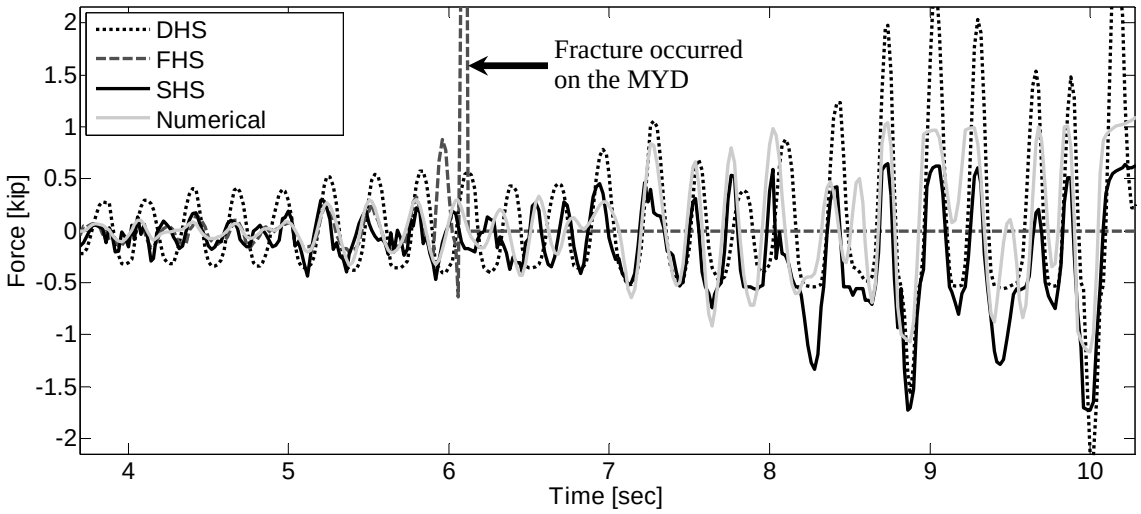

(b) Force time history

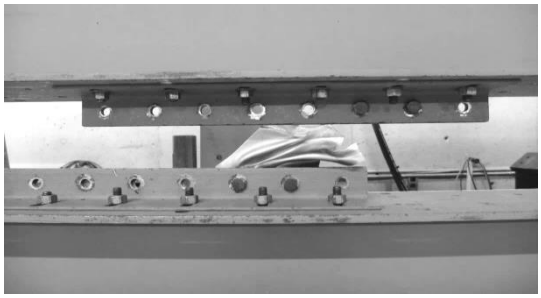

(c) FHS

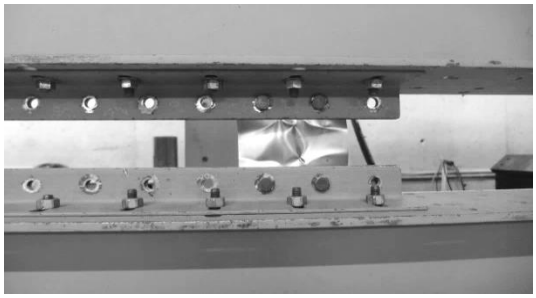

(d) SHS

Figure 4.7 Experimental study of DHS, FHS, and SHS

As presented in Figure 4.4, the switching between the DC and FC algorithms is based on the tangent stiffness of an experimental sub-assembly. For this test, the switch threshold is selected to be 80% of the specimen initial stiffness. When the tangent stiffness is less than 80% of the initial stiffness, the DC algorithm is used. Otherwise, the FC algorithm is used. The tangent stiffness is calculated based on the previous three force-displacement data collected by the load cell and LVDT. Figure 4.8 shows the control algorithm implemented to obtain the force-displacement relationship of the specimen at a given time step of the ground motion excitation. Before yielding, the specimen is elastic and hence, the test is conducted with the FC algorithm (Figure 4.8(a)). After yielding, the test switches to and continues with the DC algorithm (Figure 4.8(b)) because the tangent stiffness of the specimen during unloading and reloading does not exceed 80% of the initial stiffness.

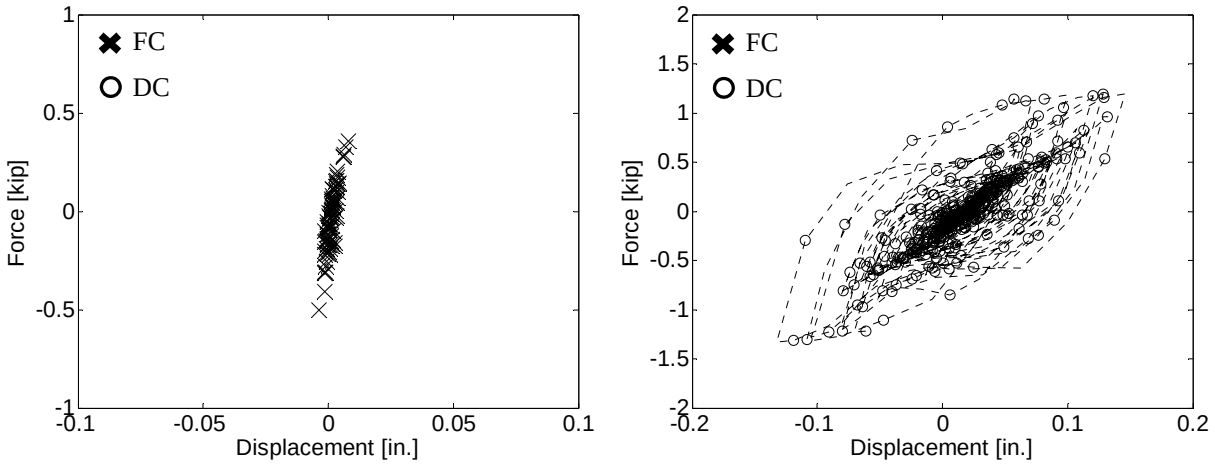

(a) Before yielding (b) After yielding

Figure 4.8 Switching of control algorithm

4.5 Summary

HS is a testing technique to study the nonlinear dynamic behaviour of a structural system without physically constructing the entire structure and testing it on a shake table. The structure is separated into analytical and experimental sub-assemblies. HS models the former in a computer and tests the latter in a laboratory. The response of the structure to an earthquake is simulated with live laboratory feedback. Such a testing technique saves time and labour. More importantly, HS is the ideal validation tool for the development of earthquake resilient fused structures where structural fuses are the yielding elements and suitable candidates of the experimental sub-assembly. Traditional HS is displacement-based where numerical integration schemes use trial displacements to check the equilibrium on the equation of motion. Such schemes are easy to implement in a laboratory because hydraulic servo actuators are typically displacement controlled. However, when DHS is used on stiff experimental sub-assemblies, a small actuator control error in displacement can result to a large error in force measurement. This causes incorrect hysteresis loops. In the extreme case, this can prematurely yield and damage a specimen. In this chapter, a finite element force-based algorithm is proposed. This algorithm uses trial forces at the local DOFs instead of trial displacements at the global DOFs. To ensure a structural system is compatible and in equilibrium, a combined equilibrium equation with compatibility conditions at each time step is solved simultaneously. Different from the previously published FHS algorithms, the

proposed FHS algorithm utilizes the finite element approach. It can test complex structures using trial forces and sub-structure techniques in a non-real-time environment. A one-storey one-bay concentrically braced moment frame is used to compare the performance of DHS and FHS. The result shows that the proposed FHS is superior to the traditional DHS when the stiffness of a specimen is high. FHS minimizes control errors and avoids incorrect hysteresis loops. It is recognized that a stiff sub-assembly eventually softens after yielding. FHS may be unstable or difficult to converge once the stiffness reduces. To address this deficiency, a switch control law is developed in this chapter to switch between the proposed FC algorithm and traditional DC algorithm. The switch to DC occurs when a reduction in stiffness is detected in the experimental sub-assembly. SHS combines the advantages of both DHS and FHS to examine a specimen undergoing changes in stiffness. With the same braced frame, the result proves that the proposed SHS has the required robustness to perform efficient and accurate simulations over an entire loading history, i.e. before and after the yielding of a stiff experimental sub-assembly. SHS not only improves numerical convergence, but also increases the safety of HS tests.

Chapter 5
Experimental Program

Chapter 2 has introduced an equivalent energy design procedure (EEDP) for fused seismic force resisting systems (SFRSs). This practical and non-iterative procedure allows engineers to design a fused system with multiple performance objectives corresponding to various seismic hazard levels. Chapter 3 has developed a fused SFRS named fused truss moment frame (FTMF) that can be easily designed using EEDP. This frame is earthquake resilient because it uses replaceable structural fuses as the primary SFRS to provide rapid return of occupancy. In addition, it has moment resisting frames as the secondary SFRS to prevent structural collapse. Chapter 4 has proposed an efficient and reliable switch-based hybrid simulation (SHS) to examine the nonlinear dynamic behaviour of a fused SFRS. In SHS, a structural fuse is designated as the experimental sub-assembly, while the remaining structure is modelled as the analytical sub-assembly. The objective of this chapter is to verify, by means of SHS from Chapter 4, that a one-storey one-bay FTMF similar to that from Chapter 3 and designed using EEDP from Chapter 2 can indeed exhibit multiple performance objectives as intended when subjected to different earthquake shaking intensities. In this chapter, Section 5.1 provides a detailed description of the structural testing facility. SHS is conducted in Section 5.2 to study the structural responses of the FTMF that uses a proprietary buckling restrained brace (BRB) as its structural fuse.

5.1 Structural testing facility

The structural testing facility will be described in terms of laboratory in Section 5.1.1 and controller in Section 5.1.2. The former includes the testing facility and mechanical hardware, while the latter comprises the control framework and data acquisition.

5.1.1 Laboratory

The Structural Laboratory in the Department of Civil Engineering at the University of British Columbia (UBC) is one of the preeminent institutes for earthquake engineering research. It consists of a 450m^2 high-head room as shown in Figure 5.1(a). The strong floor has a footprint of 9.0m by 22.0m, while the 4.9m high L-shaped strong wall has a footprint of 9.3m by 4.3m. The Laboratory can accommodate large-scale structural components and sub-assemblies. The hydraulic power unit is provided by the MTS Systems Corporation as shown in Figure 5.1(b). The model number is 506.61, and serial number is 110. The unit is located in the basement of the Laboratory and capable to supply 70gpm of hydraulic fluid at 3000psi working pressure. The hydraulic service manifold is also provided by the MTS Systems Corporation as shown in Figure 5.1(c). The model number is 293.22A-12, and serial number is 10183602. The manifold is located by the strong wall and has dual stations. It regulates hydraulic pressure for precise servo valve control as well as minimizes the effects of rapid application and removal of high pressure to a servo valve. In short, the manifold distributes the hydraulic fluid from the hydraulic power unit to a servo valve which then controls the movement of a hydraulic servo actuator shown in Figure 5.1(d). The actuator is again provided by the MTS Systems Corporation. The model number is 201.60, and serial number is 10375076A. The actuator is equipped with a Temposonics linear displacement transducer that has a stroke capacity of 20 inches and a load cell that has compression and tension capacities of 228 kips and 146 kips, respectively.

(a) Strong floor and wall (b) Hydraulic power unit

Figure 5.1 UBC Structural Laboratory

(c) Hydraulic service manifold

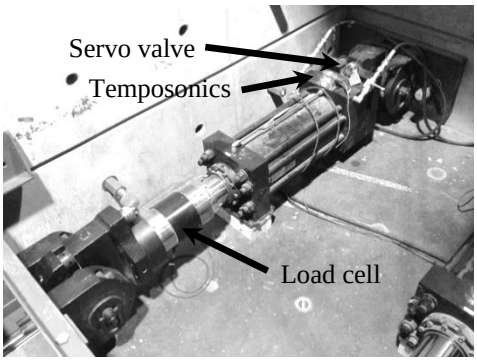

(d) Hydraulic servo actuator

Figure 5.1 UBC Structural Laboratory

As the actuator moves, it engages the UBC Smart Structure Testing Machine as shown in Figure 5.2. The Machine primarily consists of a loading carriage between the actuator and BRB. The purpose of the carriage is to apply pure axial forces onto a specimen and to protect the actuator at extreme loading conditions. The carriage is mounted on floor tracks and unidirectional bearings to minimize the effects of friction. Six bearings of one kip compression capacity each are installed under the carriage. Steel wheels at the sides and top are used to guide the carriage to ensure its unidirectional movement. Side steel plates and top steel angles are placed to provide carriage stability against any accidental misalignment due to fabrication and installation as well as during testing. Thru steel pins are used at both ends of the BRB as connections to the loading carriage and reaction seat. This detail eliminates any bending moment generated at the connections. The structural design and fabrication drawings of the Machine are provided in Appendix E. The industry sponsors include George Third & Son, Custom Plate & Profiles, Pacific Bolt Manufacturing Ltd., Canadian Institute of Steel Construction, and StarSeismic.

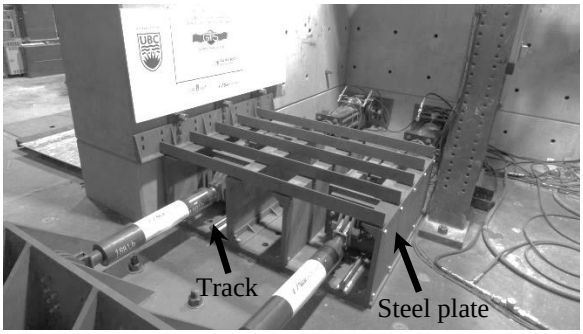

(a) Overall – front

(b) Overall – side

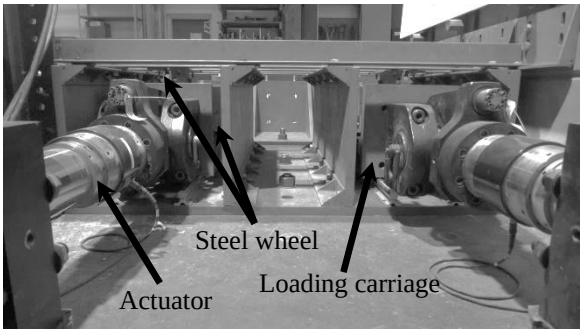

(c) Hydraulic servo actuators

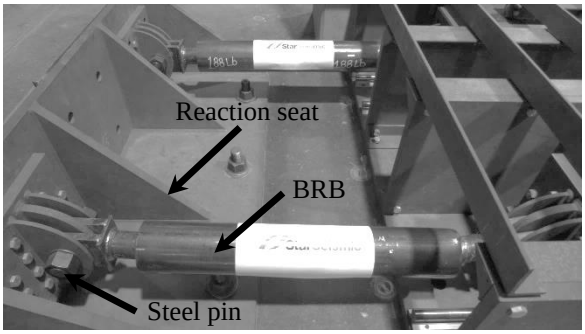

(d) Buckling restrained braces

Figure 5.2 UBC Smart Structure Testing Machine

5.1.2 Controller

A hierarchical control framework is adopted in this chapter to control the actuator. This framework is a form of control systems to handle complex control problems by decomposing them into smaller sub-problems and re-assembling their solutions via a hierarchical tree. Command signals to be achieved flow down the hierarchical tree from a high-level controller to one or multiple low-level controller(s), whereas command results flow back up the tree from the low-level controller(s) to high-level controller. The framework has been widely used to handle control challenges in different fields such as aerospace, robotic, and process industries. It has also recently been applied to earthquake engineering to control shake tables [Yang *et al.* 2015]. The framework assigns specific tasks to each level of controllers to ease the development, implementation, and adaptability of advanced testing techniques such as SHS in a laboratory.

The job of a low-level controller in the hierarchical control framework is to receive a command signal, either in displacement or force, from a high-level controller and accurately

implement it through a closed loop control as shown in Figure 5.3. The error in the figure is calculated as the difference between a command signal and displacement or force feedback measured by a displacement or force sensor, respectively. To correct this error, a traditional proportional-integral-derivative (PID) controller is utilized to determine the voltage required to move an actuator. Typically, this voltage signal goes through a voltage-current converter to control the spool inside a servo valve. The position of the spool determines the amount of hydraulic oil into the cylinder barrel of an actuator. The oil in turn pushes or pulls on the piston to move the cylinder rod of an actuator. Finally, the rod achieves the command signal onto a specimen to provide displacement or force feedback. The control strategy is termed closed loop because feedback is used to correct error.

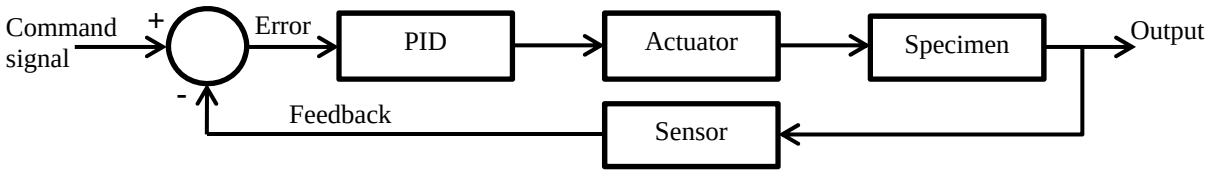

Figure 5.3 Closed loop block diagram of low-level controller

For a low-level controller to perform, a data acquisition system as shown in Figure 5.4 is required to process all sensor signals. The Temposonics linear displacement transducer uses 5V excitation. It produces single ended analog signals that are filtered by a 50Hz low-pass filter with a gain of 0.5. The load cell needs 10V excitation. It produces Wheatstone bridge analog signals that are filtered by a 1.6kHz low-pass filter with a gain of 100.

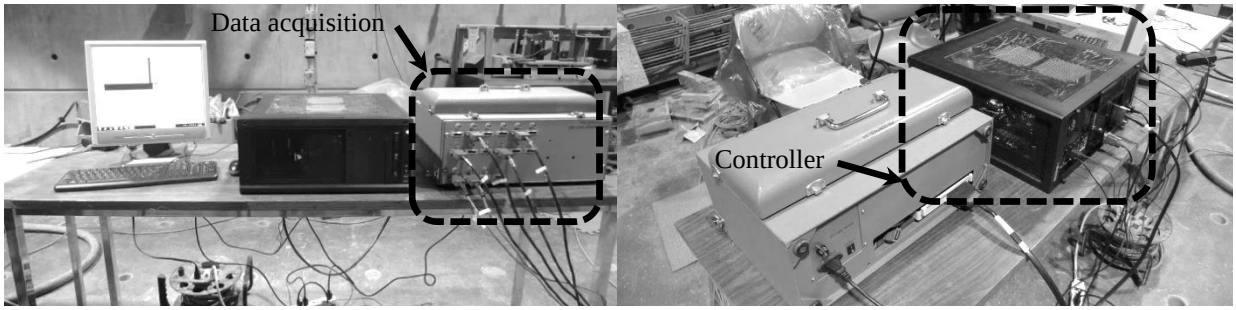

(a) Front view (b) Rear view

Figure 5.4 Advanced Control Testing System

The job of a high-level controller in the hierarchical control framework is to generate command signals, either in displacement or force. Such a controller can be as simple as a function generator that produces step, ramp, or sinusoidal signals to perform component testing. In the case of hybrid simulation, a high-level controller can be the displacement-based, force-based, or switch-based control algorithms explained in Chapter 4.

5.2 Hybrid simulation

Prior to implementing the innovative earthquake resilient FTMF proposed in Chapter 3 in practice, it is imperative to validate it through testing. Chapter 4 has demonstrated that SHS is an economical and robust experimental technique to study fused SFRSs. Hence, it is utilized to validate the proposed FTMF. Section 5.2.1 and Section 5.2.2 provide the setup and parameter of the SHS conducted on a simple one-storey one-bay FTMF prototype building. The results are given in Section 5.2.3. The design of the prototype using EEDP is given in Appendix F.

5.2.1 Sub-assembly setup

The first step to conduct hybrid simulation is to identify the analytical and experimental sub-assemblies. Figure 5.5(a) shows the FTMF under investigation, and Figure 5.5(b) gives the model element number for each of the structural members.

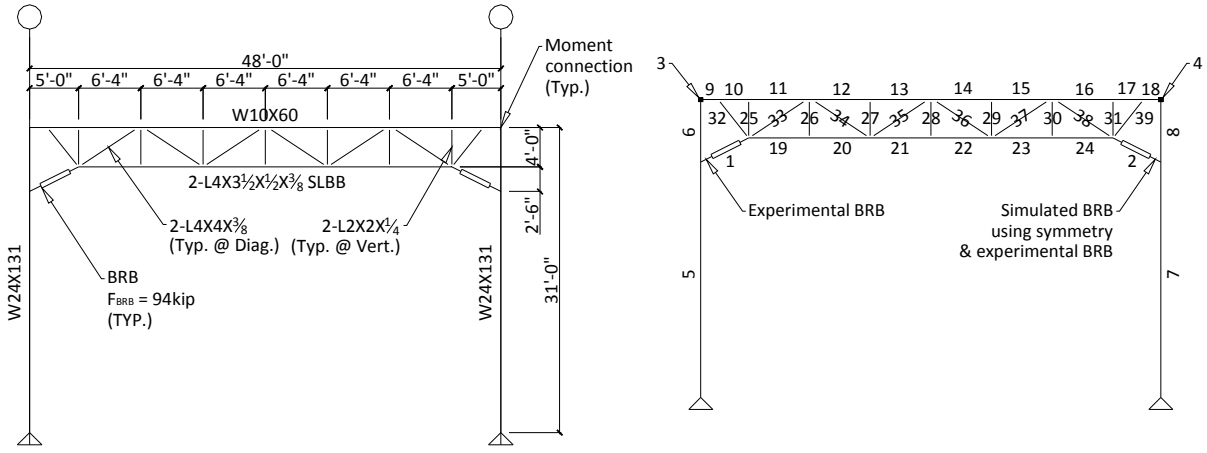

(a) Elevation view (b) Model element number

Figure 5.5 One-storey one-bay FTMF designed by EEDP

The left-hand side BRB whose element number is 1 is chosen as the experimental sub-assembly because this structural fuse is newly developed by StarSeismic. As a proprietary product, the BRB internal structure and mechanism cannot be disclosed. Hence, its force-deformation relationship is unknown and cannot be modelled effectively. The remaining system is designated as the analytical sub-assembly. Due to the limited number of available specimen from StarSeismic, the right-hand side BRB has to be a part of the analytical sub-assembly in order to conduct three tests and study the FTMF responses under three earthquake shaking intensities. The behaviour of the right-hand side BRB during a ground motion excitation is simulated by live updating from the experimental sub-assembly. This simulation is valid due to structural symmetry.

Table 5.1 lists the model parameters for all the elements. The primary SFRS consists of elements 1 and 2, while the secondary SFRS are elements 3 and 4. The force-deformation relationship of the primary SFRS is unknown and hence determined in the laboratory. The moment-rotation response of the secondary SFRS is assumed to be elastic-plastic with yielding moment, M_y, and rotational stiffness, E_{MC}, defined based on the calibrated zero-length element from Chapter 3. The columns are elements 5 to 8, and truss chords are elements 9 to 24. These are modeled as elastic beam-column elements. The truss webs are elastic truss elements whose element numbers are 25 to 39. The area, A, and moment of inertia, I, of these elastic elements are based on the design sections shown in Figure 5.5(a).

Table 5.1 Model element parameters

Element number	Element type	Numerical model	Parameters
1	Experimental BRB (experimental sub-assembly)		
2	Simulated BRB (updated using symmetry & experimental BRB data)		
3-4	Zero-length	Rigid axial & shear, Elastic-plastic moment	M_y = 1100kip-in E_{MC} = 398618kip-in
5-8	Beam-column	Elastic	A = 38.5in^2 & I = 4020in^4
9-18	Beam-column	Elastic	A = 17.6in^2 & I = 341in^4
19-24	Beam-column	Elastic	A = 7.0in^2 & I = 7.5in^4
25-31	Truss	Elastic	A = 1.9in^2
32-39	Truss	Elastic	A = 5.7in^2

The laboratory and controller described in Section 5.1 are used to conduct SHS. Figure 5.6(a) shows the left-hand side BRB of the FTMF in position of the UBC Smart Structure Testing Machine. This represents the experimental sub-assembly. Both ends of the BRB are pinned connected to the Machine. The pin in Figure 5.6(b) is attached to the reaction seat. The pin in Figure 5.6(c) is connected to the loading carriage. Two displacement sensors parallel to the BRB are used. Figure 5.6(d) shows the linear pot attached directly to the BRB shaft. This measures the BRB core displacement. Figure 5.6(e) shows the linear pot attached to the thru pin. This measures the displacement between the pins. Both sensors use swivels at the attachments so that they remain level throughout the test. A third displacement sensor is the Temposonics linear displacement transducer located on the actuator. This sensor measures the movement of the actuator.

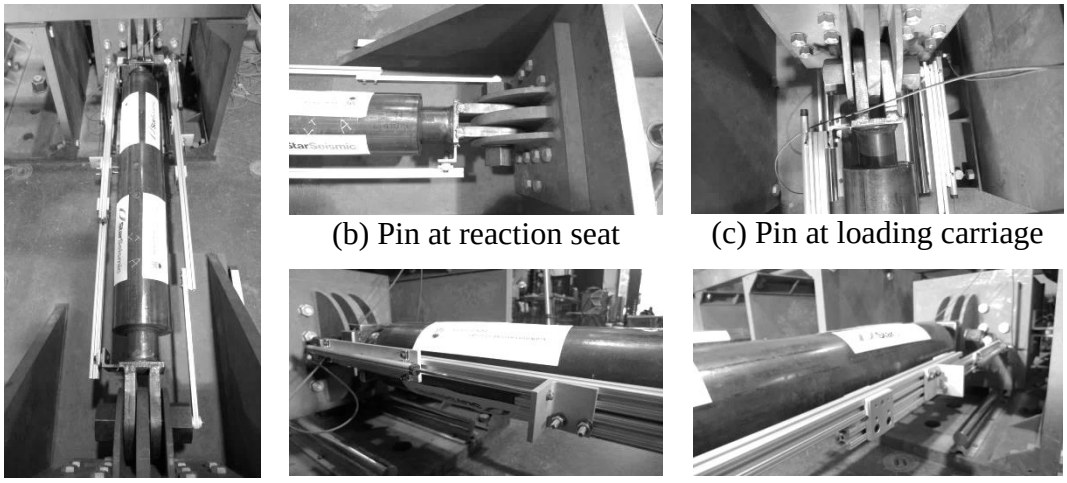

(a) Overall (b) Pin at reaction seat (c) Pin at loading carriage (d) Core displacement (e) Pin displacement

Figure 5.6 Setup of experimental sub-assembly

5.2.2 Simulation parameter

The second step to conduct hybrid simulation is to determine matrix parameters needed in the displacement-based and force-based algorithms as explained in Chapter 4. In both algorithms, it is necessary to transform displacement between the global and local degree-of-freedom (DOF) using a compatibility matrix. The matrices for truss, beam-column, and zero-length elements are derived in Appendix G. Once the compatibility matrices are determined for all the elements, they are assembled to obtain the system compatibility matrix, $[A_f]$.

According to Table 5.1, there are 17 truss elements, 20 beam-column elements, and 2 zero-length elements in the FTMF. These elements result in 83 local DOFs. Figure 5.5(b) shows that the FTMF has 24 nodes. Except the nodes at the pinned foundation which have 1 global rotational DOF, each node has 3 global DOFs. These nodes result in 68 global DOFs. Therefore, $[A_f]$ of the FTMF has a size of 83 by 68 to transform displacement from the local to global DOF.

The basic stiffness matrix is used to relate displacement to force in the local DOF. The matrices for truss, beam-column, and zero-length elements are given in Appendix G. Once the basic stiffness matrices are determined for all the elements, they are assembled to obtain the system stiffness matrix at the local DOF, $[K_s]$. Based on the elements of the FTMF as presented in Table 5.1, the size of $[K_s]$ is 83 by 83. Finally, the system stiffness matrix at the global DOF, $[K]$, can be calculated by the following equation to be a size of 68 by 68.

$$[K] = [A_f]^T \times [K_s] \times [A_f] \qquad \text{Equation 5.1}$$

Appendix G shows the available element force, q, that matches the available local DOF for each element type. With the 39 elements of the FTMF in Figure 5.5(b), Table 5.2 provides the number assignment of each element force for all the elements. In total, there are 83 element forces. Since there are 68 global DOFs corresponding to 68 available equilibrium equations, the FTMF is statically indeterminate to the 15th degree. Therefore, 15 redundant forces need to be selected in order to create the primary structure and solve the system using the force-based algorithm. These forces are identified as bold text with dark shade in Table 5.2. Different selections can be made to conduct hybrid simulation. In the force-based algorithm, $[B_x]$ is known as the force influence matrix that relates the redundant forces to all the element forces. Each column vector of $[B_x]$ represents the 83 element forces in the primary structure due to a unit value of the corresponding component of the redundant forces with all the other components set to zero. Since there are 15 redundant forces in the FTMF, $[B_x]$ has a size of 83 by 15. $[B_i]$ is known as the equilibrium matrix of the primary structure. Each column vector of $[B_i]$ represents the 83 element forces in the primary structure due to a

unit force applied at the corresponding global DOF with the redundant forces set to zero. Since there are 68 global DOFs in the FTMF, $[B_i]$ has a size of 83 by 68.

Table 5.2 Element force assignment

El.	q1	q2	q3		El.	q1	q2	q3		El.	q1	q2	q3		El.	q1	q2	q3
1	1	-	-		11	27	28	29		21	57	58	59		31	***75***	-	-
2	2	-	-		12	30	31	32		22	60	61	62		32	76	-	-
3	3	4	5		13	33	34	35		23	63	64	65		33	***77***	-	-
4	6	7	8		14	36	37	38		24	66	67	68		34	***78***	-	-
5	9	10	11		15	39	40	41		25	***69***	-	-		35	***79***	-	-
6	12	13	***14***		16	42	43	44		26	***70***	-	-		36	***80***	-	-
7	15	16	17		17	45	46	47		27	***71***	-	-		37	***81***	-	-
8	***18***	19	20		18	48	49	50		28	***72***	-	-		38	***82***	-	-
9	21	22	23		19	51	52	53		29	***73***	-	-		39	83	-	-
10	24	25	26		20	54	55	56		30	***74***	-	-					

5.2.3 Simulation result

The near-field ground motion record of the 1999 Chi-Chi earthquake is selected for hybrid simulation. Figure 5.7(a) and Figure 5.7(b) show the time history and response spectrum of the acceleration record, respectively. Figure 5.7(b) also shows the design target spectrum which is the maximum considered earthquake shaking intensity at Berkeley based on ASCE/SEI 7-10 [2010]. The ground motion response spectrum is amplitude scaled to match the target. To account for modal elongation and higher modes, the ground motion is scaled to match in the period range between $0.2T$ and $1.5T$, where T is the fundamental period of about one second for the FTMF.

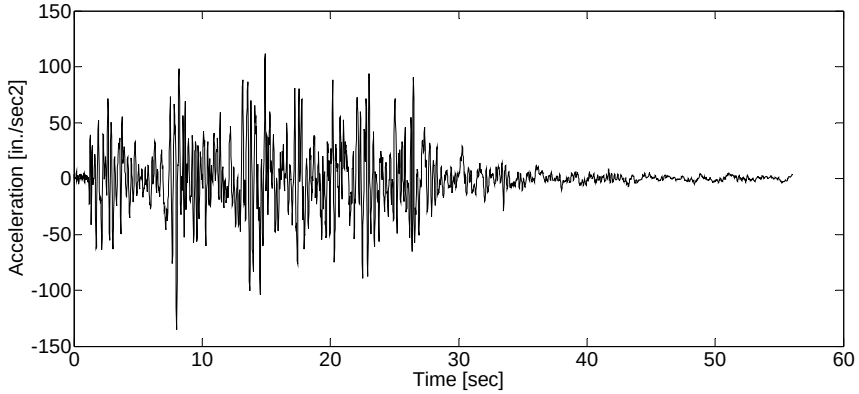

(a) Time history

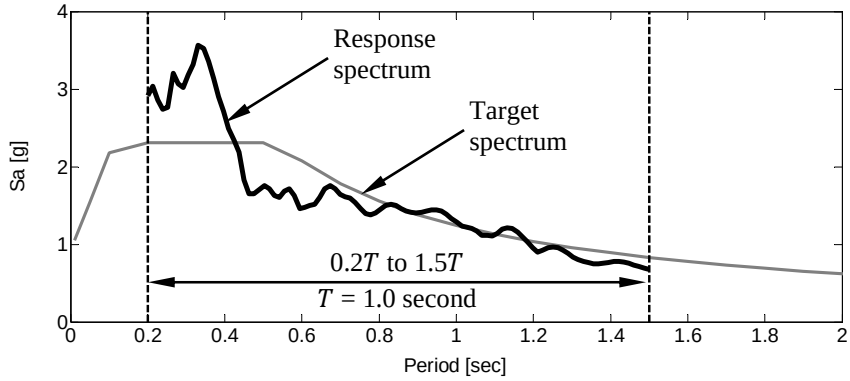

(b) Response spectrum

Figure 5.7 Ground motion record of 1999 Chi-Chi earthquake (RSN#1521, CHICHI-TCU089-E)

The FTMF is designed to have three performance objectives under three earthquake shaking intensities: 1) immediate occupancy (IO) under the service level earthquake (SLE); 2) rapid return (RR) under the design based earthquake (DBE); 3) collapse prevention (CP) under the maximum considered earthquake (MCE). To validate that the proposed FTMF can be efficiently designed using the proposed EEDP and perform as intended, the developed SHS is utilized to conduct full-scale hybrid simulation. Figure 5.8 shows the roof drift ratio (RDR) time history of the FTMF subjected to the ground motion presented in Figure 5.7(a). The motion is amplitude scaled to the three shaking intensities. According to EEDP, the performance target of RDR is 0.6%, 1.8%, and 2.8% under SLE, DBE, and MCE, respectively. These target RDRs are shown as dashed lines in Figure 5.8. Each SHS shows that the result RDR is bounded by the target RDR with only slight over-target for the case of SLE. In other words, the FTMF designed using EEDP can practically achieve the target

RDRs. Figure 5.9 shows the roof acceleration time history due to the three shaking intensities.

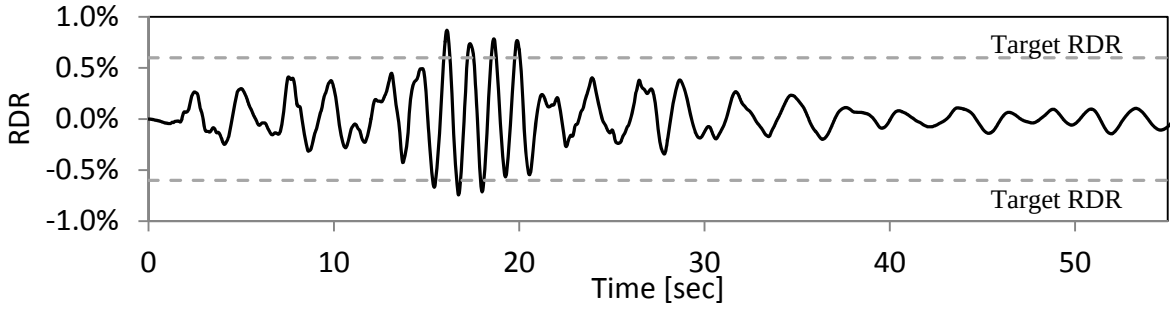

(a) SLE

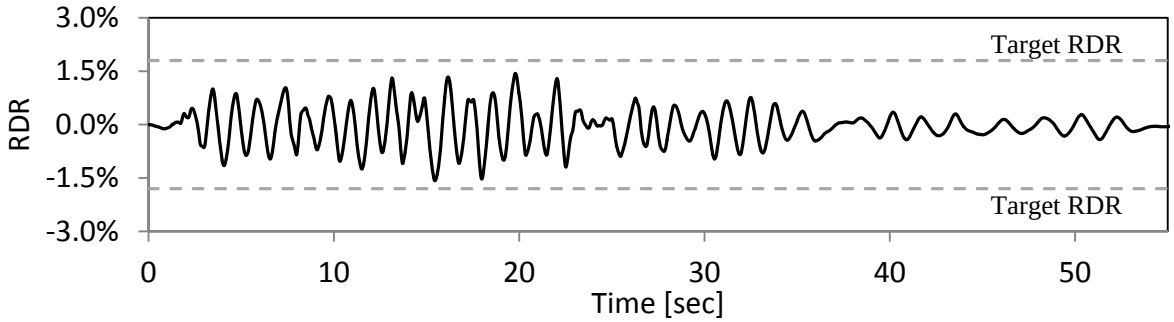

(b) DBE

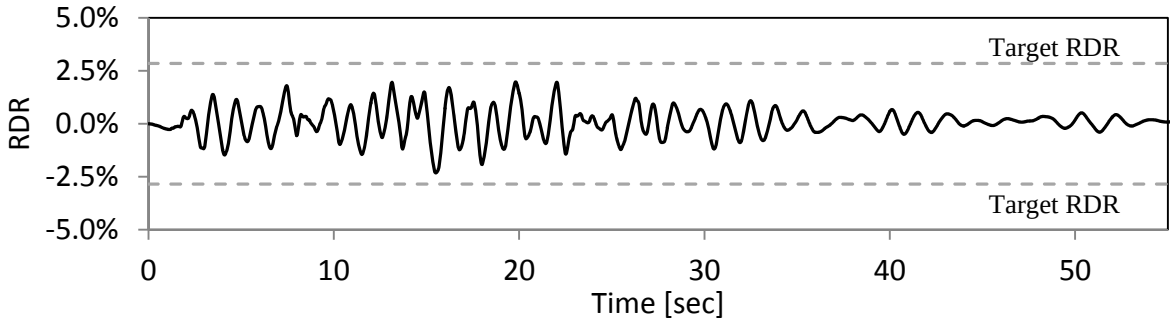

(c)MCE

Figure 5.8 Comparison of RDR

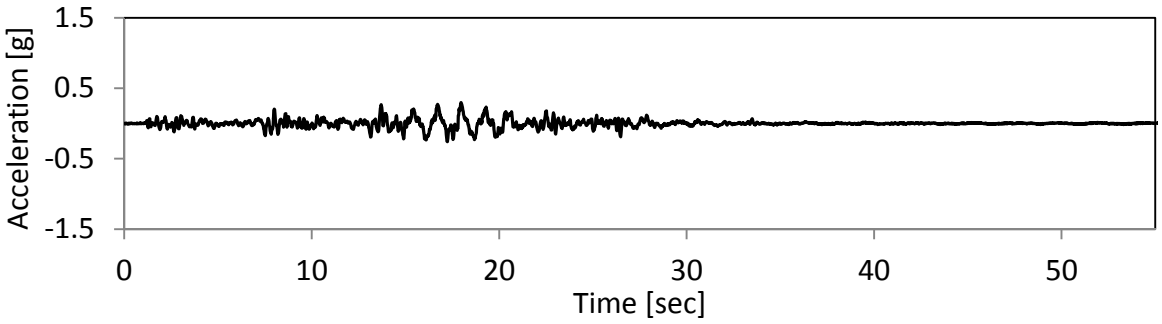

(a) SLE

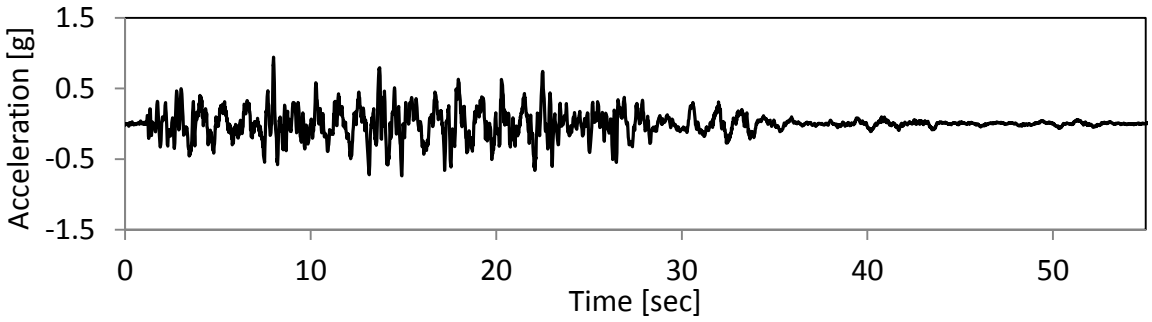

(b) DBE

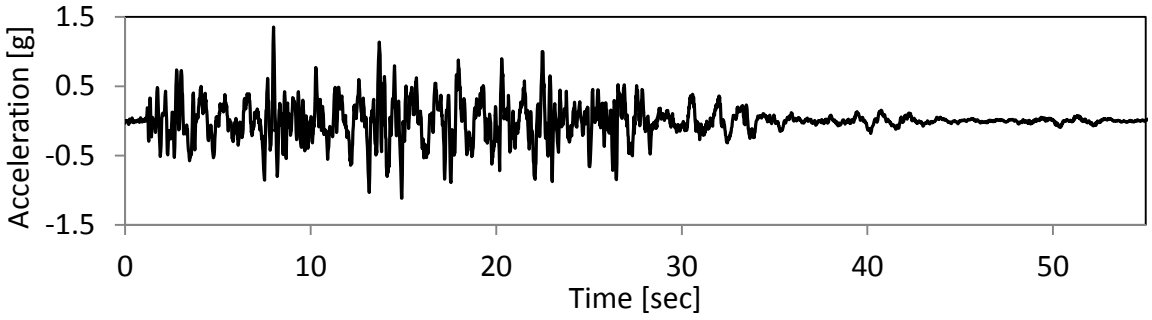

(c) MCE

Figure 5.9 Roof acceleration

The FTMF uses BRBs and moment connections (MCs) to resist lateral forces. The formal is the primary SFRS, while the latter is the secondary SFRS. During the frequently occurred earthquake, the FTMF is designed to achieve the IO performance objective. Figure 5.10(a) and Figure 5.10(b) show that, at the SLE shaking intensity, the BRB and MC remain elastic. In other words, the FTMF is damage-free to provide the IO performance objective. During the DBE shaking intensity, the BRB is designed to act as structural fuse and protect the remaining system from yielding. Figure 5.10(c) and Figure 5.10(d) show that the BRB has yielded while the MC remains elastic. After the earthquake, the BRB can be replaced to

achieve the RR performance objective. During the MCE shaking intensity, Figure 5.10(e) and Figure 5.10(f) indicate that both the BRB and MC are capable to dissipate earthquake energy without degradation. This satisfies the CP performance objective.

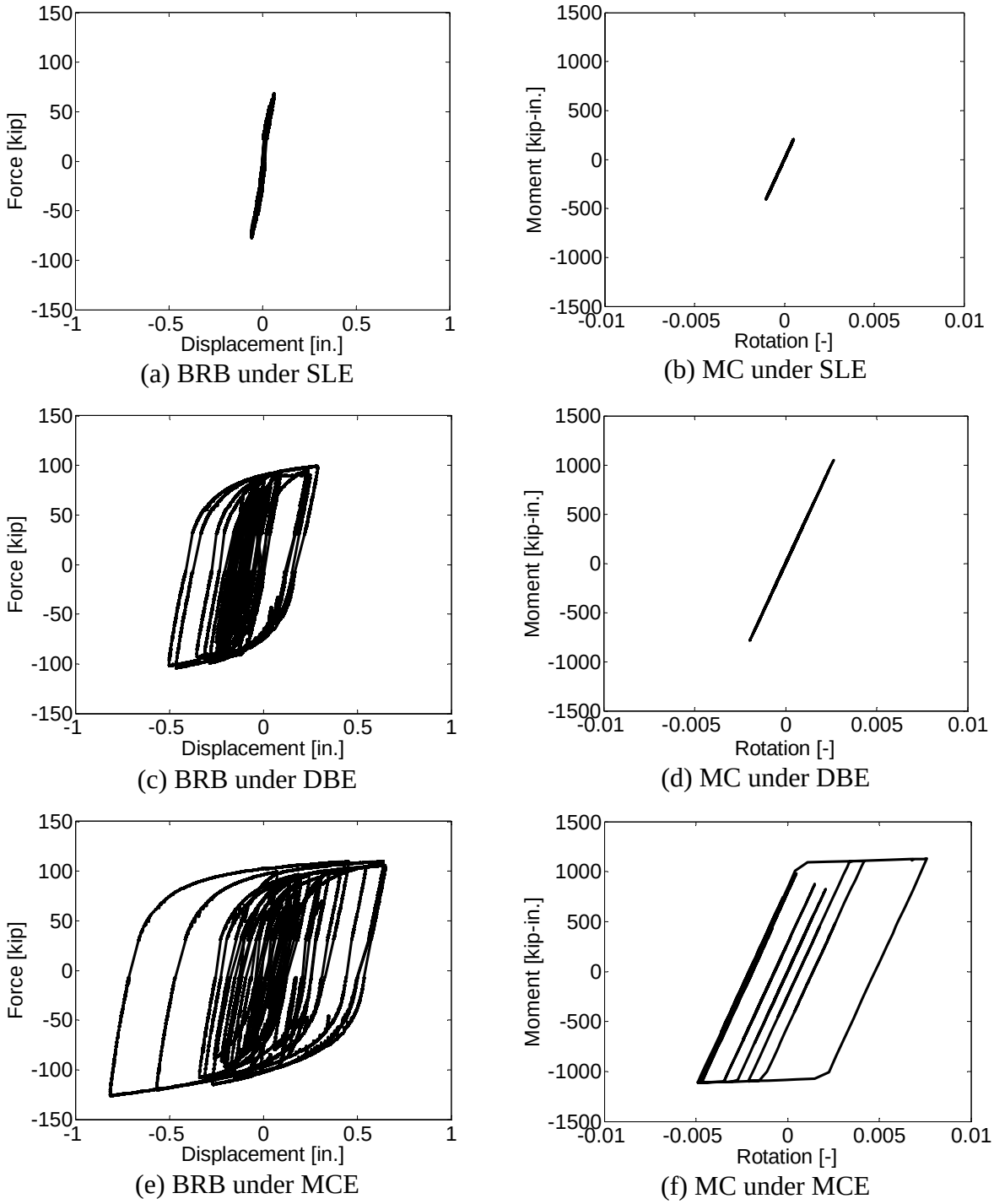

(a) BRB under SLE

(b) MC under SLE

(c) BRB under DBE

(d) MC under DBE

(e) BRB under MCE

(f) MC under MCE

Figure 5.10 Hysteresis of yielding elements

Figure 5.11 shows the maximum force demand capacity ratio (DCR) time history of the non-yielding members under the MCE shaking intensity. The capacity is defined by the nominal strength of the member per ANSI/AISC 360-10 [2010]. For the columns as well as truss top and bottom chords, axial-moment interaction is considered. To be thorough, the DCRs are obtained at various locations. For the columns, the ratios are calculated at the foundation, roof, as well as above and below the BRB connection. For the top and bottom chords of the truss, the ratios are determined at each panel point. For the web of the truss, each vertical and diagonal member is examined. According to the figure, all the DCRs are less than unity. This suggests that the non-yielding members indeed remain elastic and hence can be modeled as elastic elements.

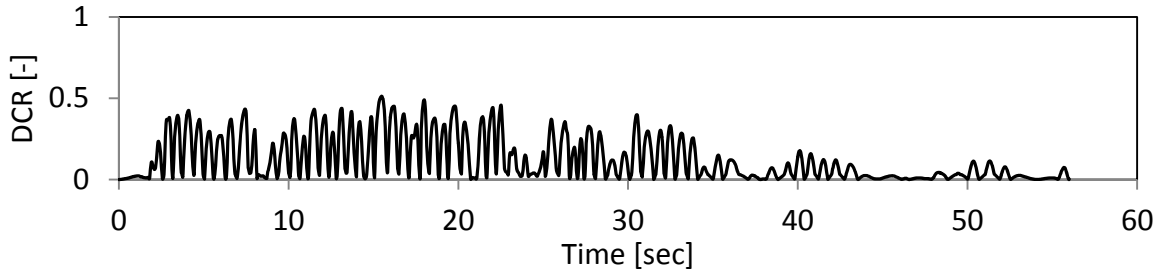

(a) Column

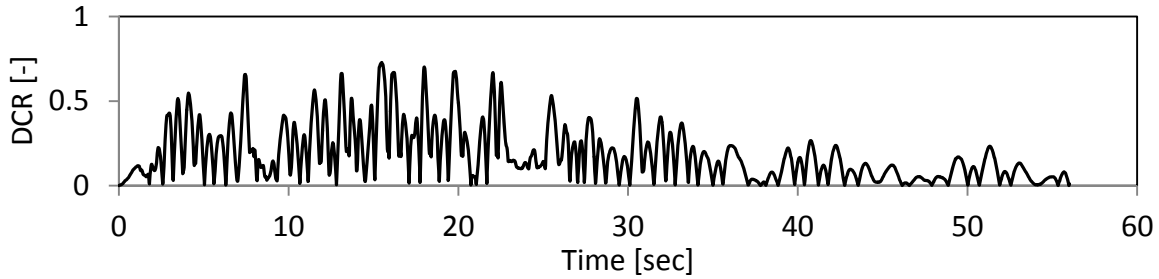

(b) Truss top chord

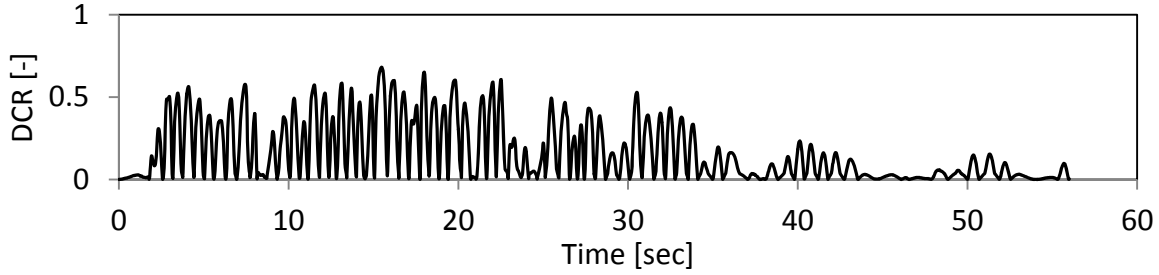

(c) Truss bottom chord

Figure 5.11 DCR of non-yielding elements under MCE

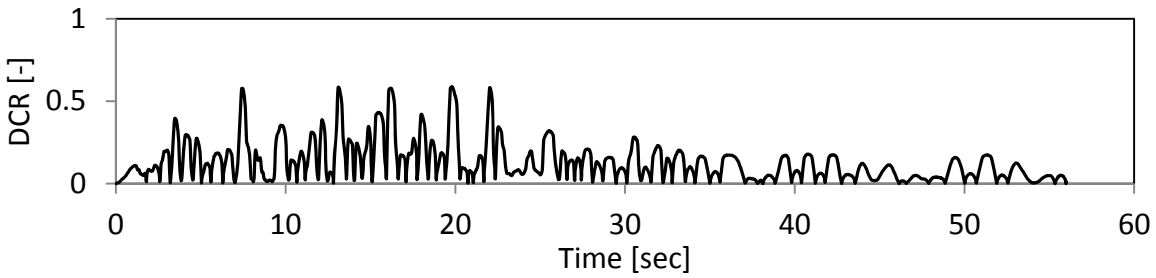

(d) Truss vertical web

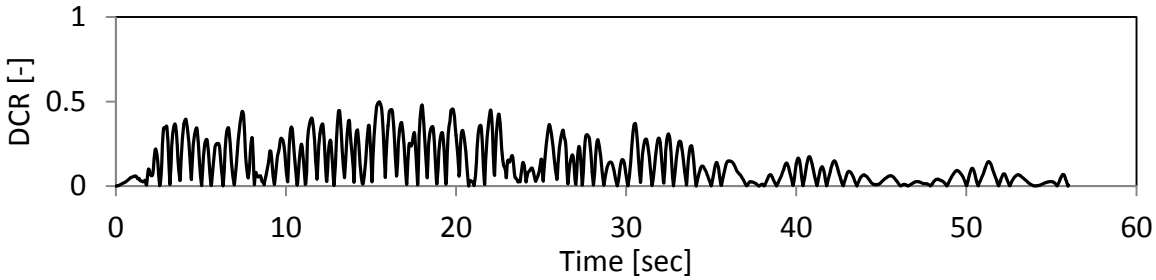

(e) Truss diagonal web

Figure 5.11 DCR of non-yielding elements under MCE

The hybrid simulation of the FTMF assigns the BRB as the experimental sub-assembly. Due to its high initial stiffness and stiffness reduction after yielding, displacement-based or force-based algorithm alone is not adequate for the BRB. Therefore, SHS is utilized to switch between these algorithms and provide robust hybrid simulation. SHS avoids incorrect hysteresis during the elastic phase of the BRB and eliminates actuator instability. As explained in Chapter 4, the switching is based on the tangent stiffness of an experimental sub-assembly. For this test, the switch threshold is selected to be 80% of the BRB initial stiffness. When the tangent stiffness is less than 80% of the initial stiffness, the displacement-based algorithm is used. Otherwise, the force-based algorithm is used. The tangent stiffness is calculated based on the previous three BRB force-displacement data collected by the load cell and linear pot.

Figure 5.12 shows the control algorithm implemented to obtain the force-displacement relationship of the BRB at a given time step of the test. During the SLE shaking intensity, the BRB is elastic, and hence the test is conducted with the force-based algorithm. During both the DBE and MCE shaking intensities, the test is generally conducted with the force-based

algorithm over the loading and unloading phases of the BRB. The tangent stiffness after yielding and during reloading opposite to the previous loading direction is typically less than 80% of the initial stiffness. Therefore, the displacement-based algorithm is implemented. It should be noted that the observed switching between the algorithms can only be generalized because the tangent stiffness is calculated using the data directly collected from the laboratory. Experimental data measured by sensors always contain noises, and hence, some unnecessary switching is expected. It can be minimized by improving sensors but may not be avoided entirely.

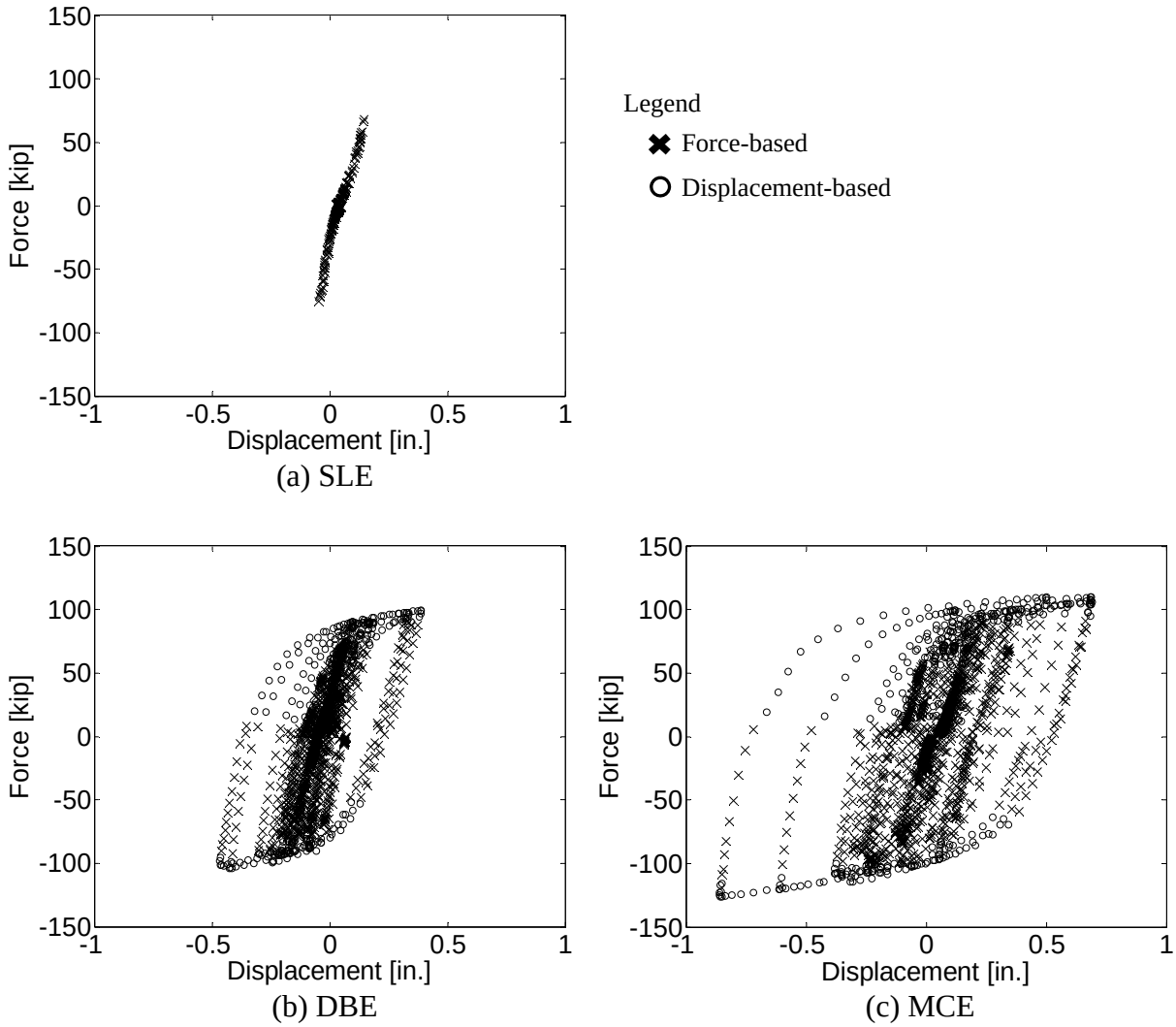

(a) SLE

(b) DBE

(c) MCE

Figure 5.12 Switching of control algorithm

5.3 Summary

Chapter 2 proposes EEDP as an alternative design procedure. Chapter 3 applies it to the innovative FTMF to demonstrate that a fused structure can be easily designed using EEDP and exhibit three performance levels under three earthquake shaking intensities. This chapter uses the robust and reliable SHS from Chapter 4 to experimentally examine the behaviour of the FTMF designed using EEDP. SHS is implemented in the University of British Columbia via a hierarchical control framework. The high-level controller consists of the numerical simulation to generate trial displacement or force commands. The low-level controller accurately implements these commands to obtain feedback of the experimental sub-assembly. The result shows that SHS can successfully verify the various target RDRs of the FTMF under different earthquake shaking intensities. In addition, SHS shows that the FTMF is damage free during the SLE shaking intensity. As the intensity increases to DBE, the structural fuse is activated to protect the remaining structure from damages. The fuse can be efficiently replaced after an earthquake to achieve resilience. At the MCE intensity, the secondary SFRS is engaged to prevent structural collapse. Throughout the three tests, SHS not only improves numerical convergence, but also increases the safety of HS tests. Therefore, the experimental program conducted in this chapter should be an essential part of the framework for researchers and engineers to develop future earthquake resilient fused structures.

Chapter 6
Conclusion

The previous chapters have presented an efficient design procedure and effective testing technique for an innovative earthquake resilient fused structure. This chapter discusses how each topic contributes to developing future fused structures and concludes the dissertation with future research suggestions.

6.1 Developing earthquake resilient fused structures

With an increasing trend to build resilient communities for future earthquakes, innovative resilient fused structures are being developed. These structures use structural fuses to dissipate earthquake energy. These fuses are designed to be efficiently repairable or replaceable without affecting the functionality of a structure. This dissertation aims to provide a consistent approach to design and validate earthquake resilient fused structures. It consists of the following: 1) an alternative design approach namely equivalent energy design procedure (EEDP) to obtain member sizes of a fused structure that satisfies system strength and ductility without iterations; 2) an experimental technique called switch-based hybrid simulation (SHS) to validate a fused structure designed using EEDP.

6.1.1 Design of earthquake resilient fused structures

The implementation of innovative earthquake resilient fused structures will not be possible unless there is a simple and practical design procedure. In this dissertation, EEDP is presented to design fused seismic force resisting systems (SFRSs). This procedure directly takes structural strength and ductility into consideration. It does not require an estimation of member sizes nor design iterations. It allows designers to select multiple performance

objectives at different earthquake shaking intensities. While the procedure is based on simple energy equivalence between inelastic and elastic systems, it recognizes the difference in energy dissipation between a system which is subjected to a monotonic pushover and that subjected to a cyclic dynamic load. This difference is addressed via energy modification factors developed using the responses of nonlinear single degree-of-freedom (DOF) systems through time history analysis. The detailed derivation and validation of EEDP is presented in this dissertation. To illustrate the implementation of EEDP, a fused truss moment frame (FTMF) is proposed and designed using EEDP to achieve multi-level performance objectives at different earthquake shaking intensities. A calibrated numerical model of the FTMF is constructed to conduct nonlinear dynamic analysis. As shown by the analysis, the EEDP designed FTMF can achieve the target roof drift ratios (RDRs) without an iterative design process. This implies significant time and cost savings to the engineering community. This also allows designers to select appropriate non-structural components that are capable to withstand the anticipated system deformations. The analysis results indicate that the FTMF can control the location and degree of damages to the designated elements. At the low level shaking intensity, the FTMF is damage free. The structural fuses start to yield at the median level shaking intensity to protect the remaining system. During severe shakings, the secondary SFRS are then activated to prevent building collapse. In addition, incremental dynamic analysis is performed to obtain the collapse fragility curve of the FTMF. Based on the methodology described in FEMA-P695, the proposed FTMF designed using EEDP has adequate seismic safety against collapse.

6.1.2 Validation of earthquake resilient fused structures

An essential step in developing an innovative earthquake resilient fused structure is validation via testing. Although full-scale shake table testing is the most comprehensive study of structural behaviour during a ground excitation, it is typically cost prohibitive to conduct such testing on a regular basis. Hybrid simulation (HS) is an innovative experimental technique which separates a complex structure into analytical and experimental sub-assemblies. Such a technique saves time and labour. Traditional HS is displacement-based (DHS), where numerical integration schemes use trial displacements to check the equilibrium on the equation of motion. However, when DHS is used on stiff experimental

sub-assemblies, a small hydraulic servo actuator control error in displacement can result to a large error in force measurement. This causes incorrect hysteresis loops. In the extreme case, this can prematurely yield and damage a specimen. In this dissertation, a finite element force-based HS (FHS) algorithm is proposed. This algorithm uses trial forces at the local DOFs instead of trial displacements at the global DOFs. To ensure a structural system is compatible and in equilibrium, a combined equilibrium equation with compatibility conditions at each time step is solved simultaneously. However, FHS may be unstable or difficult to converge once the stiffness of a specimen reduces. To address this deficiency, switch-based HS (SHS) is proposed. It combines the advantages of both DHS and FHS to examine a specimen undergoing changes in stiffness. A one-storey one-bay concentrically braced moment frame is used to prove that the proposed SHS has superior performance over DHS and FHS regardless of stiffness. SHS is then utilized to examine the seismic performance of the proposed FTMF. SHS successfully verifies that the FTMF designed using EEDP can achieve the various target RDRs under different earthquake shaking intensities. In addition, SHS shows that the FTMF is damage free during the low level shaking intensity. As the intensity increases to median, the structural fuse is activated to protect the remaining structure from damages. The fuse can be efficiently replaced after an earthquake to achieve resilience. At the maximum considered intensity, the secondary SFRS is engaged to prevent structural collapse. Throughout the three tests, SHS not only improves numerical convergence, but also increases the safety of HS tests.

6.2 Future research

Innovative earthquake resilient fused structures are building blocks to achieve earthquake resilient communities. The design procedure and validation technique developed in this dissertation provide a unified approach to research and implement such structures. This dissertation has demonstrated that the application of EEDP is simple so that it is practical for design offices. In addition, the setup of SHS is cost-effective so that full-scale testing can be routinely conducted in research facilities. The combined use of EEDP and SHS allows researchers and designers to obtain accurate dynamic responses and post-earthquake performances of a fused structure when subjected to ground shakings. The following is a list of suggested topics for future research and improvement:

1. The current EEDP is based on the dynamic responses of an equivalent single DOF system. It is most applicable to structures whose behaviour is dominated by the fundamental mode. This might not be the case for tall buildings. Future research should determine formulation adjustments and/or modification factors needed for EEDP to directly consider higher mode effects.
2. The current EEDP is applicable to earthquake resilient fused structures with a tri-linear force-deformation relationship. This relationship is decomposed into two bi-linear ones which are for the primary and secondary SFRSs. It is possible that either the primary or secondary system already has a tri-linear relationship. An example is concrete shear walls whose stiffness changes at concrete cracking in addition to steel yielding. Future research should expand EEDP so that it is applicable to structures with other force-deformation relationship.
3. The current EEDP is based on the primary and secondary SFRSs working in parallel and concurrently to provide resistance to earthquake loadings. It is possible to have the secondary system engaged or triggered only by the yielding of the first, i.e. the primary and secondary SFRSs act in series. Future research should determine formulation adjustments needed for EEDP to design structural systems with SFRSs in series.
4. The current energy modification factors used in EEDP are determined via nonlinear dynamic analysis. They have been validated using three different sets of seismic hazards. However, the data is still limited. Effects associated to long duration and fault mechanism are implicitly considered. Future research should conduct additional analysis to fine tune the factors and/or categorize them for each effect.
5. The current FHS algorithm is implicit and requires iterations. Therefore, it is not suitable to conduct real-time testing. Future research should develop explicit algorithms suitable for real-time testing and applicable to rate dependent experimental sub-assemblies.
6. The current SHS algorithm is capable to track and calculate tangent stiffness of multiple experimental sub-assemblies. Once a reduction in stiffness is detected in any one of the sub-assemblies, SHS switches to use the DHS algorithm for the entire structure that is under investigation. This includes the experimental sub-assemblies

that have not yet yielded. Future research should switch between the DHS and FHS algorithms on an individual basis, i.e. each experimental sub-assembly switches between the algorithms at different time steps of a ground motion record depending on its own tangent stiffness. Such a switching algorithm effectively mixed controls hydraulic servo actuators throughout a test.

7. In order to provide a common measure of earthquake resilience among different types of structures for the general public, future research should draft a rating system for structural resilience. The rating system can promote the use of innovative earthquake resilient fused structures and eventually achieve community-wide resilience.

Bibliography

1. Akiyama H. *Earthquake-Resistant Limit-State Design for Buildings*. University of Tokyo Press, Tokyo, 1985.

2. Akiyama H. Earthquake Resistant Design Based on the Energy Concept. *Proceedings of the 9th World Conference on Earthquake Engineering* 1988; V: 905-910.

3. Akiyama H. *Seismic Resistant Steel Structures: Method Based on Energy Criteria (Chapter 3)*. International Centre for Mechanical Sciences, Springer Verlag Wien, New York, 2000.

4. ANSI/AISC 360-10. *Specification for Structural Steel Buildings*. American Institute of Steel Construction, Chicago, 2010.

5. ASCE/SEI 7-10. *Minimum Design Loads for Buildings and Other Structures*. American Society of Civil Engineers, Virginia, 2010.

6. ASCE/SEI 31-03. *Seismic Evaluation of Existing Buildings*. American Society of Civil Engineers, Virginia, 2003.

7. ASCE/SEI 41-06. *Seismic Evaluation and Retrofit of Existing Buildings*. American Society of Civil Engineers, Virginia, 2006.

8. Black CJ, Makris N, Aiken ID. Component Testing, Seismic Evaluation and Characterization of Buckling-Restrained Braces. *Journal of Structural Engineering* 2004; 130(6): 880-894.

9. Bruneau M, Chang SE, Eguchi RT, Lee GC, O'Rourke TD, Reinhorn AM, Shinozuka M, Tierney K, Wallace WA, Winterfeldt D. A Framework to Quantitatively Assess and Enhance the Seismic Resilience of Communities. *Earthquake Spectra* 2003; 19(4): 733-752.

10. Burden RL, Faires JD. *Numerical Analysis* Seventh Edition. Brooks/Cole, California, 2001.

11. Chang S. Explicit Pseudodynamic Algorithm with Unconditional Stability. *Journal of Engineering Mechanics* 2002; 128(9): 935-947.

12. Chang S. Enhanced, Unconditionally Stable, Explicit Pseudodynamic Algorithm. *Journal of Engineering Mechanics* 2007; 133(5): 541-554.

13. Chao SH, Goel SC, Lee SS. A Seismic Design Lateral Force Distribution Based on Inelastic State of Structures. *Earthquake Spectra* 2007; 23(3): 547-569.

14. Chen C. *Development and Numerical Simulation of Hybrid Effective Force Testing Method*. Dissertations and Theses, (UMI No. 3285753), Lehigh University, Bethlehem, 2007.

15. Combescure D, Pegon P. α-Operator Splitting Time Integration Technique for Pseudodynamic Testing Error Propagation Analysis. *Soil Dynamics and Earthquake Engineering* 1997; 16: 427-443.

16. Cutter SL, Burton CG, Emrich CT. Disaster Resilience Indicators for Benchmarking Baseline Conditions. *Journal of Homeland Security and Emergency Management* 2010; 7(1): 51.

17. Dermitzakis SN, Mahin SA. *Development of Substructuring Techniques for On-line Computer Controlled Seismic Performance Testing*. Report No. UCB/EERC-85/04, University of California, Berkeley, 1985.

18. DHS. *National Infrastructure Protection Plan*. US Department of Homeland Security, Washington, DC, 2006.

19. Eguchi R, Elwood K, Lee EK, Greene M (technical editors). *The 2010 Canterbury and the 2011 Christchurch New Zealand Earthquakes and the 2011 Tohoku Japan Earthquake: Emerging Research Needs and Opportunities*. Workshop Report, Earthquake Engineering Research Institute, Oakland, 2012.

20. El-Bahey S, Bruneau M. Structural Fuse Concept for Bridges. *Proceedings of the 9th U.S. National and 10th Canadian Conference on Earthquake Engineering* 2010.

21. Elkhoraibi T, Mosalam KM. Towards Error-free Hybrid Simulation Using Mixed Variables. *Earthquake Engineering and Structural Dynamics* 2007; 36: 1497-1522.

22. Erochko J, Christopoulos C, Tremblay R, Kim H. Shake Table Testing and Numerical Simulation of a Self-centering Energy Dissipative Braced Frame. *Earthquake Engineering and Structural Dynamics* 2013; 42(11): 1617-1635.

23. ESR-2802. *ICC-ES Evaluation Report: Simpson Strong-tie® Strong Frame® Steel Special Moment Frame Connection*. International Code Council, Washington, DC, 2013.

24. FEMA-355C. *State of the Art Report on Systems Performance of Steel Moment Frames Subject to Earthquake Ground Shaking – Program to Reduce the Earthquake Hazards of*

Steel Moment-Frame Structures. Federal Emergency Management Agency, Washington, DC, 2000.

25. FEMA-440. *Improvement of Nonlinear Static Seismic Analysis Procedures*. Federal Emergency Management Agency, Washington, DC, 2006.

26. FEMA-P58. *Seismic Performance Assessment of Buildings*. Federal Emergency Management Agency, Washington, DC, 2012.

27. FEMA-P695. *Quantification of Building Seismic Performance Factors*. Federal Emergency Management Agency, Washington, DC, 2009.

28. Filippou FC, Popov EP, Bertero VV. *Effects of Bond Deterioration on Hysteretic Behavior of Reinforced Concrete Joints*. Report No. EERC-83/19, University of California, Berkeley, 1983.

29. Fischinger M (editor). *Performance-Based Seismic Engineering: Vision for an Earthquake Resilient Society*. Springer Dordrecht Heidelberg, New York, 2014.

30. Goel SC, Chao S. *Performance-Based Plastic Design Earthquake-Resistant Steel Structures*. International Code Council, Washington, DC, 2008.

31. Goel SC, Rai DC, Basha HS. *Special Truss Moment Frames Design Guide*. Report No. UMCEE-98/44, University of Michigan, Ann Arbor, 1998.

32. Gray MG, Christopoulos C, Packer JA. Cast Steel Yielding Brace System for Concentrically Braced Frames: Concept Development and Experimental Validations. *Journal of Structural Engineering* 2014; 140(4): 04013095.

33. Guo JWW, Christopoulos C. Performance Spectra Based Method for the Seismic Design of Structures Equipped with Passive Supplemental Damping Systems. *Earthquake Engineering Structural Dynamics* 2013; 13(42): 935-952.

34. Hoffman RM. A Generalized Concept of Resilience. *Textile Research Journal* 1948; 18(3): 141-148.

35. Holling CS. Resilience and Stability of Ecological Systems. *Annual Review of Ecology and Systematics* 1973; 4:1-23.

36. Housner GW. Limit Design of Structures to Resist Earthquakes. *Proceedings of the 1st World Conference on Earthquake Engineering* 1956; 5.1-5.13.

37. Housner GW. The Plastic Failure of Frames during Earthquakes. *Proceedings of the 2nd World Conference on Earthquake Engineering* 1960; 997-1012.

38. Hoveidae N, Tremblay R, Rafezy B, Davaran A. Numerical Investigation of Seismic Behavior of Short-core All-steel Buckling Restrained Braces. *Journal of Constructional Steel Research* 2015; 114(2015): 89-99.

39. Ibarra LF, Krawinkler H. *Global Collapse of Frame Structures under Seismic Excitations*. Report No. PEER-05/06, University of California, Berkeley, 2005.

40. Janhunen B, Tipping S, Wolfe J. Seismic Retrofit of a 1960s Steel Moment-Frame Highrise Using a Pivoting Spine. *Proceedings of the 2013 Structural Engineers Association of California Convention* 2013.

41. Koetaka Y, Chusilp P, Zhang Z, Ando M, Suita K, Inoue K, Uno N. Mechanical Property of Beam-to-Column Moment Connection with Hysteretic Dampers for Column Weak Axis. *Engineering Structures* 2005; 27(2005): 109-117.

42. Kurama YC. Seismic Design of Unbonded Post-Tensioned Precast Concrete Walls with Supplemental Viscous Damping. *ACI Structural Journal* 2000; 97(4): 648-658.

43. Li Y. *Performance-based Design and Evaluation of Innovative Steel Knee Braced Truss Moment Frames*. Dissertations and Theses, The University of British Columbia, 2012.

44. Liao WC, Goel SC. Performance-Based Seismic Design of RC SMF Using Target Drift and Yield Mechanism as Performance Criteria. *Advances in Structural Engineering* 2014; 17(4): 529-542.

45. Lopes AP, Dusicka P, Berman JW. Design of the Linked Column Frame Structural System. *Proceedings of the 7th International Conference on Behaviour of Steel Structures in Seismic Areas* 2012; 311-318.

46. Ma X, Krawinkler H, Deierlein GG. *Seismic Design and Behavior of Self-Centering Braced Frame with Controlled Rocking and Energy Dissipating Fuses*. Report No.174, John A. Blume Earthquake Engineering Center, Stanford Digital Repository, 2013.

47. Malakoutian M. *Seismic Response Evaluation of the Linked Column Frame System*. Dissertations and Theses, University of Washington, 2012.

48. MathWorks. MATLAB®, Version 7.12.0.635 (R2011a). www.mathworks.com.

49. MCEER (Multidisciplinary Center for Earthquake Engineering Research). MCEER Research: Enabling Disaster-Resilient Communities. *SeismicWaves* 2008; 1-2.

50. Merritt S, Uang CM, Benzoni G. *Subassemblage Testing of Star Seismic Buckling Restrained Braces*. Report No. TR-03/04, University of California, San Diego, 2003.

51. Miranda E, Bertero VV. Evaluation of Strength Reduction Factors for Earthquake-Resistant Design. *Earthquake Spectra* 1994; 10(2): 357-379.

52. Mosqueda G, Stojadinovic B, Mahin SA. *Implementation and Accuracy of Continuous Hybrid Simulation with Geographically Distributed Substructures*. Report No. UCB/EERC-05/02, University of California, Berkeley, 2005.

53. Nakashima M, Ishii K, Kamagata S, Tsutsumi H, Ando K. Feasibility of Pseudo Dynamic Test Using Substructuring Techniques. *Proceedings of Ninth World Conference on Earthquake Engineering* 1988; IV47-52.

54. NER. *National Earthquake Resilience: Research, Implementation, and Outreach*. National Research Council of the National Academies, Washington, DC, 2011.

55. National Instruments. LabVIEW™ 2012, Service pack 1. www.ni.com.

56. NBCC. *National Building Code of Canada*. Canadian Commission on Building and Fire Codes, National Research Council of Canada, Ottawa, 2005.

57. Newmark NM. A Method of Computation for Structural Dynamics. *Journal of the Engineering Mechanics Division* 1959; 85: 67-94.

58. Newmark NM, Hall WJ. *Earthquake Spectra and Design*. Earthquake Engineering Research Institute, El Cerrito, California, 1982.

59. OpenSees (Open System for Earthquake Engineering Simulation) Version 2.4.6., Pacific Earthquake Engineering Research (PEER) Center, 2013, University of California, Berkeley. http://opensees.berkeley.edu.

60. Pan P, Nakashima M, Tomofuji H. Online Test Using Displacement-force Mixed Control. *Earthquake Engineering and Structural Dynamics* 2005; 34: 869-888.

61. Pan P, Wang T, Zhong DZA. *Development of Online Hybrid Test – Theory and Applications*. Tsinghua University Press, China, 2013.

62. PEER (Pacific Earthquake Engineering Research) Center Strong Motion Database 2010 BETA version, University of California, Berkeley. http://peer.berkeley.edu/products/strong_ground_motion_db.html.

63. Priestley MJN, Calvi GM, Kowalsky MJ. *Displacement-Based Seismic Design of Structures*. IUSS Press, Pavia, Italy, 2007.

64. Pryor SE, Murray TM. Next Generation Partial Strength Steel Moment Frame Connections for Seismic Resistance. *Research, Development, and Practice in Structural Engineering and Construction* 2012; St-145-0423.

65. Raju NRBK, Nagabhushanam J. Nonlinear Structural Analysis Using Integrated Force Method. *Sādhanā* 2000; 25(4): 353-365.

66. REDi™ Rating System. *Resilience-based Earthquake Design Initiative for the Next Generation of Buildings*. Arup, 2013.

67. Reinhorn AM, Sivaselvan MV, Liang Z, Shao X. Real-time Dynamic Hybrid Testing of Structural Systems. *Proceedings of the 13th World Conference on Earthquake Engineering* 2004; Paper No. 1644.

68. Rutter M. Psychosocial Resilience and Protective Mechanisms. *American Journal of Orthopsychiatry* 1987; 57(3): 316-331.

69. SAC/BD-97/02. *Protocol for Fabrication, Inspection, Testing, and Documentation of Beam-Column Connection Tests and Other Experimental Specimens*. Report No. SAC/BD-97-02, Federal Emergency Management Agency/SAC (SEAOC, ATC, and CUREe) Joint Venture, 1997.

70. Schellenberg AH, Mahin SA, Fenves GL. *Advanced Implementation of Hybrid Simulation*. Report No. PEER-09/104, University of California, Berkeley, 2009.

71. SEAOC. *Vision 2000 Report: Performance-Based Seismic Engineering of Buildings*. Structural Engineers Association of California, Sacramento, 1995.

72. Shen Y, Christopoulos C, Mansour N, Tremblay R. Seismic Design and Performance of Steel Moment-resisting Frames with Nonlinear Replaceable Links. *Journal of Structural Engineering* 2011; 137(10): 1107-1117.

73. Shield CK, French CW, Timm J. Development and Implementation of the Effective Force Testing Method for Seismic Simulation of Large-scale Structures. *Philosophical Transactions of the Royal Society* 2001; 359: 1911-1929.

74. Shing PB, Mahin SA. *Pseudodynamic Test Method for Seismic Performance Evaluation: Theory and Implementation*. Report No. UCB/EERC-84/01, University of California, Berkeley, 1984.

75. Sivaselvan MV, Reinhorn AM, Shao X, Weinreber S. Dynamic Force Control with Hydraulic Actuators Using Added Compliance and Displacement Compensation. *Earthquake Engineering and Structural Dynamics* 2008; (37): 1785-1800.

76. StarSeismic. *Perform Nonlinear Component Modeling of StarSeismic PowercatTM BRBs*. unpublished report to StarSeismic LLC, 2011.

77. Takanashi K. Non-linear Earthquake Response Analysis of Structures by a Computer-actuator On-line System. *Bulletin of Earthquake Resistant Structure Research Center* 1975; 1-17.

78. Takanashi K, Nakashima M. Japanese Activities on On-line Testing. *Journal of Engineering Mechanics* 1987; 113(7): 1014-1032.

79. Tremblay R, St-Onge E, Rogers CA, Morrison T, Légeron F, Desjardins E, Tirca L, Gray MG, Christopoulos C, Packer JA. Overview of Ductile Seismic Brace Fuse Systems in Canada. *Proceedings of the 6th European Conference on Steel and Composite Structures* 2011; 939-944.

80. Uang C, Bertero VV. *Use of Energy as a Design Criterion in Earthquake-Resistant Design*. Report No. UCB/EERC-88/18, University of California, Berkeley, 1988.

81. UCB. *U.C. Berkeley Seismic Guidelines Appendix I: Probabilistic Ground-motion Analysis for Central Campus*. 2003.

82. USRC. (U.S. Resiliency Council) 2015. www.usrc.org.

83. Vamvatsikos D, Cornell CA. Incremental Dynamic Analysis. *Earthquake Engineering and Structural Dynamic* 2002; 02(31): 491-514.

84. Vannan MT. *The pseudodynamic test method with substructuring applications*. Dissertations and Theses, (Order No. 9220459), University of Colorado, Boulder, 1991.

85. Vargas R, Bruneau M. Analytical Response and Design of Buildings with Metallic Structural Fuses I. *Journal of Structural Engineering* 2009a; 09(135): 386-393.

86. Vargas R, Bruneau M. Experimental Response of Buildings Designed with Metallic Structural Fuses II. *Journal of Structural Engineering* 2009b; 09(135): 394-403.

87. Verrucci E, Rossetto T, Twigg J, Adams BJ. Multi-disciplinary Indicators for Evaluating the Seismic Resilience of Urban Areas. *Proceedings of the 15th World Conference on Earthquake Engineering* 2012.

88. Wongpakdee N, Leelataviwat S, Goel SC, Liao WC. Performance-based Design and Collapse Evaluation of Buckling Restrained Knee Braced Truss Moment Frames. *Engineering Structures* 2014; 60: 23-31.

89. Yang TY. *Performance Evaluation of Innovative Steel Braced Frames*. Dissertations and Theses, (UMI No. 3254146), University of California, Berkeley, 2006.

90. Yang TY, Li K, Lin JY, Li Y, Tung DP. Development of High-performance Shake Tables Using the Hierarchical Control Strategy and Nonlinear Control Techniques. *Earthquake Engineering and Structural Dynamics* 2015; 44: 1717-1728.

91. Yang TY, Li Y, Goel SC. Seismic Performance Evaluation of Long-Span Conventional Moment Frames and Buckling-Restrained Knee-Braced Truss Moment Frames. *Journal of Structural Engineering* 2016; 142(1): 04015081.

92. Yang TY, Li Y, Leelataviwat S. Performance-based Design and Optimization of Buckling Restrained Knee Braced Truss Moment Frame. *Journal of Performance of Constructed Facilities* 2014; 28(6): A4014007.

93. Yang TY, Moehle JP, Bozorgnia Y, Zareian F, Wallace JW. Performance Assessment of Tall Concrete Core-wall Building Designed Using Two Alternative Approaches. *Earthquake Engineering and Structural Dynamics* 2012; 41(11): 1515-1531.

94. Yang TY, Stojadinovic B, Moehle JP. Hybrid Simulation of a Zipper-braced Steel Frame under Earthquake Excitation. *Earthquake Engineering and Structural Dynamics* 2009; 38(1): 95-113.

95. Yang TY, Tung DP, Li Y. Performance-based Plastic Design and Evaluation of Linked Column Frames. *Progress in Steel Building Structures* 2015; 17(1): 27-35.

96. Yi W. *Towards Reducing the Effect of Control Errors in Pseudodynamic Testing: Formulation, Implementation, and Evaluation*. Dissertations and Theses, (Order No. 9124144), University of Michigan, Ann Arbor, 1991.

Appendix A
Determination of γ_a

γ_a relates the incremental monotonic and cyclic energies of the equivalent nonlinear single degree-of-freedom (ENLSDOF) system as the earthquake shaking intensity increases from the service level earthquake (SLE) to design based earthquake (DBE) hazard level. For a selected Δ_p, there are many possible post-yielding behaviour depending on the value of γ_a. To determine the appropriate factor for the selected Δ_p, all possible values of γ_a are tried. For each trial, the force-deformation backbone curve defined by the equivalent energy design procedure (EEDP) is assigned to the ENLSDOF system which is then excited by the 20 ground motions as presented in Table 2.2. The motions are amplitude scaled to match the DBE target spectrum. The medium of the maximum roof drift ratio (RDR) is plotted against the trial γ_a as a point of a figure in this appendix. EEDP only uses the converged γ_a such that the RDR due to ground motions at the DBE shaking intensity matches the selected Δ_p. This converged γ_a is identified as the intersection of the selected and calculated RDRs on the figure.

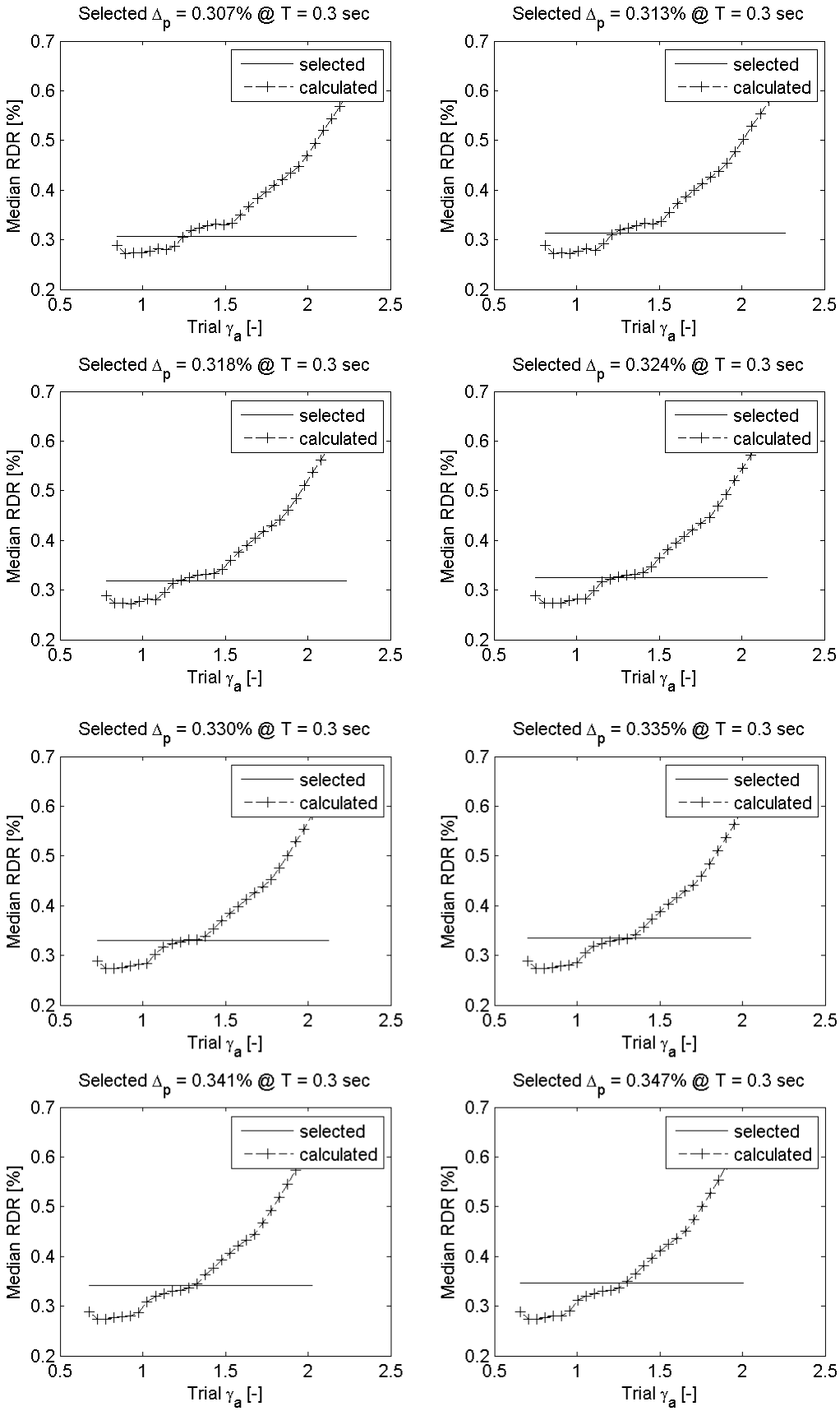
Selected Δp = 0.307% @ T = 0.3 sec
Selected Δp = 0.313% @ T = 0.3 sec
Selected Δp = 0.318% @ T = 0.3 sec
Selected Δp = 0.324% @ T = 0.3 sec
Selected Δp = 0.330% @ T = 0.3 sec
Selected Δp = 0.335% @ T = 0.3 sec
Selected Δp = 0.341% @ T = 0.3 sec
Selected Δp = 0.347% @ T = 0.3 sec
selected
calculated
Median RDR [%]
Trial γa [-]
0.2
0.3
0.4
0.5
0.6
0.7
0.5
1
1.5
2
2.5

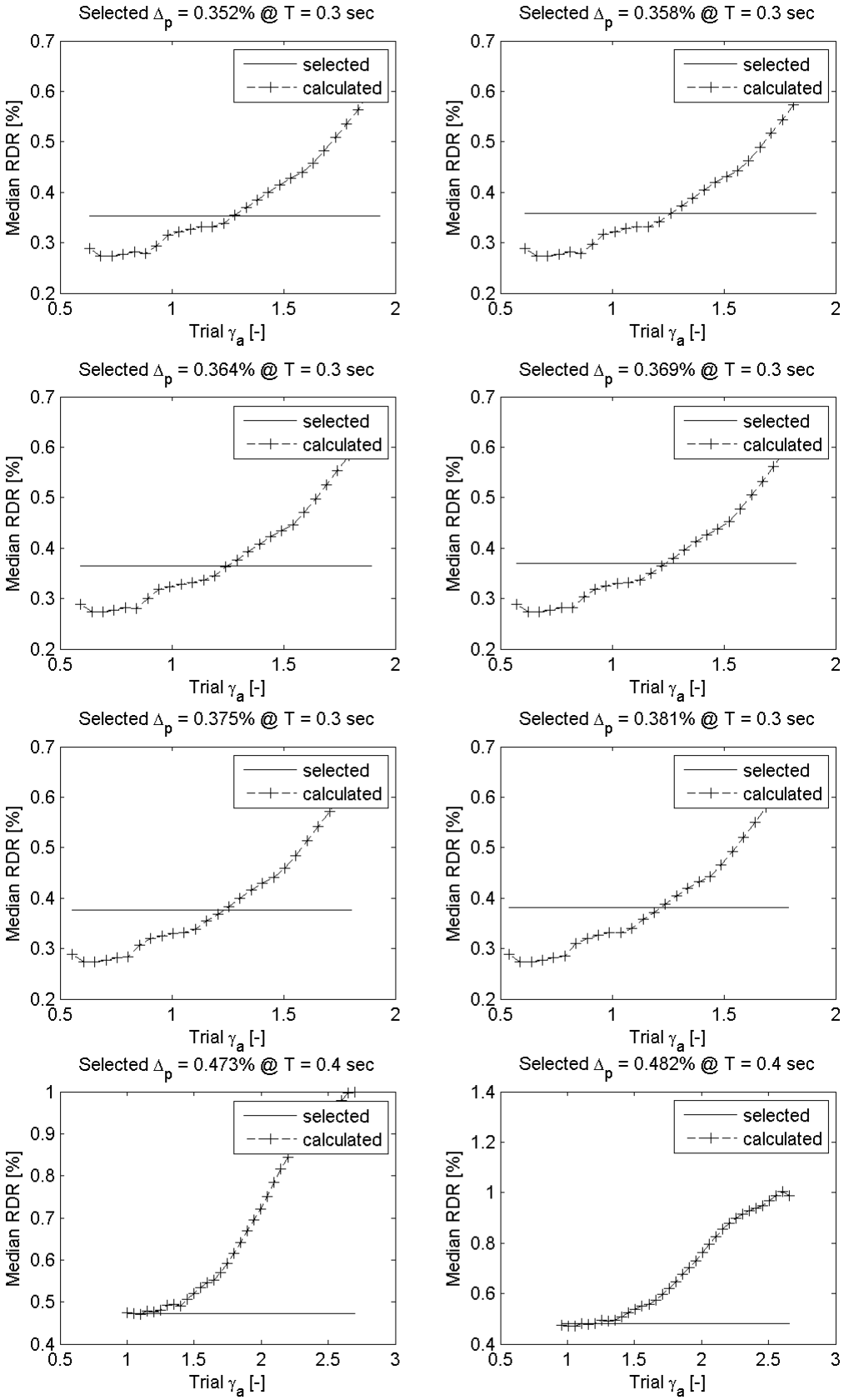
Selected Δp = 0.352% @ T = 0.3 sec
Selected Δp = 0.358% @ T = 0.3 sec
Selected Δp = 0.364% @ T = 0.3 sec
Selected Δp = 0.369% @ T = 0.3 sec
Selected Δp = 0.375% @ T = 0.3 sec
Selected Δp = 0.381% @ T = 0.3 sec
Selected Δp = 0.473% @ T = 0.4 sec
Selected Δp = 0.482% @ T = 0.4 sec
selected
calculated
Median RDR [%]
Trial γa [-]

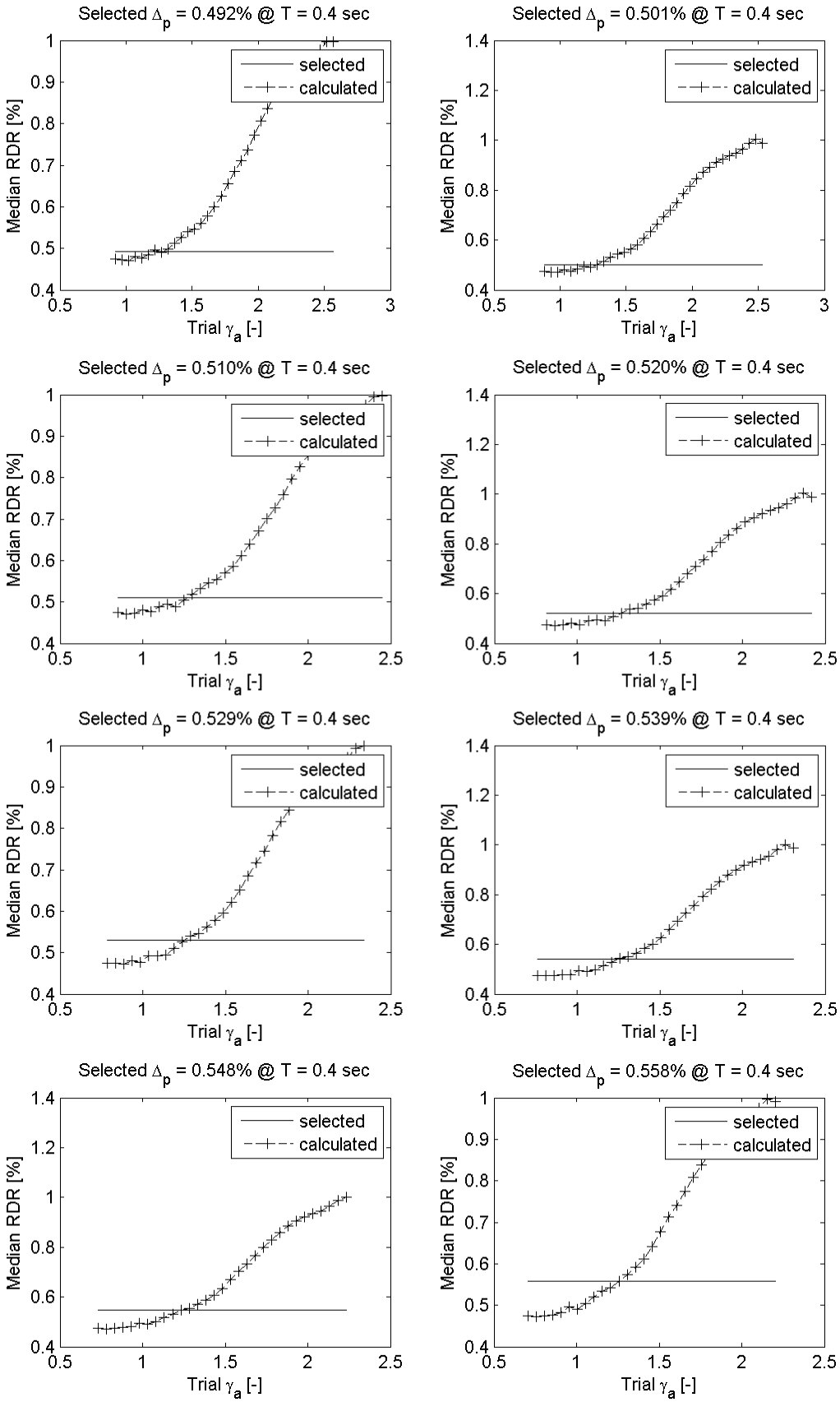
Selected Δp = 0.492% @ T = 0.4 sec
Selected Δp = 0.501% @ T = 0.4 sec
Selected Δp = 0.510% @ T = 0.4 sec
Selected Δp = 0.520% @ T = 0.4 sec
Selected Δp = 0.529% @ T = 0.4 sec
Selected Δp = 0.539% @ T = 0.4 sec
Selected Δp = 0.548% @ T = 0.4 sec
Selected Δp = 0.558% @ T = 0.4 sec
selected
calculated
Median RDR [%]
Trial γa [-]

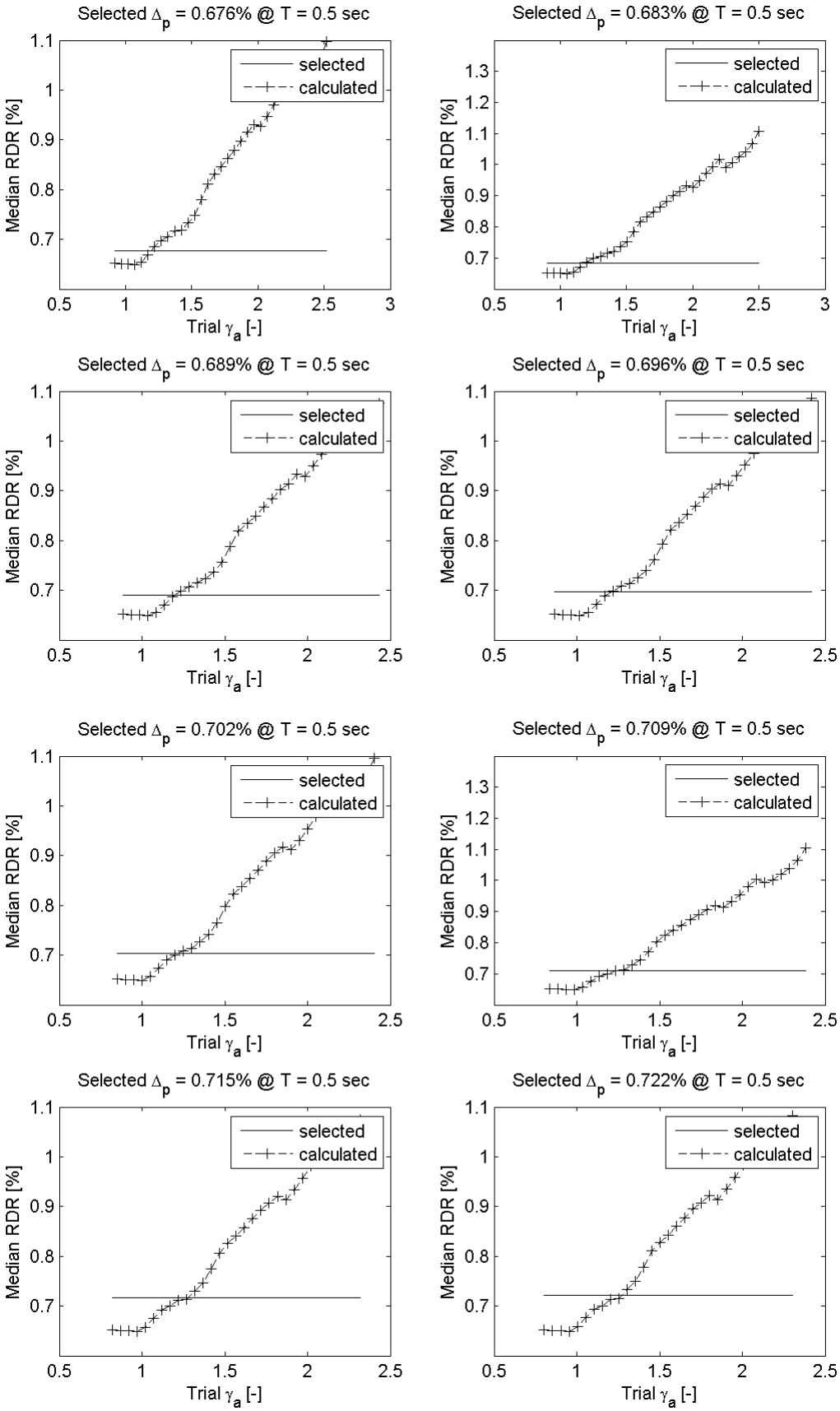
Selected Δp = 0.676% @ T = 0.5 sec
Selected Δp = 0.683% @ T = 0.5 sec
Selected Δp = 0.689% @ T = 0.5 sec
Selected Δp = 0.696% @ T = 0.5 sec
Selected Δp = 0.702% @ T = 0.5 sec
Selected Δp = 0.709% @ T = 0.5 sec
Selected Δp = 0.715% @ T = 0.5 sec
Selected Δp = 0.722% @ T = 0.5 sec
selected
calculated
Median RDR [%]
Trial γa [-]

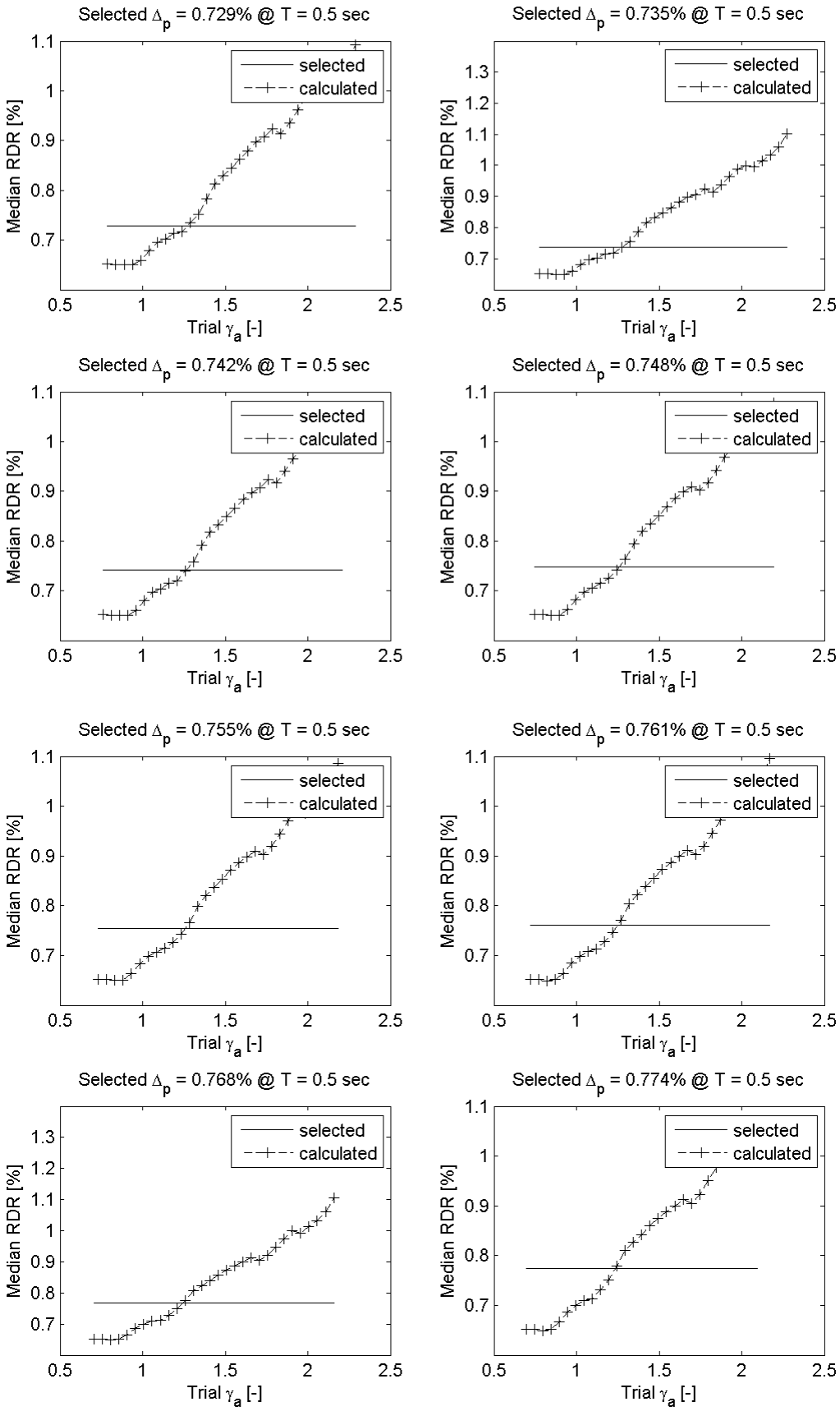
Selected Δp = 0.729% @ T = 0.5 sec
Selected Δp = 0.735% @ T = 0.5 sec
Selected Δp = 0.742% @ T = 0.5 sec
Selected Δp = 0.748% @ T = 0.5 sec
Selected Δp = 0.755% @ T = 0.5 sec
Selected Δp = 0.761% @ T = 0.5 sec
Selected Δp = 0.768% @ T = 0.5 sec
Selected Δp = 0.774% @ T = 0.5 sec
selected
calculated
Median RDR [%]
Trial γa [-]

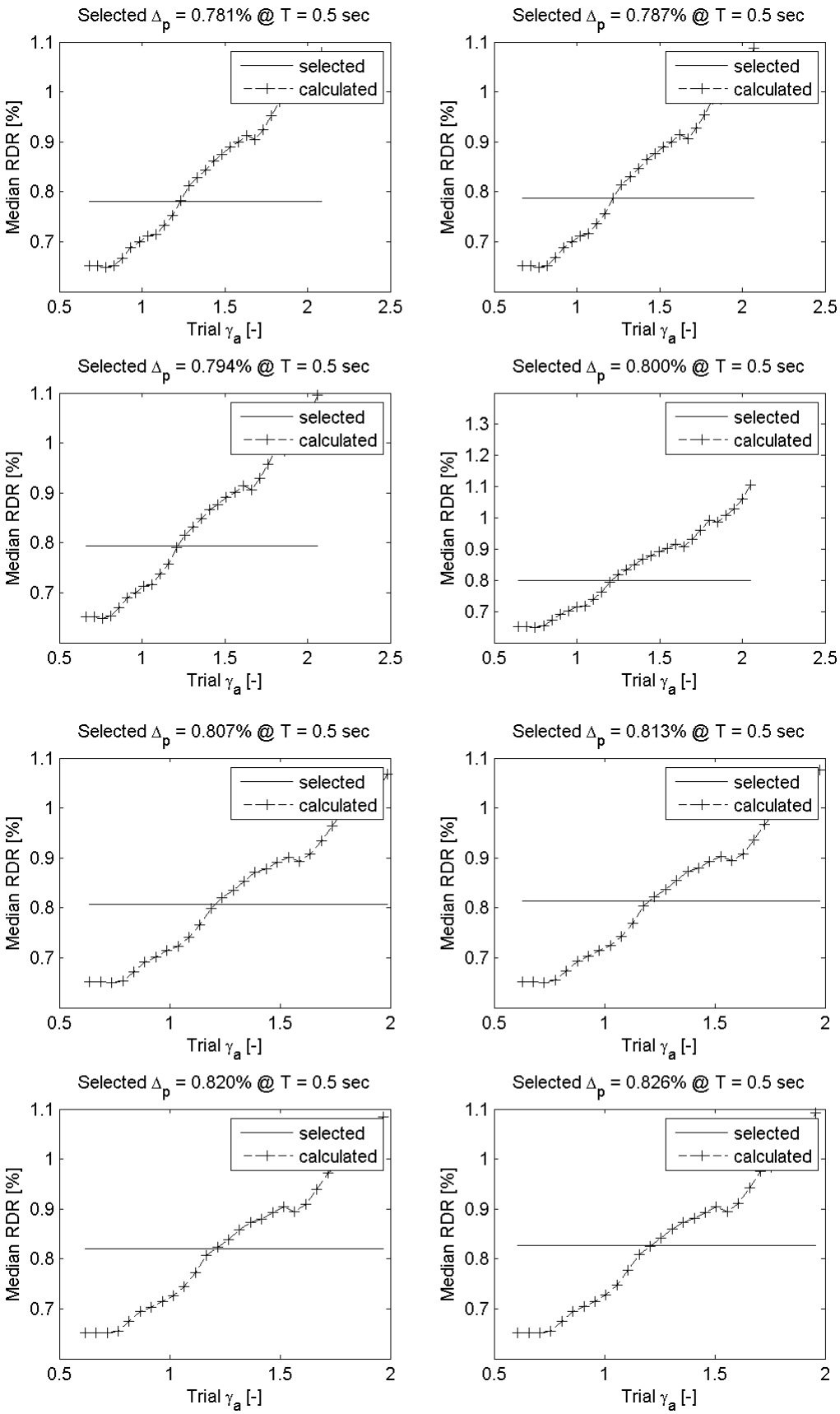
Selected Δp = 0.781% @ T = 0.5 sec
Selected Δp = 0.787% @ T = 0.5 sec
Selected Δp = 0.794% @ T = 0.5 sec
Selected Δp = 0.800% @ T = 0.5 sec
Selected Δp = 0.807% @ T = 0.5 sec
Selected Δp = 0.813% @ T = 0.5 sec
Selected Δp = 0.820% @ T = 0.5 sec
Selected Δp = 0.826% @ T = 0.5 sec
selected
calculated
Median RDR [%]
Trial γa [-]

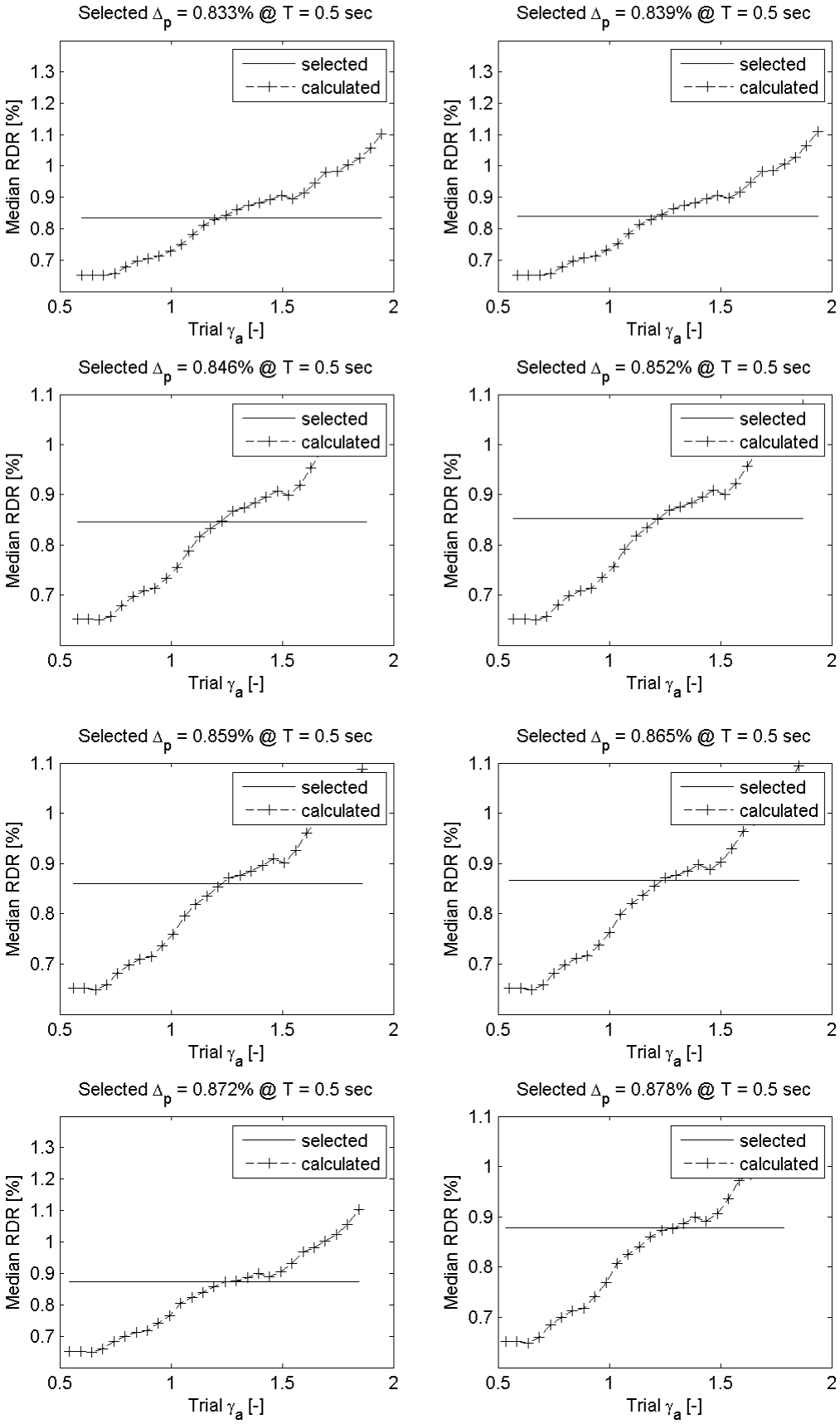
Selected Δp = 0.833% @ T = 0.5 sec
Selected Δp = 0.839% @ T = 0.5 sec
Selected Δp = 0.846% @ T = 0.5 sec
Selected Δp = 0.852% @ T = 0.5 sec
Selected Δp = 0.859% @ T = 0.5 sec
Selected Δp = 0.865% @ T = 0.5 sec
Selected Δp = 0.872% @ T = 0.5 sec
Selected Δp = 0.878% @ T = 0.5 sec
selected
calculated
Median RDR [%]
Trial γa [-]

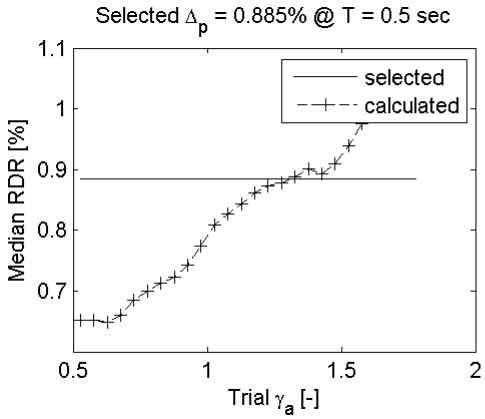
Selected Δp = 0.885% @ T = 0.5 sec
selected
calculated
Median RDR [%]
Trial γa [-]

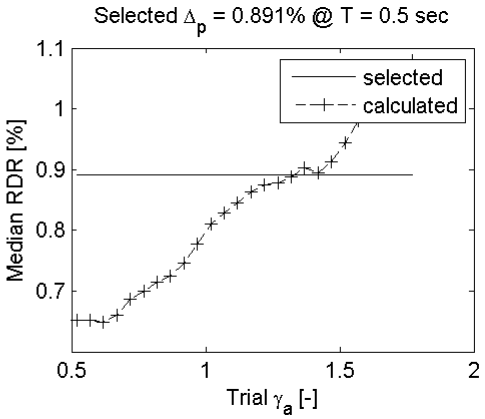
Selected Δp = 0.891% @ T = 0.5 sec
selected
calculated
Median RDR [%]
Trial γa [-]

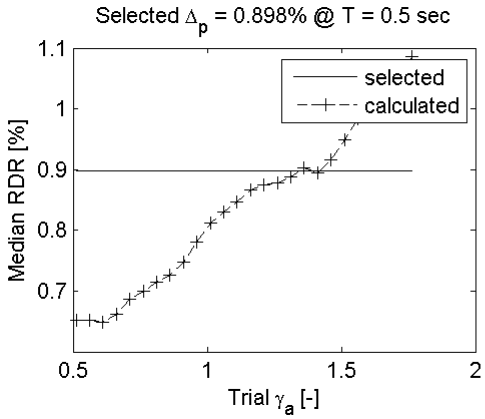
Selected Δp = 0.898% @ T = 0.5 sec
selected
calculated
Median RDR [%]
Trial γa [-]

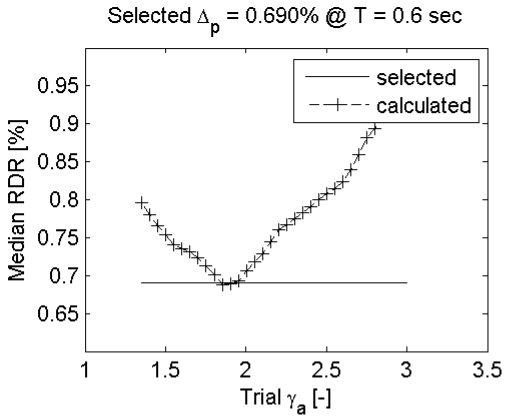
Selected Δp = 0.690% @ T = 0.6 sec
selected
calculated
Median RDR [%]
Trial γa [-]

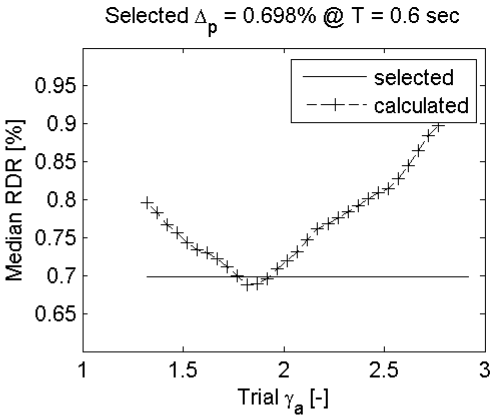
Selected Δp = 0.698% @ T = 0.6 sec
selected
calculated
Median RDR [%]
Trial γa [-]

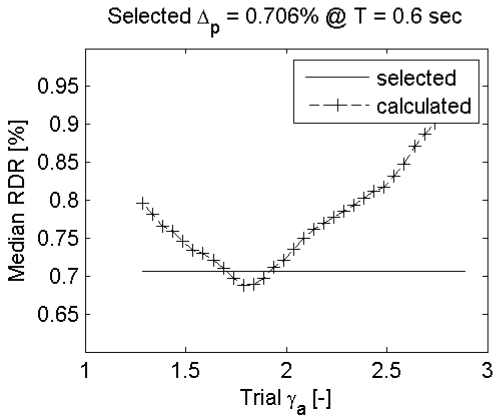
Selected Δp = 0.706% @ T = 0.6 sec
selected
calculated
Median RDR [%]
Trial γa [-]

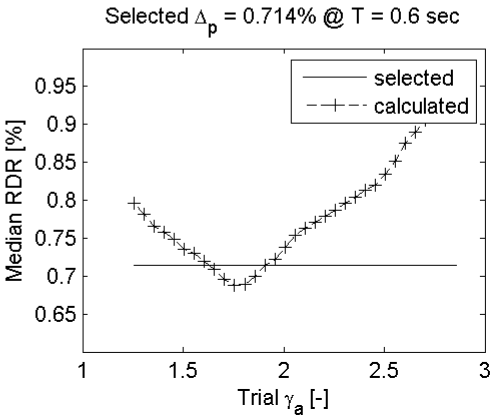
Selected Δp = 0.714% @ T = 0.6 sec
selected
calculated
Median RDR [%]
Trial γa [-]

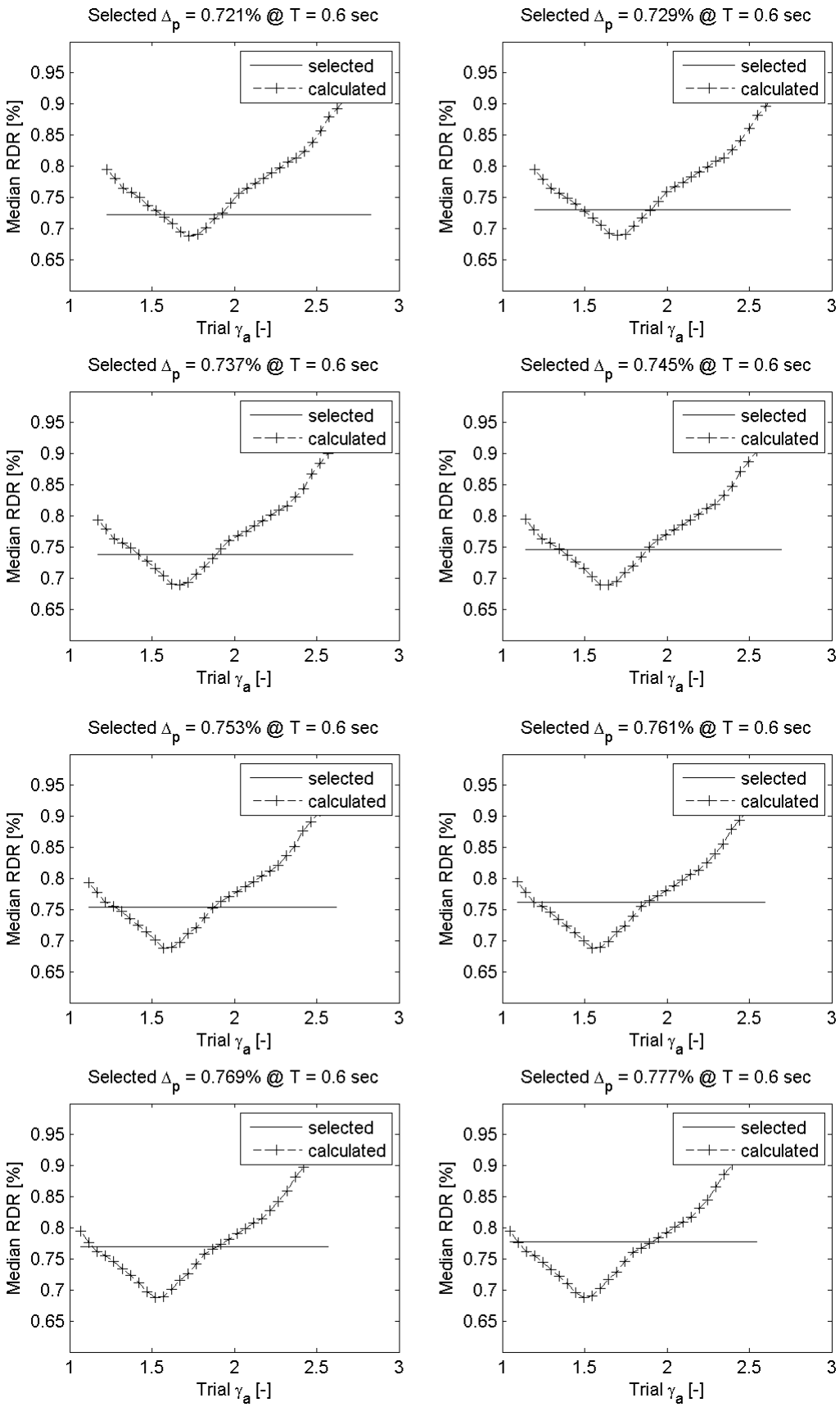
Selected Δp = 0.721% @ T = 0.6 sec
Selected Δp = 0.729% @ T = 0.6 sec
Selected Δp = 0.737% @ T = 0.6 sec
Selected Δp = 0.745% @ T = 0.6 sec
Selected Δp = 0.753% @ T = 0.6 sec
Selected Δp = 0.761% @ T = 0.6 sec
Selected Δp = 0.769% @ T = 0.6 sec
Selected Δp = 0.777% @ T = 0.6 sec
selected
calculated
Median RDR [%]
Trial γa [-]
0.65
0.7
0.75
0.8
0.85
0.9
0.95
1
1.5
2
2.5
3

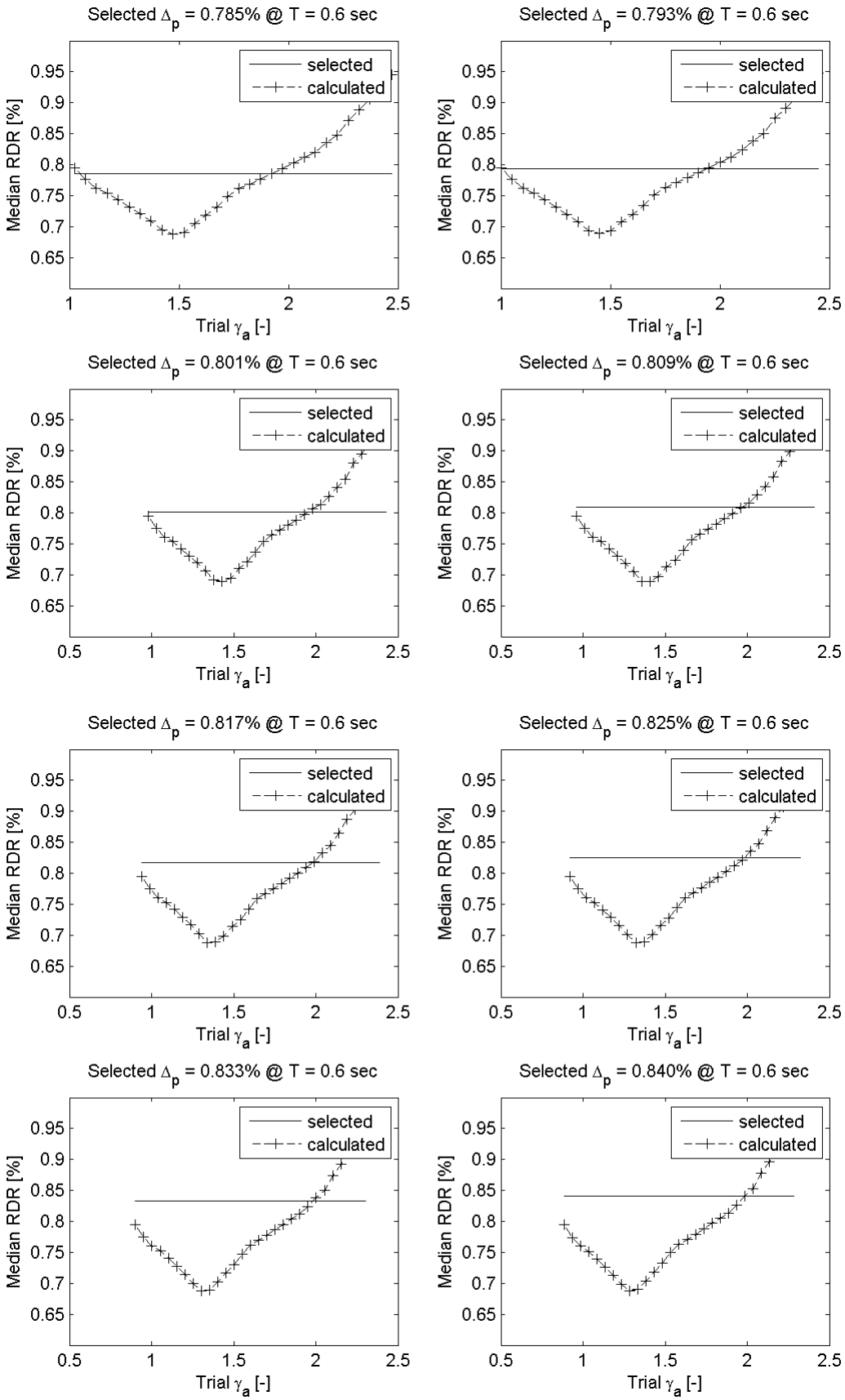
Selected Δp = 0.785% @ T = 0.6 sec
Selected Δp = 0.793% @ T = 0.6 sec
Selected Δp = 0.801% @ T = 0.6 sec
Selected Δp = 0.809% @ T = 0.6 sec
Selected Δp = 0.817% @ T = 0.6 sec
Selected Δp = 0.825% @ T = 0.6 sec
Selected Δp = 0.833% @ T = 0.6 sec
Selected Δp = 0.840% @ T = 0.6 sec
selected
calculated
Median RDR [%]
Trial γa [-]

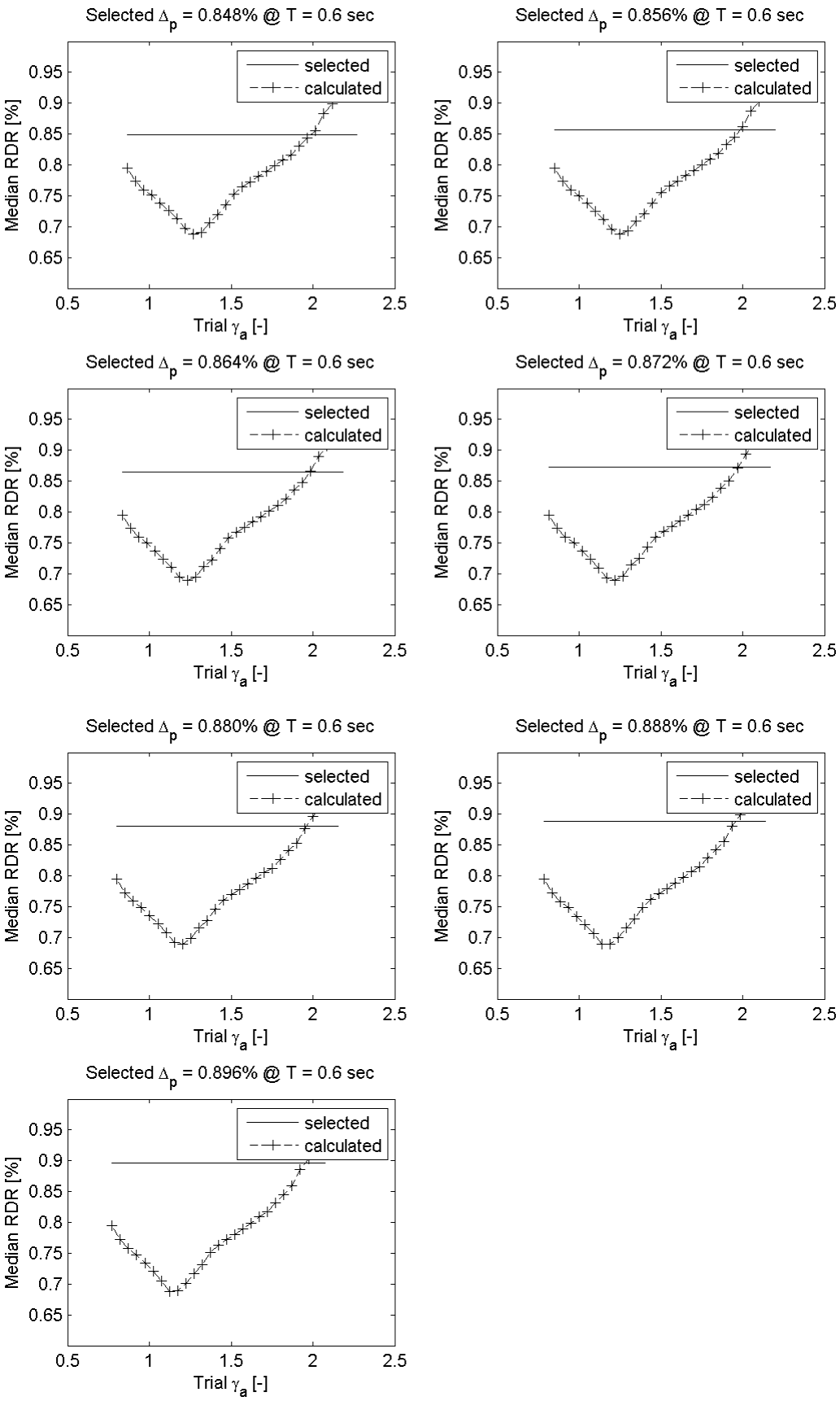
Selected Δp = 0.848% @ T = 0.6 sec
Selected Δp = 0.856% @ T = 0.6 sec
Selected Δp = 0.864% @ T = 0.6 sec
Selected Δp = 0.872% @ T = 0.6 sec
Selected Δp = 0.880% @ T = 0.6 sec
Selected Δp = 0.888% @ T = 0.6 sec
Selected Δp = 0.896% @ T = 0.6 sec
selected
calculated
Median RDR [%]
Trial γa [-]

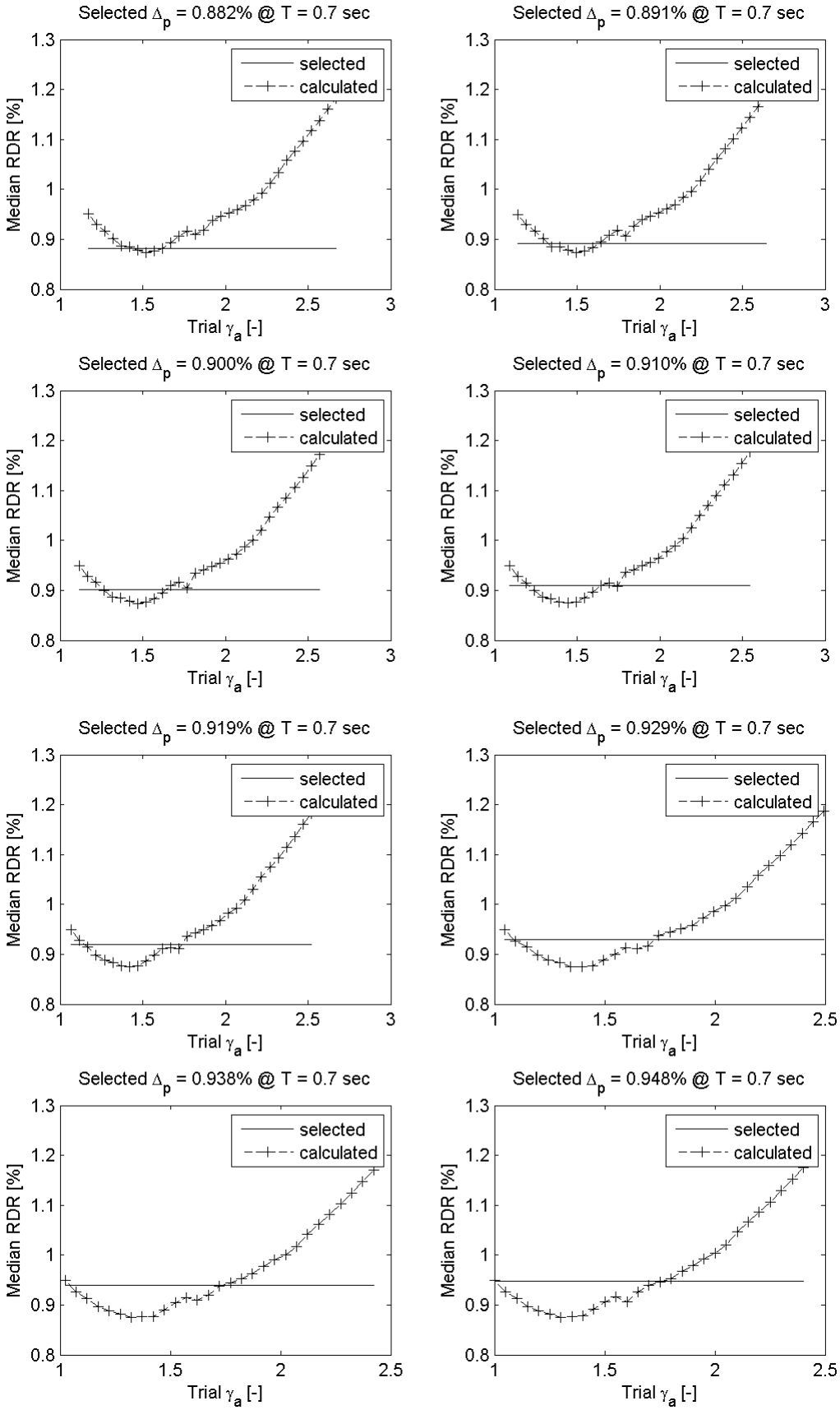
Selected Δp = 0.882% @ T = 0.7 sec
Selected Δp = 0.891% @ T = 0.7 sec
Selected Δp = 0.900% @ T = 0.7 sec
Selected Δp = 0.910% @ T = 0.7 sec
Selected Δp = 0.919% @ T = 0.7 sec
Selected Δp = 0.929% @ T = 0.7 sec
Selected Δp = 0.938% @ T = 0.7 sec
Selected Δp = 0.948% @ T = 0.7 sec
selected
calculated
Median RDR [%]
Trial γa [-]

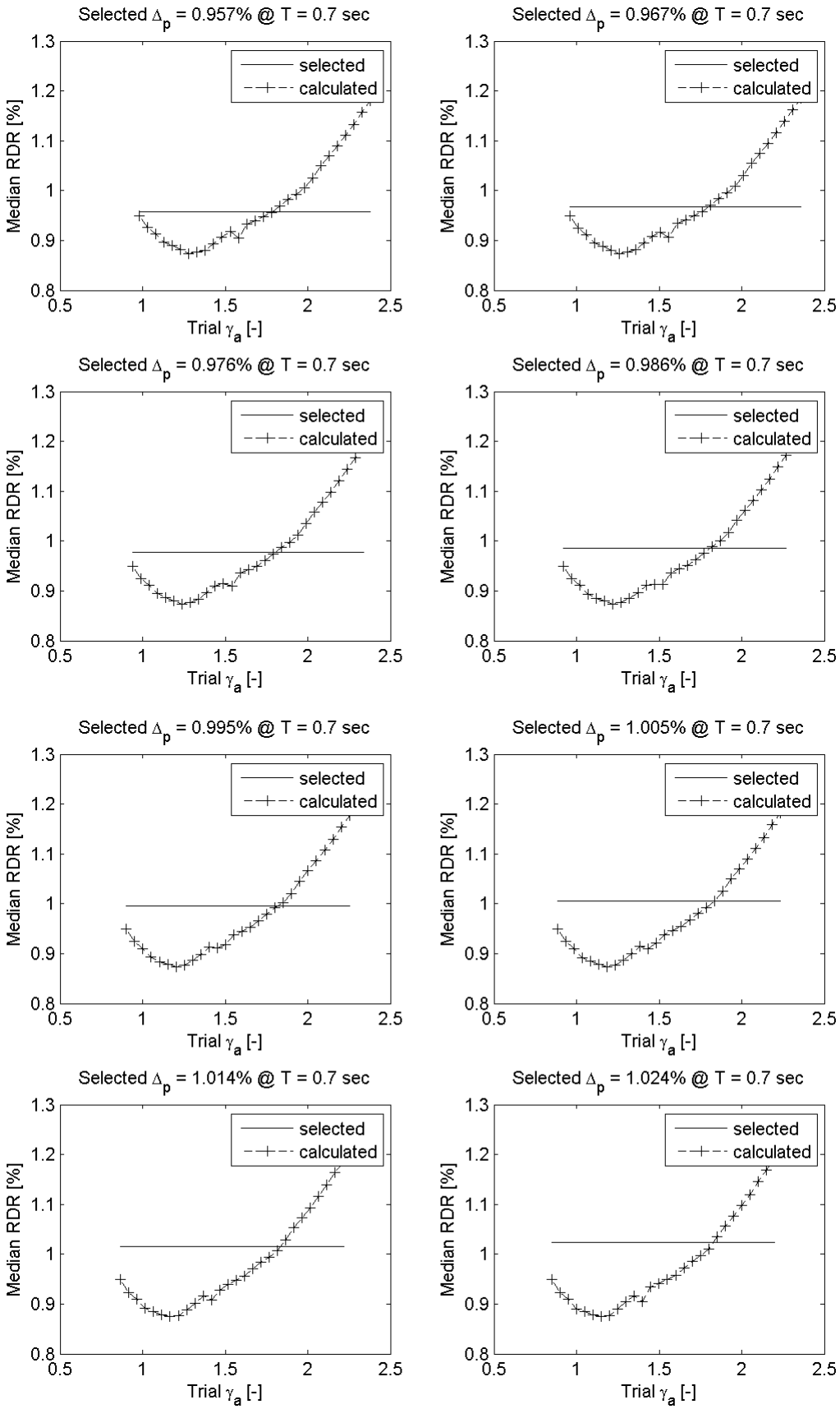
Selected Δp = 0.957% @ T = 0.7 sec
Selected Δp = 0.967% @ T = 0.7 sec
Selected Δp = 0.976% @ T = 0.7 sec
Selected Δp = 0.986% @ T = 0.7 sec
Selected Δp = 0.995% @ T = 0.7 sec
Selected Δp = 1.005% @ T = 0.7 sec
Selected Δp = 1.014% @ T = 0.7 sec
Selected Δp = 1.024% @ T = 0.7 sec
selected
calculated
Median RDR [%]
Trial γa [-]
0.8
0.9
1
1.1
1.2
1.3
0.5
1
1.5
2
2.5

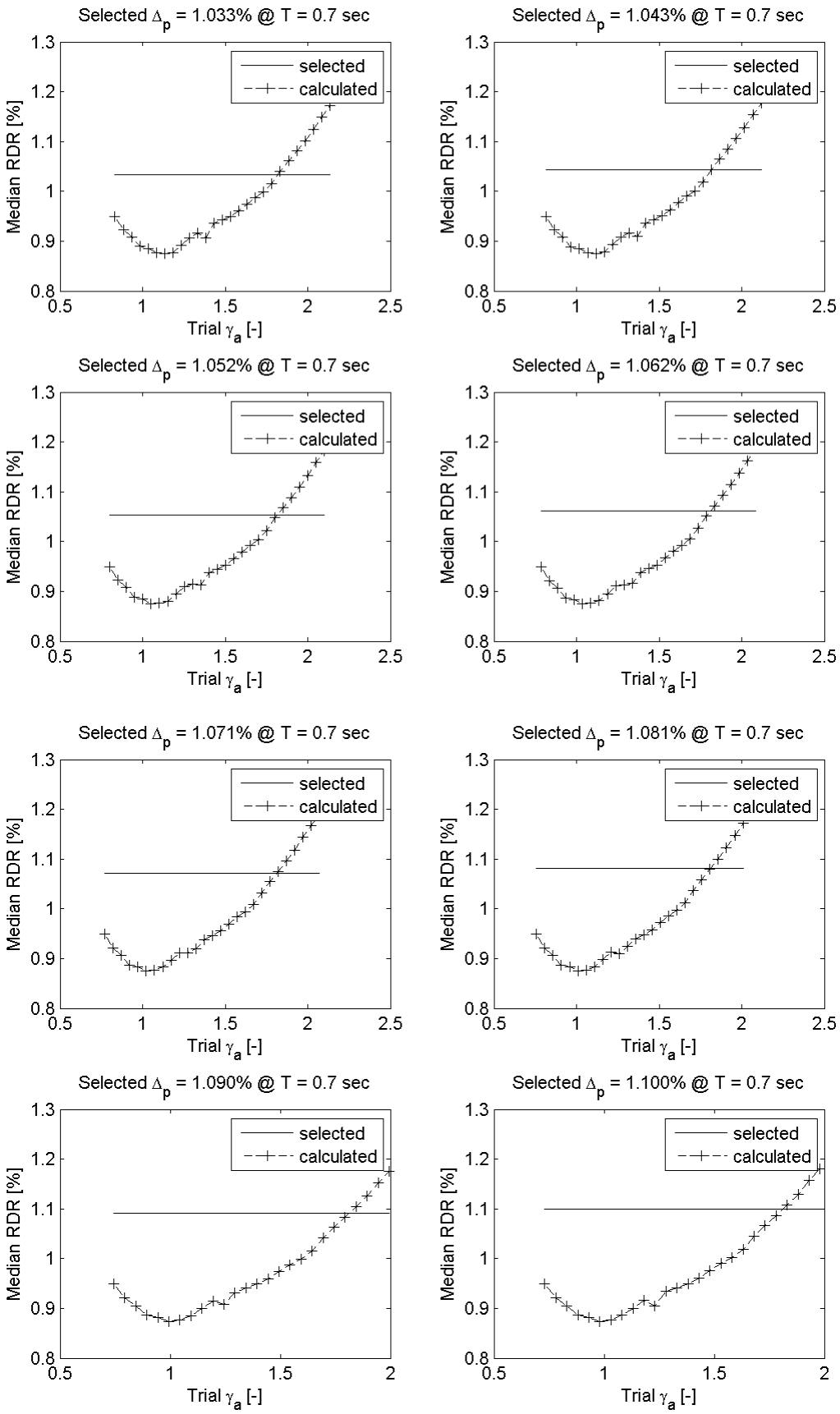
Selected Δp = 1.033% @ T = 0.7 sec
Selected Δp = 1.043% @ T = 0.7 sec
Selected Δp = 1.052% @ T = 0.7 sec
Selected Δp = 1.062% @ T = 0.7 sec
Selected Δp = 1.071% @ T = 0.7 sec
Selected Δp = 1.081% @ T = 0.7 sec
Selected Δp = 1.090% @ T = 0.7 sec
Selected Δp = 1.100% @ T = 0.7 sec
selected
calculated
Median RDR [%]
Trial γa [-]

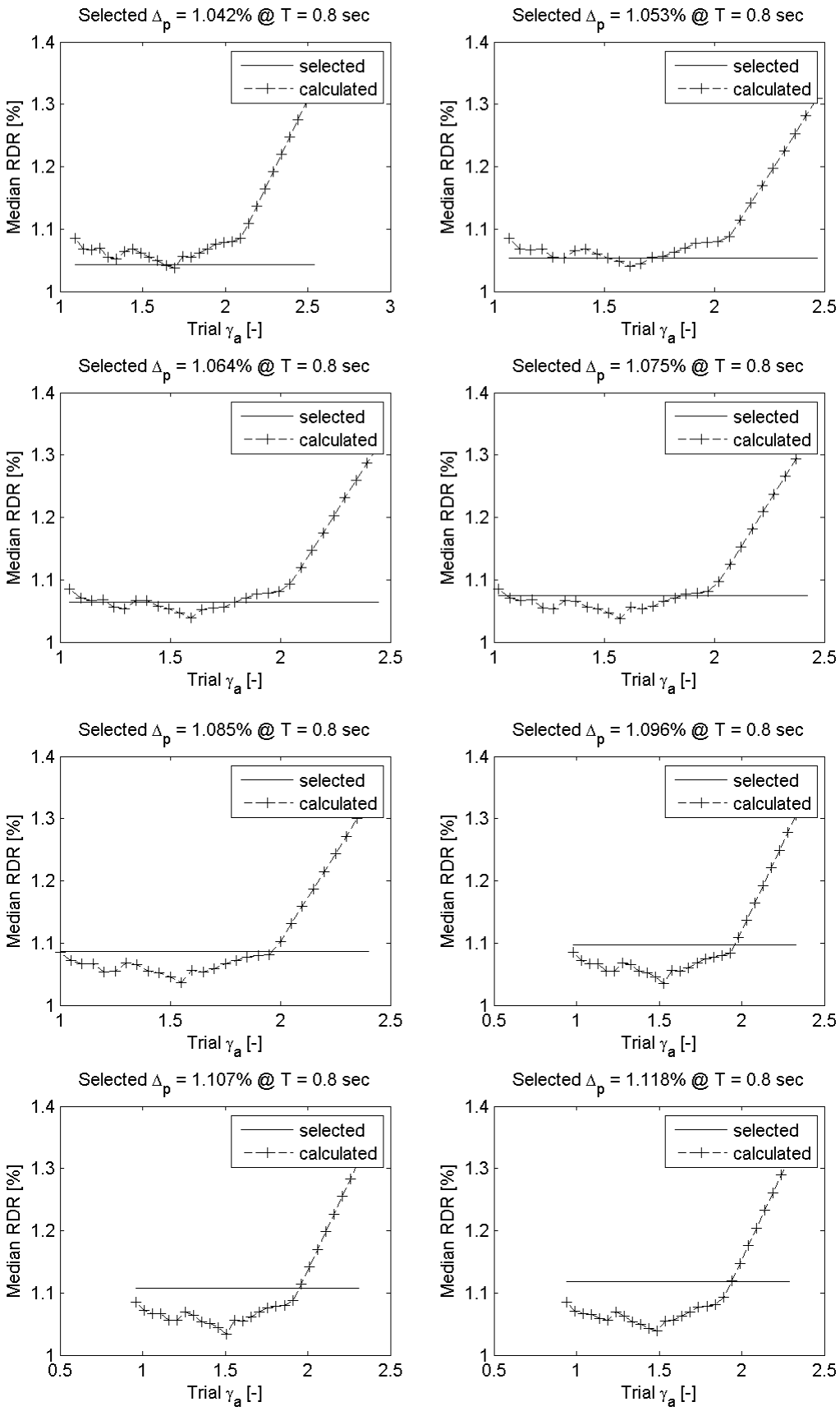
Selected Δp = 1.042% @ T = 0.8 sec
Selected Δp = 1.053% @ T = 0.8 sec
Selected Δp = 1.064% @ T = 0.8 sec
Selected Δp = 1.075% @ T = 0.8 sec
Selected Δp = 1.085% @ T = 0.8 sec
Selected Δp = 1.096% @ T = 0.8 sec
Selected Δp = 1.107% @ T = 0.8 sec
Selected Δp = 1.118% @ T = 0.8 sec
selected
calculated
Median RDR [%]
Trial γa [-]

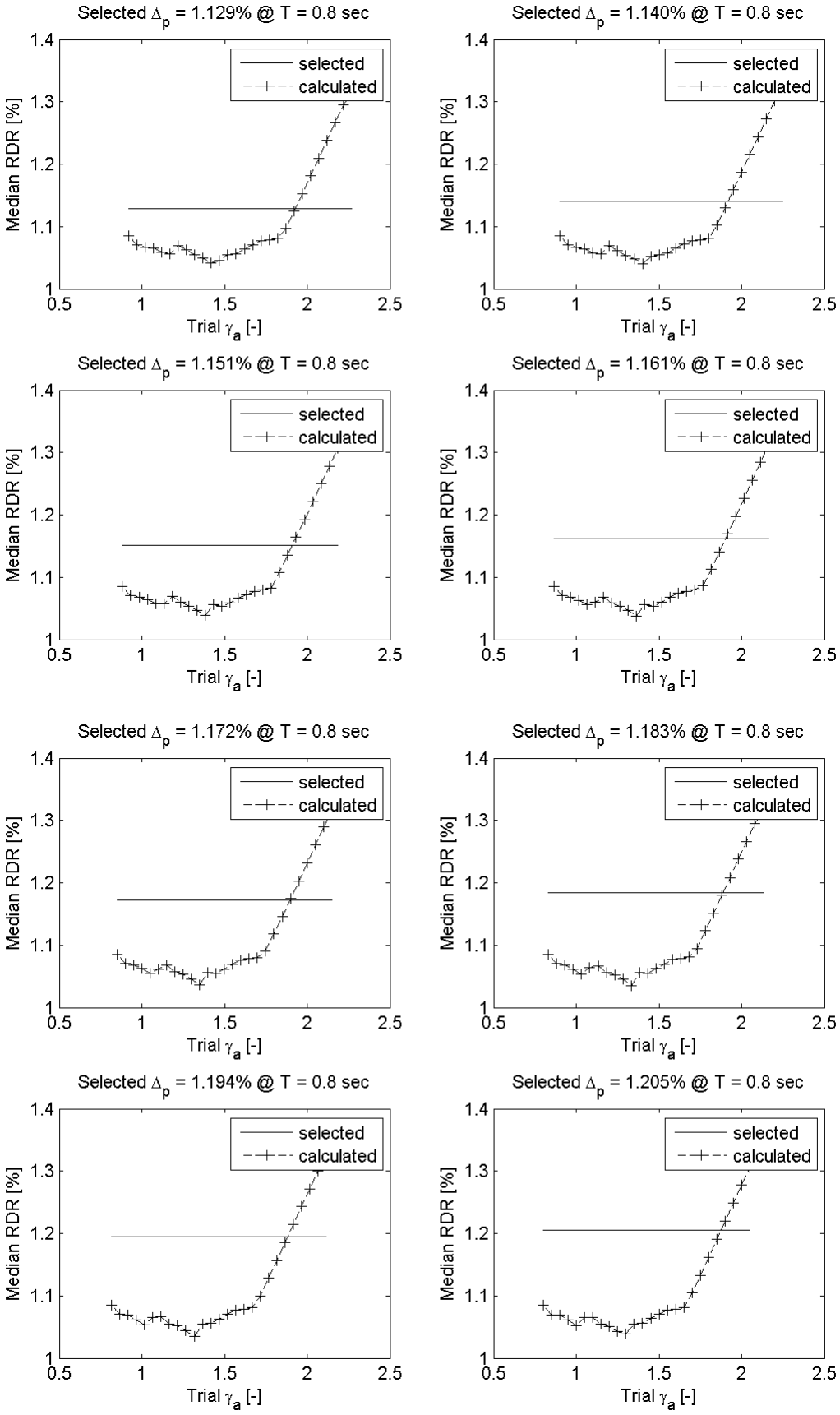
Selected Δp = 1.129% @ T = 0.8 sec
Selected Δp = 1.140% @ T = 0.8 sec
Selected Δp = 1.151% @ T = 0.8 sec
Selected Δp = 1.161% @ T = 0.8 sec
Selected Δp = 1.172% @ T = 0.8 sec
Selected Δp = 1.183% @ T = 0.8 sec
Selected Δp = 1.194% @ T = 0.8 sec
Selected Δp = 1.205% @ T = 0.8 sec
selected
calculated
Median RDR [%]
Trial γa [-]
1
1.1
1.2
1.3
1.4
0.5
1
1.5
2
2.5

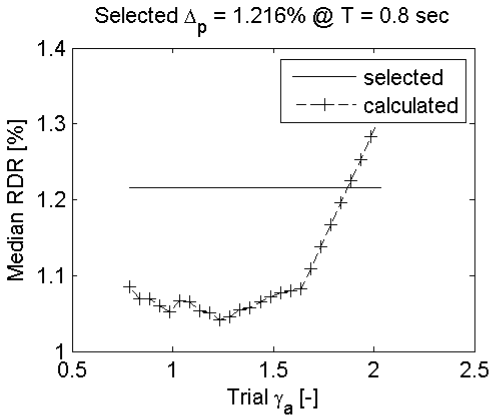
Selected Δp = 1.216% @ T = 0.8 sec
selected
calculated
Median RDR [%]
Trial γa [-]

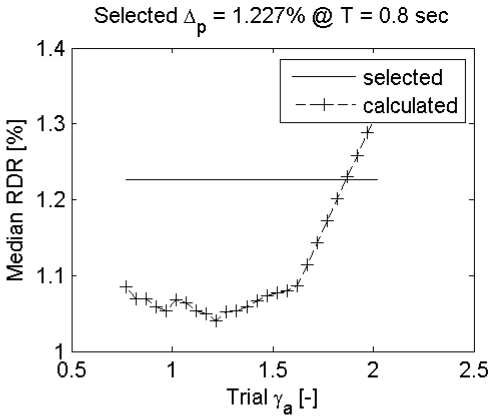
Selected Δp = 1.227% @ T = 0.8 sec
selected
calculated
Median RDR [%]
Trial γa [-]

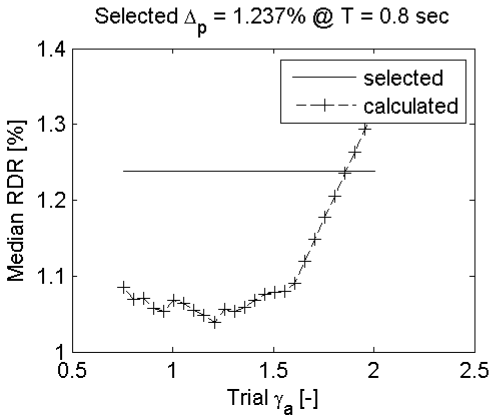
Selected Δp = 1.237% @ T = 0.8 sec
selected
calculated
Median RDR [%]
Trial γa [-]

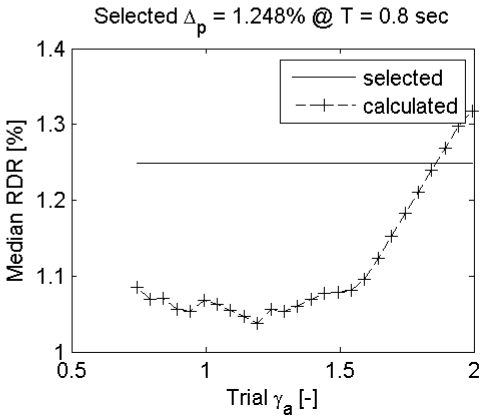
Selected Δp = 1.248% @ T = 0.8 sec
selected
calculated
Median RDR [%]
Trial γa [-]

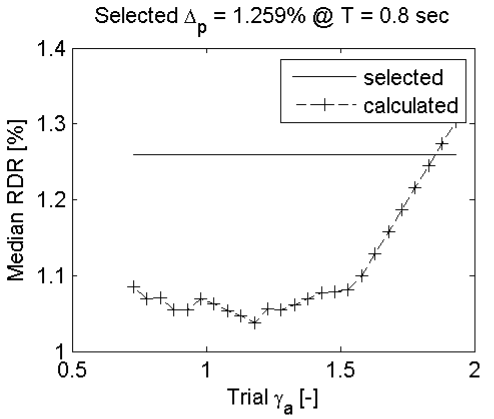
Selected Δp = 1.259% @ T = 0.8 sec
selected
calculated
Median RDR [%]
Trial γa [-]

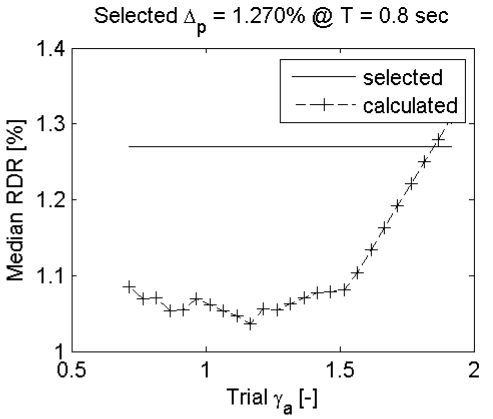
Selected Δp = 1.270% @ T = 0.8 sec
selected
calculated
Median RDR [%]
Trial γa [-]

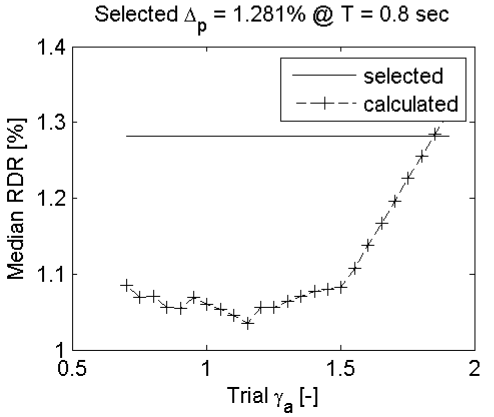
Selected Δp = 1.281% @ T = 0.8 sec
selected
calculated
Median RDR [%]
Trial γa [-]

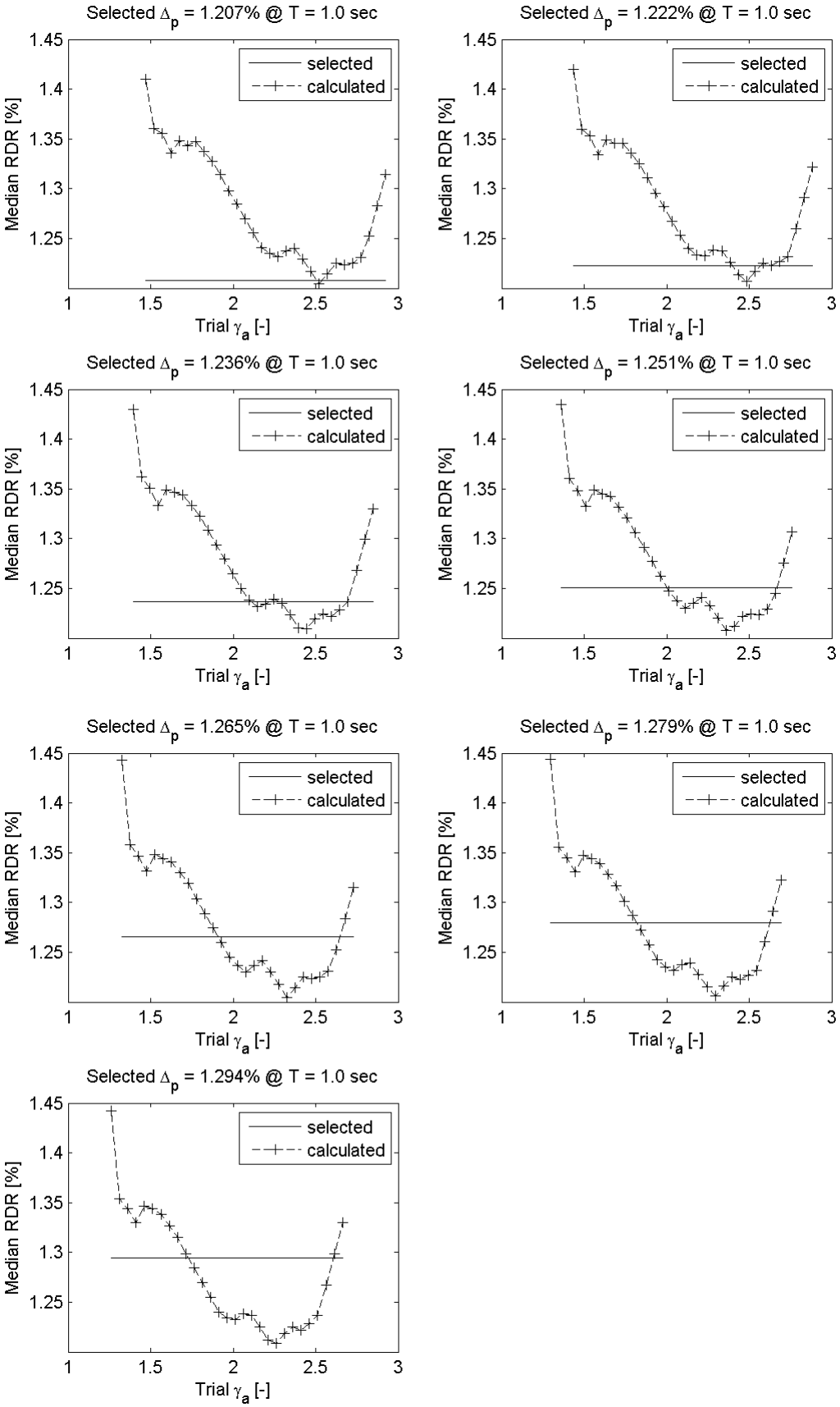
Selected Δp = 1.207% @ T = 1.0 sec
Selected Δp = 1.222% @ T = 1.0 sec
Selected Δp = 1.236% @ T = 1.0 sec
Selected Δp = 1.251% @ T = 1.0 sec
Selected Δp = 1.265% @ T = 1.0 sec
Selected Δp = 1.279% @ T = 1.0 sec
Selected Δp = 1.294% @ T = 1.0 sec
selected
calculated
Median RDR [%]
Trial γa [-]
1.45
1.4
1.35
1.3
1.25
1
1.5
2
2.5
3

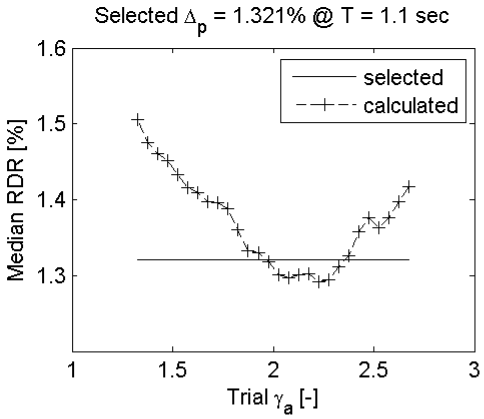
Selected Δp = 1.321% @ T = 1.1 sec
selected
calculated
Median RDR [%]
Trial γa [-]

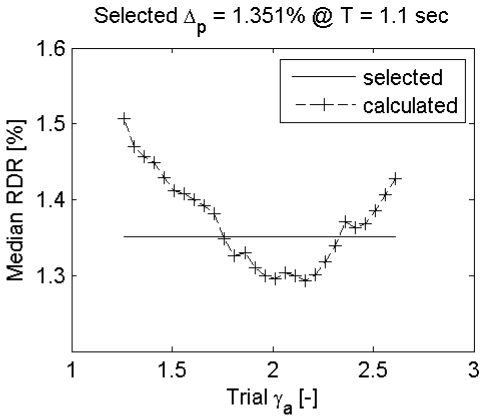
Selected Δp = 1.351% @ T = 1.1 sec
selected
calculated
Median RDR [%]
Trial γa [-]

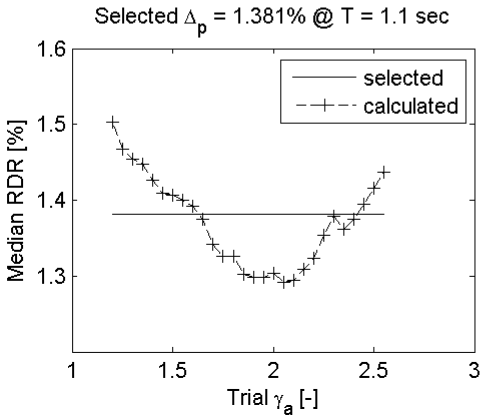
Selected Δp = 1.381% @ T = 1.1 sec
selected
calculated
Median RDR [%]
Trial γa [-]

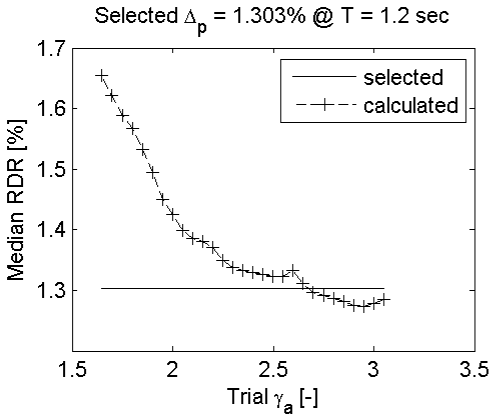
Selected Δp = 1.303% @ T = 1.2 sec
selected
calculated
Median RDR [%]
Trial γa [-]

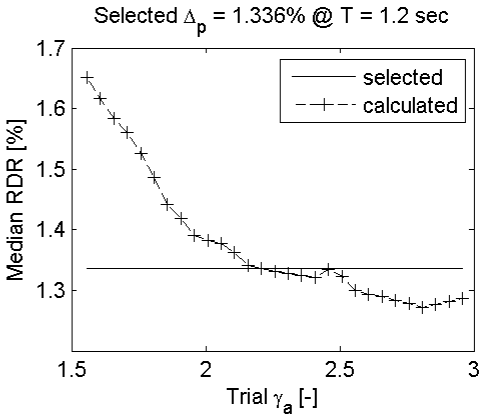
Selected Δp = 1.336% @ T = 1.2 sec
selected
calculated
Median RDR [%]
Trial γa [-]

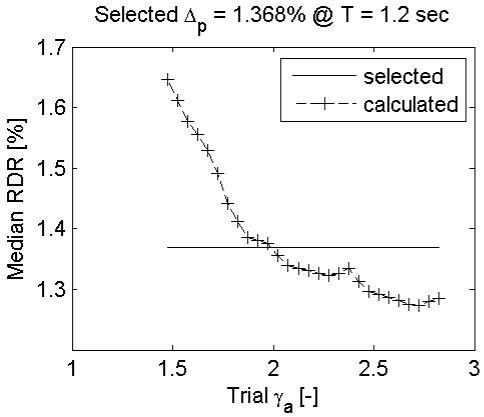
Selected Δp = 1.368% @ T = 1.2 sec
selected
calculated
Median RDR [%]
Trial γa [-]

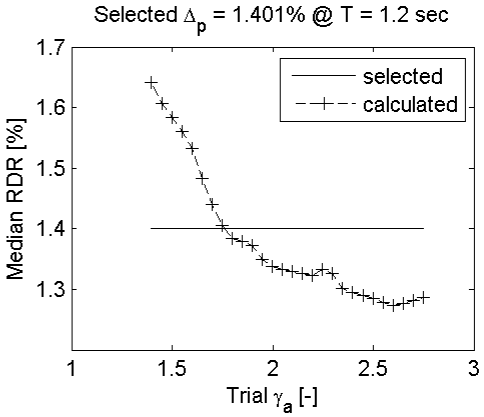
Selected Δp = 1.401% @ T = 1.2 sec
selected
calculated
Median RDR [%]
Trial γa [-]

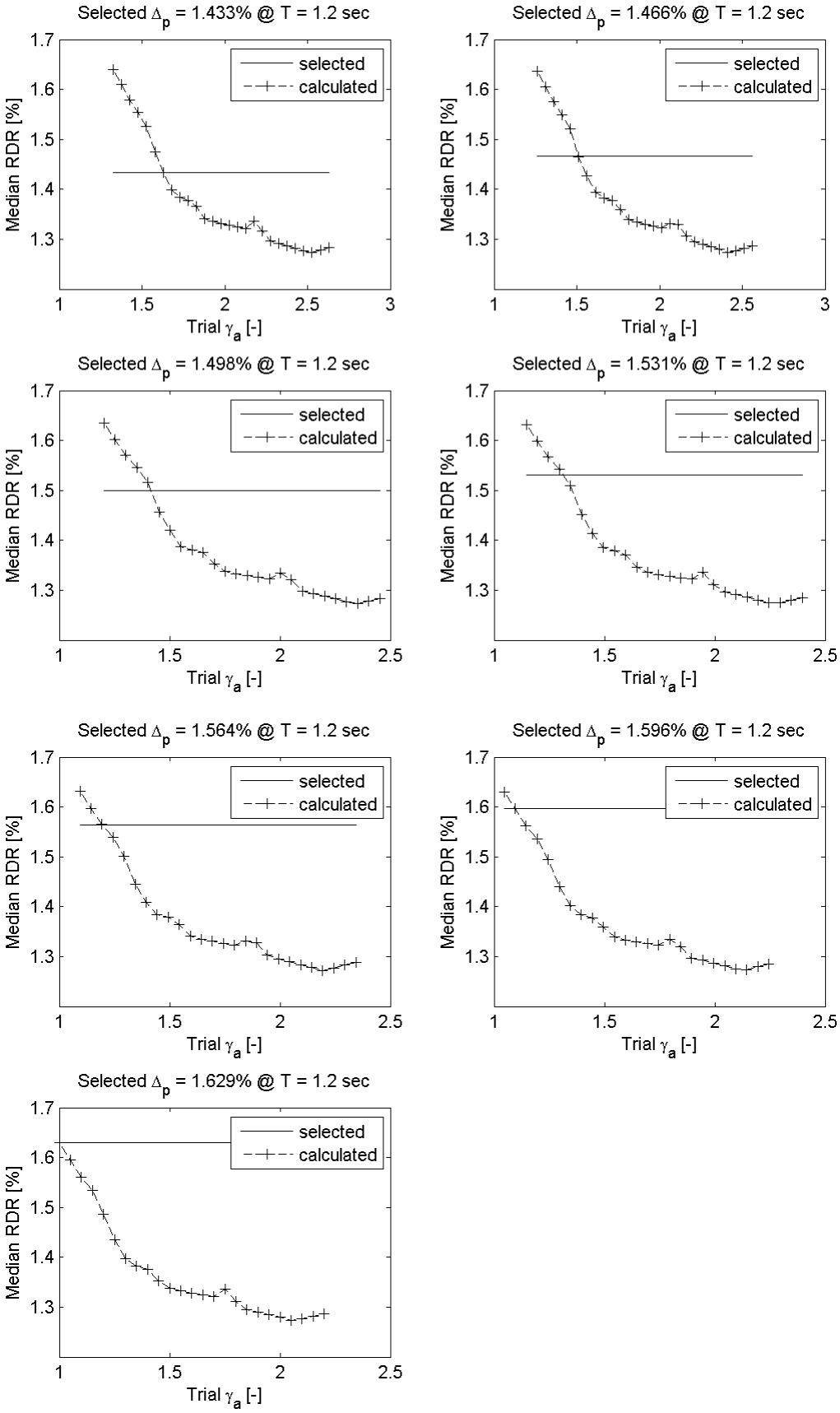
Selected Δp = 1.433% @ T = 1.2 sec
Selected Δp = 1.466% @ T = 1.2 sec
Selected Δp = 1.498% @ T = 1.2 sec
Selected Δp = 1.531% @ T = 1.2 sec
Selected Δp = 1.564% @ T = 1.2 sec
Selected Δp = 1.596% @ T = 1.2 sec
Selected Δp = 1.629% @ T = 1.2 sec
selected
calculated
Median RDR [%]
Trial γa [-]

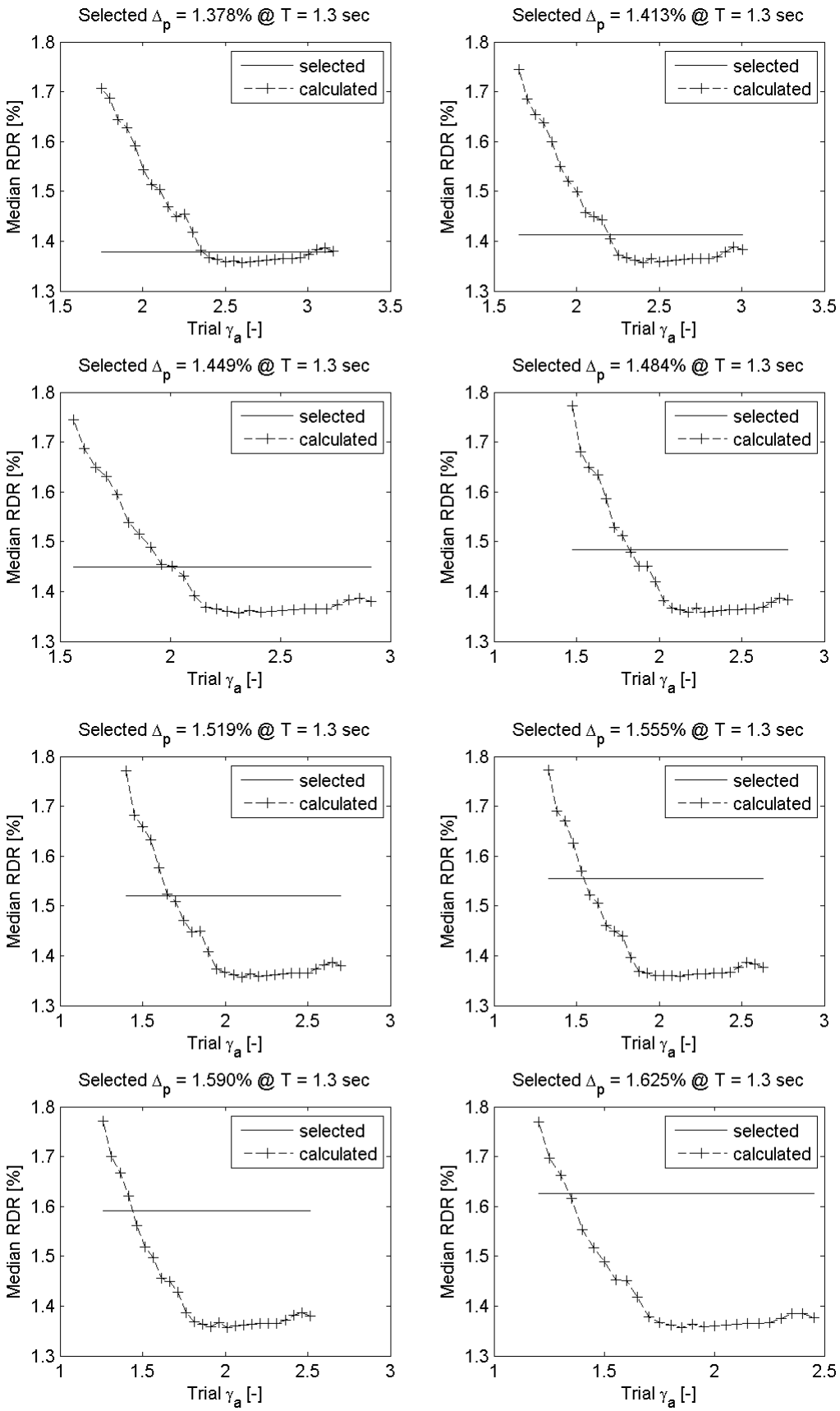
Selected Δp = 1.378% @ T = 1.3 sec
Selected Δp = 1.413% @ T = 1.3 sec
Selected Δp = 1.449% @ T = 1.3 sec
Selected Δp = 1.484% @ T = 1.3 sec
Selected Δp = 1.519% @ T = 1.3 sec
Selected Δp = 1.555% @ T = 1.3 sec
Selected Δp = 1.590% @ T = 1.3 sec
Selected Δp = 1.625% @ T = 1.3 sec
selected
calculated
Median RDR [%]
Trial γa [-]

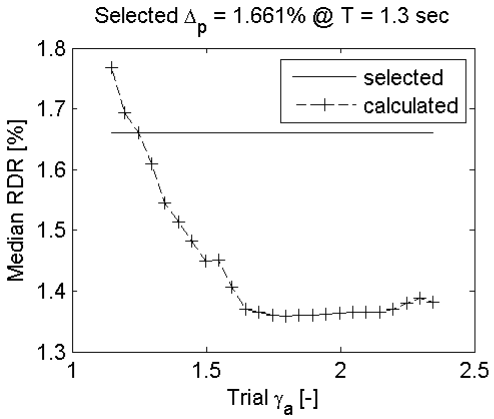
Selected Δ_p = 1.661% @ T = 1.3 sec
selected
calculated
Median RDR [%]
Trial γ_a [-]

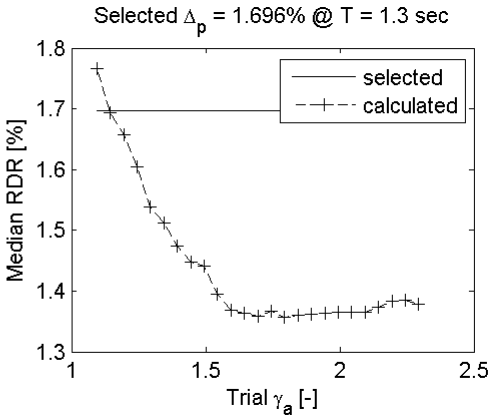
Selected Δ_p = 1.696% @ T = 1.3 sec
selected
calculated
Median RDR [%]
Trial γ_a [-]

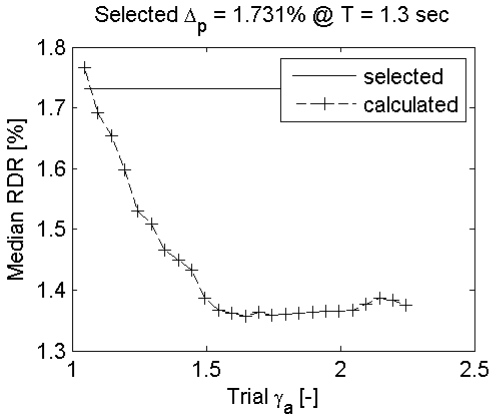
Selected Δ_p = 1.731% @ T = 1.3 sec
selected
calculated
Median RDR [%]
Trial γ_a [-]

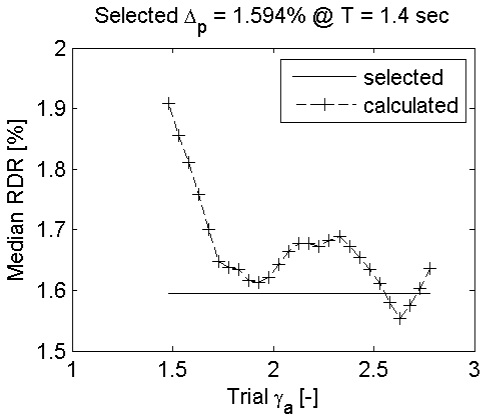
Selected Δ_p = 1.594% @ T = 1.4 sec
selected
calculated
Median RDR [%]
Trial γ_a [-]

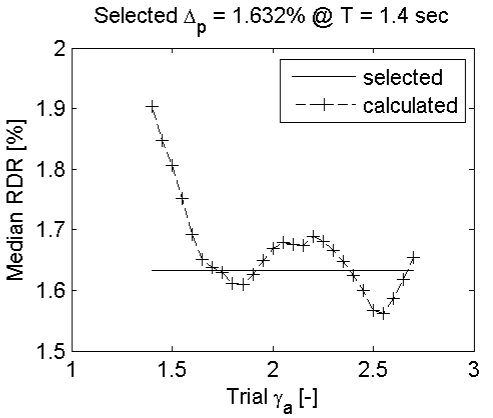
Selected Δ_p = 1.632% @ T = 1.4 sec
selected
calculated
Median RDR [%]
Trial γ_a [-]

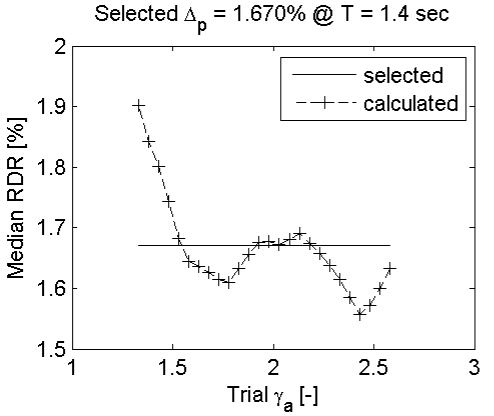
Selected Δ_p = 1.670% @ T = 1.4 sec
selected
calculated
Median RDR [%]
Trial γ_a [-]

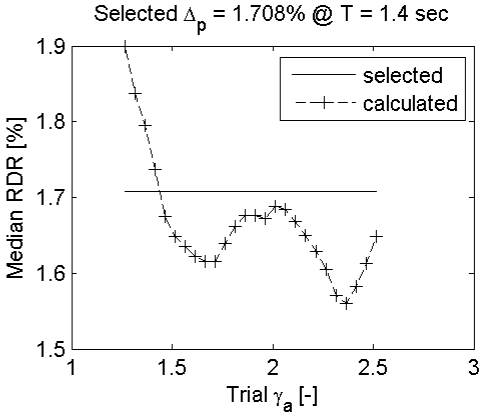
Selected Δ_p = 1.708% @ T = 1.4 sec
selected
calculated
Median RDR [%]
Trial γ_a [-]

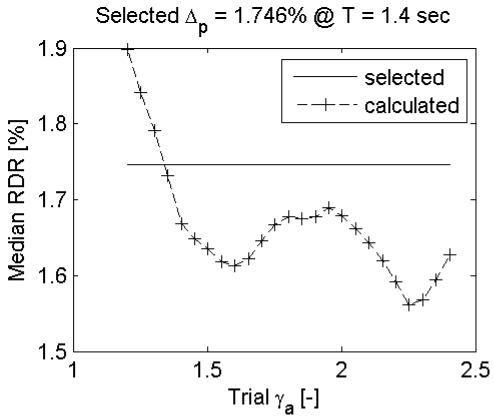
Selected Δp = 1.746% @ T = 1.4 sec
selected
calculated
Median RDR [%]
Trial γa [-]

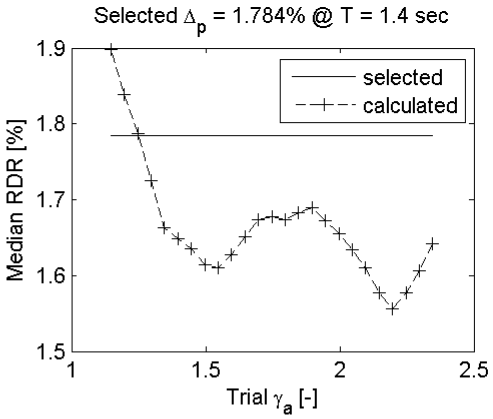
Selected Δp = 1.784% @ T = 1.4 sec
selected
calculated
Median RDR [%]
Trial γa [-]

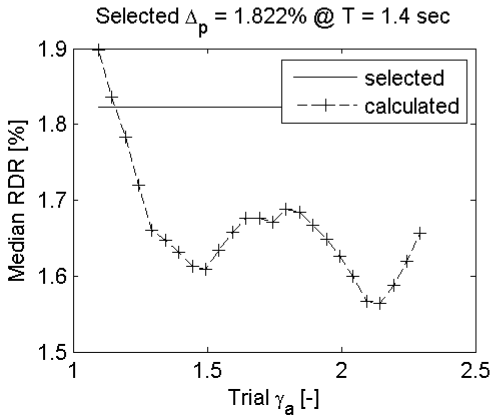
Selected Δp = 1.822% @ T = 1.4 sec
selected
calculated
Median RDR [%]
Trial γa [-]

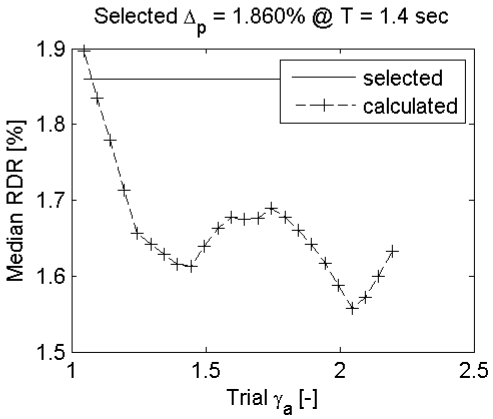
Selected Δp = 1.860% @ T = 1.4 sec
selected
calculated
Median RDR [%]
Trial γa [-]

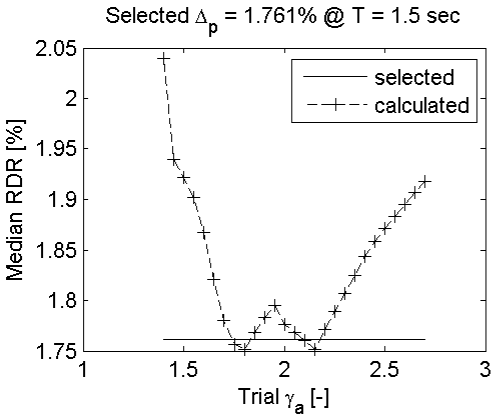
Selected Δp = 1.761% @ T = 1.5 sec
selected
calculated
Median RDR [%]
Trial γa [-]

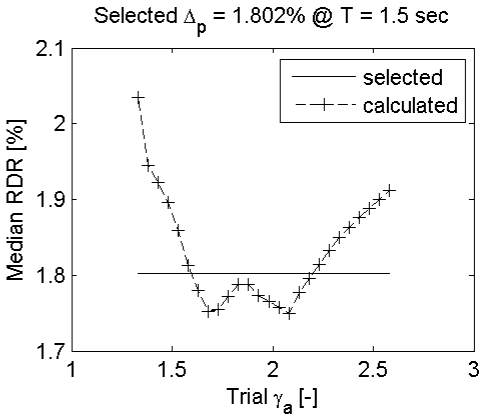
Selected Δp = 1.802% @ T = 1.5 sec
selected
calculated
Median RDR [%]
Trial γa [-]

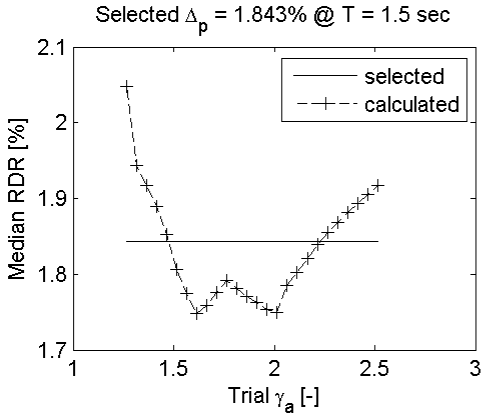
Selected Δp = 1.843% @ T = 1.5 sec
selected
calculated
Median RDR [%]
Trial γa [-]

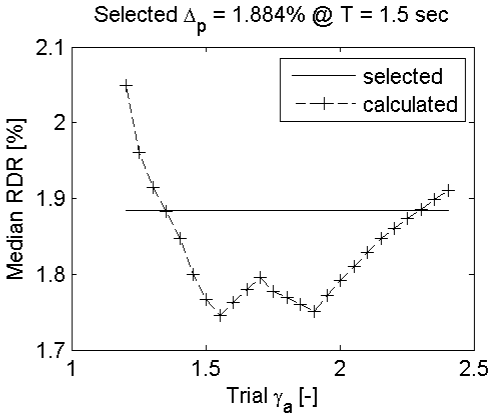
Selected Δp = 1.884% @ T = 1.5 sec
selected
calculated
Median RDR [%]
Trial γa [-]

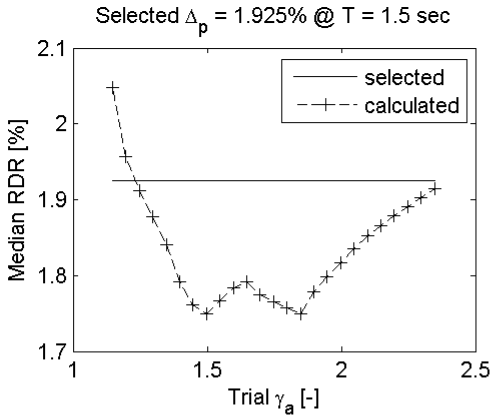
Selected Δ_p = 1.925% @ T = 1.5 sec
selected
calculated
Median RDR [%]
Trial γ_a [-]

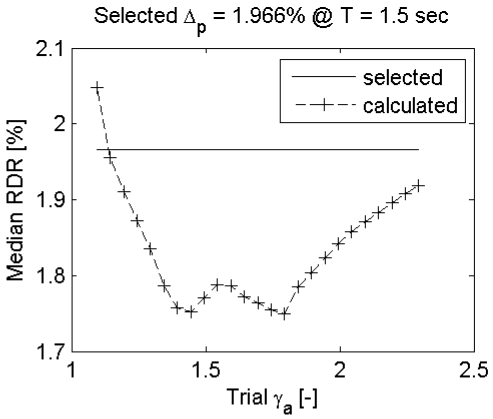
Selected Δ_p = 1.966% @ T = 1.5 sec
selected
calculated
Median RDR [%]
Trial γ_a [-]

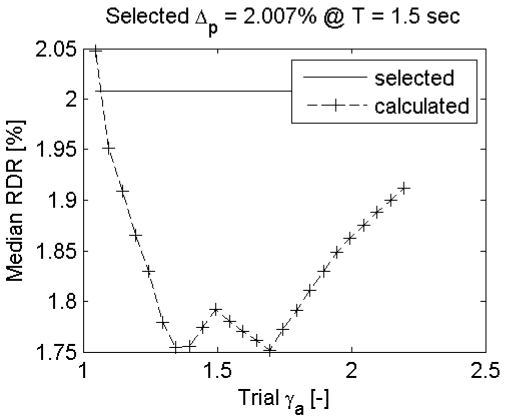
Selected Δ_p = 2.007% @ T = 1.5 sec
selected
calculated
Median RDR [%]
Trial γ_a [-]

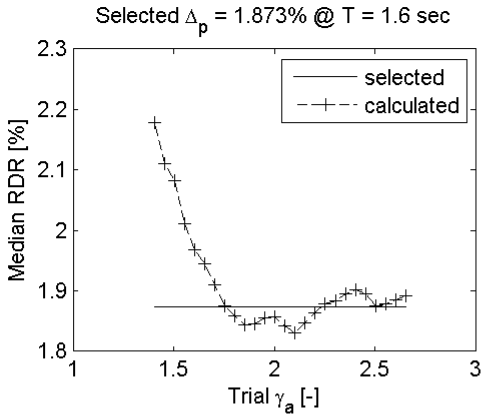
Selected Δ_p = 1.873% @ T = 1.6 sec
selected
calculated
Median RDR [%]
Trial γ_a [-]

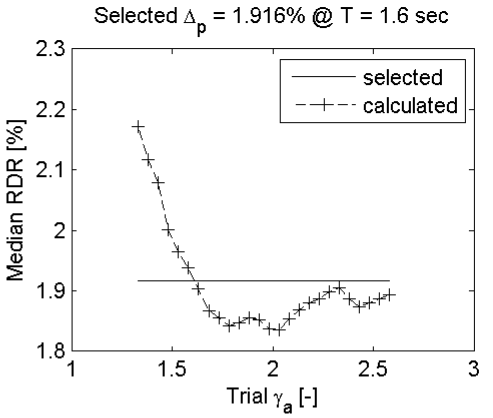
Selected Δ_p = 1.916% @ T = 1.6 sec
selected
calculated
Median RDR [%]
Trial γ_a [-]

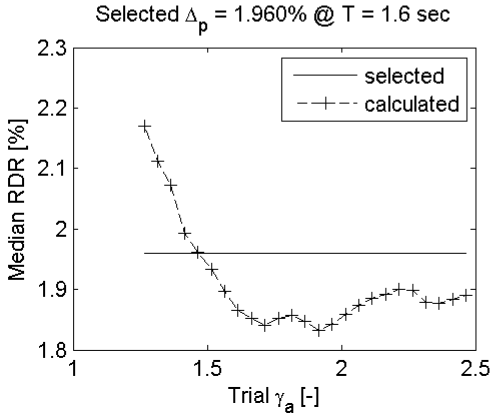
Selected Δ_p = 1.960% @ T = 1.6 sec
selected
calculated
Median RDR [%]
Trial γ_a [-]

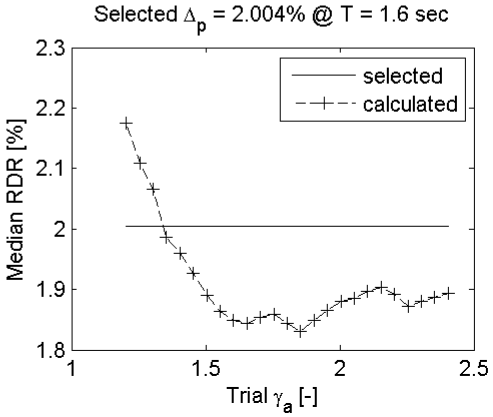
Selected Δ_p = 2.004% @ T = 1.6 sec
selected
calculated
Median RDR [%]
Trial γ_a [-]

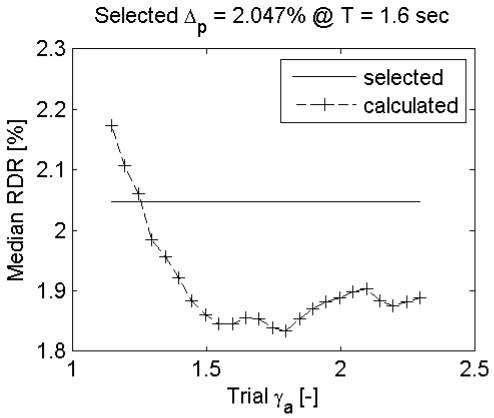
Selected Δp = 2.047% @ T = 1.6 sec
selected
calculated
Median RDR [%]
Trial γa [-]

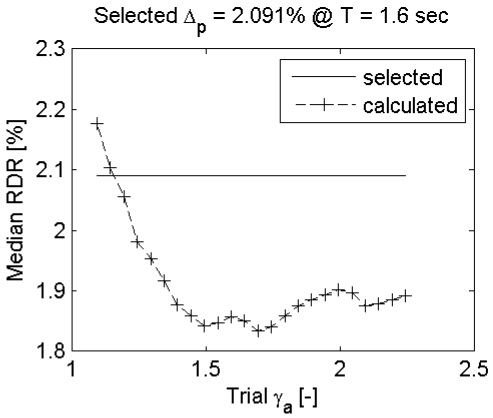
Selected Δp = 2.091% @ T = 1.6 sec
selected
calculated
Median RDR [%]
Trial γa [-]

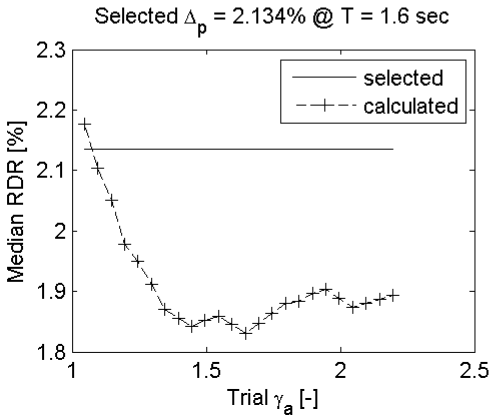
Selected Δp = 2.134% @ T = 1.6 sec
selected
calculated
Median RDR [%]
Trial γa [-]

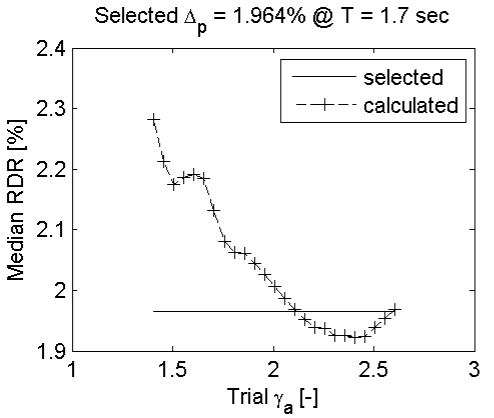
Selected Δp = 1.964% @ T = 1.7 sec
selected
calculated
Median RDR [%]
Trial γa [-]

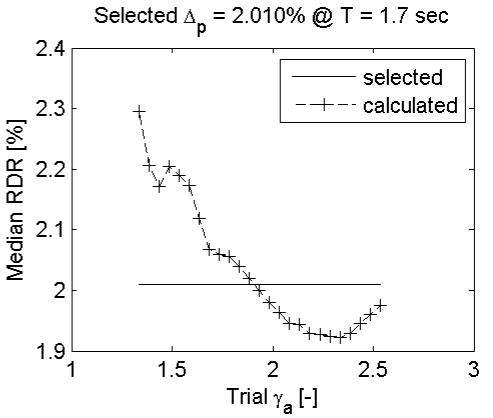
Selected Δp = 2.010% @ T = 1.7 sec
selected
calculated
Median RDR [%]
Trial γa [-]

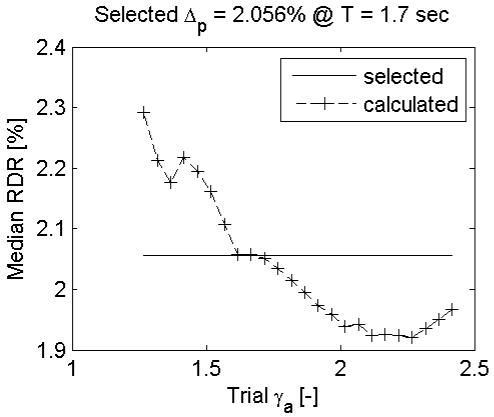
Selected Δp = 2.056% @ T = 1.7 sec
selected
calculated
Median RDR [%]
Trial γa [-]

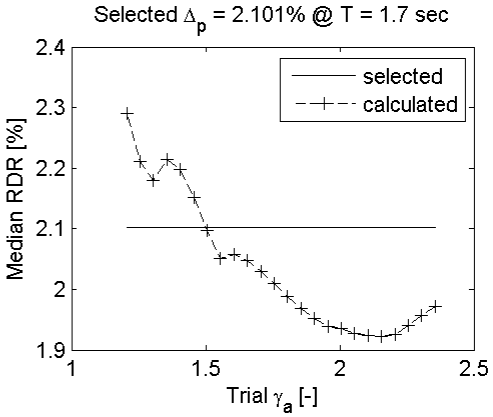
Selected Δp = 2.101% @ T = 1.7 sec
selected
calculated
Median RDR [%]
Trial γa [-]

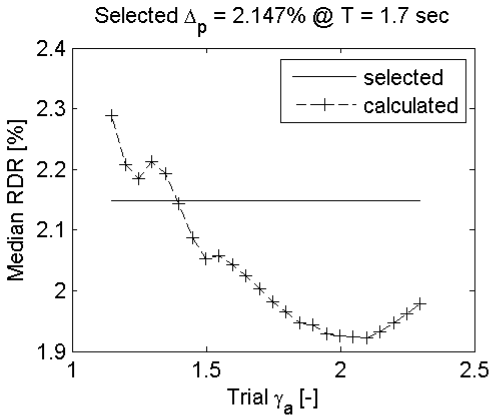
Selected Δp = 2.147% @ T = 1.7 sec
selected
calculated
Median RDR [%]
Trial γa [-]

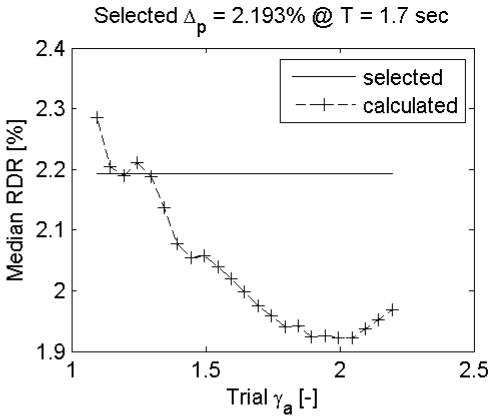
Selected Δp = 2.193% @ T = 1.7 sec
selected
calculated
Median RDR [%]
Trial γa [-]

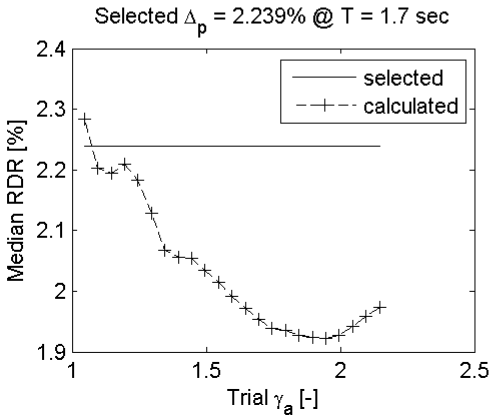
Selected Δp = 2.239% @ T = 1.7 sec
selected
calculated
Median RDR [%]
Trial γa [-]

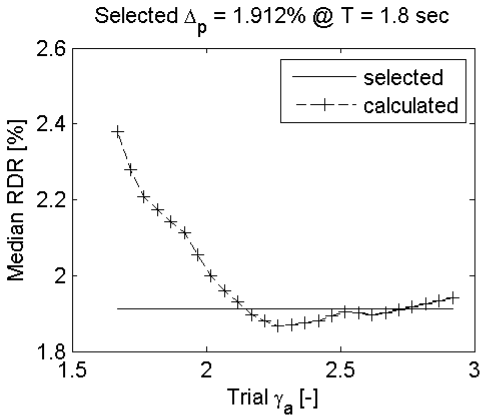
Selected Δp = 1.912% @ T = 1.8 sec
selected
calculated
Median RDR [%]
Trial γa [-]

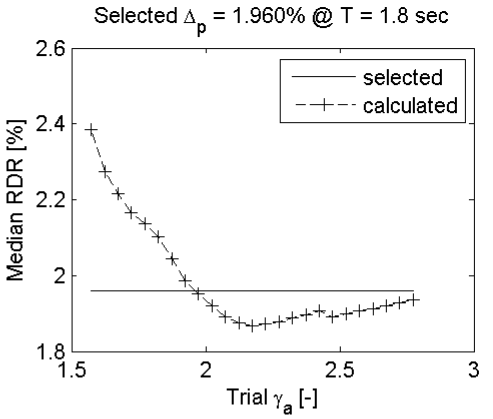
Selected Δp = 1.960% @ T = 1.8 sec
selected
calculated
Median RDR [%]
Trial γa [-]

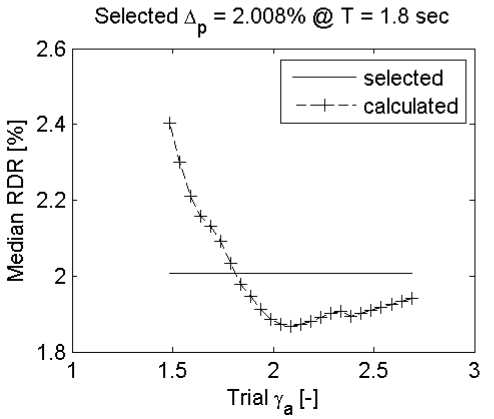
Selected Δp = 2.008% @ T = 1.8 sec
selected
calculated
Median RDR [%]
Trial γa [-]

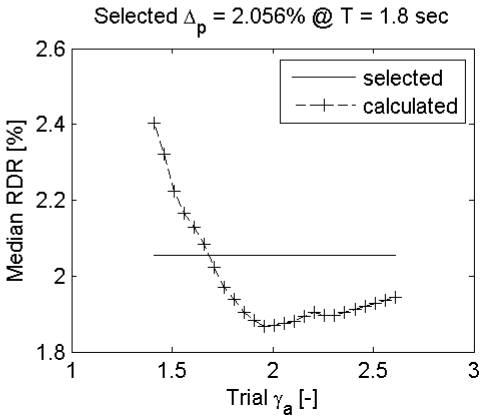
Selected Δp = 2.056% @ T = 1.8 sec
selected
calculated
Median RDR [%]
Trial γa [-]

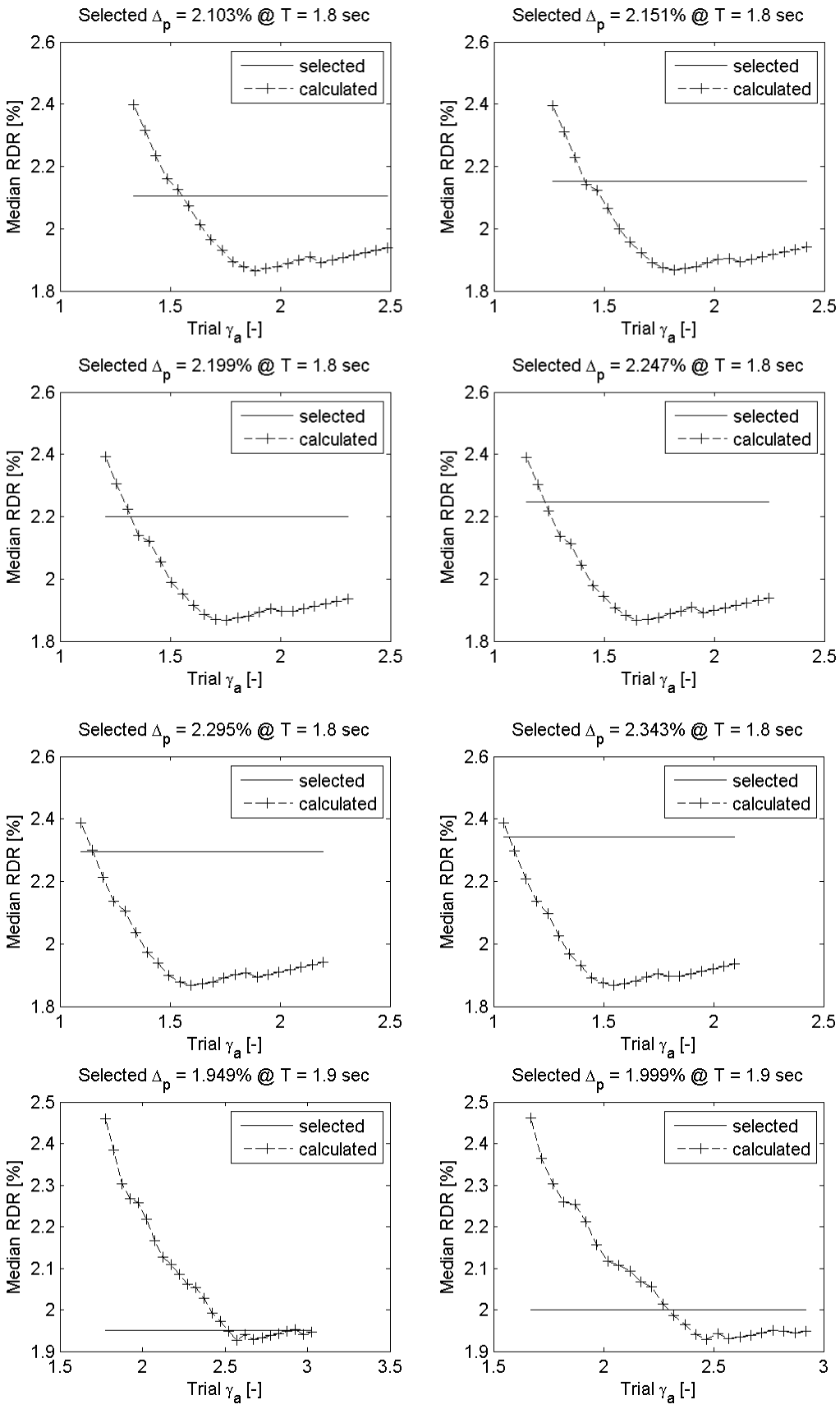
Selected Δp = 2.103% @ T = 1.8 sec
Selected Δp = 2.151% @ T = 1.8 sec
Selected Δp = 2.199% @ T = 1.8 sec
Selected Δp = 2.247% @ T = 1.8 sec
Selected Δp = 2.295% @ T = 1.8 sec
Selected Δp = 2.343% @ T = 1.8 sec
Selected Δp = 1.949% @ T = 1.9 sec
Selected Δp = 1.999% @ T = 1.9 sec
selected
calculated
Median RDR [%]
Trial γa [-]

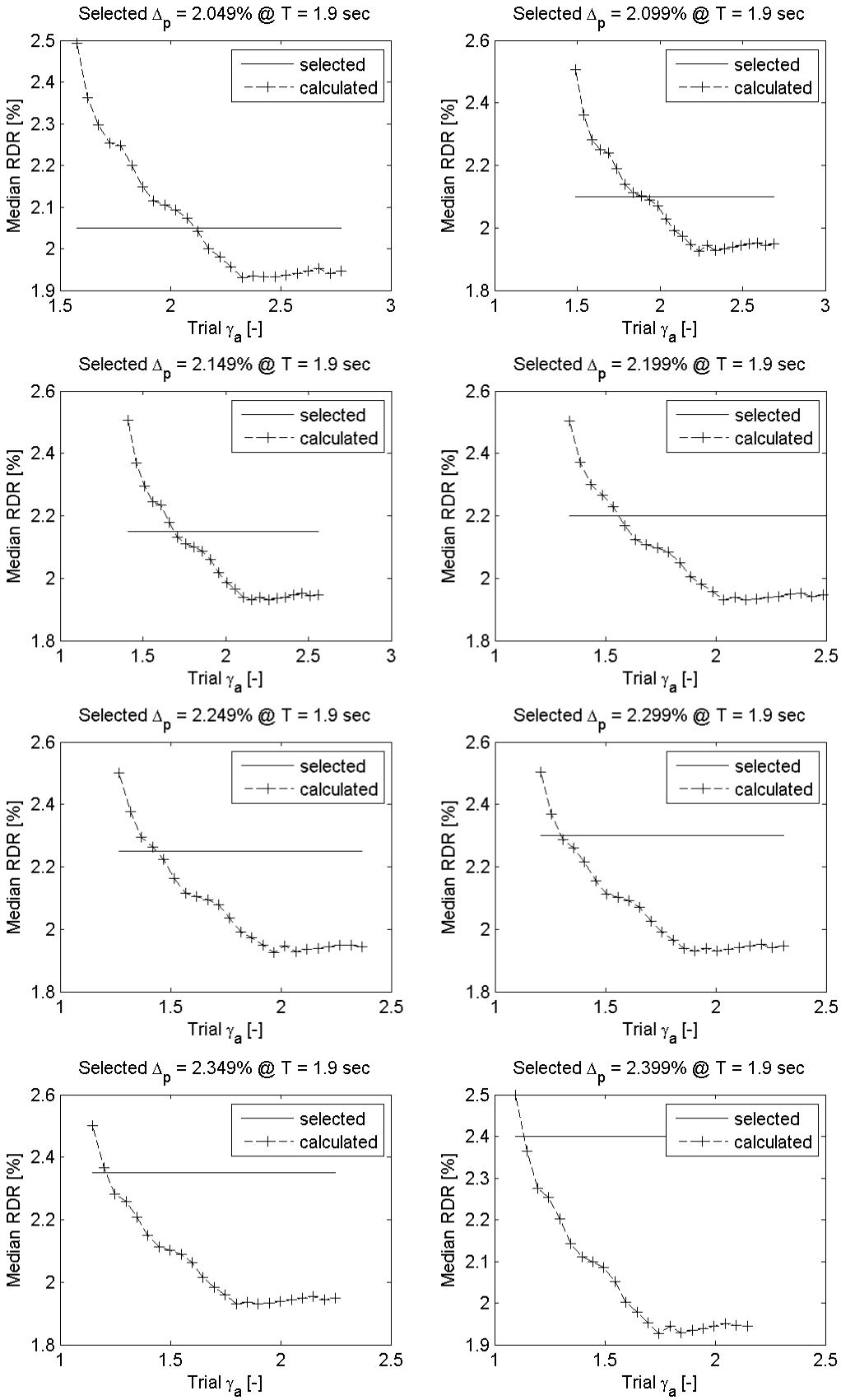
Selected Δp = 2.049% @ T = 1.9 sec
Selected Δp = 2.099% @ T = 1.9 sec
Selected Δp = 2.149% @ T = 1.9 sec
Selected Δp = 2.199% @ T = 1.9 sec
Selected Δp = 2.249% @ T = 1.9 sec
Selected Δp = 2.299% @ T = 1.9 sec
Selected Δp = 2.349% @ T = 1.9 sec
Selected Δp = 2.399% @ T = 1.9 sec
selected
calculated
Median RDR [%]
Trial γa [-]

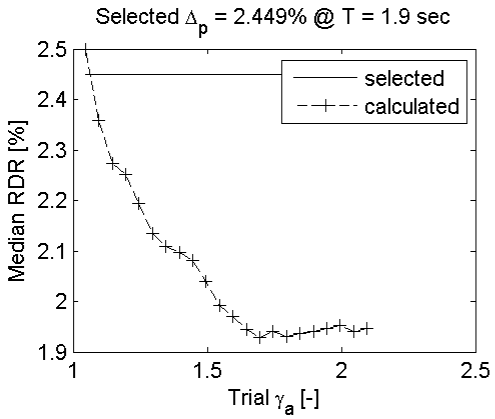
Selected Δp = 2.449% @ T = 1.9 sec
selected
calculated
Median RDR [%]
Trial γa [-]

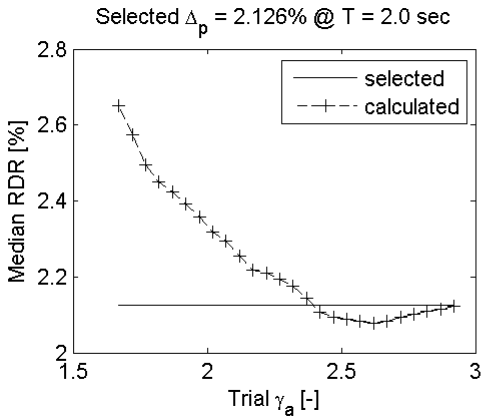
Selected Δp = 2.126% @ T = 2.0 sec
selected
calculated
Median RDR [%]
Trial γa [-]

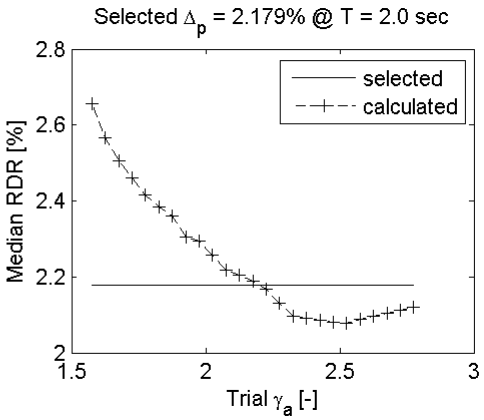
Selected Δp = 2.179% @ T = 2.0 sec
selected
calculated
Median RDR [%]
Trial γa [-]

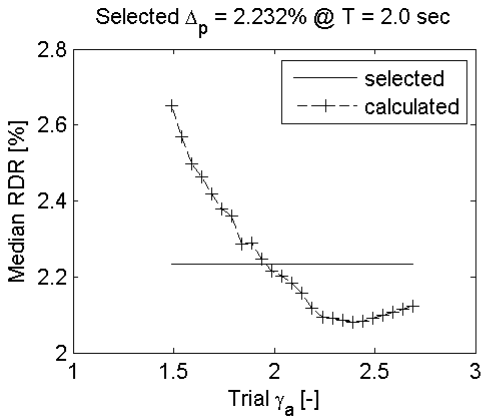
Selected Δp = 2.232% @ T = 2.0 sec
selected
calculated
Median RDR [%]
Trial γa [-]

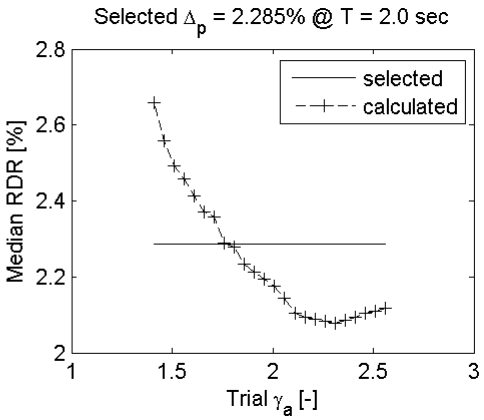
Selected Δp = 2.285% @ T = 2.0 sec
selected
calculated
Median RDR [%]
Trial γa [-]

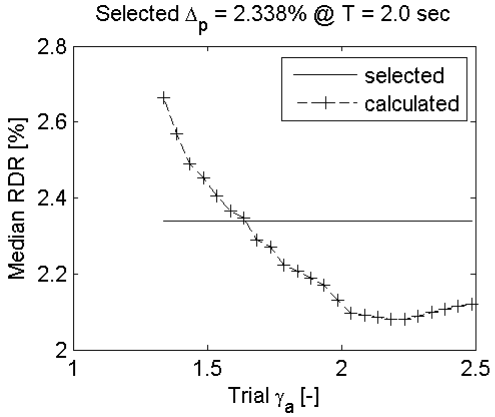
Selected Δp = 2.338% @ T = 2.0 sec
selected
calculated
Median RDR [%]
Trial γa [-]

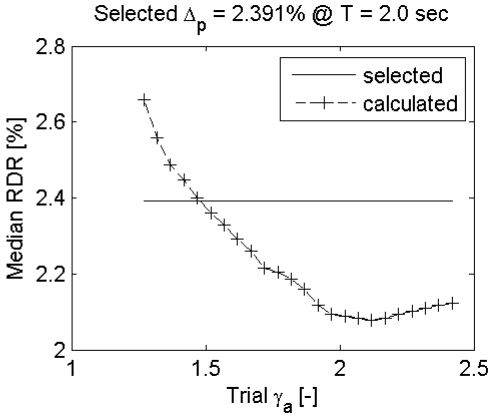
Selected Δp = 2.391% @ T = 2.0 sec
selected
calculated
Median RDR [%]
Trial γa [-]

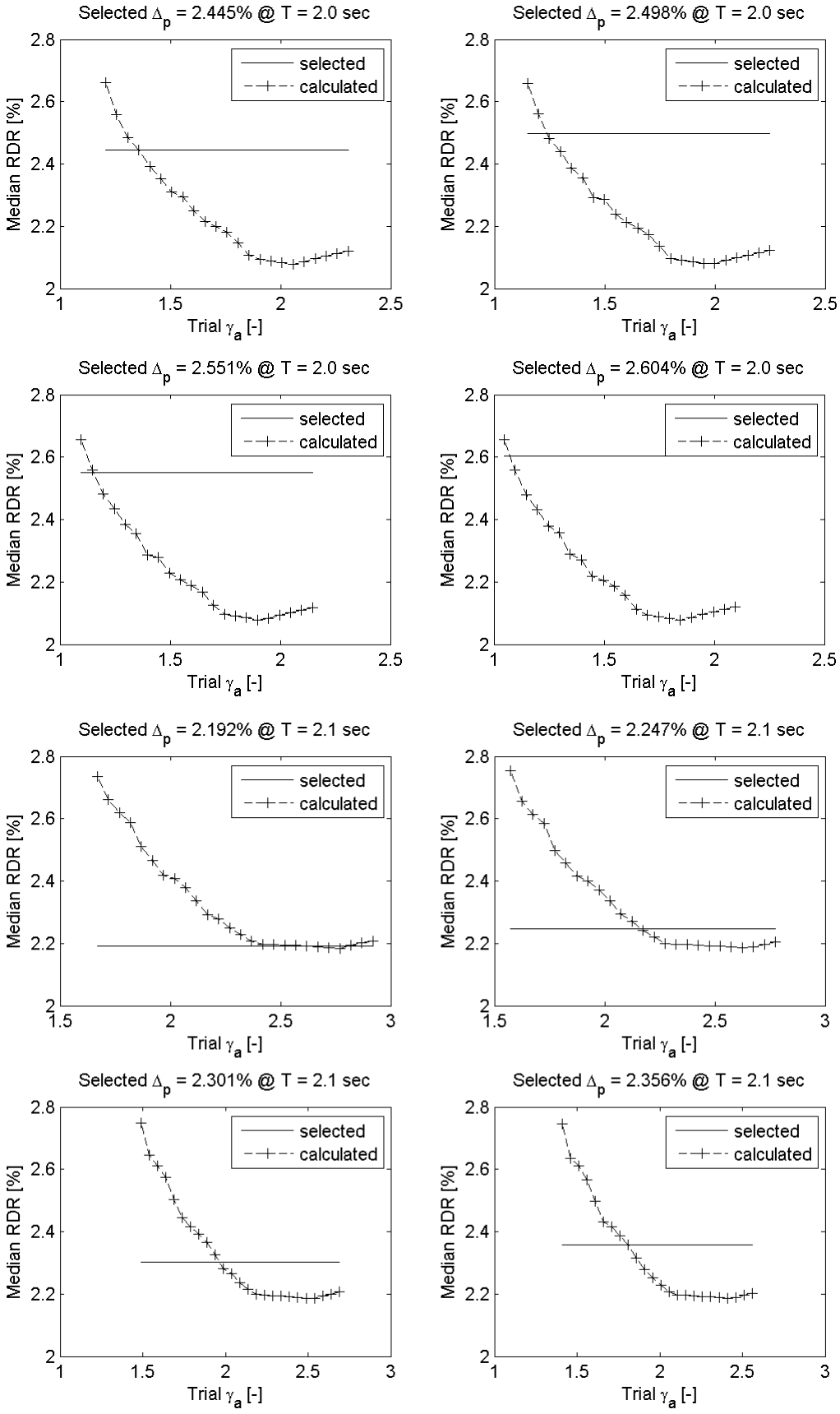
Selected Δp = 2.445% @ T = 2.0 sec
Selected Δp = 2.498% @ T = 2.0 sec
Selected Δp = 2.551% @ T = 2.0 sec
Selected Δp = 2.604% @ T = 2.0 sec
Selected Δp = 2.192% @ T = 2.1 sec
Selected Δp = 2.247% @ T = 2.1 sec
Selected Δp = 2.301% @ T = 2.1 sec
Selected Δp = 2.356% @ T = 2.1 sec
selected
calculated
Median RDR [%]
Trial γa [-]

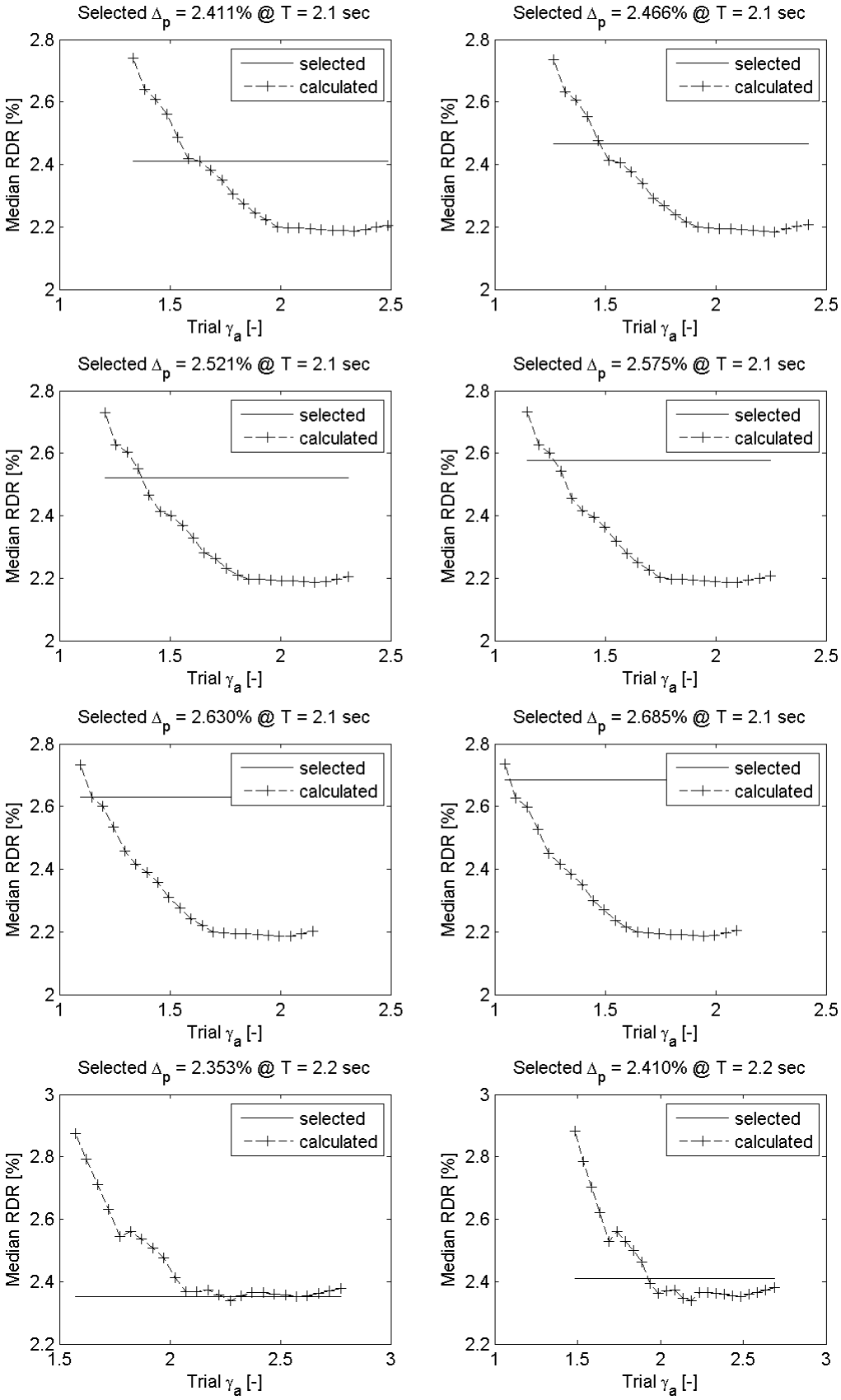
Selected Δp = 2.411% @ T = 2.1 sec
Selected Δp = 2.466% @ T = 2.1 sec
Selected Δp = 2.521% @ T = 2.1 sec
Selected Δp = 2.575% @ T = 2.1 sec
Selected Δp = 2.630% @ T = 2.1 sec
Selected Δp = 2.685% @ T = 2.1 sec
Selected Δp = 2.353% @ T = 2.2 sec
Selected Δp = 2.410% @ T = 2.2 sec
selected
calculated
Median RDR [%]
Trial γa [-]

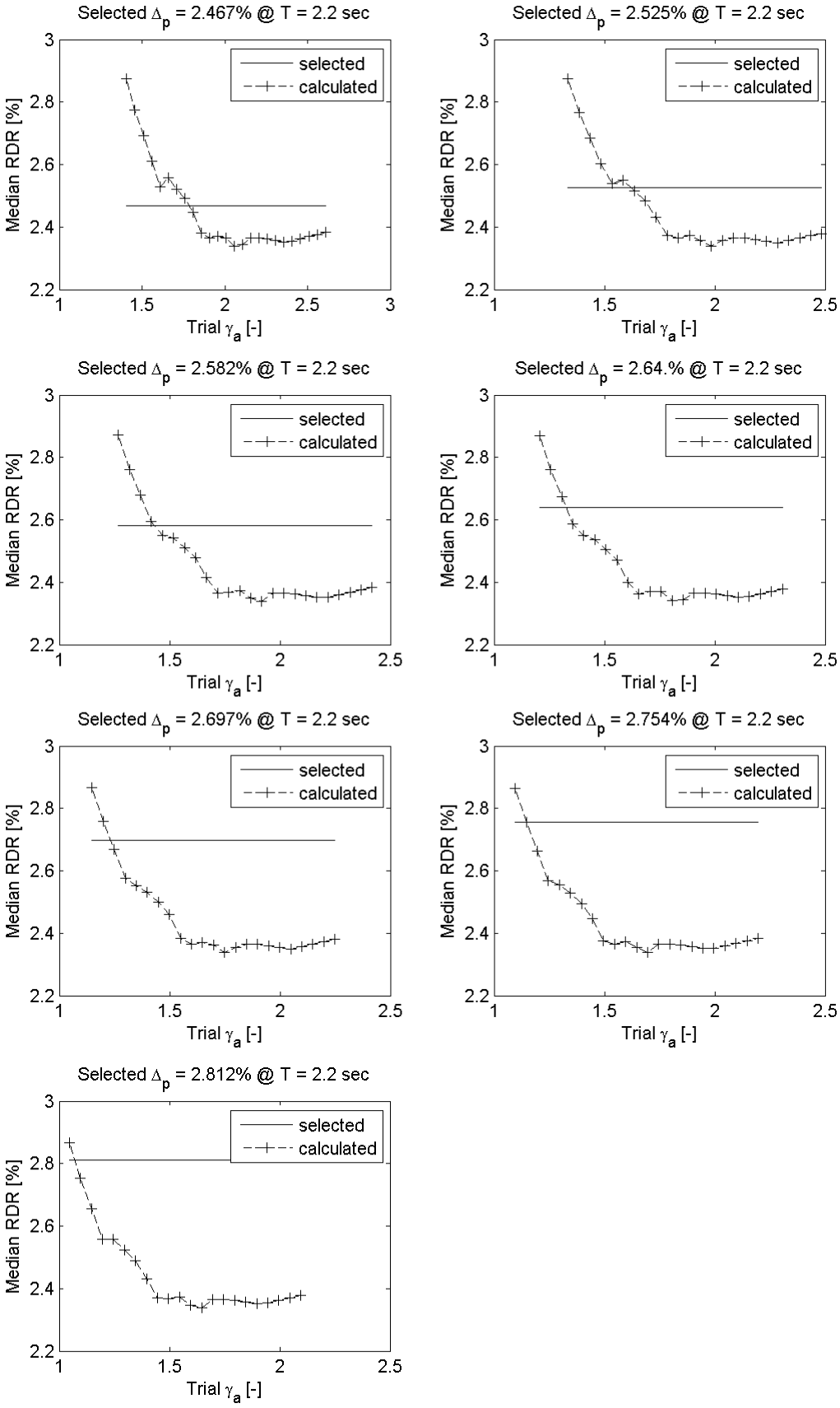
Selected Δp = 2.467% @ T = 2.2 sec
Selected Δp = 2.525% @ T = 2.2 sec
Selected Δp = 2.582% @ T = 2.2 sec
Selected Δp = 2.64.% @ T = 2.2 sec
Selected Δp = 2.697% @ T = 2.2 sec
Selected Δp = 2.754% @ T = 2.2 sec
Selected Δp = 2.812% @ T = 2.2 sec
selected
calculated
Median RDR [%]
Trial γa [-]

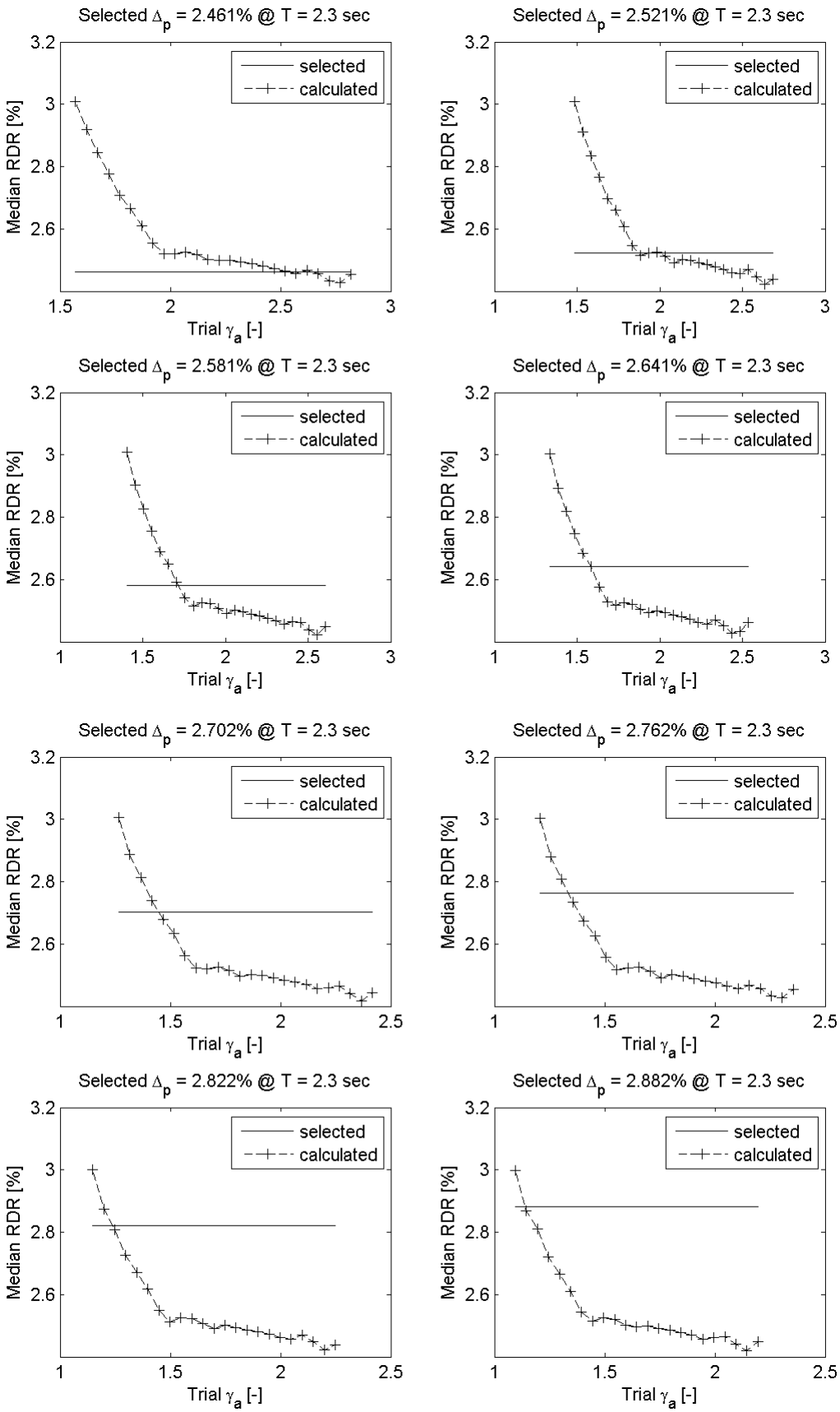
Selected Δp = 2.461% @ T = 2.3 sec
Selected Δp = 2.521% @ T = 2.3 sec
Selected Δp = 2.581% @ T = 2.3 sec
Selected Δp = 2.641% @ T = 2.3 sec
Selected Δp = 2.702% @ T = 2.3 sec
Selected Δp = 2.762% @ T = 2.3 sec
Selected Δp = 2.822% @ T = 2.3 sec
Selected Δp = 2.882% @ T = 2.3 sec
selected
calculated
Median RDR [%]
Trial γa [-]

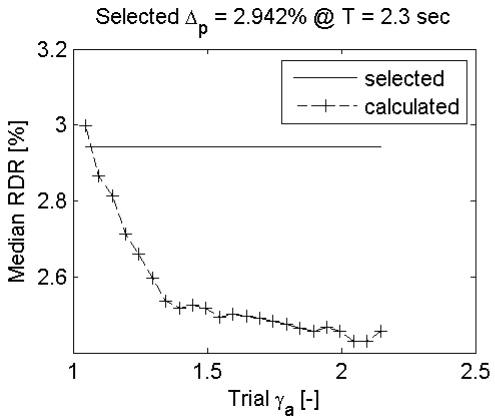
Selected Δp = 2.942% @ T = 2.3 sec
selected
calculated
Median RDR [%]
Trial γa [-]

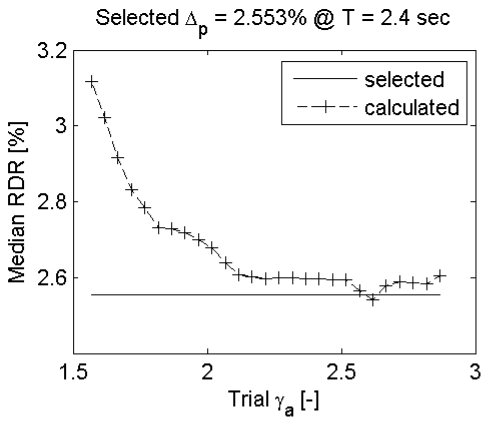
Selected Δp = 2.553% @ T = 2.4 sec
selected
calculated
Median RDR [%]
Trial γa [-]

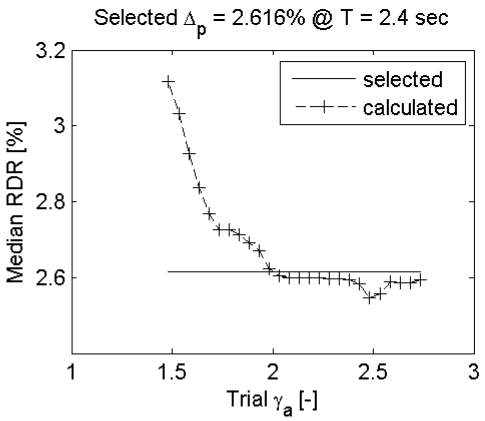
Selected Δp = 2.616% @ T = 2.4 sec
selected
calculated
Median RDR [%]
Trial γa [-]

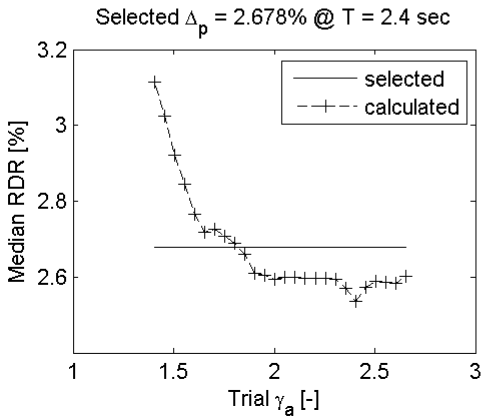
Selected Δp = 2.678% @ T = 2.4 sec
selected
calculated
Median RDR [%]
Trial γa [-]

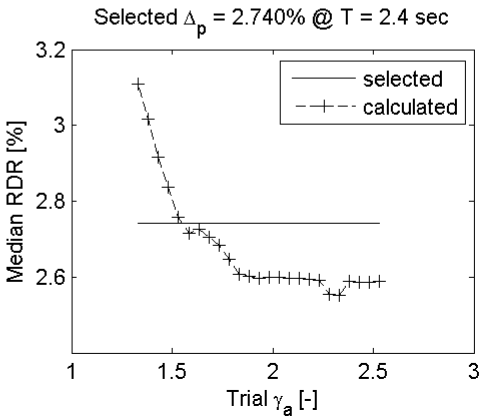
Selected Δp = 2.740% @ T = 2.4 sec
selected
calculated
Median RDR [%]
Trial γa [-]

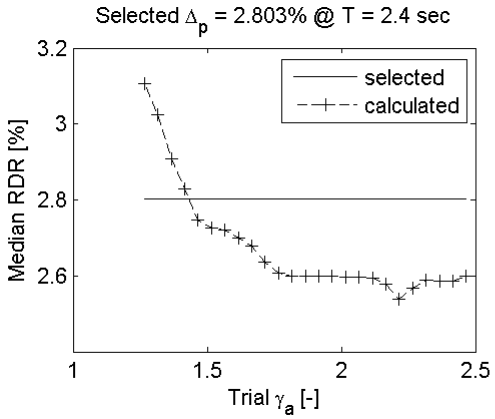
Selected Δp = 2.803% @ T = 2.4 sec
selected
calculated
Median RDR [%]
Trial γa [-]

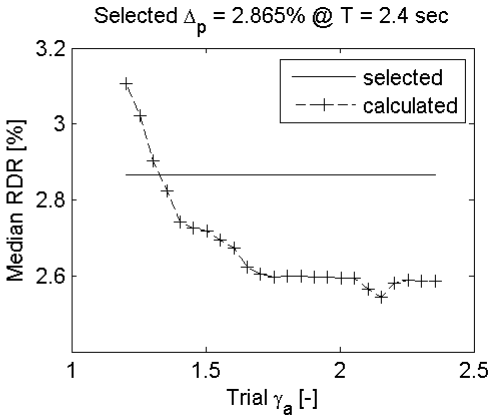
Selected Δp = 2.865% @ T = 2.4 sec
selected
calculated
Median RDR [%]
Trial γa [-]

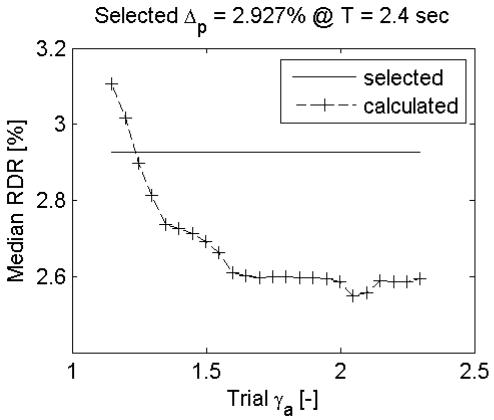
Selected Δ_p = 2.927% @ T = 2.4 sec
selected
calculated
Median RDR [%]
Trial γ_a [-]

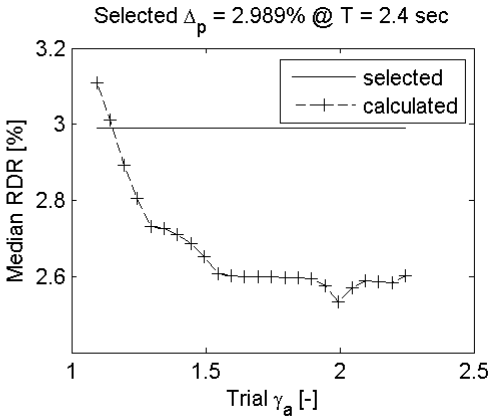
Selected Δ_p = 2.989% @ T = 2.4 sec
selected
calculated
Median RDR [%]
Trial γ_a [-]

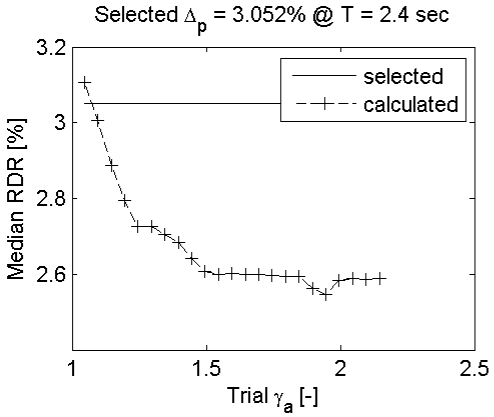
Selected Δ_p = 3.052% @ T = 2.4 sec
selected
calculated
Median RDR [%]
Trial γ_a [-]

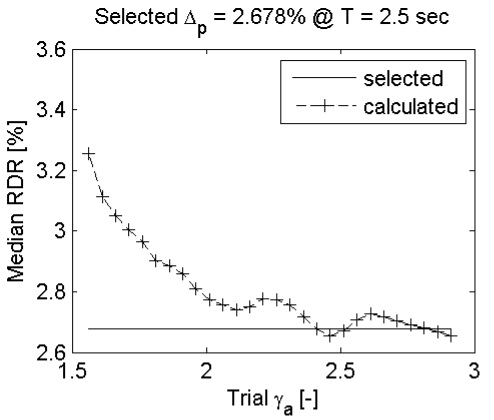
Selected Δ_p = 2.678% @ T = 2.5 sec
selected
calculated
Median RDR [%]
Trial γ_a [-]

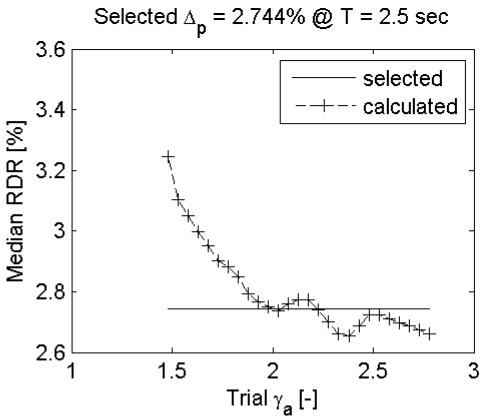
Selected Δ_p = 2.744% @ T = 2.5 sec
selected
calculated
Median RDR [%]
Trial γ_a [-]

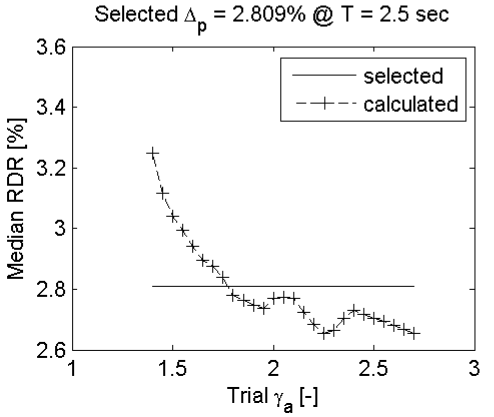
Selected Δ_p = 2.809% @ T = 2.5 sec
selected
calculated
Median RDR [%]
Trial γ_a [-]

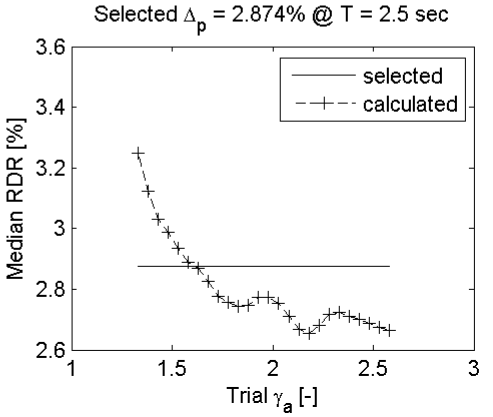
Selected Δ_p = 2.874% @ T = 2.5 sec
selected
calculated
Median RDR [%]
Trial γ_a [-]

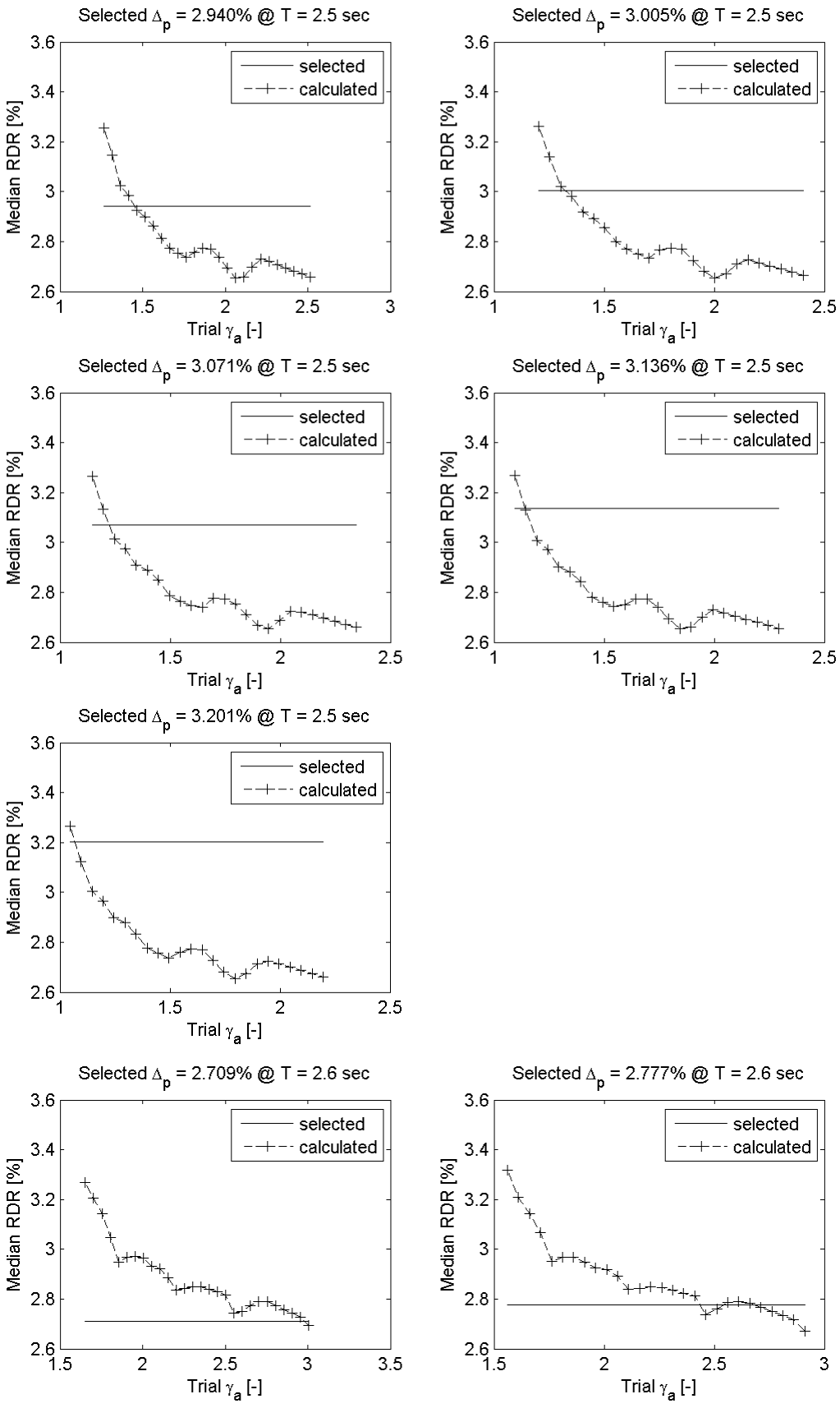
Selected Δp = 2.940% @ T = 2.5 sec
Selected Δp = 3.005% @ T = 2.5 sec
Selected Δp = 3.071% @ T = 2.5 sec
Selected Δp = 3.136% @ T = 2.5 sec
Selected Δp = 3.201% @ T = 2.5 sec
Selected Δp = 2.709% @ T = 2.6 sec
Selected Δp = 2.777% @ T = 2.6 sec
selected
calculated
Median RDR [%]
Trial γa [-]

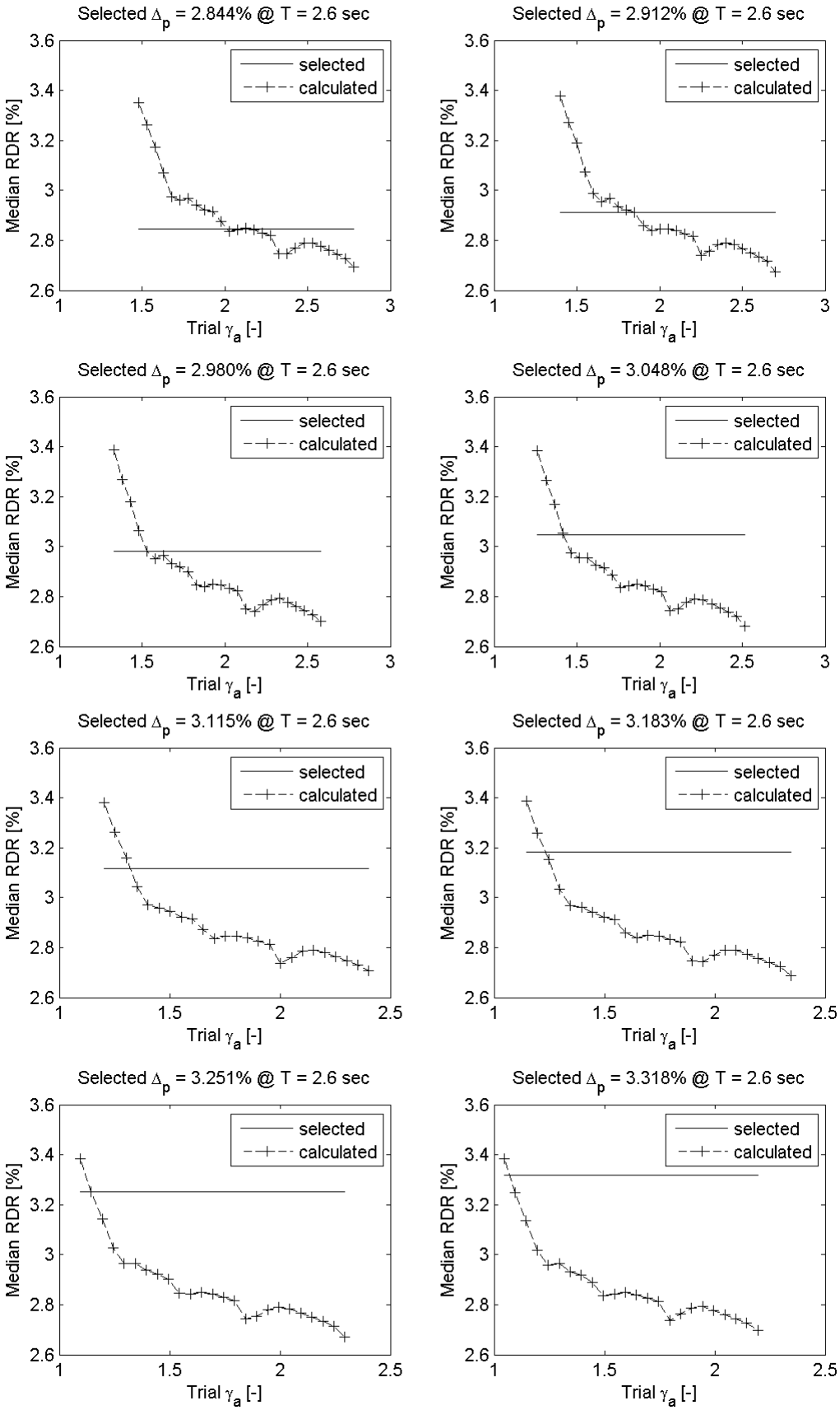
Selected Δp = 2.844% @ T = 2.6 sec
Selected Δp = 2.912% @ T = 2.6 sec
Selected Δp = 2.980% @ T = 2.6 sec
Selected Δp = 3.048% @ T = 2.6 sec
Selected Δp = 3.115% @ T = 2.6 sec
Selected Δp = 3.183% @ T = 2.6 sec
Selected Δp = 3.251% @ T = 2.6 sec
Selected Δp = 3.318% @ T = 2.6 sec
selected
calculated
Median RDR [%]
Trial γa [-]

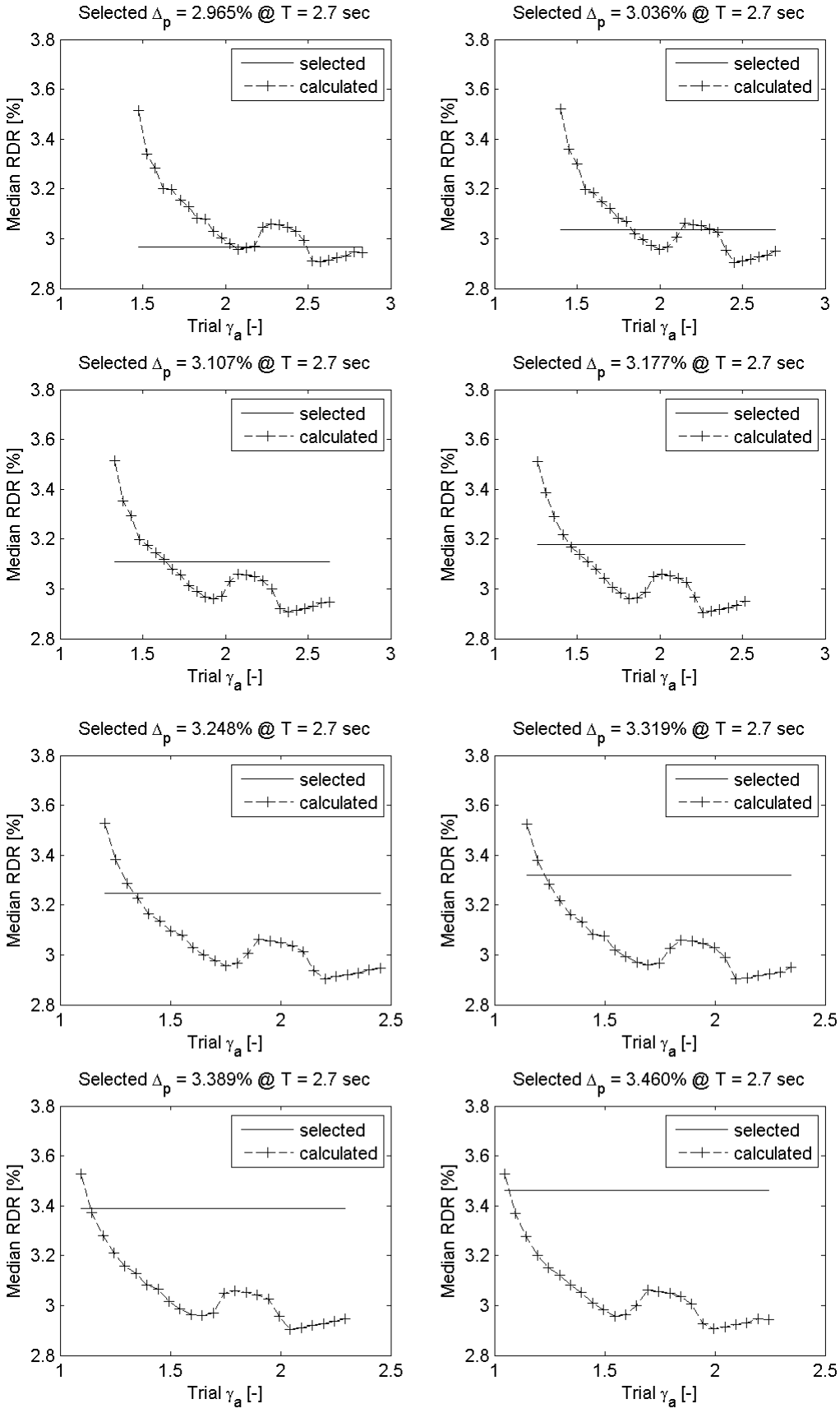
Selected Δp = 2.965% @ T = 2.7 sec
Selected Δp = 3.036% @ T = 2.7 sec
Selected Δp = 3.107% @ T = 2.7 sec
Selected Δp = 3.177% @ T = 2.7 sec
Selected Δp = 3.248% @ T = 2.7 sec
Selected Δp = 3.319% @ T = 2.7 sec
Selected Δp = 3.389% @ T = 2.7 sec
Selected Δp = 3.460% @ T = 2.7 sec
selected
calculated
Median RDR [%]
Trial γa [-]

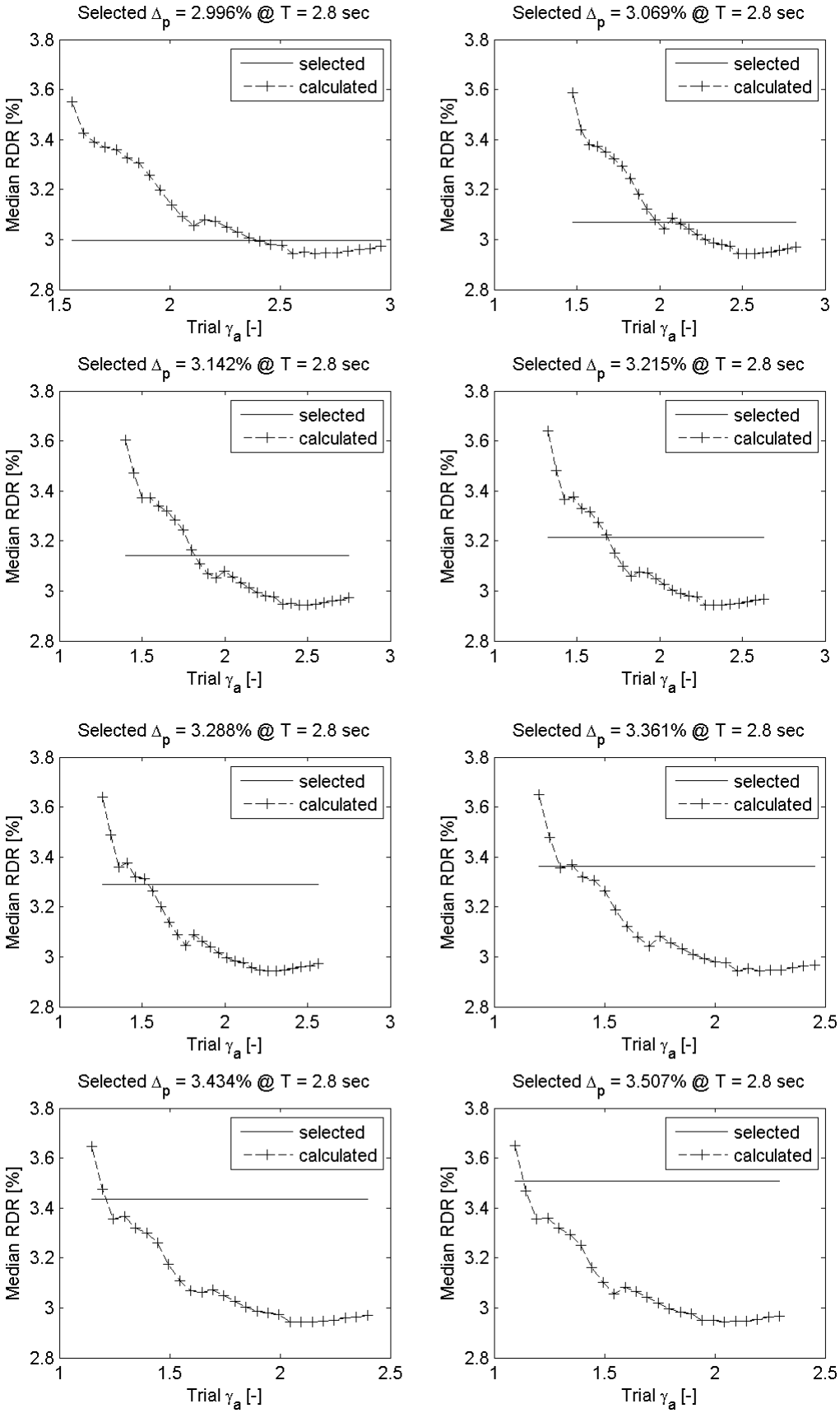
Selected Δp = 2.996% @ T = 2.8 sec
Selected Δp = 3.069% @ T = 2.8 sec
Selected Δp = 3.142% @ T = 2.8 sec
Selected Δp = 3.215% @ T = 2.8 sec
Selected Δp = 3.288% @ T = 2.8 sec
Selected Δp = 3.361% @ T = 2.8 sec
Selected Δp = 3.434% @ T = 2.8 sec
Selected Δp = 3.507% @ T = 2.8 sec
selected
calculated
Median RDR [%]
Trial γa [-]

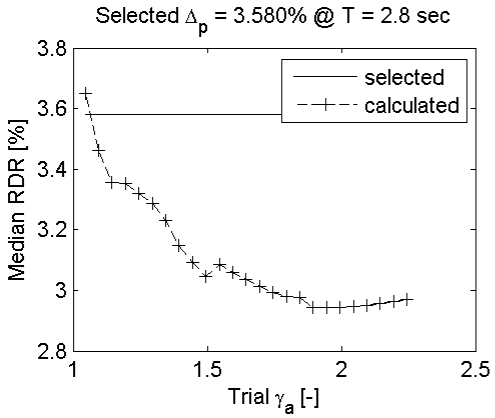
Selected Δp = 3.580% @ T = 2.8 sec
selected
calculated
Median RDR [%]
Trial γa [-]

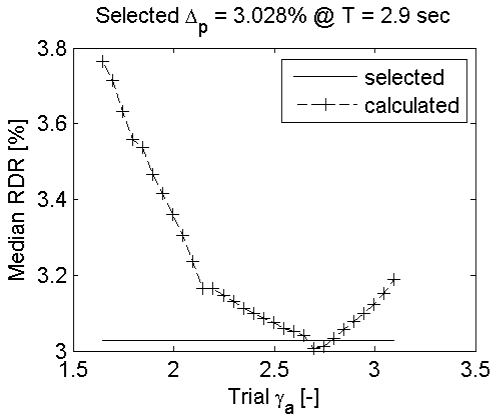
Selected Δp = 3.028% @ T = 2.9 sec
selected
calculated
Median RDR [%]
Trial γa [-]

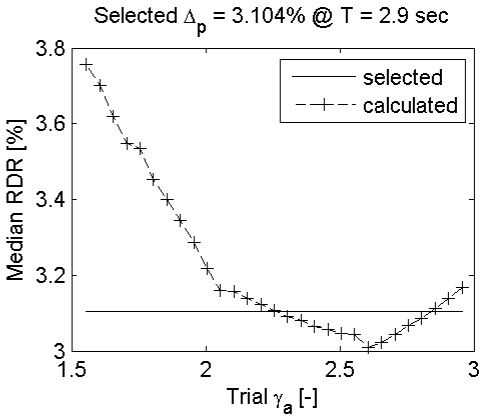
Selected Δp = 3.104% @ T = 2.9 sec
selected
calculated
Median RDR [%]
Trial γa [-]

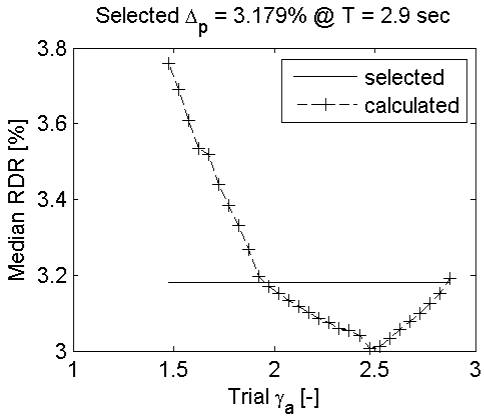
Selected Δp = 3.179% @ T = 2.9 sec
selected
calculated
Median RDR [%]
Trial γa [-]

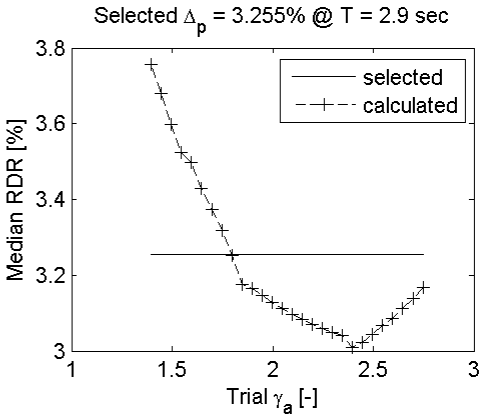
Selected Δp = 3.255% @ T = 2.9 sec
selected
calculated
Median RDR [%]
Trial γa [-]

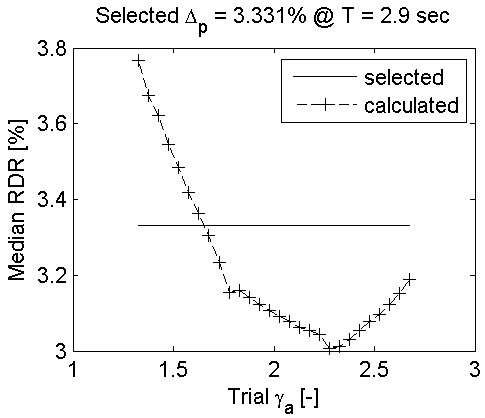
Selected Δp = 3.331% @ T = 2.9 sec
selected
calculated
Median RDR [%]
Trial γa [-]

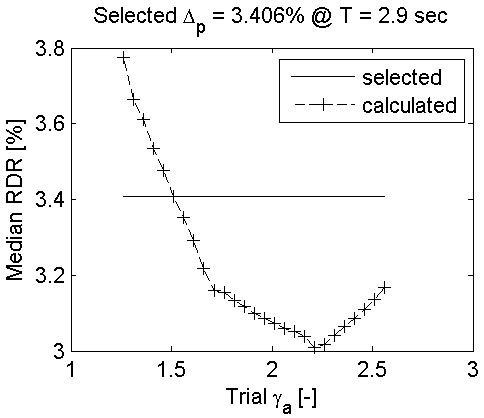
Selected Δp = 3.406% @ T = 2.9 sec
selected
calculated
Median RDR [%]
Trial γa [-]

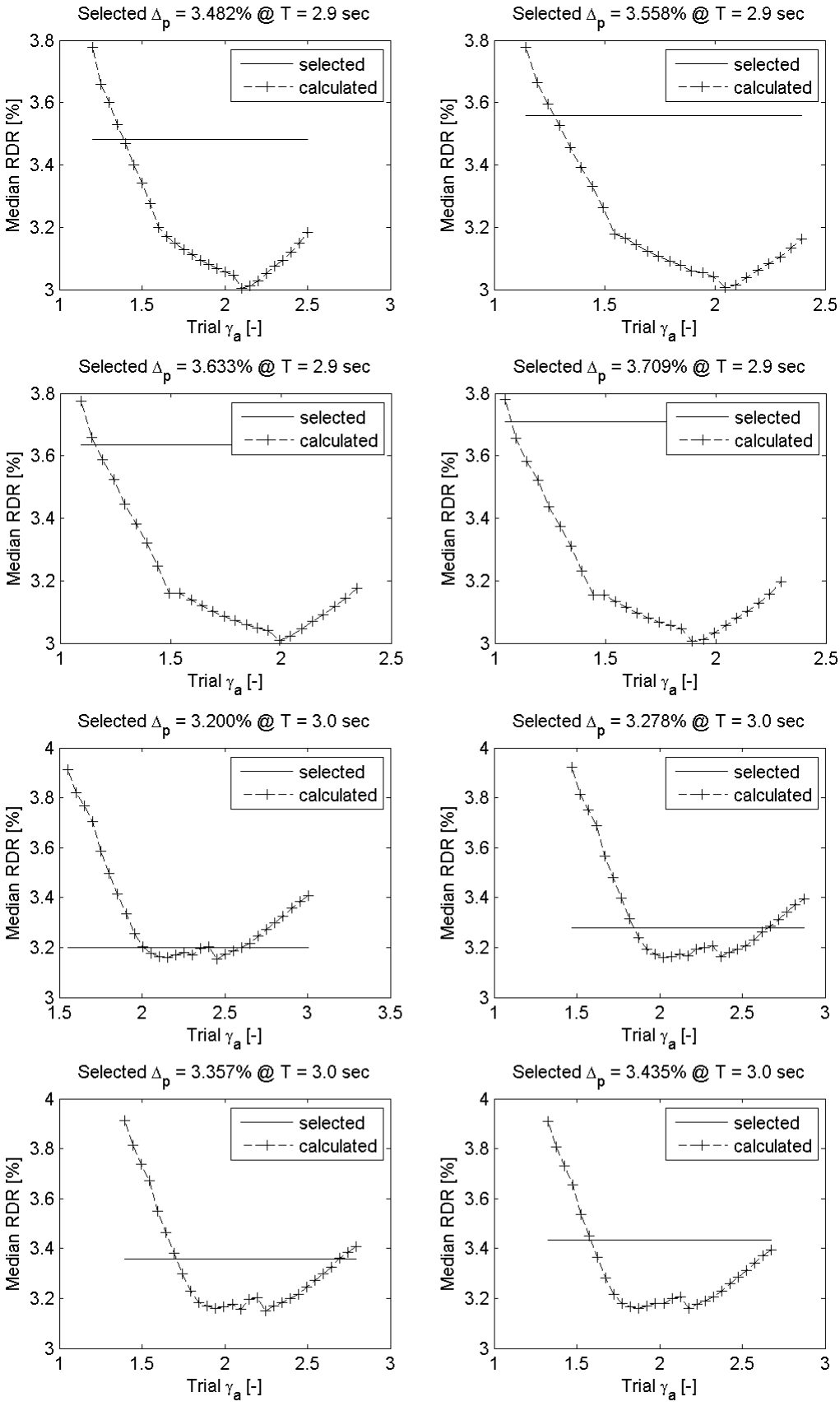
Selected Δp = 3.482% @ T = 2.9 sec
Selected Δp = 3.558% @ T = 2.9 sec
Selected Δp = 3.633% @ T = 2.9 sec
Selected Δp = 3.709% @ T = 2.9 sec
Selected Δp = 3.200% @ T = 3.0 sec
Selected Δp = 3.278% @ T = 3.0 sec
Selected Δp = 3.357% @ T = 3.0 sec
Selected Δp = 3.435% @ T = 3.0 sec
selected
calculated
Median RDR [%]
Trial γa [-]

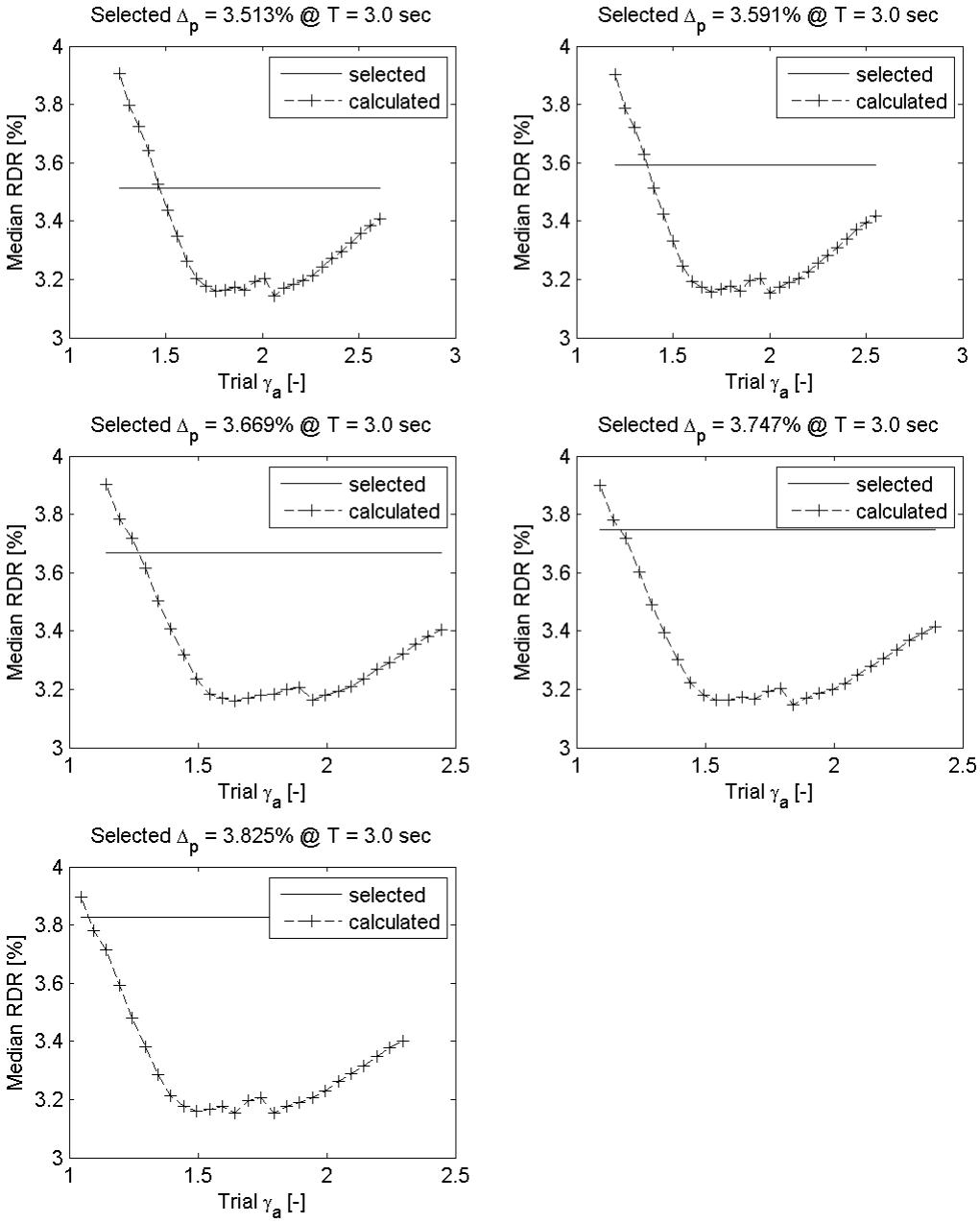
Selected Δp = 3.513% @ T = 3.0 sec
Selected Δp = 3.591% @ T = 3.0 sec
Selected Δp = 3.669% @ T = 3.0 sec
Selected Δp = 3.747% @ T = 3.0 sec
Selected Δp = 3.825% @ T = 3.0 sec
selected
calculated
Median RDR [%]
Trial γa [-]

Appendix B
Roof Drift Ratio of Prototype FTMF

A three-storey office prototype building located in Los Angeles, California, is designed using the proposed equivalent energy design procedure (EEDP) from Chapter 2. The seismic force resisting system is the proposed fused truss moment frame (FTMF) from Chapter 3. Nonlinear dynamic analysis is conducted using the ground motions presetned in Table 3.1. The figures in this appendix are the roof drift ratio (RDR) time hisotries of the building subjected to the motions scaled to the service level earthquake (SLE), designed based earthquake (DBE), and maximum considered earthquake (MCE) shaking intensities.

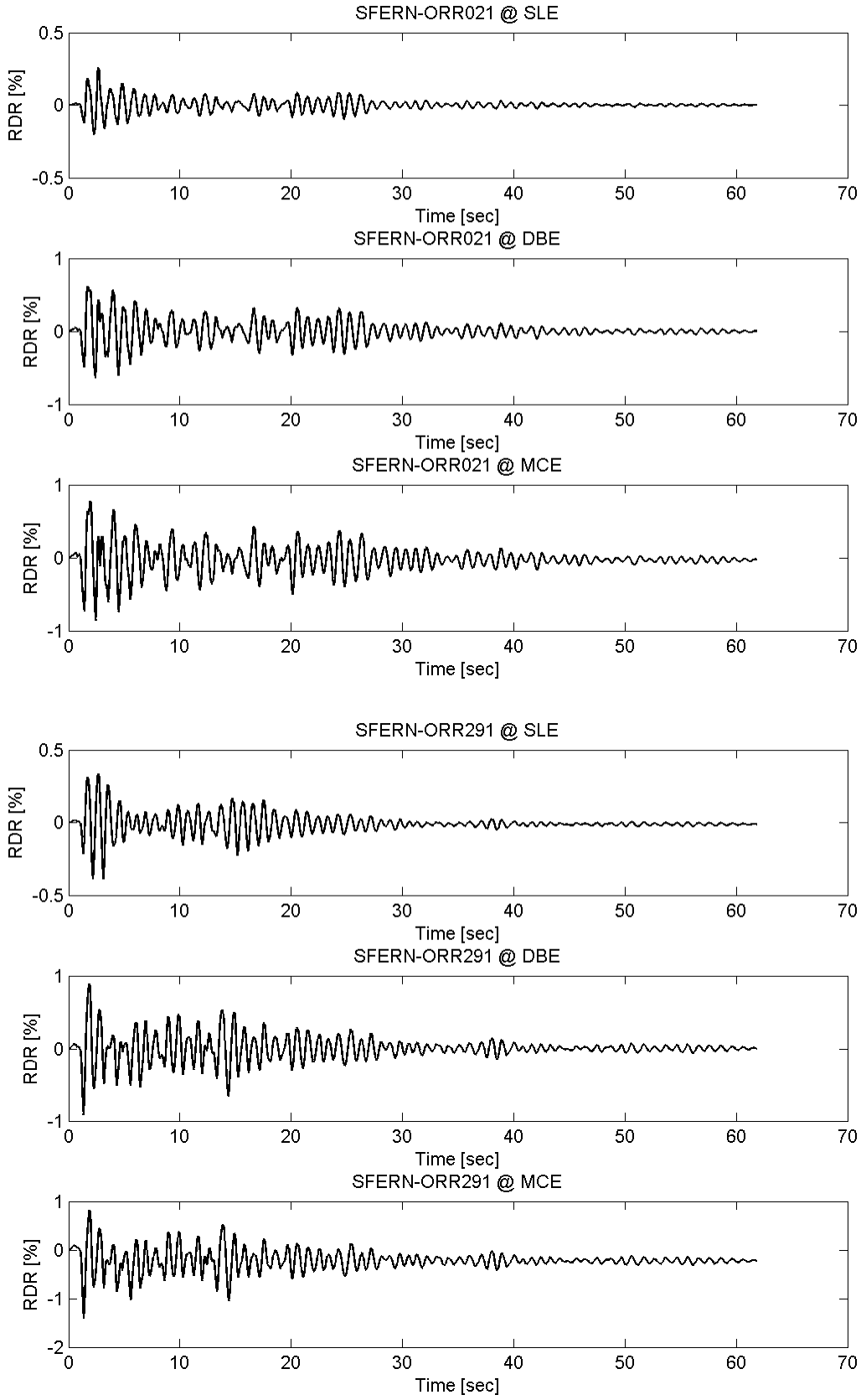
SFERN-ORR021 @ SLE
RDR [%]
Time [sec]
SFERN-ORR021 @ DBE
RDR [%]
Time [sec]
SFERN-ORR021 @ MCE
RDR [%]
Time [sec]
SFERN-ORR291 @ SLE
RDR [%]
Time [sec]
SFERN-ORR291 @ DBE
RDR [%]
Time [sec]
SFERN-ORR291 @ MCE
RDR [%]
Time [sec]

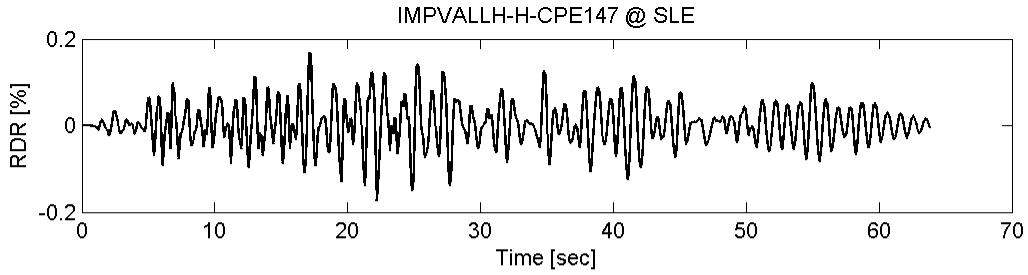
IMPVALLH-H-CPE147 @ SLE
RDR [%]
Time [sec]

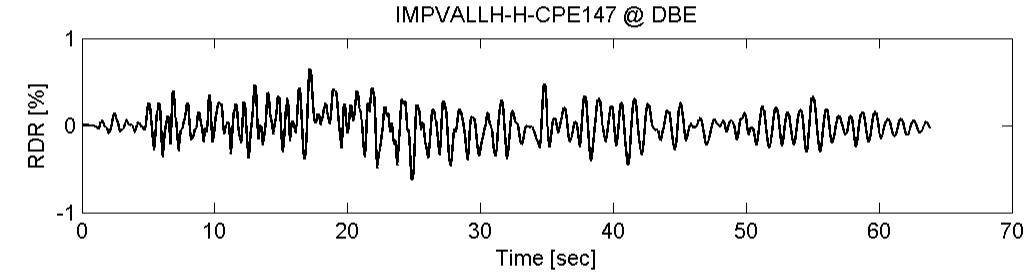
IMPVALLH-H-CPE147 @ DBE
RDR [%]
Time [sec]

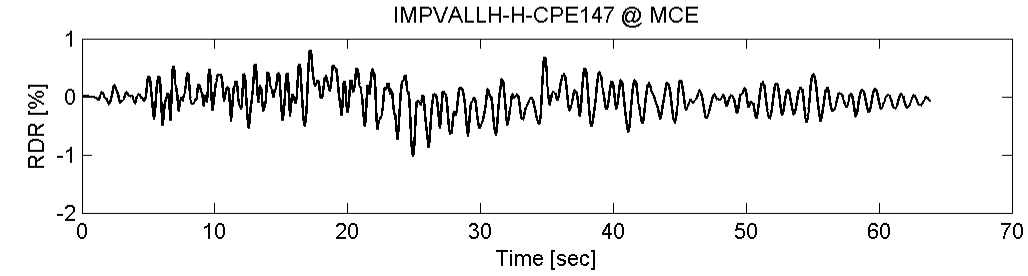
IMPVALLH-H-CPE147 @ MCE
RDR [%]
Time [sec]

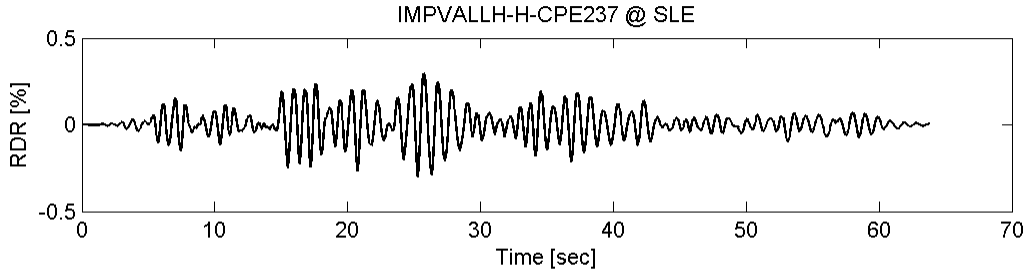
IMPVALLH-H-CPE237 @ SLE
RDR [%]
Time [sec]

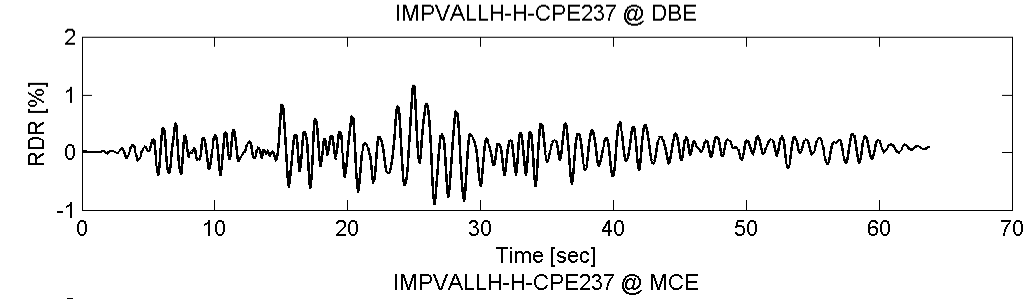
IMPVALLH-H-CPE237 @ DBE
RDR [%]
Time [sec]

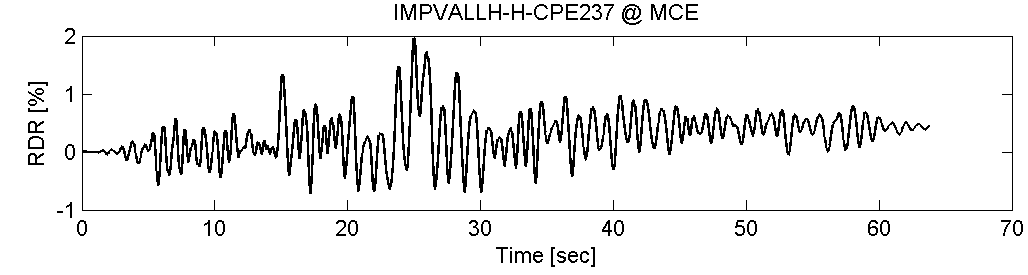
IMPVALLH-H-CPE237 @ MCE
RDR [%]
Time [sec]

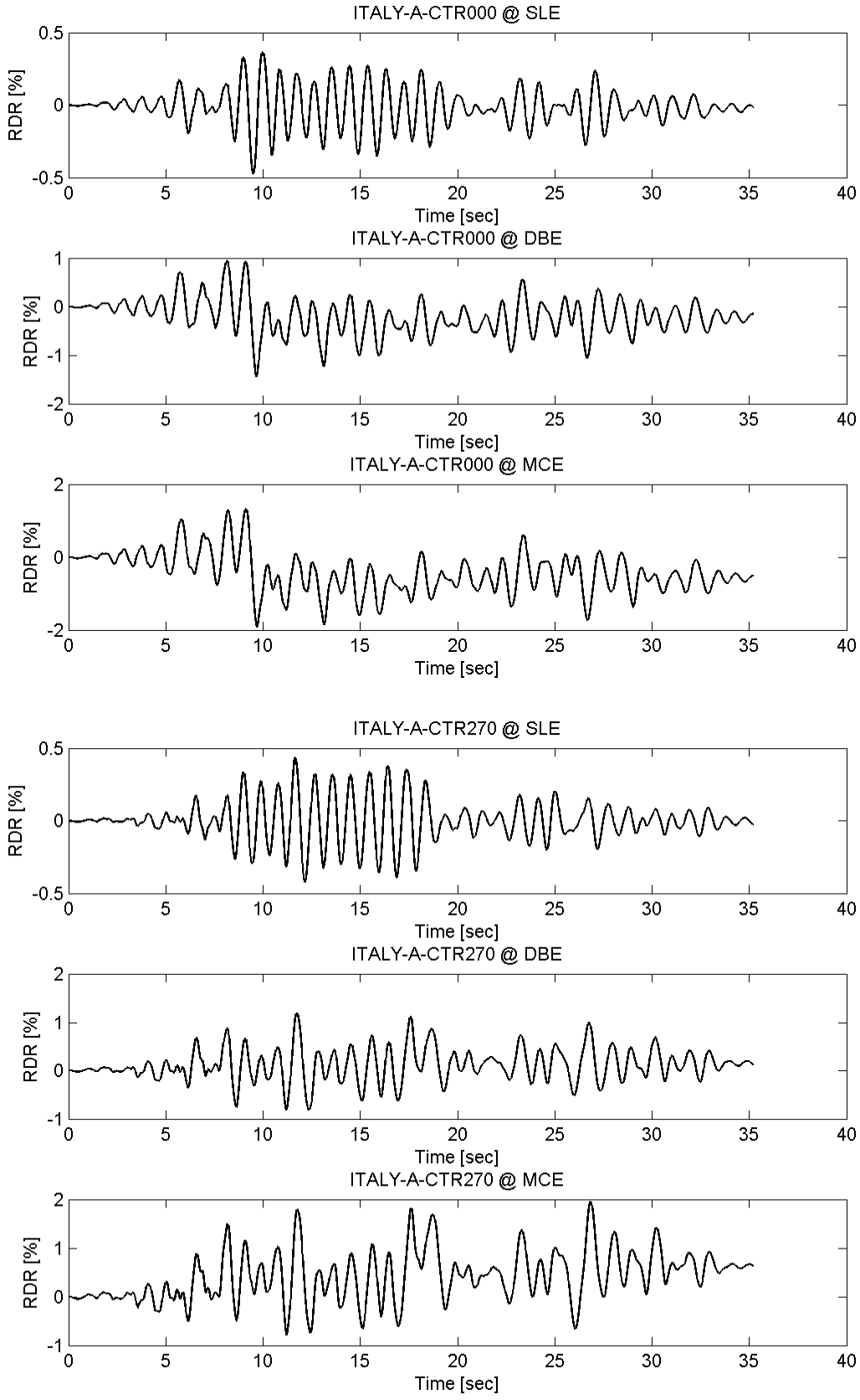
ITALY-A-CTR000 @ SLE
RDR [%]
Time [sec]
ITALY-A-CTR000 @ DBE
RDR [%]
Time [sec]
ITALY-A-CTR000 @ MCE
RDR [%]
Time [sec]
ITALY-A-CTR270 @ SLE
RDR [%]
Time [sec]
ITALY-A-CTR270 @ DBE
RDR [%]
Time [sec]
ITALY-A-CTR270 @ MCE
RDR [%]
Time [sec]

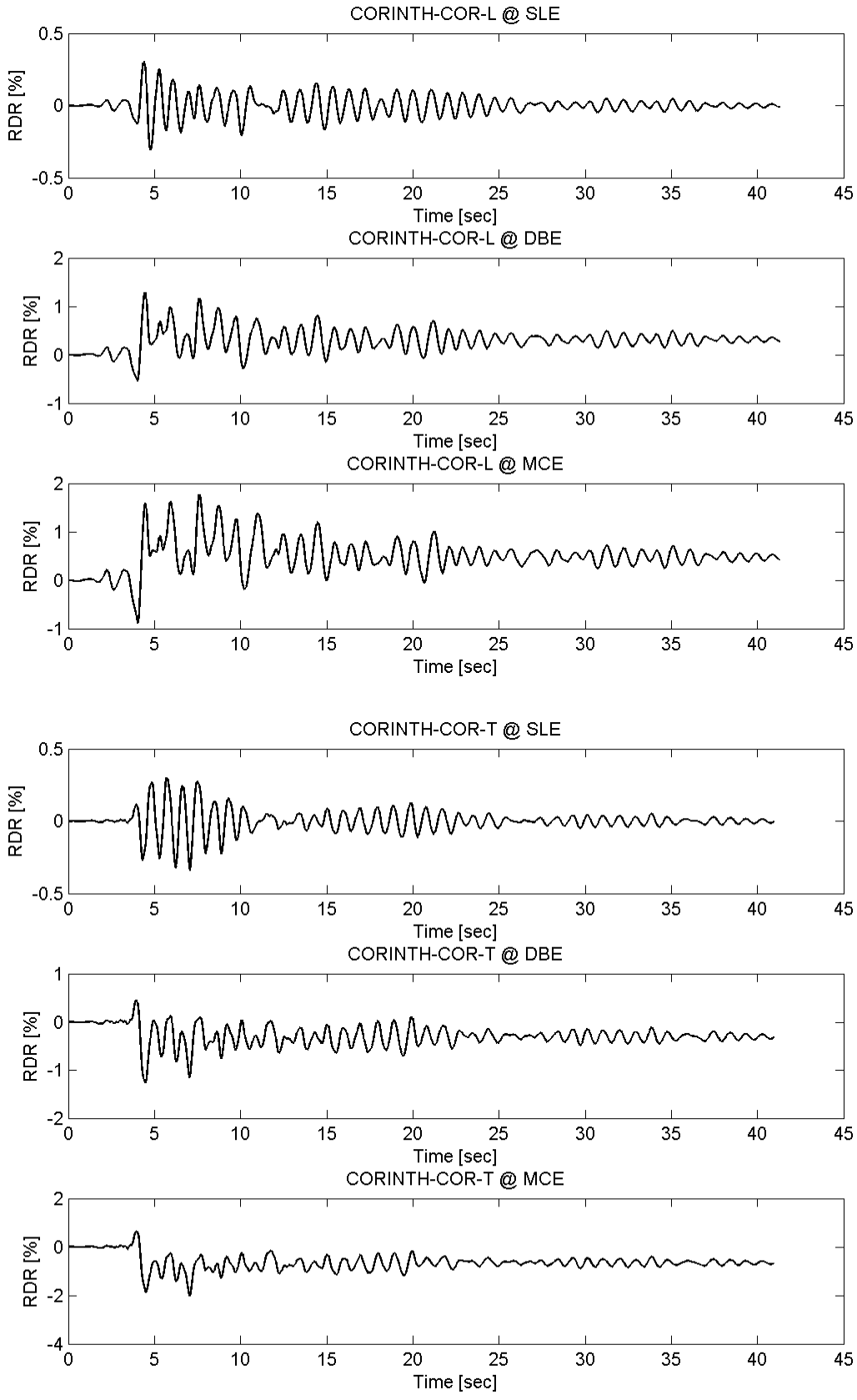
CORINTH-COR-L @ SLE
RDR [%]
Time [sec]
CORINTH-COR-L @ DBE
RDR [%]
Time [sec]
CORINTH-COR-L @ MCE
RDR [%]
Time [sec]
CORINTH-COR-T @ SLE
RDR [%]
Time [sec]
CORINTH-COR-T @ DBE
RDR [%]
Time [sec]
CORINTH-COR-T @ MCE
RDR [%]
Time [sec]

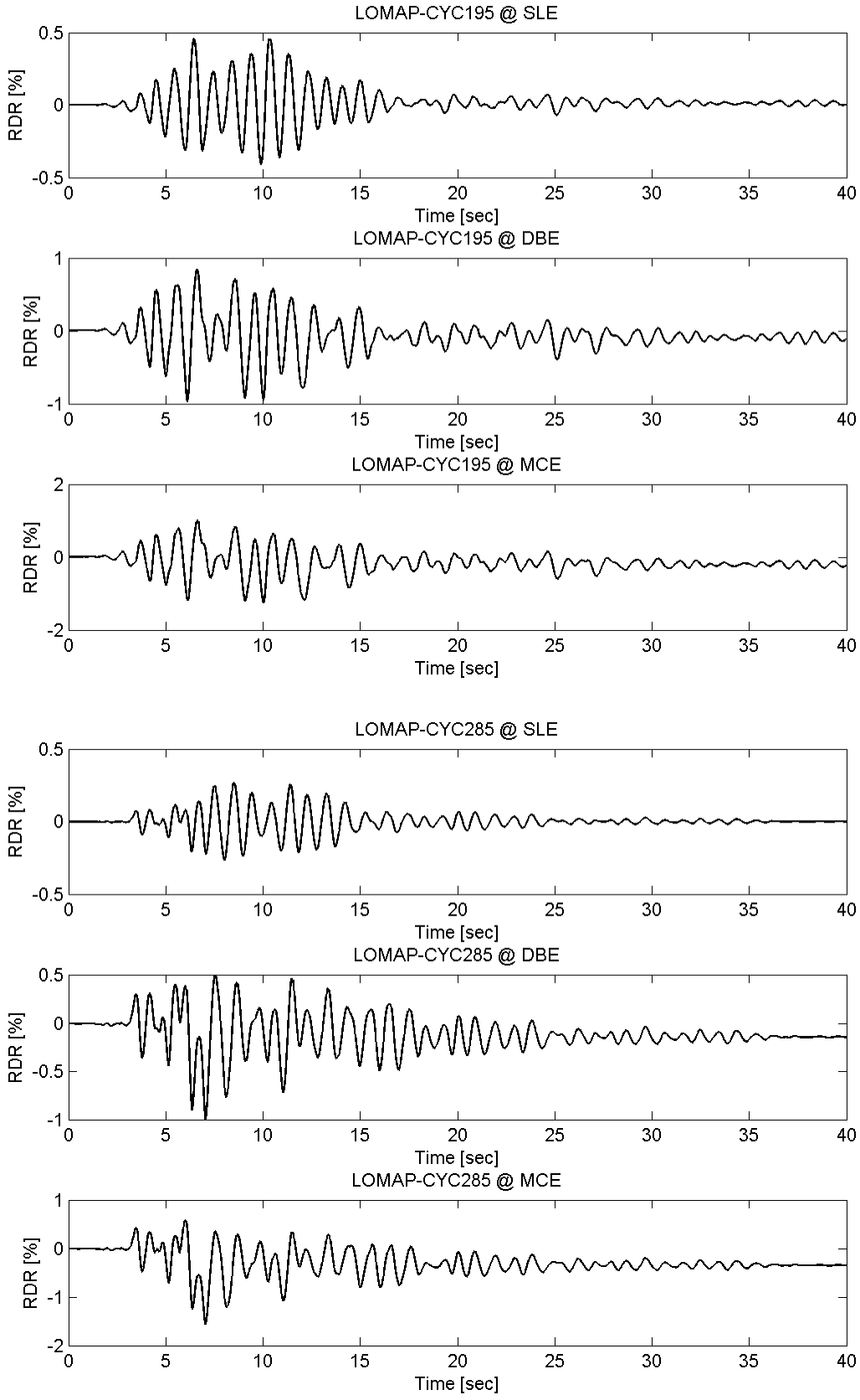
LOMAP-CYC195 @ SLE
RDR [%]
Time [sec]
LOMAP-CYC195 @ DBE
RDR [%]
Time [sec]
LOMAP-CYC195 @ MCE
RDR [%]
Time [sec]
LOMAP-CYC285 @ SLE
RDR [%]
Time [sec]
LOMAP-CYC285 @ DBE
RDR [%]
Time [sec]
LOMAP-CYC285 @ MCE
RDR [%]
Time [sec]

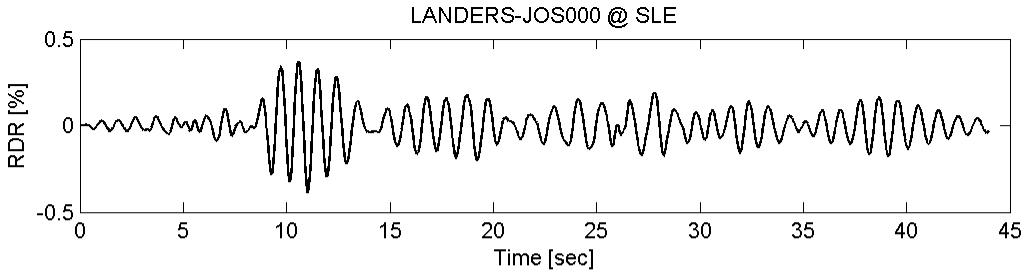
LANDERS-JOS000 @ SLE
RDR [%]
Time [sec]

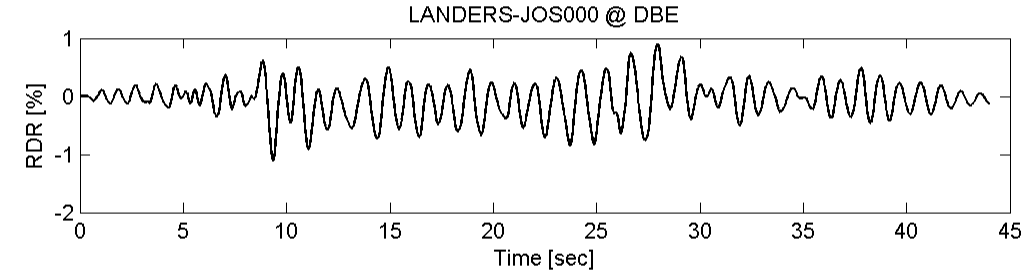
LANDERS-JOS000 @ DBE
RDR [%]
Time [sec]

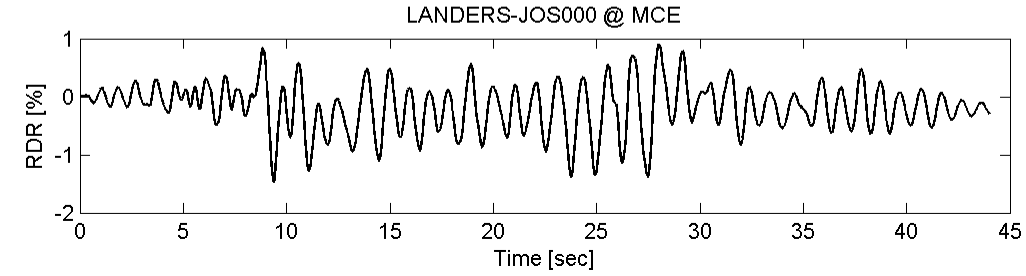
LANDERS-JOS000 @ MCE
RDR [%]
Time [sec]

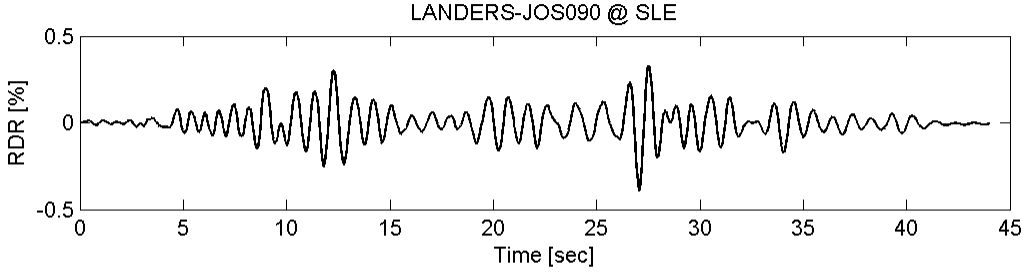
LANDERS-JOS090 @ SLE
RDR [%]
Time [sec]

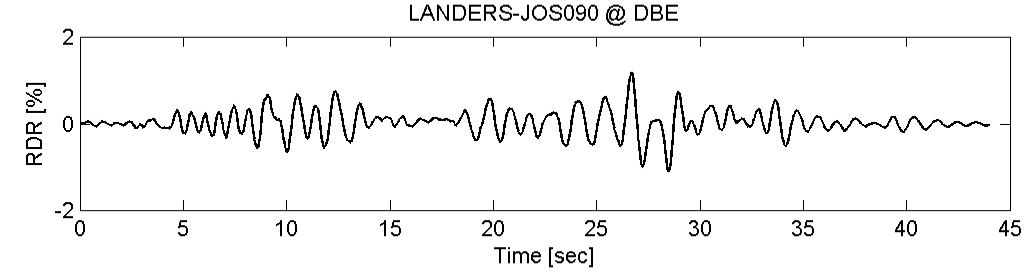
LANDERS-JOS090 @ DBE
RDR [%]
Time [sec]

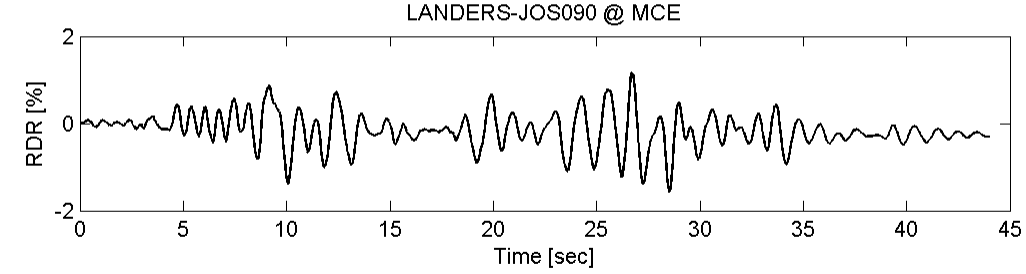
LANDERS-JOS090 @ MCE
RDR [%]
Time [sec]

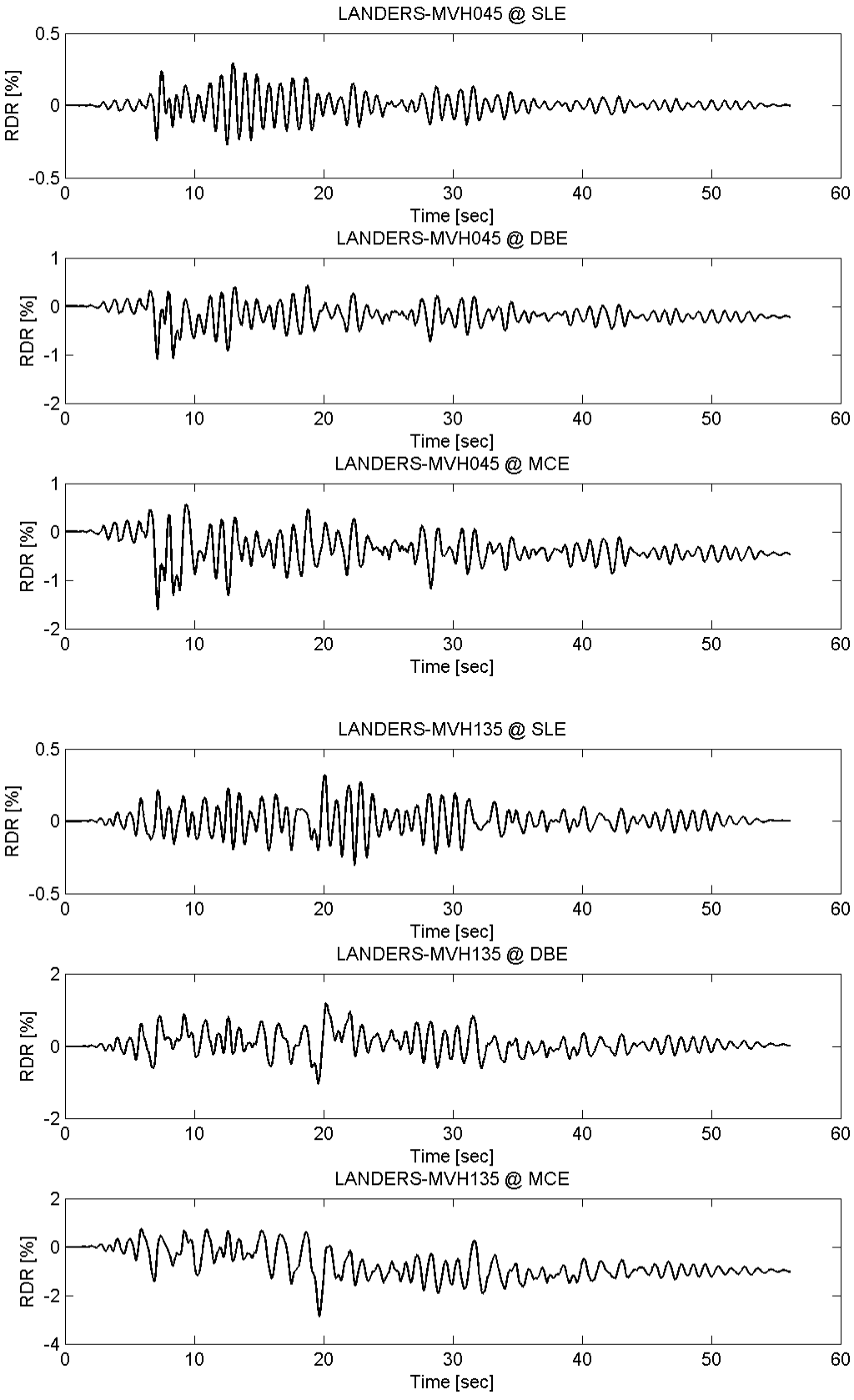
LANDERS-MVH045 @ SLE
RDR [%]
Time [sec]
LANDERS-MVH045 @ DBE
RDR [%]
Time [sec]
LANDERS-MVH045 @ MCE
RDR [%]
Time [sec]
LANDERS-MVH135 @ SLE
RDR [%]
Time [sec]
LANDERS-MVH135 @ DBE
RDR [%]
Time [sec]
LANDERS-MVH135 @ MCE
RDR [%]
Time [sec]

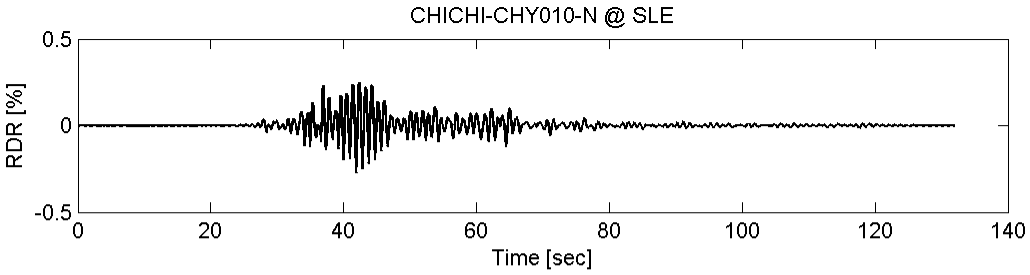
CHICHI-CHY010-N @ SLE
RDR [%]
Time [sec]

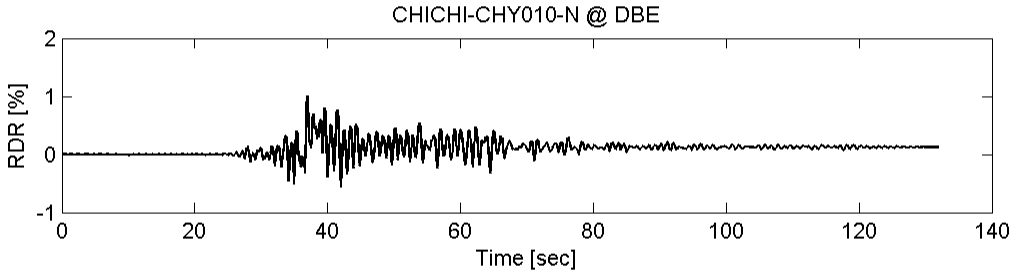
CHICHI-CHY010-N @ DBE
RDR [%]
Time [sec]

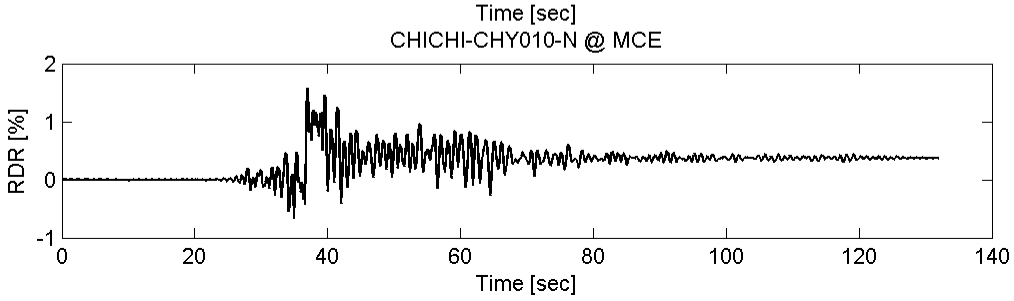
CHICHI-CHY010-N @ MCE
RDR [%]
Time [sec]

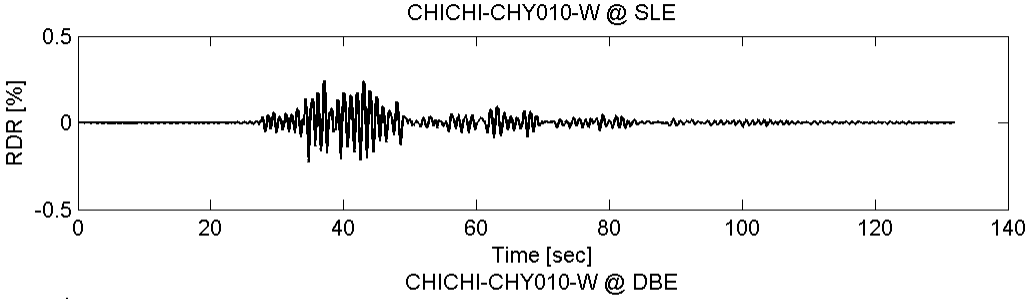
CHICHI-CHY010-W @ SLE
RDR [%]
Time [sec]

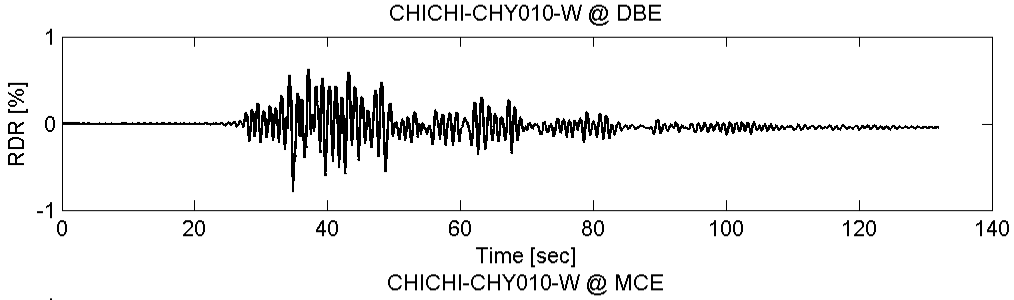
CHICHI-CHY010-W @ DBE
RDR [%]
Time [sec]

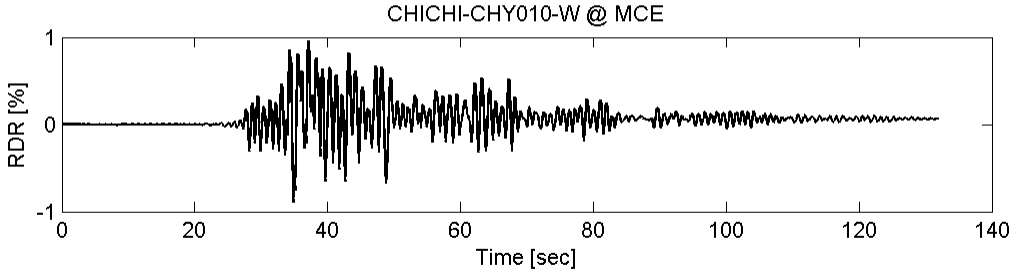
CHICHI-CHY010-W @ MCE
RDR [%]
Time [sec]

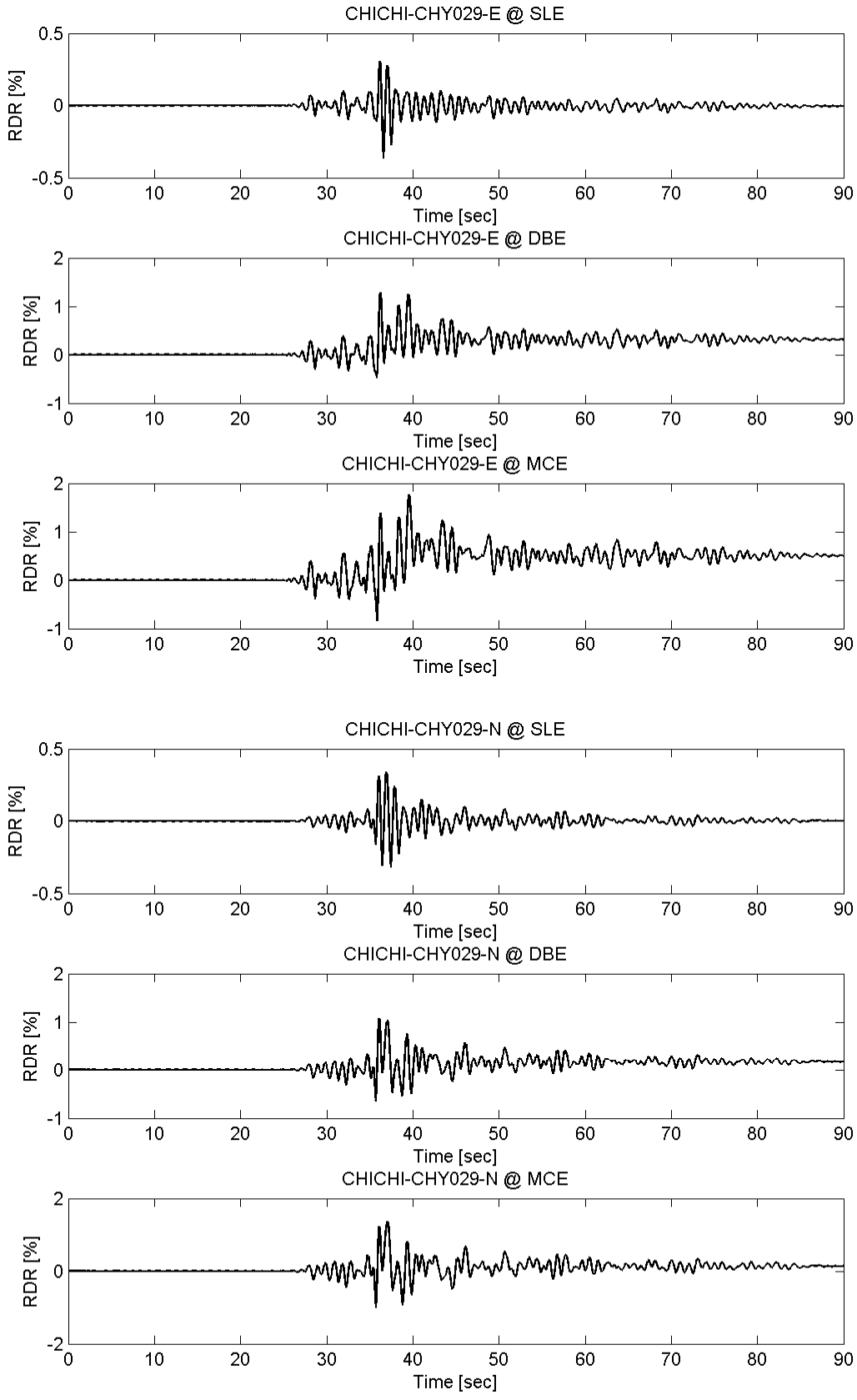
CHICHI-CHY029-E @ SLE
RDR [%]
Time [sec]
CHICHI-CHY029-E @ DBE
RDR [%]
Time [sec]
CHICHI-CHY029-E @ MCE
RDR [%]
Time [sec]
CHICHI-CHY029-N @ SLE
RDR [%]
Time [sec]
CHICHI-CHY029-N @ DBE
RDR [%]
Time [sec]
CHICHI-CHY029-N @ MCE
RDR [%]
Time [sec]

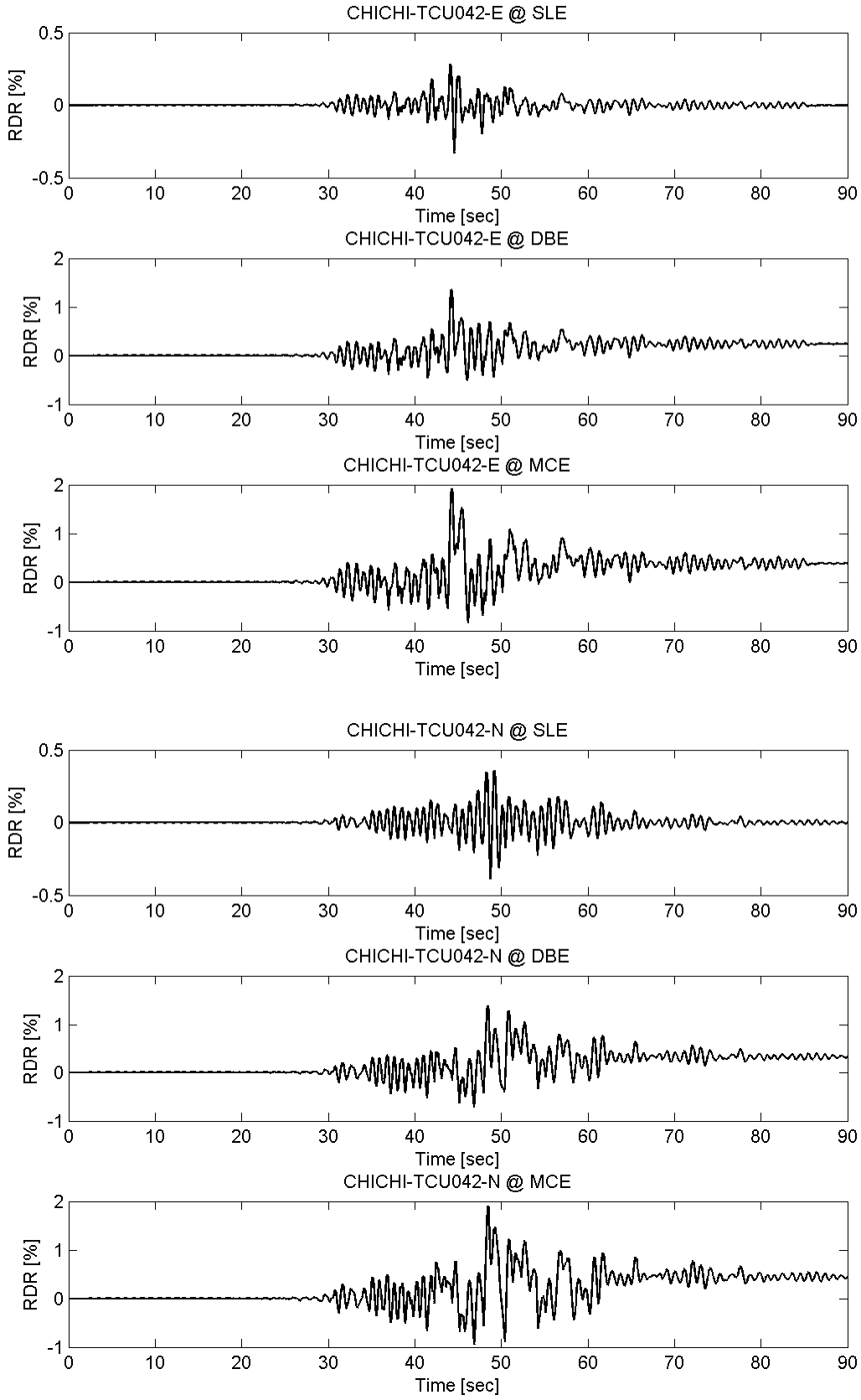
CHICHI-TCU042-E @ SLE
RDR [%]
Time [sec]
CHICHI-TCU042-E @ DBE
RDR [%]
Time [sec]
CHICHI-TCU042-E @ MCE
RDR [%]
Time [sec]
CHICHI-TCU042-N @ SLE
RDR [%]
Time [sec]
CHICHI-TCU042-N @ DBE
RDR [%]
Time [sec]
CHICHI-TCU042-N @ MCE
RDR [%]
Time [sec]

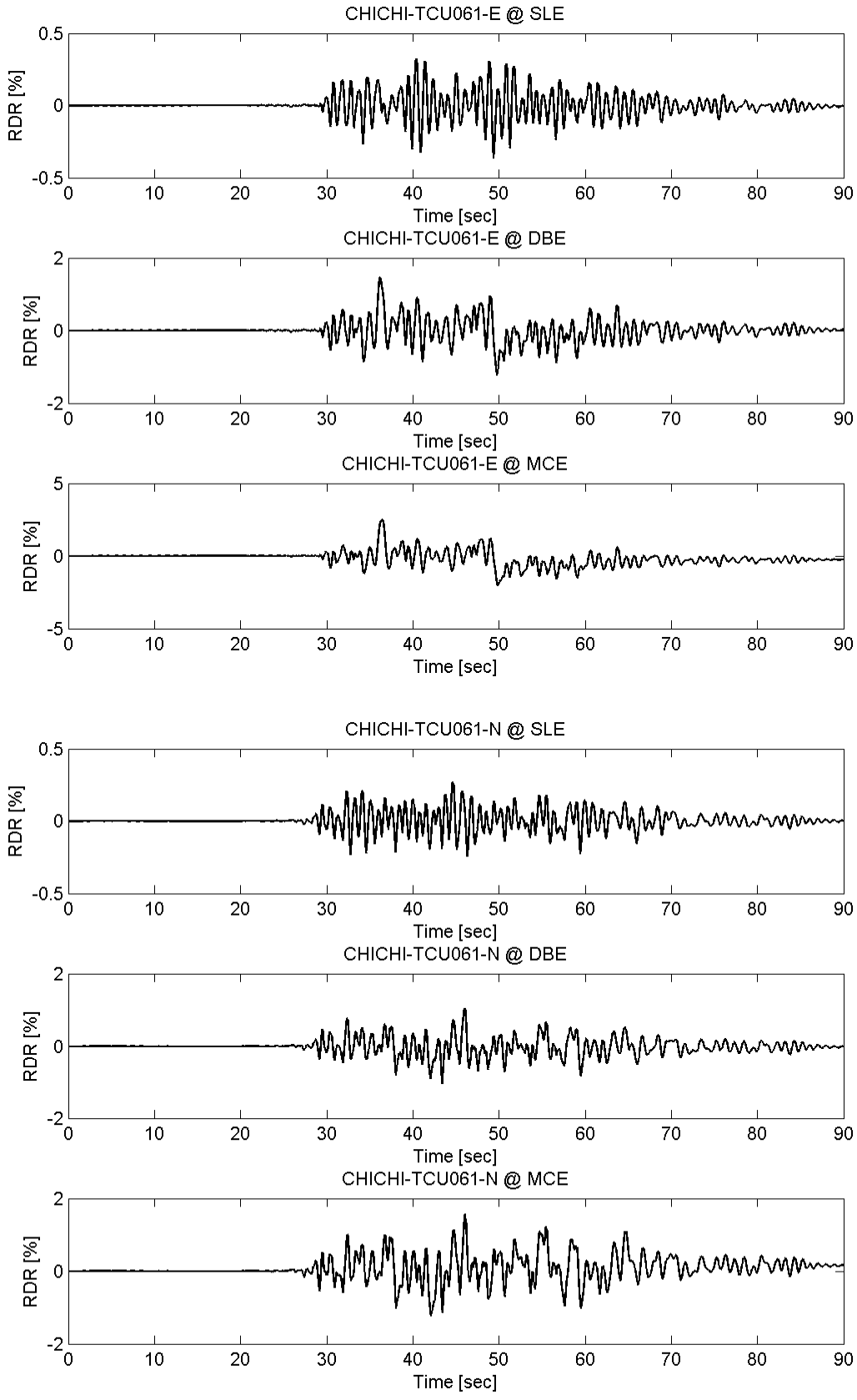
CHICHI-TCU061-E @ SLE
RDR [%]
Time [sec]
CHICHI-TCU061-E @ DBE
RDR [%]
Time [sec]
CHICHI-TCU061-E @ MCE
RDR [%]
Time [sec]
CHICHI-TCU061-N @ SLE
RDR [%]
Time [sec]
CHICHI-TCU061-N @ DBE
RDR [%]
Time [sec]
CHICHI-TCU061-N @ MCE
RDR [%]
Time [sec]

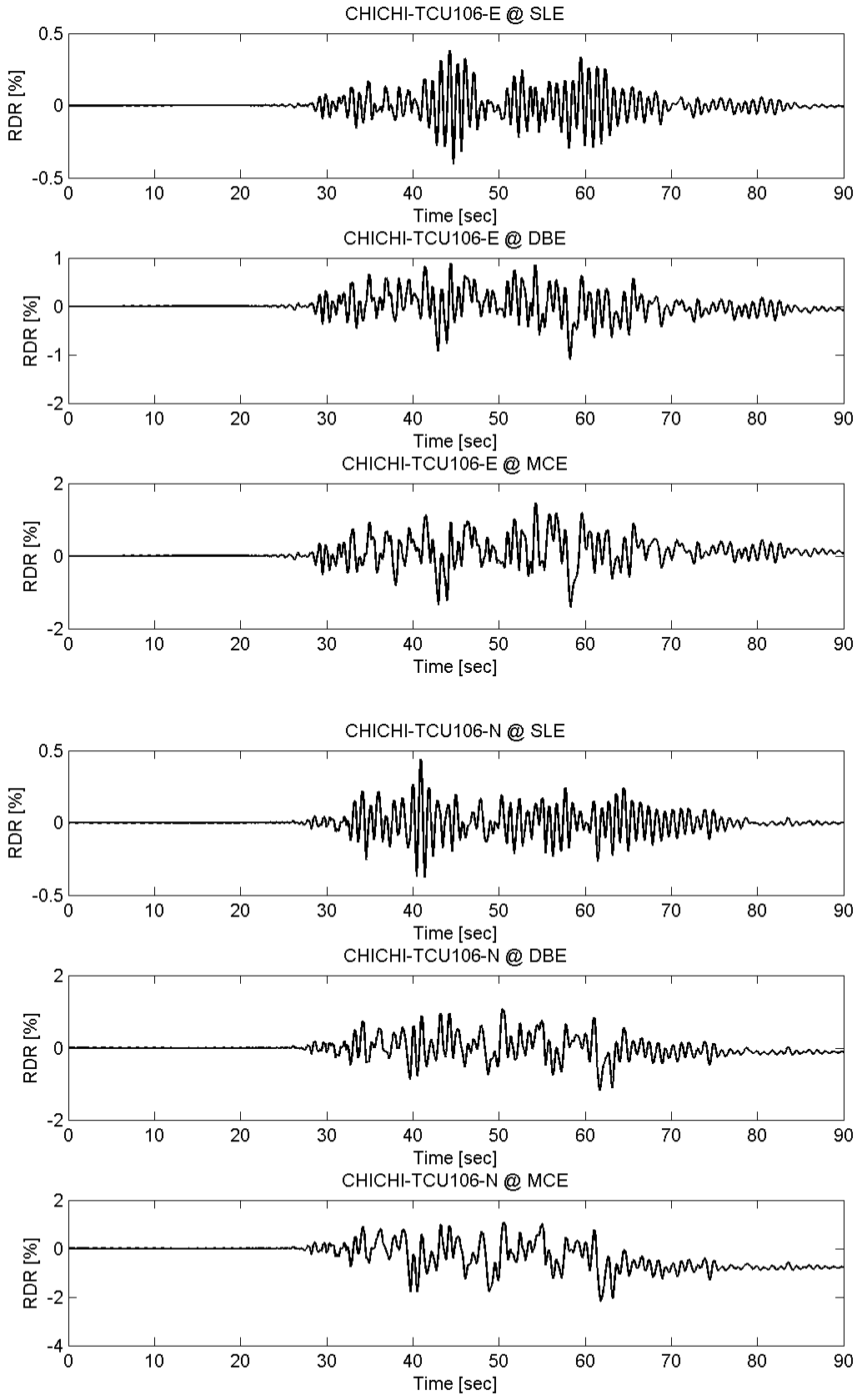
CHICHI-TCU106-E @ SLE
RDR [%]
Time [sec]
CHICHI-TCU106-E @ DBE
RDR [%]
Time [sec]
CHICHI-TCU106-E @ MCE
RDR [%]
Time [sec]
CHICHI-TCU106-N @ SLE
RDR [%]
Time [sec]
CHICHI-TCU106-N @ DBE
RDR [%]
Time [sec]
CHICHI-TCU106-N @ MCE
RDR [%]
Time [sec]

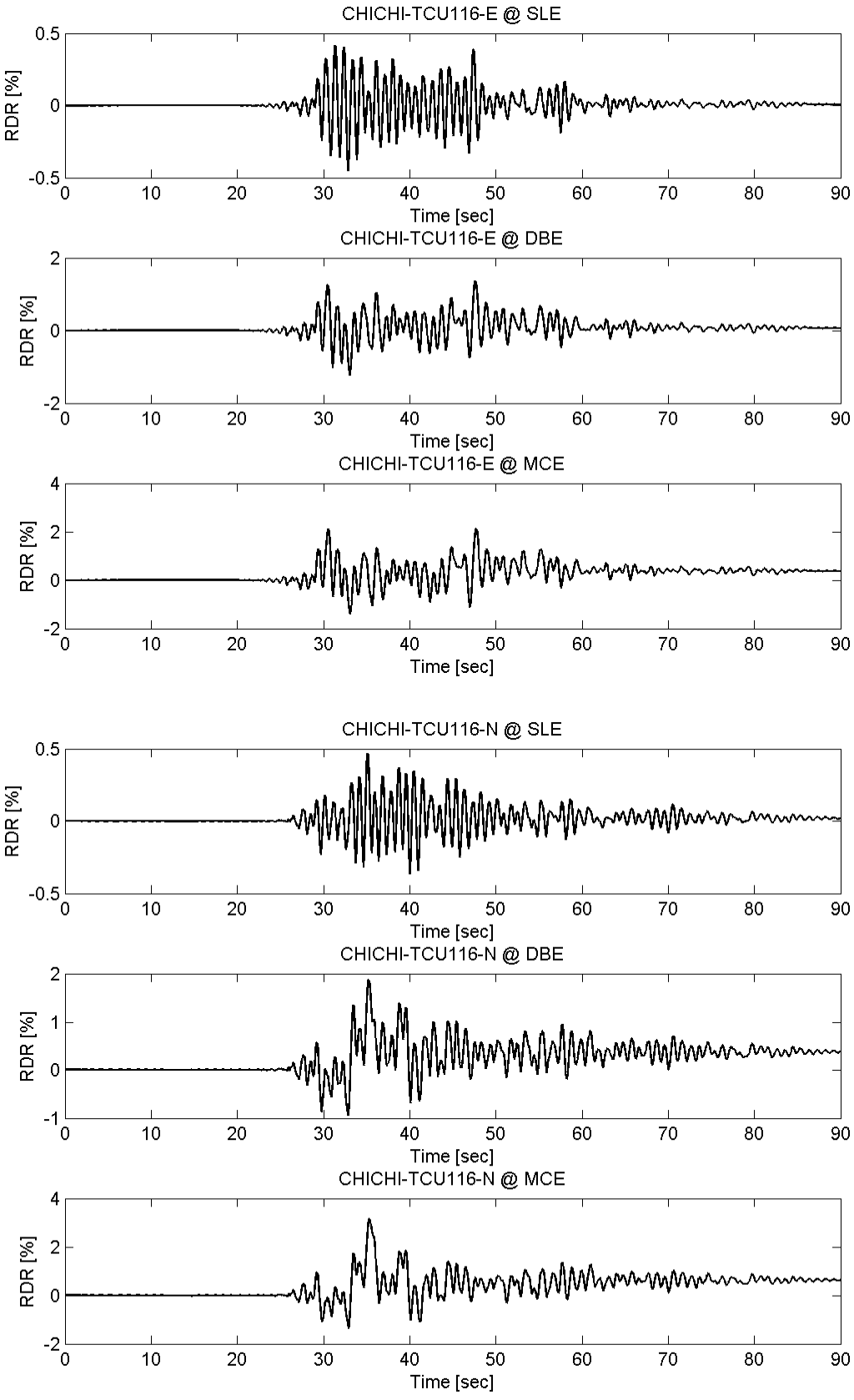
CHICHI-TCU116-E @ SLE
RDR [%]
Time [sec]
CHICHI-TCU116-E @ DBE
RDR [%]
Time [sec]
CHICHI-TCU116-E @ MCE
RDR [%]
Time [sec]
CHICHI-TCU116-N @ SLE
RDR [%]
Time [sec]
CHICHI-TCU116-N @ DBE
RDR [%]
Time [sec]
CHICHI-TCU116-N @ MCE
RDR [%]
Time [sec]

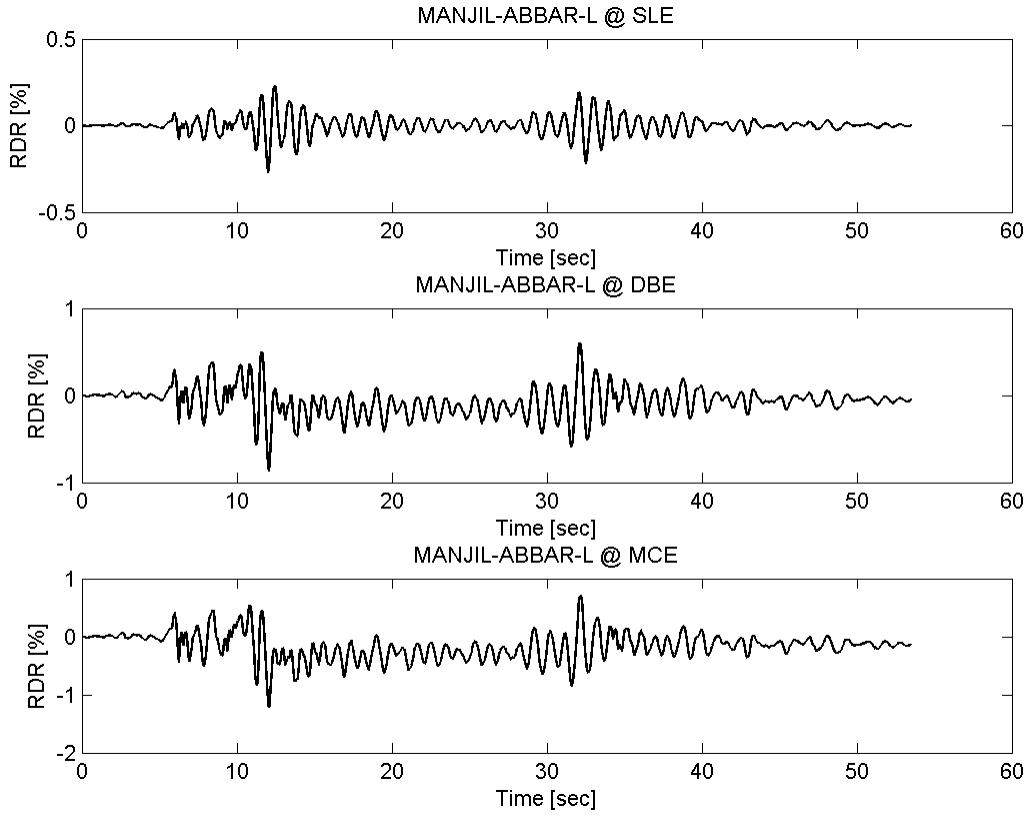
MANJIL-ABBAR-L @ SLE
RDR [%]
Time [sec]
MANJIL-ABBAR-L @ DBE
RDR [%]
Time [sec]
MANJIL-ABBAR-L @ MCE
RDR [%]
Time [sec]

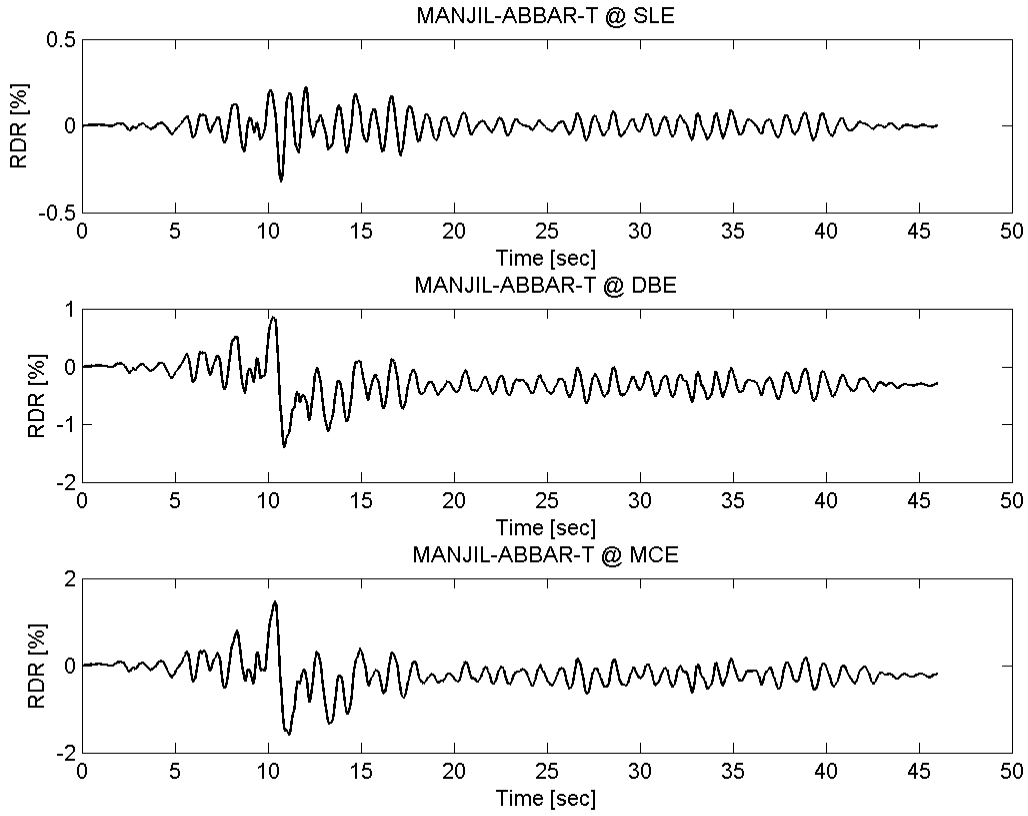
MANJIL-ABBAR-T @ SLE
RDR [%]
Time [sec]
MANJIL-ABBAR-T @ DBE
RDR [%]
Time [sec]
MANJIL-ABBAR-T @ MCE
RDR [%]
Time [sec]

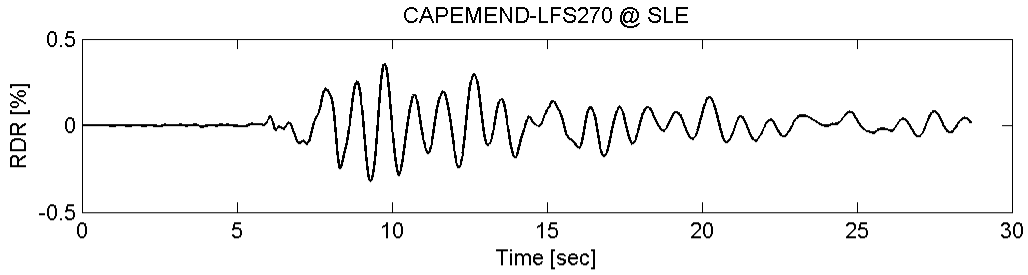
CAPEMEND-LFS270 @ SLE
RDR [%]
Time [sec]

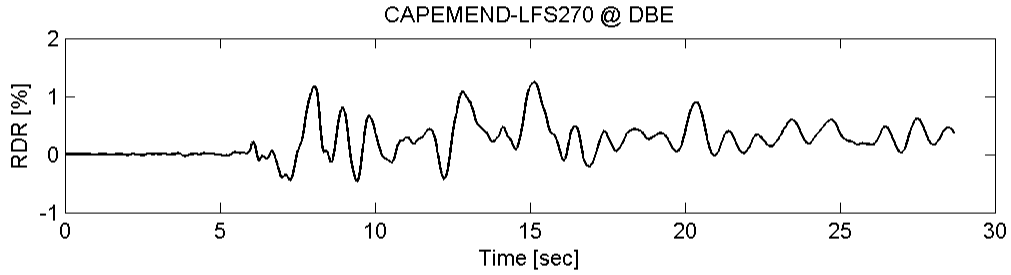
CAPEMEND-LFS270 @ DBE
RDR [%]
Time [sec]

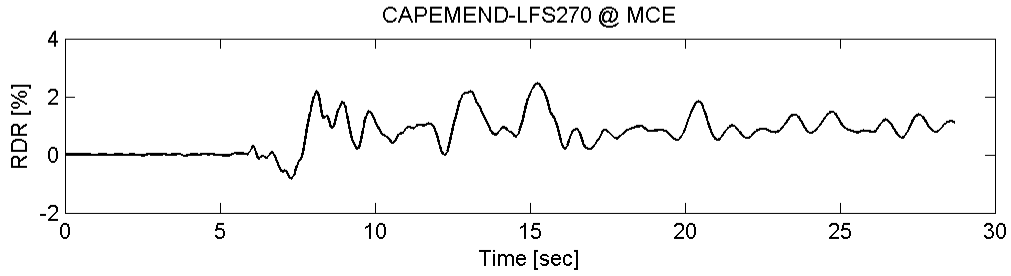
CAPEMEND-LFS270 @ MCE
RDR [%]
Time [sec]

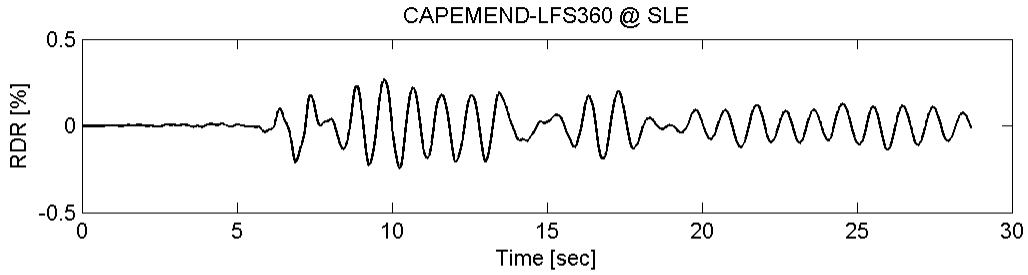
CAPEMEND-LFS360 @ SLE
RDR [%]
Time [sec]

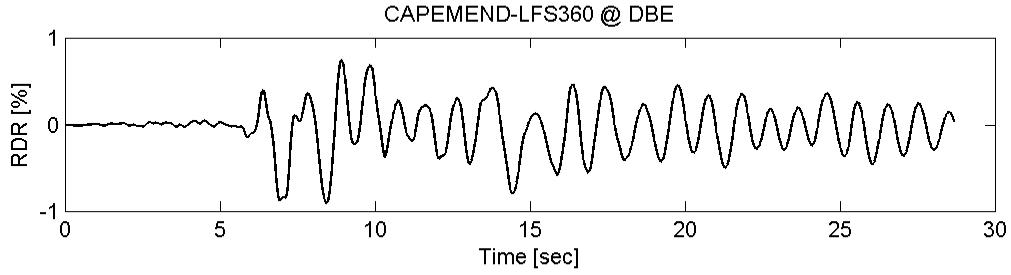
CAPEMEND-LFS360 @ DBE
RDR [%]
Time [sec]

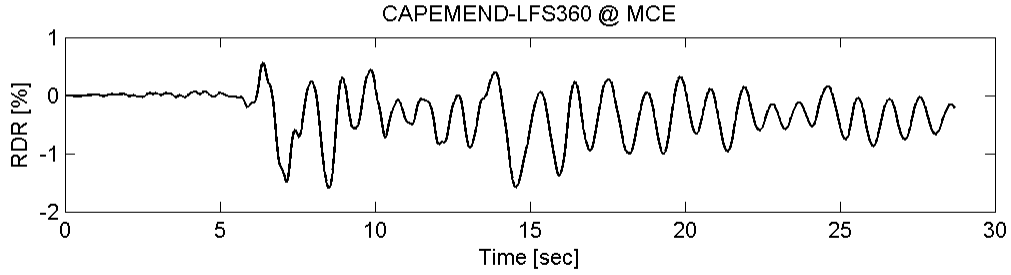
CAPEMEND-LFS360 @ MCE
RDR [%]
Time [sec]

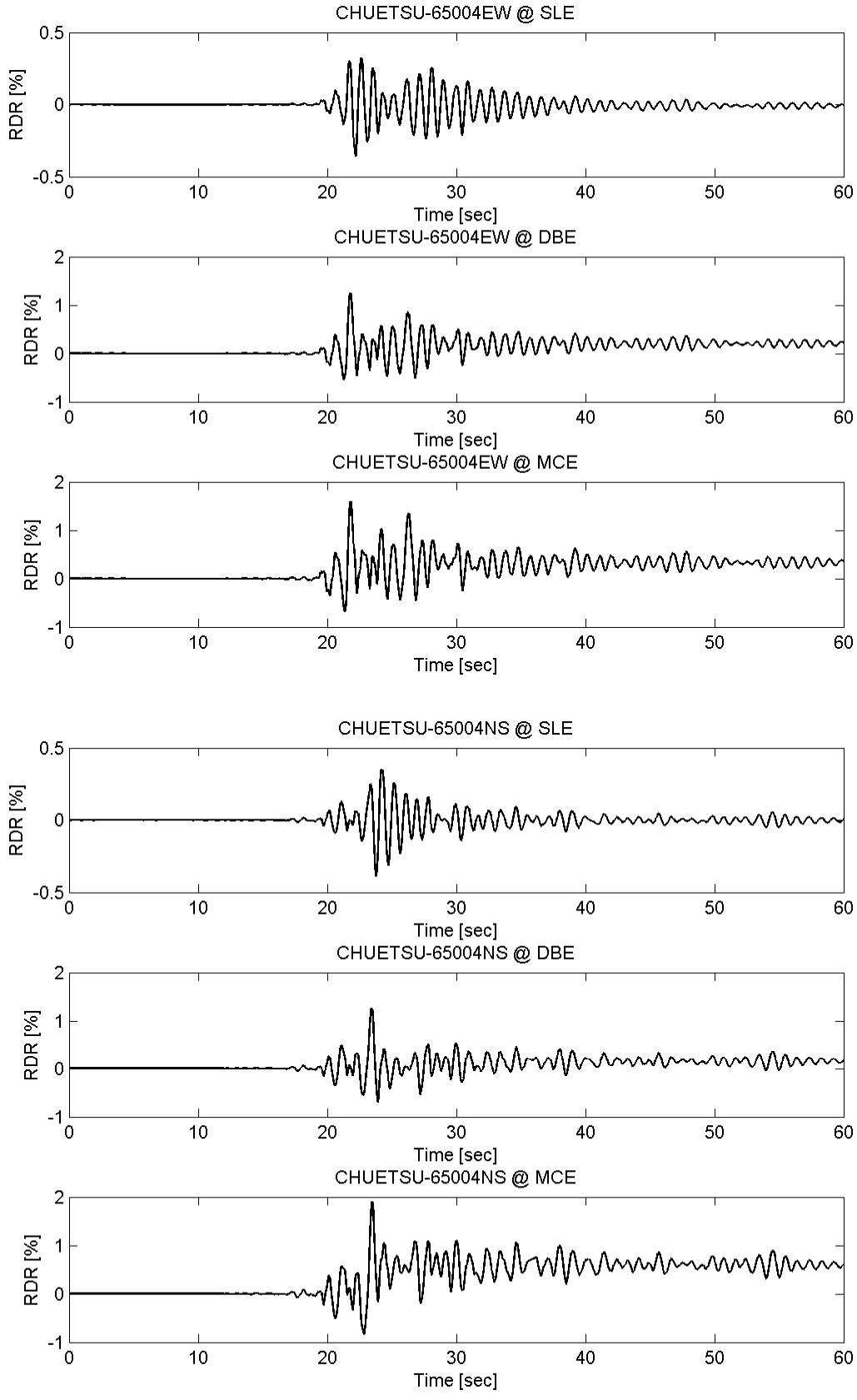
CHUETSU-65004EW @ SLE
RDR [%]
Time [sec]
CHUETSU-65004EW @ DBE
RDR [%]
Time [sec]
CHUETSU-65004EW @ MCE
RDR [%]
Time [sec]
CHUETSU-65004NS @ SLE
RDR [%]
Time [sec]
CHUETSU-65004NS @ DBE
RDR [%]
Time [sec]
CHUETSU-65004NS @ MCE
RDR [%]
Time [sec]

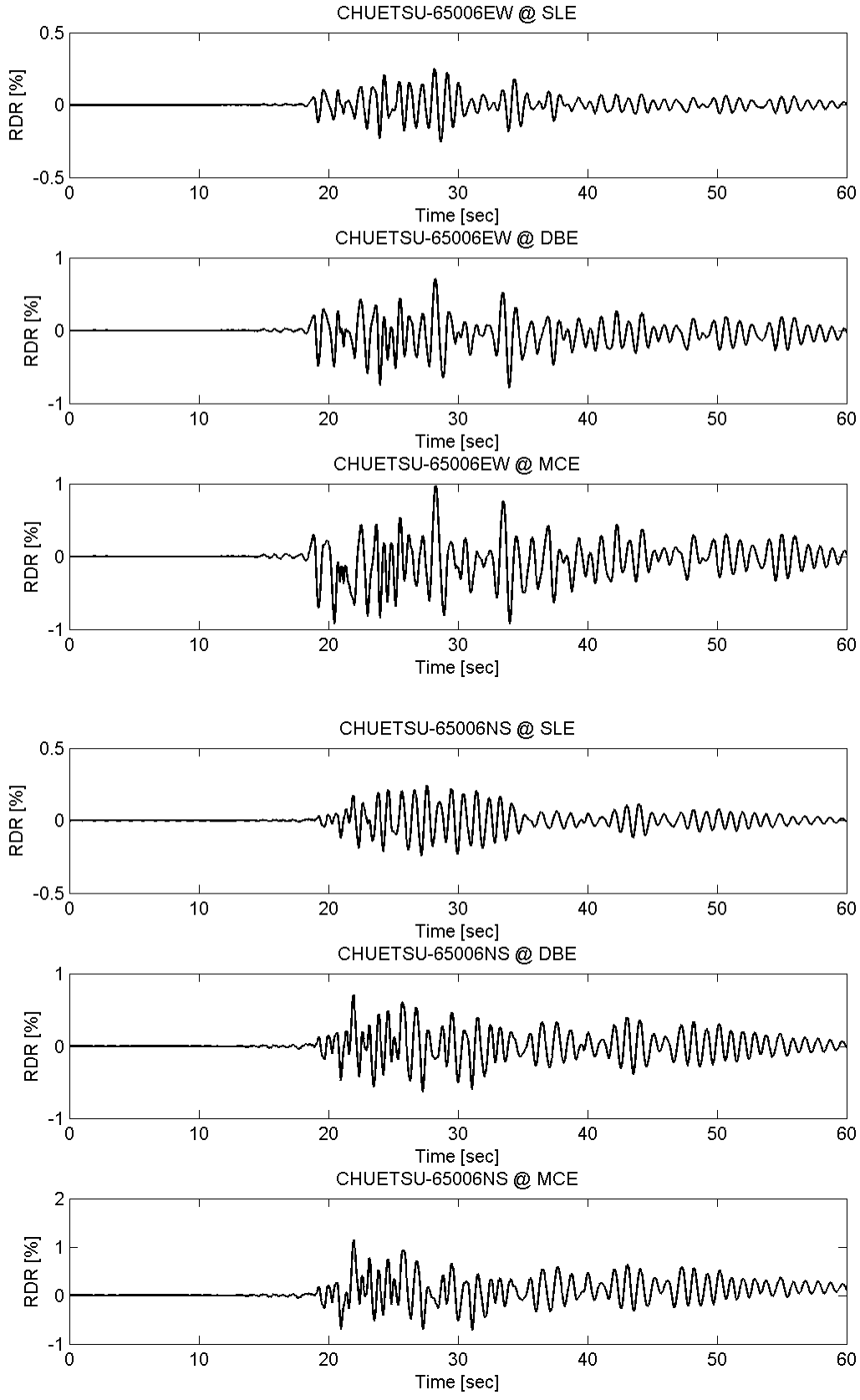
CHUETSU-65006EW @ SLE
RDR [%]
Time [sec]
CHUETSU-65006EW @ DBE
RDR [%]
Time [sec]
CHUETSU-65006EW @ MCE
RDR [%]
Time [sec]
CHUETSU-65006NS @ SLE
RDR [%]
Time [sec]
CHUETSU-65006NS @ DBE
RDR [%]
Time [sec]
CHUETSU-65006NS @ MCE
RDR [%]
Time [sec]

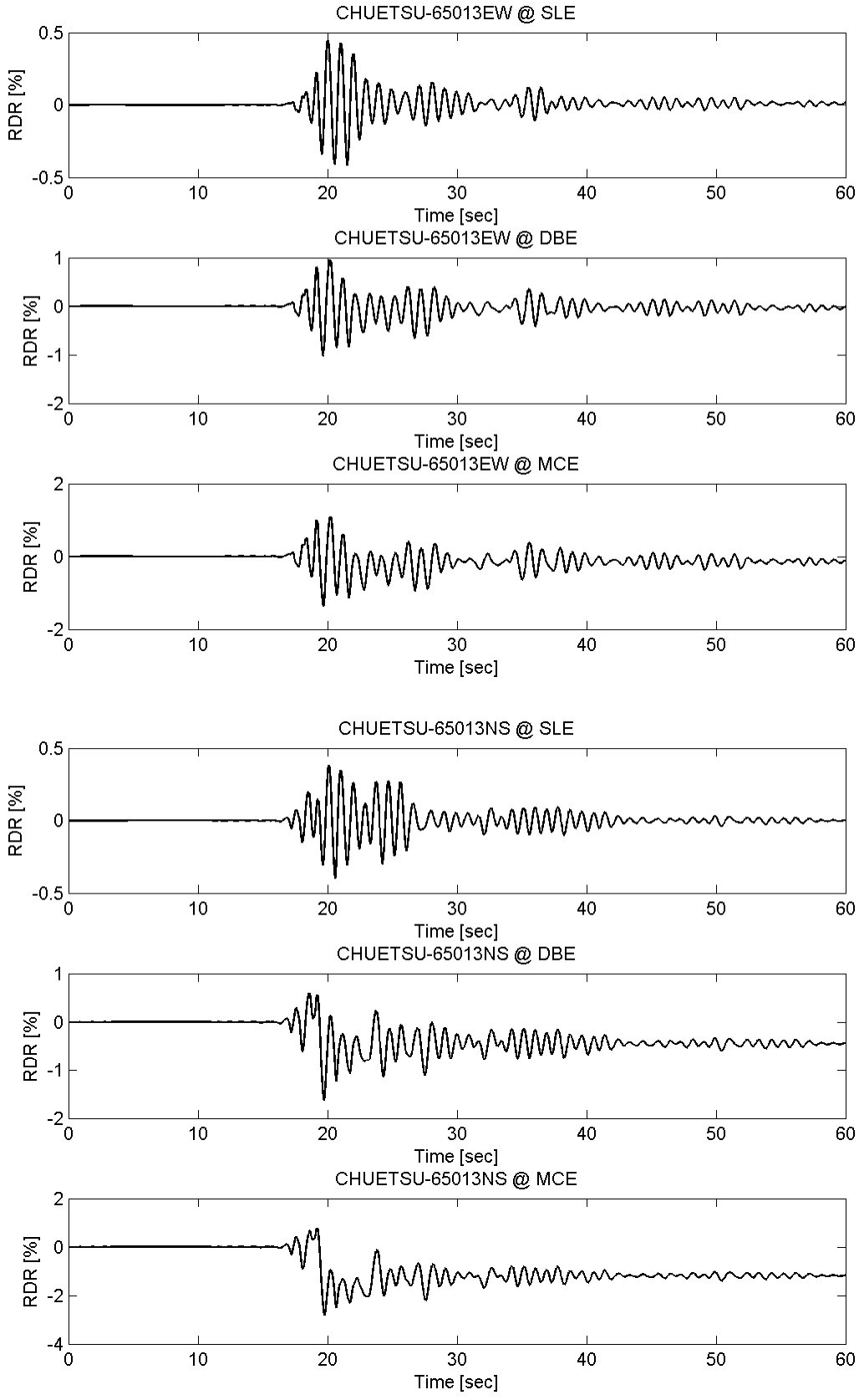
CHUETSU-65013EW @ SLE
RDR [%]
Time [sec]
CHUETSU-65013EW @ DBE
RDR [%]
Time [sec]
CHUETSU-65013EW @ MCE
RDR [%]
Time [sec]
CHUETSU-65013NS @ SLE
RDR [%]
Time [sec]
CHUETSU-65013NS @ DBE
RDR [%]
Time [sec]
CHUETSU-65013NS @ MCE
RDR [%]
Time [sec]

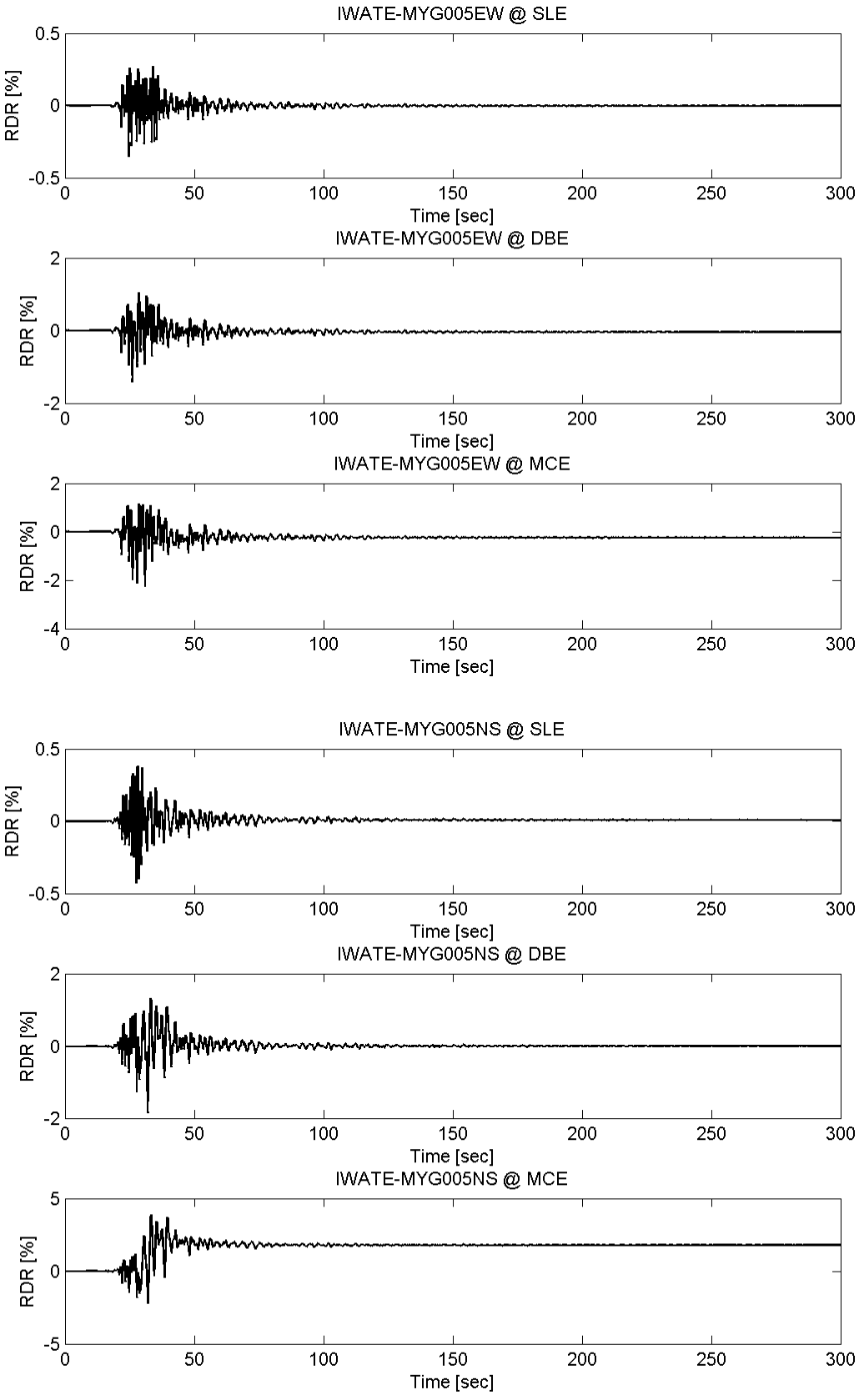
IWATE-MYG005EW @ SLE
RDR [%]
Time [sec]
IWATE-MYG005EW @ DBE
RDR [%]
Time [sec]
IWATE-MYG005EW @ MCE
RDR [%]
Time [sec]
IWATE-MYG005NS @ SLE
RDR [%]
Time [sec]
IWATE-MYG005NS @ DBE
RDR [%]
Time [sec]
IWATE-MYG005NS @ MCE
RDR [%]
Time [sec]

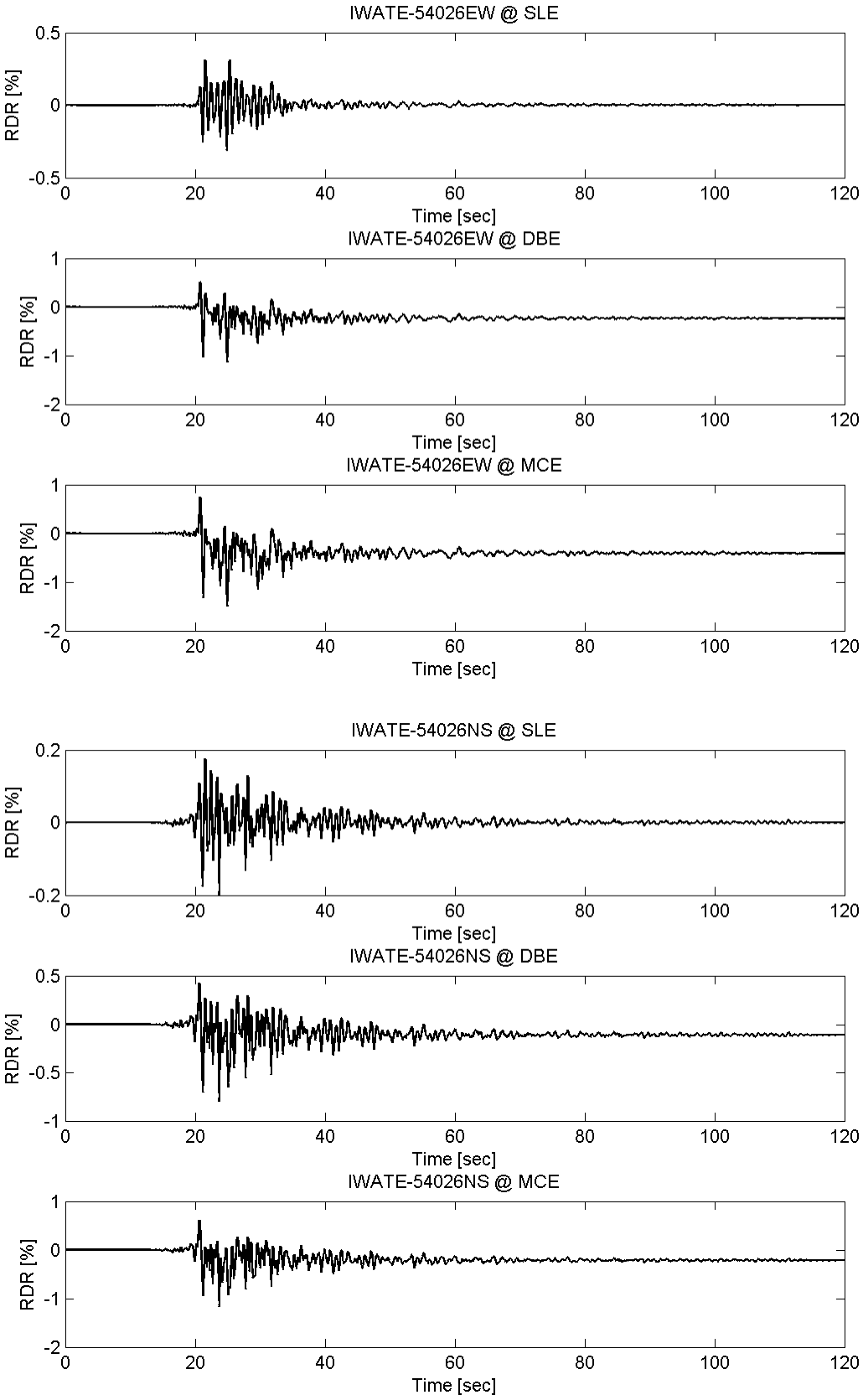
IWATE-54026EW @ SLE
RDR [%]
Time [sec]
IWATE-54026EW @ DBE
RDR [%]
Time [sec]
IWATE-54026EW @ MCE
RDR [%]
Time [sec]
IWATE-54026NS @ SLE
RDR [%]
Time [sec]
IWATE-54026NS @ DBE
RDR [%]
Time [sec]
IWATE-54026NS @ MCE
RDR [%]
Time [sec]

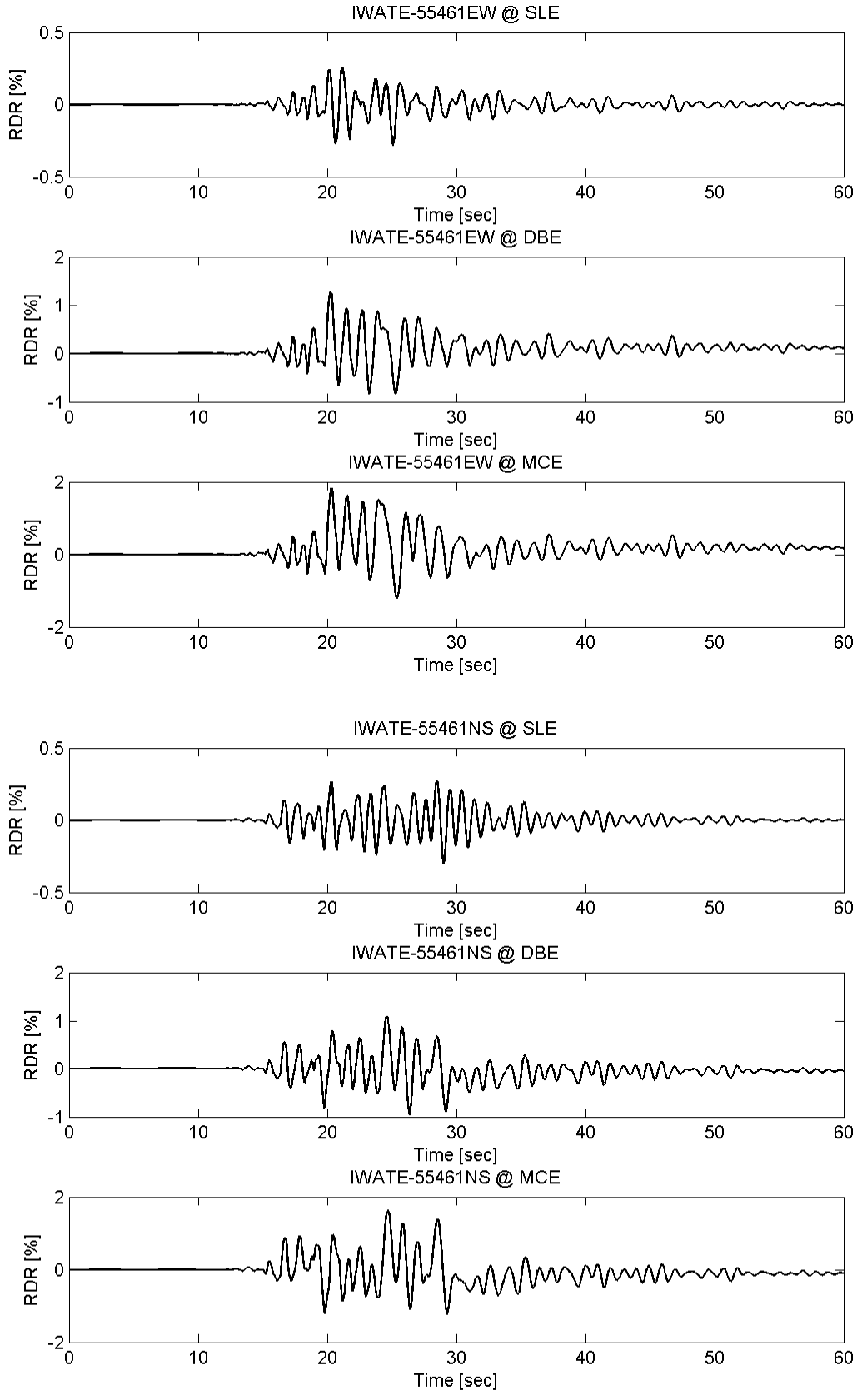
IWATE-55461EW @ SLE
RDR [%]
Time [sec]
IWATE-55461EW @ DBE
RDR [%]
Time [sec]
IWATE-55461EW @ MCE
RDR [%]
Time [sec]
IWATE-55461NS @ SLE
RDR [%]
Time [sec]
IWATE-55461NS @ DBE
RDR [%]
Time [sec]
IWATE-55461NS @ MCE
RDR [%]
Time [sec]

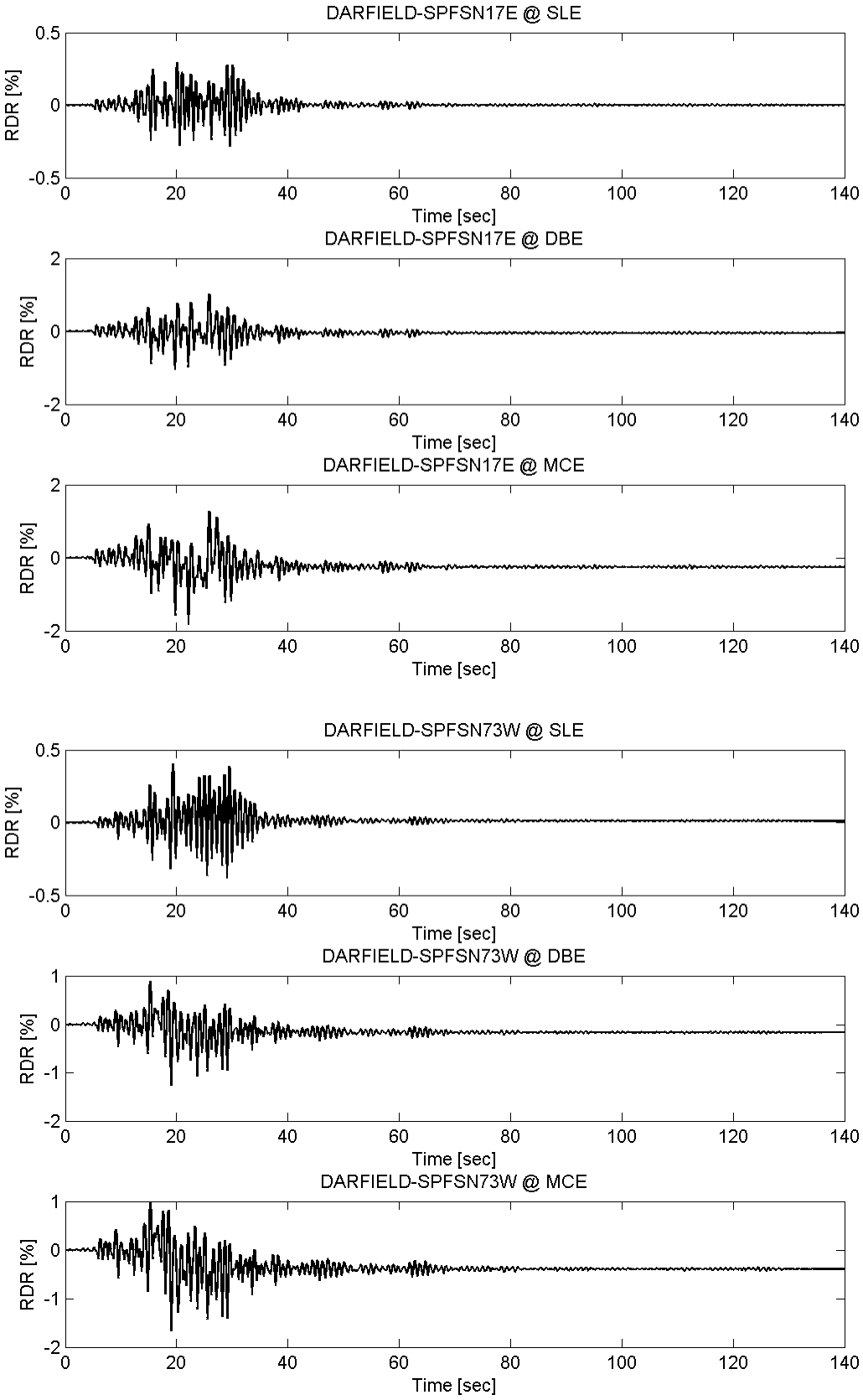
DARFIELD-SPFSN17E @ SLE
RDR [%]
Time [sec]
DARFIELD-SPFSN17E @ DBE
RDR [%]
Time [sec]
DARFIELD-SPFSN17E @ MCE
RDR [%]
Time [sec]
DARFIELD-SPFSN73W @ SLE
RDR [%]
Time [sec]
DARFIELD-SPFSN73W @ DBE
RDR [%]
Time [sec]
DARFIELD-SPFSN73W @ MCE
RDR [%]
Time [sec]

Appendix C
BRB Strain of Prototype FTMF

A three-storey office prototype building located in Los Angeles, California, is designed using the proposed equivalent energy design procedure (EEDP) from Chapter 2. The seismic force resisting system (SFRS) is the proposed fused truss moment frame (FTMF) from Chapter 3. Within the FTMF, the primary SFRS is mainly the buckling restrained braces (BRBs) located at the truss bottom chords. Nonlinear dynamic analysis is conducted using the ground motions presetned in Table 3.1. The figures in this appendix are the axial strain time hisotries of the representative BRB at each floor as the building is subjected to the motions scaled to the service level earthquake (SLE), designed based earthquake (DBE), and maximum considered earthquake (MCE) shaking intensities.

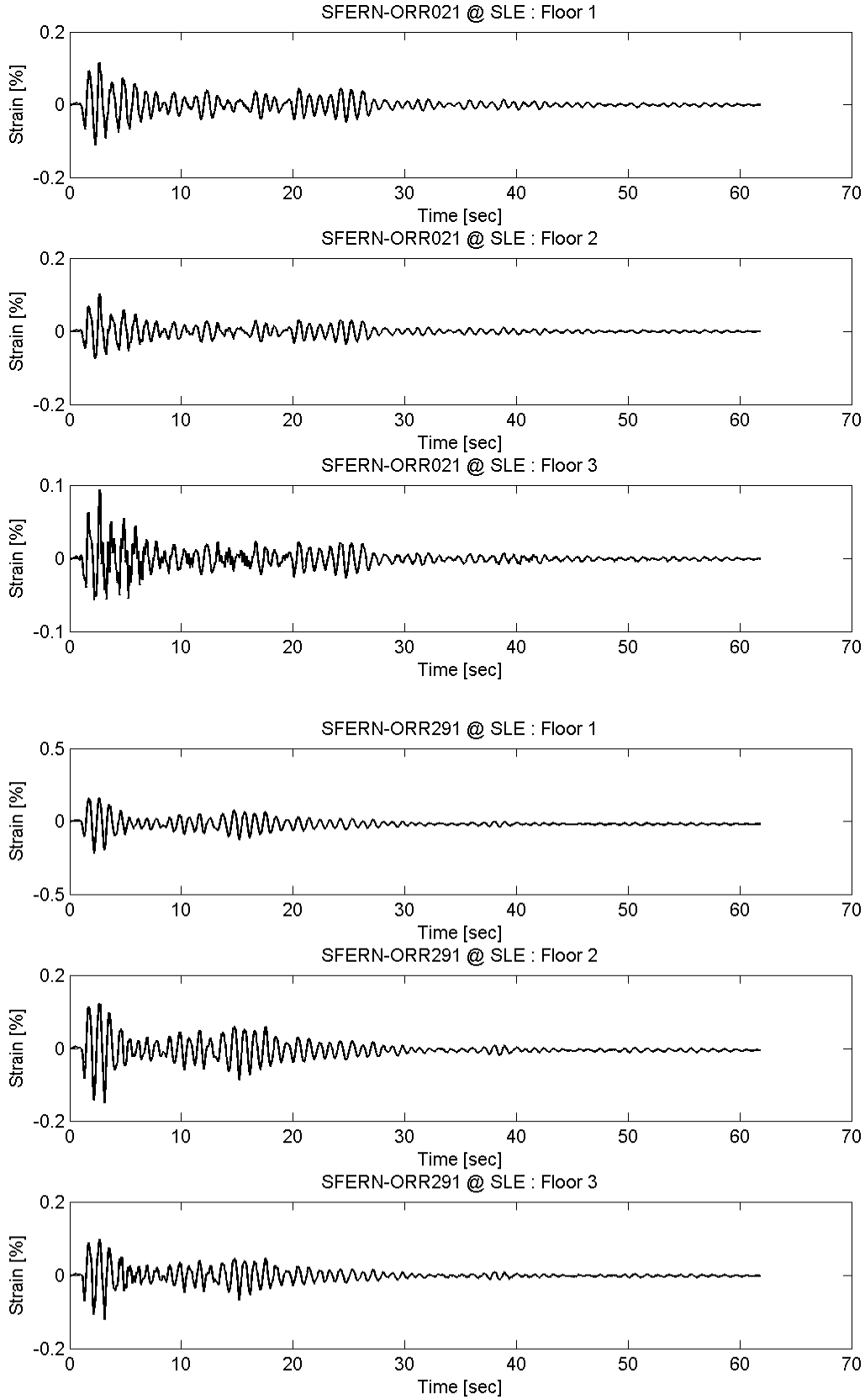
SFERN-ORR021 @ SLE : Floor 1
Strain [%]
Time [sec]
SFERN-ORR021 @ SLE : Floor 2
Strain [%]
Time [sec]
SFERN-ORR021 @ SLE : Floor 3
Strain [%]
Time [sec]
SFERN-ORR291 @ SLE : Floor 1
Strain [%]
Time [sec]
SFERN-ORR291 @ SLE : Floor 2
Strain [%]
Time [sec]
SFERN-ORR291 @ SLE : Floor 3
Strain [%]
Time [sec]

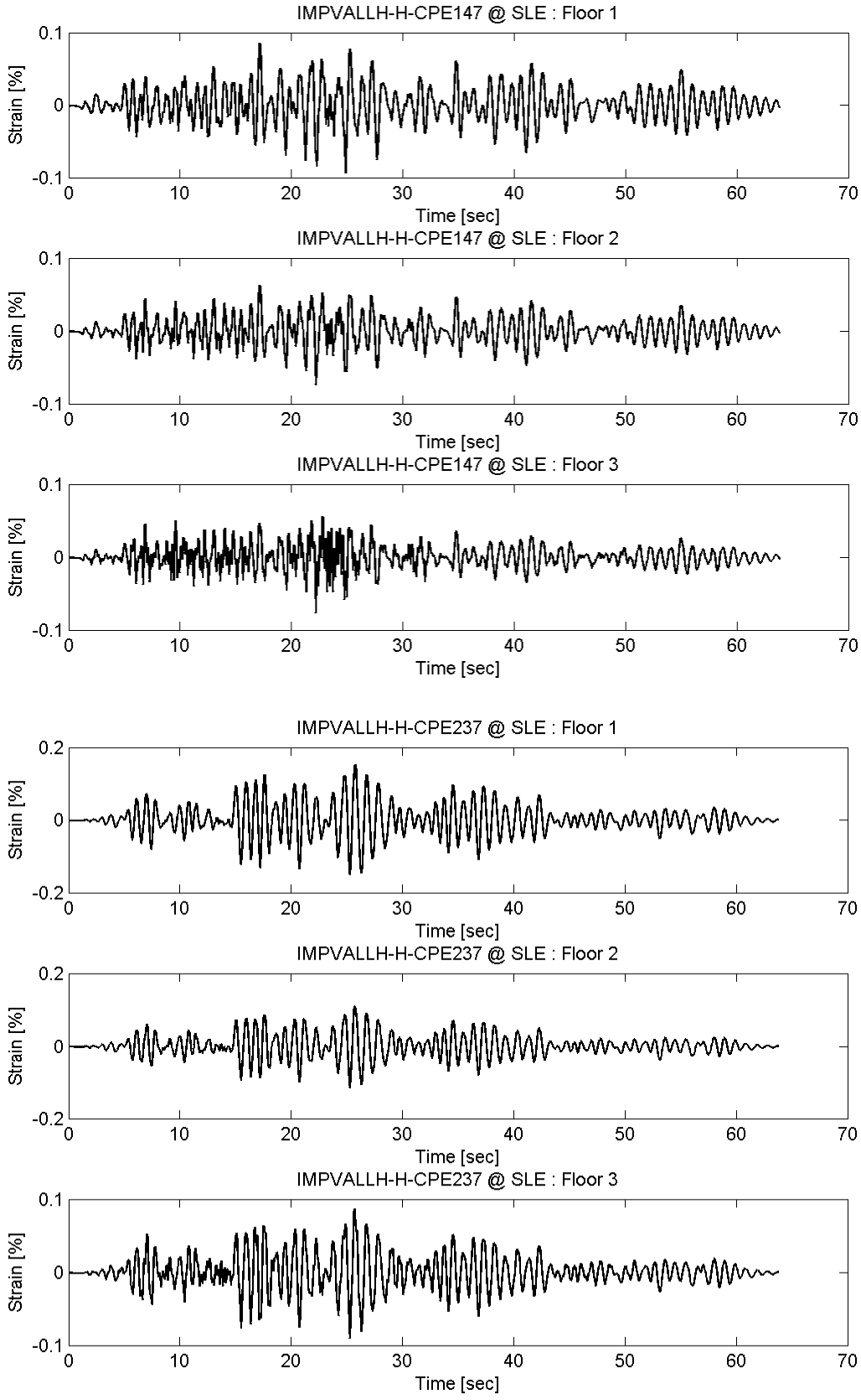
IMPVALLH-H-CPE147 @ SLE : Floor 1
Strain [%]
Time [sec]
IMPVALLH-H-CPE147 @ SLE : Floor 2
Strain [%]
Time [sec]
IMPVALLH-H-CPE147 @ SLE : Floor 3
Strain [%]
Time [sec]
IMPVALLH-H-CPE237 @ SLE : Floor 1
Strain [%]
Time [sec]
IMPVALLH-H-CPE237 @ SLE : Floor 2
Strain [%]
Time [sec]
IMPVALLH-H-CPE237 @ SLE : Floor 3
Strain [%]
Time [sec]

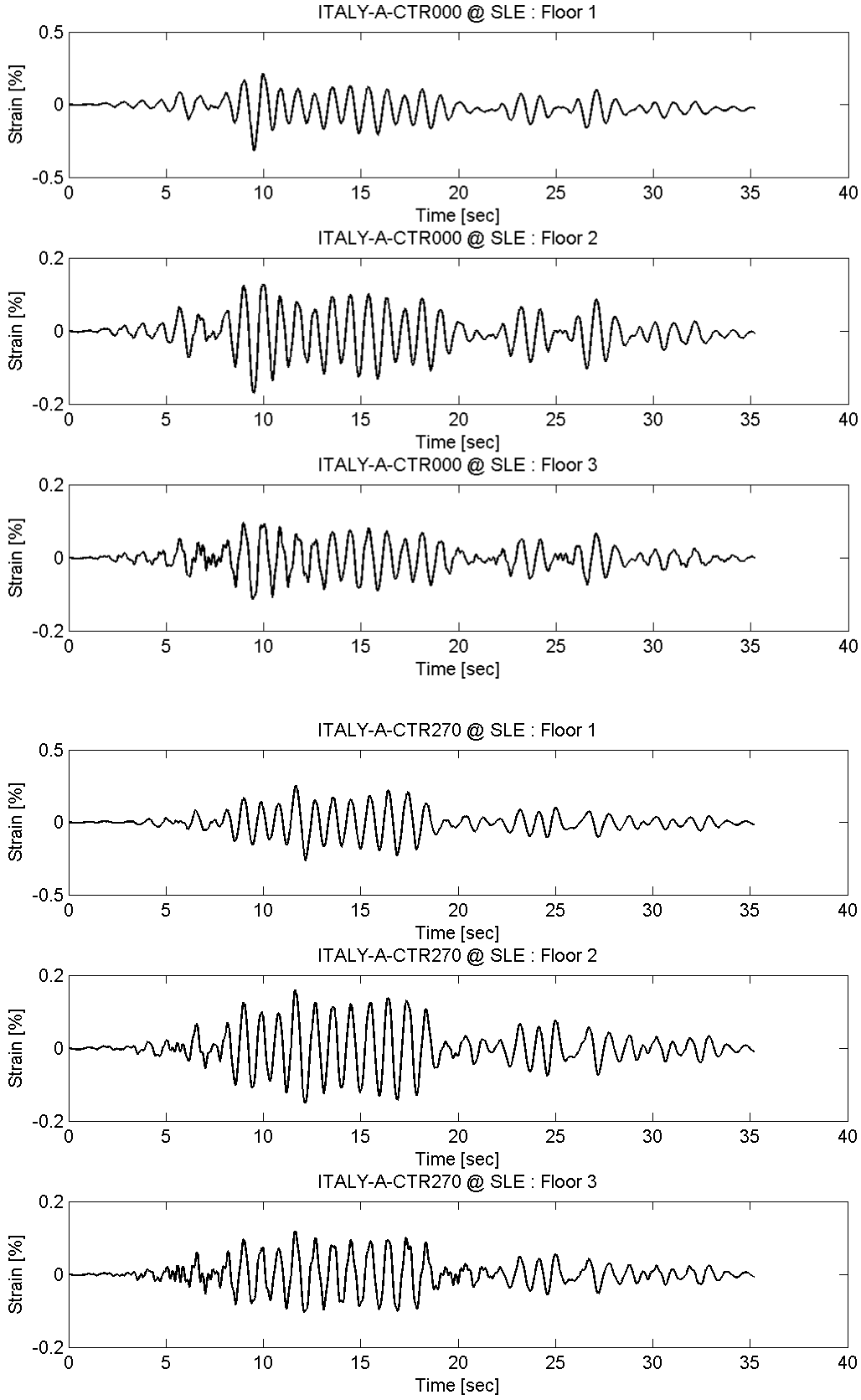
ITALY-A-CTR000 @ SLE : Floor 1
Strain [%]
Time [sec]
ITALY-A-CTR000 @ SLE : Floor 2
Strain [%]
Time [sec]
ITALY-A-CTR000 @ SLE : Floor 3
Strain [%]
Time [sec]
ITALY-A-CTR270 @ SLE : Floor 1
Strain [%]
Time [sec]
ITALY-A-CTR270 @ SLE : Floor 2
Strain [%]
Time [sec]
ITALY-A-CTR270 @ SLE : Floor 3
Strain [%]
Time [sec]

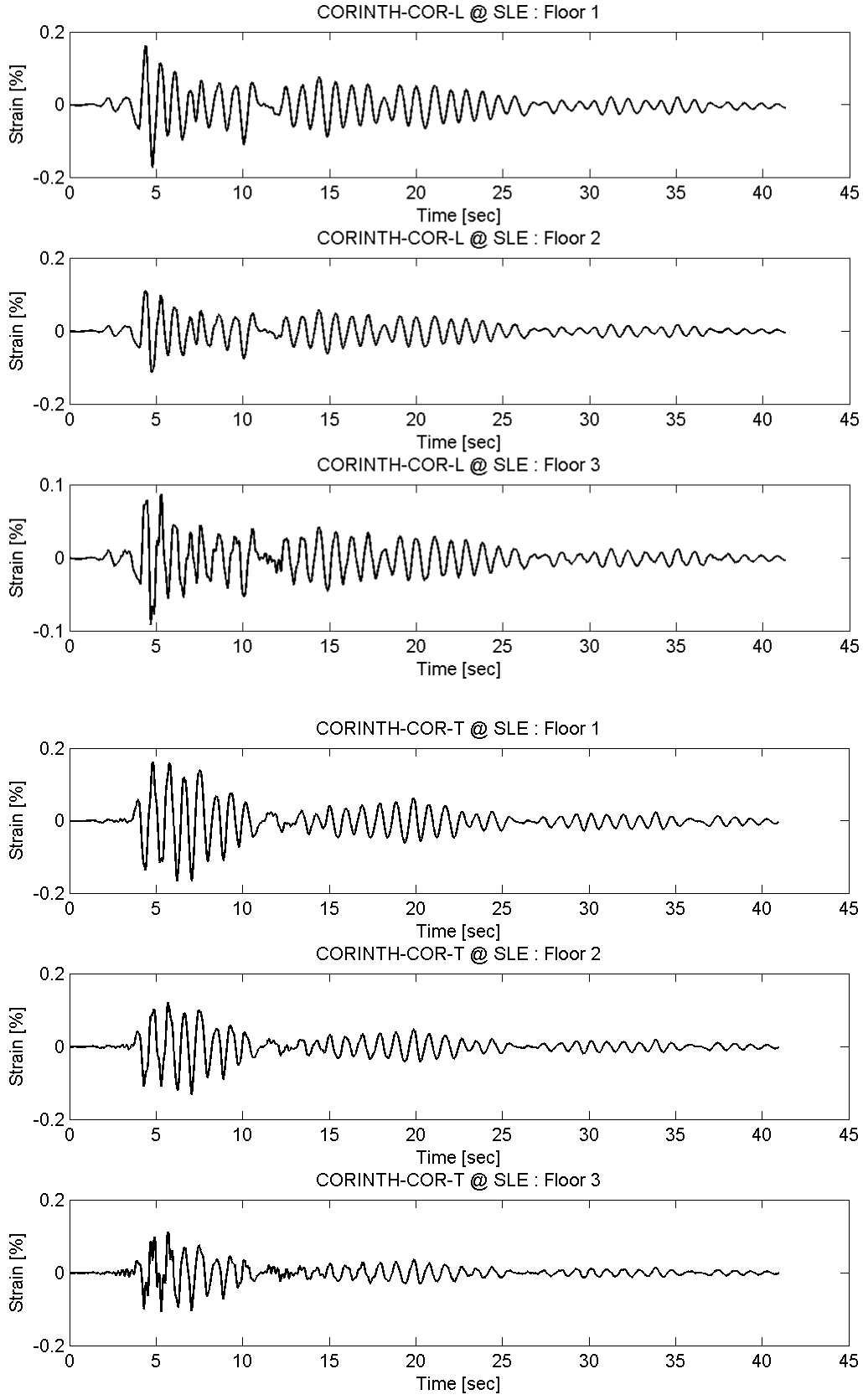
CORINTH-COR-L @ SLE : Floor 1
Strain [%]
Time [sec]
CORINTH-COR-L @ SLE : Floor 2
Strain [%]
Time [sec]
CORINTH-COR-L @ SLE : Floor 3
Strain [%]
Time [sec]
CORINTH-COR-T @ SLE : Floor 1
Strain [%]
Time [sec]
CORINTH-COR-T @ SLE : Floor 2
Strain [%]
Time [sec]
CORINTH-COR-T @ SLE : Floor 3
Strain [%]
Time [sec]

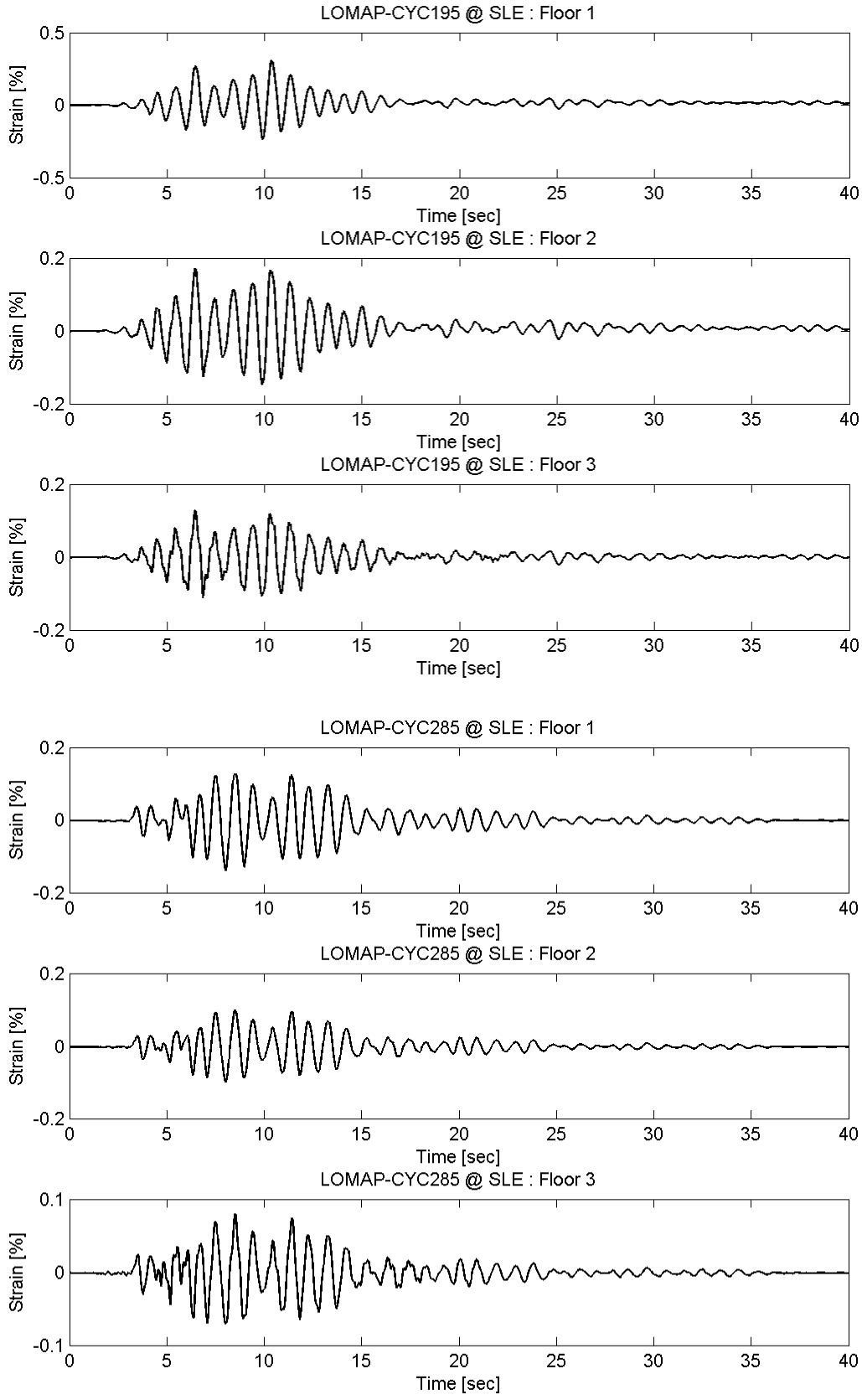
LOMAP-CYC195 @ SLE : Floor 1
Strain [%]
Time [sec]
LOMAP-CYC195 @ SLE : Floor 2
Strain [%]
Time [sec]
LOMAP-CYC195 @ SLE : Floor 3
Strain [%]
Time [sec]
LOMAP-CYC285 @ SLE : Floor 1
Strain [%]
Time [sec]
LOMAP-CYC285 @ SLE : Floor 2
Strain [%]
Time [sec]
LOMAP-CYC285 @ SLE : Floor 3
Strain [%]
Time [sec]

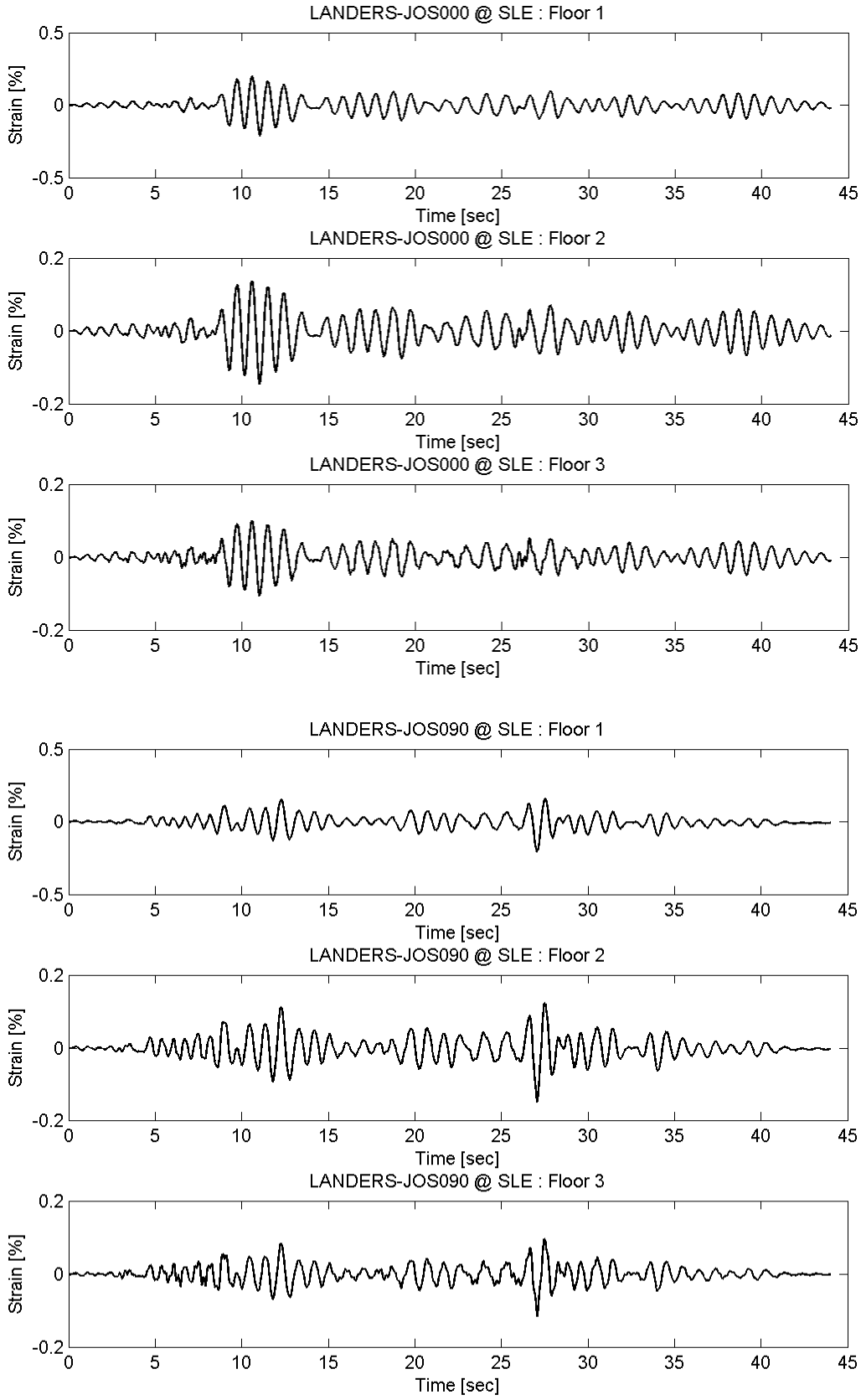
LANDERS-JOS000 @ SLE : Floor 1
Strain [%]
Time [sec]
LANDERS-JOS000 @ SLE : Floor 2
Strain [%]
Time [sec]
LANDERS-JOS000 @ SLE : Floor 3
Strain [%]
Time [sec]
LANDERS-JOS090 @ SLE : Floor 1
Strain [%]
Time [sec]
LANDERS-JOS090 @ SLE : Floor 2
Strain [%]
Time [sec]
LANDERS-JOS090 @ SLE : Floor 3
Strain [%]
Time [sec]

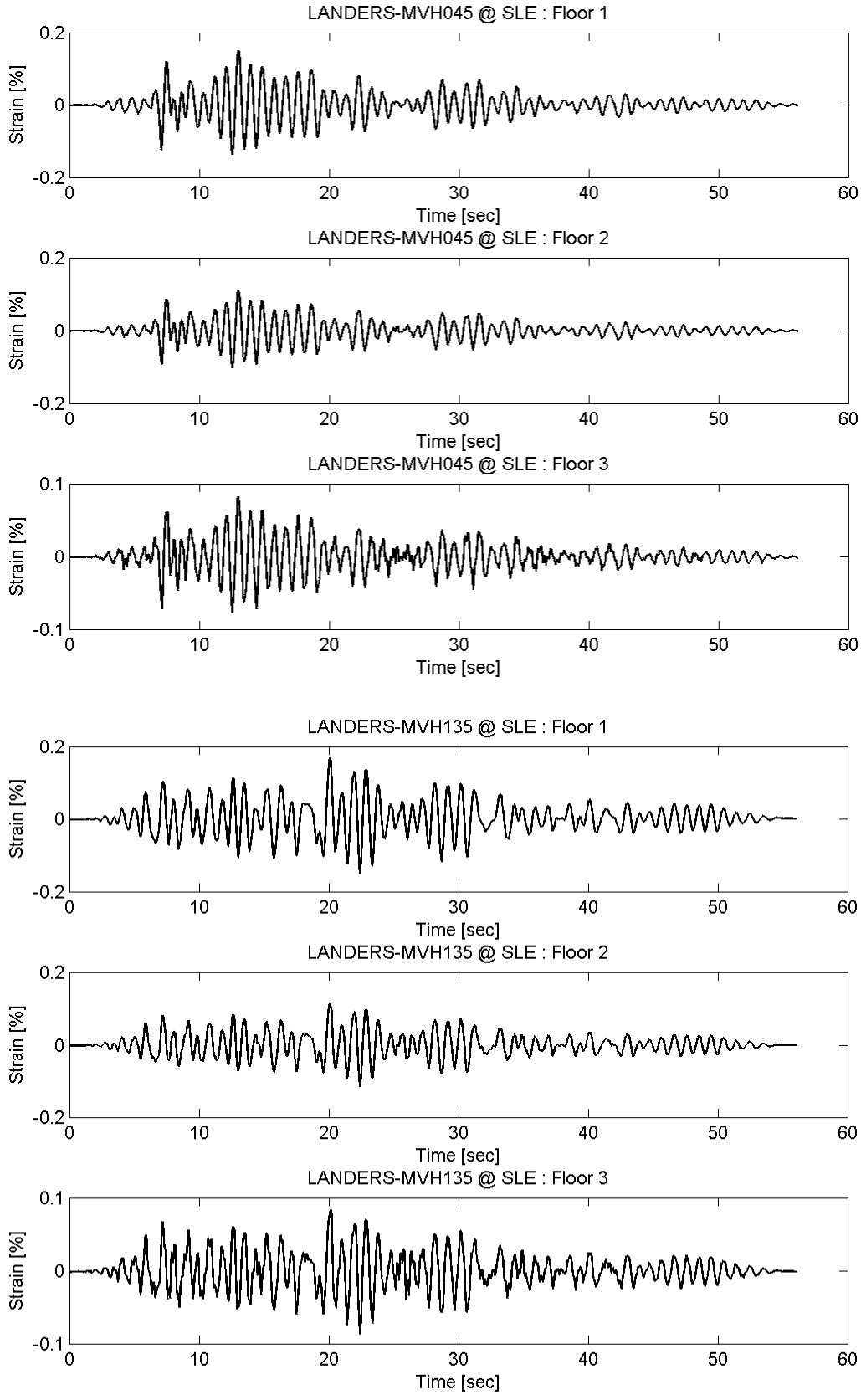
LANDERS-MVH045 @ SLE : Floor 1
Strain [%]
Time [sec]
LANDERS-MVH045 @ SLE : Floor 2
Strain [%]
Time [sec]
LANDERS-MVH045 @ SLE : Floor 3
Strain [%]
Time [sec]
LANDERS-MVH135 @ SLE : Floor 1
Strain [%]
Time [sec]
LANDERS-MVH135 @ SLE : Floor 2
Strain [%]
Time [sec]
LANDERS-MVH135 @ SLE : Floor 3
Strain [%]
Time [sec]

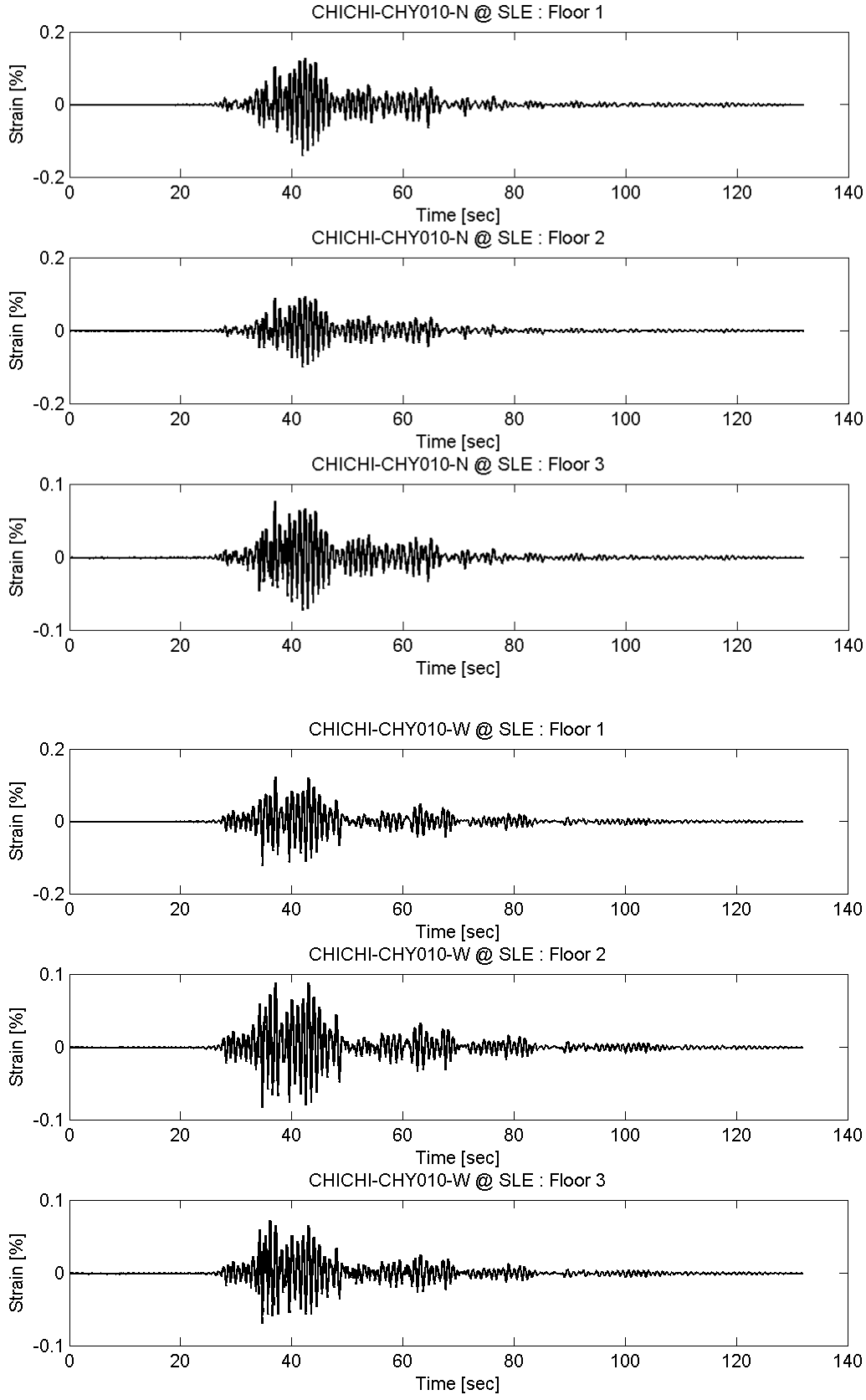
CHICHI-CHY010-N @ SLE : Floor 1
Strain [%]
Time [sec]
CHICHI-CHY010-N @ SLE : Floor 2
Strain [%]
Time [sec]
CHICHI-CHY010-N @ SLE : Floor 3
Strain [%]
Time [sec]
CHICHI-CHY010-W @ SLE : Floor 1
Strain [%]
Time [sec]
CHICHI-CHY010-W @ SLE : Floor 2
Strain [%]
Time [sec]
CHICHI-CHY010-W @ SLE : Floor 3
Strain [%]
Time [sec]

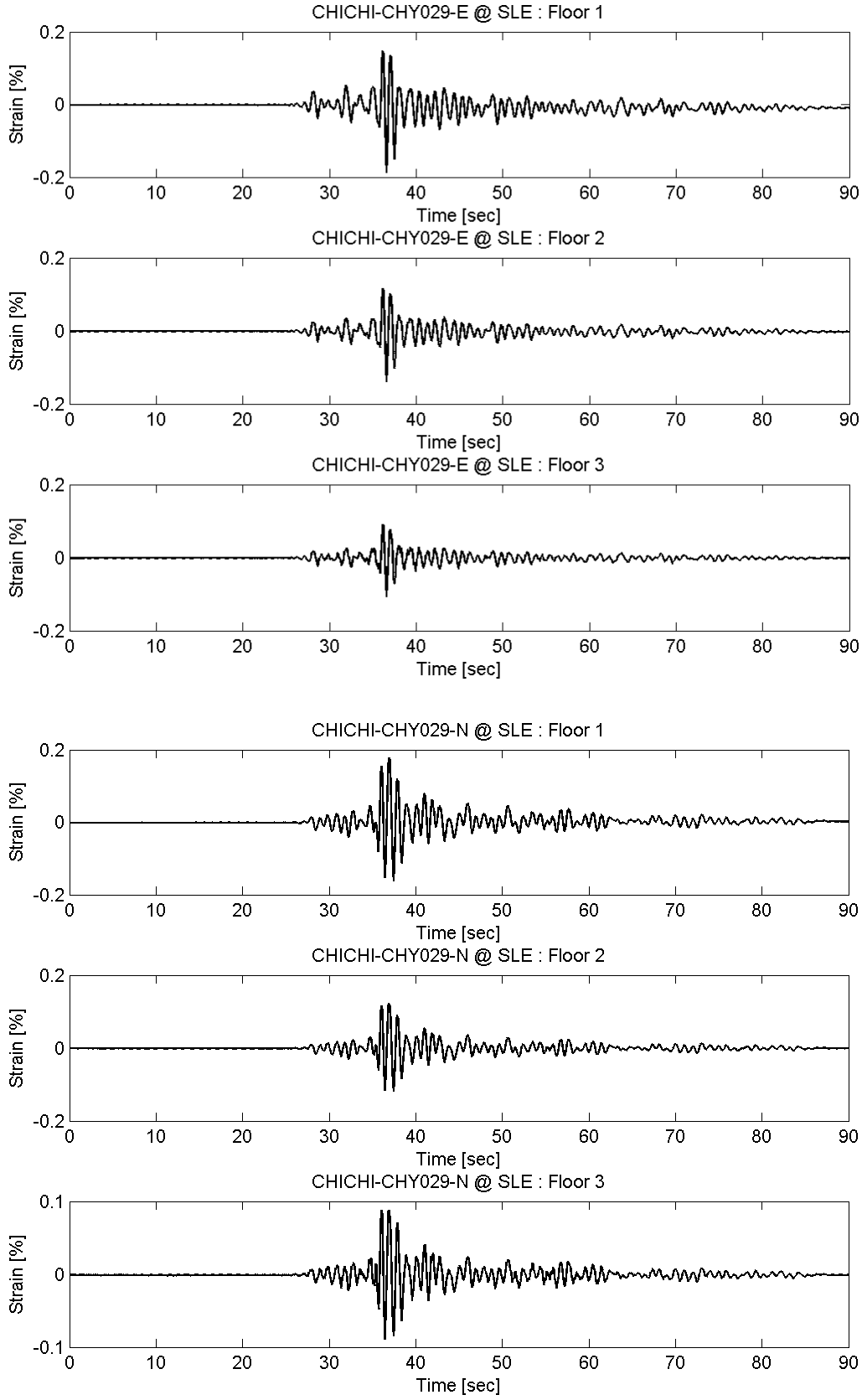
CHICHI-CHY029-E @ SLE : Floor 1
Strain [%]
Time [sec]
CHICHI-CHY029-E @ SLE : Floor 2
Strain [%]
Time [sec]
CHICHI-CHY029-E @ SLE : Floor 3
Strain [%]
Time [sec]
CHICHI-CHY029-N @ SLE : Floor 1
Strain [%]
Time [sec]
CHICHI-CHY029-N @ SLE : Floor 2
Strain [%]
Time [sec]
CHICHI-CHY029-N @ SLE : Floor 3
Strain [%]
Time [sec]

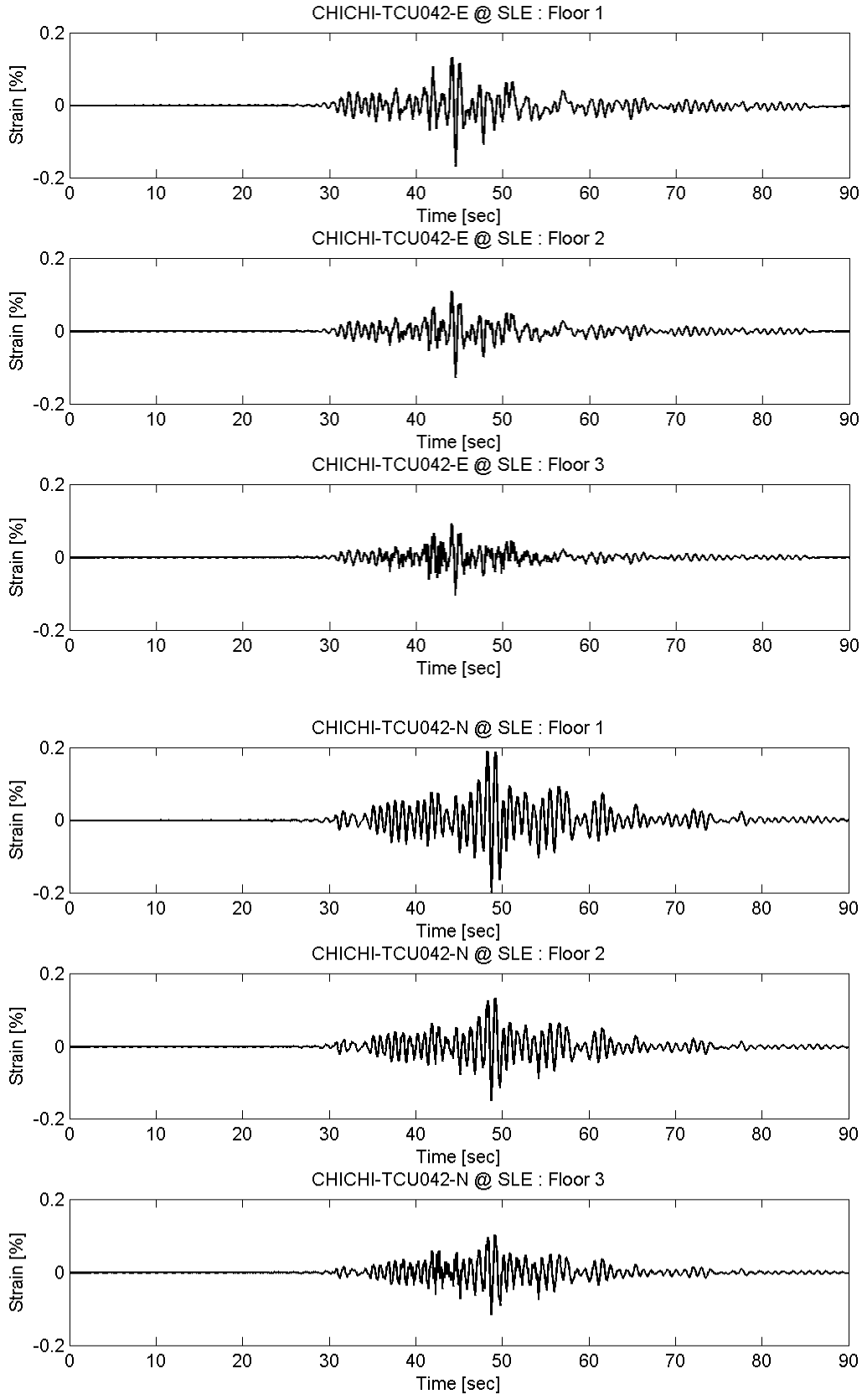
CHICHI-TCU042-E @ SLE : Floor 1
Strain [%]
Time [sec]
CHICHI-TCU042-E @ SLE : Floor 2
Strain [%]
Time [sec]
CHICHI-TCU042-E @ SLE : Floor 3
Strain [%]
Time [sec]
CHICHI-TCU042-N @ SLE : Floor 1
Strain [%]
Time [sec]
CHICHI-TCU042-N @ SLE : Floor 2
Strain [%]
Time [sec]
CHICHI-TCU042-N @ SLE : Floor 3
Strain [%]
Time [sec]

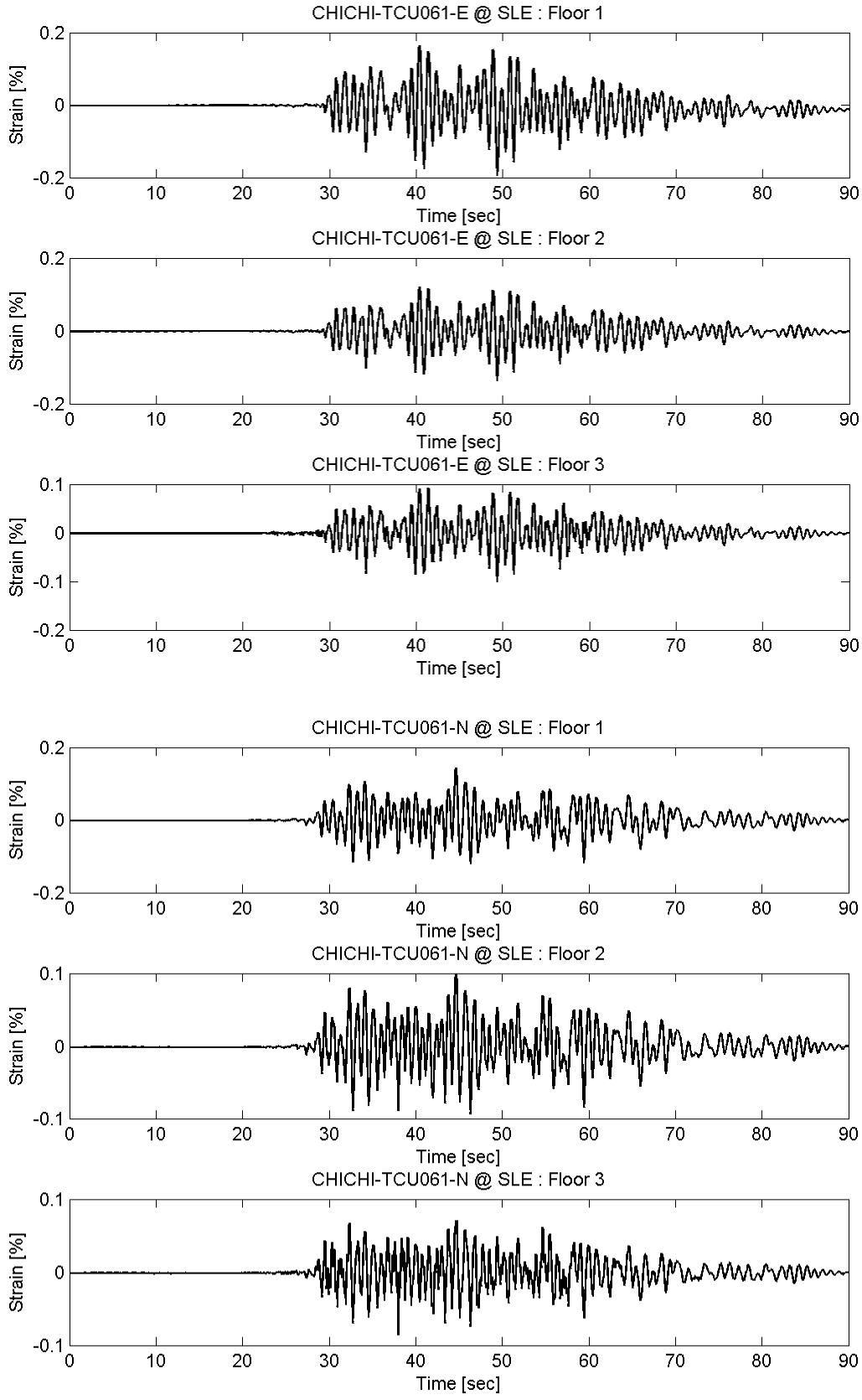
CHICHI-TCU061-E @ SLE : Floor 1
Strain [%]
Time [sec]
CHICHI-TCU061-E @ SLE : Floor 2
Strain [%]
Time [sec]
CHICHI-TCU061-E @ SLE : Floor 3
Strain [%]
Time [sec]
CHICHI-TCU061-N @ SLE : Floor 1
Strain [%]
Time [sec]
CHICHI-TCU061-N @ SLE : Floor 2
Strain [%]
Time [sec]
CHICHI-TCU061-N @ SLE : Floor 3
Strain [%]
Time [sec]

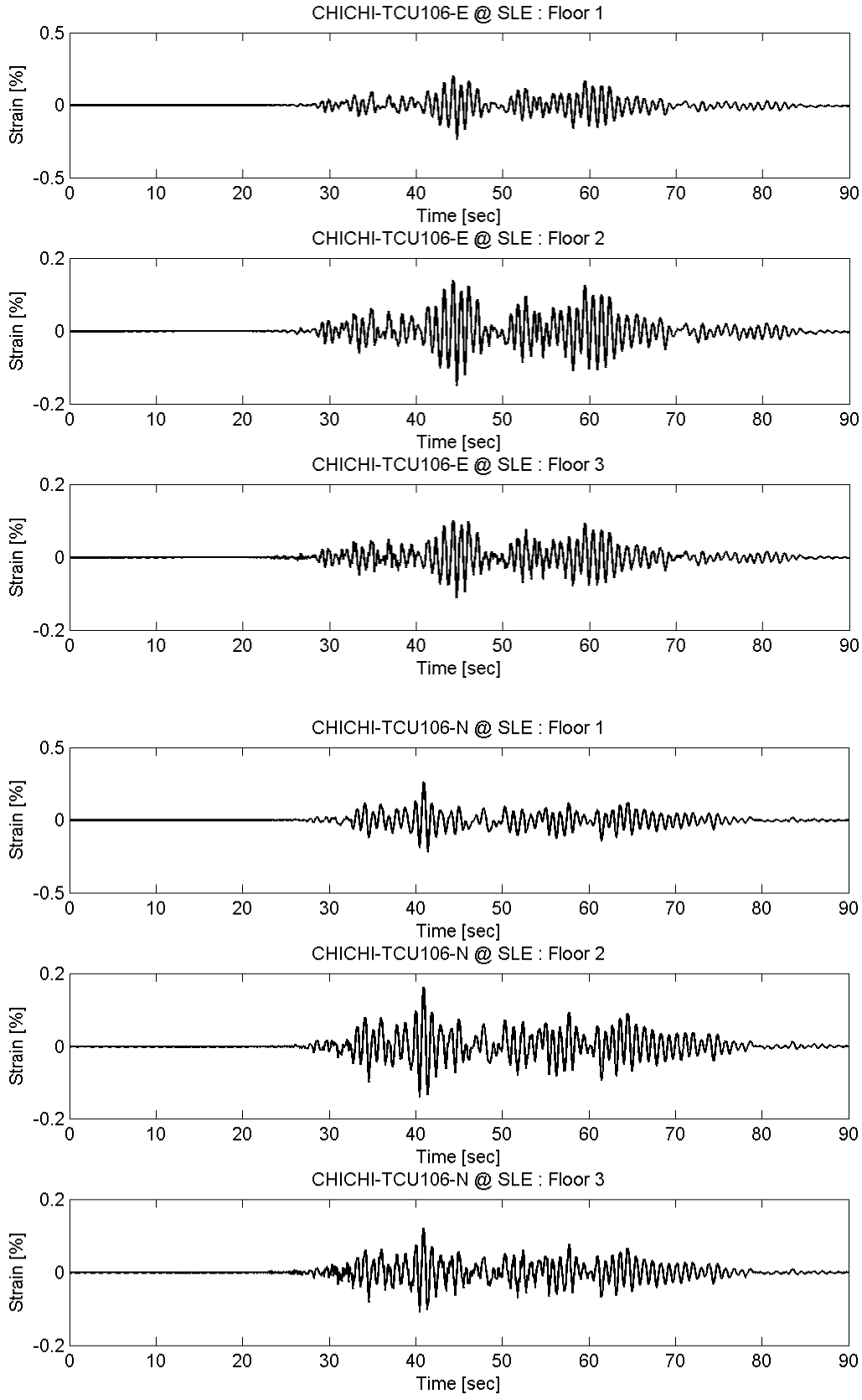
CHICHI-TCU106-E @ SLE : Floor 1
Strain [%]
Time [sec]
CHICHI-TCU106-E @ SLE : Floor 2
Strain [%]
Time [sec]
CHICHI-TCU106-E @ SLE : Floor 3
Strain [%]
Time [sec]
CHICHI-TCU106-N @ SLE : Floor 1
Strain [%]
Time [sec]
CHICHI-TCU106-N @ SLE : Floor 2
Strain [%]
Time [sec]
CHICHI-TCU106-N @ SLE : Floor 3
Strain [%]
Time [sec]

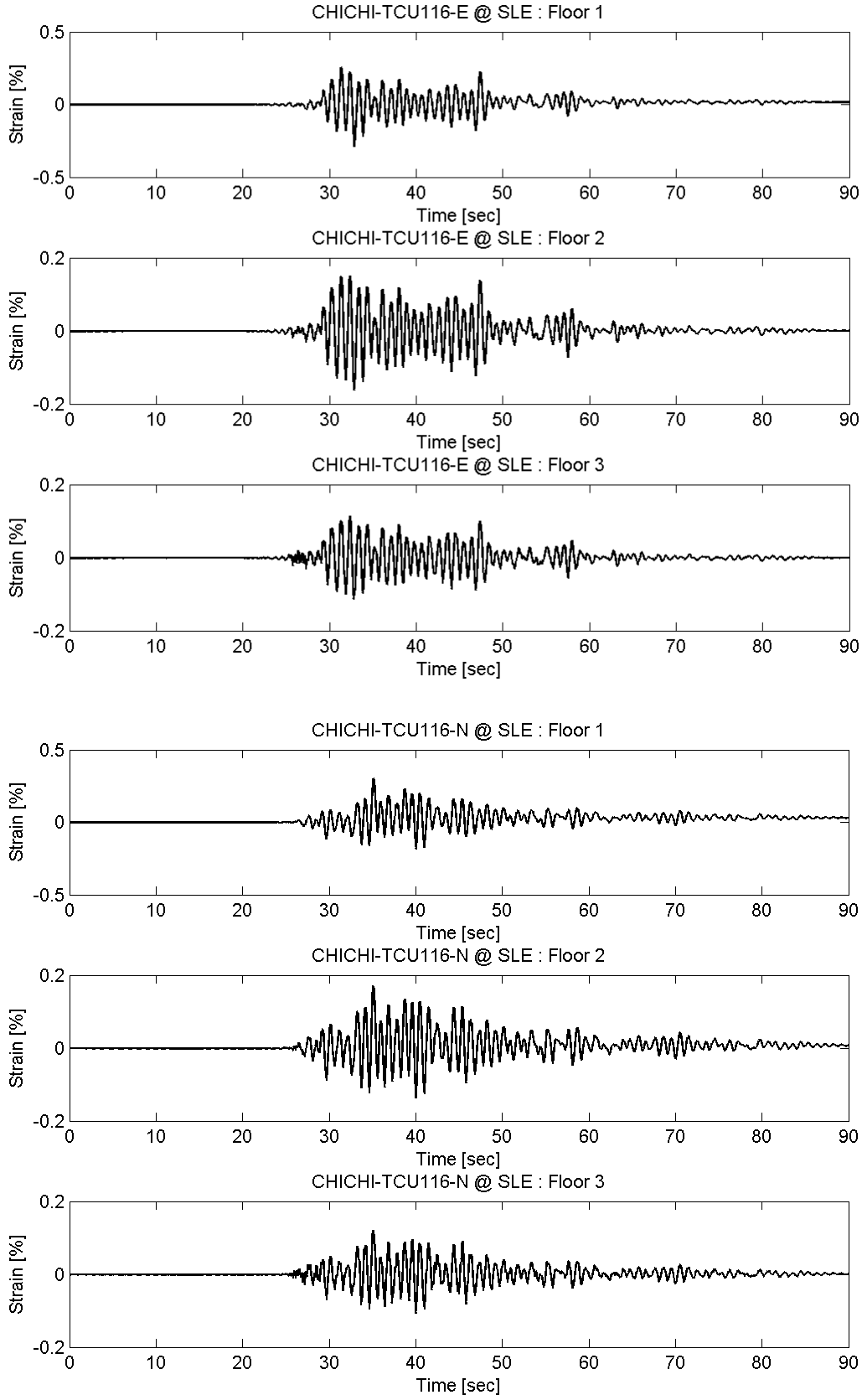
CHICHI-TCU116-E @ SLE : Floor 1
Strain [%]
Time [sec]
CHICHI-TCU116-E @ SLE : Floor 2
Strain [%]
Time [sec]
CHICHI-TCU116-E @ SLE : Floor 3
Strain [%]
Time [sec]
CHICHI-TCU116-N @ SLE : Floor 1
Strain [%]
Time [sec]
CHICHI-TCU116-N @ SLE : Floor 2
Strain [%]
Time [sec]
CHICHI-TCU116-N @ SLE : Floor 3
Strain [%]
Time [sec]

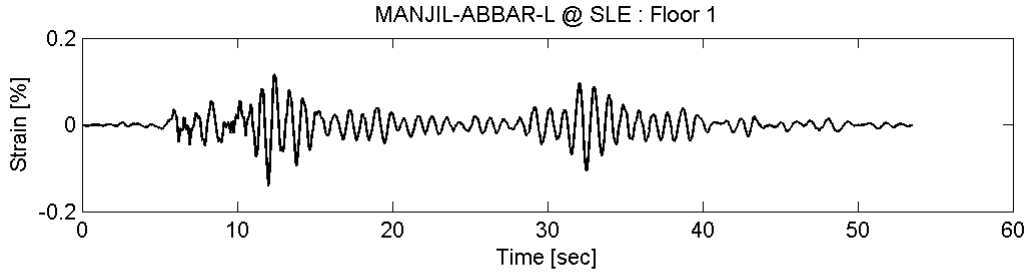
MANJIL-ABBAR-L @ SLE : Floor 1
Strain [%]
Time [sec]

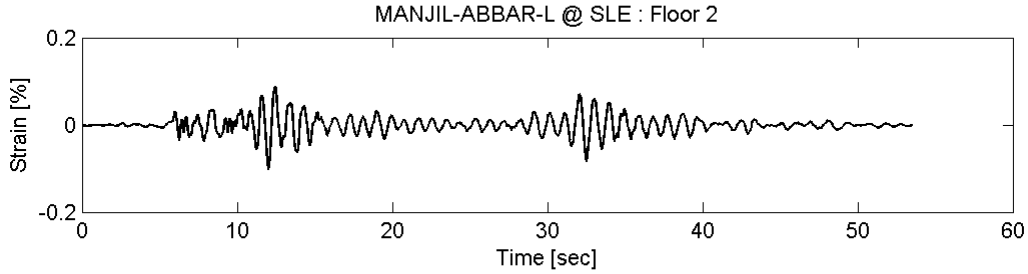
MANJIL-ABBAR-L @ SLE : Floor 2
Strain [%]
Time [sec]

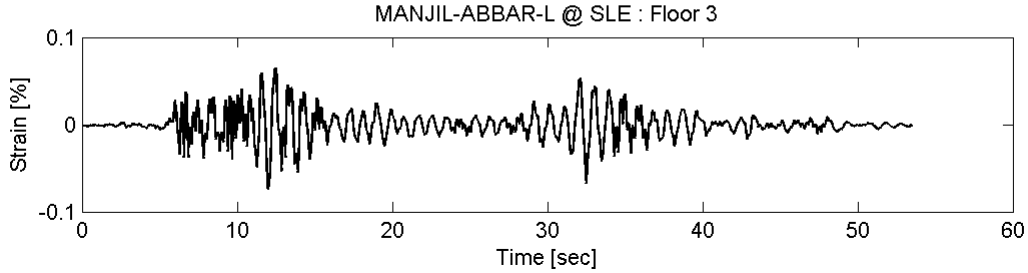
MANJIL-ABBAR-L @ SLE : Floor 3
Strain [%]
Time [sec]

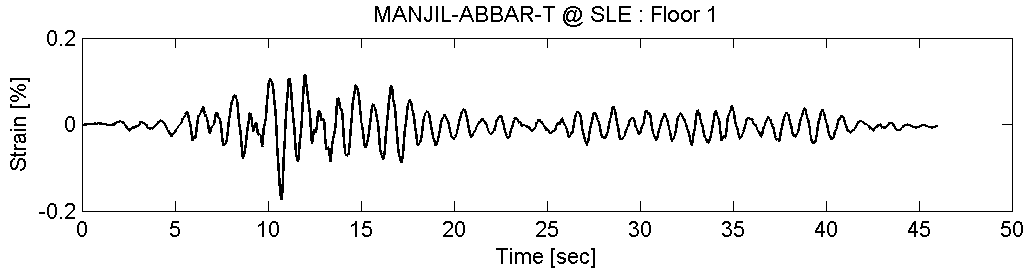
MANJIL-ABBAR-T @ SLE : Floor 1
Strain [%]
Time [sec]

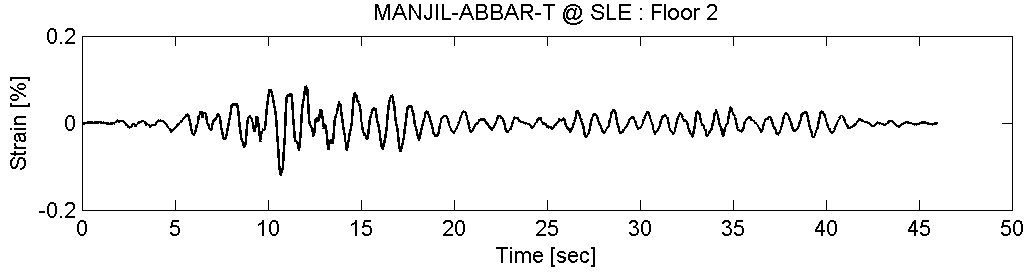
MANJIL-ABBAR-T @ SLE : Floor 2
Strain [%]
Time [sec]

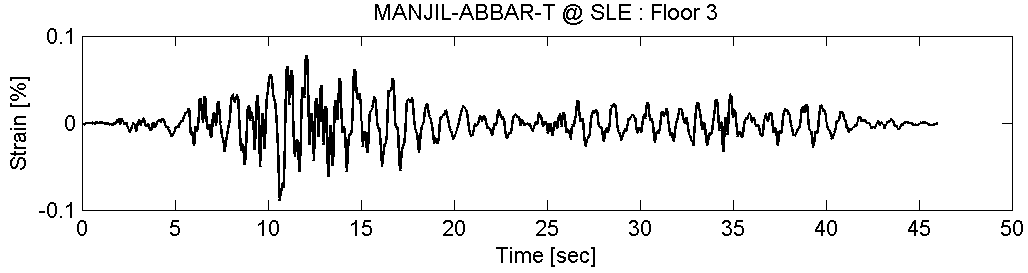
MANJIL-ABBAR-T @ SLE : Floor 3
Strain [%]
Time [sec]

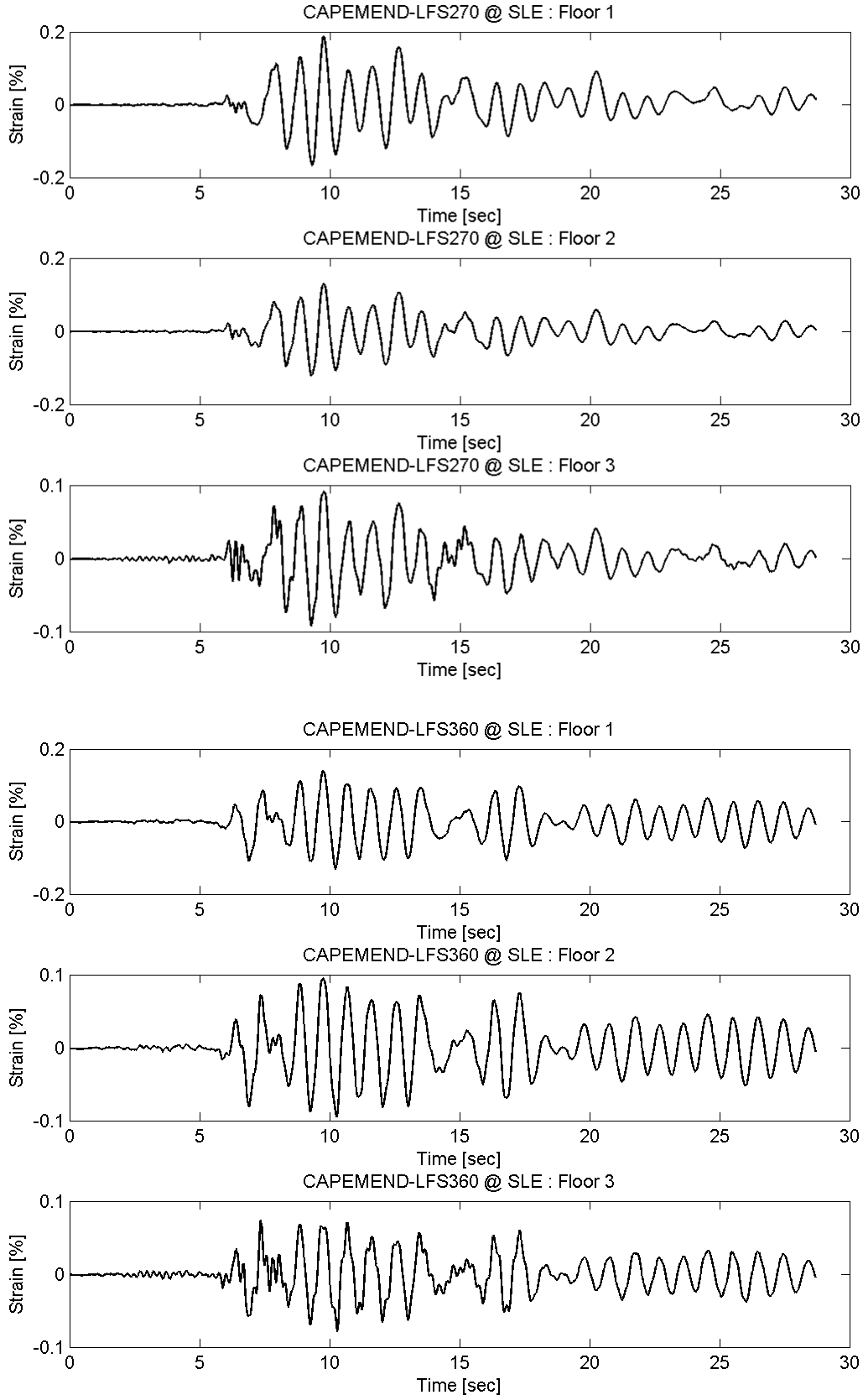
CAPEMEND-LFS270 @ SLE : Floor 1
Strain [%]
Time [sec]
CAPEMEND-LFS270 @ SLE : Floor 2
Strain [%]
Time [sec]
CAPEMEND-LFS270 @ SLE : Floor 3
Strain [%]
Time [sec]
CAPEMEND-LFS360 @ SLE : Floor 1
Strain [%]
Time [sec]
CAPEMEND-LFS360 @ SLE : Floor 2
Strain [%]
Time [sec]
CAPEMEND-LFS360 @ SLE : Floor 3
Strain [%]
Time [sec]

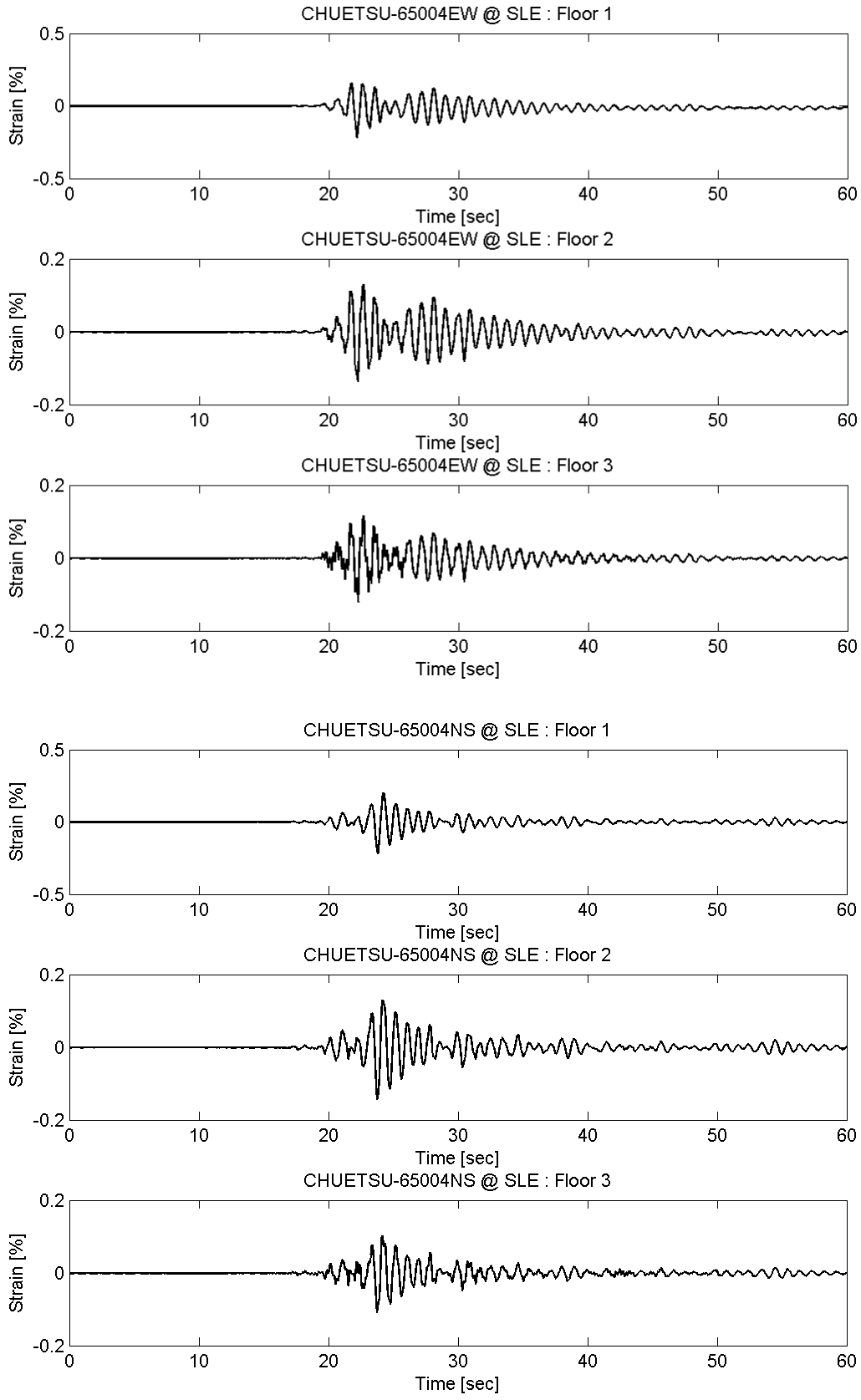
CHUETSU-65004EW @ SLE : Floor 1
Strain [%]
Time [sec]
CHUETSU-65004EW @ SLE : Floor 2
Strain [%]
Time [sec]
CHUETSU-65004EW @ SLE : Floor 3
Strain [%]
Time [sec]
CHUETSU-65004NS @ SLE : Floor 1
Strain [%]
Time [sec]
CHUETSU-65004NS @ SLE : Floor 2
Strain [%]
Time [sec]
CHUETSU-65004NS @ SLE : Floor 3
Strain [%]
Time [sec]

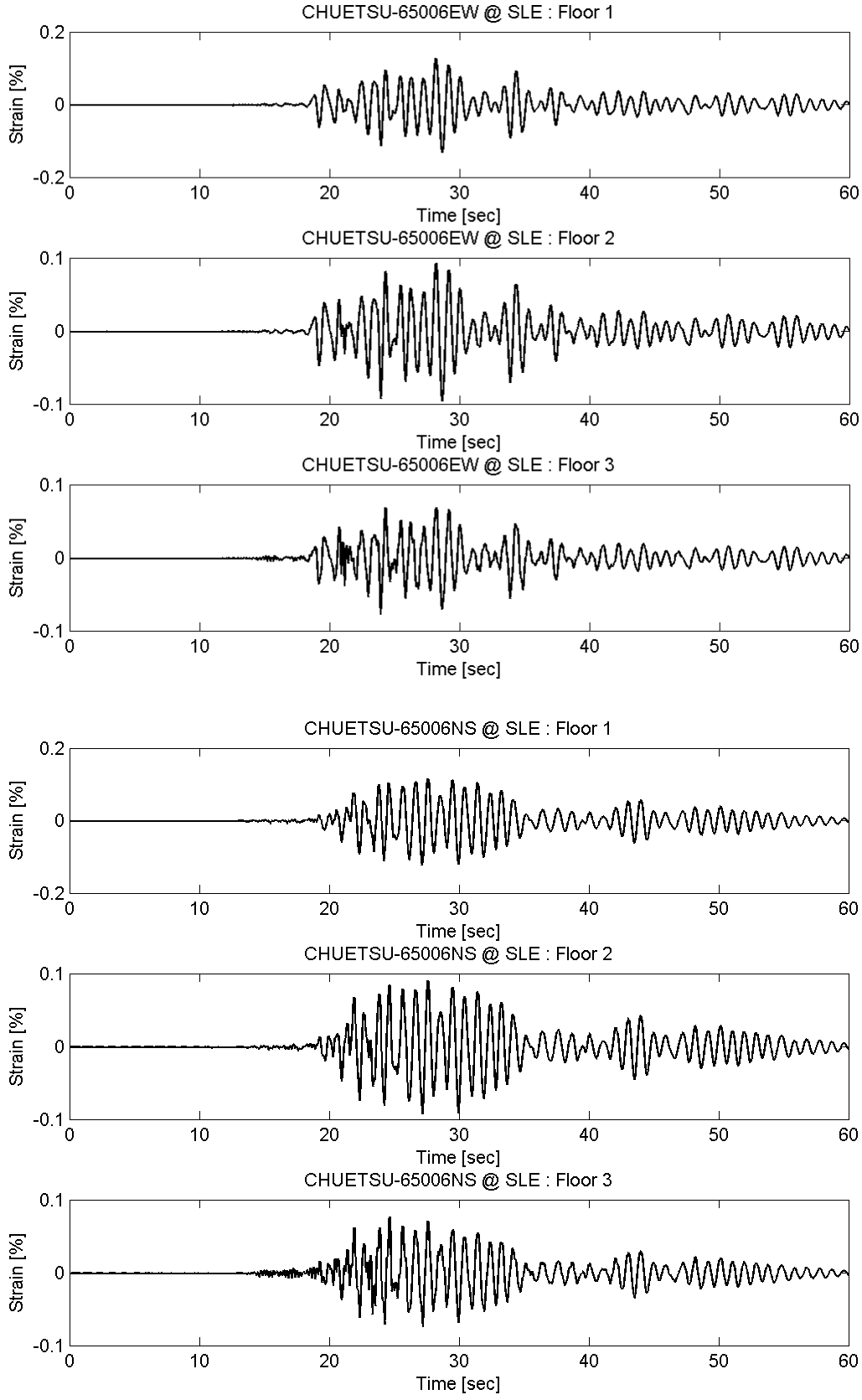
CHUETSU-65006EW @ SLE : Floor 1
Strain [%]
Time [sec]
CHUETSU-65006EW @ SLE : Floor 2
Strain [%]
Time [sec]
CHUETSU-65006EW @ SLE : Floor 3
Strain [%]
Time [sec]
CHUETSU-65006NS @ SLE : Floor 1
Strain [%]
Time [sec]
CHUETSU-65006NS @ SLE : Floor 2
Strain [%]
Time [sec]
CHUETSU-65006NS @ SLE : Floor 3
Strain [%]
Time [sec]

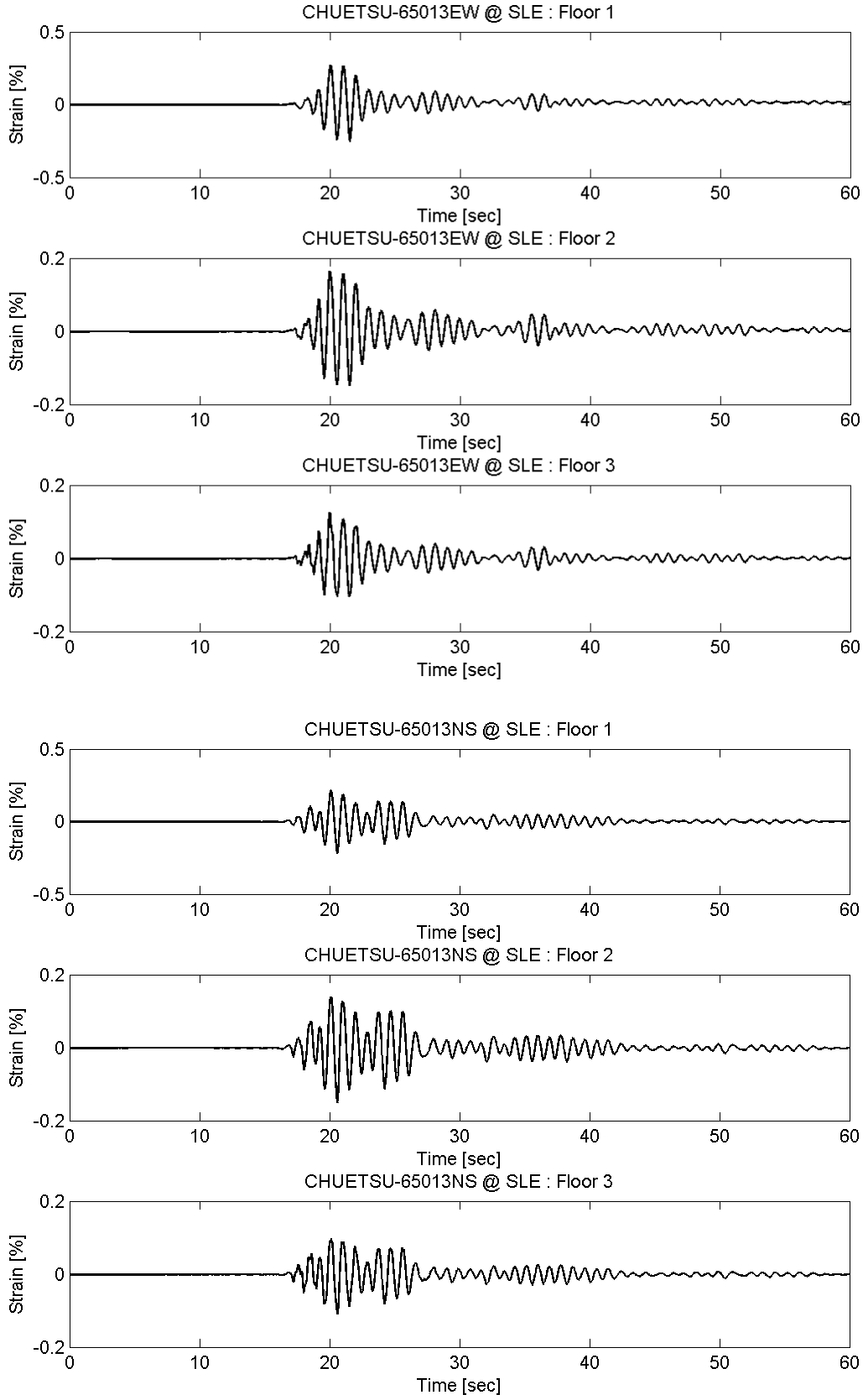
CHUETSU-65013EW @ SLE : Floor 1
Strain [%]
Time [sec]
CHUETSU-65013EW @ SLE : Floor 2
Strain [%]
Time [sec]
CHUETSU-65013EW @ SLE : Floor 3
Strain [%]
Time [sec]
CHUETSU-65013NS @ SLE : Floor 1
Strain [%]
Time [sec]
CHUETSU-65013NS @ SLE : Floor 2
Strain [%]
Time [sec]
CHUETSU-65013NS @ SLE : Floor 3
Strain [%]
Time [sec]

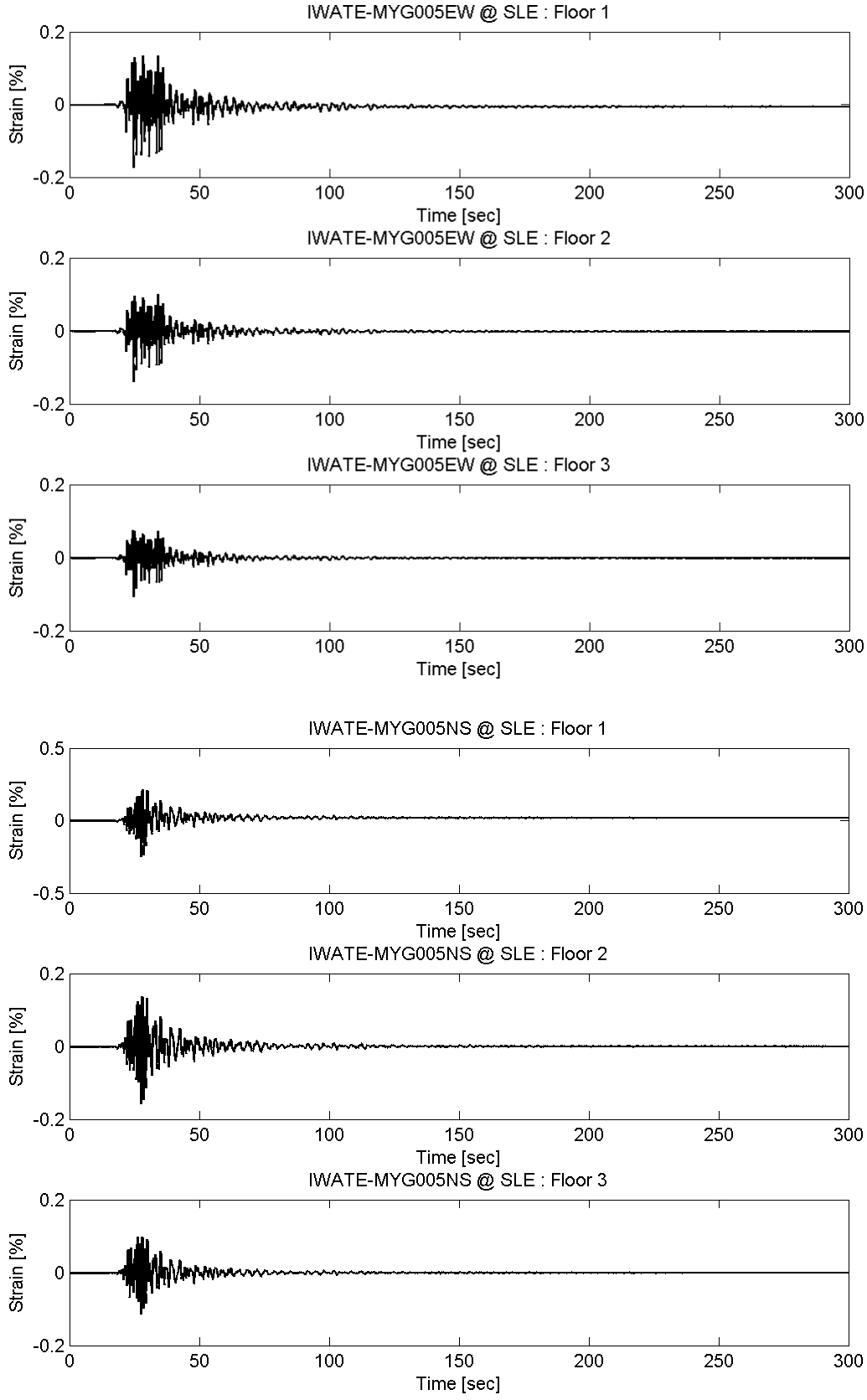
IWATE-MYG005EW @ SLE : Floor 1
Strain [%]
Time [sec]
IWATE-MYG005EW @ SLE : Floor 2
Strain [%]
Time [sec]
IWATE-MYG005EW @ SLE : Floor 3
Strain [%]
Time [sec]
IWATE-MYG005NS @ SLE : Floor 1
Strain [%]
Time [sec]
IWATE-MYG005NS @ SLE : Floor 2
Strain [%]
Time [sec]
IWATE-MYG005NS @ SLE : Floor 3
Strain [%]
Time [sec]

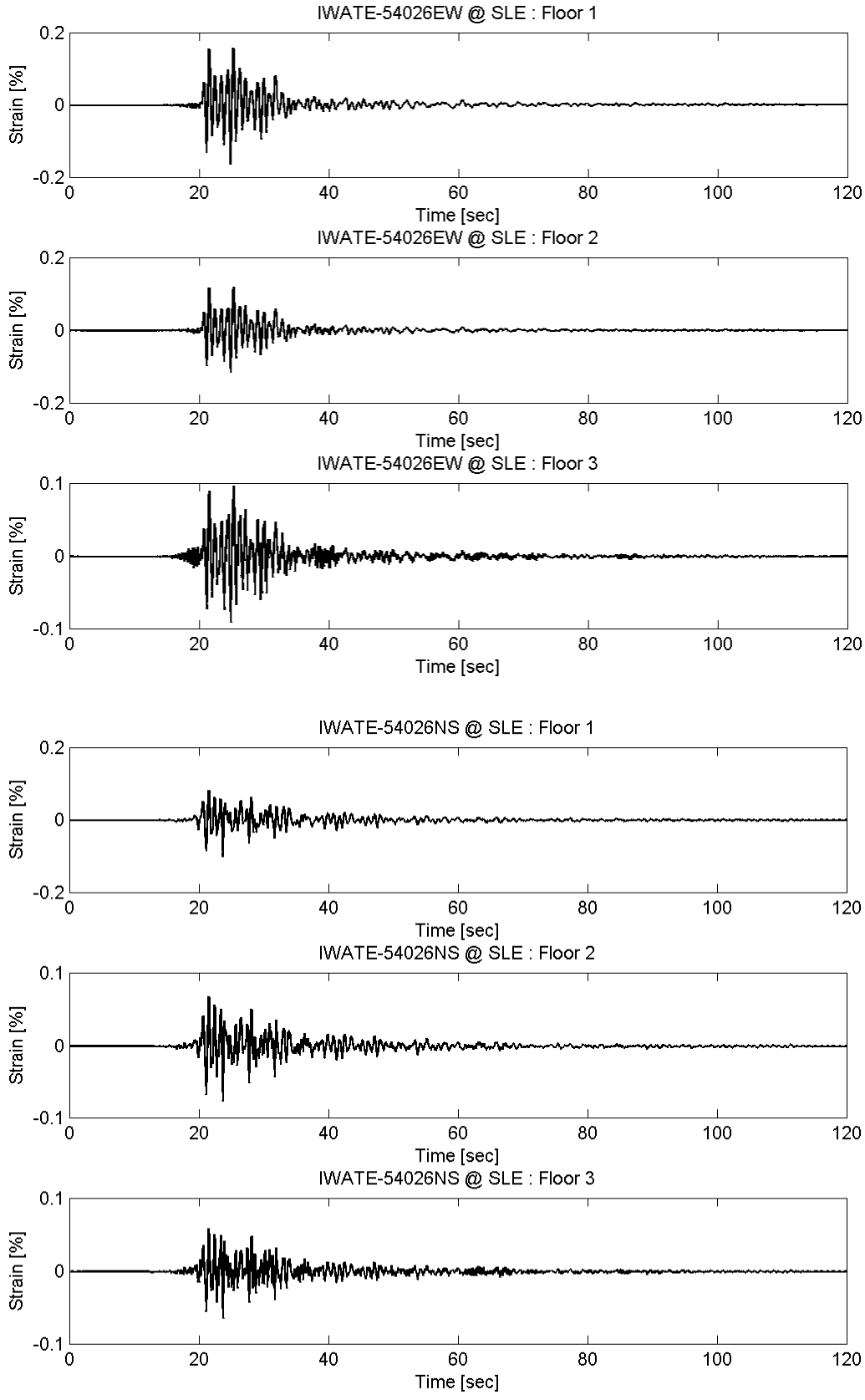
IWATE-54026EW @ SLE : Floor 1
Strain [%]
Time [sec]
IWATE-54026EW @ SLE : Floor 2
Strain [%]
Time [sec]
IWATE-54026EW @ SLE : Floor 3
Strain [%]
Time [sec]
IWATE-54026NS @ SLE : Floor 1
Strain [%]
Time [sec]
IWATE-54026NS @ SLE : Floor 2
Strain [%]
Time [sec]
IWATE-54026NS @ SLE : Floor 3
Strain [%]
Time [sec]

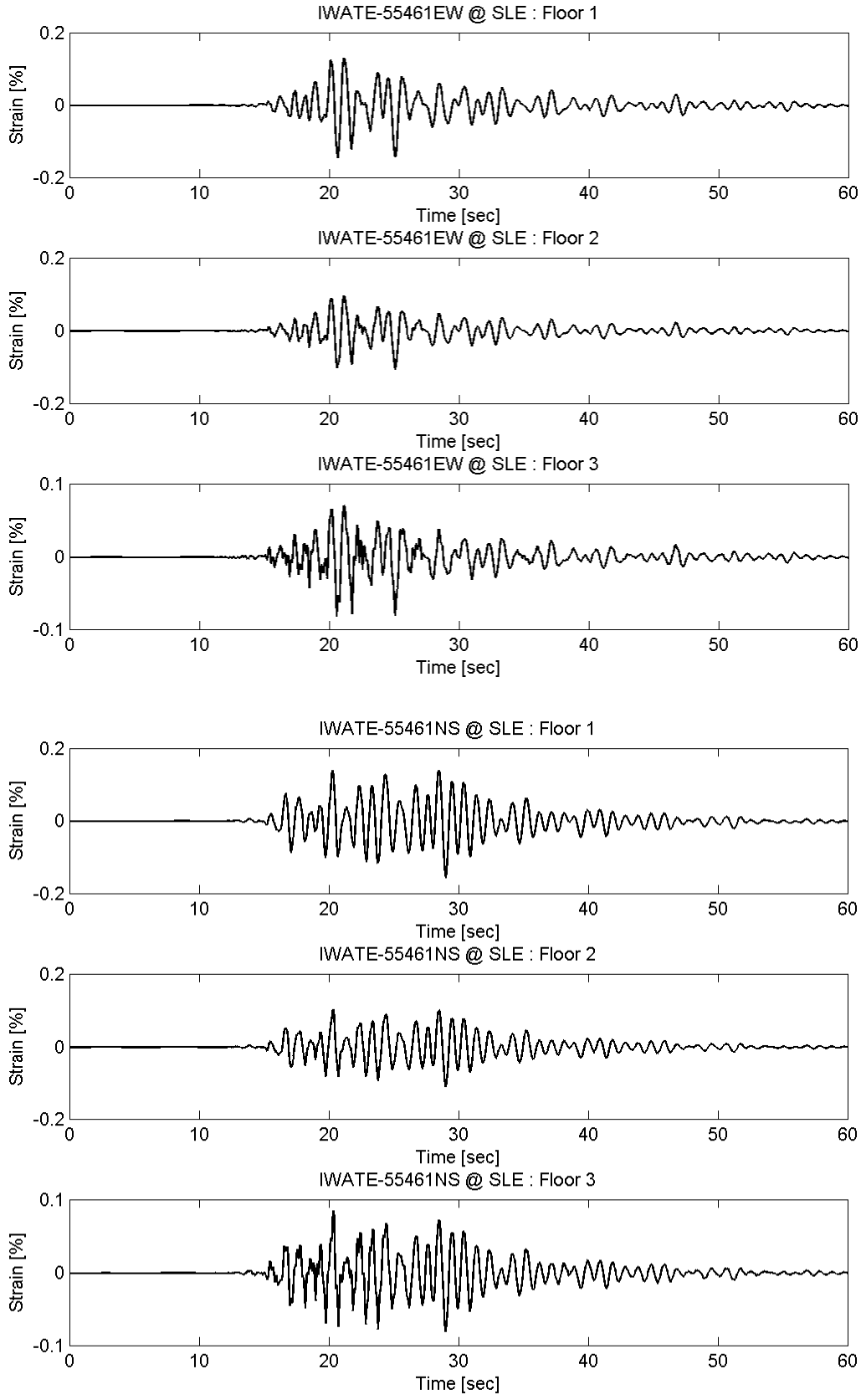
IWATE-55461EW @ SLE : Floor 1
Strain [%]
Time [sec]
IWATE-55461EW @ SLE : Floor 2
Strain [%]
Time [sec]
IWATE-55461EW @ SLE : Floor 3
Strain [%]
Time [sec]
IWATE-55461NS @ SLE : Floor 1
Strain [%]
Time [sec]
IWATE-55461NS @ SLE : Floor 2
Strain [%]
Time [sec]
IWATE-55461NS @ SLE : Floor 3
Strain [%]
Time [sec]

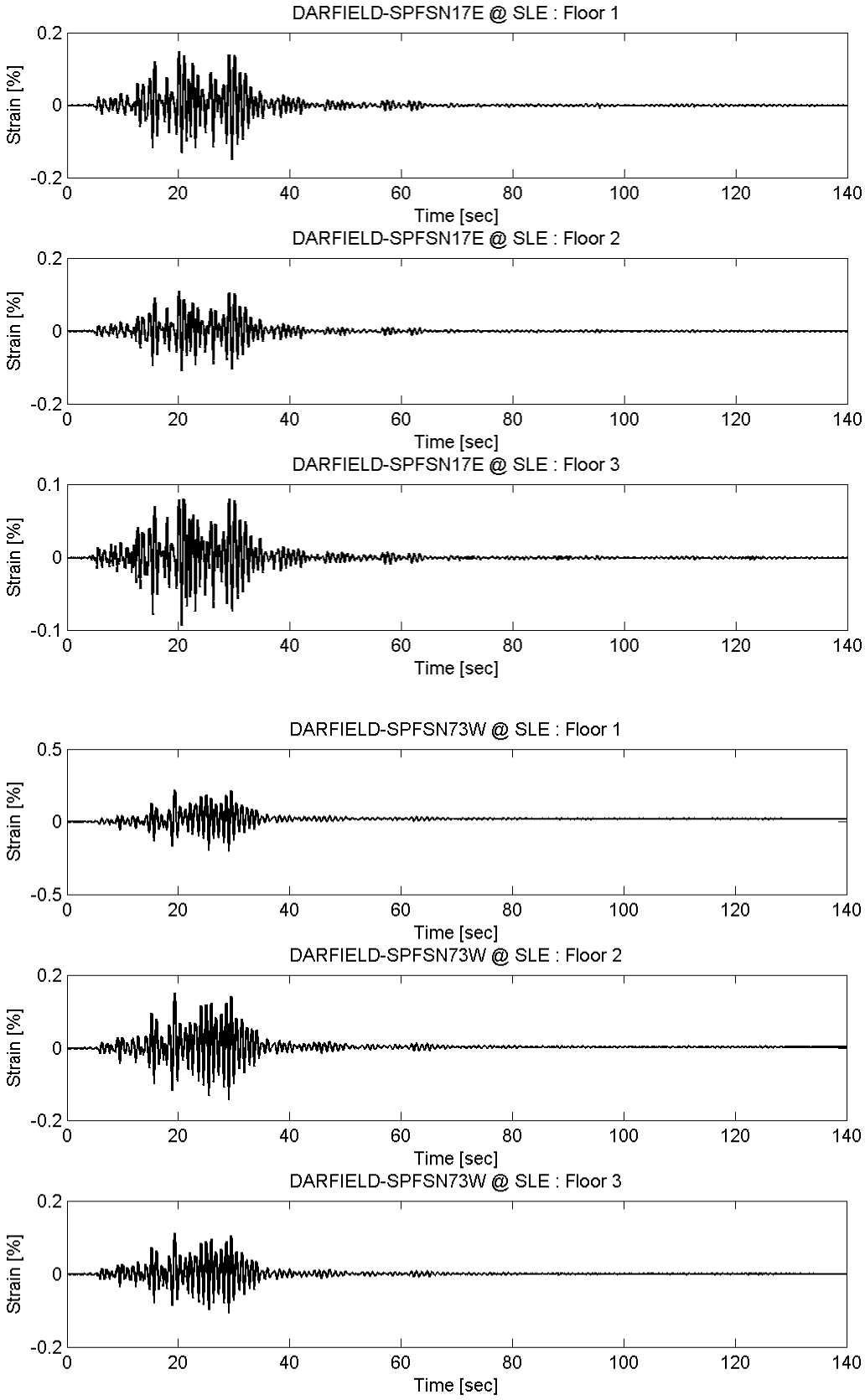
DARFIELD-SPFSN17E @ SLE : Floor 1
Strain [%]
Time [sec]
DARFIELD-SPFSN17E @ SLE : Floor 2
Strain [%]
Time [sec]
DARFIELD-SPFSN17E @ SLE : Floor 3
Strain [%]
Time [sec]
DARFIELD-SPFSN73W @ SLE : Floor 1
Strain [%]
Time [sec]
DARFIELD-SPFSN73W @ SLE : Floor 2
Strain [%]
Time [sec]
DARFIELD-SPFSN73W @ SLE : Floor 3
Strain [%]
Time [sec]

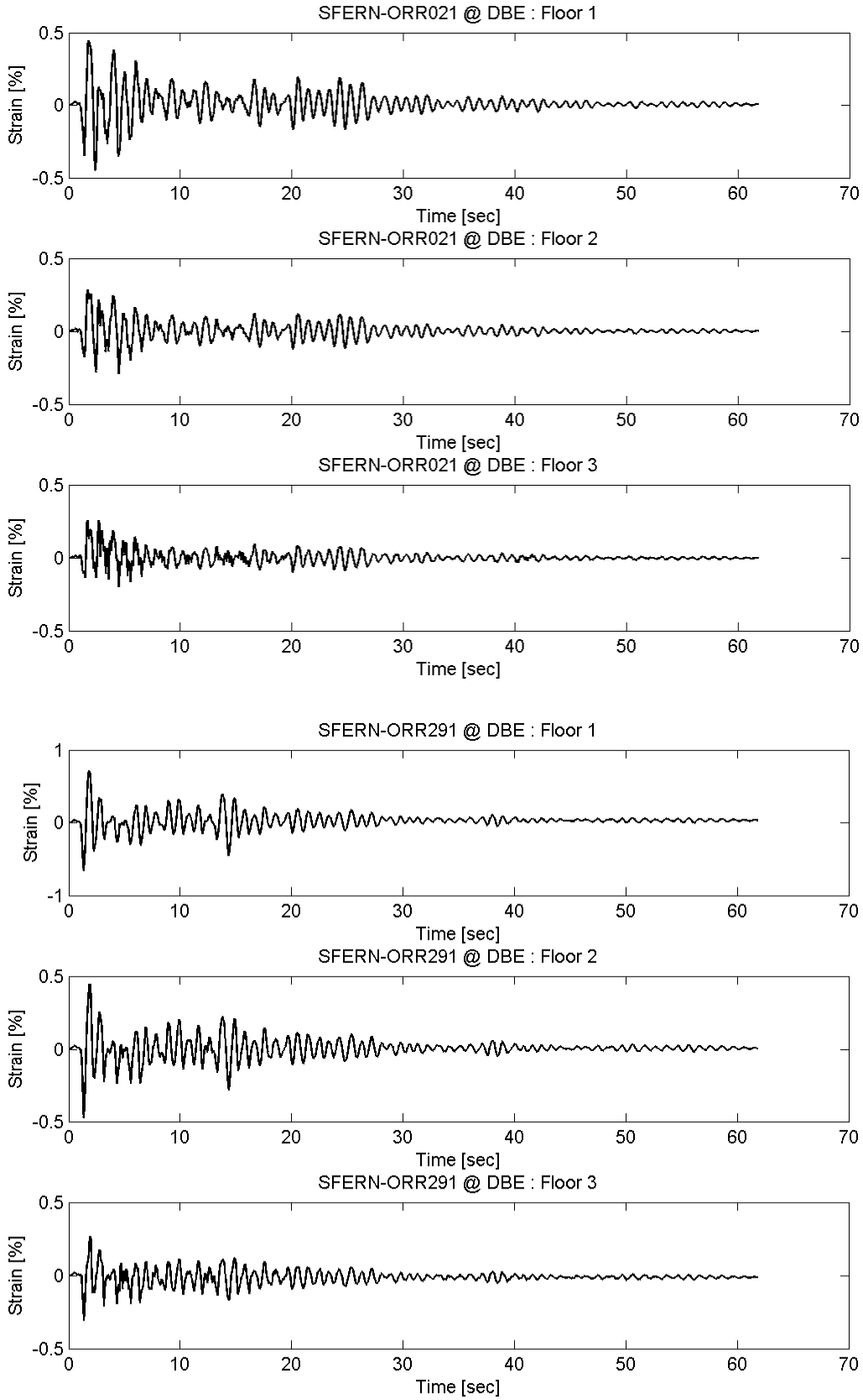
SFERN-ORR021 @ DBE : Floor 1
Strain [%]
Time [sec]
SFERN-ORR021 @ DBE : Floor 2
Strain [%]
Time [sec]
SFERN-ORR021 @ DBE : Floor 3
Strain [%]
Time [sec]
SFERN-ORR291 @ DBE : Floor 1
Strain [%]
Time [sec]
SFERN-ORR291 @ DBE : Floor 2
Strain [%]
Time [sec]
SFERN-ORR291 @ DBE : Floor 3
Strain [%]
Time [sec]

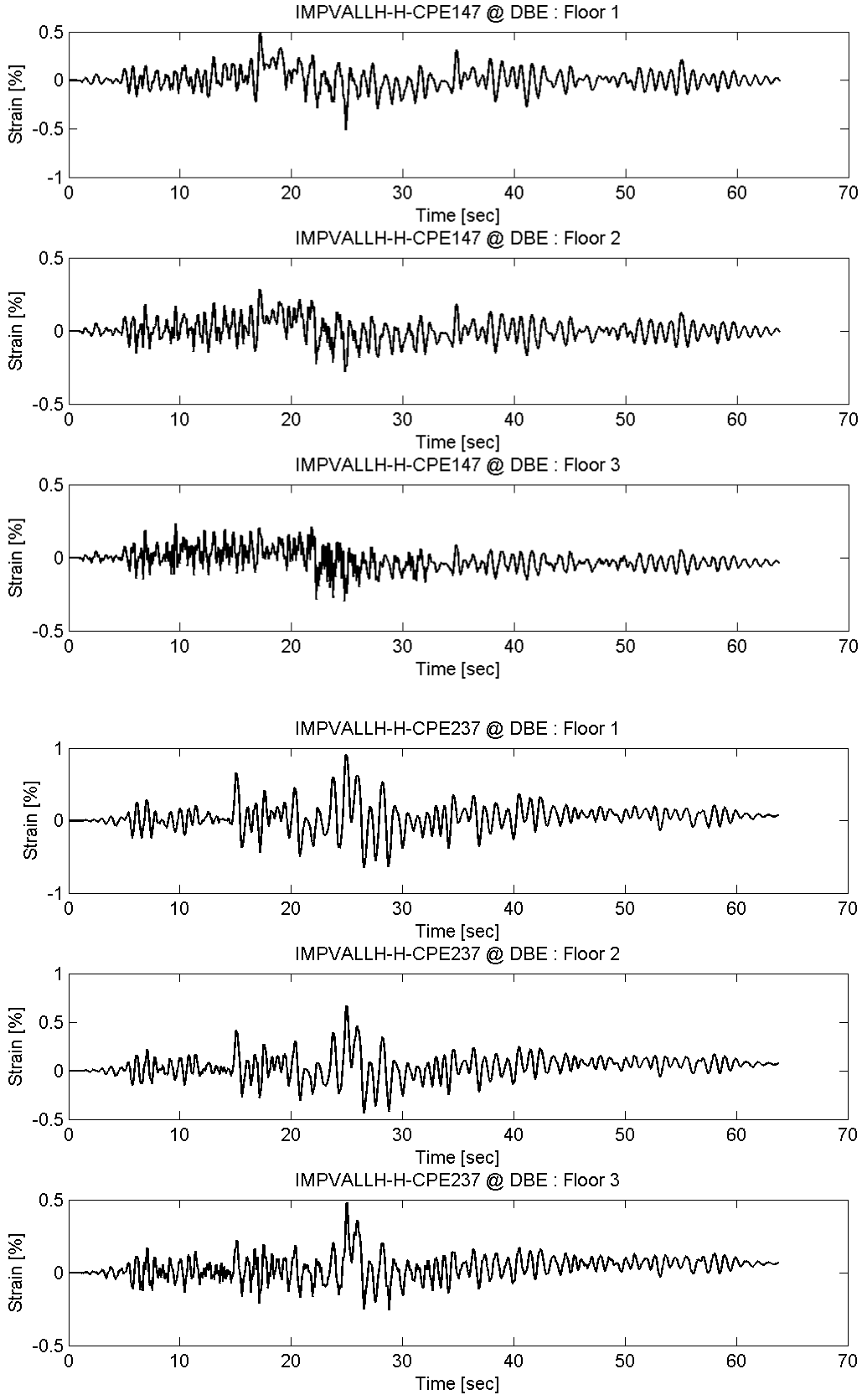
IMPVALLH-H-CPE147 @ DBE : Floor 1
Strain [%]
Time [sec]
IMPVALLH-H-CPE147 @ DBE : Floor 2
Strain [%]
Time [sec]
IMPVALLH-H-CPE147 @ DBE : Floor 3
Strain [%]
Time [sec]
IMPVALLH-H-CPE237 @ DBE : Floor 1
Strain [%]
Time [sec]
IMPVALLH-H-CPE237 @ DBE : Floor 2
Strain [%]
Time [sec]
IMPVALLH-H-CPE237 @ DBE : Floor 3
Strain [%]
Time [sec]

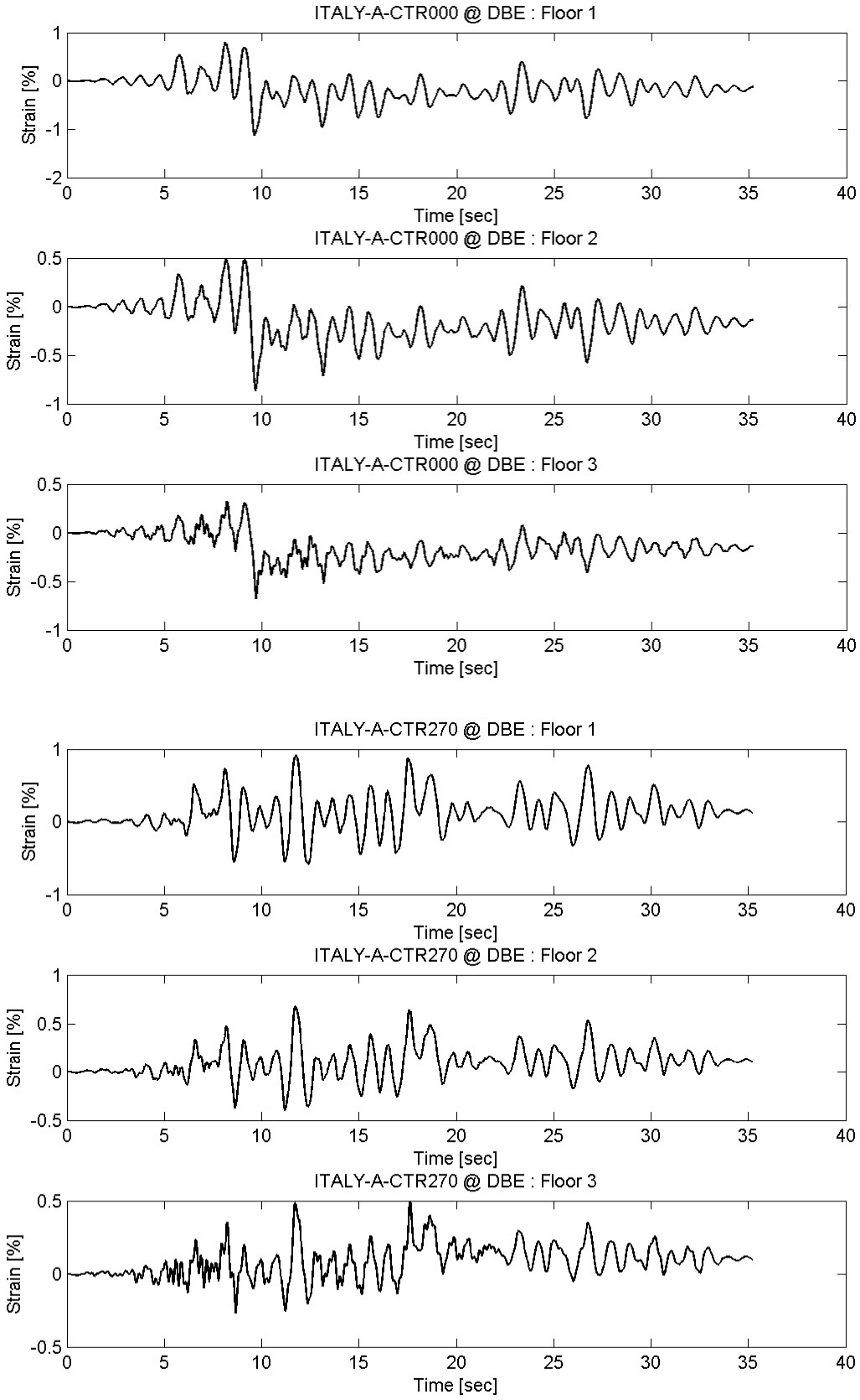
ITALY-A-CTR000 @ DBE : Floor 1
Strain [%]
Time [sec]
ITALY-A-CTR000 @ DBE : Floor 2
Strain [%]
Time [sec]
ITALY-A-CTR000 @ DBE : Floor 3
Strain [%]
Time [sec]
ITALY-A-CTR270 @ DBE : Floor 1
Strain [%]
Time [sec]
ITALY-A-CTR270 @ DBE : Floor 2
Strain [%]
Time [sec]
ITALY-A-CTR270 @ DBE : Floor 3
Strain [%]
Time [sec]

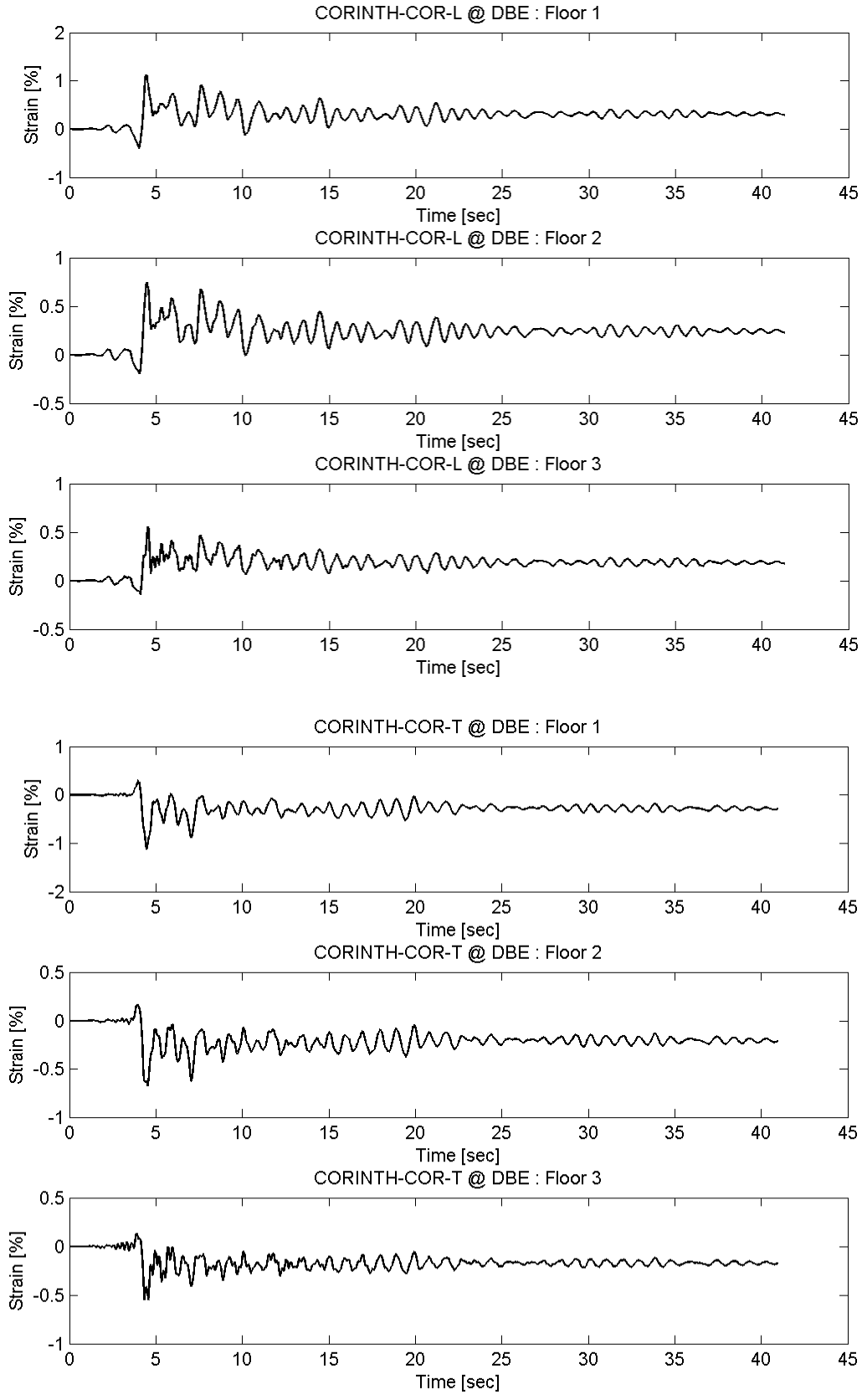
CORINTH-COR-L @ DBE : Floor 1
Strain [%]
Time [sec]
CORINTH-COR-L @ DBE : Floor 2
Strain [%]
Time [sec]
CORINTH-COR-L @ DBE : Floor 3
Strain [%]
Time [sec]
CORINTH-COR-T @ DBE : Floor 1
Strain [%]
Time [sec]
CORINTH-COR-T @ DBE : Floor 2
Strain [%]
Time [sec]
CORINTH-COR-T @ DBE : Floor 3
Strain [%]
Time [sec]

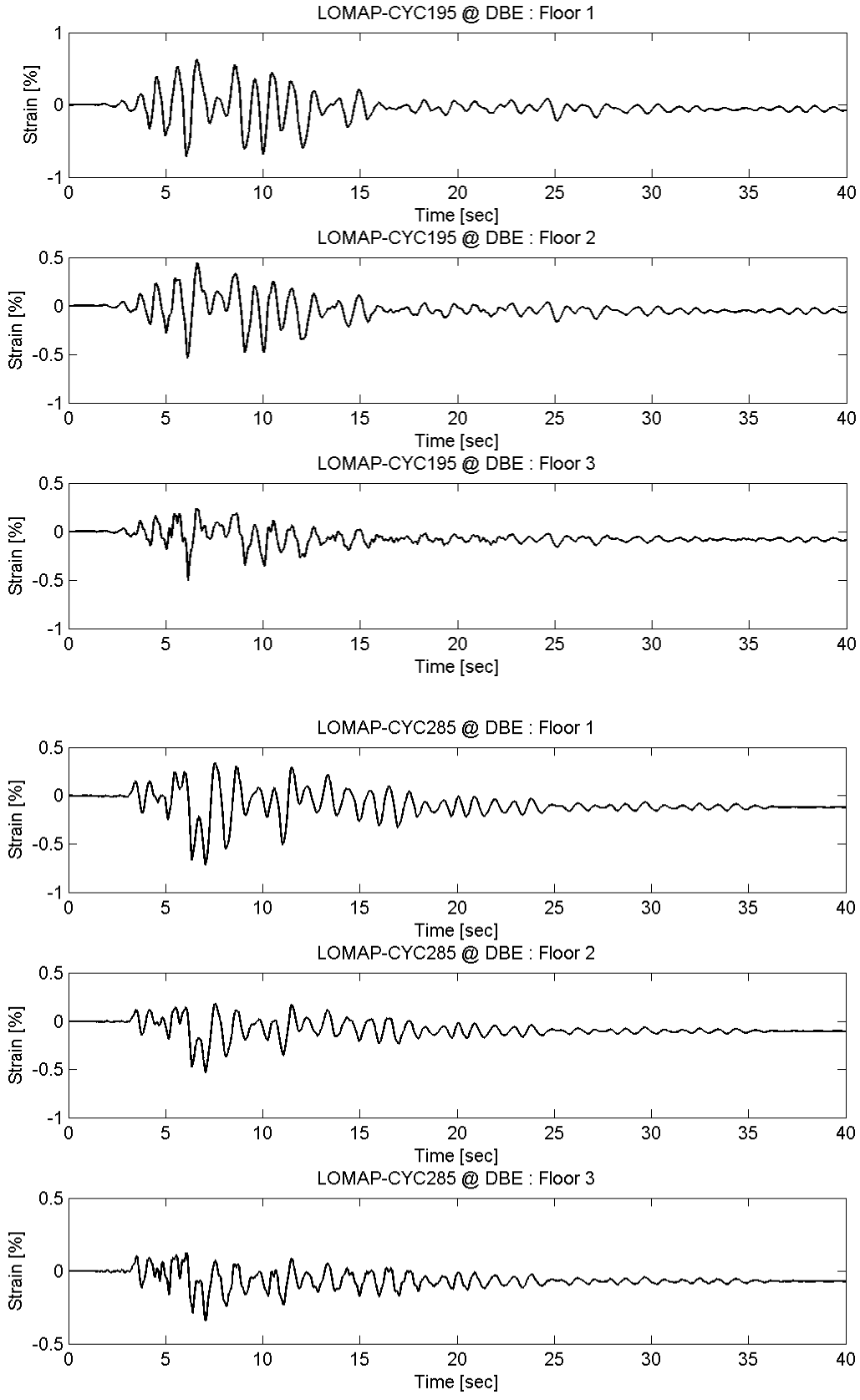
LOMAP-CYC195 @ DBE : Floor 1
Strain [%]
Time [sec]
LOMAP-CYC195 @ DBE : Floor 2
Strain [%]
Time [sec]
LOMAP-CYC195 @ DBE : Floor 3
Strain [%]
Time [sec]
LOMAP-CYC285 @ DBE : Floor 1
Strain [%]
Time [sec]
LOMAP-CYC285 @ DBE : Floor 2
Strain [%]
Time [sec]
LOMAP-CYC285 @ DBE : Floor 3
Strain [%]
Time [sec]

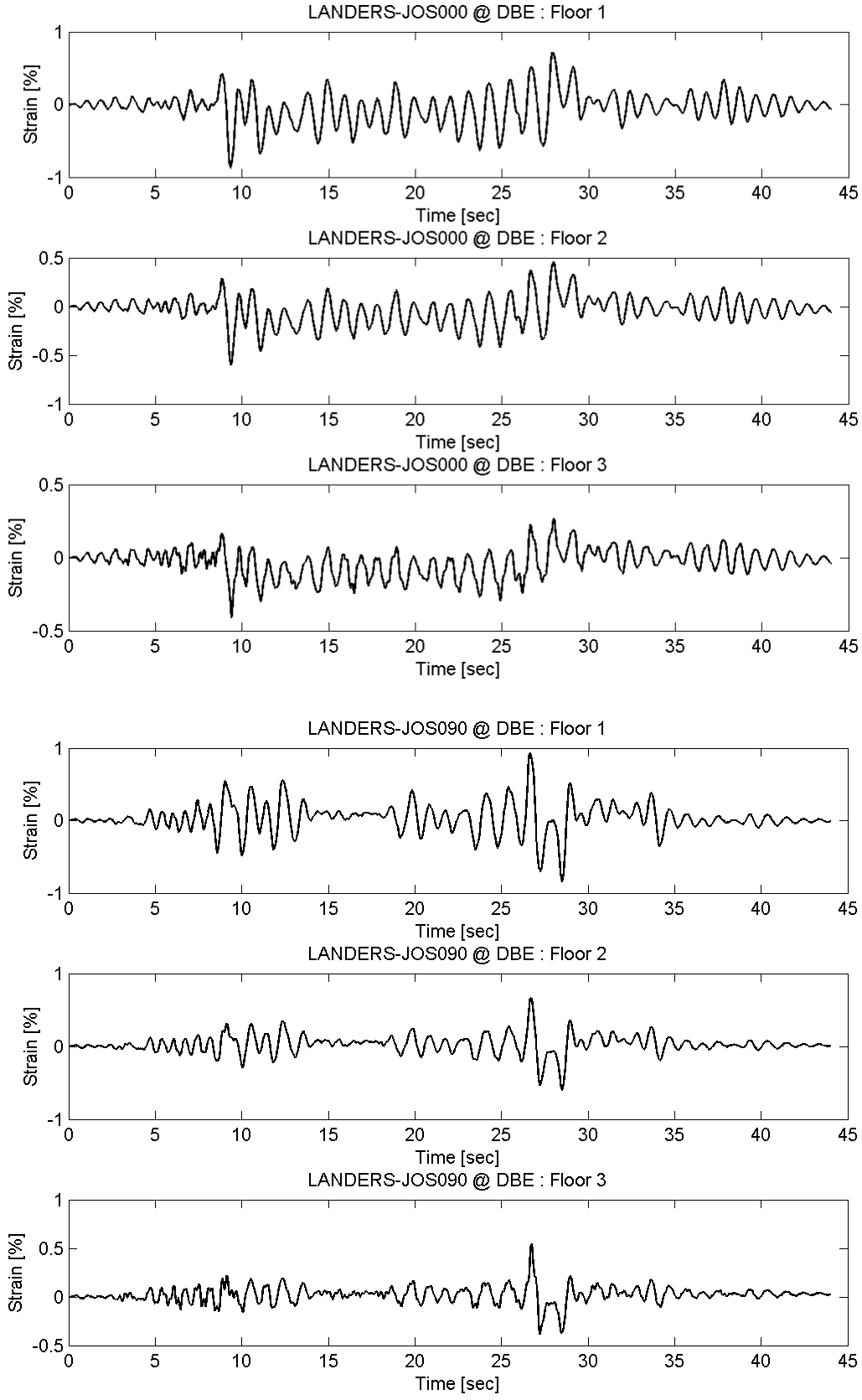
LANDERS-JOS000 @ DBE : Floor 1
Strain [%]
Time [sec]
LANDERS-JOS000 @ DBE : Floor 2
Strain [%]
Time [sec]
LANDERS-JOS000 @ DBE : Floor 3
Strain [%]
Time [sec]
LANDERS-JOS090 @ DBE : Floor 1
Strain [%]
Time [sec]
LANDERS-JOS090 @ DBE : Floor 2
Strain [%]
Time [sec]
LANDERS-JOS090 @ DBE : Floor 3
Strain [%]
Time [sec]

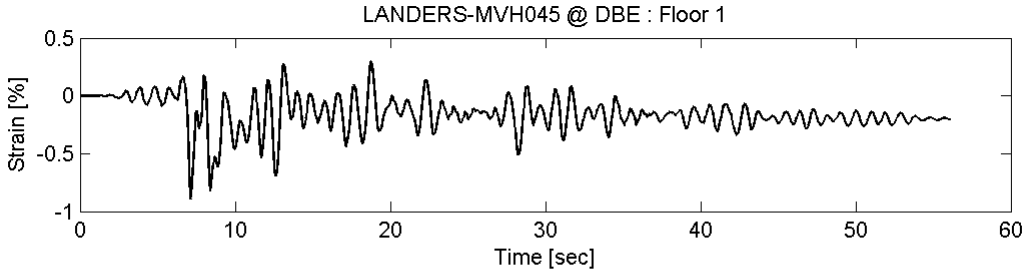
LANDERS-MVH045 @ DBE : Floor 1
Strain [%]
Time [sec]

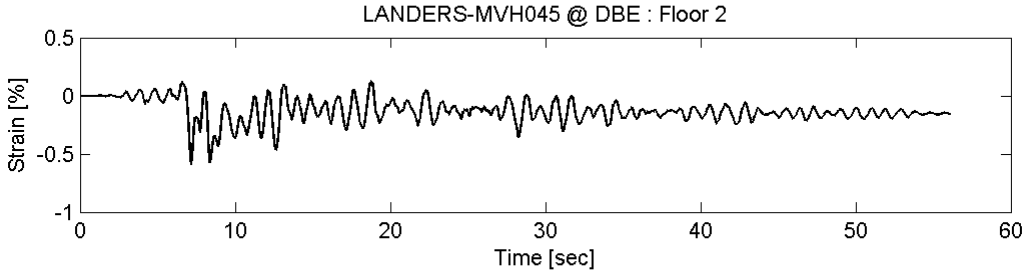
LANDERS-MVH045 @ DBE : Floor 2
Strain [%]
Time [sec]

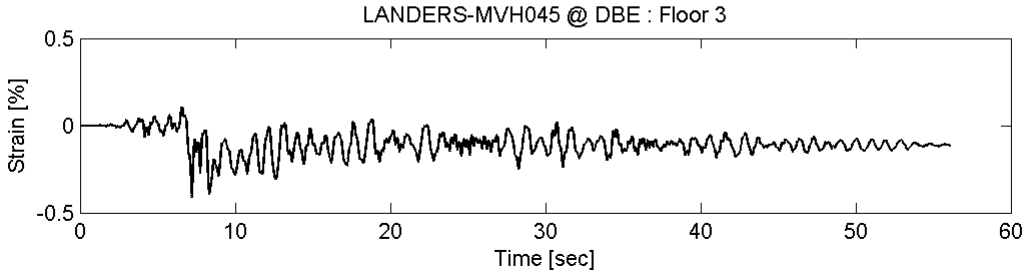
LANDERS-MVH045 @ DBE : Floor 3
Strain [%]
Time [sec]

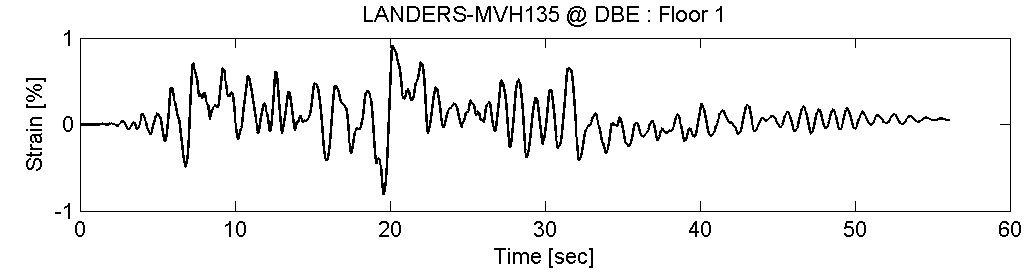
LANDERS-MVH135 @ DBE : Floor 1
Strain [%]
Time [sec]

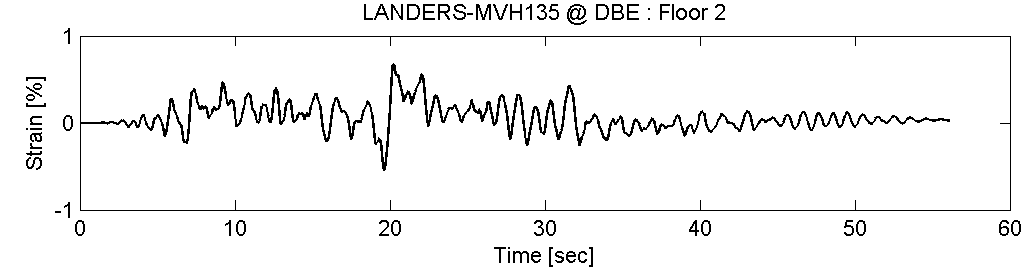
LANDERS-MVH135 @ DBE : Floor 2
Strain [%]
Time [sec]

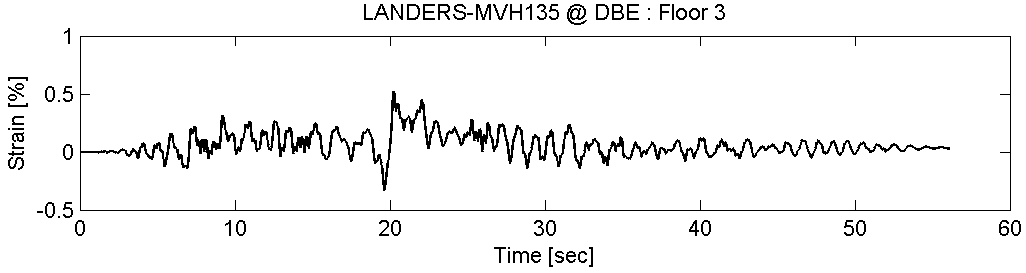
LANDERS-MVH135 @ DBE : Floor 3
Strain [%]
Time [sec]

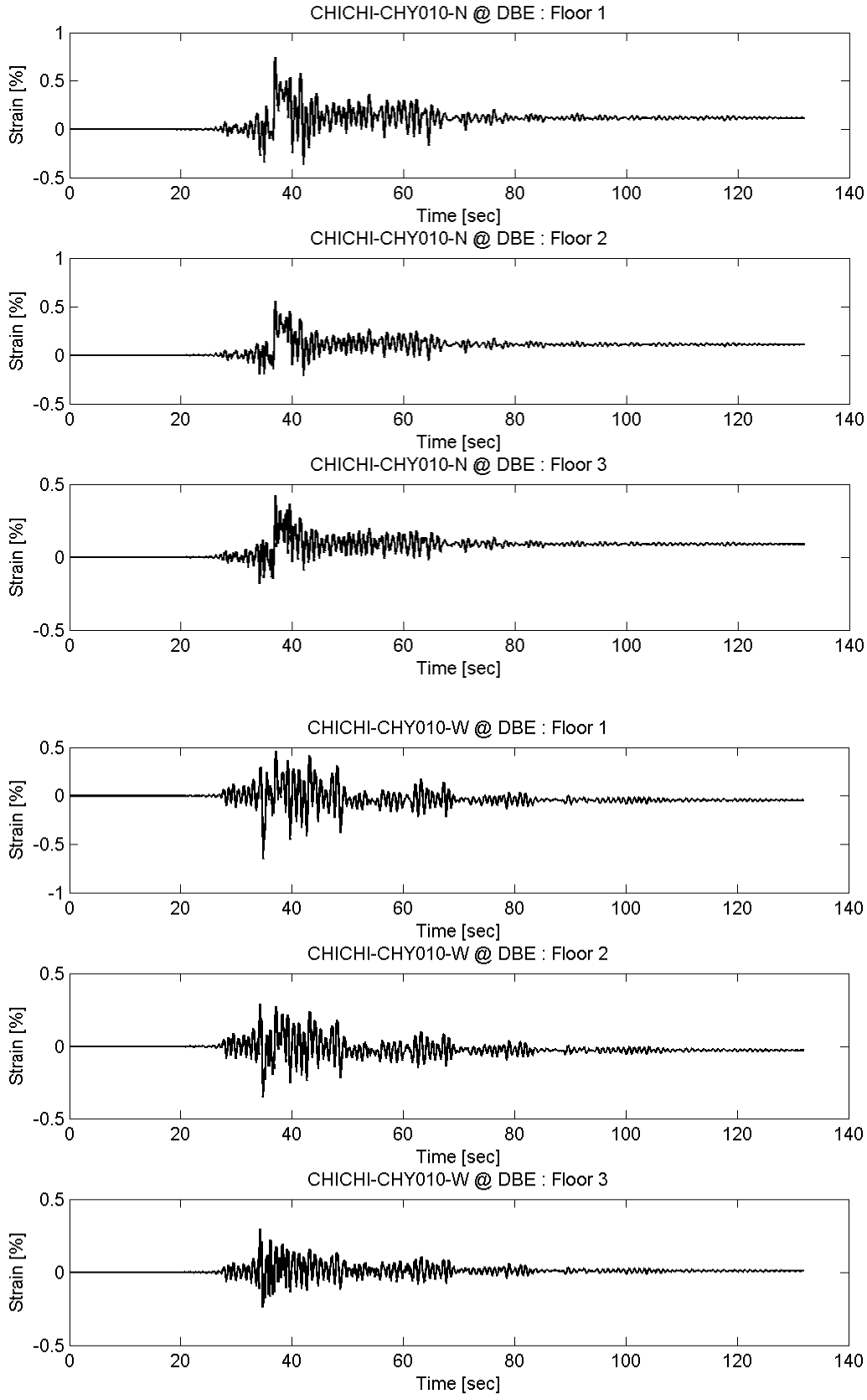
CHICHI-CHY010-N @ DBE : Floor 1
Strain [%]
Time [sec]
CHICHI-CHY010-N @ DBE : Floor 2
Strain [%]
Time [sec]
CHICHI-CHY010-N @ DBE : Floor 3
Strain [%]
Time [sec]
CHICHI-CHY010-W @ DBE : Floor 1
Strain [%]
Time [sec]
CHICHI-CHY010-W @ DBE : Floor 2
Strain [%]
Time [sec]
CHICHI-CHY010-W @ DBE : Floor 3
Strain [%]
Time [sec]

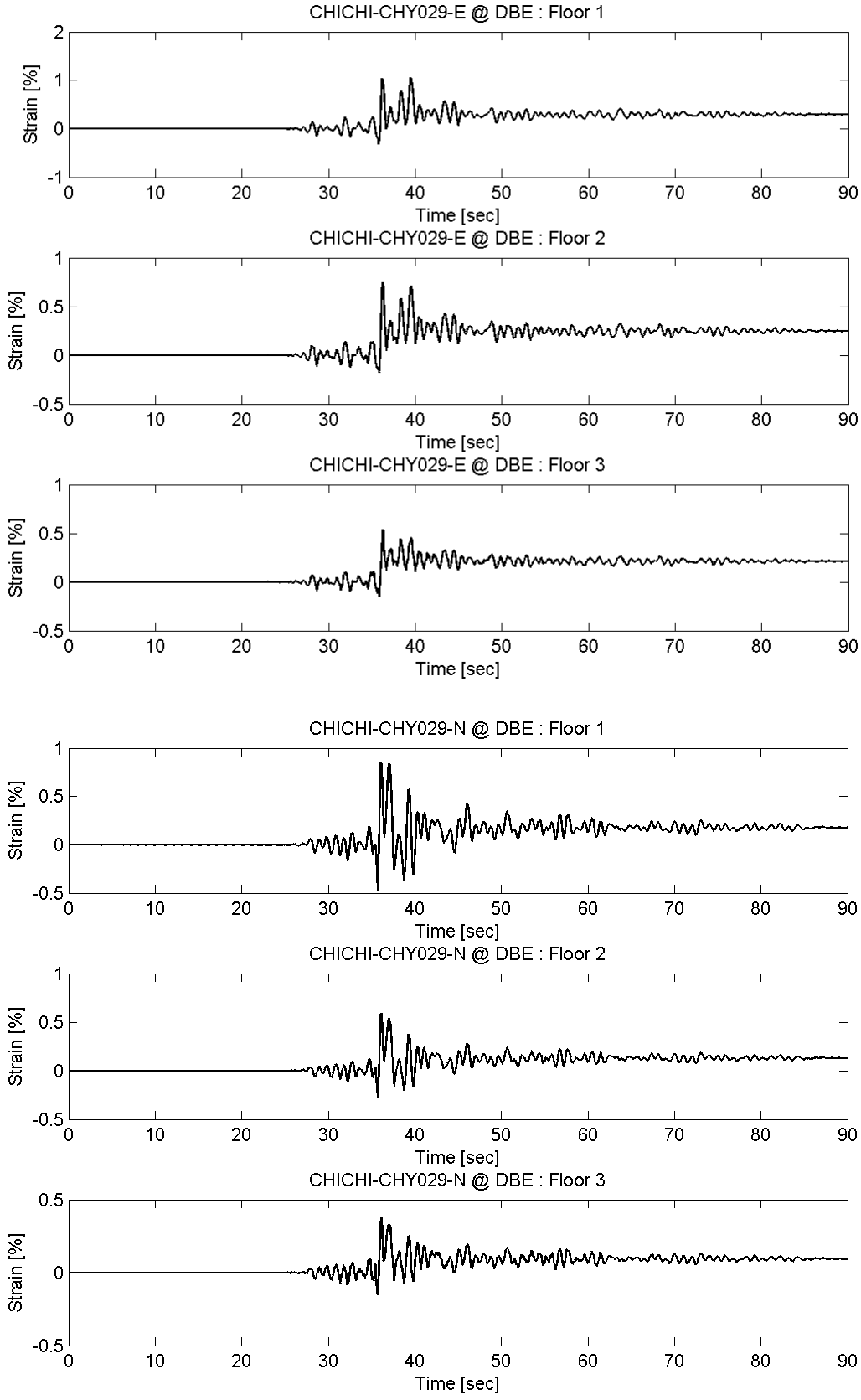
CHICHI-CHY029-E @ DBE : Floor 1
Strain [%]
Time [sec]
CHICHI-CHY029-E @ DBE : Floor 2
Strain [%]
Time [sec]
CHICHI-CHY029-E @ DBE : Floor 3
Strain [%]
Time [sec]
CHICHI-CHY029-N @ DBE : Floor 1
Strain [%]
Time [sec]
CHICHI-CHY029-N @ DBE : Floor 2
Strain [%]
Time [sec]
CHICHI-CHY029-N @ DBE : Floor 3
Strain [%]
Time [sec]

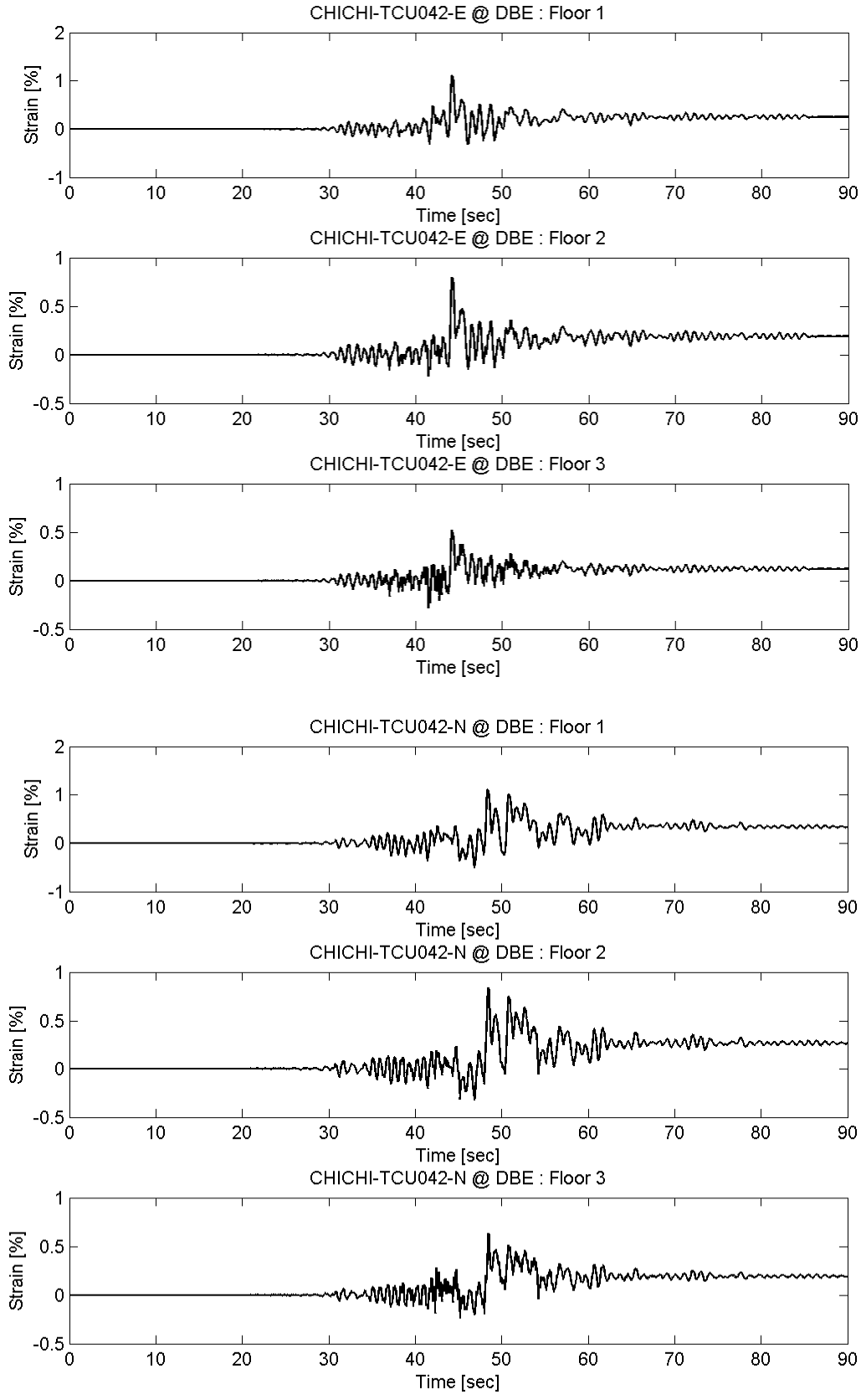
CHICHI-TCU042-E @ DBE : Floor 1
Strain [%]
Time [sec]
CHICHI-TCU042-E @ DBE : Floor 2
Strain [%]
Time [sec]
CHICHI-TCU042-E @ DBE : Floor 3
Strain [%]
Time [sec]
CHICHI-TCU042-N @ DBE : Floor 1
Strain [%]
Time [sec]
CHICHI-TCU042-N @ DBE : Floor 2
Strain [%]
Time [sec]
CHICHI-TCU042-N @ DBE : Floor 3
Strain [%]
Time [sec]

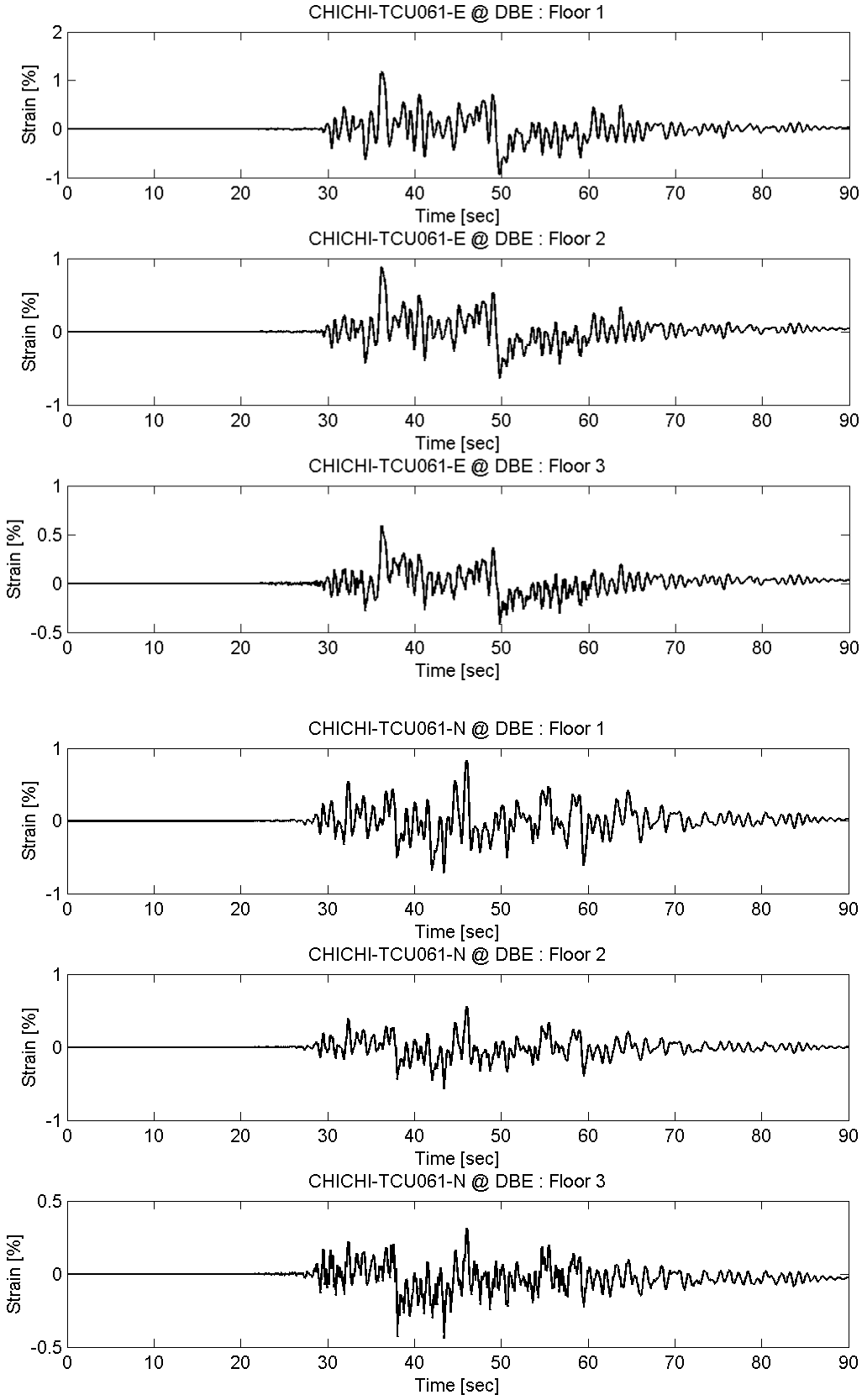
CHICHI-TCU061-E @ DBE : Floor 1
Strain [%]
Time [sec]
CHICHI-TCU061-E @ DBE : Floor 2
Strain [%]
Time [sec]
CHICHI-TCU061-E @ DBE : Floor 3
Strain [%]
Time [sec]
CHICHI-TCU061-N @ DBE : Floor 1
Strain [%]
Time [sec]
CHICHI-TCU061-N @ DBE : Floor 2
Strain [%]
Time [sec]
CHICHI-TCU061-N @ DBE : Floor 3
Strain [%]
Time [sec]

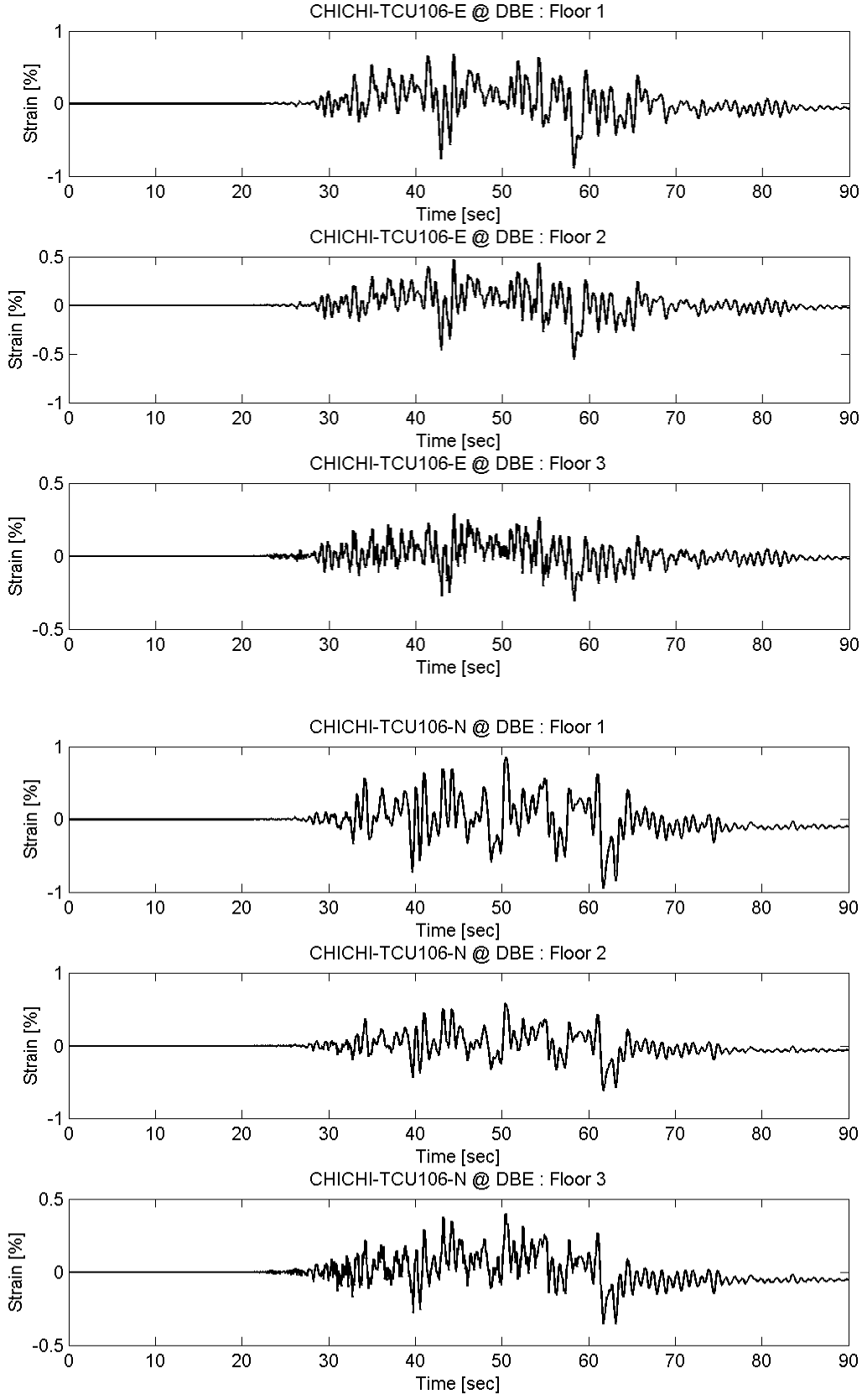
CHICHI-TCU106-E @ DBE : Floor 1
Strain [%]
Time [sec]
CHICHI-TCU106-E @ DBE : Floor 2
Strain [%]
Time [sec]
CHICHI-TCU106-E @ DBE : Floor 3
Strain [%]
Time [sec]
CHICHI-TCU106-N @ DBE : Floor 1
Strain [%]
Time [sec]
CHICHI-TCU106-N @ DBE : Floor 2
Strain [%]
Time [sec]
CHICHI-TCU106-N @ DBE : Floor 3
Strain [%]
Time [sec]

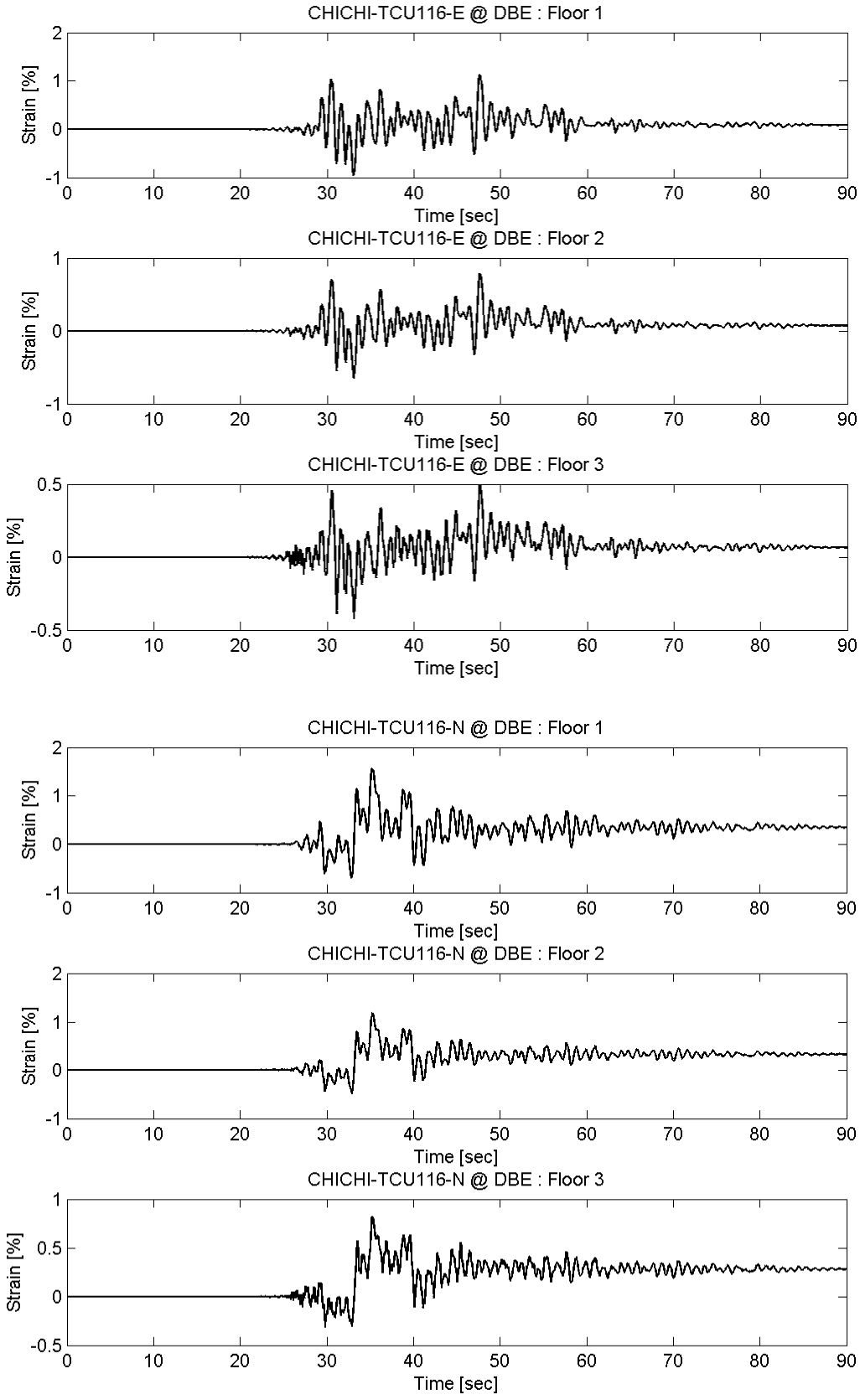
CHICHI-TCU116-E @ DBE : Floor 1
Strain [%]
Time [sec]
CHICHI-TCU116-E @ DBE : Floor 2
Strain [%]
Time [sec]
CHICHI-TCU116-E @ DBE : Floor 3
Strain [%]
Time [sec]
CHICHI-TCU116-N @ DBE : Floor 1
Strain [%]
Time [sec]
CHICHI-TCU116-N @ DBE : Floor 2
Strain [%]
Time [sec]
CHICHI-TCU116-N @ DBE : Floor 3
Strain [%]
Time [sec]

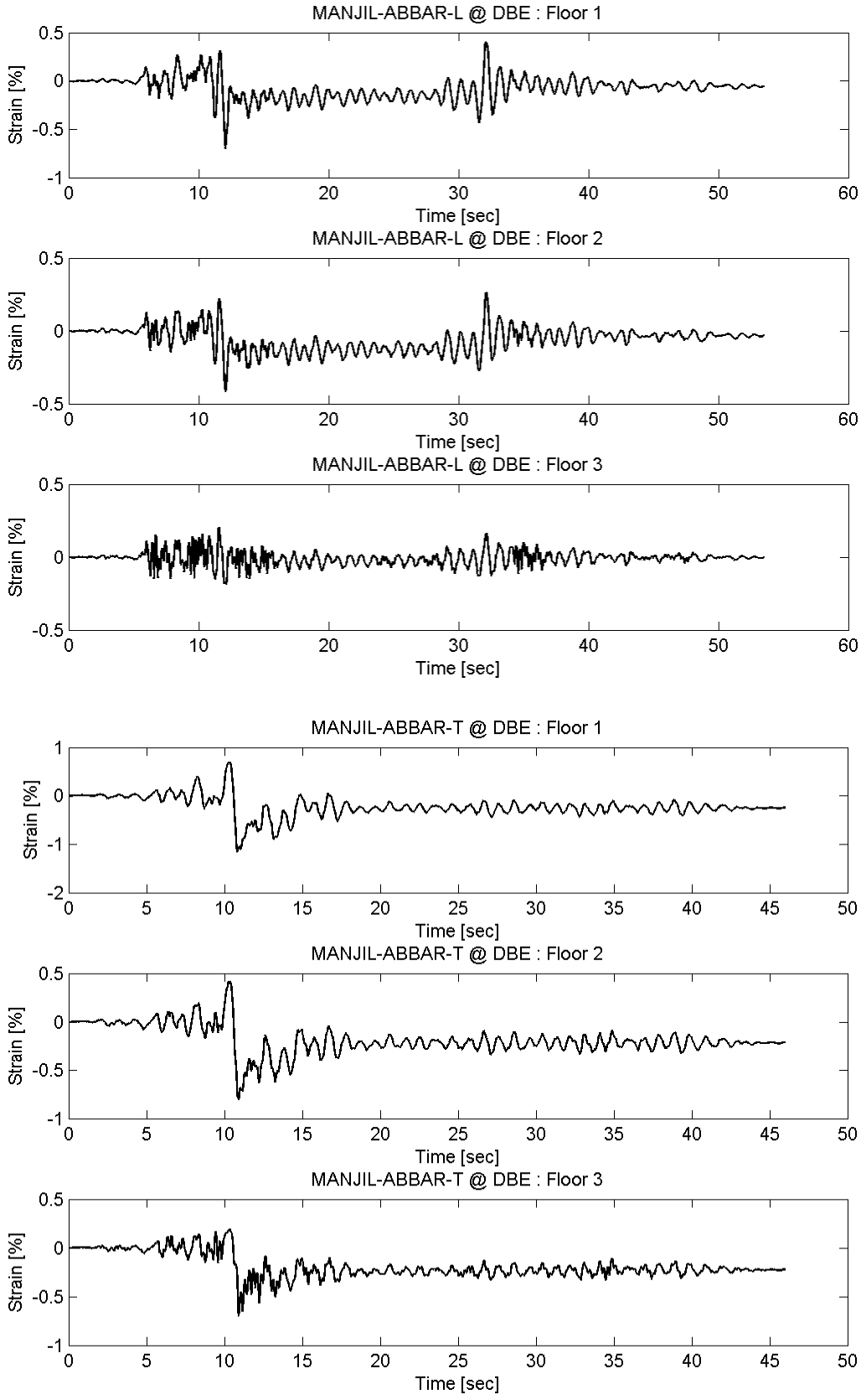
MANJIL-ABBAR-L @ DBE : Floor 1
Strain [%]
Time [sec]
MANJIL-ABBAR-L @ DBE : Floor 2
Strain [%]
Time [sec]
MANJIL-ABBAR-L @ DBE : Floor 3
Strain [%]
Time [sec]
MANJIL-ABBAR-T @ DBE : Floor 1
Strain [%]
Time [sec]
MANJIL-ABBAR-T @ DBE : Floor 2
Strain [%]
Time [sec]
MANJIL-ABBAR-T @ DBE : Floor 3
Strain [%]
Time [sec]

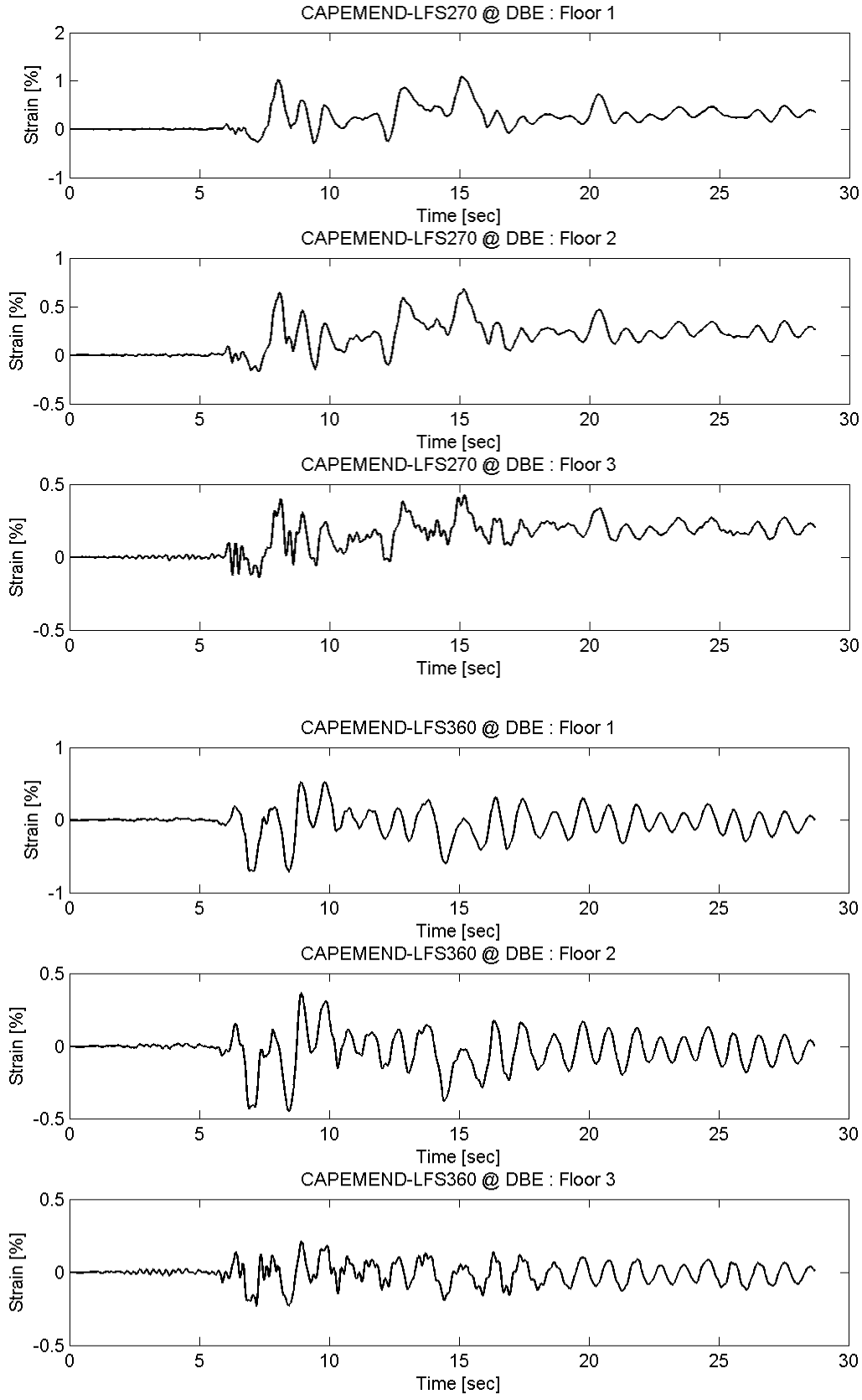
CAPEMEND-LFS270 @ DBE : Floor 1
Strain [%]
Time [sec]
CAPEMEND-LFS270 @ DBE : Floor 2
Strain [%]
Time [sec]
CAPEMEND-LFS270 @ DBE : Floor 3
Strain [%]
Time [sec]
CAPEMEND-LFS360 @ DBE : Floor 1
Strain [%]
Time [sec]
CAPEMEND-LFS360 @ DBE : Floor 2
Strain [%]
Time [sec]
CAPEMEND-LFS360 @ DBE : Floor 3
Strain [%]
Time [sec]

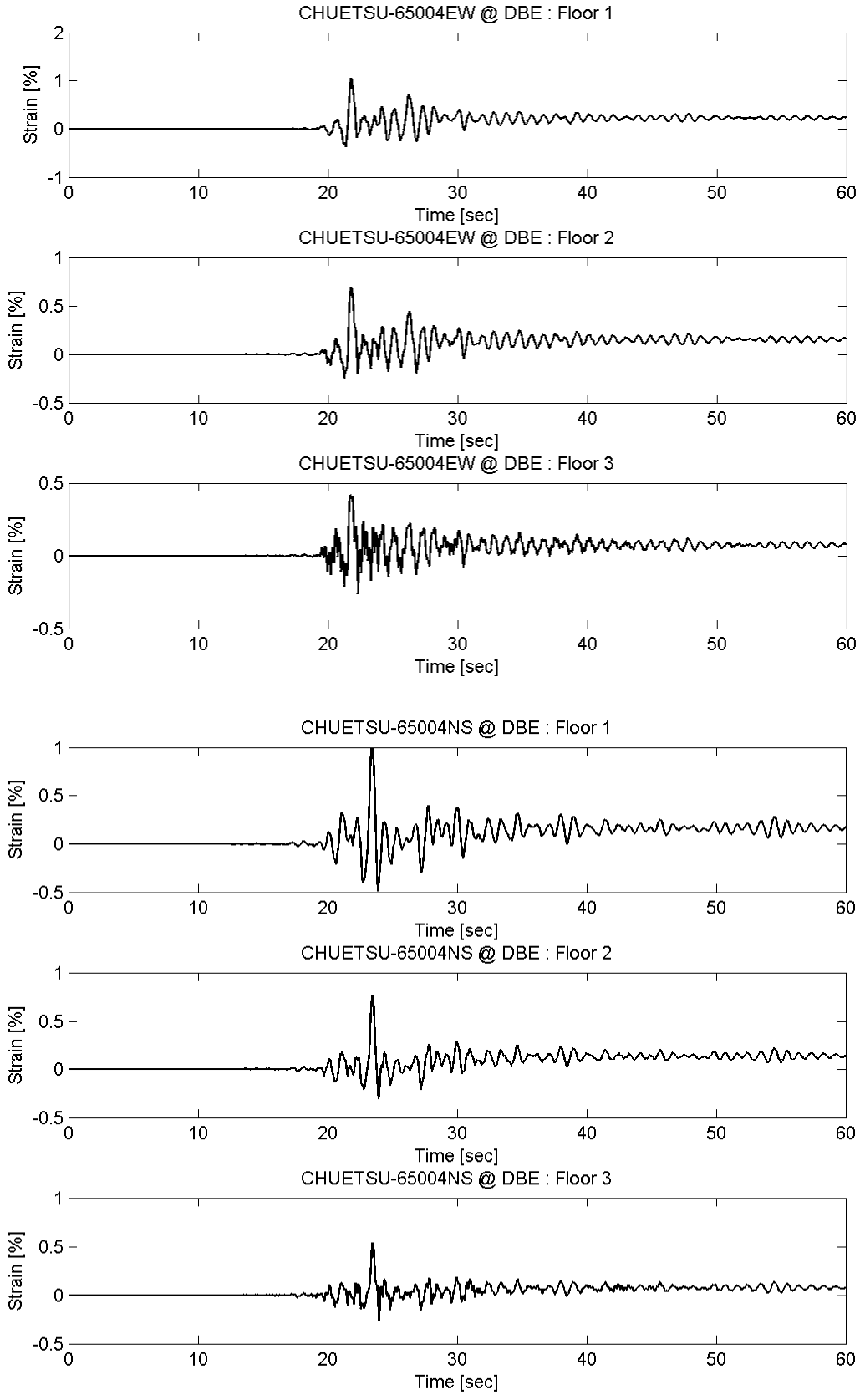
CHUETSU-65004EW @ DBE : Floor 1
Strain [%]
Time [sec]
CHUETSU-65004EW @ DBE : Floor 2
Strain [%]
Time [sec]
CHUETSU-65004EW @ DBE : Floor 3
Strain [%]
Time [sec]
CHUETSU-65004NS @ DBE : Floor 1
Strain [%]
Time [sec]
CHUETSU-65004NS @ DBE : Floor 2
Strain [%]
Time [sec]
CHUETSU-65004NS @ DBE : Floor 3
Strain [%]
Time [sec]

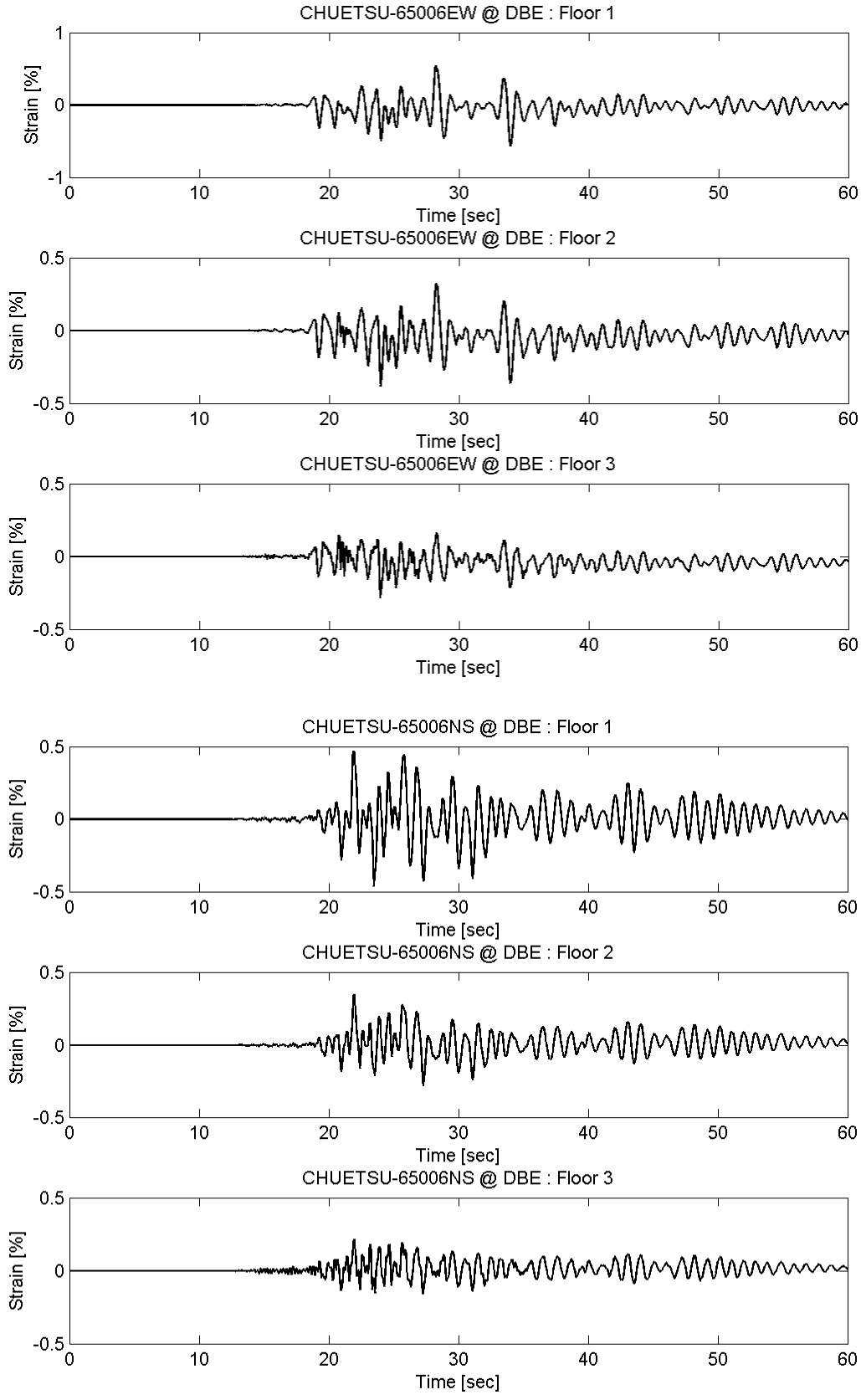
CHUETSU-65006EW @ DBE : Floor 1
Strain [%]
Time [sec]
CHUETSU-65006EW @ DBE : Floor 2
Strain [%]
Time [sec]
CHUETSU-65006EW @ DBE : Floor 3
Strain [%]
Time [sec]
CHUETSU-65006NS @ DBE : Floor 1
Strain [%]
Time [sec]
CHUETSU-65006NS @ DBE : Floor 2
Strain [%]
Time [sec]
CHUETSU-65006NS @ DBE : Floor 3
Strain [%]
Time [sec]

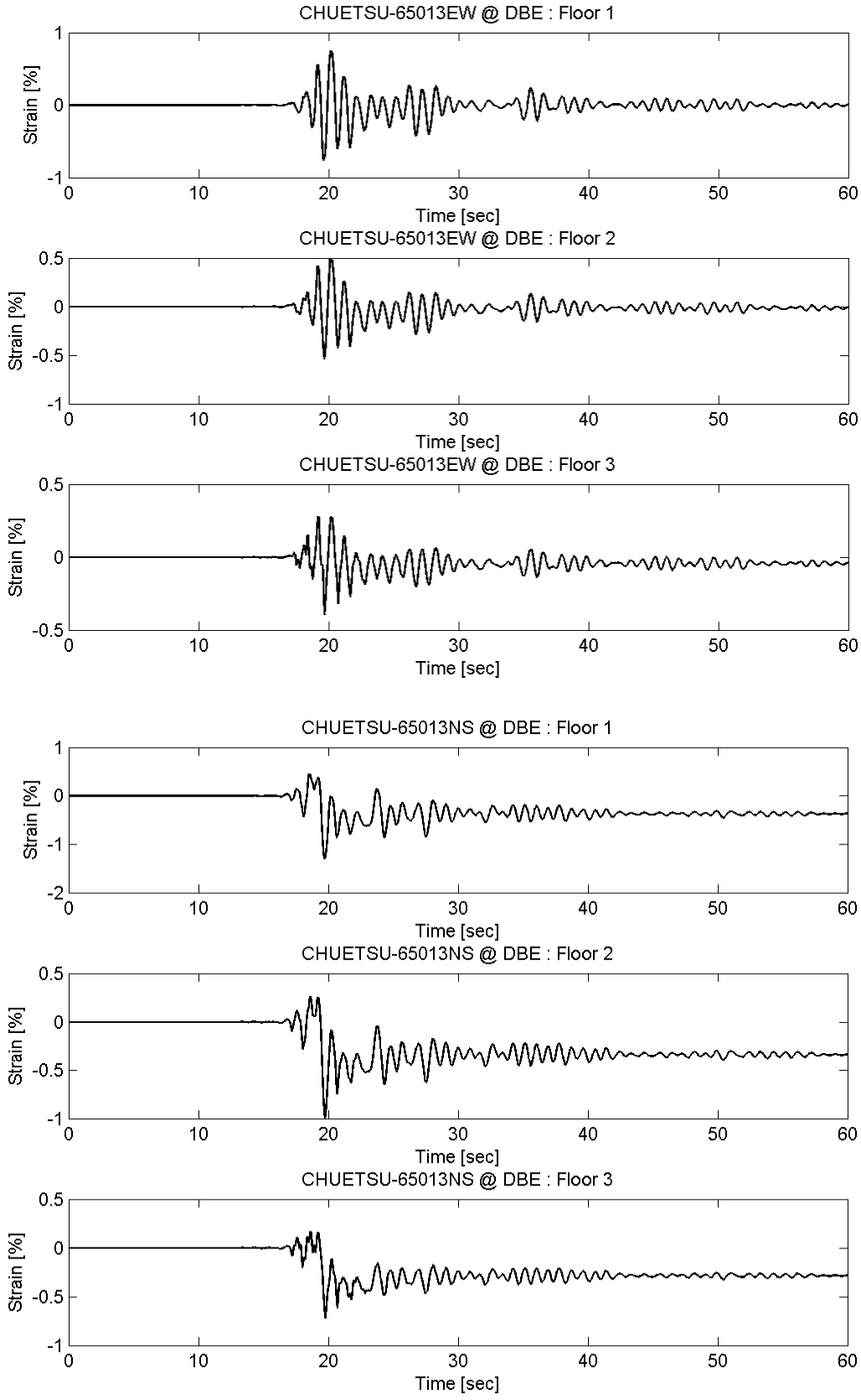
CHUETSU-65013EW @ DBE : Floor 1
Strain [%]
Time [sec]
CHUETSU-65013EW @ DBE : Floor 2
Strain [%]
Time [sec]
CHUETSU-65013EW @ DBE : Floor 3
Strain [%]
Time [sec]
CHUETSU-65013NS @ DBE : Floor 1
Strain [%]
Time [sec]
CHUETSU-65013NS @ DBE : Floor 2
Strain [%]
Time [sec]
CHUETSU-65013NS @ DBE : Floor 3
Strain [%]
Time [sec]

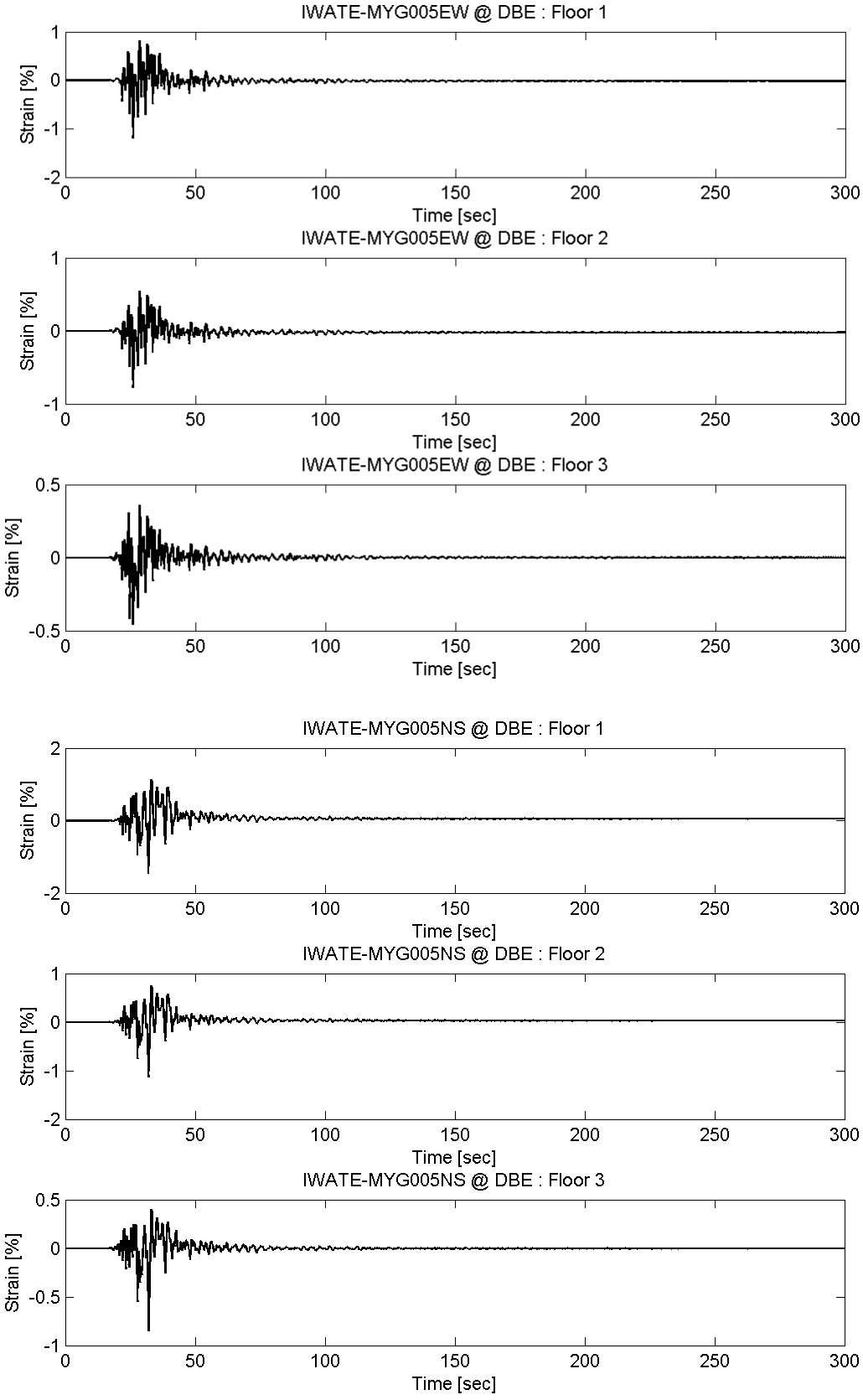
IWATE-MYG005EW @ DBE : Floor 1
Strain [%]
Time [sec]
IWATE-MYG005EW @ DBE : Floor 2
Strain [%]
Time [sec]
IWATE-MYG005EW @ DBE : Floor 3
Strain [%]
Time [sec]
IWATE-MYG005NS @ DBE : Floor 1
Strain [%]
Time [sec]
IWATE-MYG005NS @ DBE : Floor 2
Strain [%]
Time [sec]
IWATE-MYG005NS @ DBE : Floor 3
Strain [%]
Time [sec]

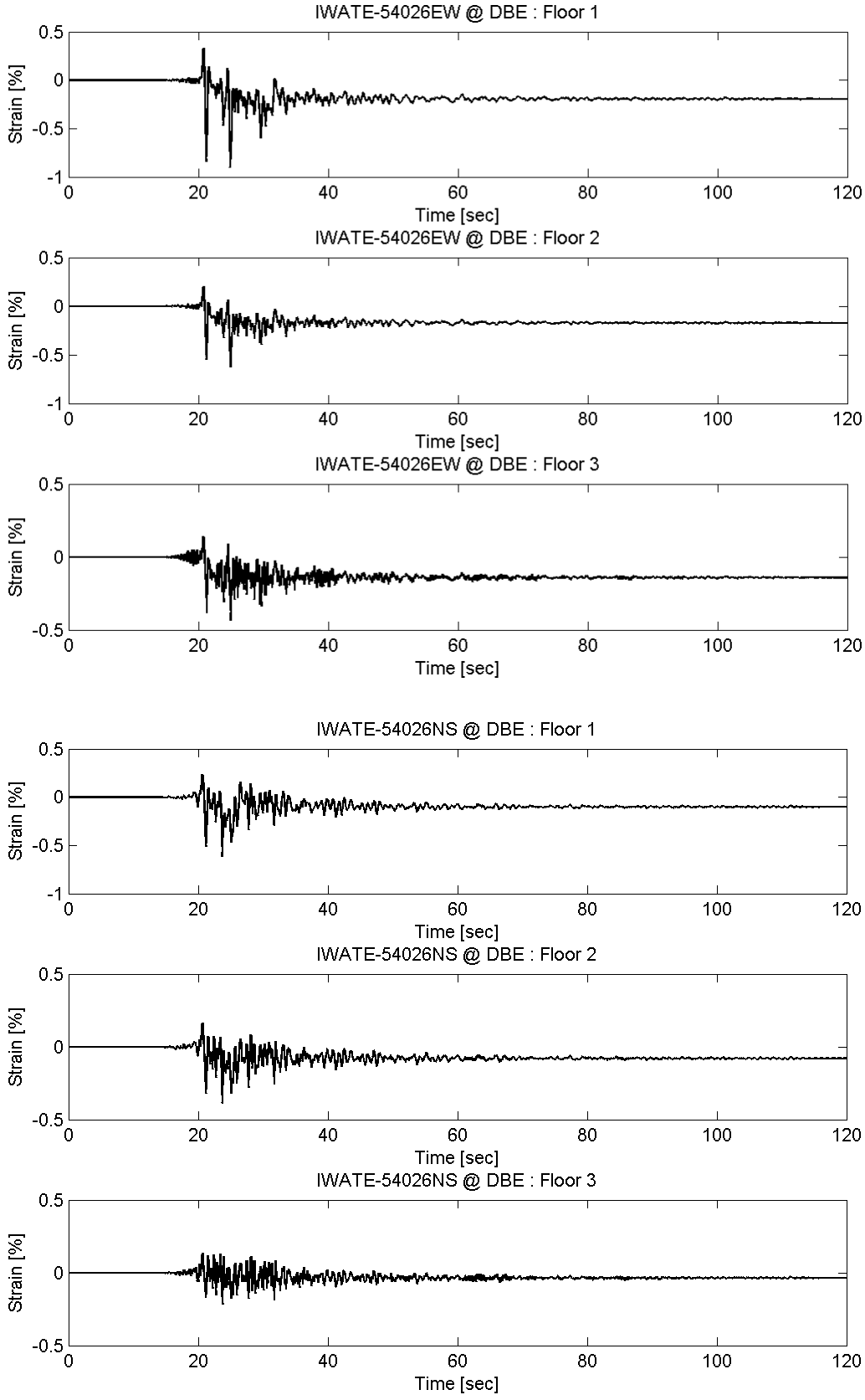
IWATE-54026EW @ DBE : Floor 1
Strain [%]
Time [sec]
IWATE-54026EW @ DBE : Floor 2
Strain [%]
Time [sec]
IWATE-54026EW @ DBE : Floor 3
Strain [%]
Time [sec]
IWATE-54026NS @ DBE : Floor 1
Strain [%]
Time [sec]
IWATE-54026NS @ DBE : Floor 2
Strain [%]
Time [sec]
IWATE-54026NS @ DBE : Floor 3
Strain [%]
Time [sec]

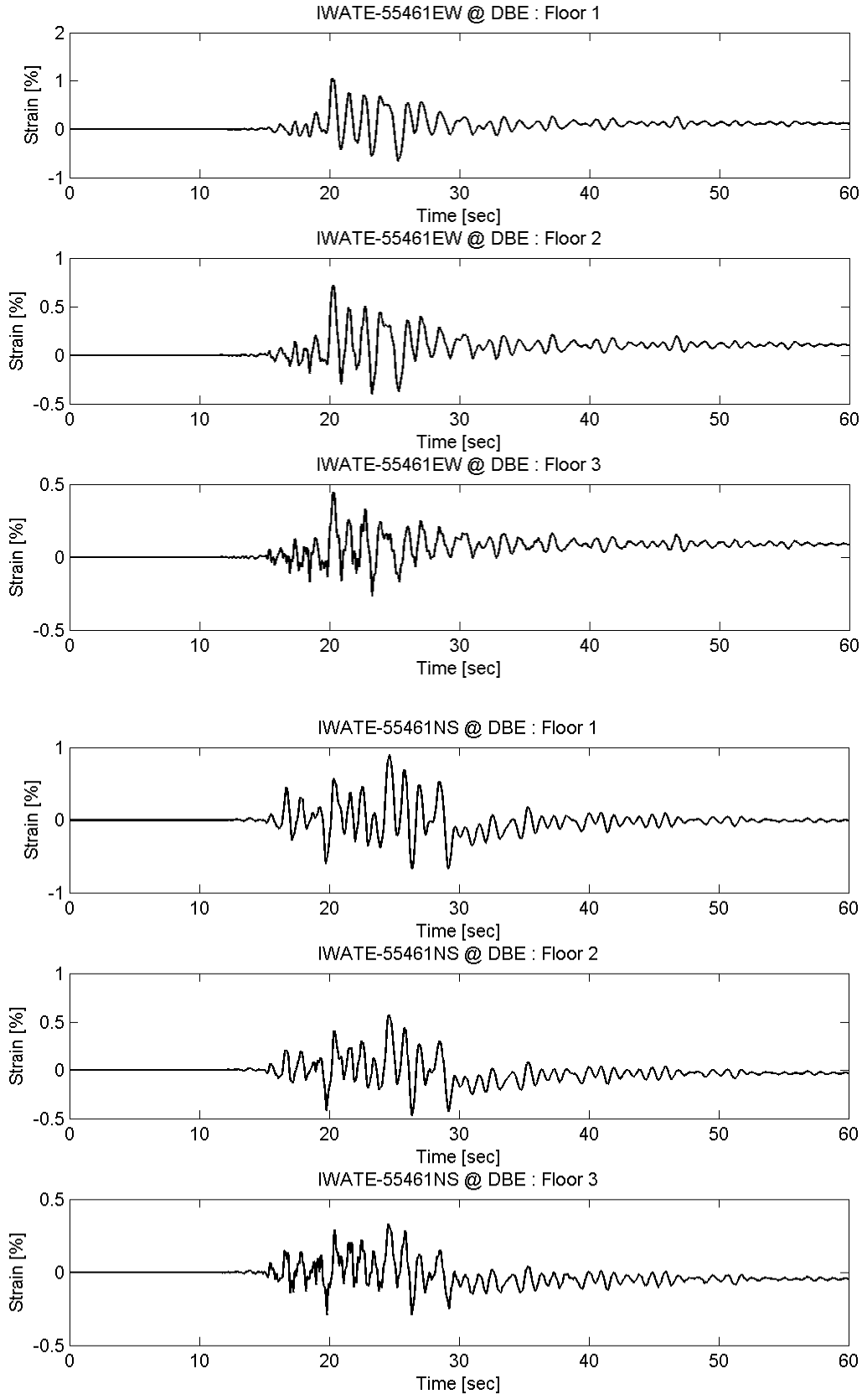
IWATE-55461EW @ DBE : Floor 1
Strain [%]
Time [sec]
IWATE-55461EW @ DBE : Floor 2
Strain [%]
Time [sec]
IWATE-55461EW @ DBE : Floor 3
Strain [%]
Time [sec]
IWATE-55461NS @ DBE : Floor 1
Strain [%]
Time [sec]
IWATE-55461NS @ DBE : Floor 2
Strain [%]
Time [sec]
IWATE-55461NS @ DBE : Floor 3
Strain [%]
Time [sec]

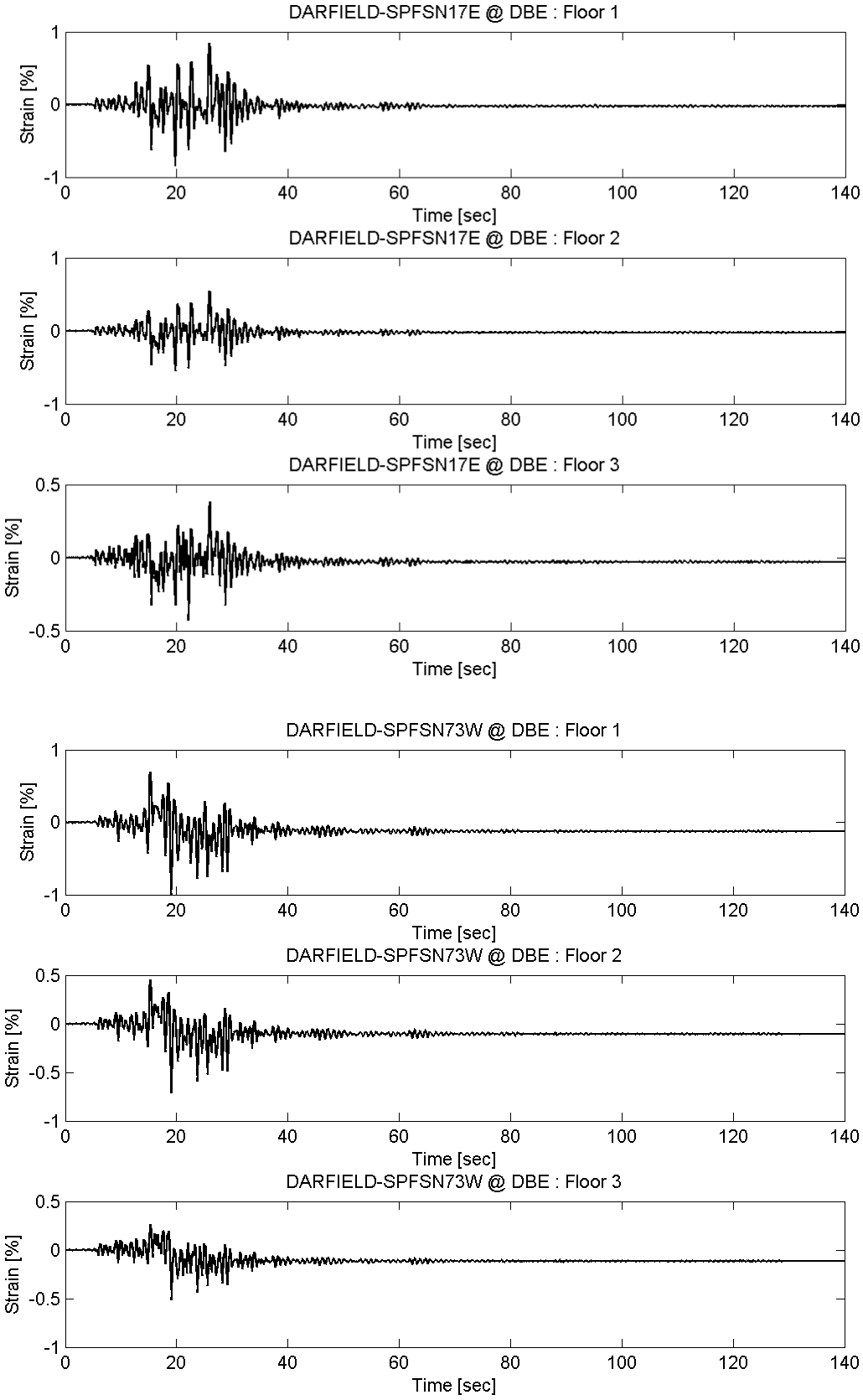
DARFIELD-SPFSN17E @ DBE : Floor 1
Strain [%]
Time [sec]
DARFIELD-SPFSN17E @ DBE : Floor 2
Strain [%]
Time [sec]
DARFIELD-SPFSN17E @ DBE : Floor 3
Strain [%]
Time [sec]
DARFIELD-SPFSN73W @ DBE : Floor 1
Strain [%]
Time [sec]
DARFIELD-SPFSN73W @ DBE : Floor 2
Strain [%]
Time [sec]
DARFIELD-SPFSN73W @ DBE : Floor 3
Strain [%]
Time [sec]

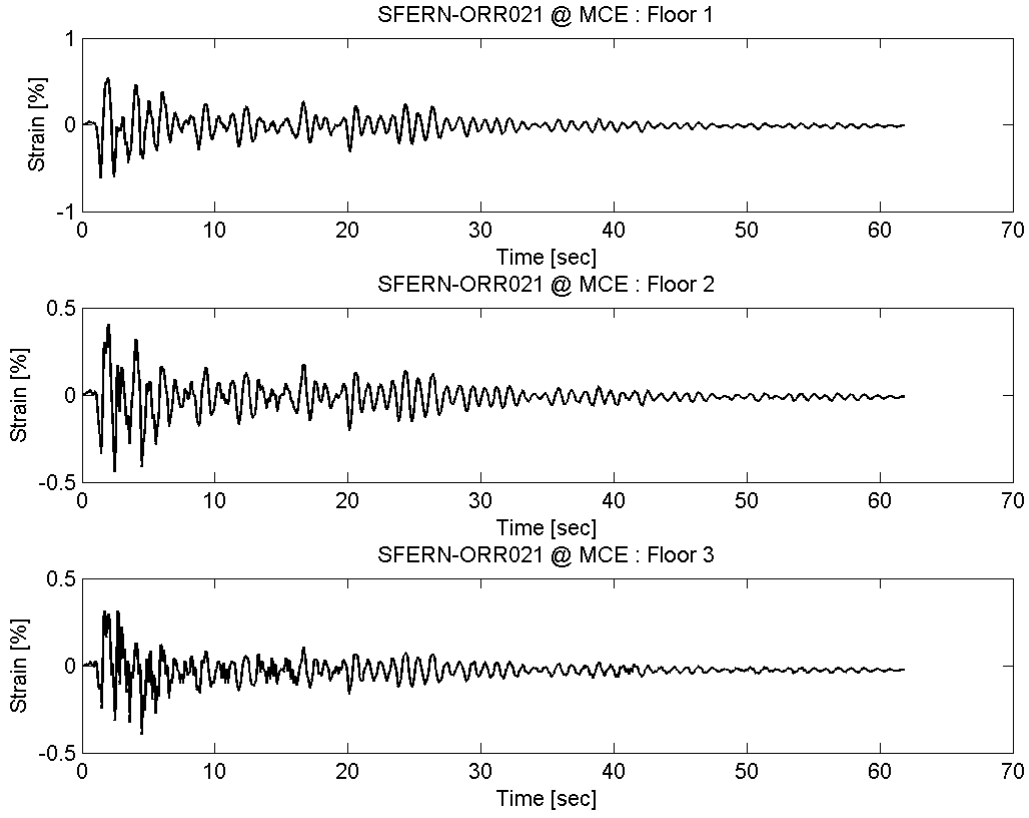
SFERN-ORR021 @ MCE : Floor 1
Strain [%]
Time [sec]
SFERN-ORR021 @ MCE : Floor 2
Strain [%]
Time [sec]
SFERN-ORR021 @ MCE : Floor 3
Strain [%]
Time [sec]

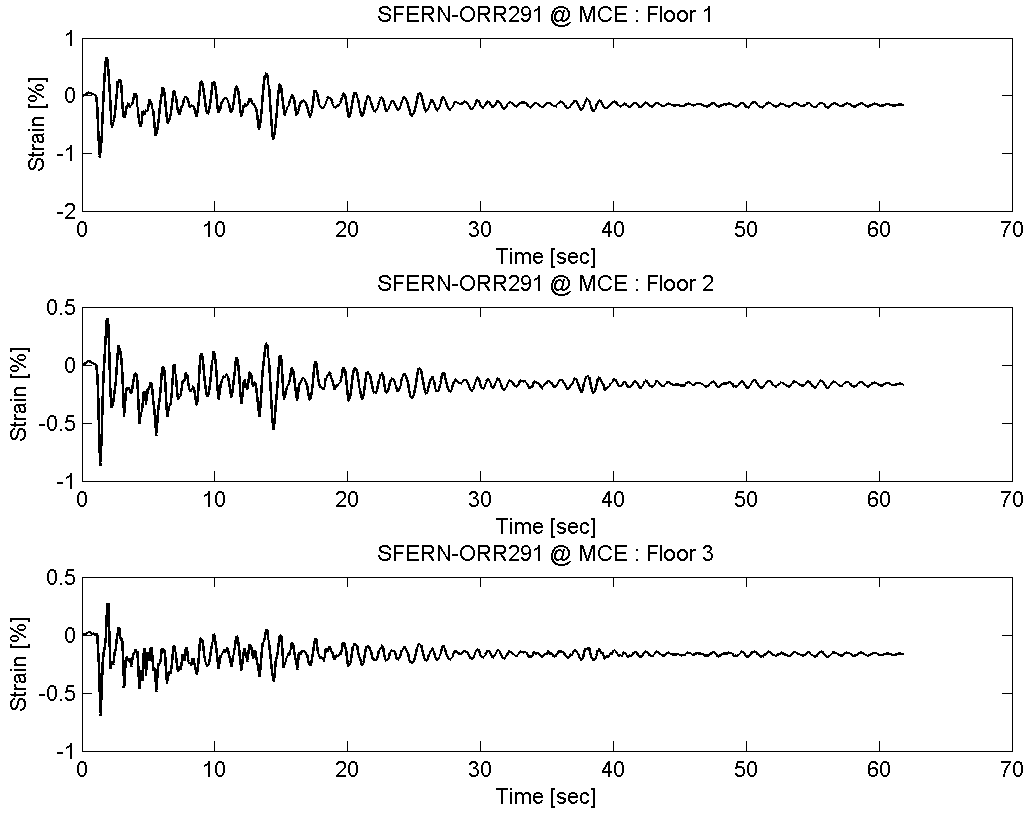
SFERN-ORR291 @ MCE : Floor 1
Strain [%]
Time [sec]
SFERN-ORR291 @ MCE : Floor 2
Strain [%]
Time [sec]
SFERN-ORR291 @ MCE : Floor 3
Strain [%]
Time [sec]

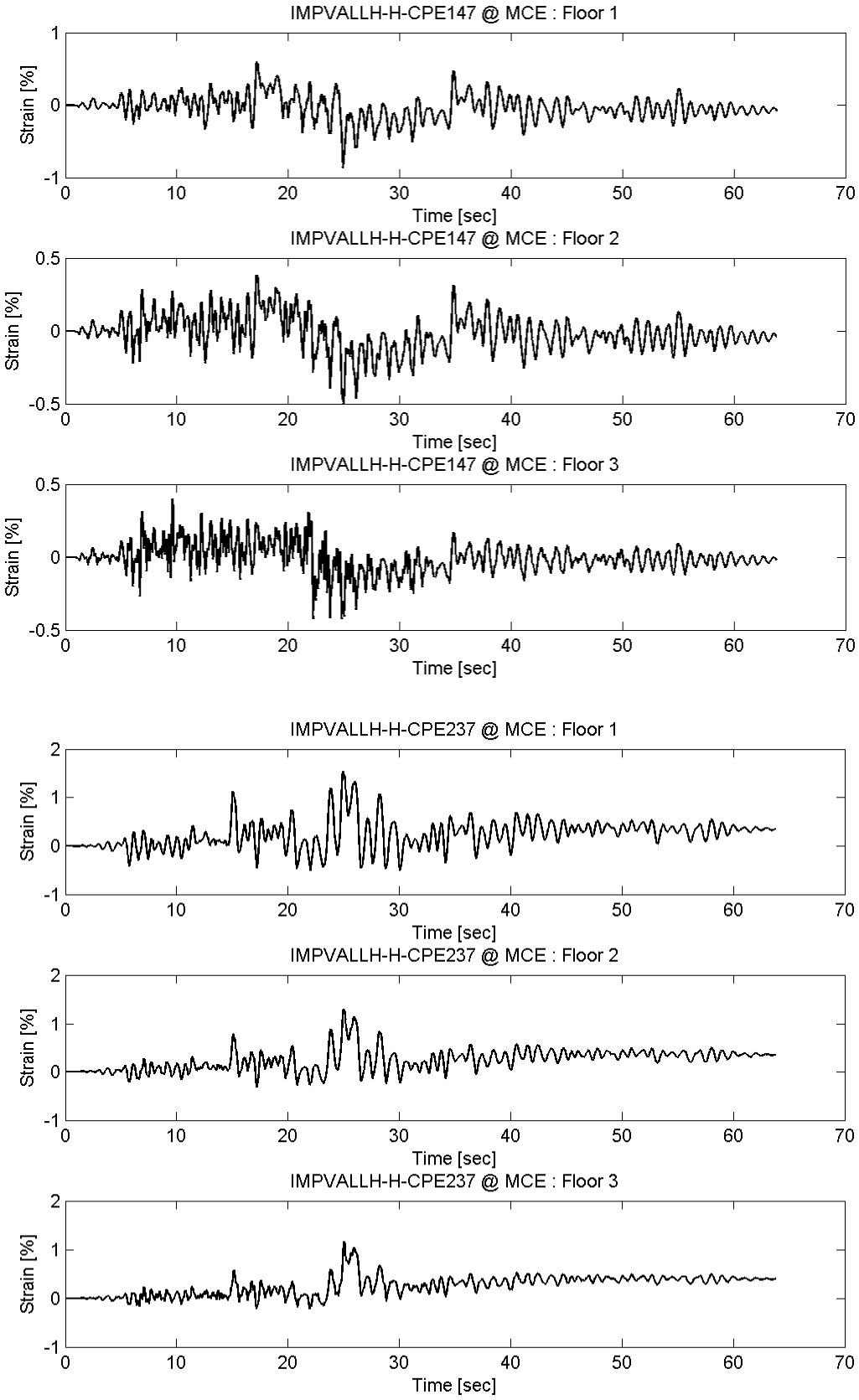
IMPVALLH-H-CPE147 @ MCE : Floor 1
Strain [%]
Time [sec]
IMPVALLH-H-CPE147 @ MCE : Floor 2
Strain [%]
Time [sec]
IMPVALLH-H-CPE147 @ MCE : Floor 3
Strain [%]
Time [sec]
IMPVALLH-H-CPE237 @ MCE : Floor 1
Strain [%]
Time [sec]
IMPVALLH-H-CPE237 @ MCE : Floor 2
Strain [%]
Time [sec]
IMPVALLH-H-CPE237 @ MCE : Floor 3
Strain [%]
Time [sec]

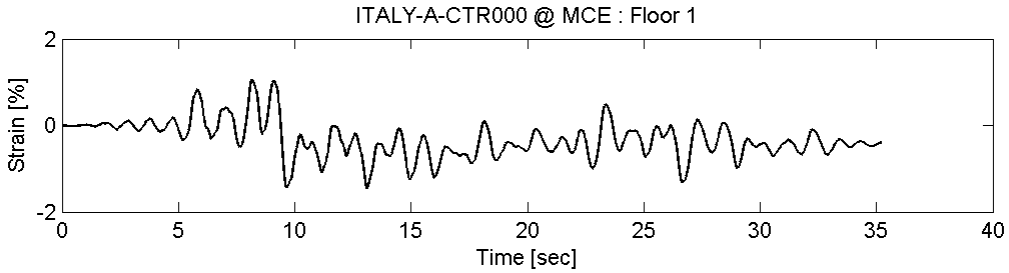
ITALY-A-CTR000 @ MCE : Floor 1
Strain [%]
Time [sec]

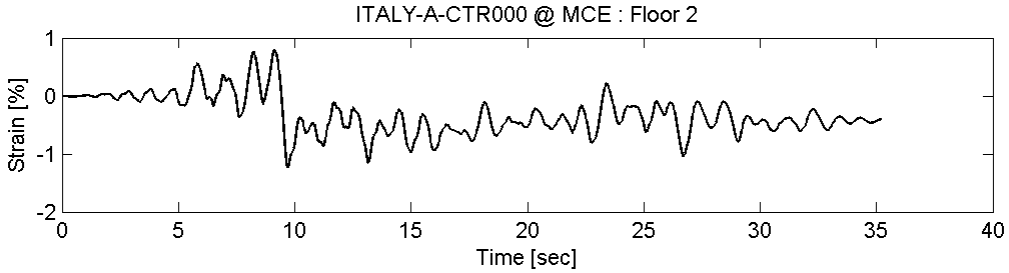
ITALY-A-CTR000 @ MCE : Floor 2
Strain [%]
Time [sec]

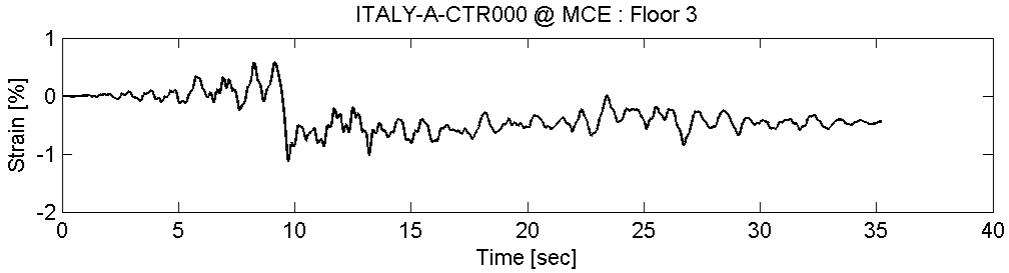
ITALY-A-CTR000 @ MCE : Floor 3
Strain [%]
Time [sec]

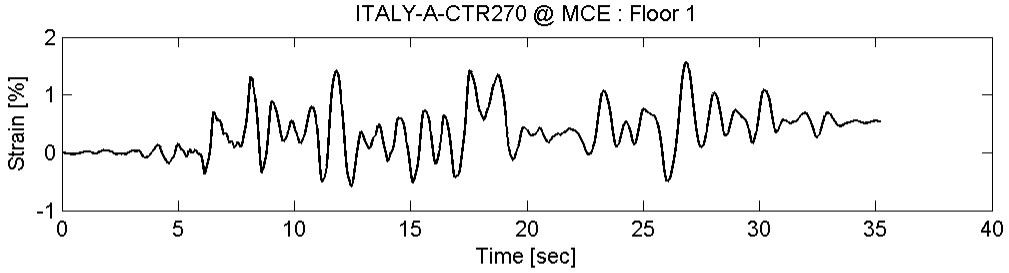
ITALY-A-CTR270 @ MCE : Floor 1
Strain [%]
Time [sec]

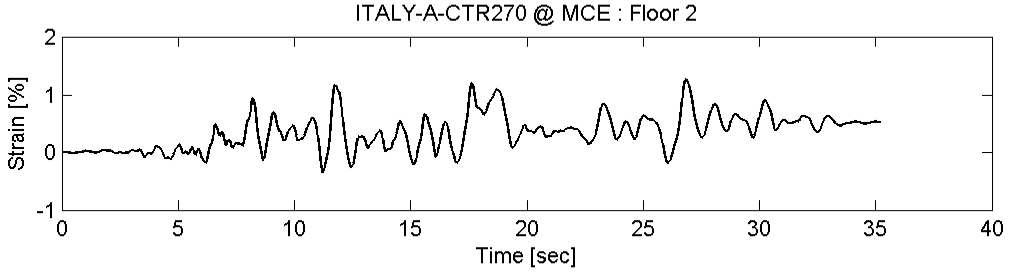
ITALY-A-CTR270 @ MCE : Floor 2
Strain [%]
Time [sec]

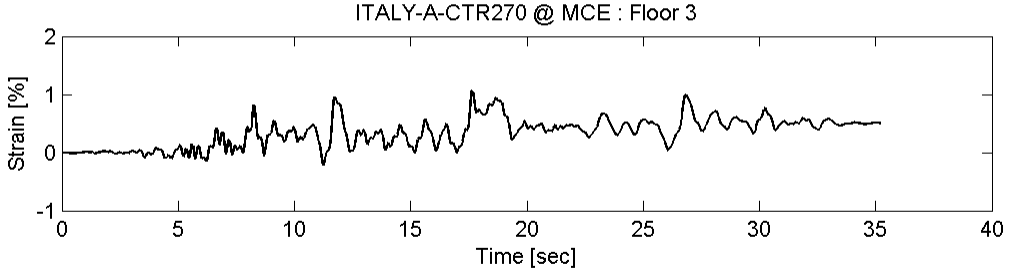
ITALY-A-CTR270 @ MCE : Floor 3
Strain [%]
Time [sec]

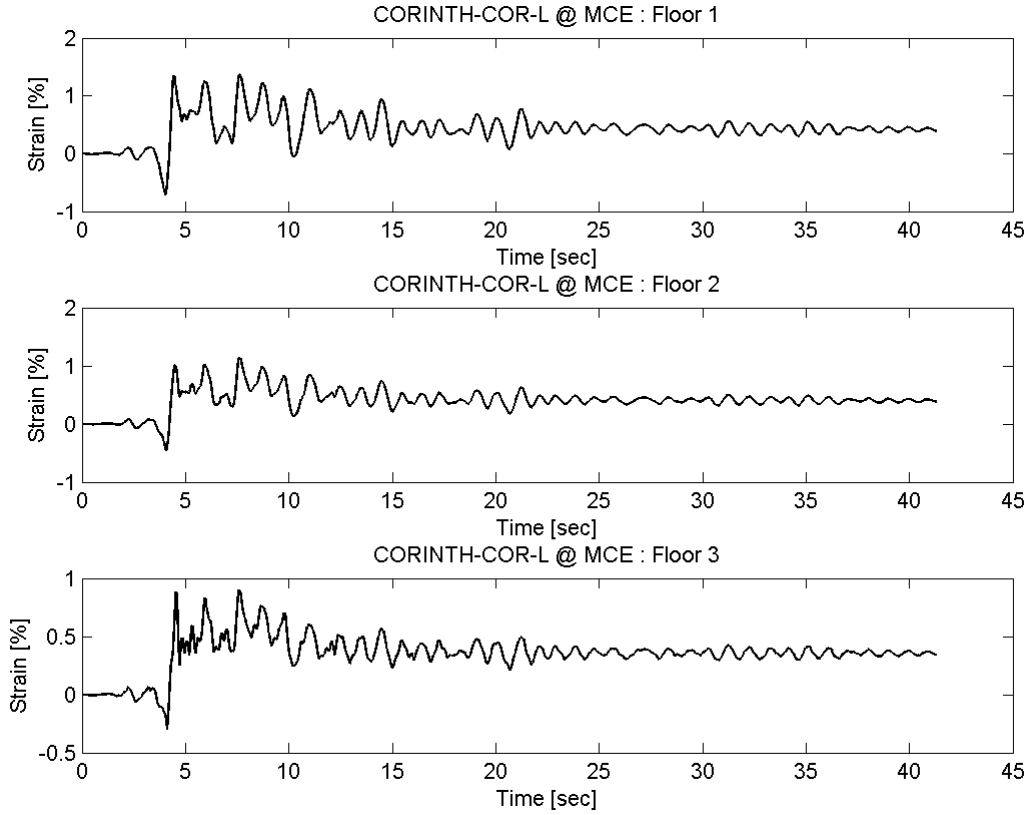
CORINTH-COR-L @ MCE : Floor 1
Strain [%]
Time [sec]
CORINTH-COR-L @ MCE : Floor 2
Strain [%]
Time [sec]
CORINTH-COR-L @ MCE : Floor 3
Strain [%]
Time [sec]

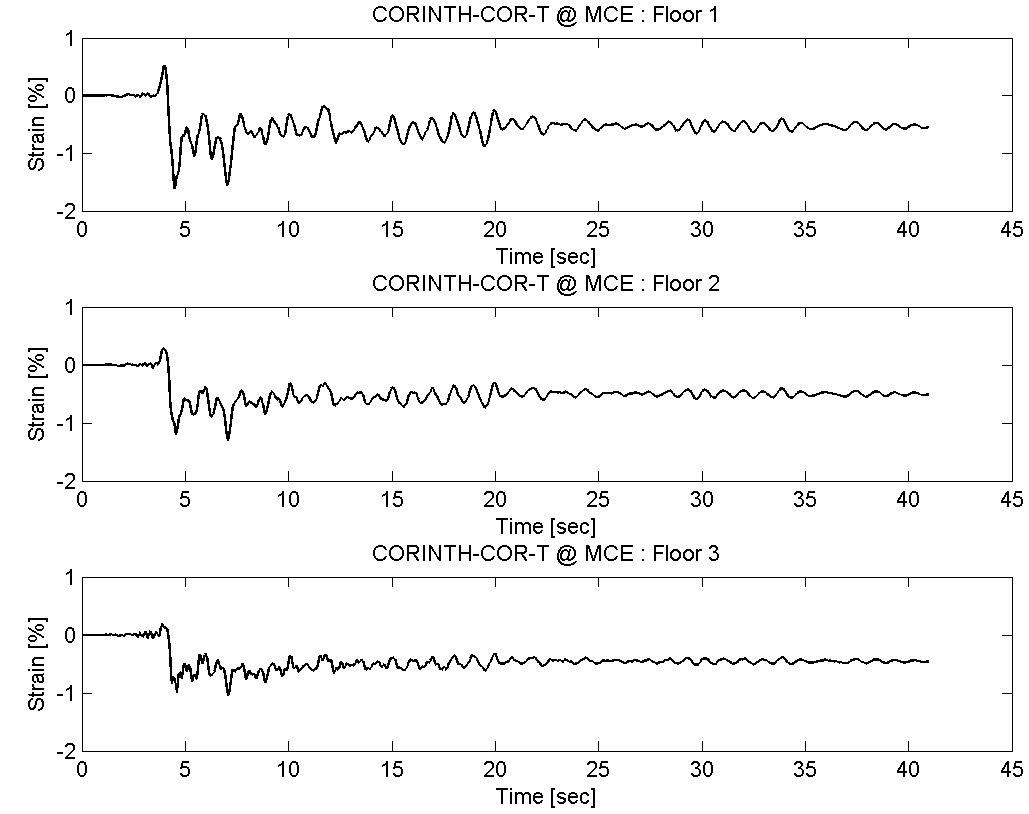
CORINTH-COR-T @ MCE : Floor 1
Strain [%]
Time [sec]
CORINTH-COR-T @ MCE : Floor 2
Strain [%]
Time [sec]
CORINTH-COR-T @ MCE : Floor 3
Strain [%]
Time [sec]

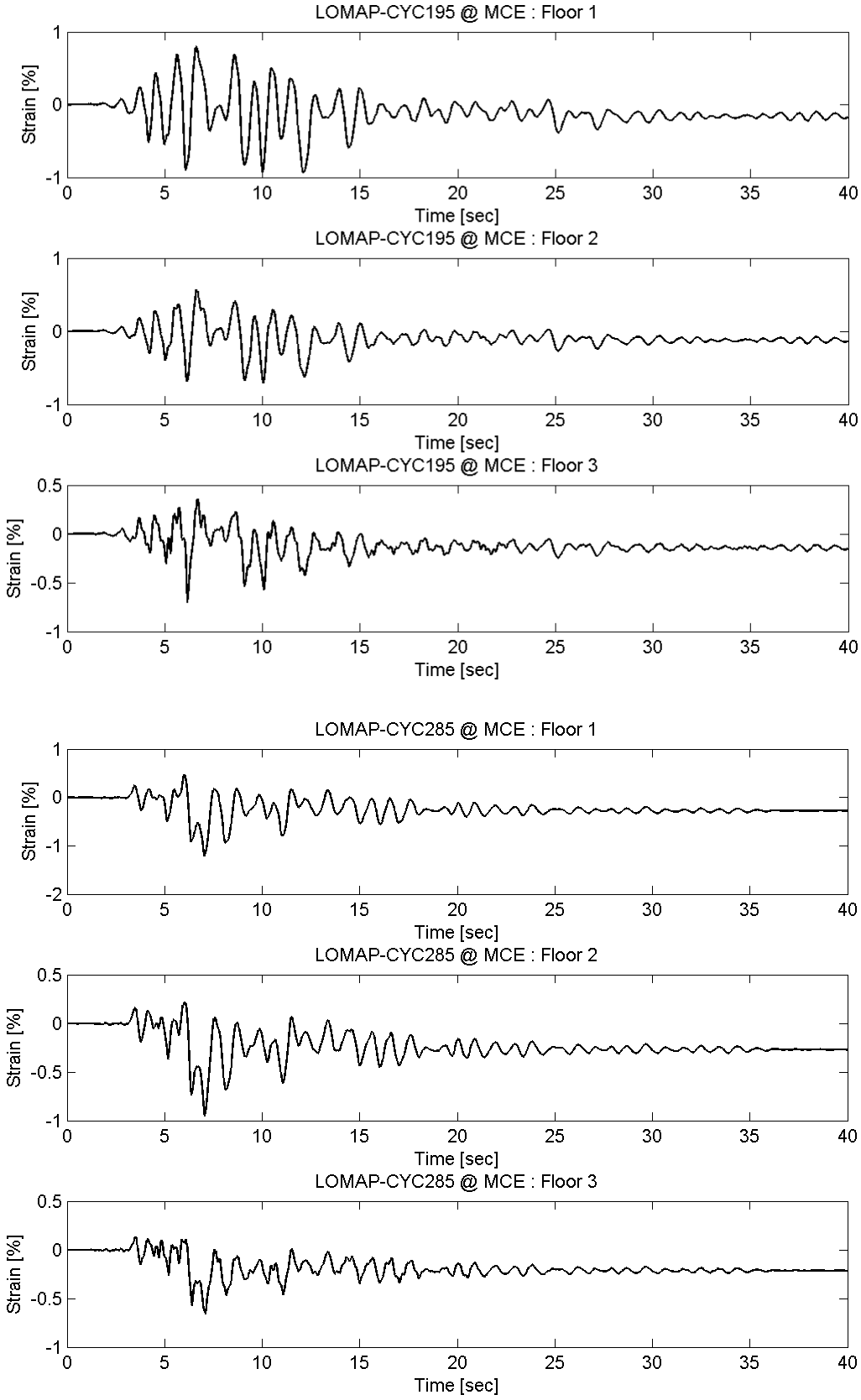
LOMAP-CYC195 @ MCE : Floor 1
Strain [%]
Time [sec]
LOMAP-CYC195 @ MCE : Floor 2
Strain [%]
Time [sec]
LOMAP-CYC195 @ MCE : Floor 3
Strain [%]
Time [sec]
LOMAP-CYC285 @ MCE : Floor 1
Strain [%]
Time [sec]
LOMAP-CYC285 @ MCE : Floor 2
Strain [%]
Time [sec]
LOMAP-CYC285 @ MCE : Floor 3
Strain [%]
Time [sec]

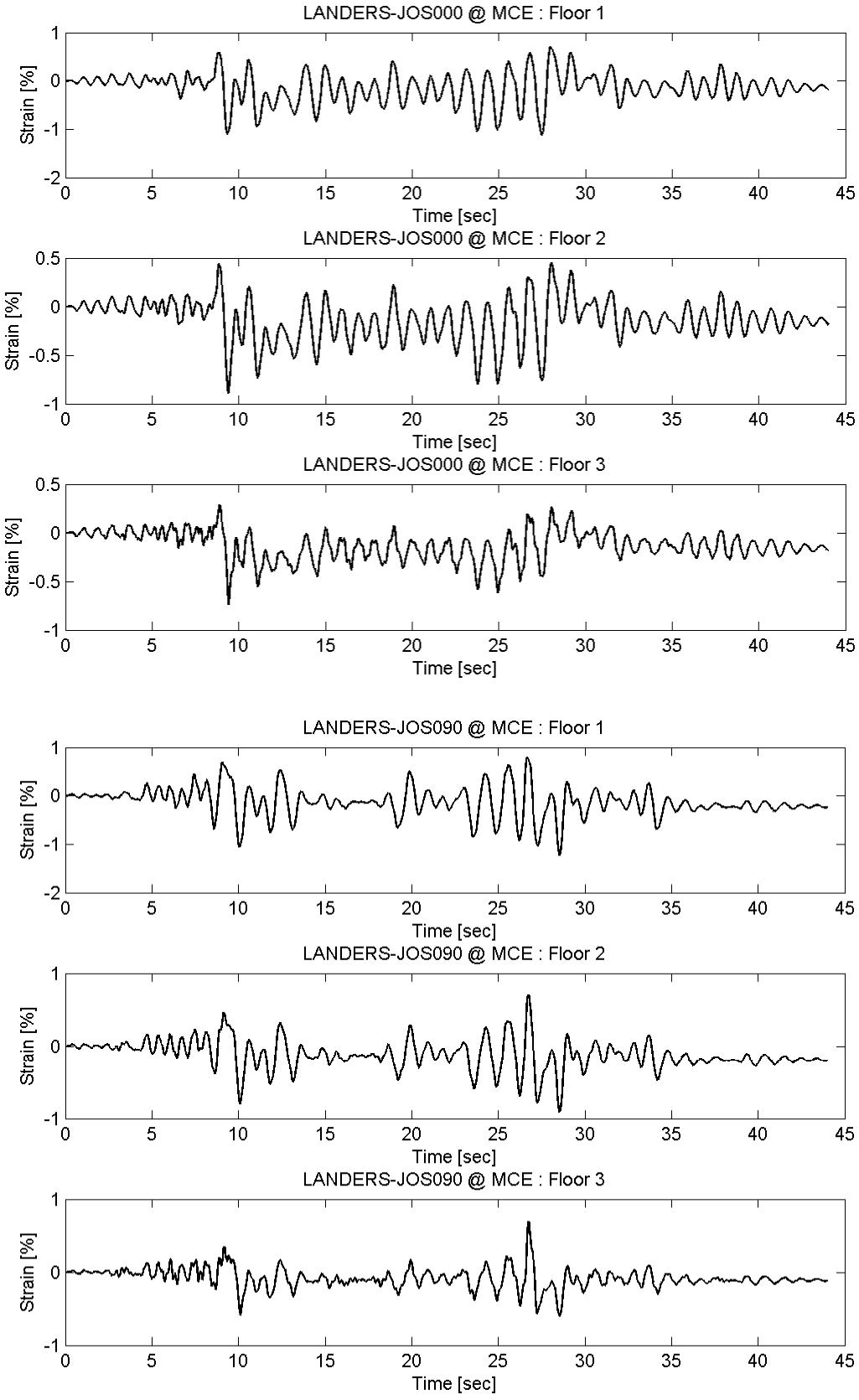
LANDERS-JOS000 @ MCE : Floor 1
Strain [%]
Time [sec]
LANDERS-JOS000 @ MCE : Floor 2
Strain [%]
Time [sec]
LANDERS-JOS000 @ MCE : Floor 3
Strain [%]
Time [sec]
LANDERS-JOS090 @ MCE : Floor 1
Strain [%]
Time [sec]
LANDERS-JOS090 @ MCE : Floor 2
Strain [%]
Time [sec]
LANDERS-JOS090 @ MCE : Floor 3
Strain [%]
Time [sec]

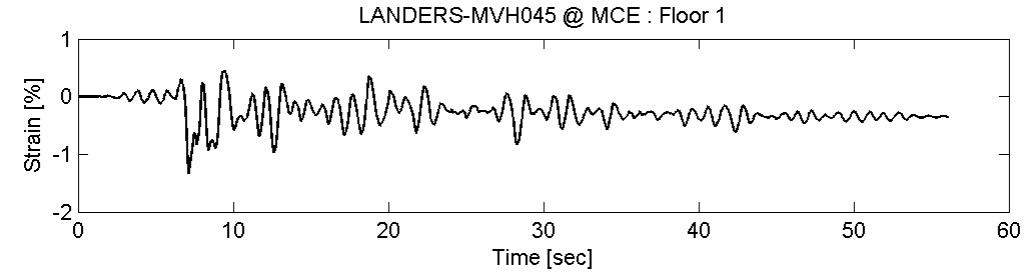
LANDERS-MVH045 @ MCE : Floor 1
Strain [%]
Time [sec]

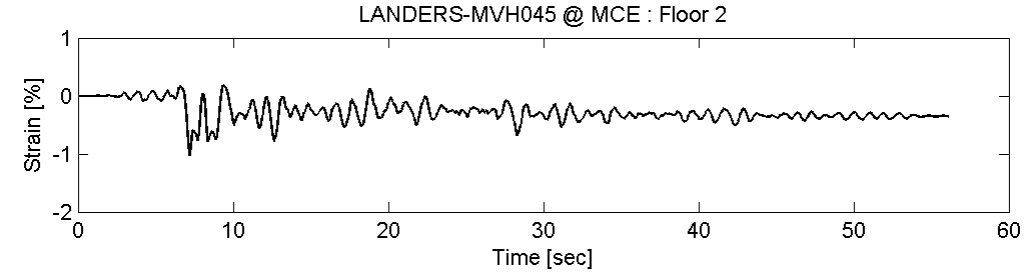
LANDERS-MVH045 @ MCE : Floor 2
Strain [%]
Time [sec]

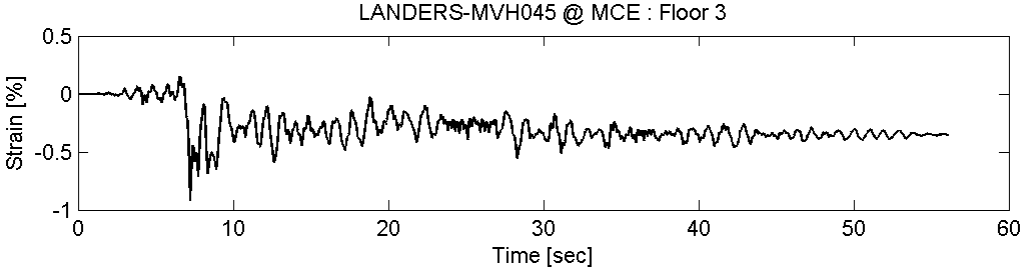
LANDERS-MVH045 @ MCE : Floor 3
Strain [%]
Time [sec]

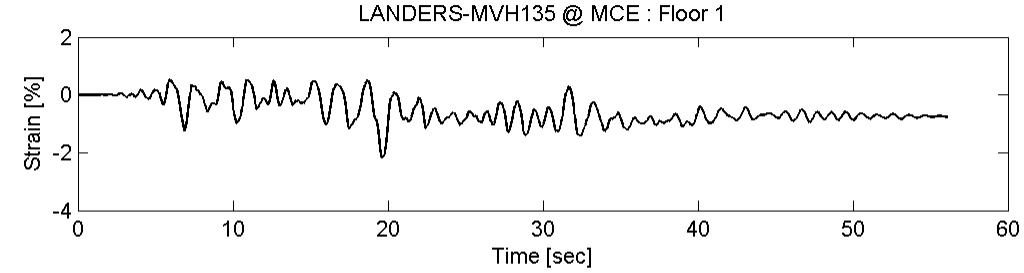
LANDERS-MVH135 @ MCE : Floor 1
Strain [%]
Time [sec]

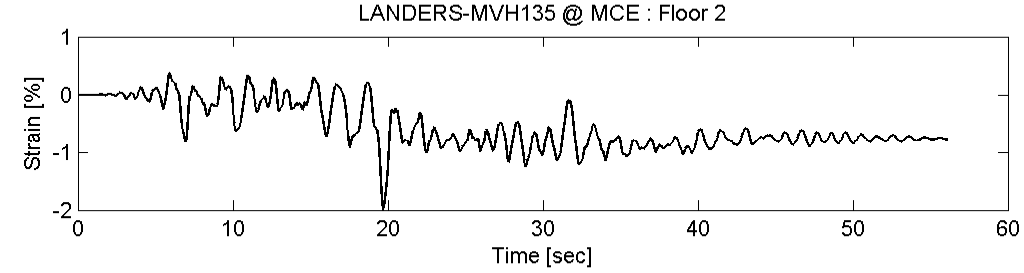
LANDERS-MVH135 @ MCE : Floor 2
Strain [%]
Time [sec]

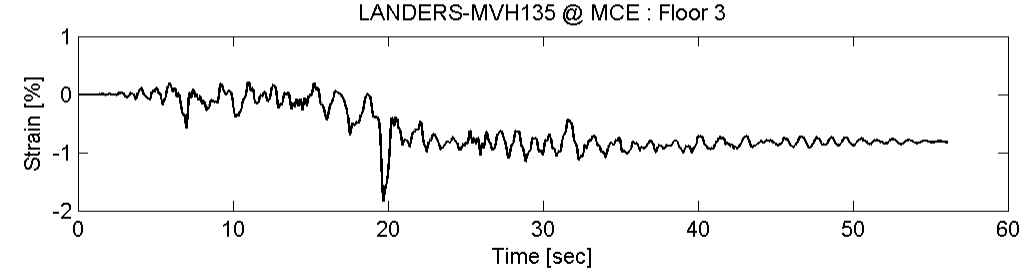
LANDERS-MVH135 @ MCE : Floor 3
Strain [%]
Time [sec]

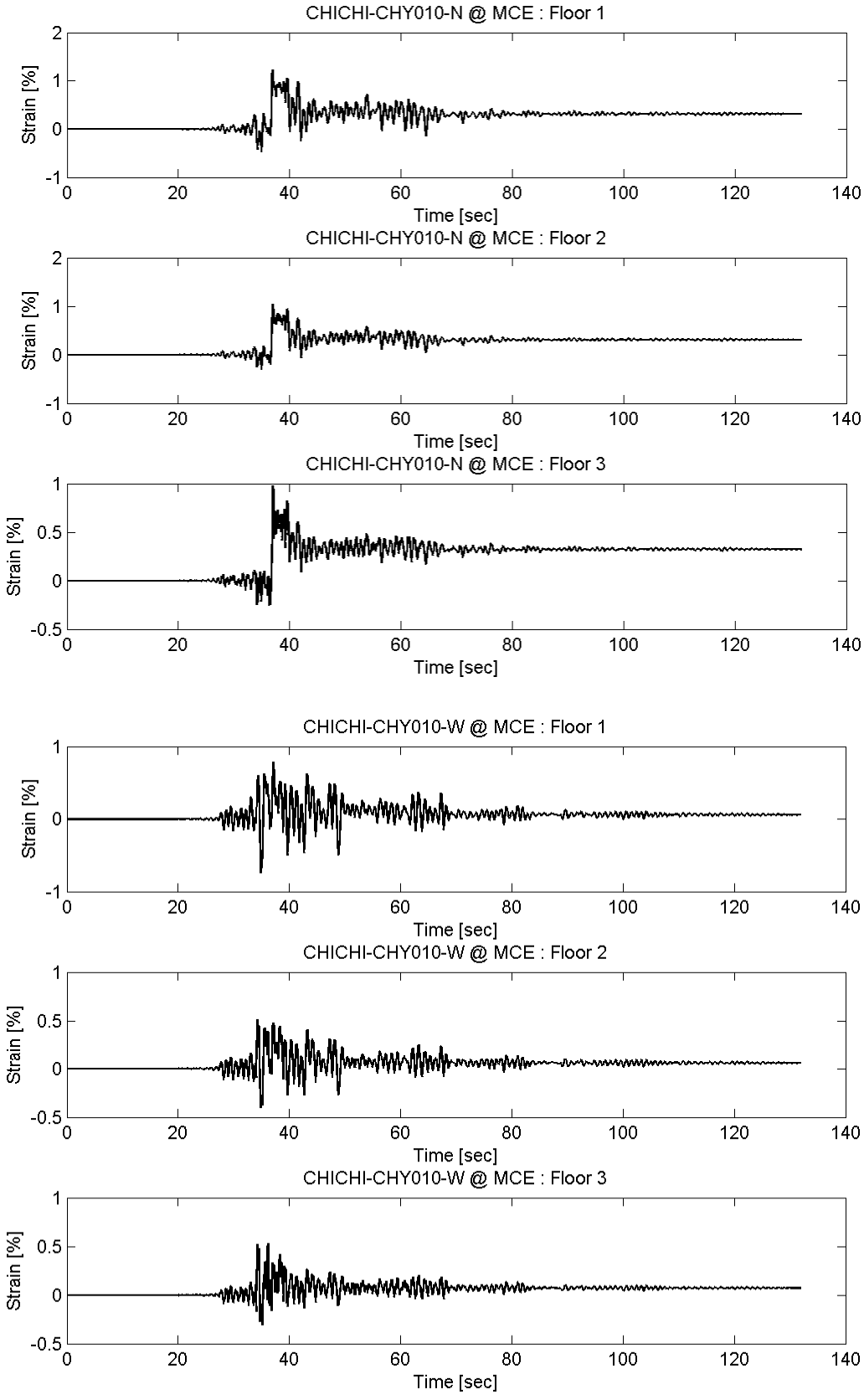
CHICHI-CHY010-N @ MCE : Floor 1
Strain [%]
Time [sec]
CHICHI-CHY010-N @ MCE : Floor 2
Strain [%]
Time [sec]
CHICHI-CHY010-N @ MCE : Floor 3
Strain [%]
Time [sec]
CHICHI-CHY010-W @ MCE : Floor 1
Strain [%]
Time [sec]
CHICHI-CHY010-W @ MCE : Floor 2
Strain [%]
Time [sec]
CHICHI-CHY010-W @ MCE : Floor 3
Strain [%]
Time [sec]

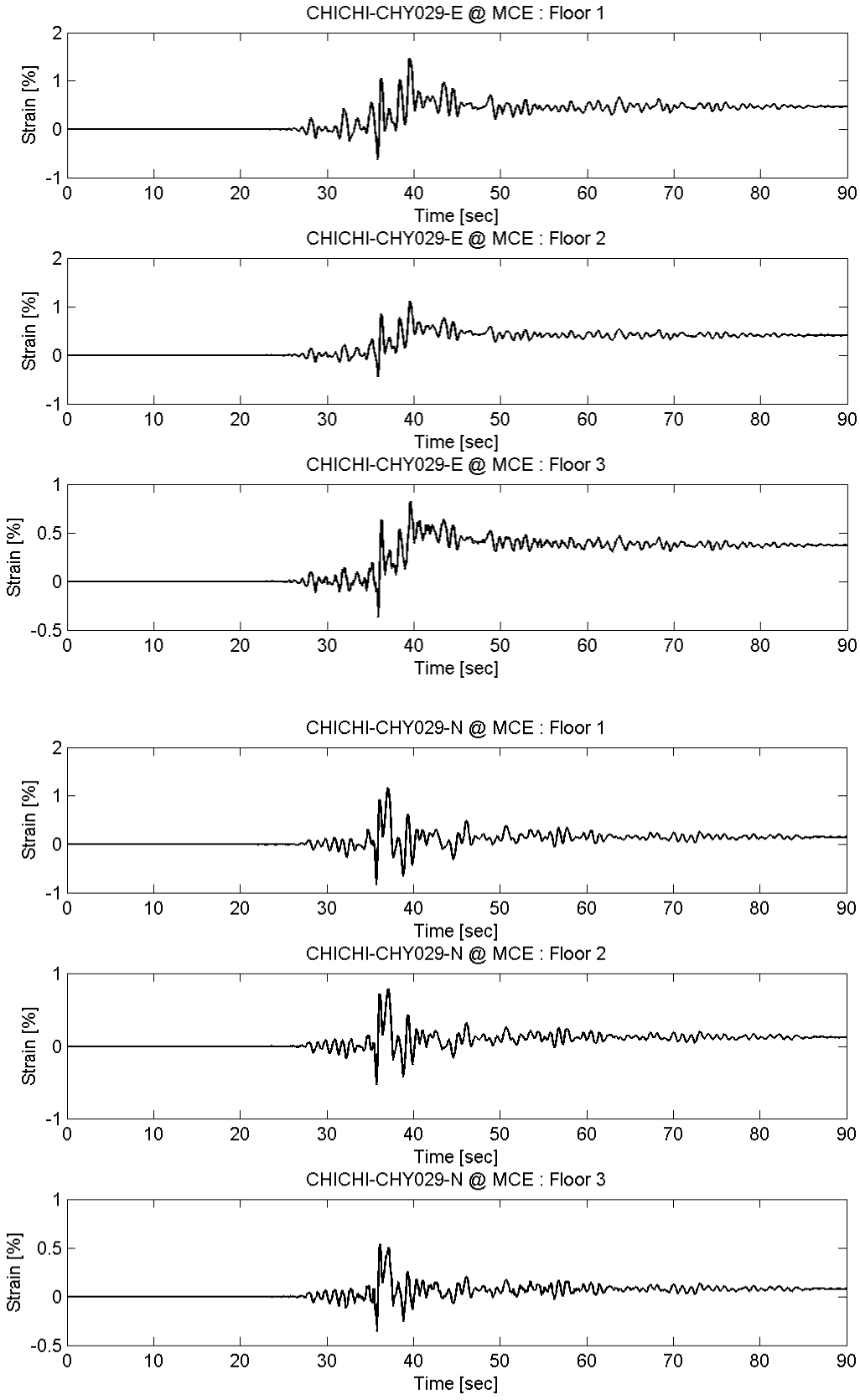
CHICHI-CHY029-E @ MCE : Floor 1
Strain [%]
Time [sec]
CHICHI-CHY029-E @ MCE : Floor 2
Strain [%]
Time [sec]
CHICHI-CHY029-E @ MCE : Floor 3
Strain [%]
Time [sec]
CHICHI-CHY029-N @ MCE : Floor 1
Strain [%]
Time [sec]
CHICHI-CHY029-N @ MCE : Floor 2
Strain [%]
Time [sec]
CHICHI-CHY029-N @ MCE : Floor 3
Strain [%]
Time [sec]

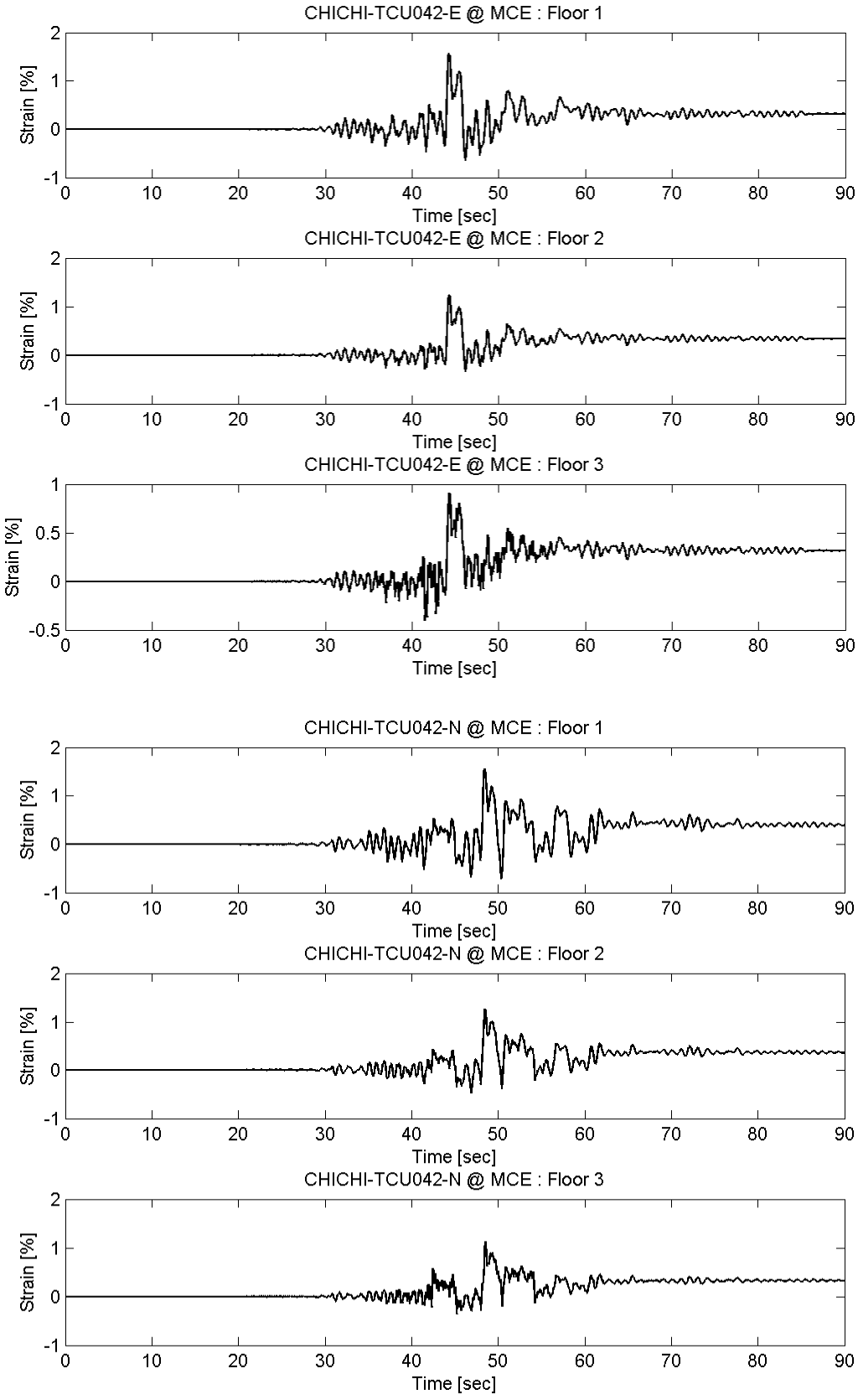
CHICHI-TCU042-E @ MCE : Floor 1
Strain [%]
Time [sec]
CHICHI-TCU042-E @ MCE : Floor 2
Strain [%]
Time [sec]
CHICHI-TCU042-E @ MCE : Floor 3
Strain [%]
Time [sec]
CHICHI-TCU042-N @ MCE : Floor 1
Strain [%]
Time [sec]
CHICHI-TCU042-N @ MCE : Floor 2
Strain [%]
Time [sec]
CHICHI-TCU042-N @ MCE : Floor 3
Strain [%]
Time [sec]

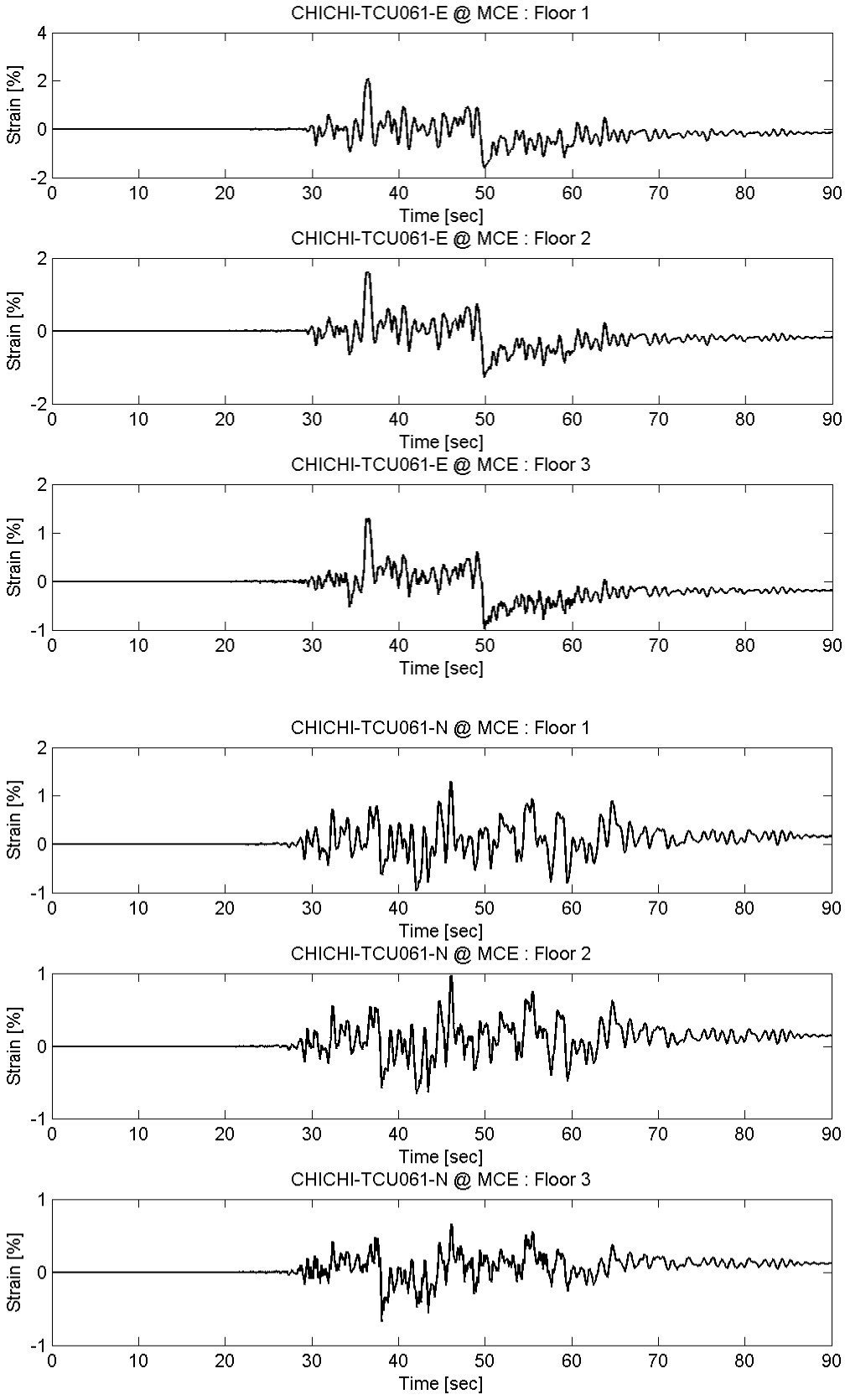
CHICHI-TCU061-E @ MCE : Floor 1
Strain [%]
Time [sec]
CHICHI-TCU061-E @ MCE : Floor 2
Strain [%]
Time [sec]
CHICHI-TCU061-E @ MCE : Floor 3
Strain [%]
Time [sec]
CHICHI-TCU061-N @ MCE : Floor 1
Strain [%]
Time [sec]
CHICHI-TCU061-N @ MCE : Floor 2
Strain [%]
Time [sec]
CHICHI-TCU061-N @ MCE : Floor 3
Strain [%]
Time [sec]

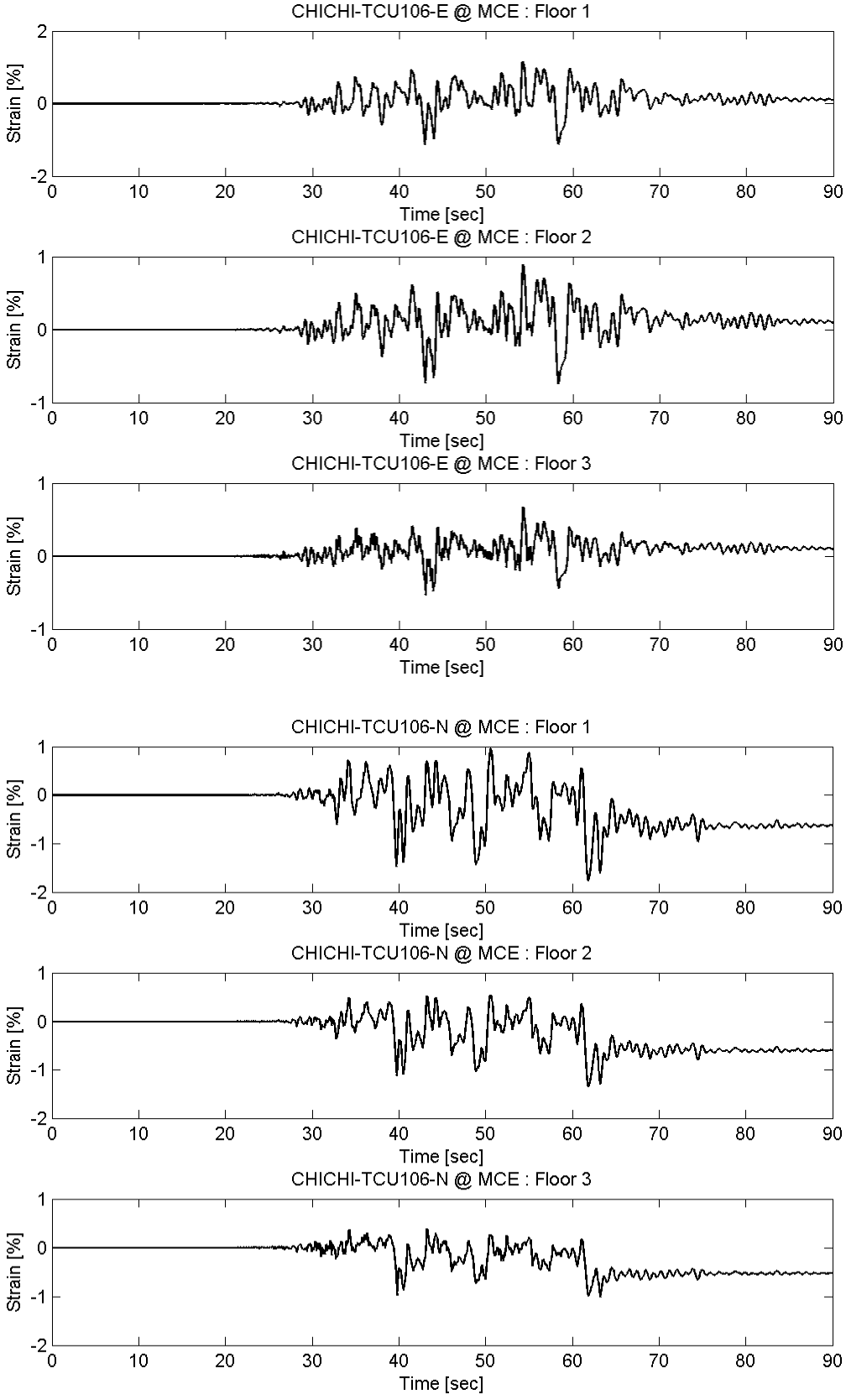
CHICHI-TCU106-E @ MCE : Floor 1
Strain [%]
Time [sec]
CHICHI-TCU106-E @ MCE : Floor 2
Strain [%]
Time [sec]
CHICHI-TCU106-E @ MCE : Floor 3
Strain [%]
Time [sec]
CHICHI-TCU106-N @ MCE : Floor 1
Strain [%]
Time [sec]
CHICHI-TCU106-N @ MCE : Floor 2
Strain [%]
Time [sec]
CHICHI-TCU106-N @ MCE : Floor 3
Strain [%]
Time [sec]

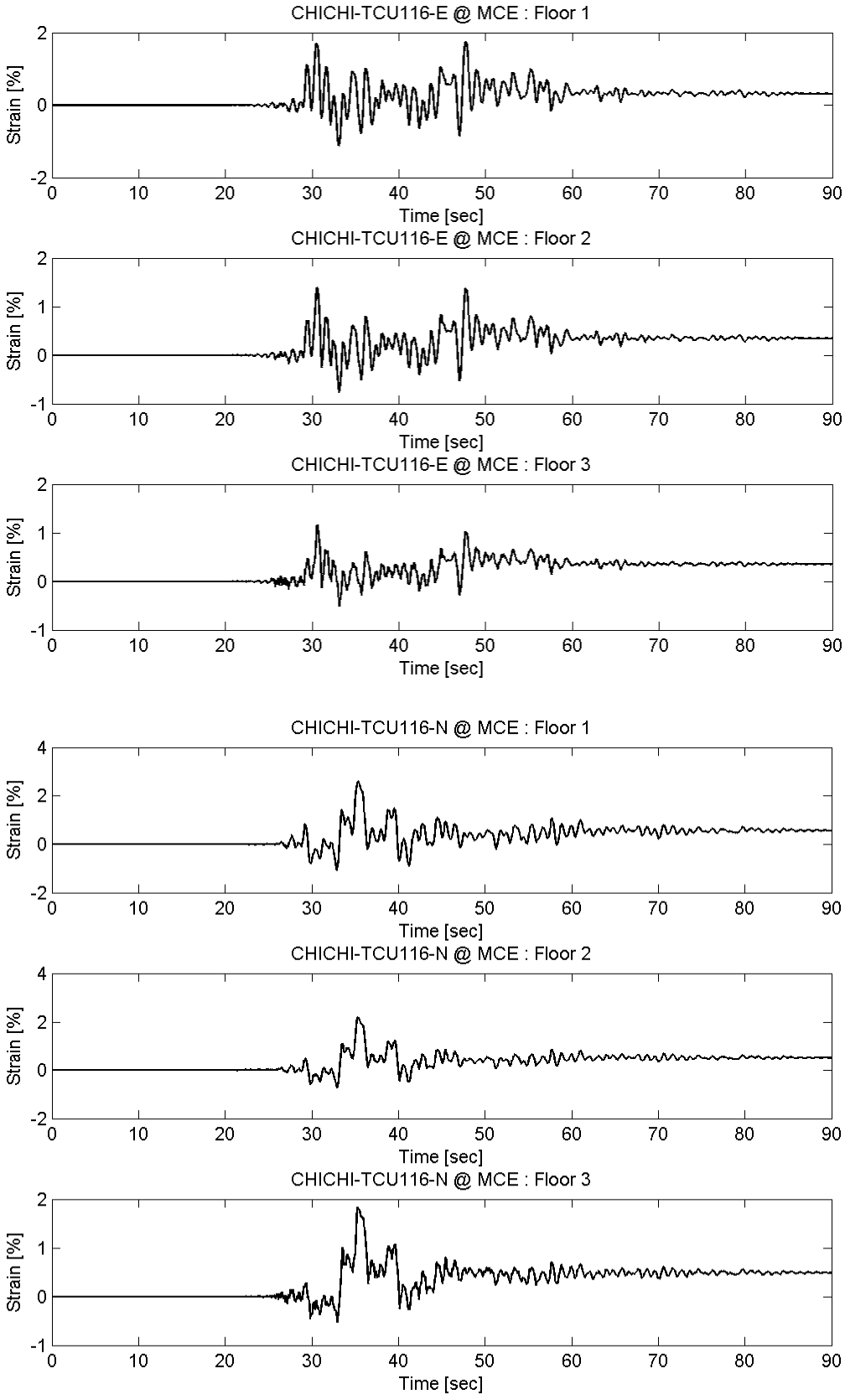
CHICHI-TCU116-E @ MCE : Floor 1
Strain [%]
Time [sec]
CHICHI-TCU116-E @ MCE : Floor 2
Strain [%]
Time [sec]
CHICHI-TCU116-E @ MCE : Floor 3
Strain [%]
Time [sec]
CHICHI-TCU116-N @ MCE : Floor 1
Strain [%]
Time [sec]
CHICHI-TCU116-N @ MCE : Floor 2
Strain [%]
Time [sec]
CHICHI-TCU116-N @ MCE : Floor 3
Strain [%]
Time [sec]

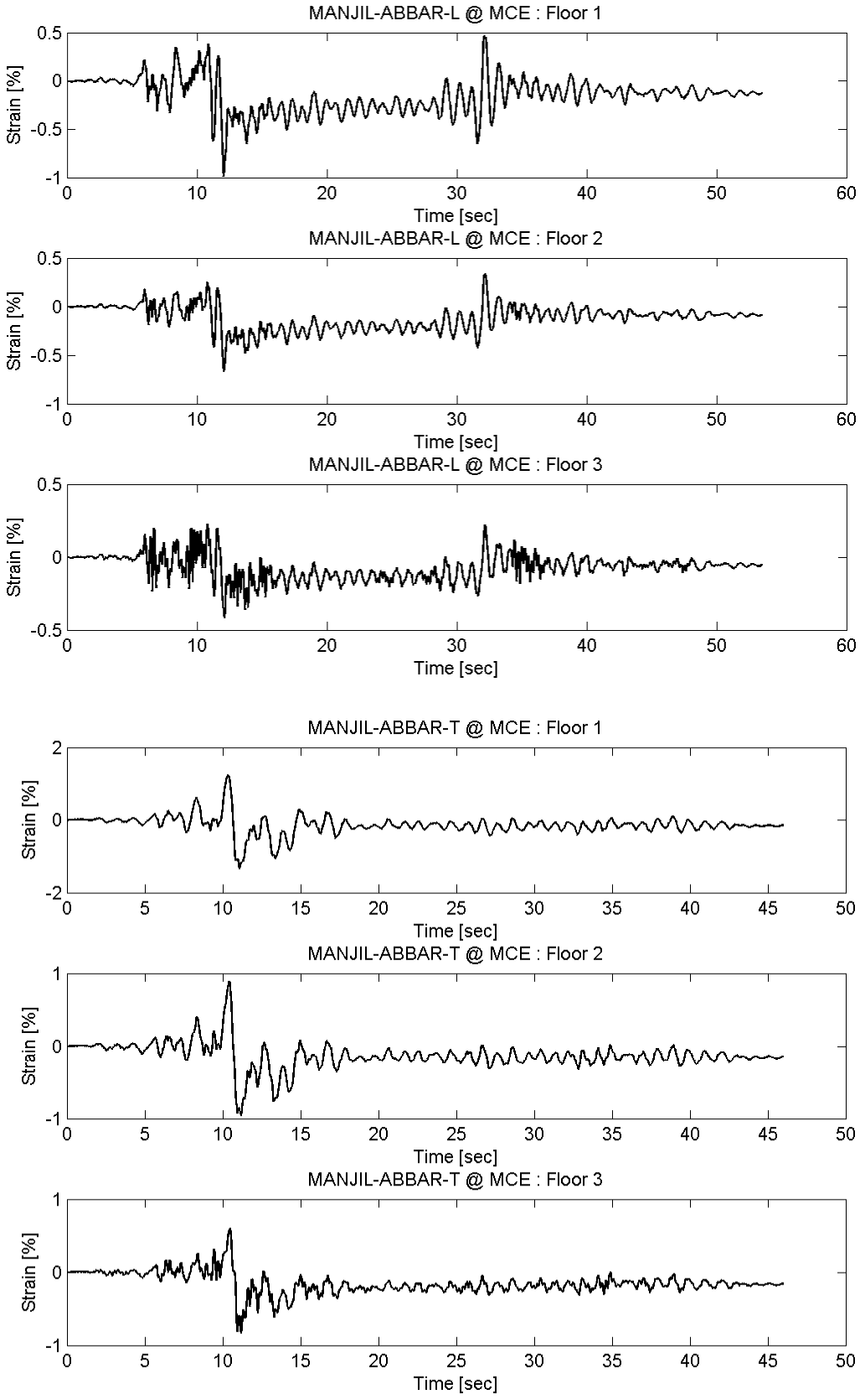
MANJIL-ABBAR-L @ MCE : Floor 1
Strain [%]
Time [sec]
MANJIL-ABBAR-L @ MCE : Floor 2
Strain [%]
Time [sec]
MANJIL-ABBAR-L @ MCE : Floor 3
Strain [%]
Time [sec]
MANJIL-ABBAR-T @ MCE : Floor 1
Strain [%]
Time [sec]
MANJIL-ABBAR-T @ MCE : Floor 2
Strain [%]
Time [sec]
MANJIL-ABBAR-T @ MCE : Floor 3
Strain [%]
Time [sec]

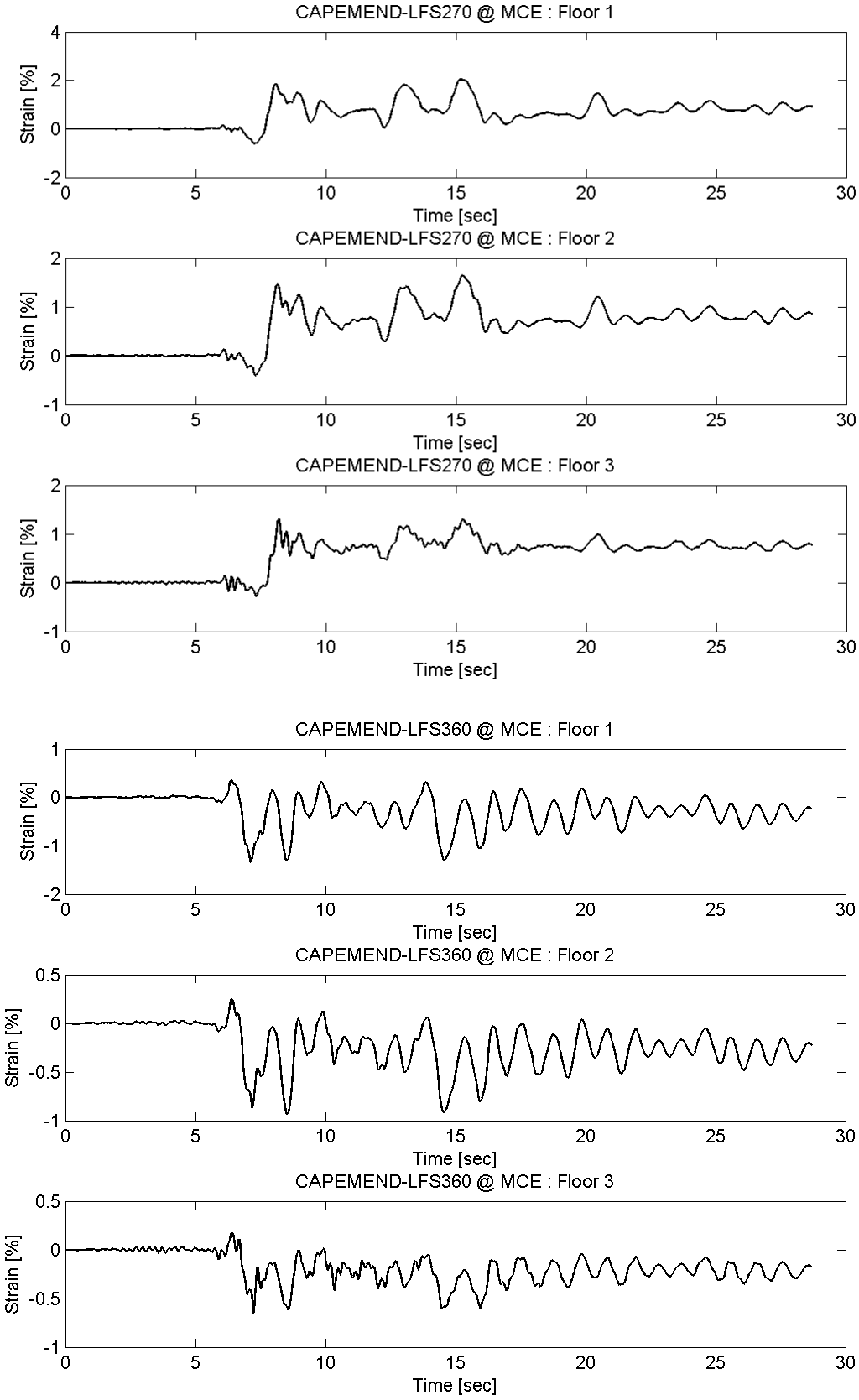
CAPEMEND-LFS270 @ MCE : Floor 1
Strain [%]
Time [sec]
CAPEMEND-LFS270 @ MCE : Floor 2
Strain [%]
Time [sec]
CAPEMEND-LFS270 @ MCE : Floor 3
Strain [%]
Time [sec]
CAPEMEND-LFS360 @ MCE : Floor 1
Strain [%]
Time [sec]
CAPEMEND-LFS360 @ MCE : Floor 2
Strain [%]
Time [sec]
CAPEMEND-LFS360 @ MCE : Floor 3
Strain [%]
Time [sec]

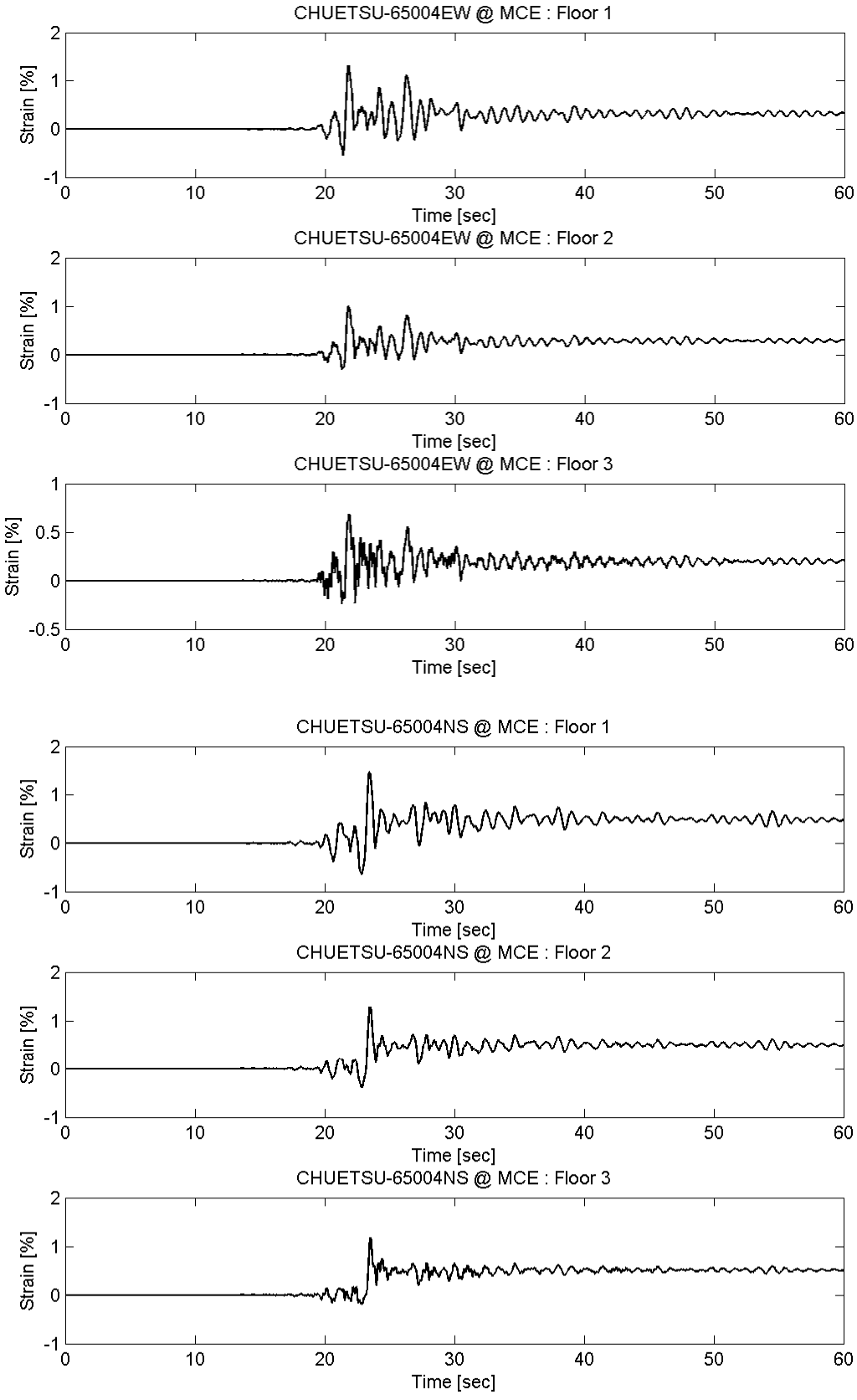
CHUETSU-65004EW @ MCE : Floor 1
Strain [%]
Time [sec]
CHUETSU-65004EW @ MCE : Floor 2
Strain [%]
Time [sec]
CHUETSU-65004EW @ MCE : Floor 3
Strain [%]
Time [sec]
CHUETSU-65004NS @ MCE : Floor 1
Strain [%]
Time [sec]
CHUETSU-65004NS @ MCE : Floor 2
Strain [%]
Time [sec]
CHUETSU-65004NS @ MCE : Floor 3
Strain [%]
Time [sec]

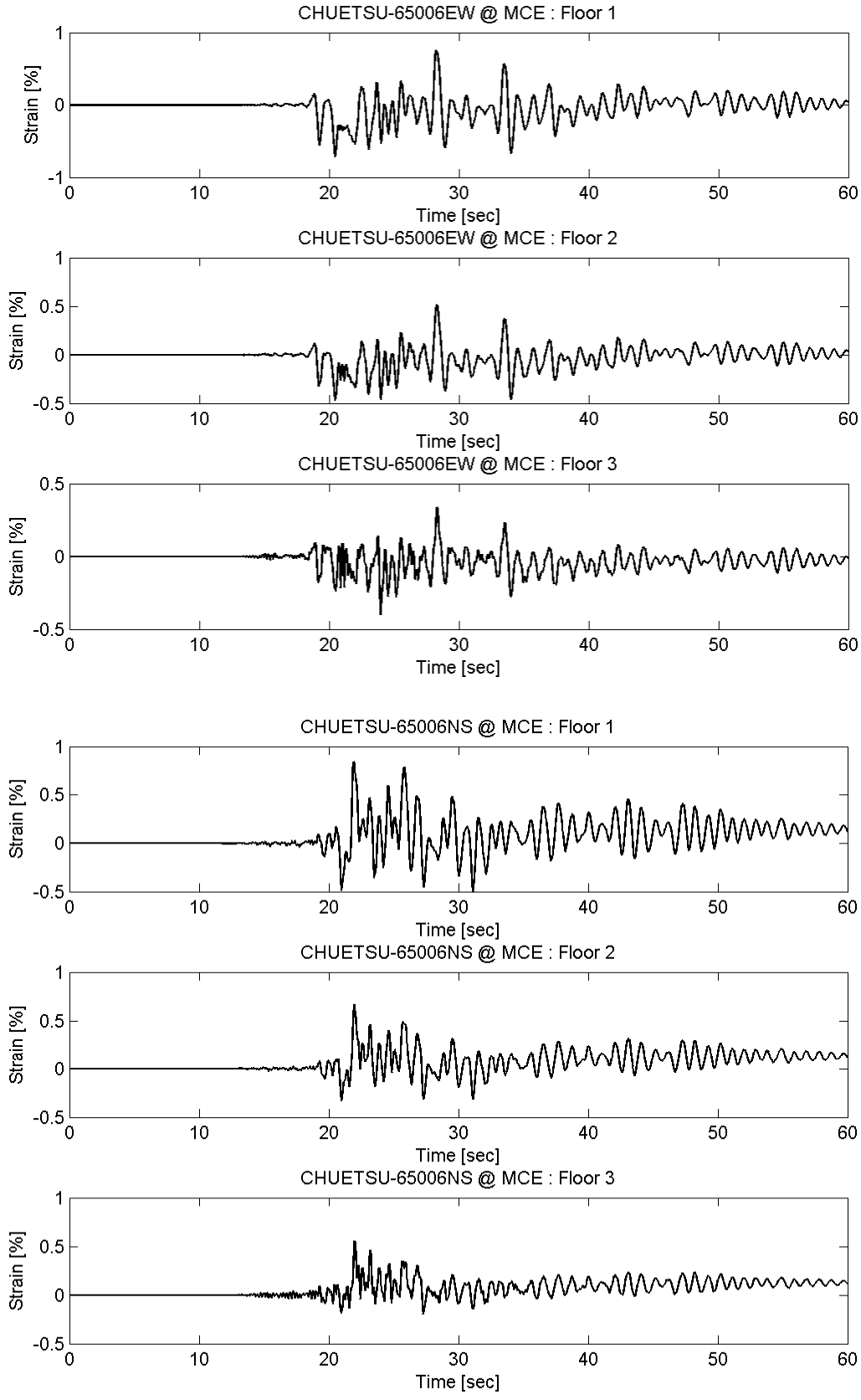
CHUETSU-65006EW @ MCE : Floor 1
Strain [%]
Time [sec]
CHUETSU-65006EW @ MCE : Floor 2
Strain [%]
Time [sec]
CHUETSU-65006EW @ MCE : Floor 3
Strain [%]
Time [sec]
CHUETSU-65006NS @ MCE : Floor 1
Strain [%]
Time [sec]
CHUETSU-65006NS @ MCE : Floor 2
Strain [%]
Time [sec]
CHUETSU-65006NS @ MCE : Floor 3
Strain [%]
Time [sec]

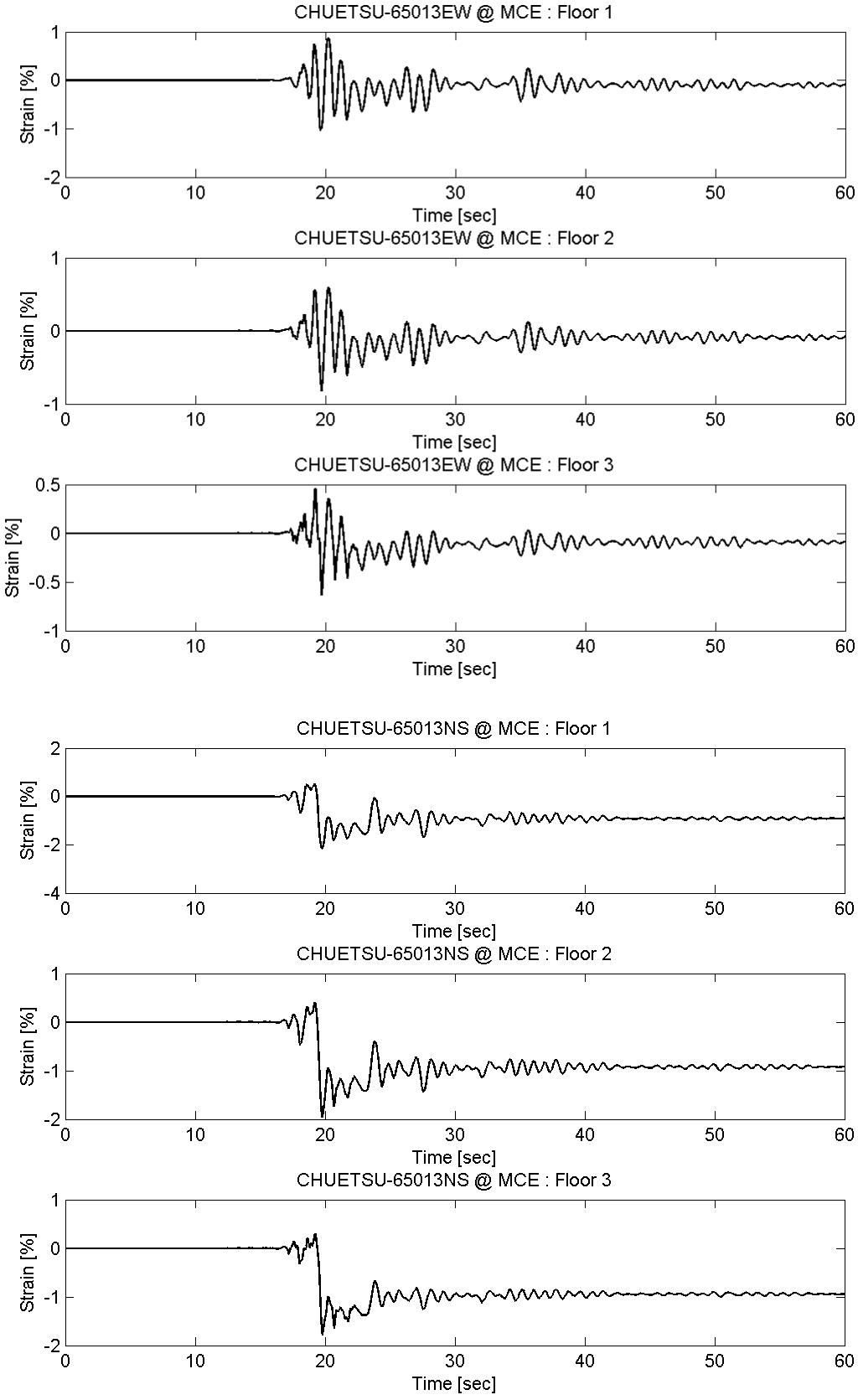
CHUETSU-65013EW @ MCE : Floor 1
Strain [%]
Time [sec]
CHUETSU-65013EW @ MCE : Floor 2
Strain [%]
Time [sec]
CHUETSU-65013EW @ MCE : Floor 3
Strain [%]
Time [sec]
CHUETSU-65013NS @ MCE : Floor 1
Strain [%]
Time [sec]
CHUETSU-65013NS @ MCE : Floor 2
Strain [%]
Time [sec]
CHUETSU-65013NS @ MCE : Floor 3
Strain [%]
Time [sec]

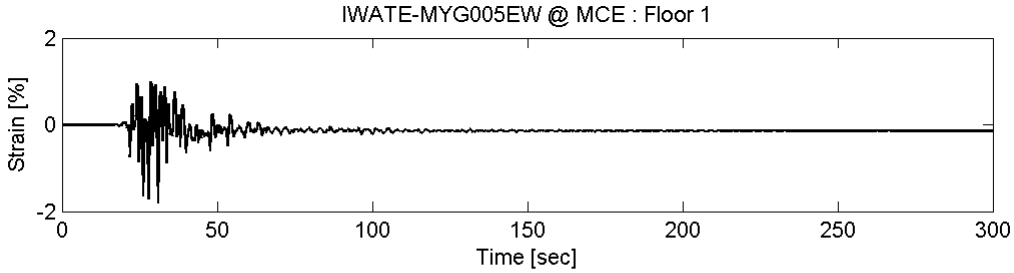
IWATE-MYG005EW @ MCE : Floor 1
Strain [%]
Time [sec]

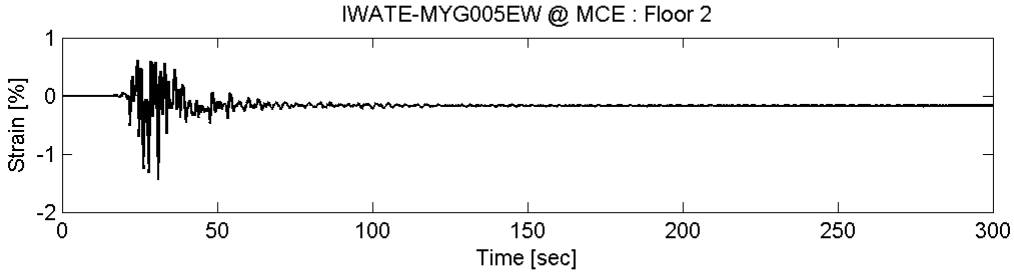
IWATE-MYG005EW @ MCE : Floor 2
Strain [%]
Time [sec]

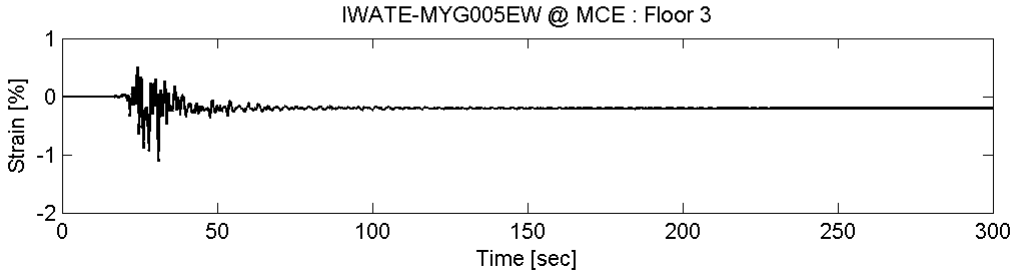
IWATE-MYG005EW @ MCE : Floor 3
Strain [%]
Time [sec]

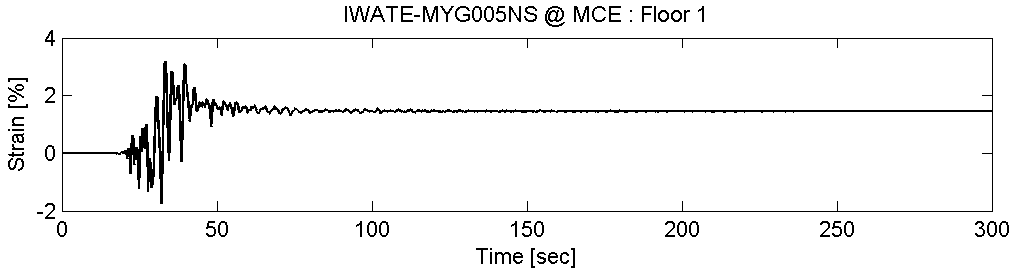
IWATE-MYG005NS @ MCE : Floor 1
Strain [%]
Time [sec]

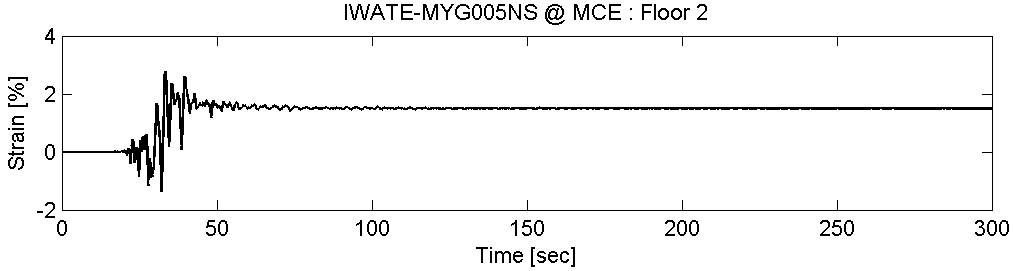
IWATE-MYG005NS @ MCE : Floor 2
Strain [%]
Time [sec]

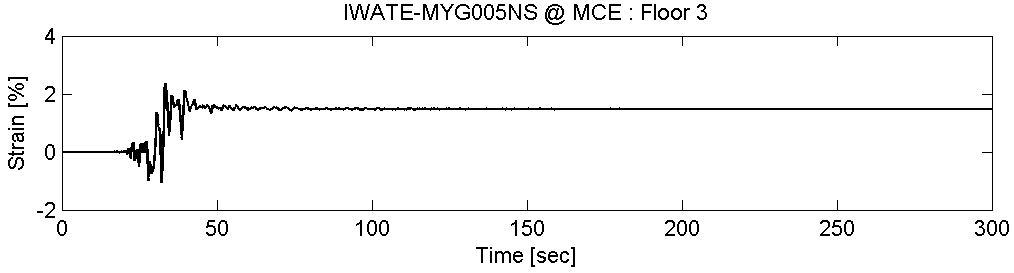
IWATE-MYG005NS @ MCE : Floor 3
Strain [%]
Time [sec]

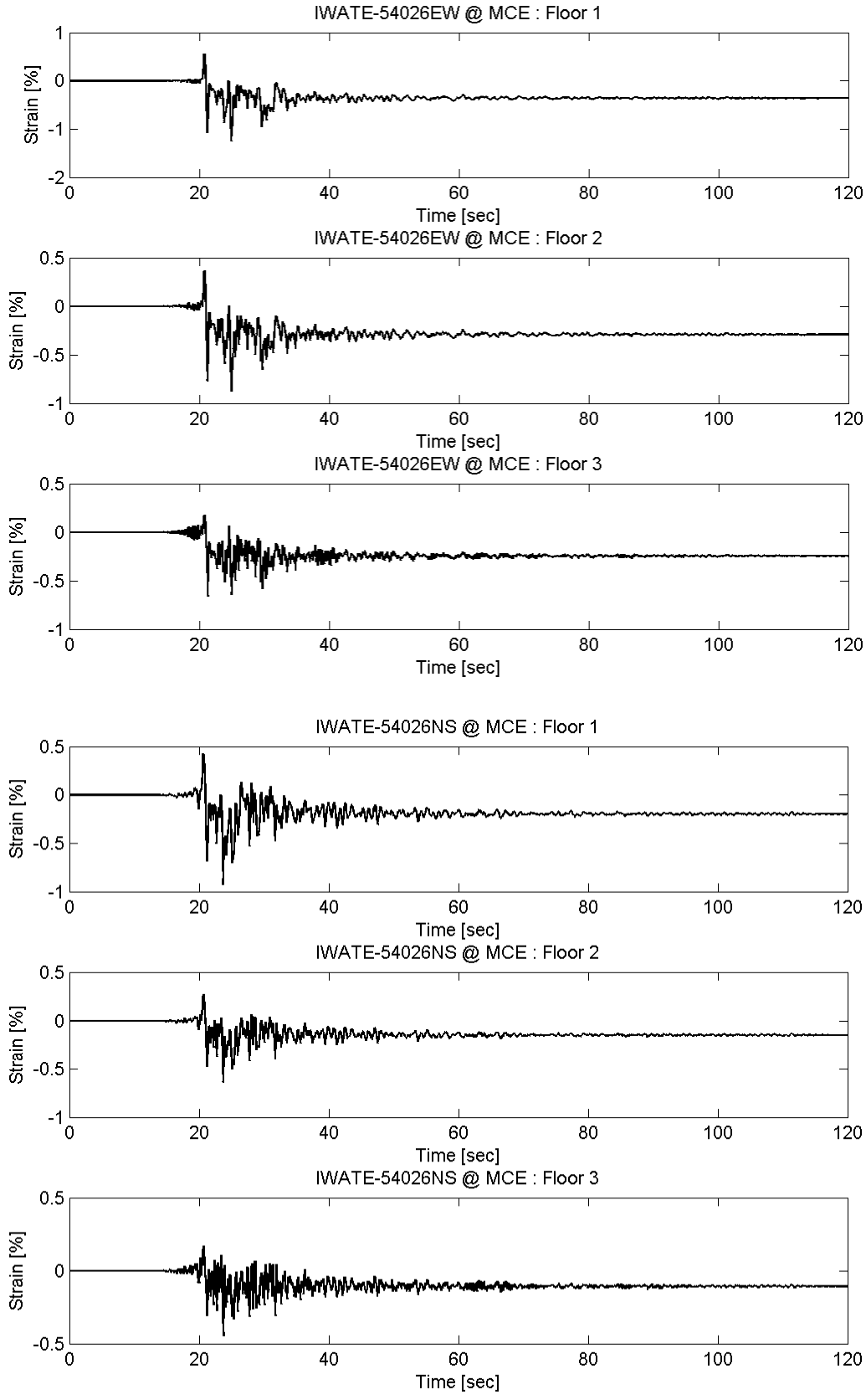
IWATE-54026EW @ MCE : Floor 1
Strain [%]
Time [sec]
IWATE-54026EW @ MCE : Floor 2
Strain [%]
Time [sec]
IWATE-54026EW @ MCE : Floor 3
Strain [%]
Time [sec]
IWATE-54026NS @ MCE : Floor 1
Strain [%]
Time [sec]
IWATE-54026NS @ MCE : Floor 2
Strain [%]
Time [sec]
IWATE-54026NS @ MCE : Floor 3
Strain [%]
Time [sec]

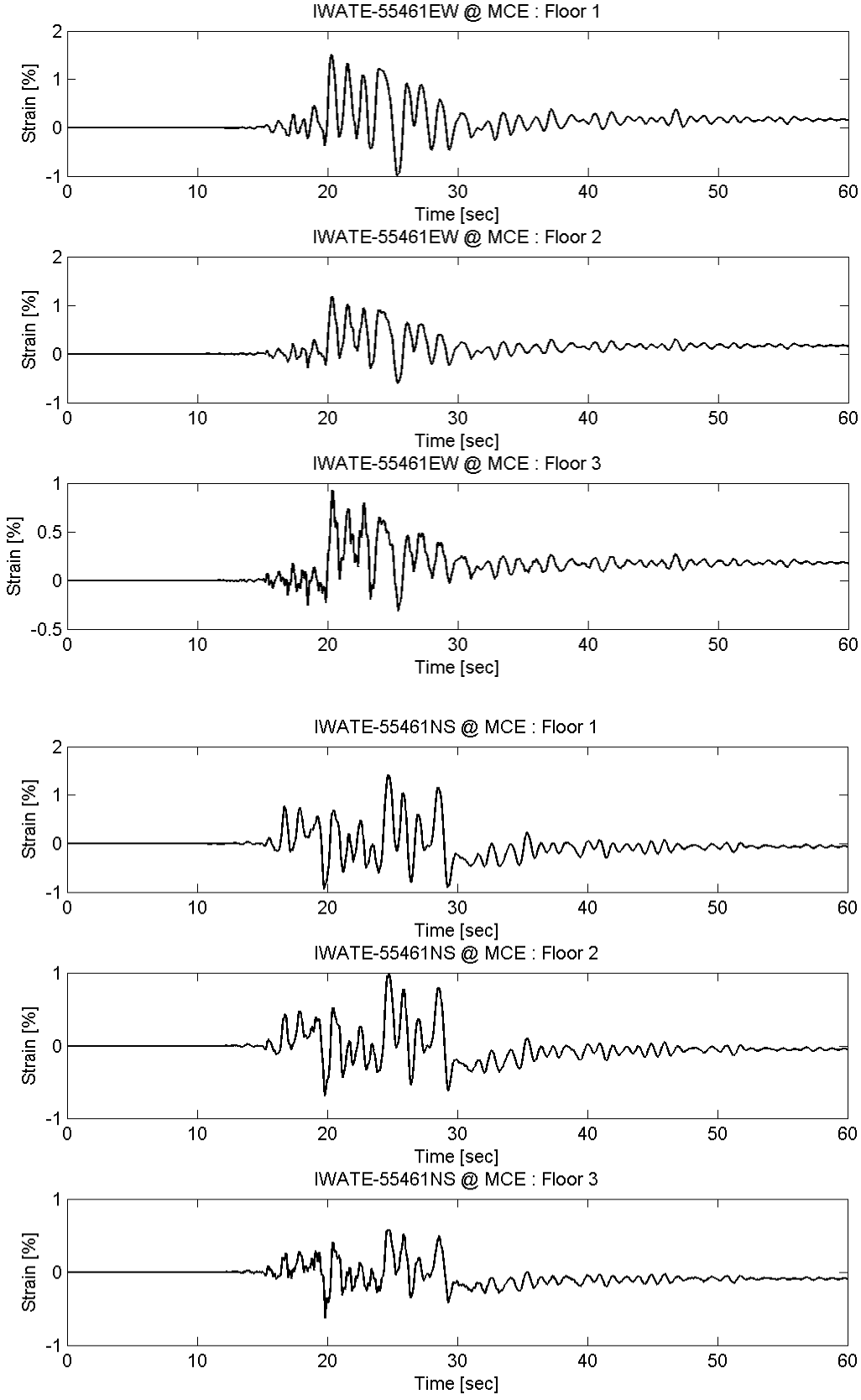
IWATE-55461EW @ MCE : Floor 1
Strain [%]
Time [sec]
IWATE-55461EW @ MCE : Floor 2
Strain [%]
Time [sec]
IWATE-55461EW @ MCE : Floor 3
Strain [%]
Time [sec]
IWATE-55461NS @ MCE : Floor 1
Strain [%]
Time [sec]
IWATE-55461NS @ MCE : Floor 2
Strain [%]
Time [sec]
IWATE-55461NS @ MCE : Floor 3
Strain [%]
Time [sec]

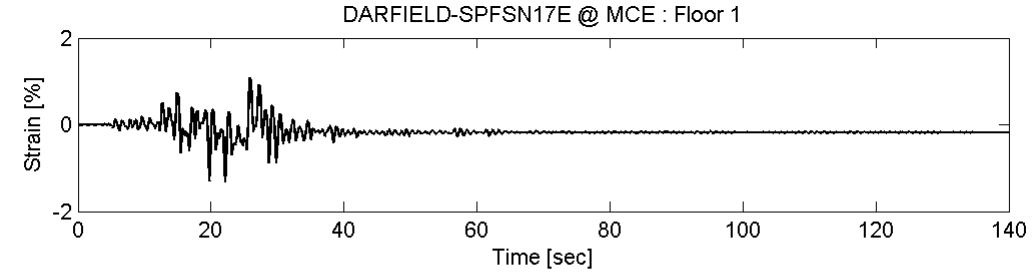
DARFIELD-SPFSN17E @ MCE : Floor 1
Strain [%]
Time [sec]

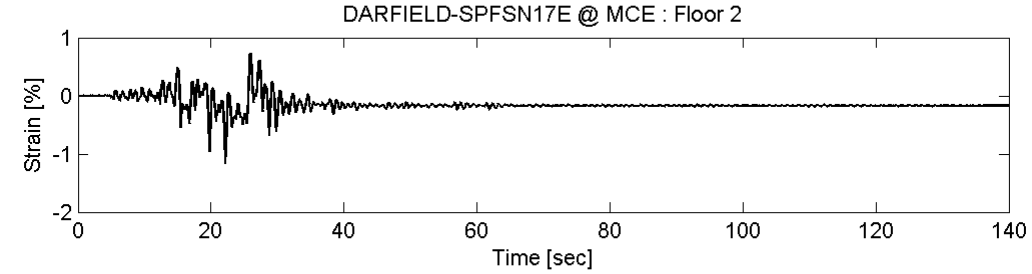
DARFIELD-SPFSN17E @ MCE : Floor 2
Strain [%]
Time [sec]

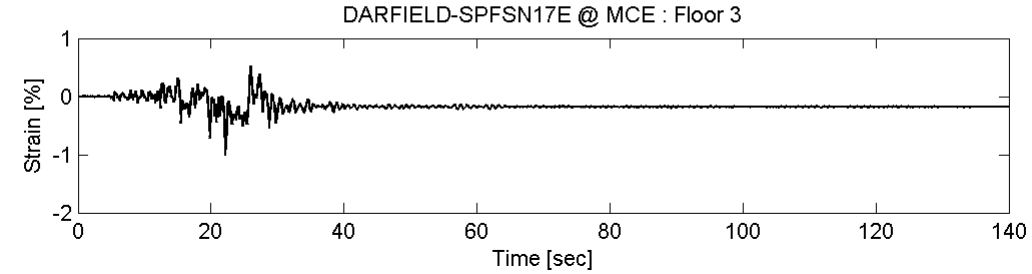
DARFIELD-SPFSN17E @ MCE : Floor 3
Strain [%]
Time [sec]

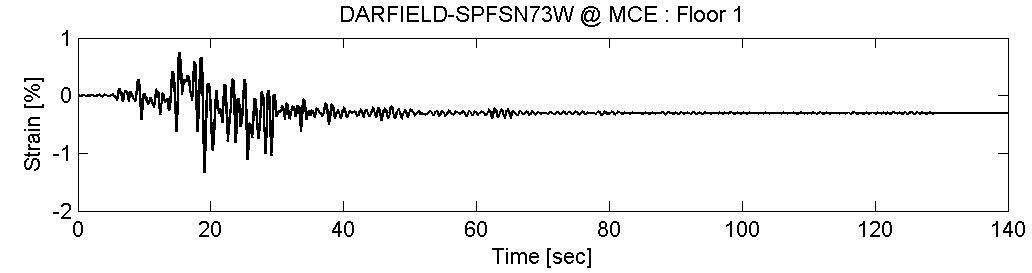
DARFIELD-SPFSN73W @ MCE : Floor 1
Strain [%]
Time [sec]

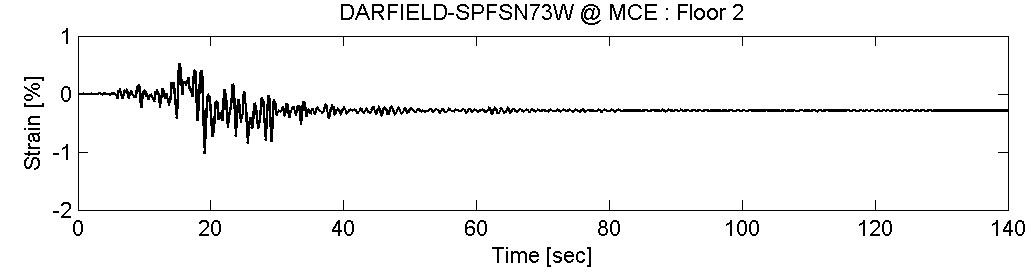
DARFIELD-SPFSN73W @ MCE : Floor 2
Strain [%]
Time [sec]

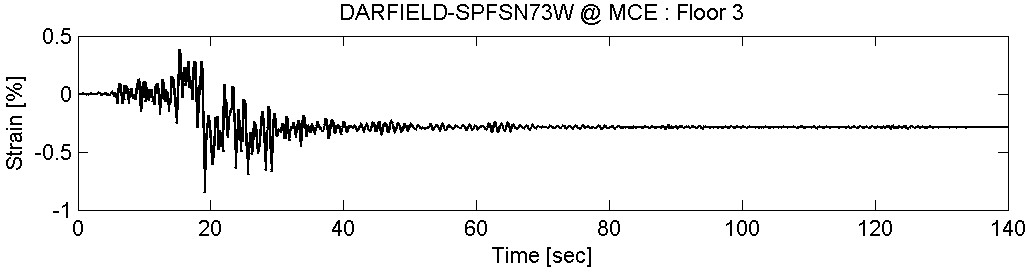
DARFIELD-SPFSN73W @ MCE : Floor 3
Strain [%]
Time [sec]

Appendix D
MC Rotation of Prototype FTMF

A three-storey office prototype building located in Los Angeles, California, is designed using the proposed equivalent energy design procedure (EEDP) from Chapter 2. The seismic force resisting system (SFRS) is the proposed fused truss moment frame (FTMF) from Chapter 3. Within the FTMF, the secondary SFRS is mainly the moment connections (MCs) located at the truss top chords. Nonlinear dynamic analysis is conducted using the ground motions presetned in Table 3.1. The figures in this appendix are the joint rotation time hisotries of the representative MC at each floor as the building is subjected to the motions scaled to the service level earthquake (SLE), designed based earthquake (DBE), and maximum considered earthquake (MCE) shaking intensities.

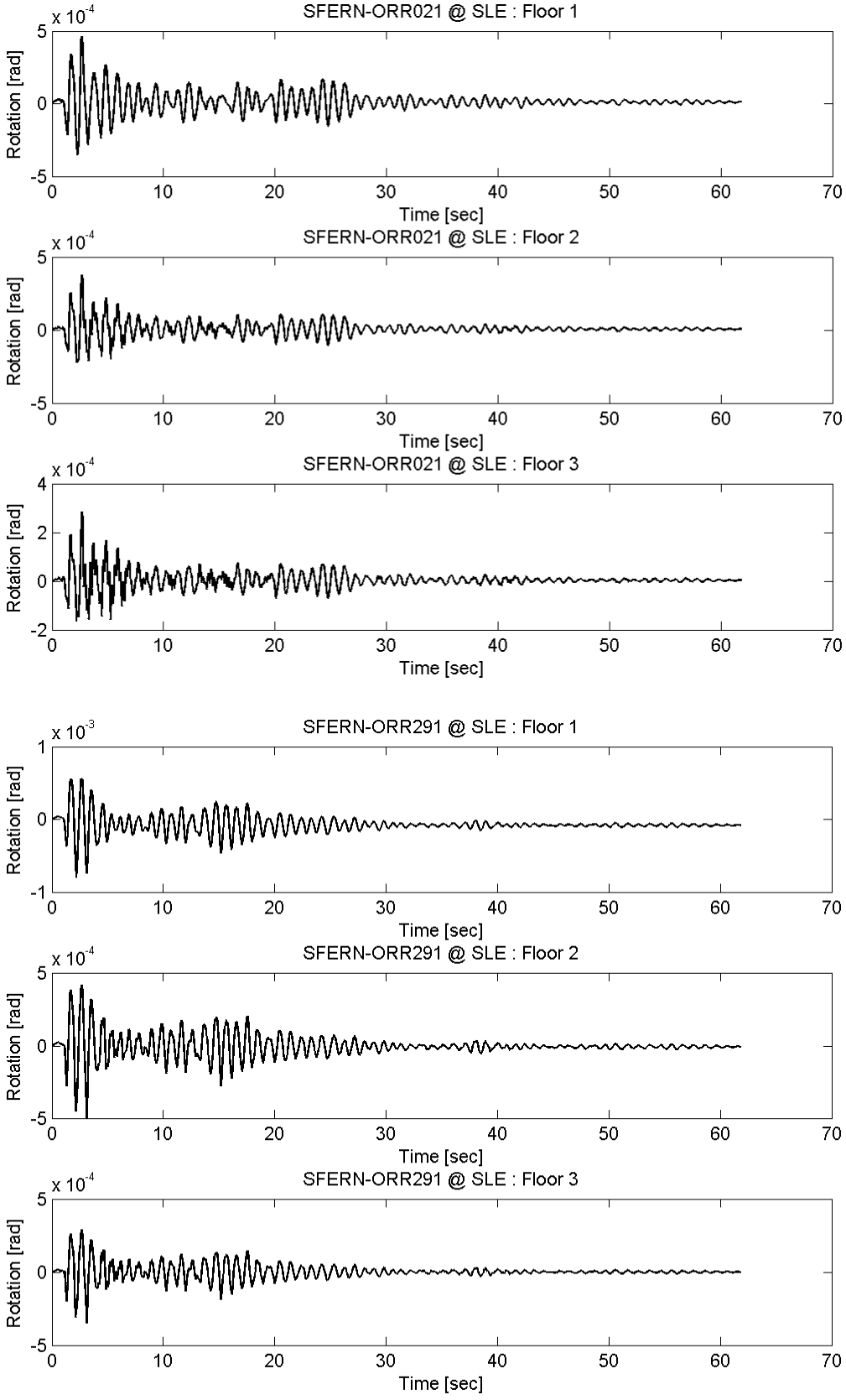
SFERN-ORR021 @ SLE : Floor 1
x 10^-4
Rotation [rad]
Time [sec]
SFERN-ORR021 @ SLE : Floor 2
x 10^-4
Rotation [rad]
Time [sec]
SFERN-ORR021 @ SLE : Floor 3
x 10^-4
Rotation [rad]
Time [sec]
SFERN-ORR291 @ SLE : Floor 1
x 10^-3
Rotation [rad]
Time [sec]
SFERN-ORR291 @ SLE : Floor 2
x 10^-4
Rotation [rad]
Time [sec]
SFERN-ORR291 @ SLE : Floor 3
x 10^-4
Rotation [rad]
Time [sec]

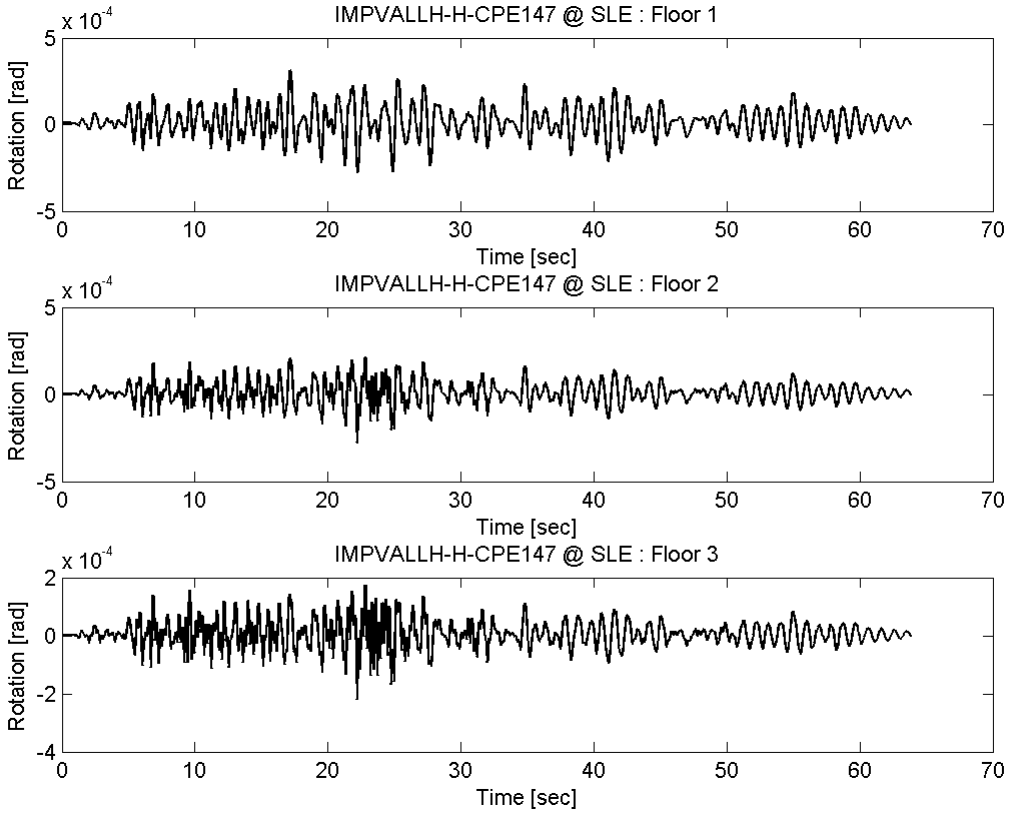
IMPVALLH-H-CPE147 @ SLE : Floor 1
x 10^-4
Rotation [rad]
Time [sec]
IMPVALLH-H-CPE147 @ SLE : Floor 2
x 10^-4
Rotation [rad]
Time [sec]
IMPVALLH-H-CPE147 @ SLE : Floor 3
x 10^-4
Rotation [rad]
Time [sec]

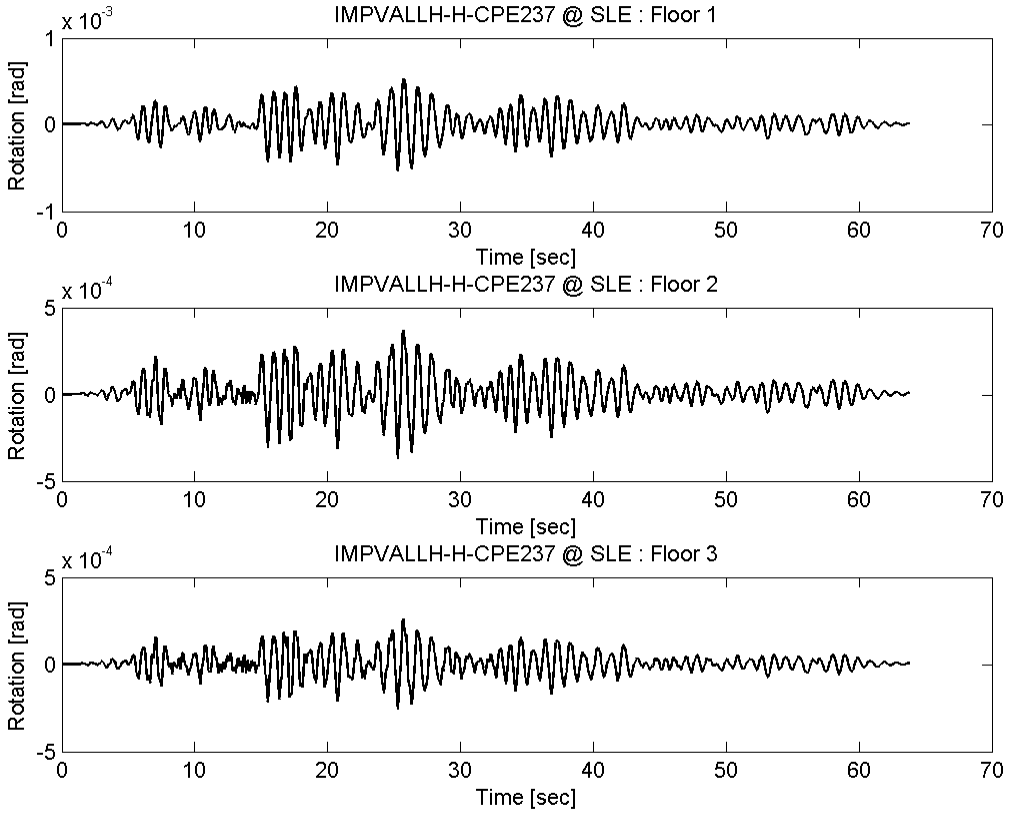
IMPVALLH-H-CPE237 @ SLE : Floor 1
x 10^-3
Rotation [rad]
Time [sec]
IMPVALLH-H-CPE237 @ SLE : Floor 2
x 10^-4
Rotation [rad]
Time [sec]
IMPVALLH-H-CPE237 @ SLE : Floor 3
x 10^-4
Rotation [rad]
Time [sec]

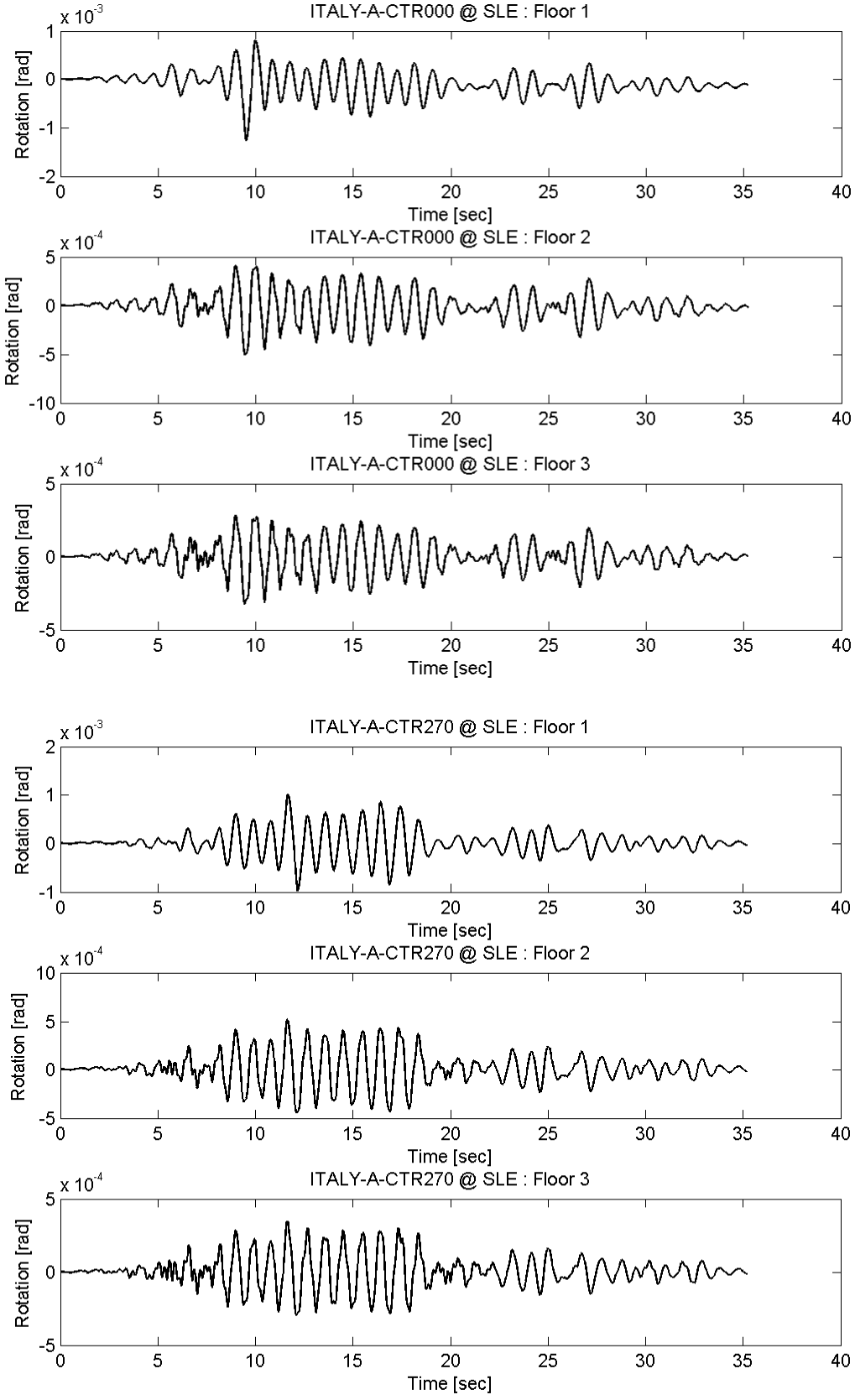
ITALY-A-CTR000 @ SLE : Floor 1
x 10^-3
Rotation [rad]
Time [sec]
ITALY-A-CTR000 @ SLE : Floor 2
x 10^-4
Rotation [rad]
Time [sec]
ITALY-A-CTR000 @ SLE : Floor 3
x 10^-4
Rotation [rad]
Time [sec]
ITALY-A-CTR270 @ SLE : Floor 1
x 10^-3
Rotation [rad]
Time [sec]
ITALY-A-CTR270 @ SLE : Floor 2
x 10^-4
Rotation [rad]
Time [sec]
ITALY-A-CTR270 @ SLE : Floor 3
x 10^-4
Rotation [rad]
Time [sec]

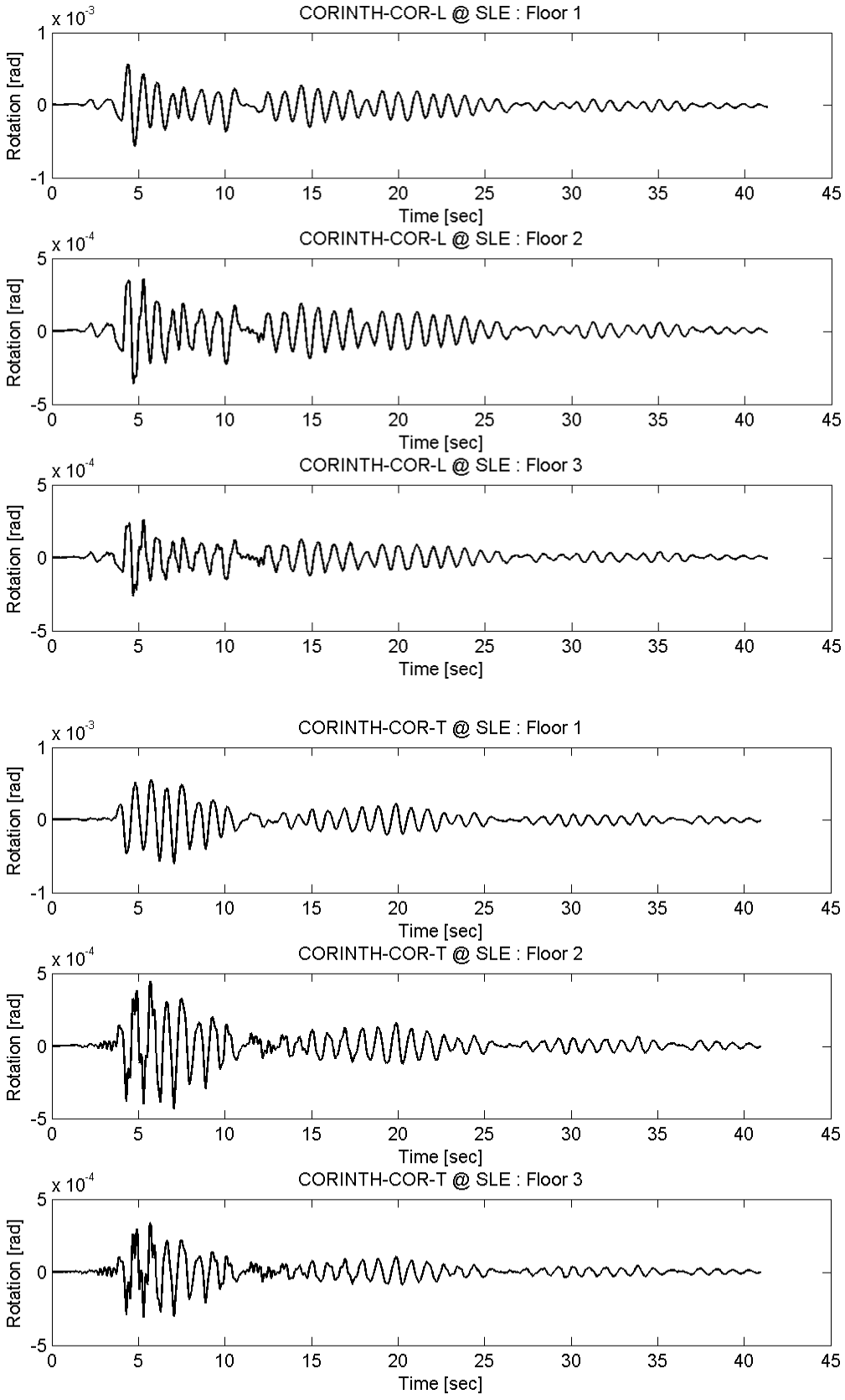
CORINTH-COR-L @ SLE : Floor 1
x 10^-3
Rotation [rad]
Time [sec]
CORINTH-COR-L @ SLE : Floor 2
x 10^-4
Rotation [rad]
Time [sec]
CORINTH-COR-L @ SLE : Floor 3
x 10^-4
Rotation [rad]
Time [sec]
CORINTH-COR-T @ SLE : Floor 1
x 10^-3
Rotation [rad]
Time [sec]
CORINTH-COR-T @ SLE : Floor 2
x 10^-4
Rotation [rad]
Time [sec]
CORINTH-COR-T @ SLE : Floor 3
x 10^-4
Rotation [rad]
Time [sec]

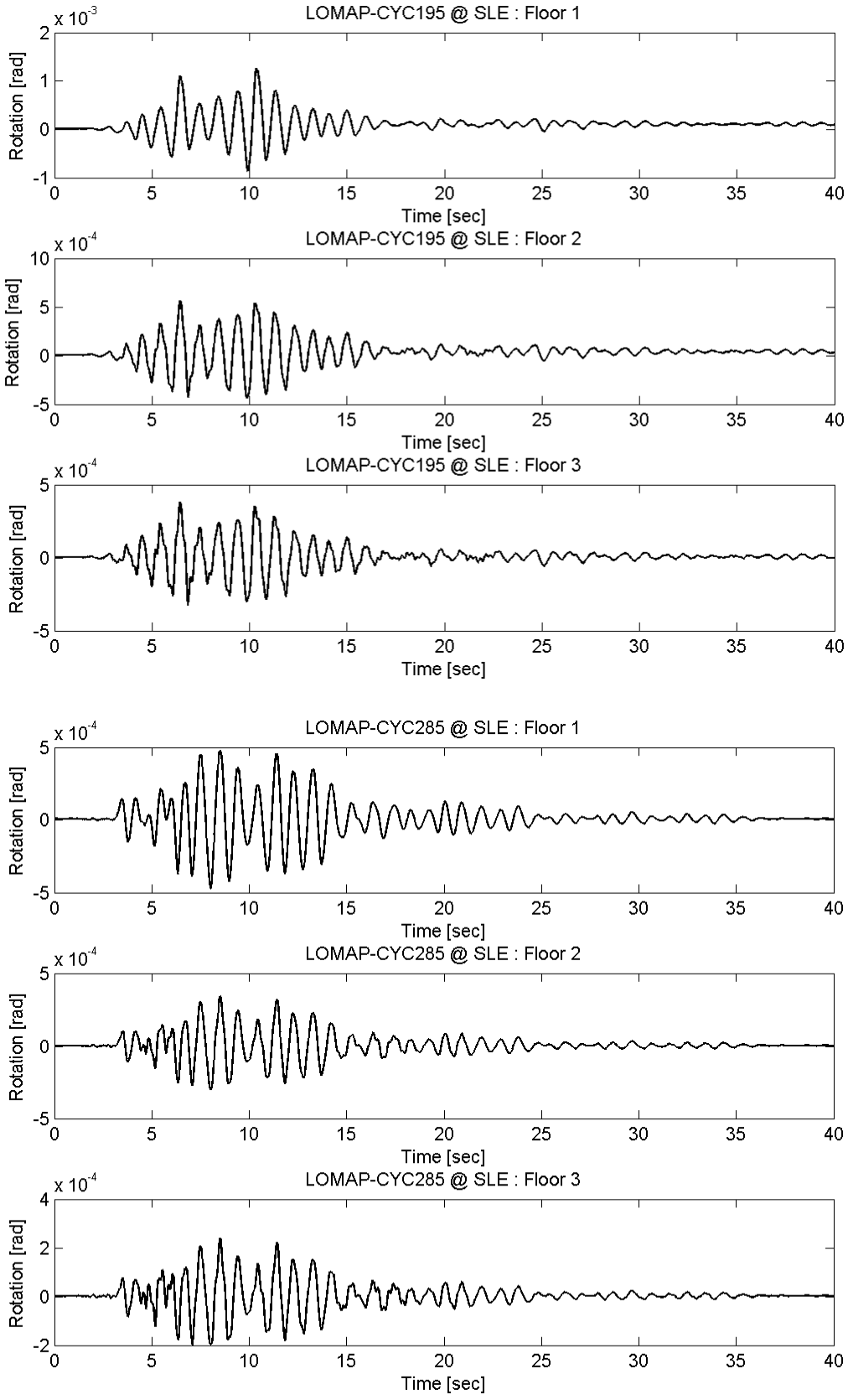
LOMAP-CYC195 @ SLE : Floor 1
x 10^-3
Rotation [rad]
Time [sec]
LOMAP-CYC195 @ SLE : Floor 2
x 10^-4
Rotation [rad]
Time [sec]
LOMAP-CYC195 @ SLE : Floor 3
x 10^-4
Rotation [rad]
Time [sec]
LOMAP-CYC285 @ SLE : Floor 1
x 10^-4
Rotation [rad]
Time [sec]
LOMAP-CYC285 @ SLE : Floor 2
x 10^-4
Rotation [rad]
Time [sec]
LOMAP-CYC285 @ SLE : Floor 3
x 10^-4
Rotation [rad]
Time [sec]

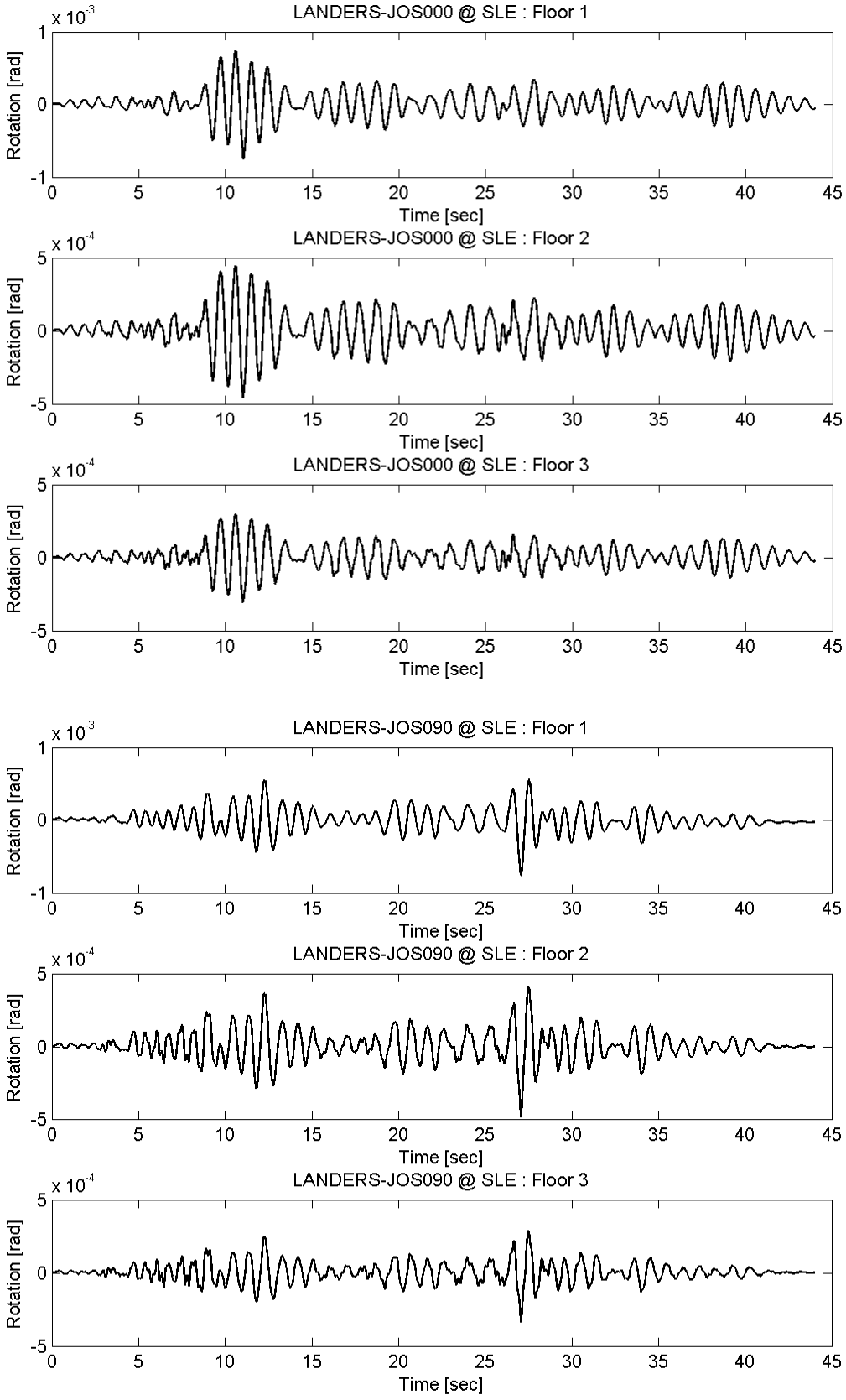
LANDERS-JOS000 @ SLE : Floor 1
x 10^-3
Rotation [rad]
Time [sec]
LANDERS-JOS000 @ SLE : Floor 2
x 10^-4
Rotation [rad]
Time [sec]
LANDERS-JOS000 @ SLE : Floor 3
x 10^-4
Rotation [rad]
Time [sec]
LANDERS-JOS090 @ SLE : Floor 1
x 10^-3
Rotation [rad]
Time [sec]
LANDERS-JOS090 @ SLE : Floor 2
x 10^-4
Rotation [rad]
Time [sec]
LANDERS-JOS090 @ SLE : Floor 3
x 10^-4
Rotation [rad]
Time [sec]

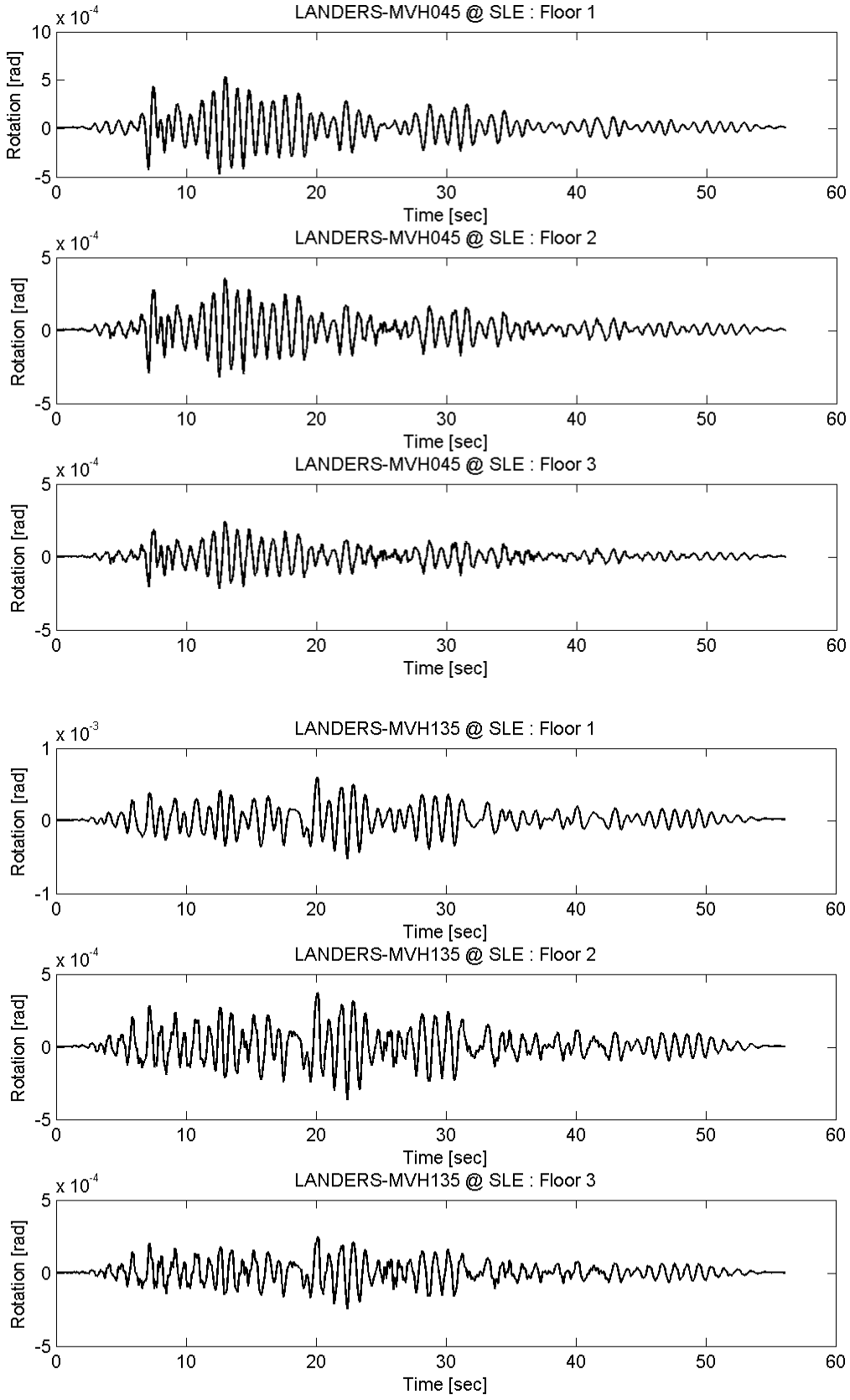
LANDERS-MVH045 @ SLE : Floor 1
x 10^-4
Rotation [rad]
Time [sec]
LANDERS-MVH045 @ SLE : Floor 2
x 10^-4
Rotation [rad]
Time [sec]
LANDERS-MVH045 @ SLE : Floor 3
x 10^-4
Rotation [rad]
Time [sec]
LANDERS-MVH135 @ SLE : Floor 1
x 10^-3
Rotation [rad]
Time [sec]
LANDERS-MVH135 @ SLE : Floor 2
x 10^-4
Rotation [rad]
Time [sec]
LANDERS-MVH135 @ SLE : Floor 3
x 10^-4
Rotation [rad]
Time [sec]

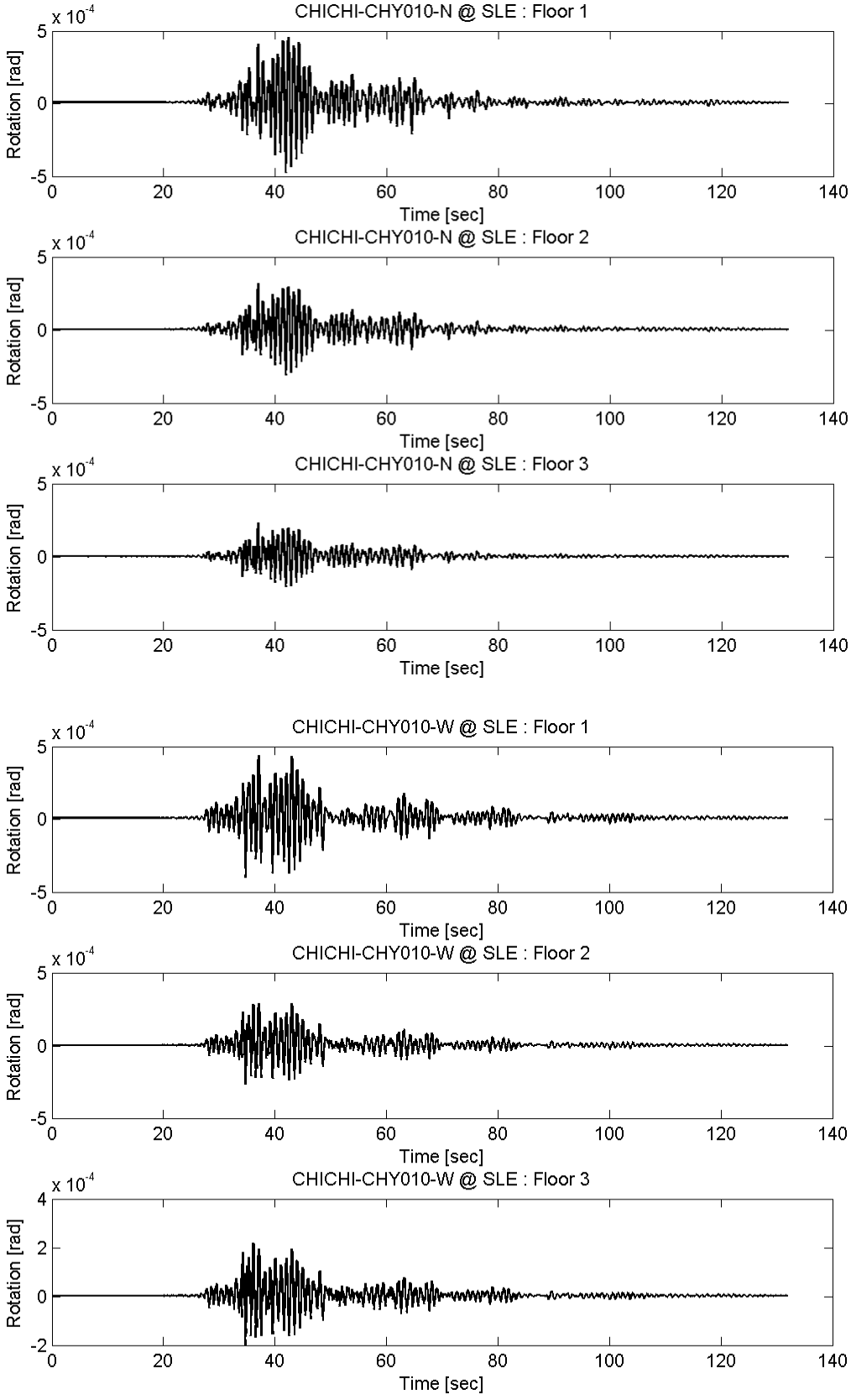
CHICHI-CHY010-N @ SLE : Floor 1
CHICHI-CHY010-N @ SLE : Floor 2
CHICHI-CHY010-N @ SLE : Floor 3
CHICHI-CHY010-W @ SLE : Floor 1
CHICHI-CHY010-W @ SLE : Floor 2
CHICHI-CHY010-W @ SLE : Floor 3
x 10^-4
Rotation [rad]
Time [sec]

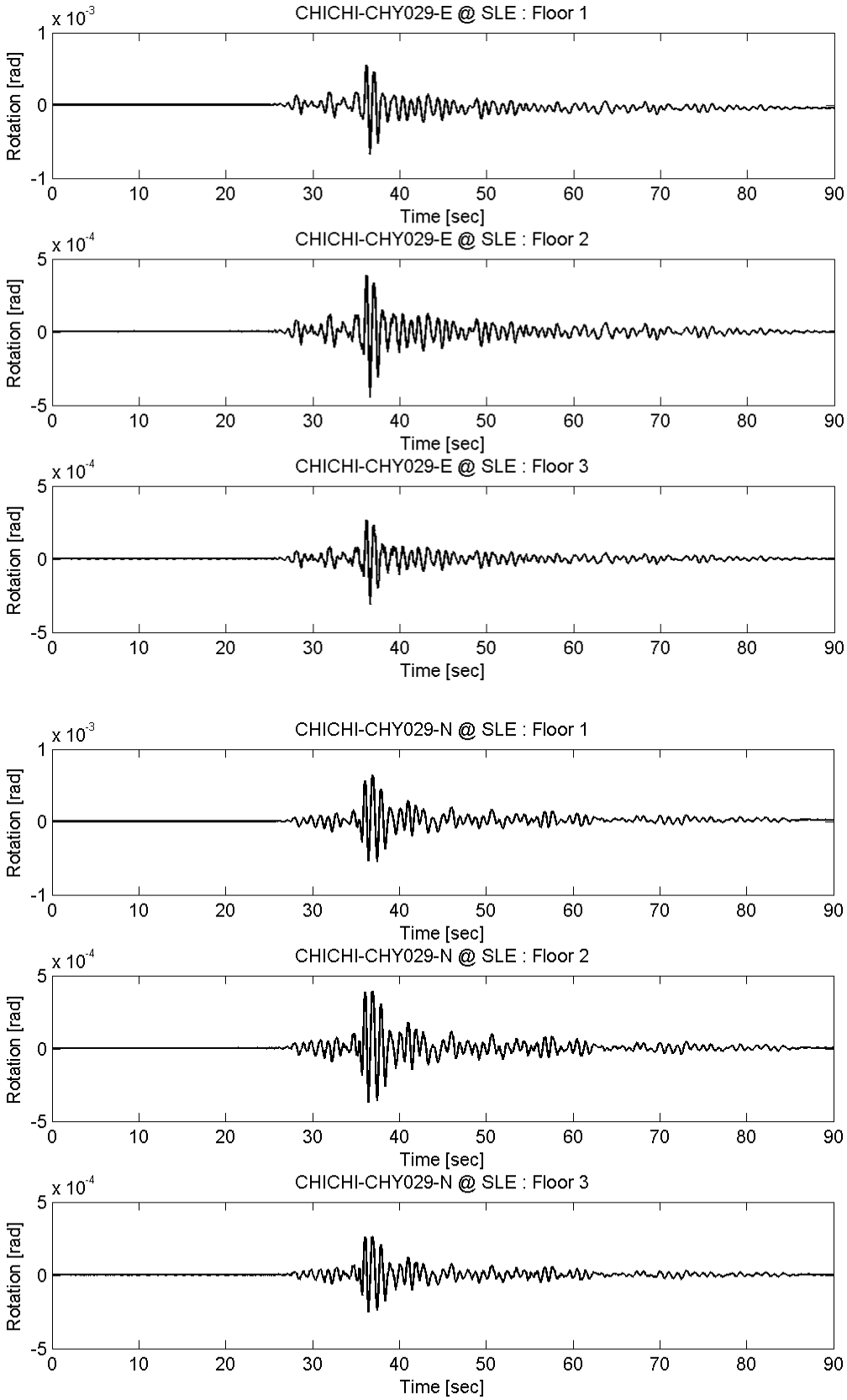
CHICHI-CHY029-E @ SLE : Floor 1
x 10^-3
Rotation [rad]
Time [sec]
CHICHI-CHY029-E @ SLE : Floor 2
x 10^-4
Rotation [rad]
Time [sec]
CHICHI-CHY029-E @ SLE : Floor 3
x 10^-4
Rotation [rad]
Time [sec]
CHICHI-CHY029-N @ SLE : Floor 1
x 10^-3
Rotation [rad]
Time [sec]
CHICHI-CHY029-N @ SLE : Floor 2
x 10^-4
Rotation [rad]
Time [sec]
CHICHI-CHY029-N @ SLE : Floor 3
x 10^-4
Rotation [rad]
Time [sec]

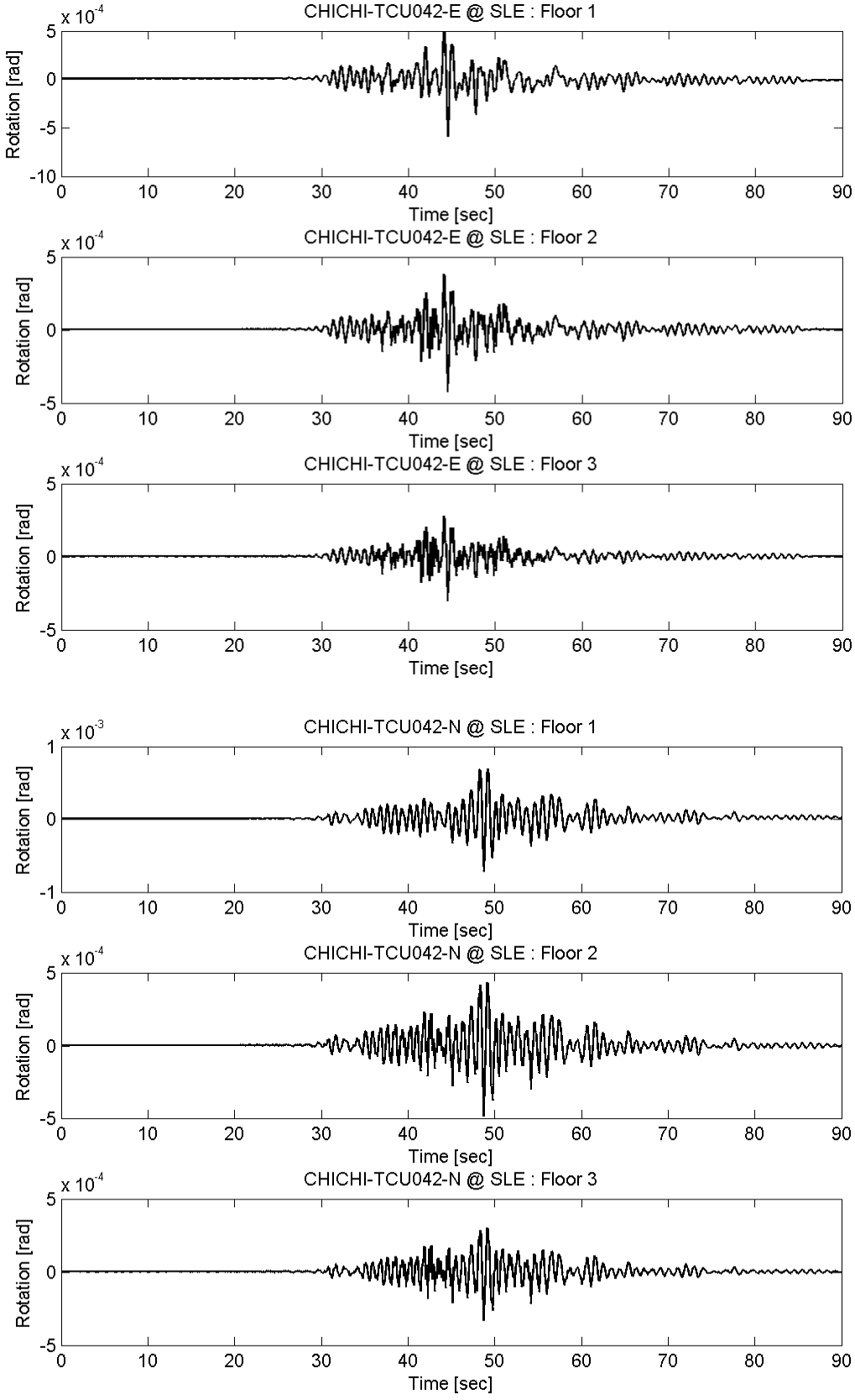
CHICHI-TCU042-E @ SLE : Floor 1
x 10^-4
Rotation [rad]
Time [sec]
CHICHI-TCU042-E @ SLE : Floor 2
x 10^-4
Rotation [rad]
Time [sec]
CHICHI-TCU042-E @ SLE : Floor 3
x 10^-4
Rotation [rad]
Time [sec]
CHICHI-TCU042-N @ SLE : Floor 1
x 10^-3
Rotation [rad]
Time [sec]
CHICHI-TCU042-N @ SLE : Floor 2
x 10^-4
Rotation [rad]
Time [sec]
CHICHI-TCU042-N @ SLE : Floor 3
x 10^-4
Rotation [rad]
Time [sec]

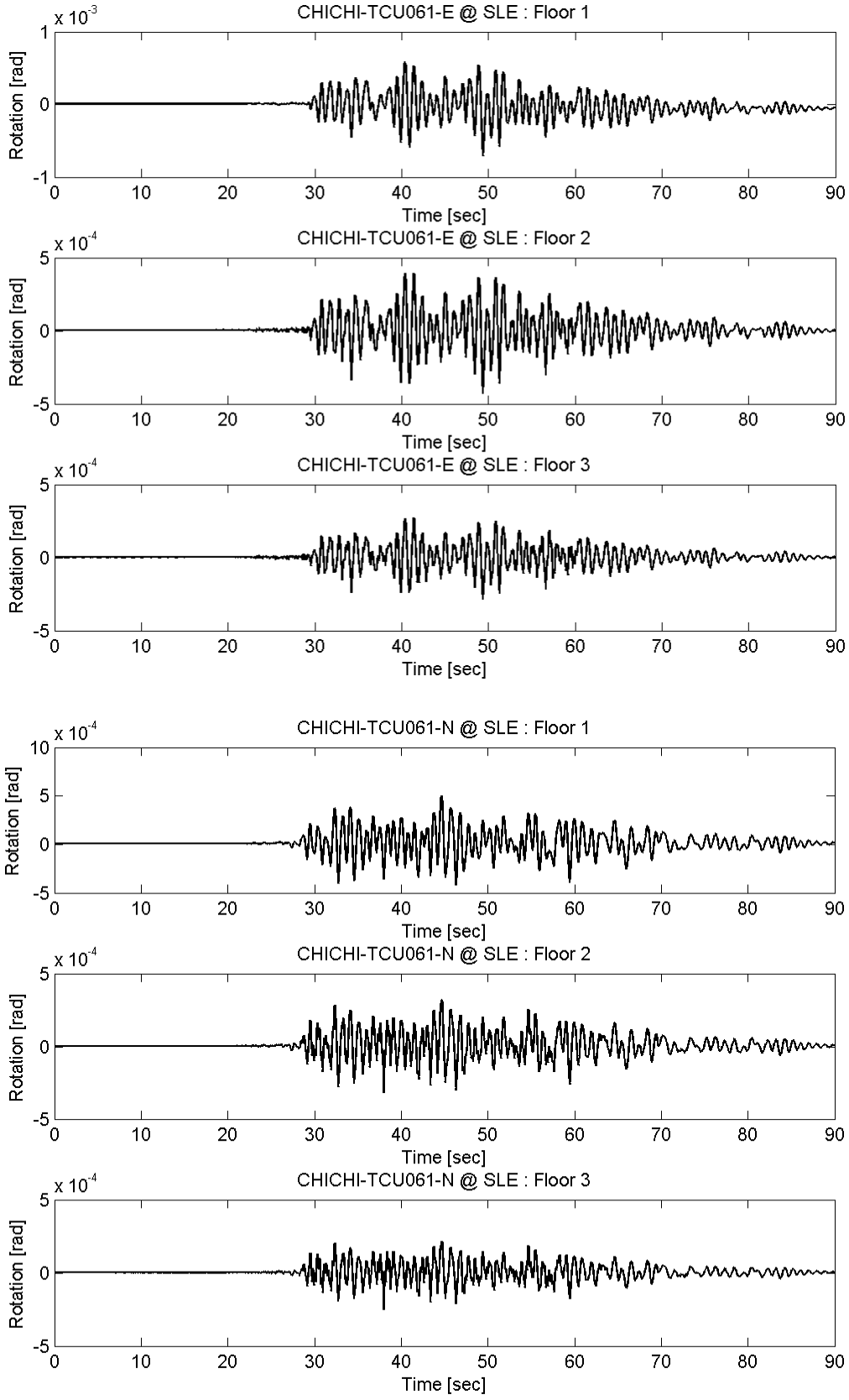
CHICHI-TCU061-E @ SLE : Floor 1
x 10^-3
Rotation [rad]
Time [sec]
CHICHI-TCU061-E @ SLE : Floor 2
x 10^-4
Rotation [rad]
Time [sec]
CHICHI-TCU061-E @ SLE : Floor 3
x 10^-4
Rotation [rad]
Time [sec]
CHICHI-TCU061-N @ SLE : Floor 1
x 10^-4
Rotation [rad]
Time [sec]
CHICHI-TCU061-N @ SLE : Floor 2
x 10^-4
Rotation [rad]
Time [sec]
CHICHI-TCU061-N @ SLE : Floor 3
x 10^-4
Rotation [rad]
Time [sec]

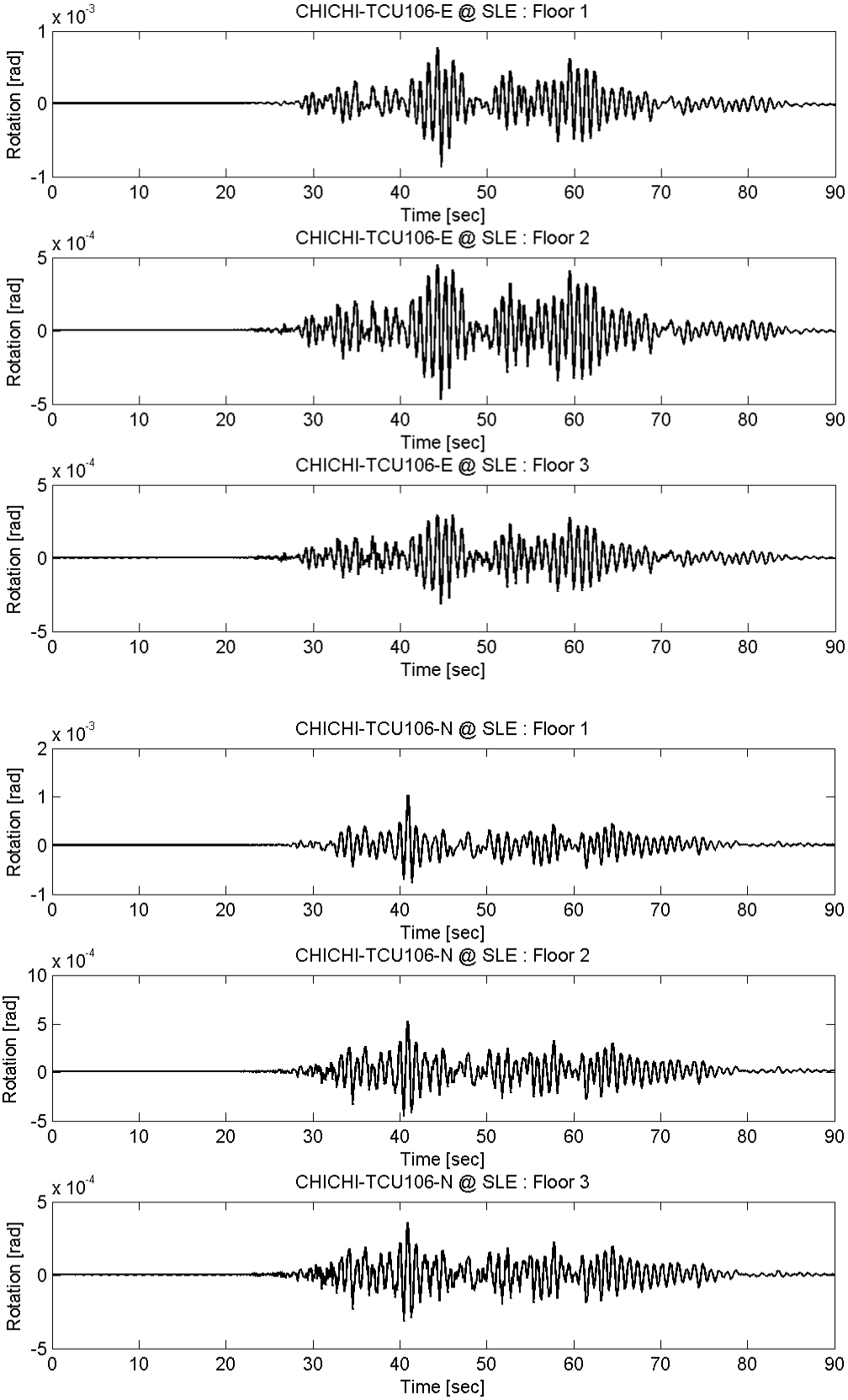
CHICHI-TCU106-E @ SLE : Floor 1
x 10^-3
Rotation [rad]
Time [sec]
CHICHI-TCU106-E @ SLE : Floor 2
x 10^-4
Rotation [rad]
Time [sec]
CHICHI-TCU106-E @ SLE : Floor 3
x 10^-4
Rotation [rad]
Time [sec]
CHICHI-TCU106-N @ SLE : Floor 1
x 10^-3
Rotation [rad]
Time [sec]
CHICHI-TCU106-N @ SLE : Floor 2
x 10^-4
Rotation [rad]
Time [sec]
CHICHI-TCU106-N @ SLE : Floor 3
x 10^-4
Rotation [rad]
Time [sec]

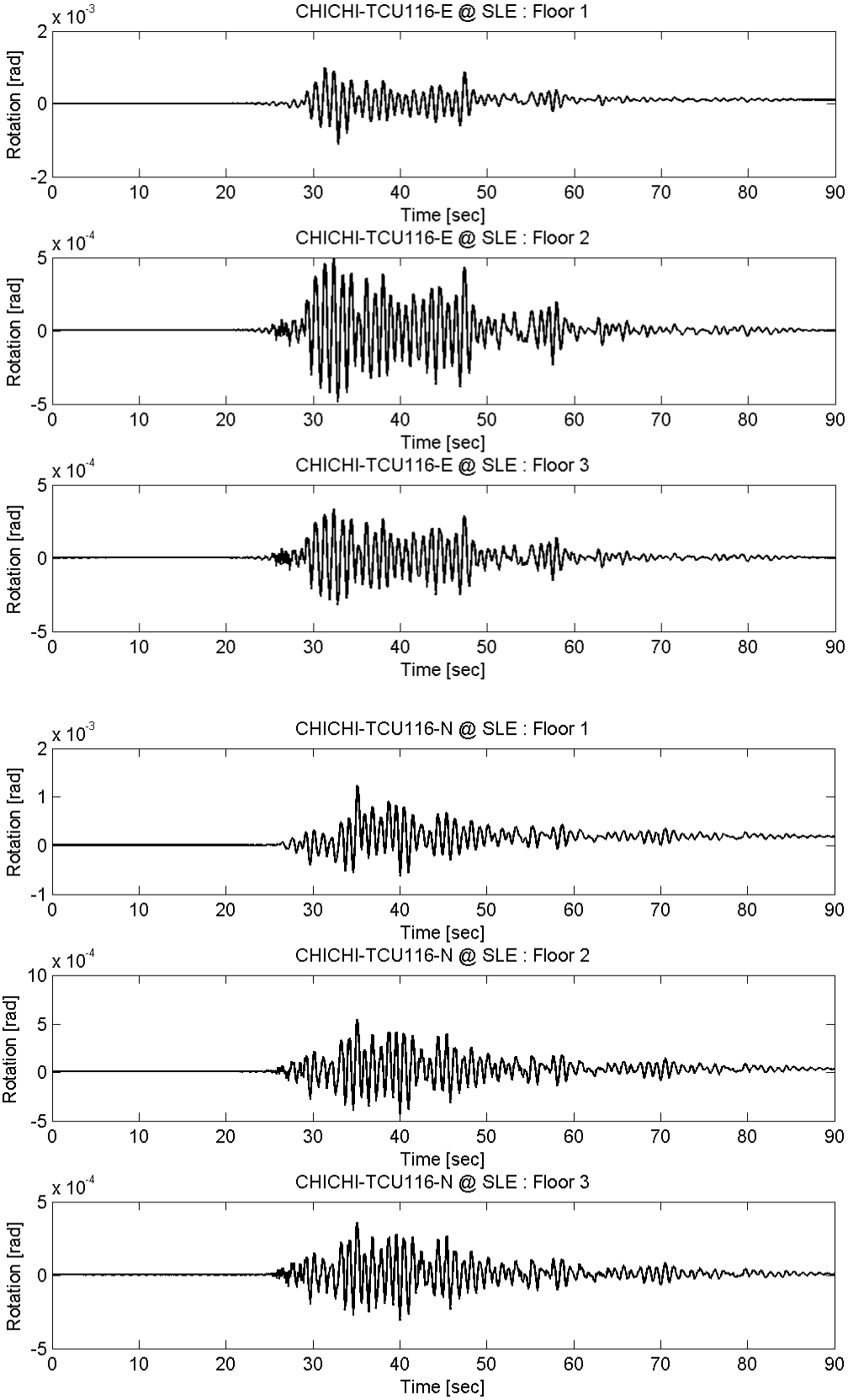
CHICHI-TCU116-E @ SLE : Floor 1
x 10^-3
Rotation [rad]
Time [sec]
CHICHI-TCU116-E @ SLE : Floor 2
x 10^-4
Rotation [rad]
Time [sec]
CHICHI-TCU116-E @ SLE : Floor 3
x 10^-4
Rotation [rad]
Time [sec]
CHICHI-TCU116-N @ SLE : Floor 1
x 10^-3
Rotation [rad]
Time [sec]
CHICHI-TCU116-N @ SLE : Floor 2
x 10^-4
Rotation [rad]
Time [sec]
CHICHI-TCU116-N @ SLE : Floor 3
x 10^-4
Rotation [rad]
Time [sec]

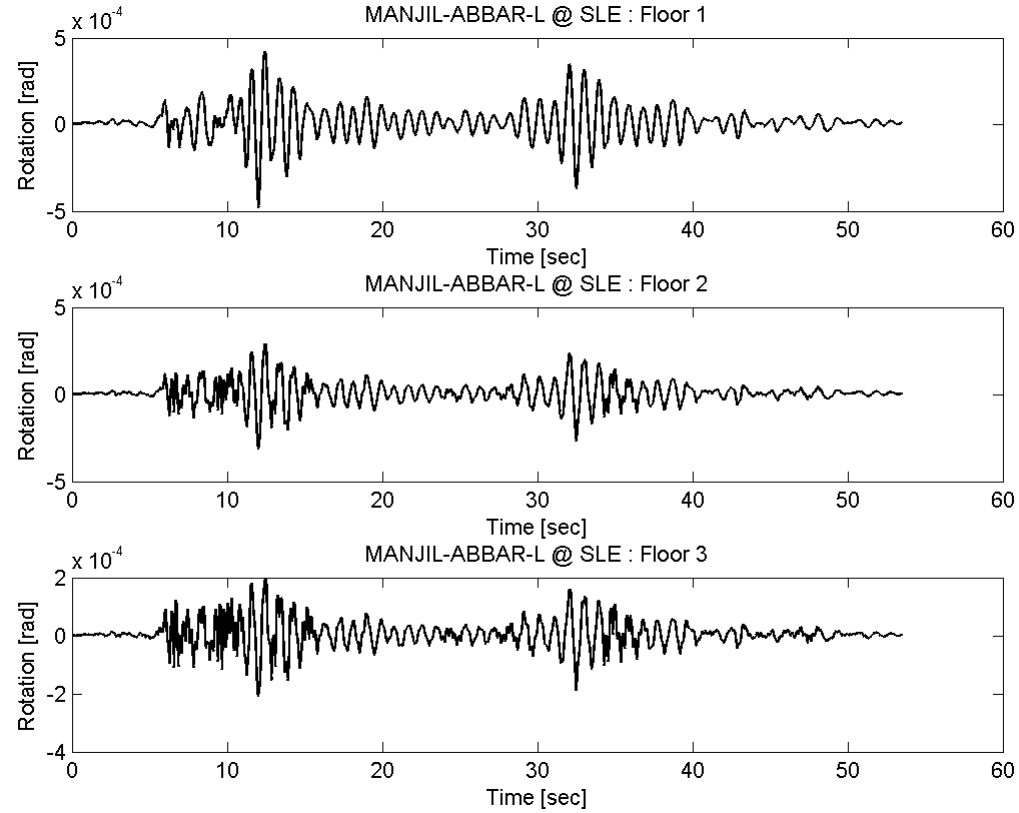
MANJIL-ABBAR-L @ SLE : Floor 1
MANJIL-ABBAR-L @ SLE : Floor 2
MANJIL-ABBAR-L @ SLE : Floor 3
Rotation [rad]
Time [sec]
x 10^-4

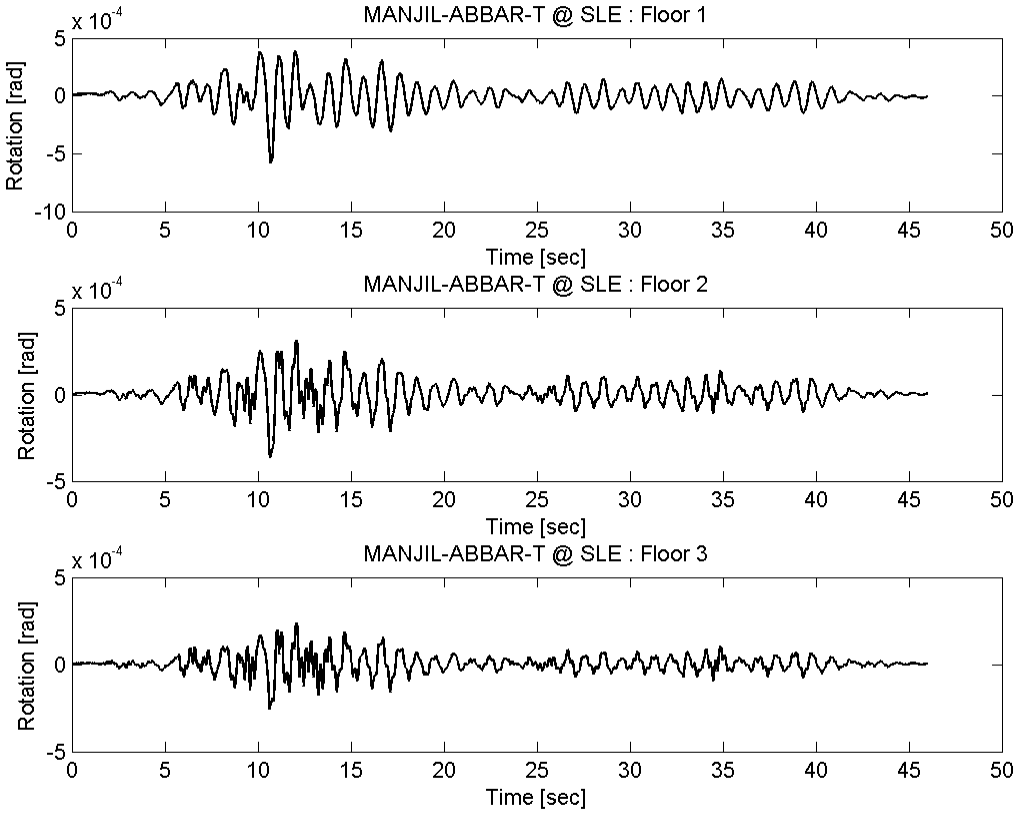
MANJIL-ABBAR-T @ SLE : Floor 1
MANJIL-ABBAR-T @ SLE : Floor 2
MANJIL-ABBAR-T @ SLE : Floor 3
Rotation [rad]
Time [sec]
x 10^-4

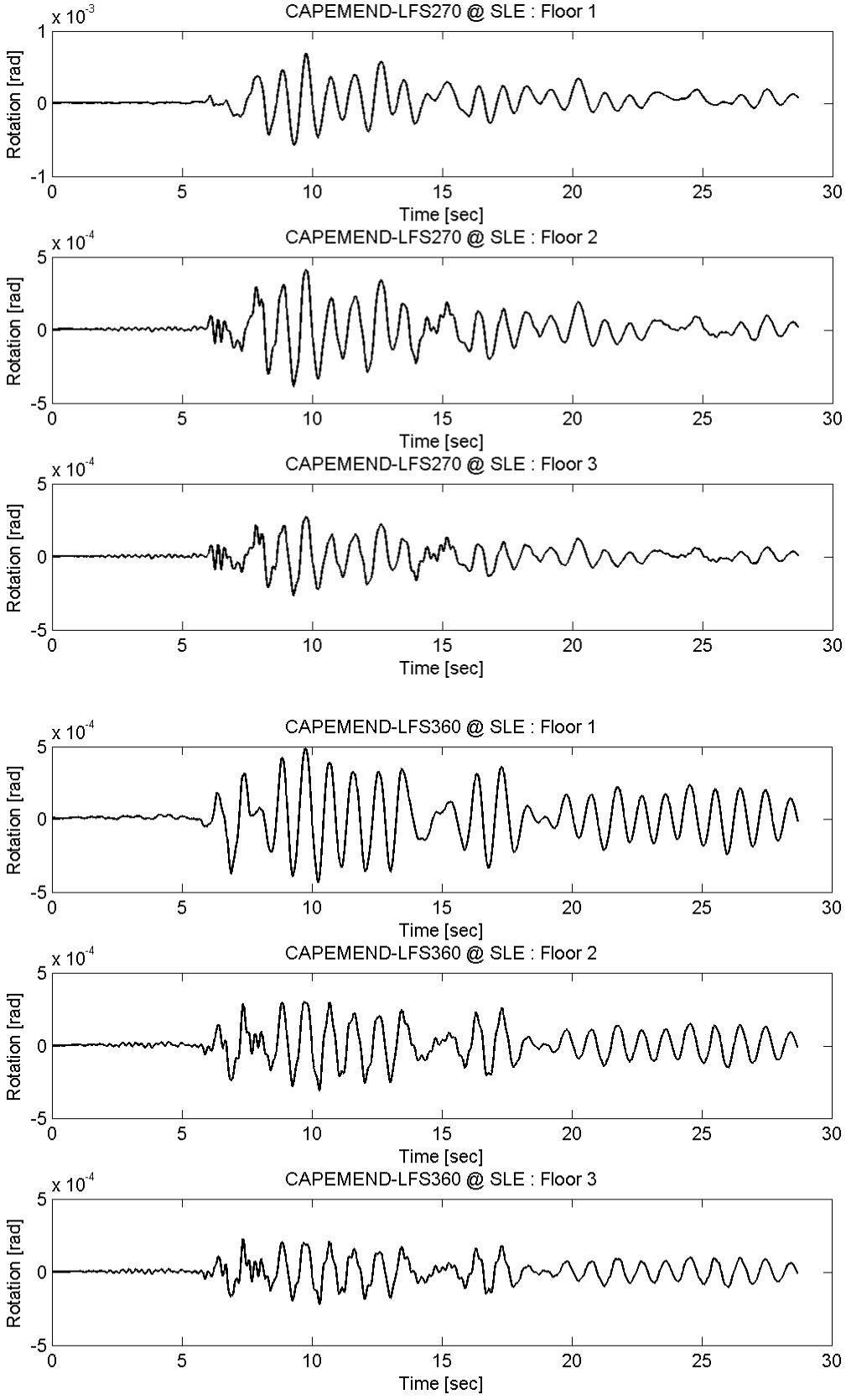
CAPEMEND-LFS270 @ SLE : Floor 1
x 10^-3
Rotation [rad]
Time [sec]
CAPEMEND-LFS270 @ SLE : Floor 2
x 10^-4
Rotation [rad]
Time [sec]
CAPEMEND-LFS270 @ SLE : Floor 3
x 10^-4
Rotation [rad]
Time [sec]
CAPEMEND-LFS360 @ SLE : Floor 1
x 10^-4
Rotation [rad]
Time [sec]
CAPEMEND-LFS360 @ SLE : Floor 2
x 10^-4
Rotation [rad]
Time [sec]
CAPEMEND-LFS360 @ SLE : Floor 3
x 10^-4
Rotation [rad]
Time [sec]

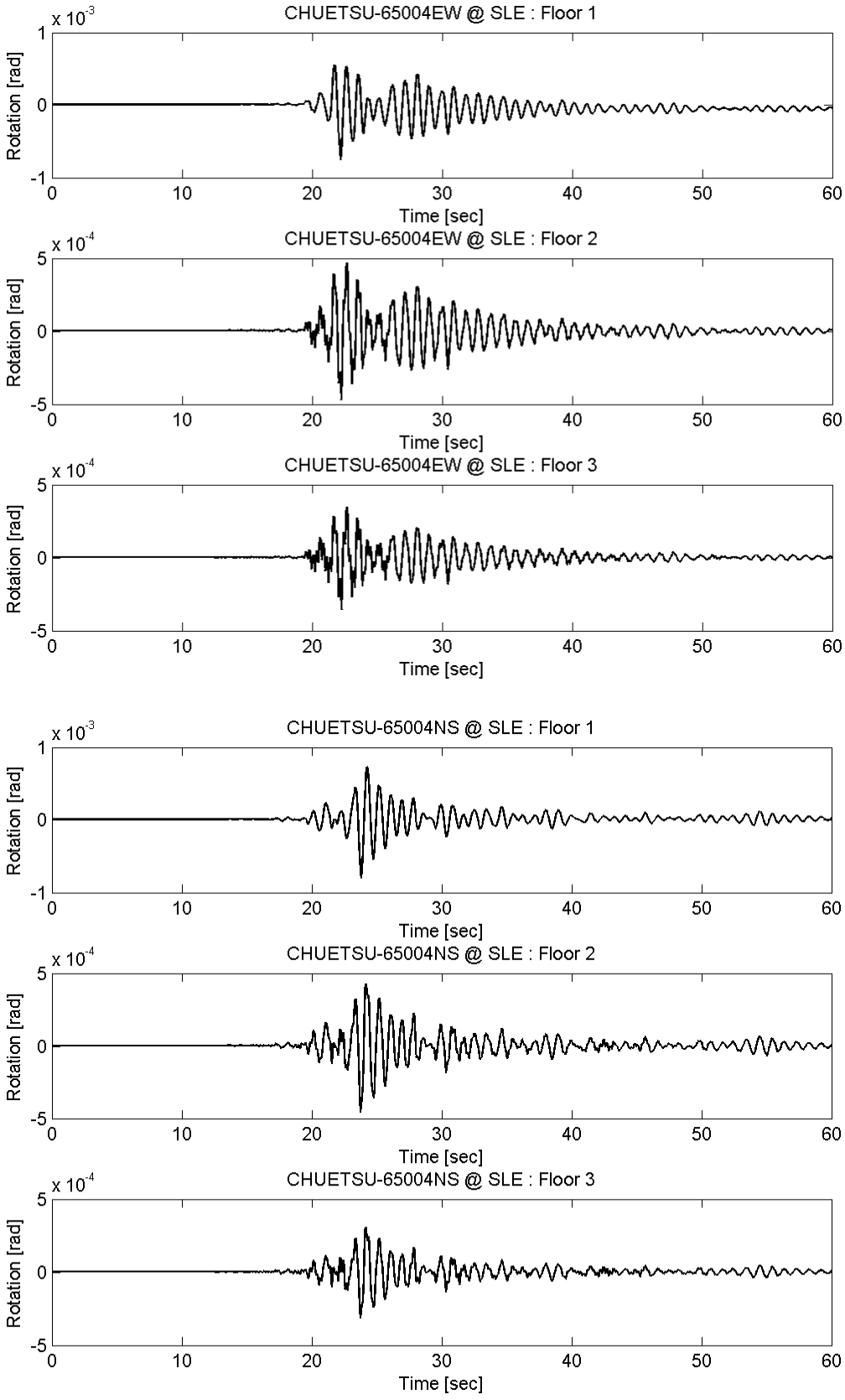
CHUETSU-65004EW @ SLE : Floor 1
x 10^-3
Rotation [rad]
Time [sec]
CHUETSU-65004EW @ SLE : Floor 2
x 10^-4
Rotation [rad]
Time [sec]
CHUETSU-65004EW @ SLE : Floor 3
x 10^-4
Rotation [rad]
Time [sec]
CHUETSU-65004NS @ SLE : Floor 1
x 10^-3
Rotation [rad]
Time [sec]
CHUETSU-65004NS @ SLE : Floor 2
x 10^-4
Rotation [rad]
Time [sec]
CHUETSU-65004NS @ SLE : Floor 3
x 10^-4
Rotation [rad]
Time [sec]

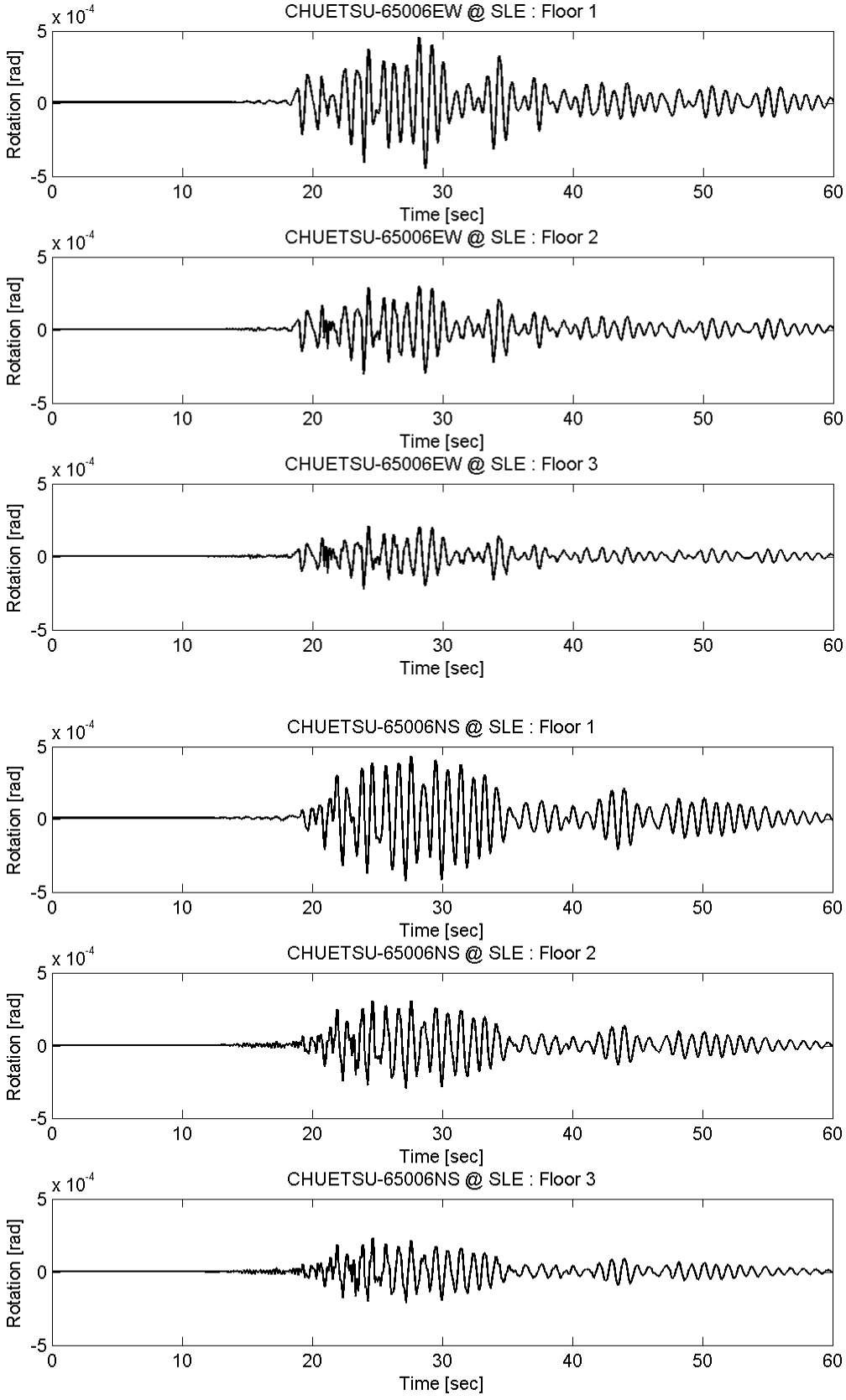
CHUETSU-65006EW @ SLE : Floor 1
CHUETSU-65006EW @ SLE : Floor 2
CHUETSU-65006EW @ SLE : Floor 3
CHUETSU-65006NS @ SLE : Floor 1
CHUETSU-65006NS @ SLE : Floor 2
CHUETSU-65006NS @ SLE : Floor 3
x 10^-4
Rotation [rad]
Time [sec]
5
0
-5
0
10
20
30
40
50
60

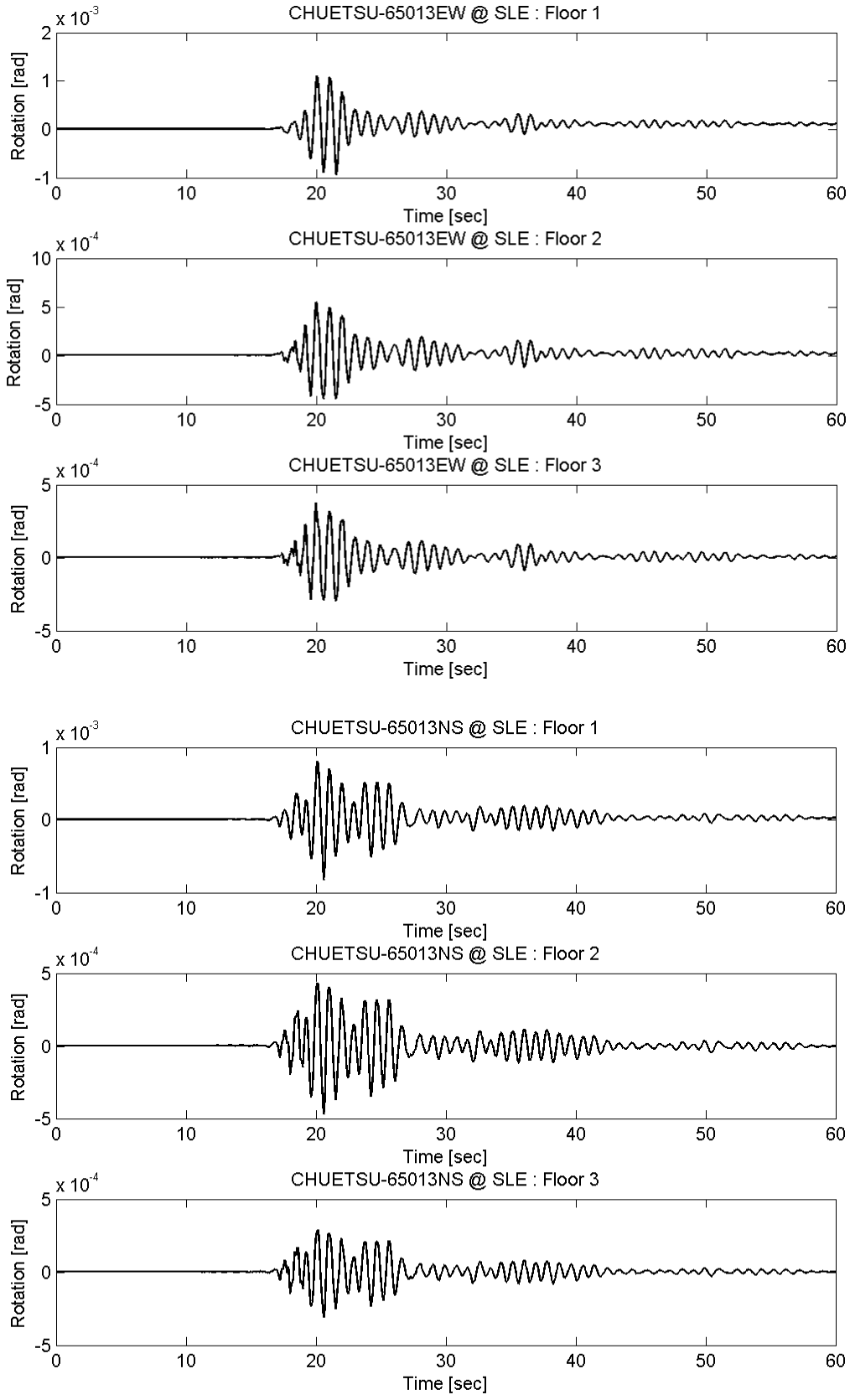
CHUETSU-65013EW @ SLE : Floor 1
x 10^-3
Rotation [rad]
Time [sec]
CHUETSU-65013EW @ SLE : Floor 2
x 10^-4
Rotation [rad]
Time [sec]
CHUETSU-65013EW @ SLE : Floor 3
x 10^-4
Rotation [rad]
Time [sec]
CHUETSU-65013NS @ SLE : Floor 1
x 10^-3
Rotation [rad]
Time [sec]
CHUETSU-65013NS @ SLE : Floor 2
x 10^-4
Rotation [rad]
Time [sec]
CHUETSU-65013NS @ SLE : Floor 3
x 10^-4
Rotation [rad]
Time [sec]

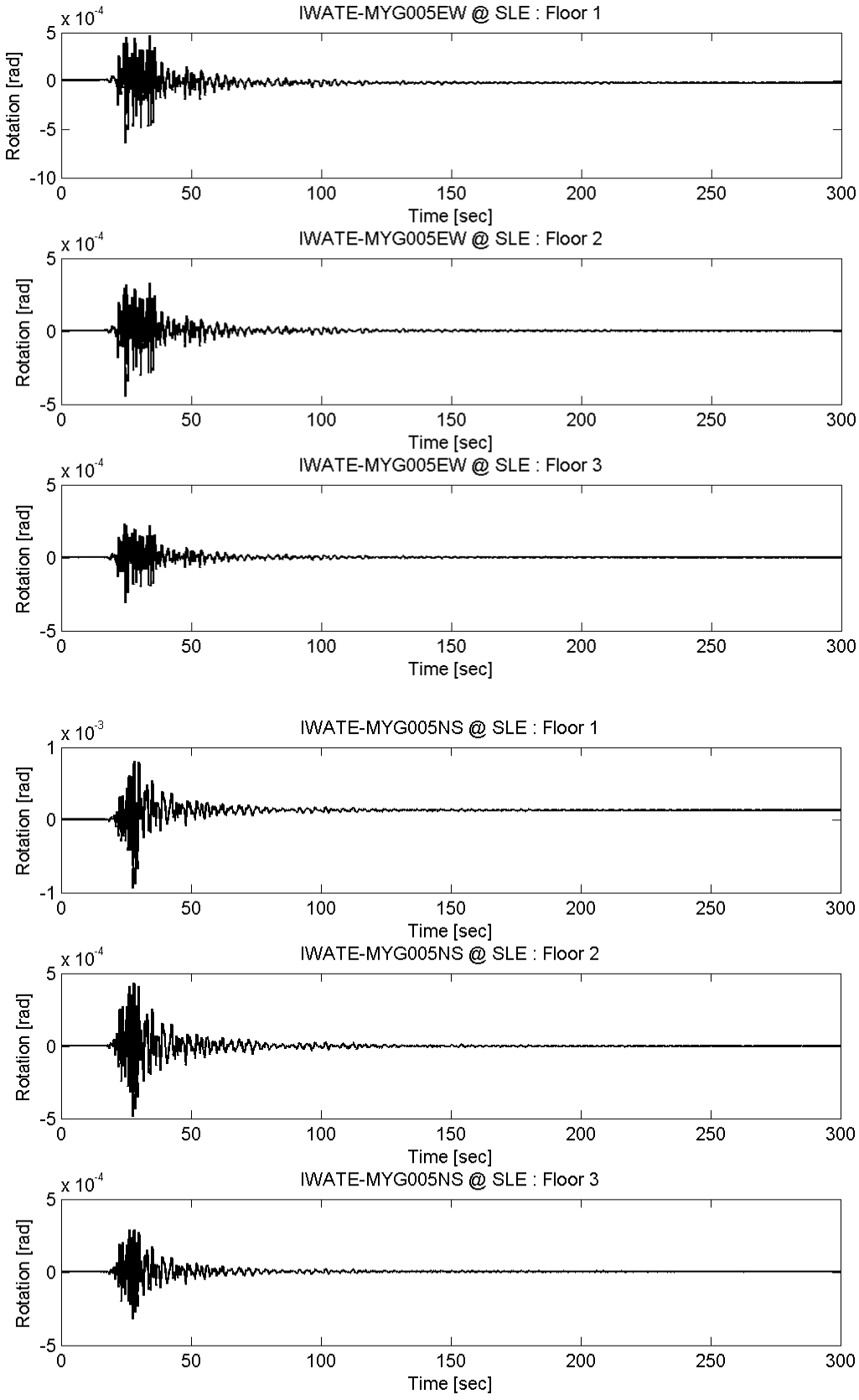
IWATE-MYG005EW @ SLE : Floor 1
x 10^-4
Rotation [rad]
Time [sec]
IWATE-MYG005EW @ SLE : Floor 2
x 10^-4
Rotation [rad]
Time [sec]
IWATE-MYG005EW @ SLE : Floor 3
x 10^-4
Rotation [rad]
Time [sec]
IWATE-MYG005NS @ SLE : Floor 1
x 10^-3
Rotation [rad]
Time [sec]
IWATE-MYG005NS @ SLE : Floor 2
x 10^-4
Rotation [rad]
Time [sec]
IWATE-MYG005NS @ SLE : Floor 3
x 10^-4
Rotation [rad]
Time [sec]

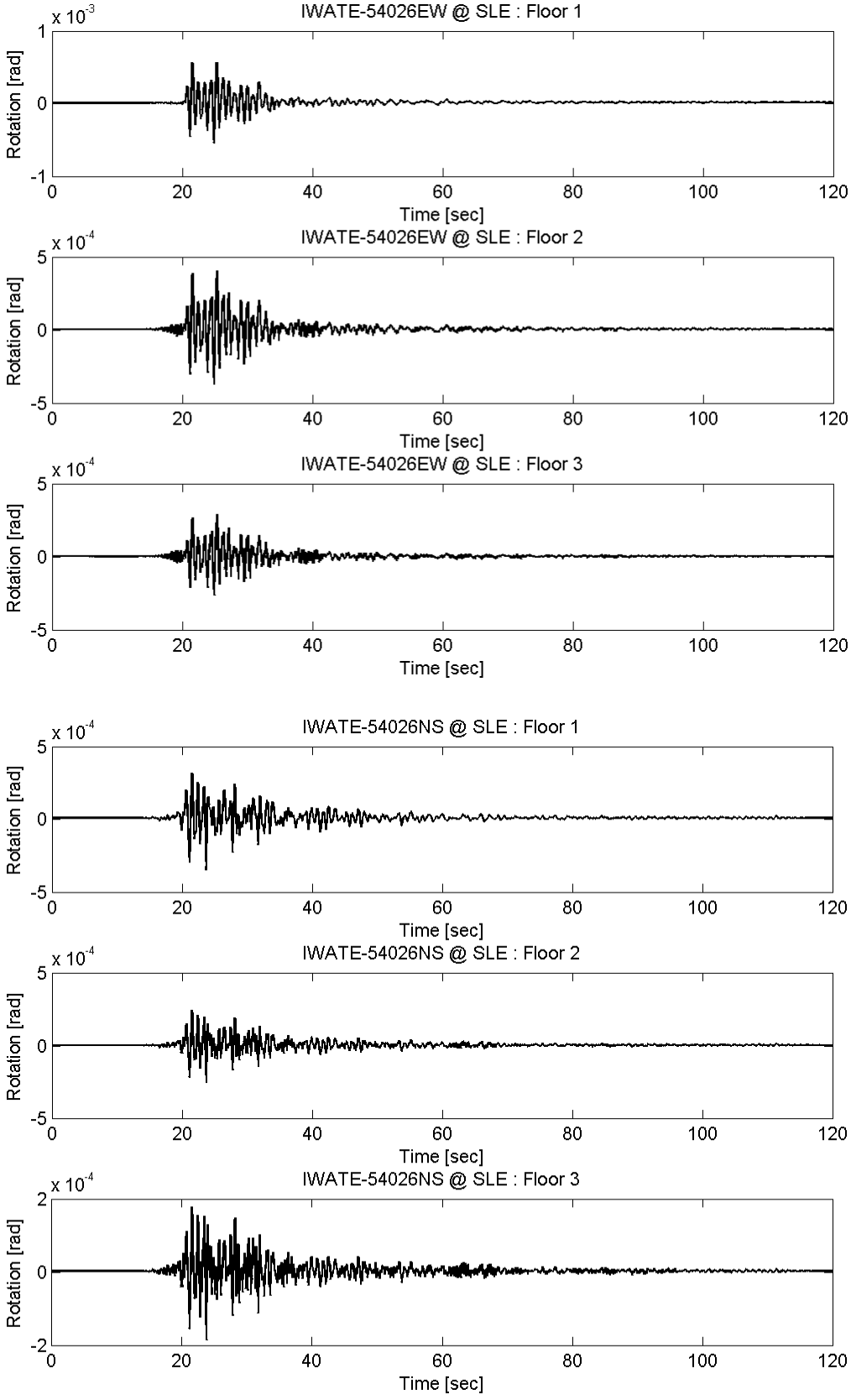
IWATE-54026EW @ SLE : Floor 1
x 10^-3
Rotation [rad]
Time [sec]
IWATE-54026EW @ SLE : Floor 2
x 10^-4
Rotation [rad]
Time [sec]
IWATE-54026EW @ SLE : Floor 3
x 10^-4
Rotation [rad]
Time [sec]
IWATE-54026NS @ SLE : Floor 1
x 10^-4
Rotation [rad]
Time [sec]
IWATE-54026NS @ SLE : Floor 2
x 10^-4
Rotation [rad]
Time [sec]
IWATE-54026NS @ SLE : Floor 3
x 10^-4
Rotation [rad]
Time [sec]

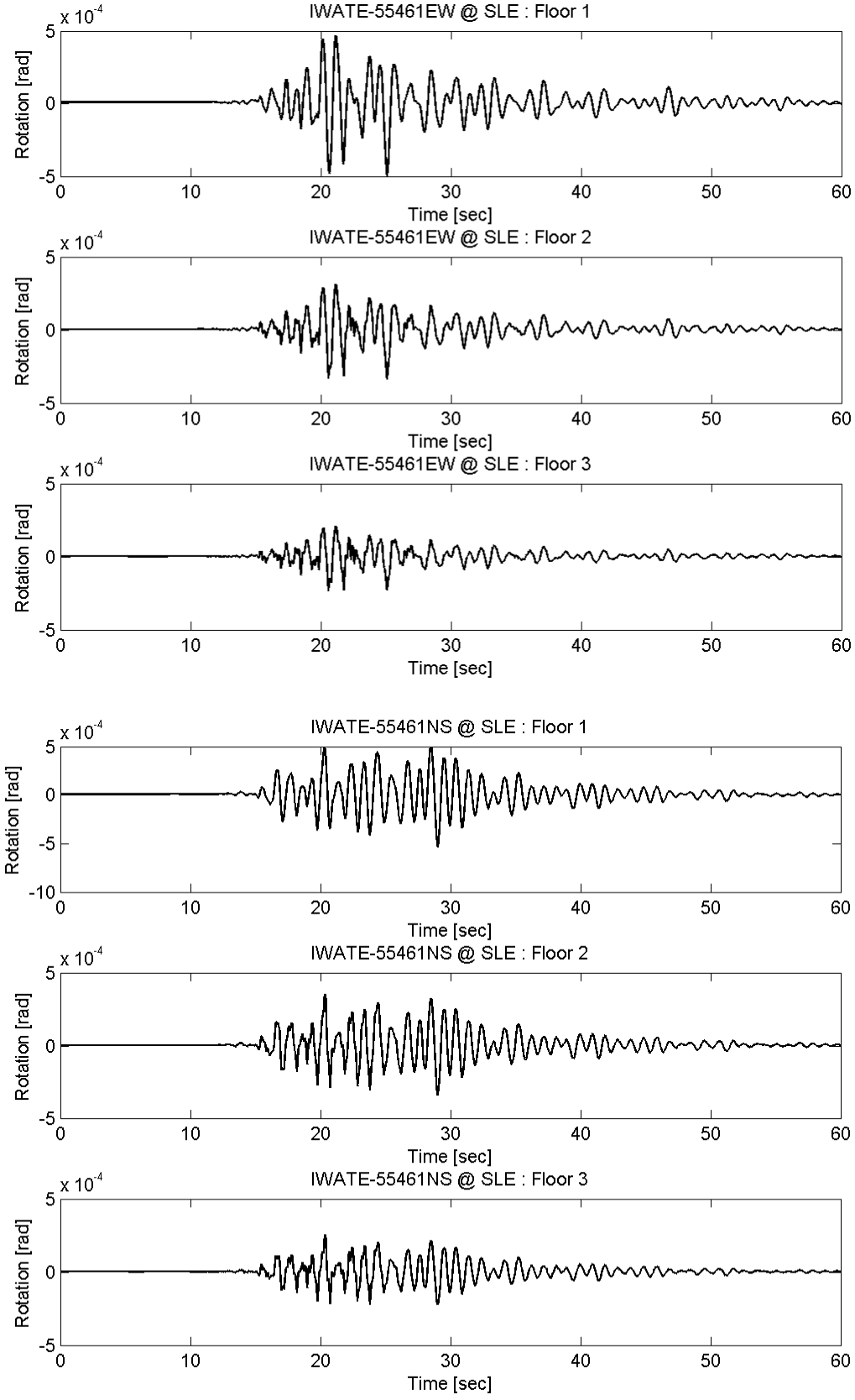
IWATE-55461EW @ SLE : Floor 1
IWATE-55461EW @ SLE : Floor 2
IWATE-55461EW @ SLE : Floor 3
IWATE-55461NS @ SLE : Floor 1
IWATE-55461NS @ SLE : Floor 2
IWATE-55461NS @ SLE : Floor 3
x 10^-4
Rotation [rad]
Time [sec]

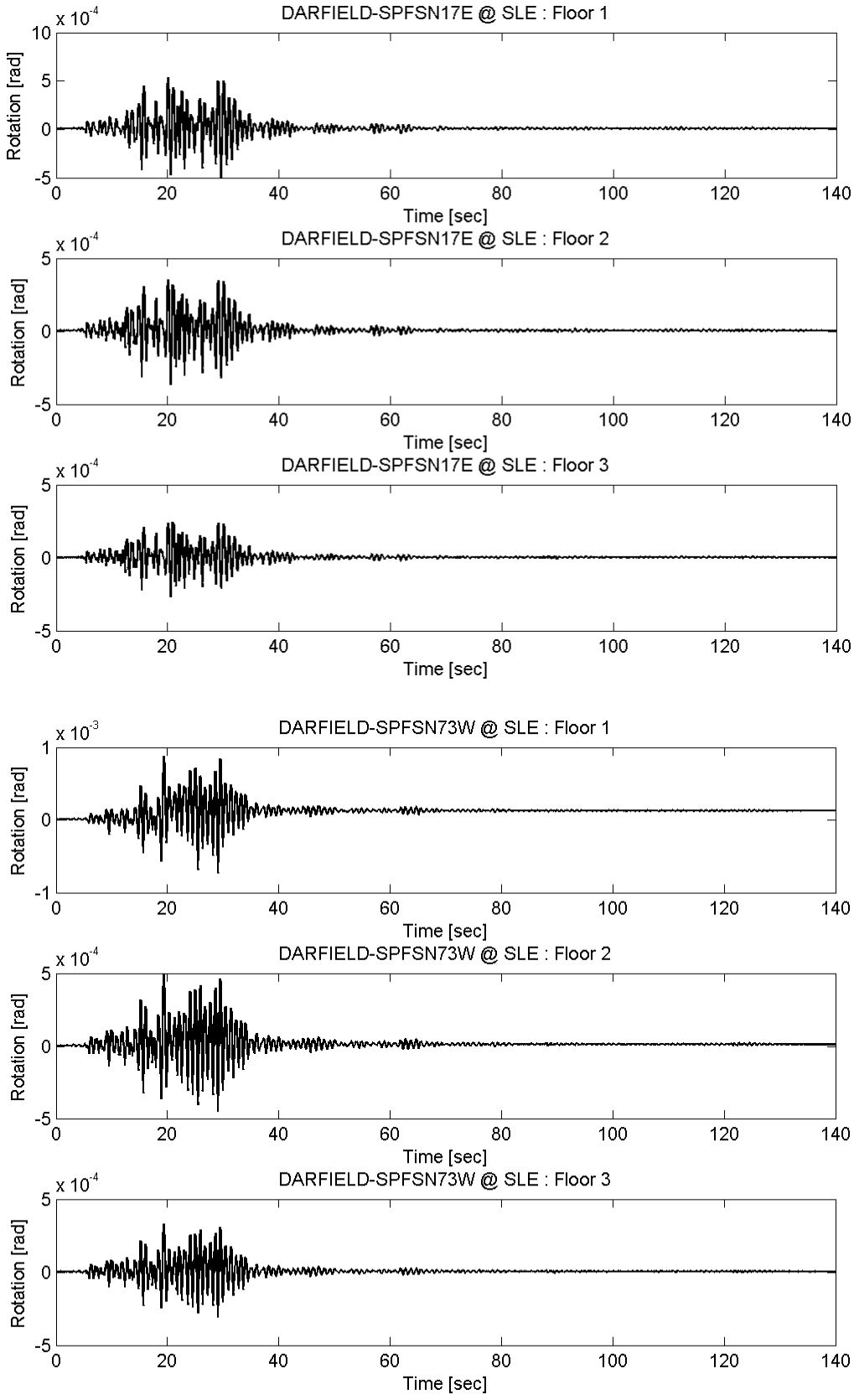
DARFIELD-SPFSN17E @ SLE : Floor 1
x 10^-4
Rotation [rad]
Time [sec]
DARFIELD-SPFSN17E @ SLE : Floor 2
x 10^-4
Rotation [rad]
Time [sec]
DARFIELD-SPFSN17E @ SLE : Floor 3
x 10^-4
Rotation [rad]
Time [sec]
DARFIELD-SPFSN73W @ SLE : Floor 1
x 10^-3
Rotation [rad]
Time [sec]
DARFIELD-SPFSN73W @ SLE : Floor 2
x 10^-4
Rotation [rad]
Time [sec]
DARFIELD-SPFSN73W @ SLE : Floor 3
x 10^-4
Rotation [rad]
Time [sec]

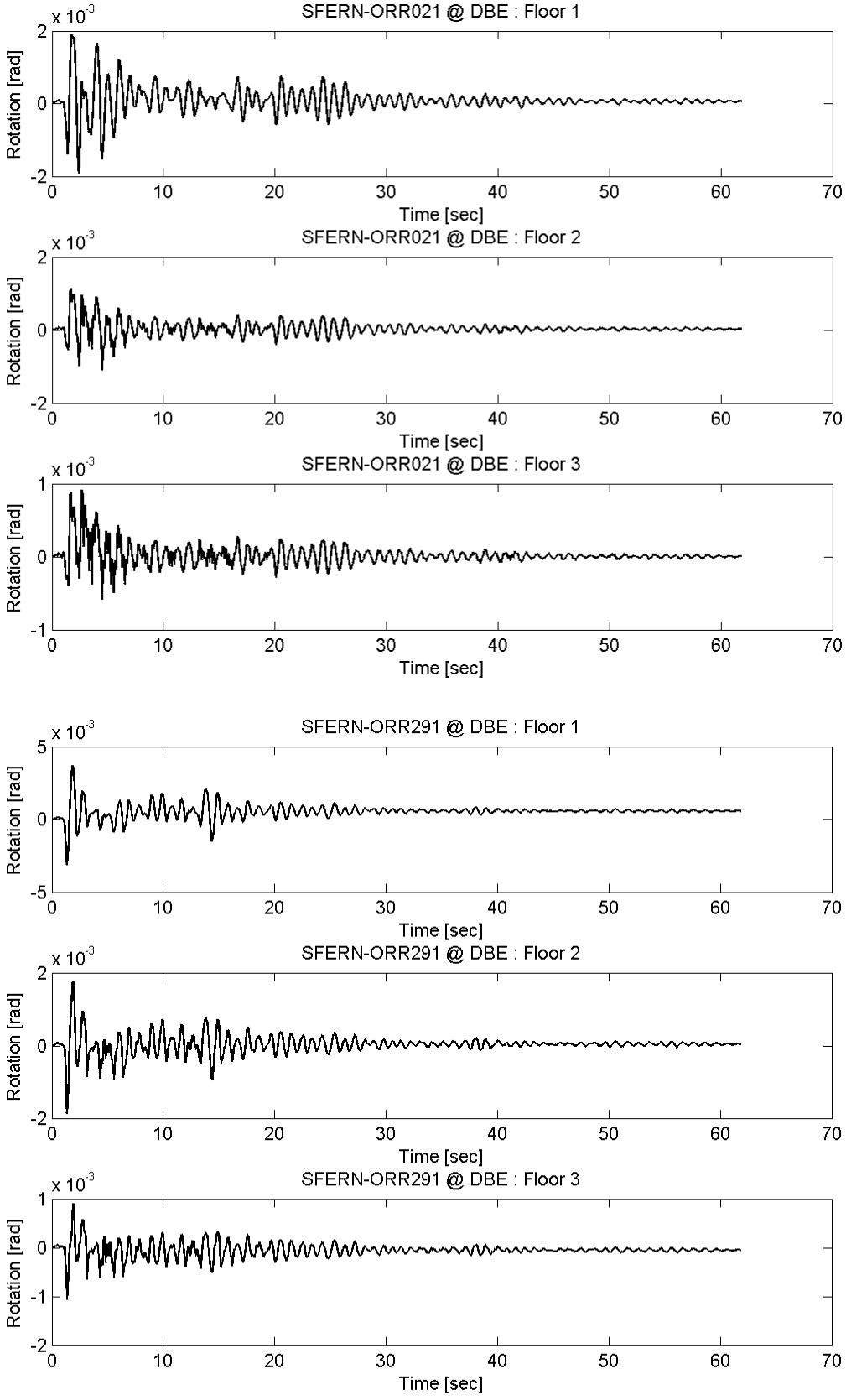
SFERN-ORR021 @ DBE : Floor 1
x 10^-3
Rotation [rad]
Time [sec]
SFERN-ORR021 @ DBE : Floor 2
x 10^-3
Rotation [rad]
Time [sec]
SFERN-ORR021 @ DBE : Floor 3
x 10^-3
Rotation [rad]
Time [sec]
SFERN-ORR291 @ DBE : Floor 1
x 10^-3
Rotation [rad]
Time [sec]
SFERN-ORR291 @ DBE : Floor 2
x 10^-3
Rotation [rad]
Time [sec]
SFERN-ORR291 @ DBE : Floor 3
x 10^-3
Rotation [rad]
Time [sec]

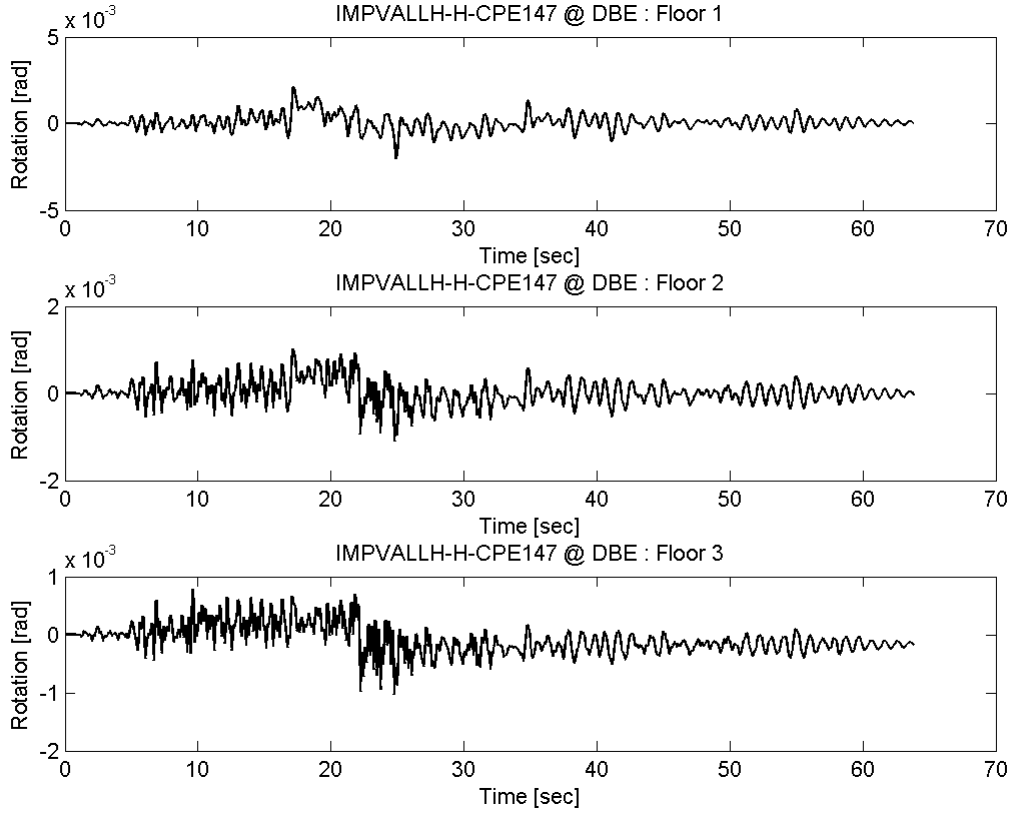
IMPVALLH-H-CPE147 @ DBE : Floor 1
x 10^-3
Rotation [rad]
Time [sec]
IMPVALLH-H-CPE147 @ DBE : Floor 2
x 10^-3
Rotation [rad]
Time [sec]
IMPVALLH-H-CPE147 @ DBE : Floor 3
x 10^-3
Rotation [rad]
Time [sec]

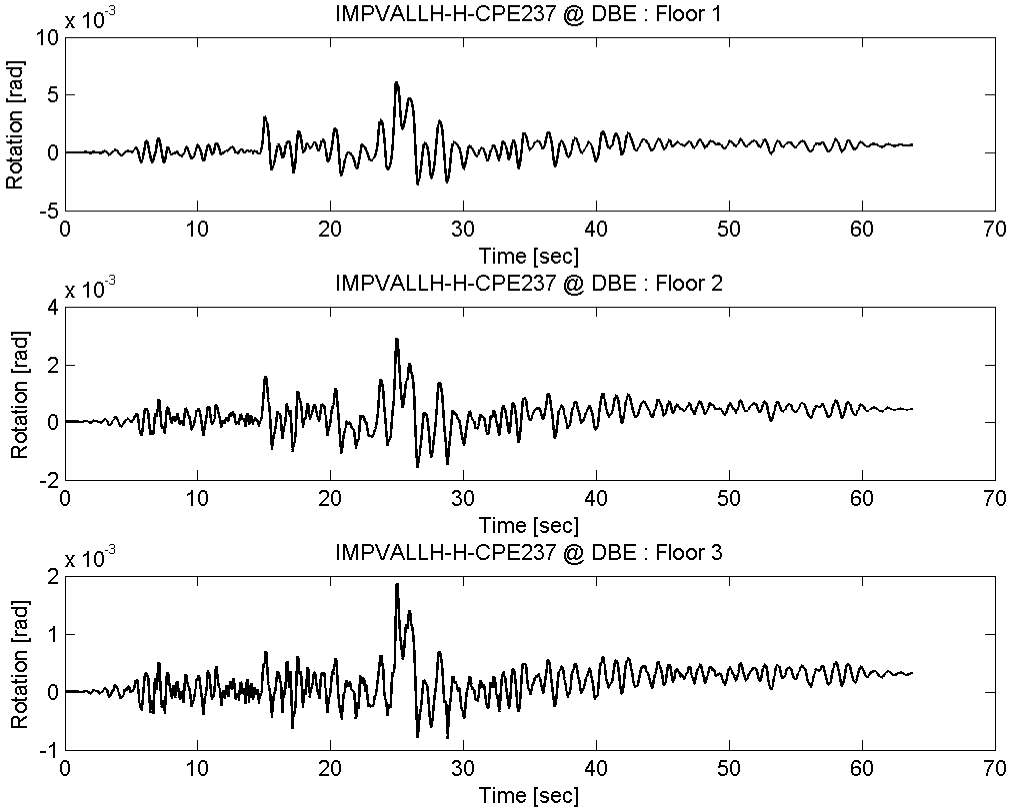
IMPVALLH-H-CPE237 @ DBE : Floor 1
x 10^-3
Rotation [rad]
Time [sec]
IMPVALLH-H-CPE237 @ DBE : Floor 2
x 10^-3
Rotation [rad]
Time [sec]
IMPVALLH-H-CPE237 @ DBE : Floor 3
x 10^-3
Rotation [rad]
Time [sec]

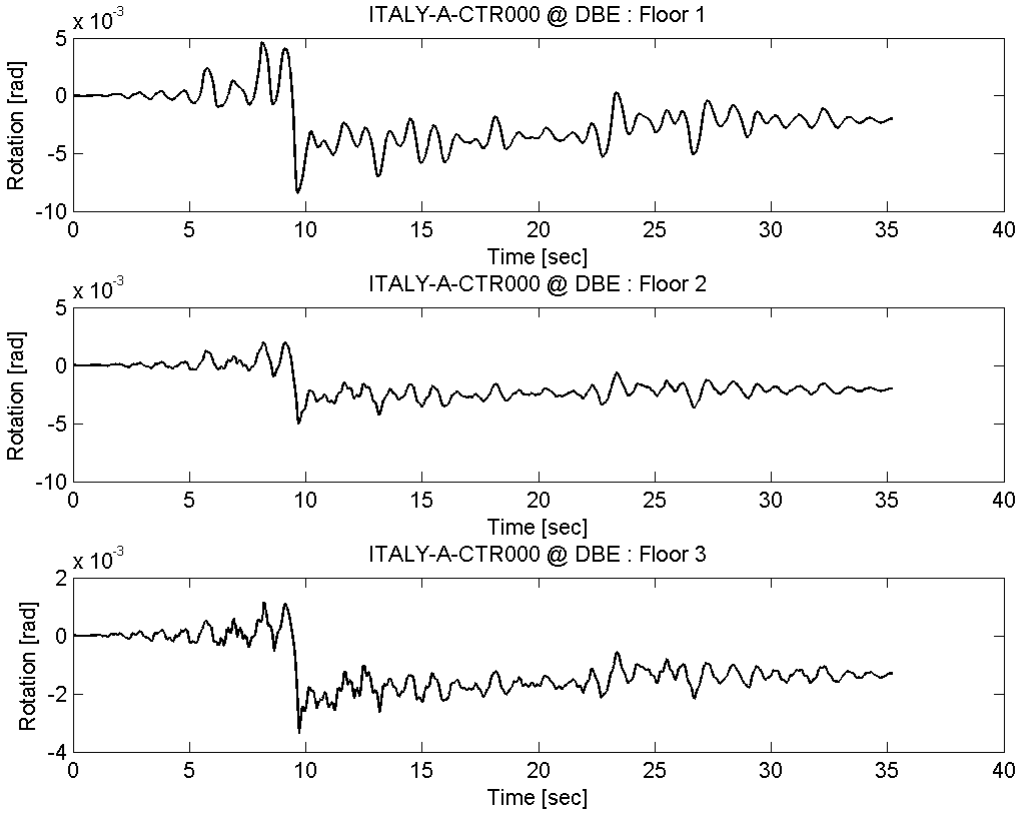
ITALY-A-CTR000 @ DBE : Floor 1
x 10^-3
Rotation [rad]
Time [sec]
ITALY-A-CTR000 @ DBE : Floor 2
x 10^-3
Rotation [rad]
Time [sec]
ITALY-A-CTR000 @ DBE : Floor 3
x 10^-3
Rotation [rad]
Time [sec]

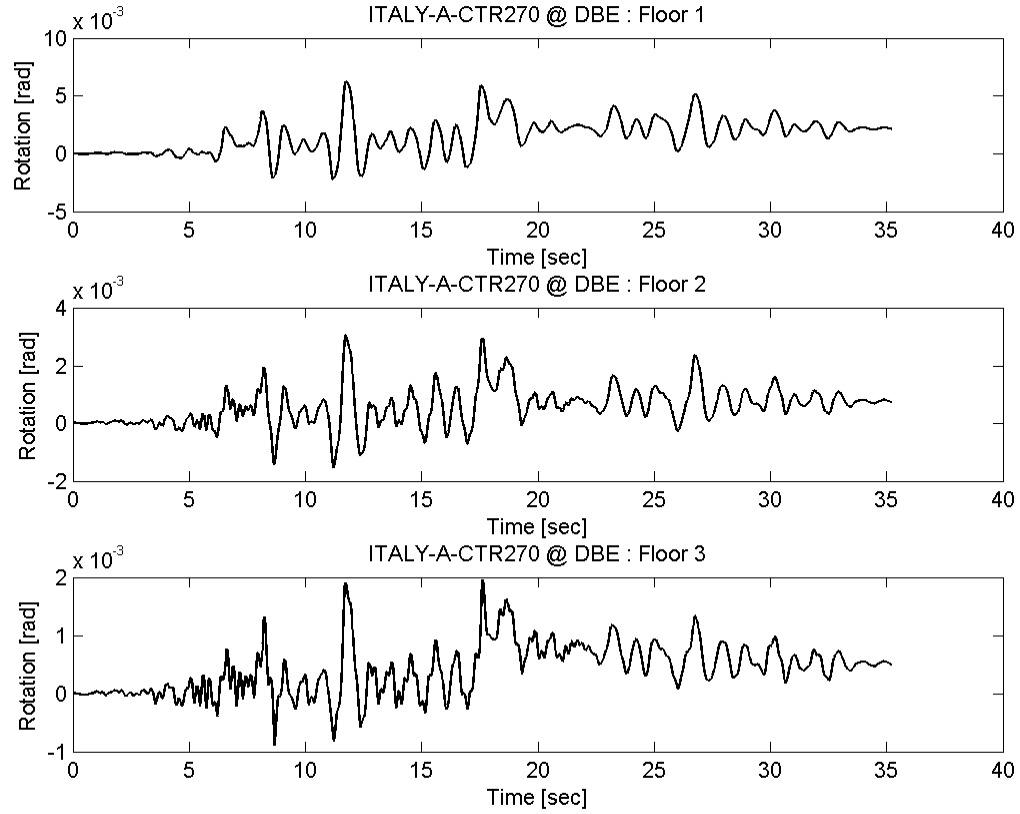
ITALY-A-CTR270 @ DBE : Floor 1
x 10^-3
Rotation [rad]
Time [sec]
ITALY-A-CTR270 @ DBE : Floor 2
x 10^-3
Rotation [rad]
Time [sec]
ITALY-A-CTR270 @ DBE : Floor 3
x 10^-3
Rotation [rad]
Time [sec]

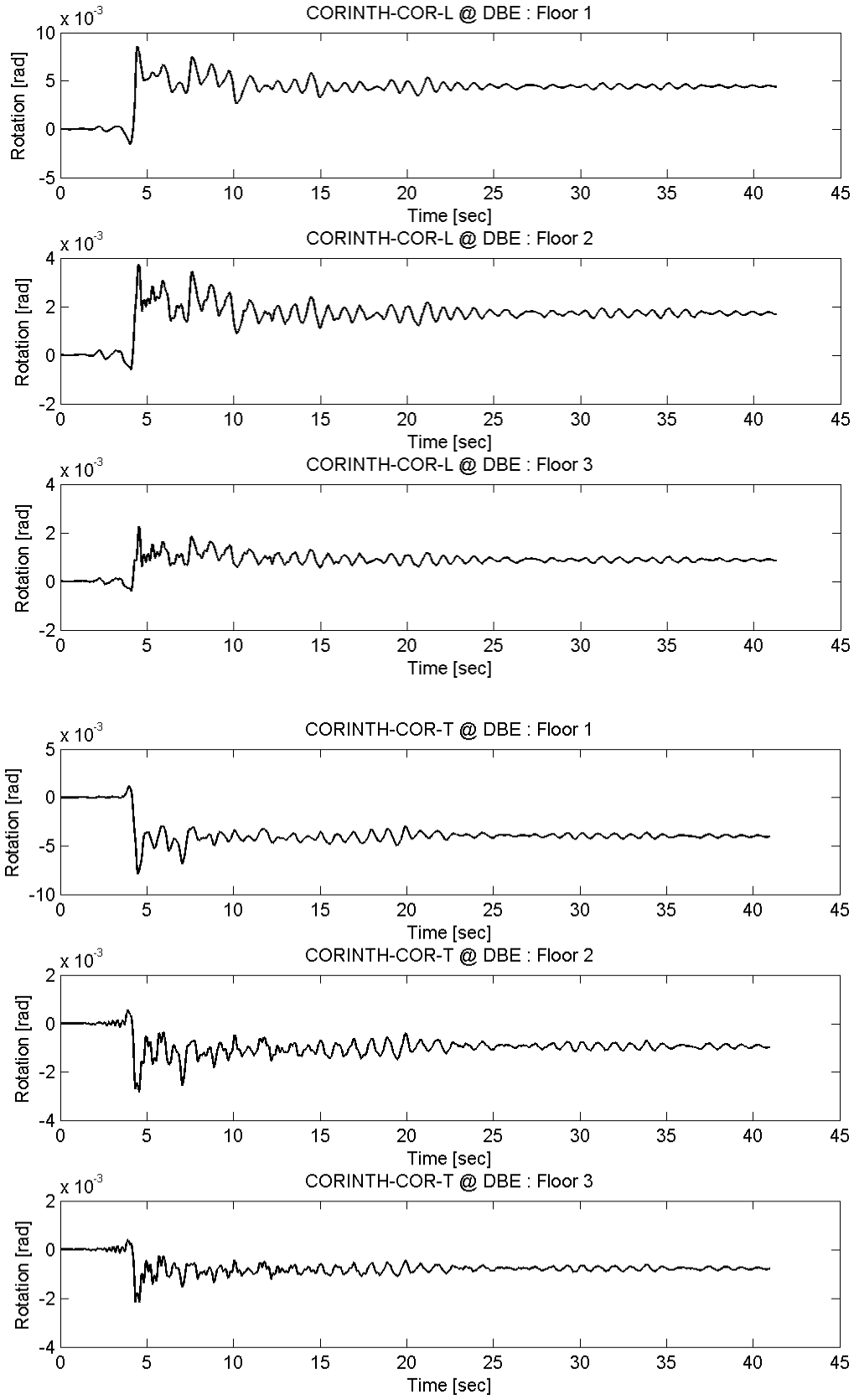
CORINTH-COR-L @ DBE : Floor 1
CORINTH-COR-L @ DBE : Floor 2
CORINTH-COR-L @ DBE : Floor 3
CORINTH-COR-T @ DBE : Floor 1
CORINTH-COR-T @ DBE : Floor 2
CORINTH-COR-T @ DBE : Floor 3
x 10^-3
Rotation [rad]
Time [sec]

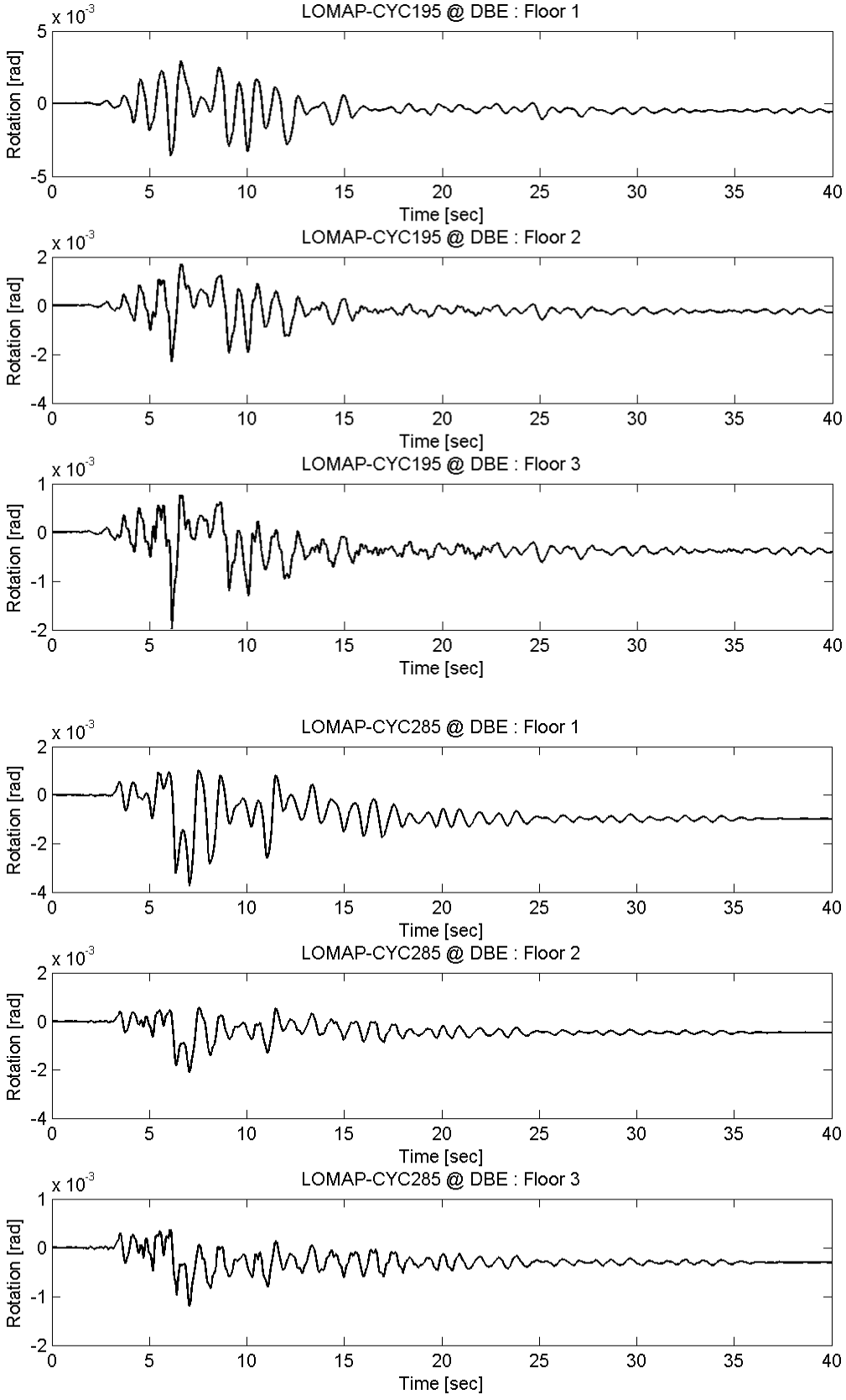
LOMAP-CYC195 @ DBE : Floor 1
LOMAP-CYC195 @ DBE : Floor 2
LOMAP-CYC195 @ DBE : Floor 3
LOMAP-CYC285 @ DBE : Floor 1
LOMAP-CYC285 @ DBE : Floor 2
LOMAP-CYC285 @ DBE : Floor 3
x 10^-3
Rotation [rad]
Time [sec]

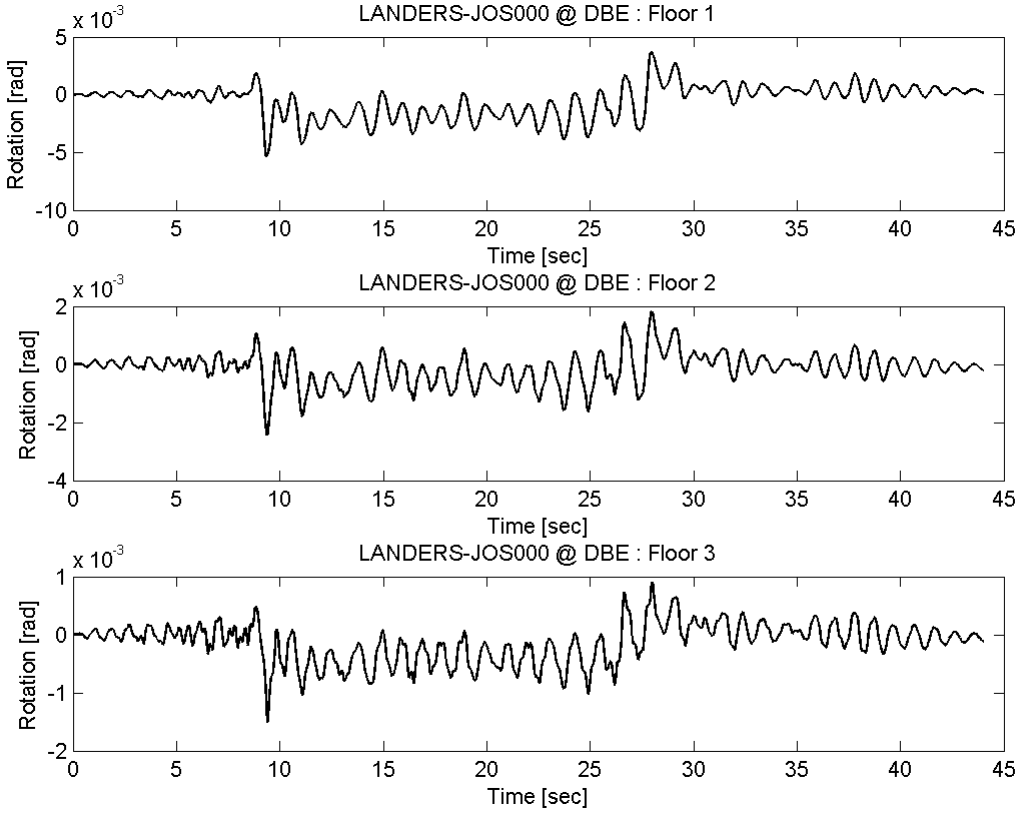
LANDERS-JOS000 @ DBE : Floor 1
x 10^-3
Rotation [rad]
Time [sec]
LANDERS-JOS000 @ DBE : Floor 2
x 10^-3
Rotation [rad]
Time [sec]
LANDERS-JOS000 @ DBE : Floor 3
x 10^-3
Rotation [rad]
Time [sec]

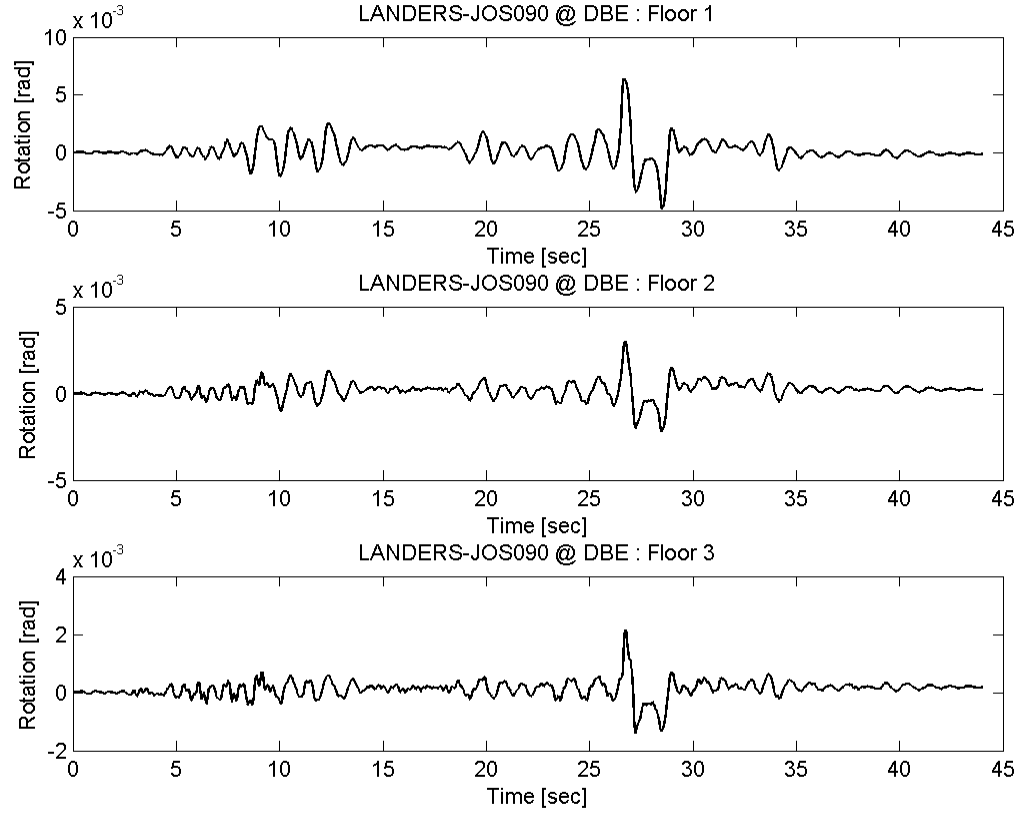
LANDERS-JOS090 @ DBE : Floor 1
x 10^-3
Rotation [rad]
Time [sec]
LANDERS-JOS090 @ DBE : Floor 2
x 10^-3
Rotation [rad]
Time [sec]
LANDERS-JOS090 @ DBE : Floor 3
x 10^-3
Rotation [rad]
Time [sec]

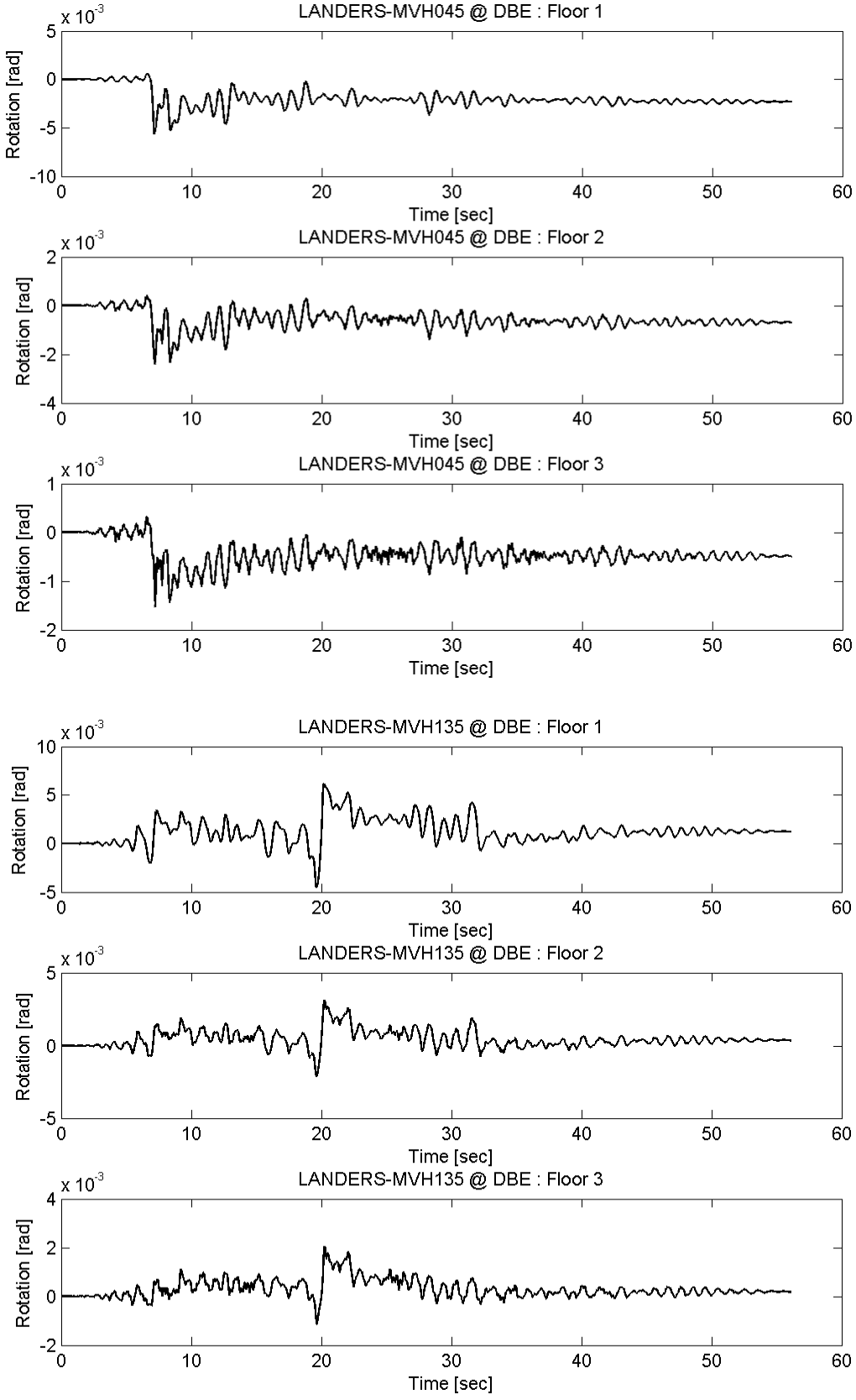
LANDERS-MVH045 @ DBE : Floor 1
x 10^-3
Rotation [rad]
Time [sec]
LANDERS-MVH045 @ DBE : Floor 2
x 10^-3
Rotation [rad]
Time [sec]
LANDERS-MVH045 @ DBE : Floor 3
x 10^-3
Rotation [rad]
Time [sec]
LANDERS-MVH135 @ DBE : Floor 1
x 10^-3
Rotation [rad]
Time [sec]
LANDERS-MVH135 @ DBE : Floor 2
x 10^-3
Rotation [rad]
Time [sec]
LANDERS-MVH135 @ DBE : Floor 3
x 10^-3
Rotation [rad]
Time [sec]

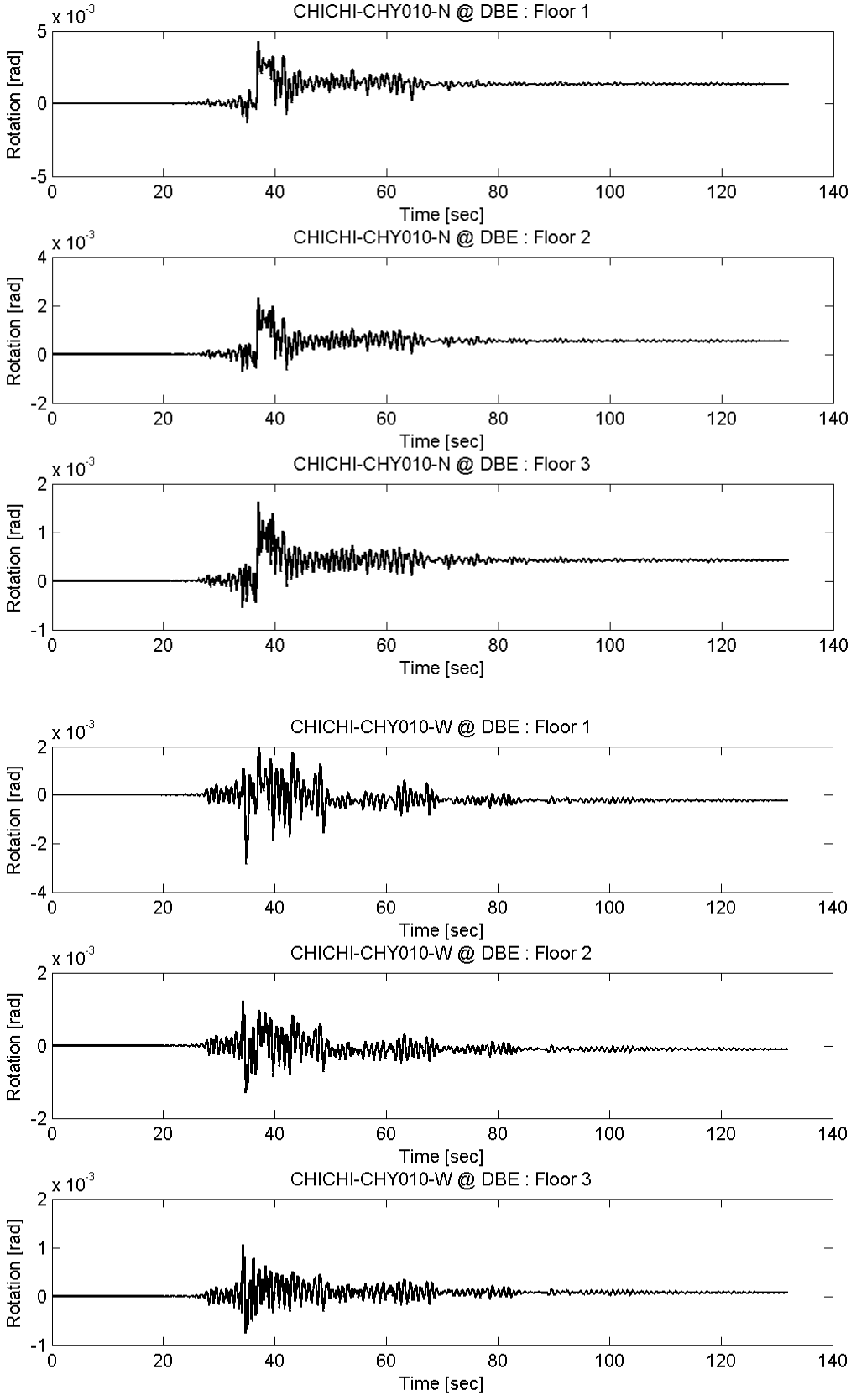
CHICHI-CHY010-N @ DBE : Floor 1
CHICHI-CHY010-N @ DBE : Floor 2
CHICHI-CHY010-N @ DBE : Floor 3
CHICHI-CHY010-W @ DBE : Floor 1
CHICHI-CHY010-W @ DBE : Floor 2
CHICHI-CHY010-W @ DBE : Floor 3
x 10^-3
Rotation [rad]
Time [sec]

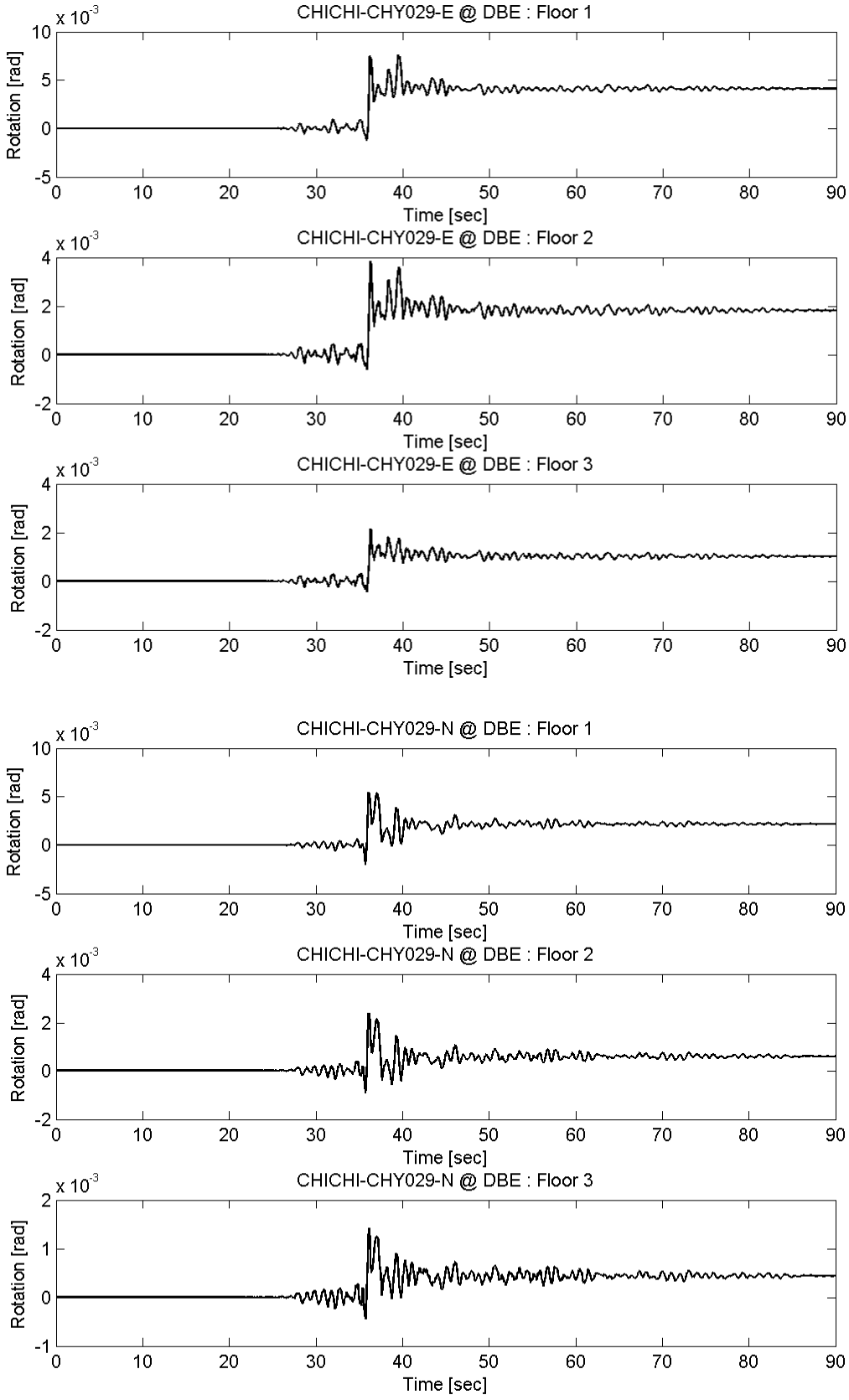
CHICHI-CHY029-E @ DBE : Floor 1
CHICHI-CHY029-E @ DBE : Floor 2
CHICHI-CHY029-E @ DBE : Floor 3
CHICHI-CHY029-N @ DBE : Floor 1
CHICHI-CHY029-N @ DBE : Floor 2
CHICHI-CHY029-N @ DBE : Floor 3
x 10^-3
Rotation [rad]
Time [sec]

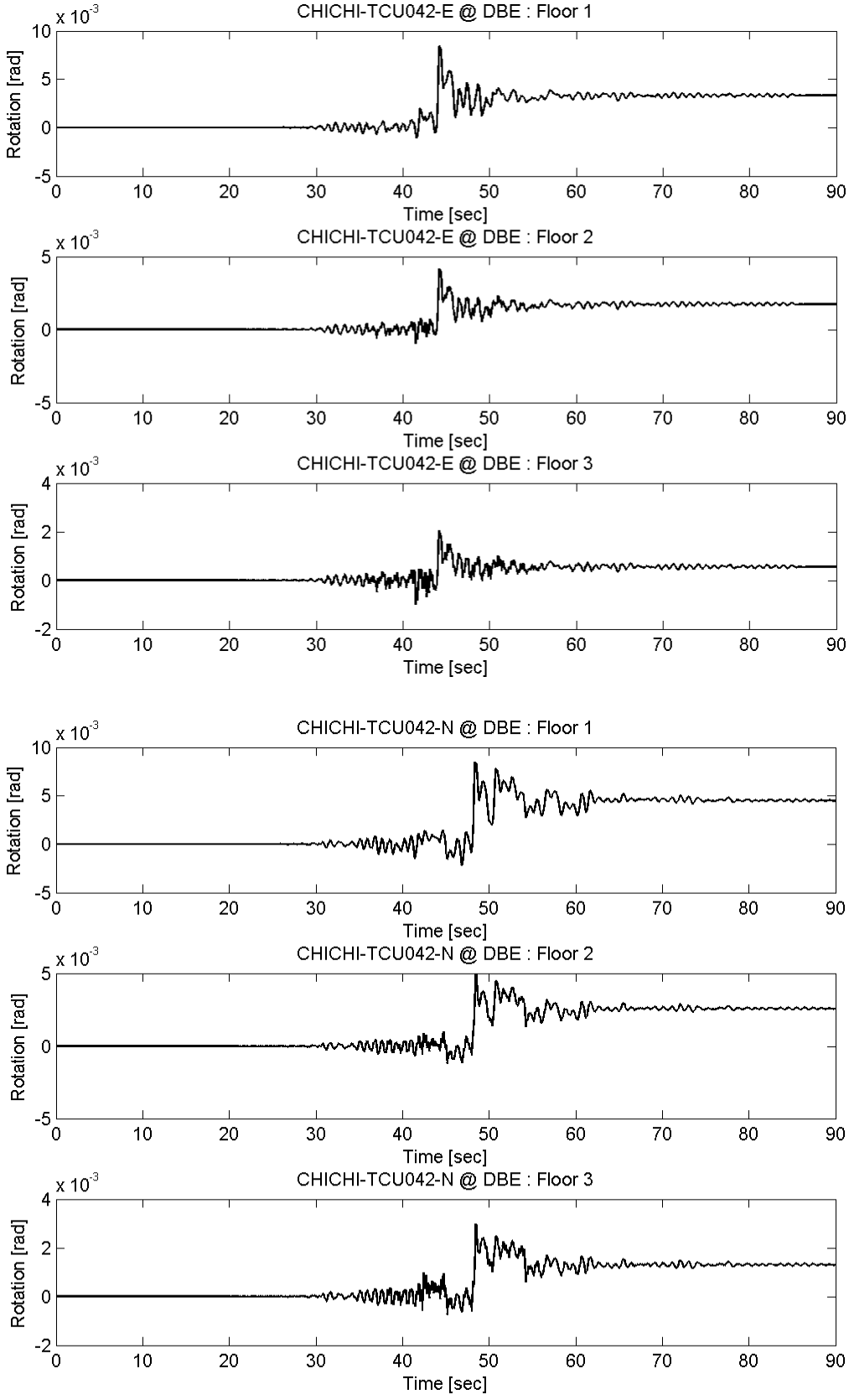
CHICHI-TCU042-E @ DBE : Floor 1
CHICHI-TCU042-E @ DBE : Floor 2
CHICHI-TCU042-E @ DBE : Floor 3
CHICHI-TCU042-N @ DBE : Floor 1
CHICHI-TCU042-N @ DBE : Floor 2
CHICHI-TCU042-N @ DBE : Floor 3
Rotation [rad]
Time [sec]
x 10^-3

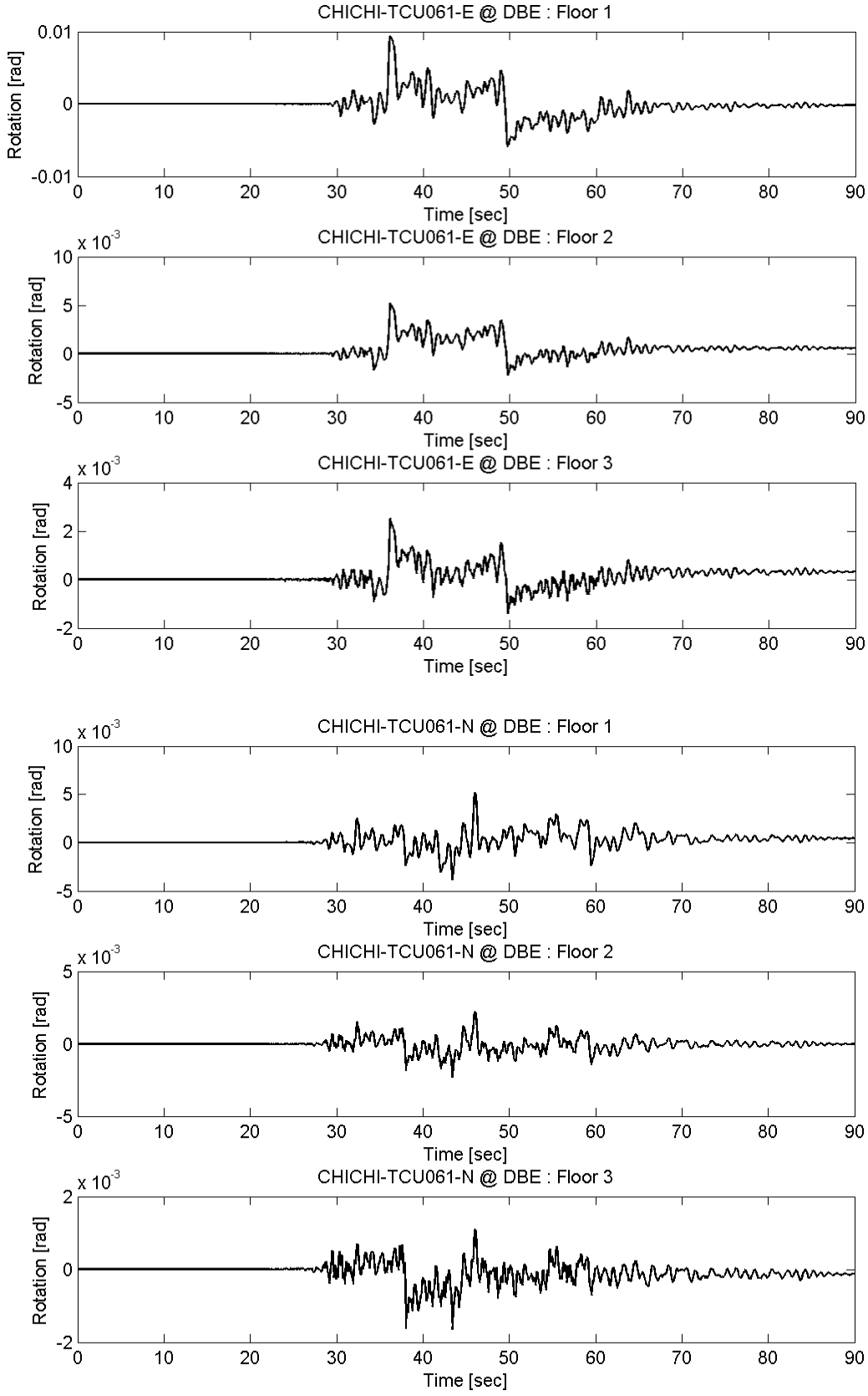
CHICHI-TCU061-E @ DBE : Floor 1
Rotation [rad]
0.01
0
-0.01
0 10 20 30 40 50 60 70 80 90
Time [sec]
CHICHI-TCU061-E @ DBE : Floor 2
x 10-3
Rotation [rad]
10
5
0
-5
0 10 20 30 40 50 60 70 80 90
Time [sec]
CHICHI-TCU061-E @ DBE : Floor 3
x 10-3
Rotation [rad]
4
2
0
-2
0 10 20 30 40 50 60 70 80 90
Time [sec]
CHICHI-TCU061-N @ DBE : Floor 1
x 10-3
Rotation [rad]
10
5
0
-5
0 10 20 30 40 50 60 70 80 90
Time [sec]
CHICHI-TCU061-N @ DBE : Floor 2
x 10-3
Rotation [rad]
5
0
-5
0 10 20 30 40 50 60 70 80 90
Time [sec]
CHICHI-TCU061-N @ DBE : Floor 3
x 10-3
Rotation [rad]
2
0
-2
0 10 20 30 40 50 60 70 80 90
Time [sec]

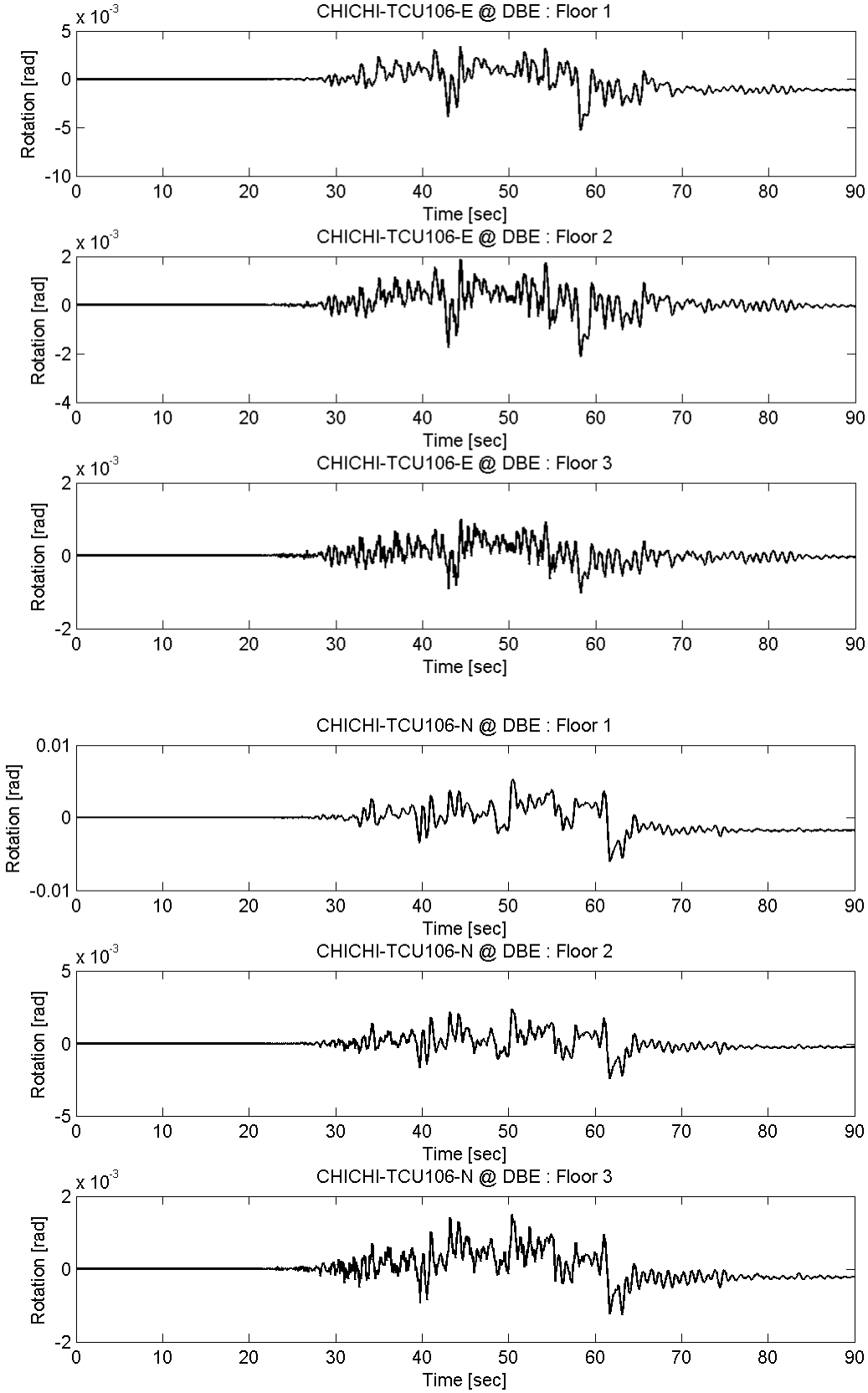
CHICHI-TCU106-E @ DBE : Floor 1
x 10^-3
Rotation [rad]
Time [sec]
CHICHI-TCU106-E @ DBE : Floor 2
x 10^-3
Rotation [rad]
Time [sec]
CHICHI-TCU106-E @ DBE : Floor 3
x 10^-3
Rotation [rad]
Time [sec]
CHICHI-TCU106-N @ DBE : Floor 1
Rotation [rad]
Time [sec]
CHICHI-TCU106-N @ DBE : Floor 2
x 10^-3
Rotation [rad]
Time [sec]
CHICHI-TCU106-N @ DBE : Floor 3
x 10^-3
Rotation [rad]
Time [sec]

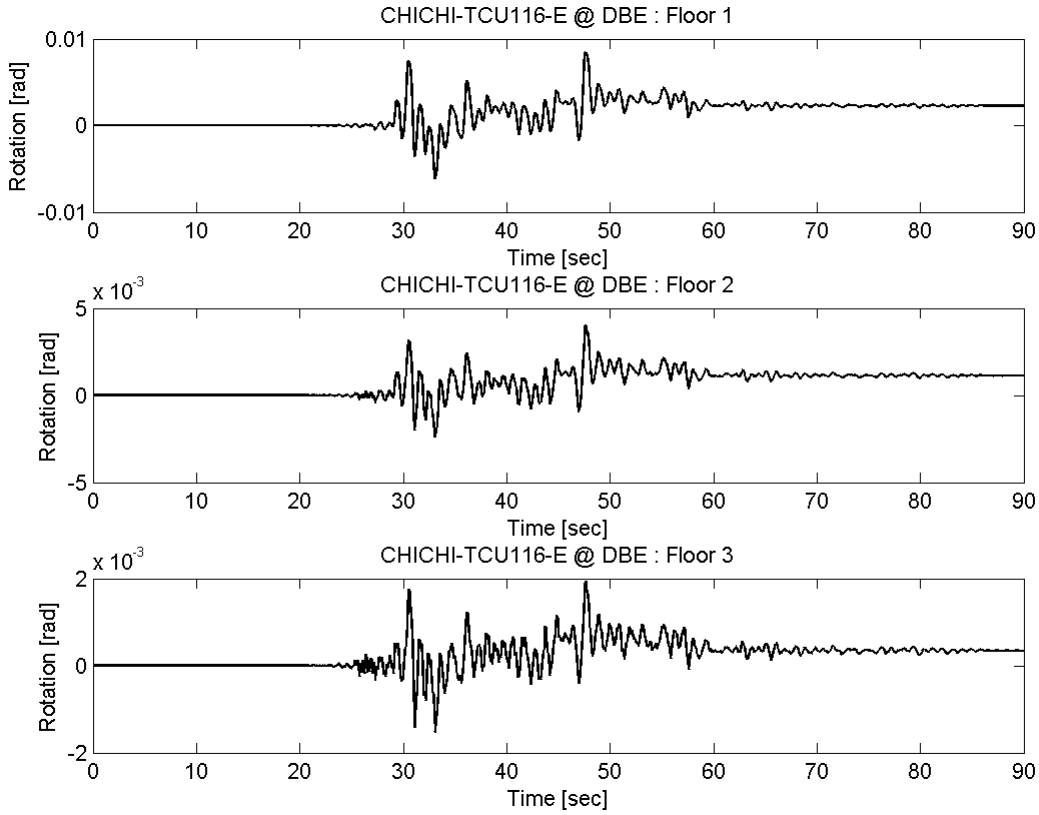
CHICHI-TCU116-E @ DBE : Floor 1
Rotation [rad]
Time [sec]
CHICHI-TCU116-E @ DBE : Floor 2
x 10^-3
Rotation [rad]
Time [sec]
CHICHI-TCU116-E @ DBE : Floor 3
x 10^-3
Rotation [rad]
Time [sec]

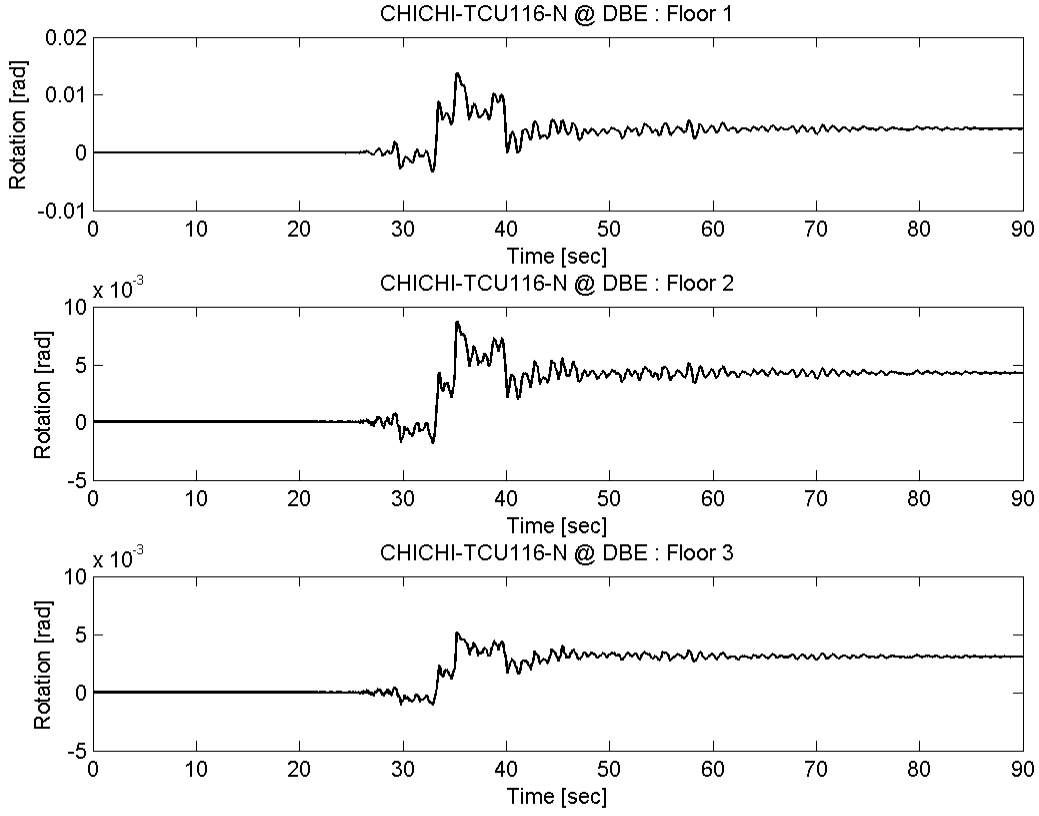
CHICHI-TCU116-N @ DBE : Floor 1
Rotation [rad]
Time [sec]
CHICHI-TCU116-N @ DBE : Floor 2
x 10^-3
Rotation [rad]
Time [sec]
CHICHI-TCU116-N @ DBE : Floor 3
x 10^-3
Rotation [rad]
Time [sec]

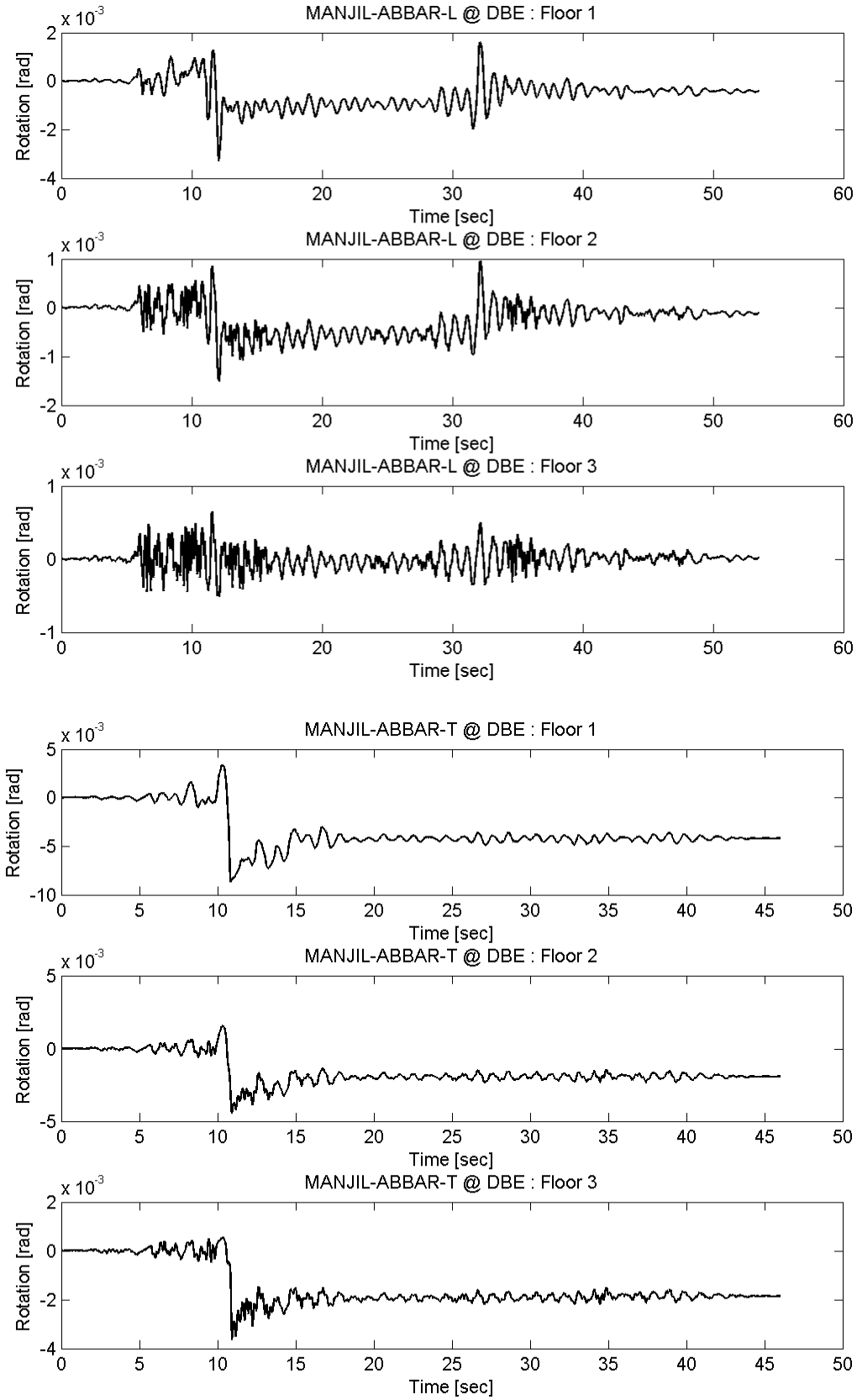
MANJIL-ABBAR-L @ DBE : Floor 1
MANJIL-ABBAR-L @ DBE : Floor 2
MANJIL-ABBAR-L @ DBE : Floor 3
MANJIL-ABBAR-T @ DBE : Floor 1
MANJIL-ABBAR-T @ DBE : Floor 2
MANJIL-ABBAR-T @ DBE : Floor 3
x 10^-3
Rotation [rad]
Time [sec]

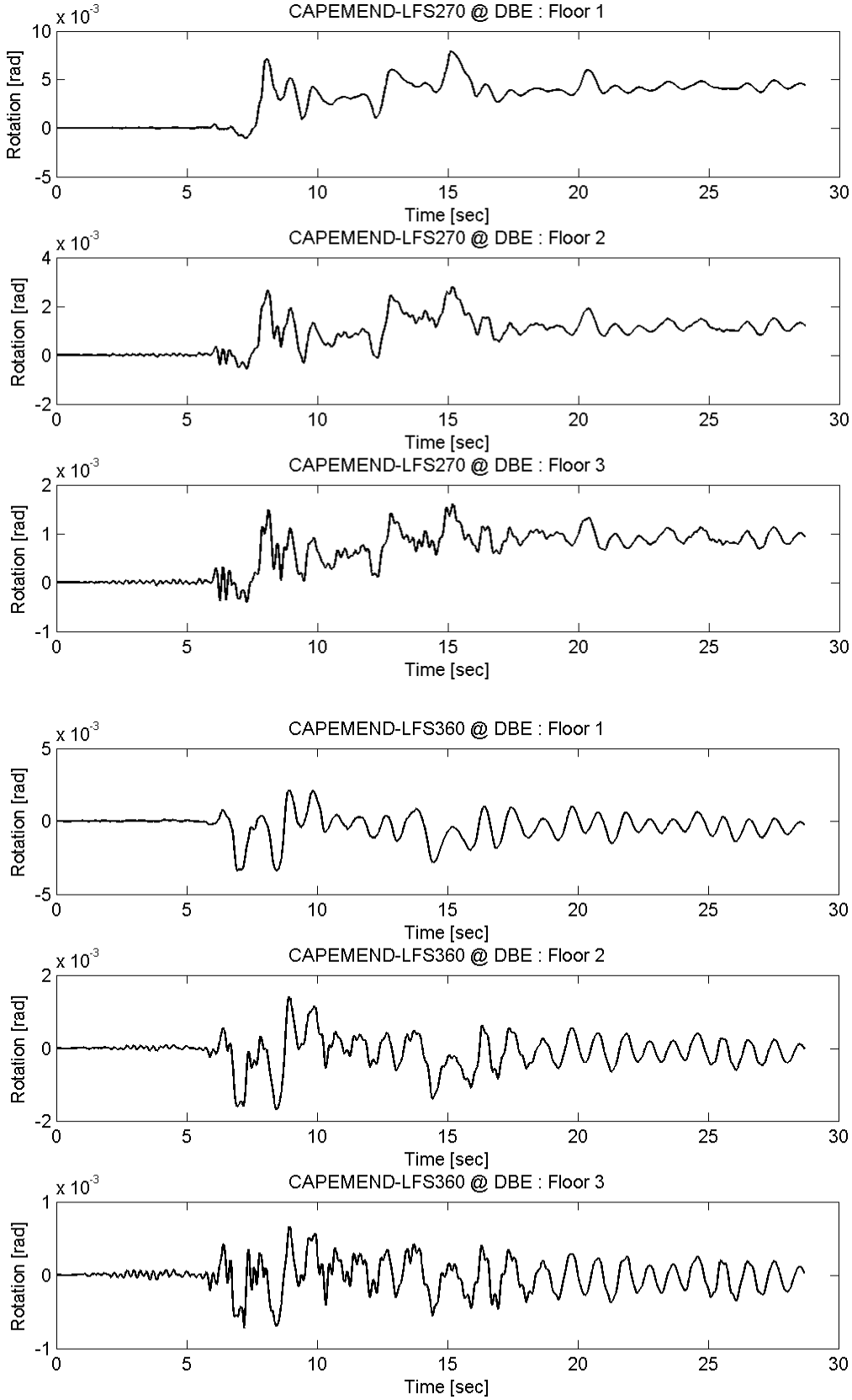
CAPEMEND-LFS270 @ DBE : Floor 1
x 10^-3
Rotation [rad]
Time [sec]
CAPEMEND-LFS270 @ DBE : Floor 2
x 10^-3
Rotation [rad]
Time [sec]
CAPEMEND-LFS270 @ DBE : Floor 3
x 10^-3
Rotation [rad]
Time [sec]
CAPEMEND-LFS360 @ DBE : Floor 1
x 10^-3
Rotation [rad]
Time [sec]
CAPEMEND-LFS360 @ DBE : Floor 2
x 10^-3
Rotation [rad]
Time [sec]
CAPEMEND-LFS360 @ DBE : Floor 3
x 10^-3
Rotation [rad]
Time [sec]

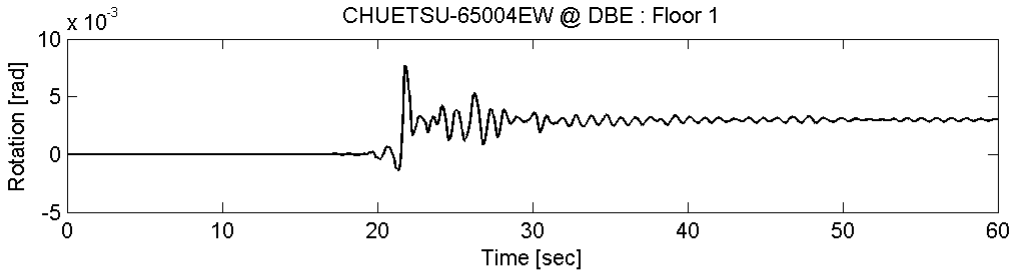
CHUETSU-65004EW @ DBE : Floor 1
x 10^-3
Rotation [rad]
Time [sec]

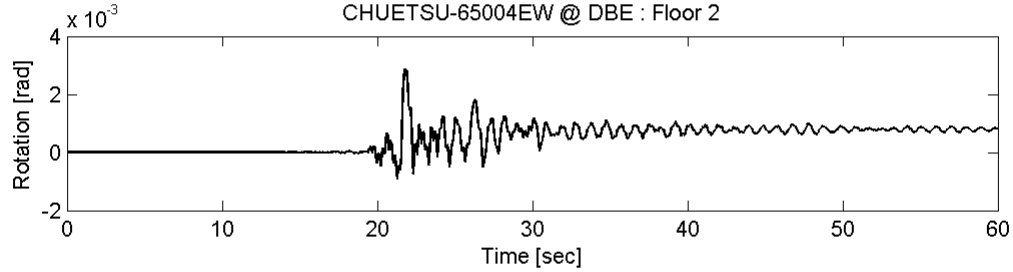
CHUETSU-65004EW @ DBE : Floor 2
x 10^-3
Rotation [rad]
Time [sec]

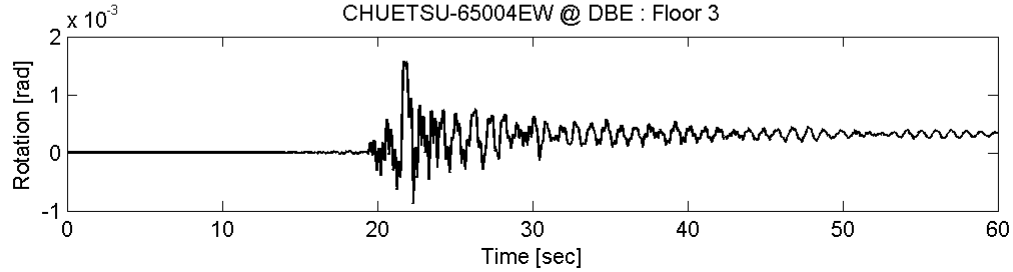
CHUETSU-65004EW @ DBE : Floor 3
x 10^-3
Rotation [rad]
Time [sec]

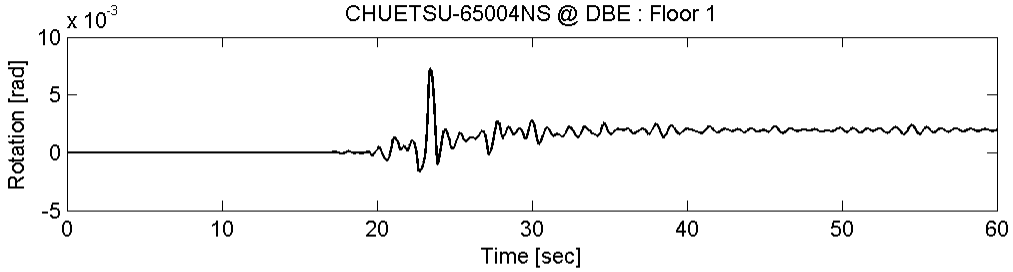
CHUETSU-65004NS @ DBE : Floor 1
x 10^-3
Rotation [rad]
Time [sec]

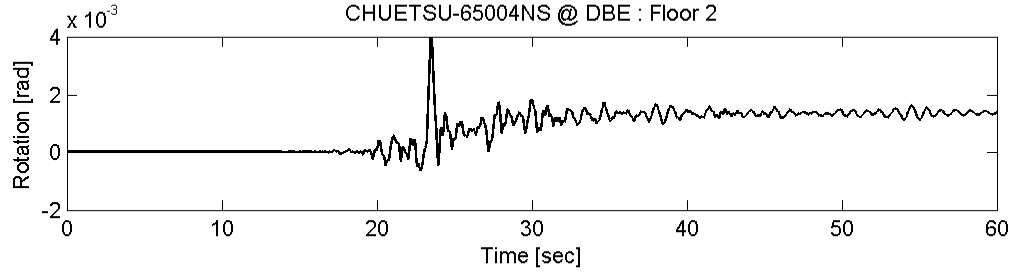
CHUETSU-65004NS @ DBE : Floor 2
x 10^-3
Rotation [rad]
Time [sec]

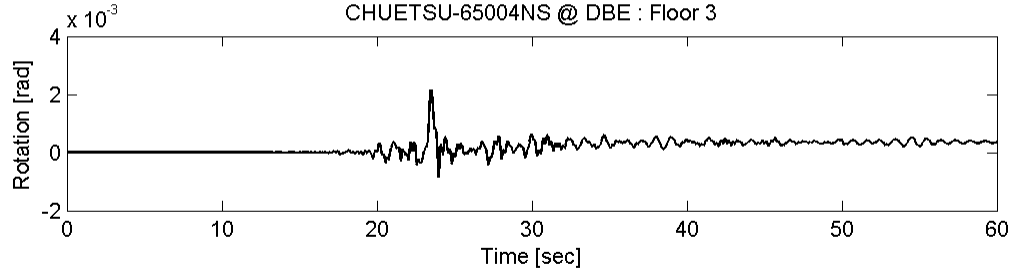
CHUETSU-65004NS @ DBE : Floor 3
x 10^-3
Rotation [rad]
Time [sec]

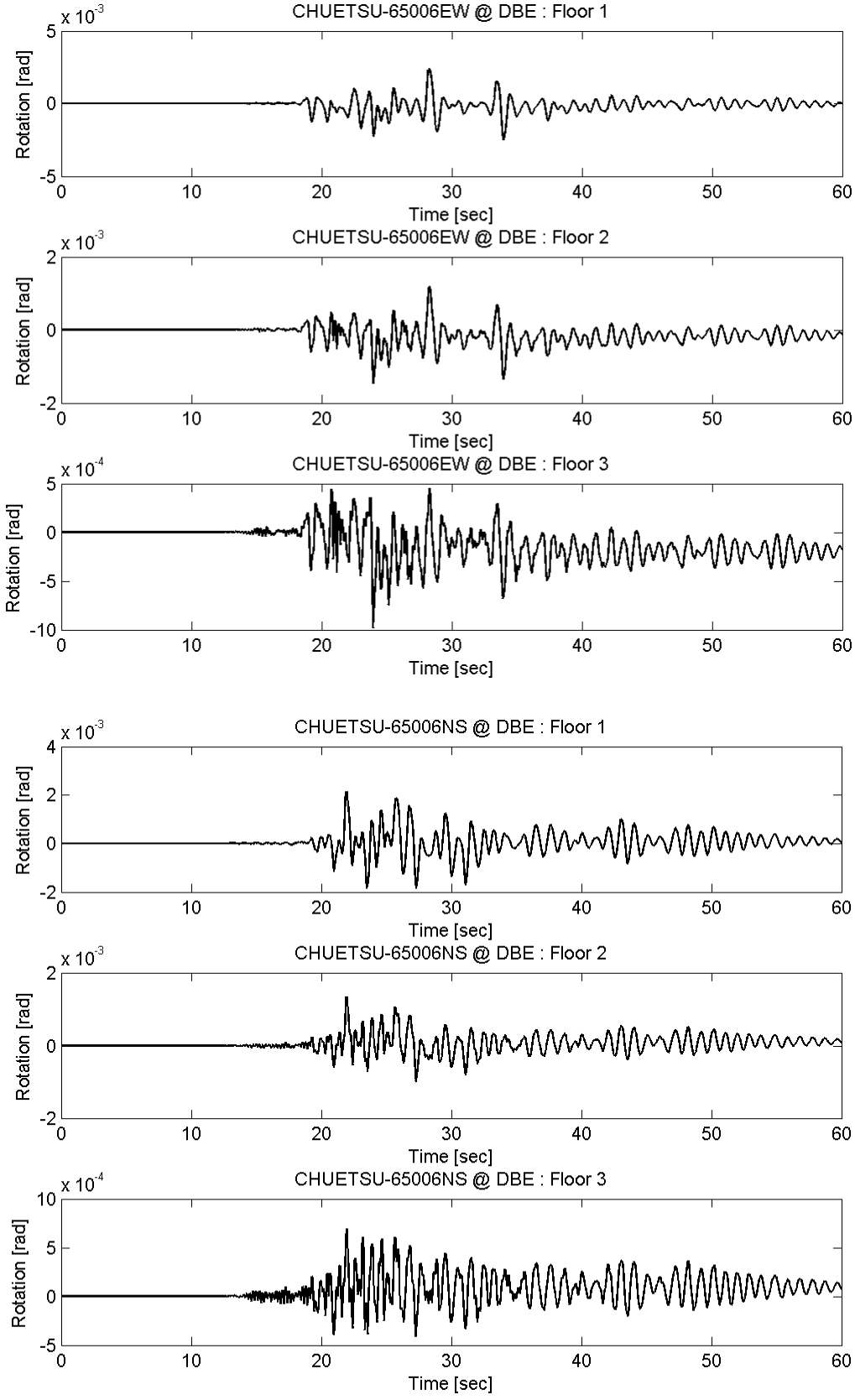
CHUETSU-65006EW @ DBE : Floor 1
x 10^-3
Rotation [rad]
Time [sec]
CHUETSU-65006EW @ DBE : Floor 2
x 10^-3
Rotation [rad]
Time [sec]
CHUETSU-65006EW @ DBE : Floor 3
x 10^-4
Rotation [rad]
Time [sec]
CHUETSU-65006NS @ DBE : Floor 1
x 10^-3
Rotation [rad]
Time [sec]
CHUETSU-65006NS @ DBE : Floor 2
x 10^-3
Rotation [rad]
Time [sec]
CHUETSU-65006NS @ DBE : Floor 3
x 10^-4
Rotation [rad]
Time [sec]

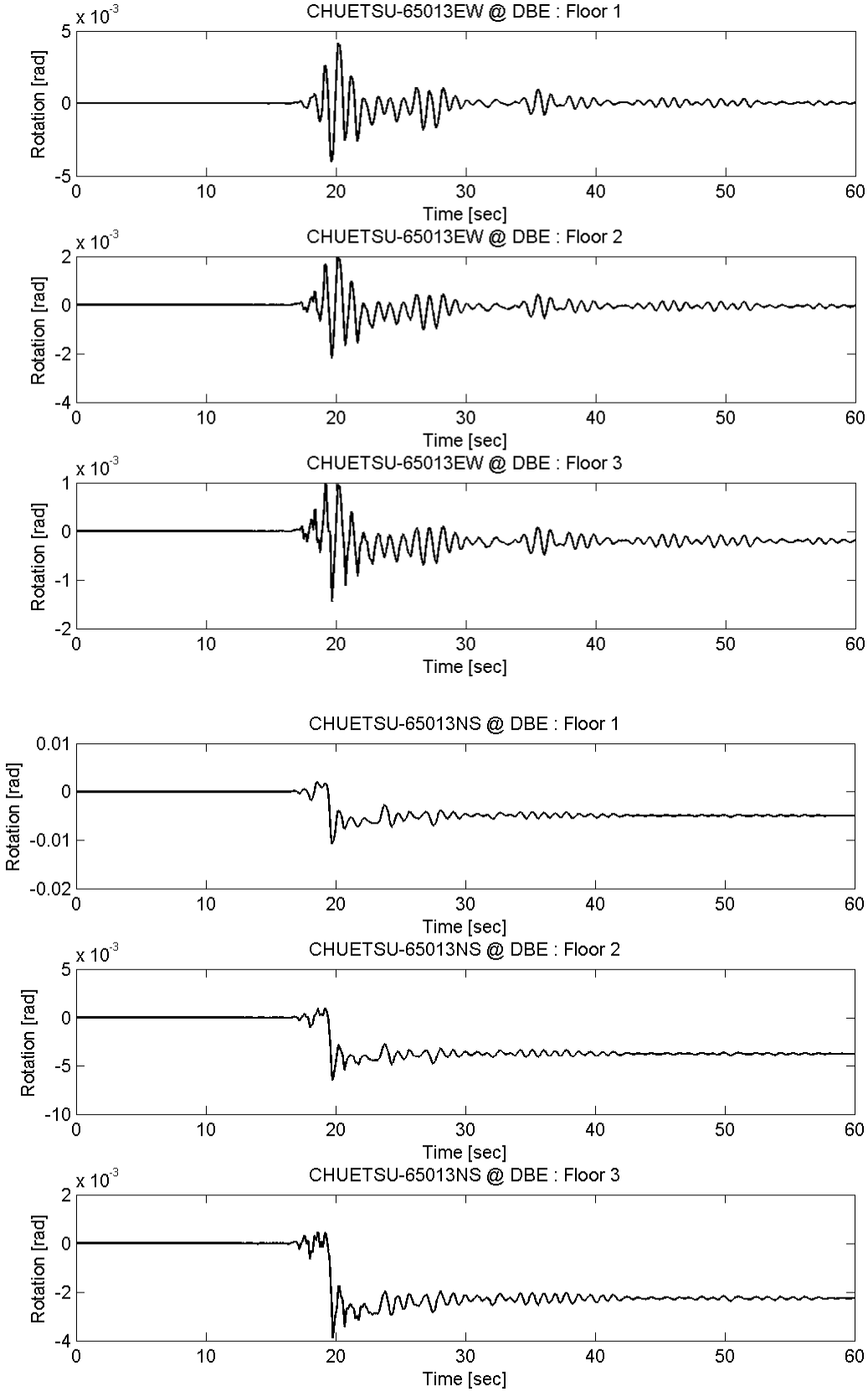
CHUETSU-65013EW @ DBE : Floor 1
x 10^-3
Rotation [rad]
Time [sec]
CHUETSU-65013EW @ DBE : Floor 2
x 10^-3
Rotation [rad]
Time [sec]
CHUETSU-65013EW @ DBE : Floor 3
x 10^-3
Rotation [rad]
Time [sec]
CHUETSU-65013NS @ DBE : Floor 1
Rotation [rad]
Time [sec]
CHUETSU-65013NS @ DBE : Floor 2
x 10^-3
Rotation [rad]
Time [sec]
CHUETSU-65013NS @ DBE : Floor 3
x 10^-3
Rotation [rad]
Time [sec]

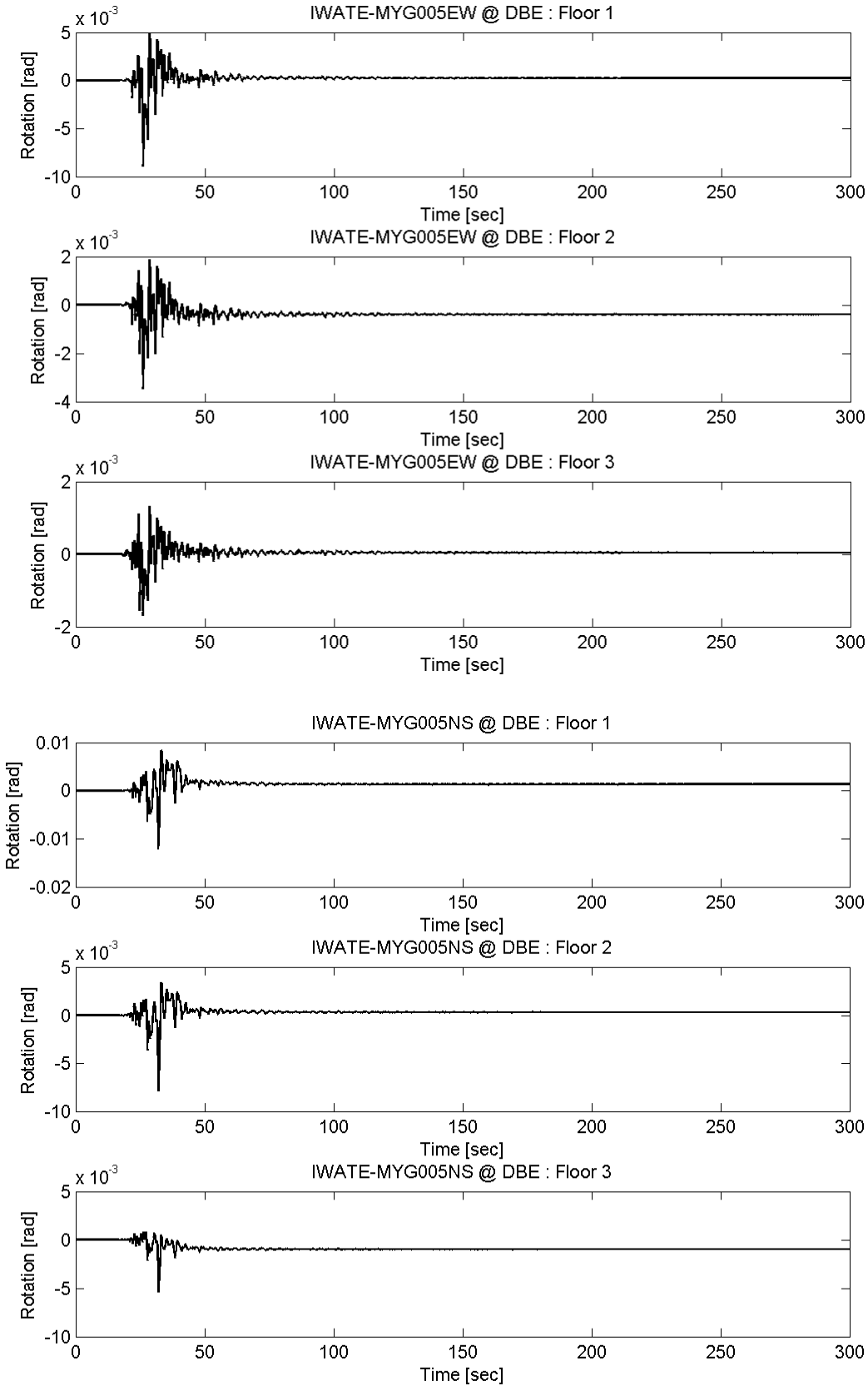
IWATE-MYG005EW @ DBE : Floor 1
x 10^-3
Rotation [rad]
Time [sec]
IWATE-MYG005EW @ DBE : Floor 2
x 10^-3
Rotation [rad]
Time [sec]
IWATE-MYG005EW @ DBE : Floor 3
x 10^-3
Rotation [rad]
Time [sec]
IWATE-MYG005NS @ DBE : Floor 1
Rotation [rad]
Time [sec]
IWATE-MYG005NS @ DBE : Floor 2
x 10^-3
Rotation [rad]
Time [sec]
IWATE-MYG005NS @ DBE : Floor 3
x 10^-3
Rotation [rad]
Time [sec]

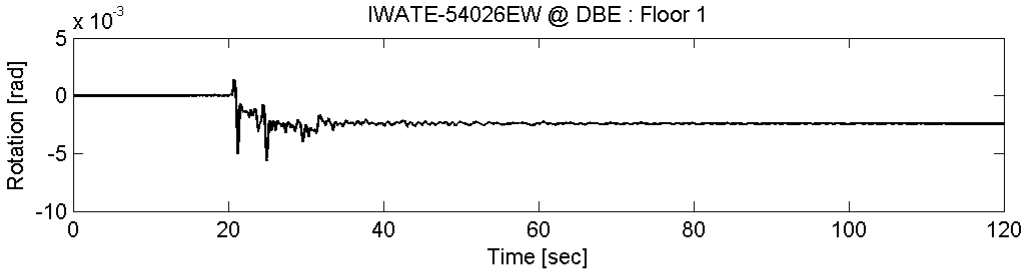
IWATE-54026EW @ DBE : Floor 1
x 10^-3
Rotation [rad]
Time [sec]

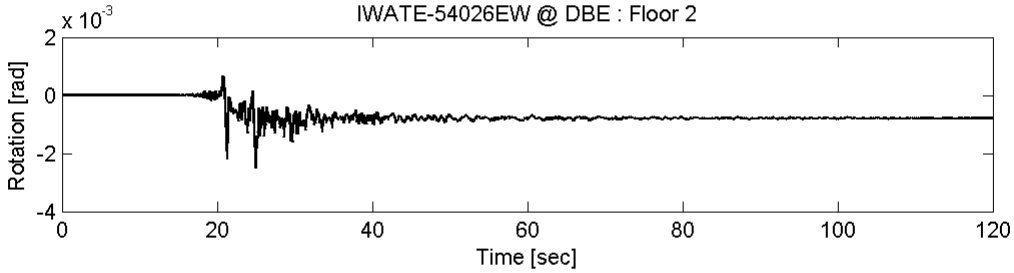
IWATE-54026EW @ DBE : Floor 2
x 10^-3
Rotation [rad]
Time [sec]

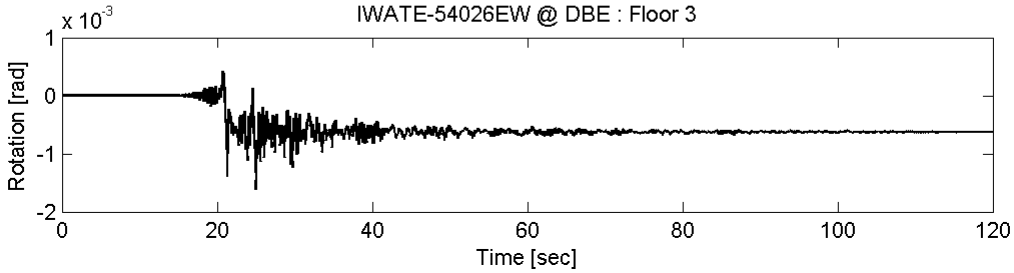
IWATE-54026EW @ DBE : Floor 3
x 10^-3
Rotation [rad]
Time [sec]

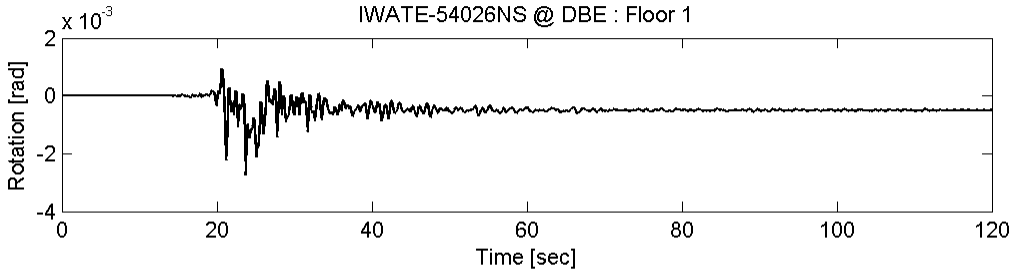
IWATE-54026NS @ DBE : Floor 1
x 10^-3
Rotation [rad]
Time [sec]

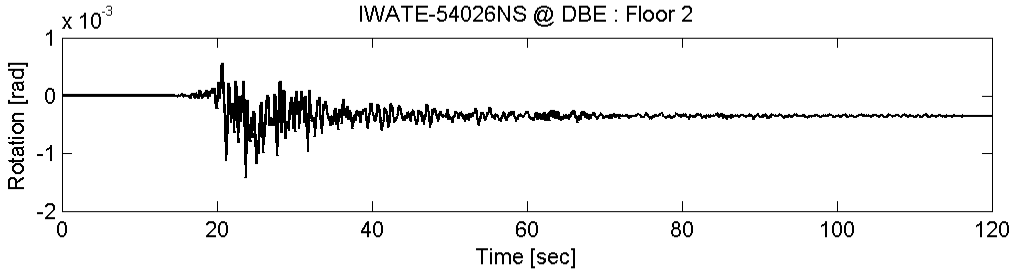
IWATE-54026NS @ DBE : Floor 2
x 10^-3
Rotation [rad]
Time [sec]

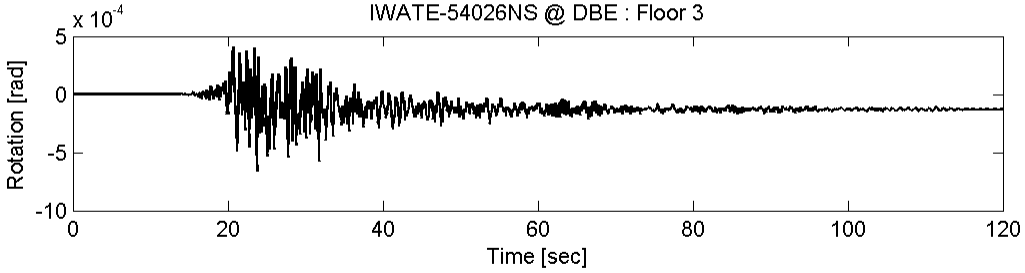
IWATE-54026NS @ DBE : Floor 3
x 10^-4
Rotation [rad]
Time [sec]

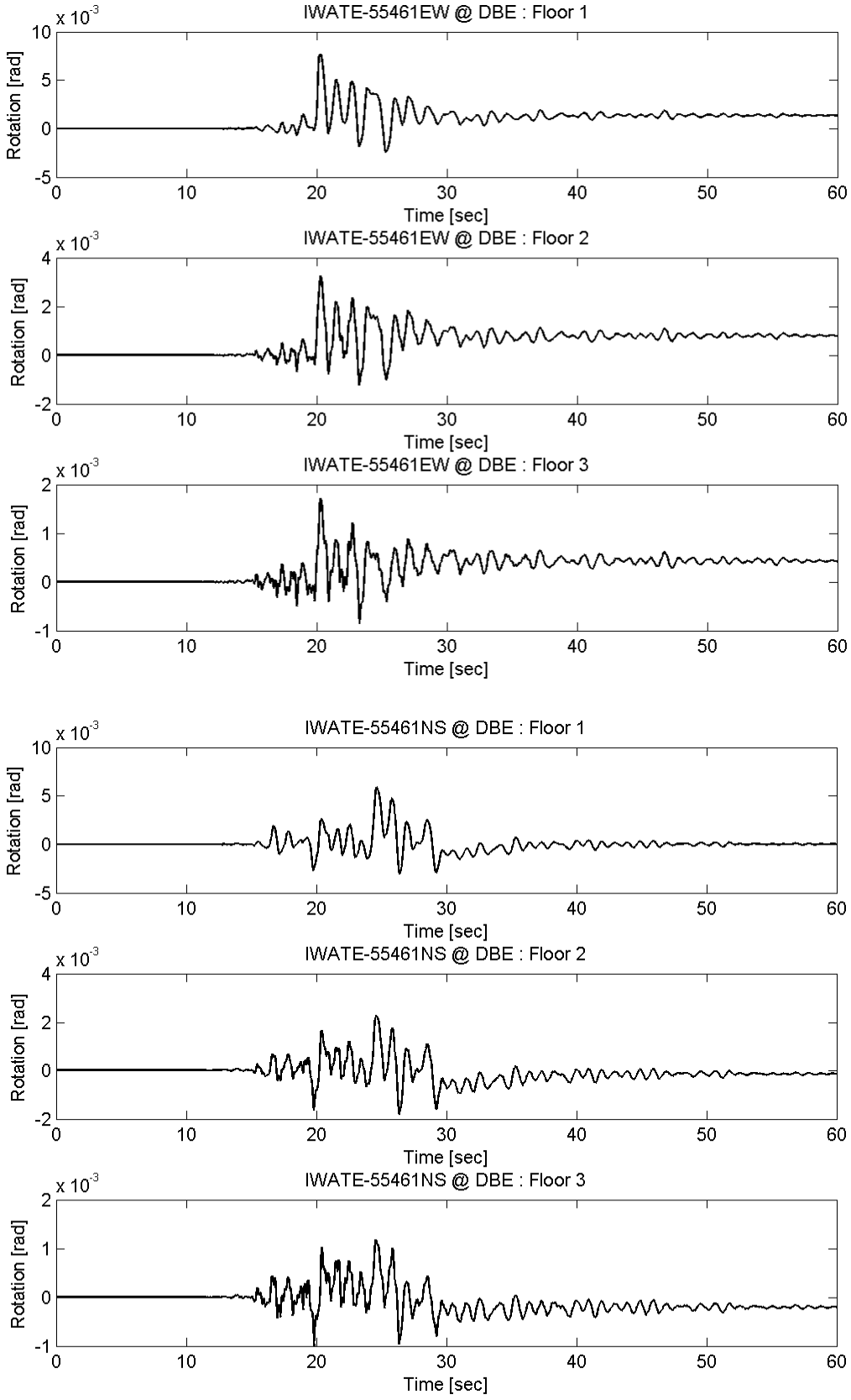
IWATE-55461EW @ DBE : Floor 1
IWATE-55461EW @ DBE : Floor 2
IWATE-55461EW @ DBE : Floor 3
IWATE-55461NS @ DBE : Floor 1
IWATE-55461NS @ DBE : Floor 2
IWATE-55461NS @ DBE : Floor 3
x 10^-3
Rotation [rad]
Time [sec]

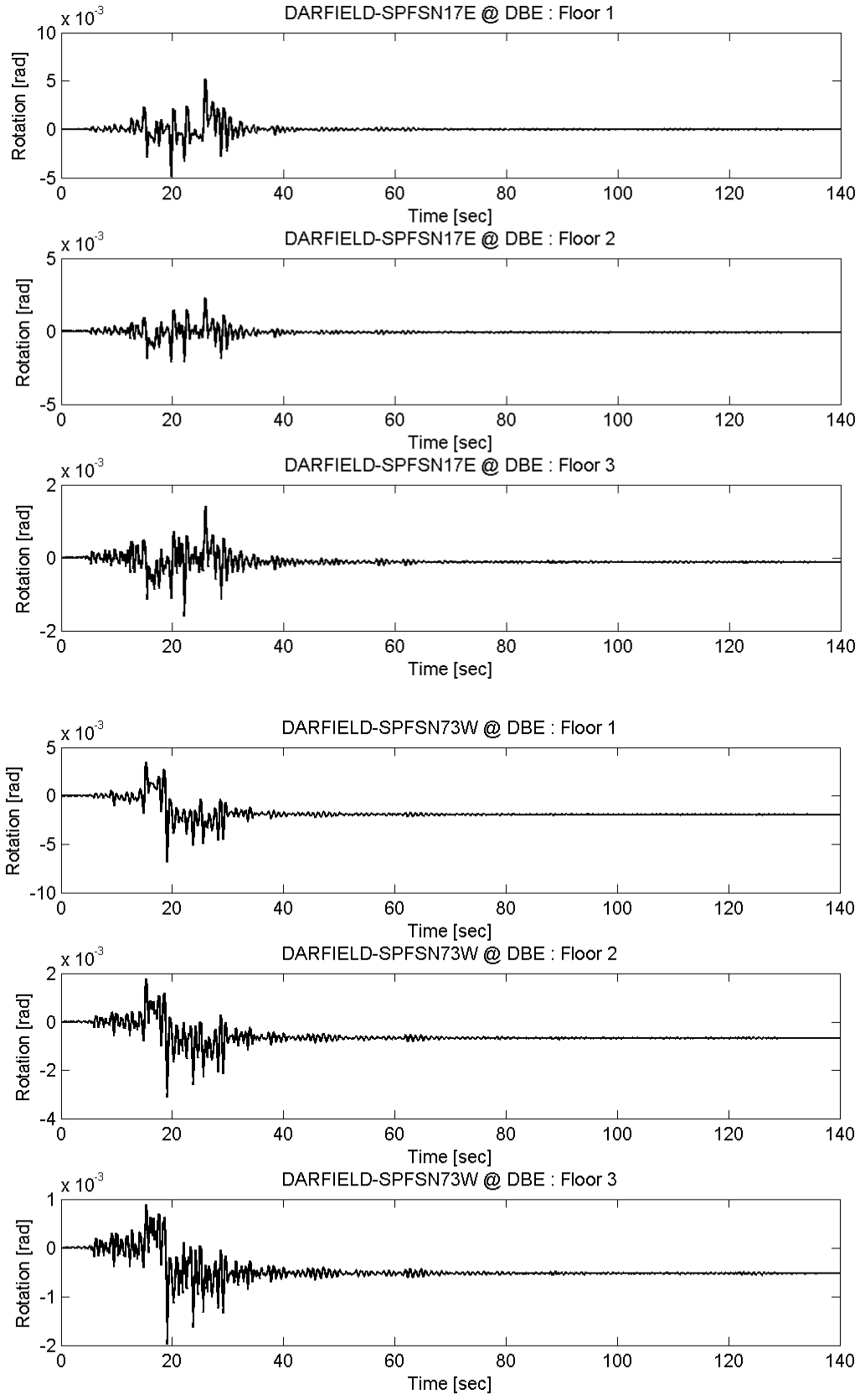
DARFIELD-SPFSN17E @ DBE : Floor 1
x 10^-3
Rotation [rad]
Time [sec]
DARFIELD-SPFSN17E @ DBE : Floor 2
x 10^-3
Rotation [rad]
Time [sec]
DARFIELD-SPFSN17E @ DBE : Floor 3
x 10^-3
Rotation [rad]
Time [sec]
DARFIELD-SPFSN73W @ DBE : Floor 1
x 10^-3
Rotation [rad]
Time [sec]
DARFIELD-SPFSN73W @ DBE : Floor 2
x 10^-3
Rotation [rad]
Time [sec]
DARFIELD-SPFSN73W @ DBE : Floor 3
x 10^-3
Rotation [rad]
Time [sec]

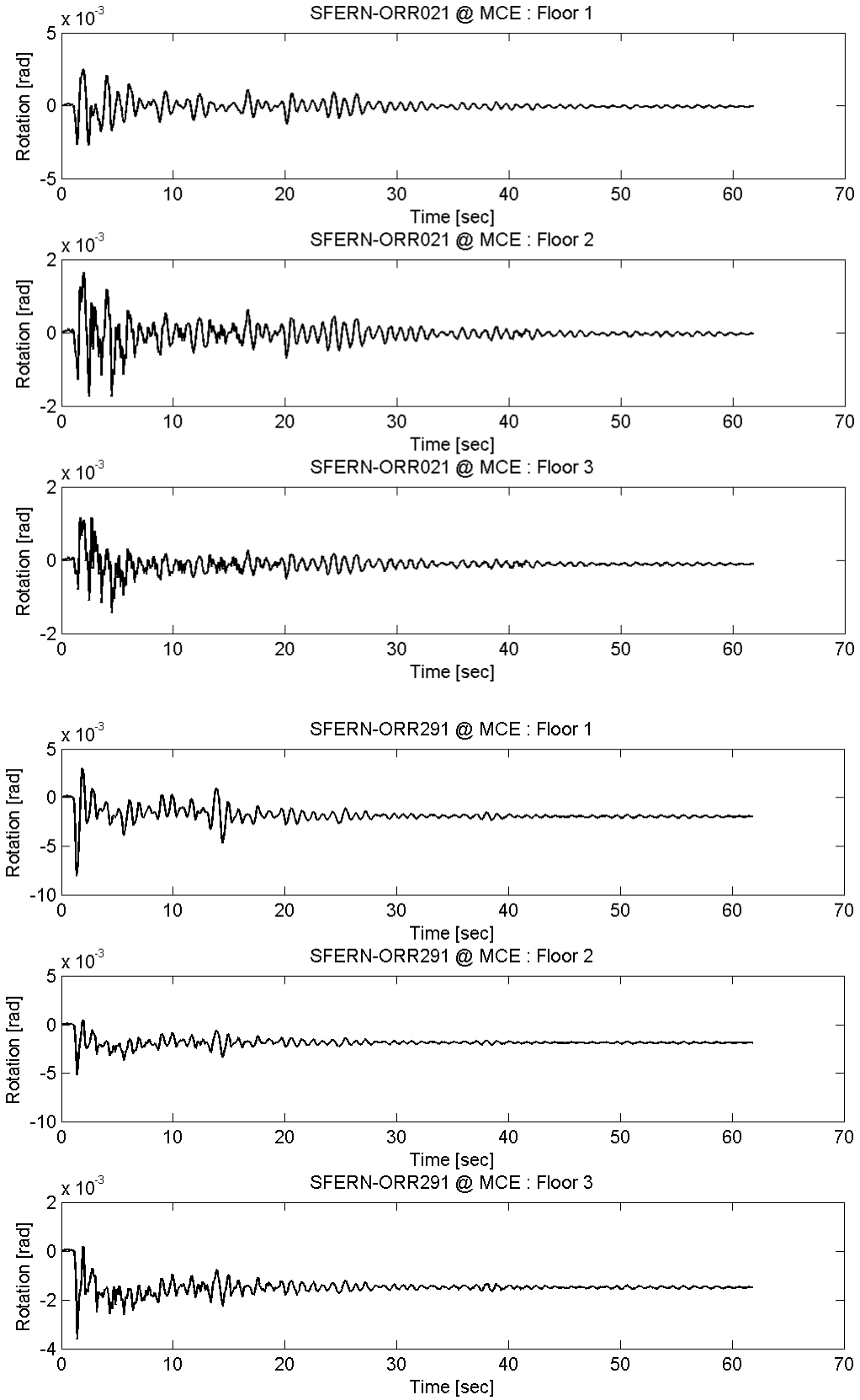
SFERN-ORR021 @ MCE : Floor 1
x 10^-3
Rotation [rad]
Time [sec]
SFERN-ORR021 @ MCE : Floor 2
x 10^-3
Rotation [rad]
Time [sec]
SFERN-ORR021 @ MCE : Floor 3
x 10^-3
Rotation [rad]
Time [sec]
SFERN-ORR291 @ MCE : Floor 1
x 10^-3
Rotation [rad]
Time [sec]
SFERN-ORR291 @ MCE : Floor 2
x 10^-3
Rotation [rad]
Time [sec]
SFERN-ORR291 @ MCE : Floor 3
x 10^-3
Rotation [rad]
Time [sec]

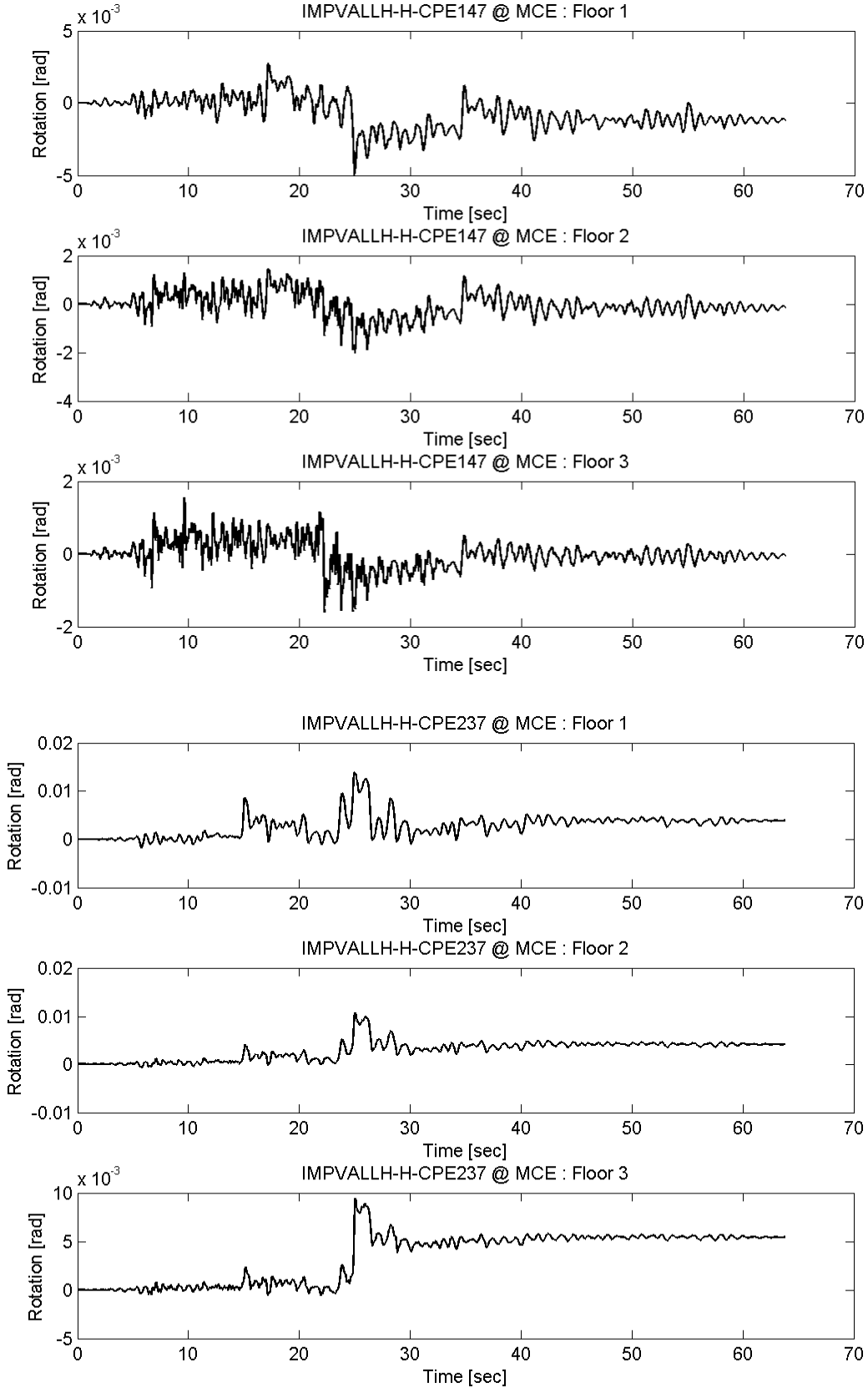
IMPVALLH-H-CPE147 @ MCE : Floor 1
x 10^-3
Rotation [rad]
Time [sec]
IMPVALLH-H-CPE147 @ MCE : Floor 2
x 10^-3
Rotation [rad]
Time [sec]
IMPVALLH-H-CPE147 @ MCE : Floor 3
x 10^-3
Rotation [rad]
Time [sec]
IMPVALLH-H-CPE237 @ MCE : Floor 1
Rotation [rad]
Time [sec]
IMPVALLH-H-CPE237 @ MCE : Floor 2
Rotation [rad]
Time [sec]
IMPVALLH-H-CPE237 @ MCE : Floor 3
x 10^-3
Rotation [rad]
Time [sec]

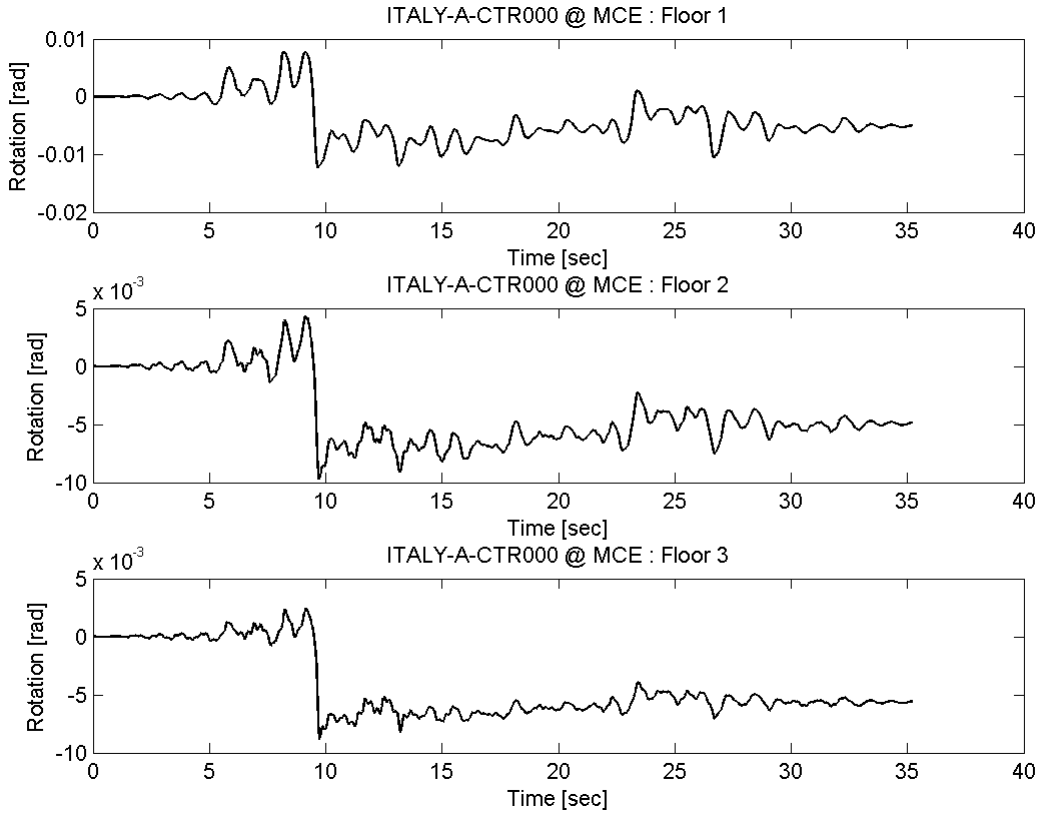
ITALY-A-CTR000 @ MCE : Floor 1
Rotation [rad]
Time [sec]
ITALY-A-CTR000 @ MCE : Floor 2
x 10^-3
Rotation [rad]
Time [sec]
ITALY-A-CTR000 @ MCE : Floor 3
x 10^-3
Rotation [rad]
Time [sec]

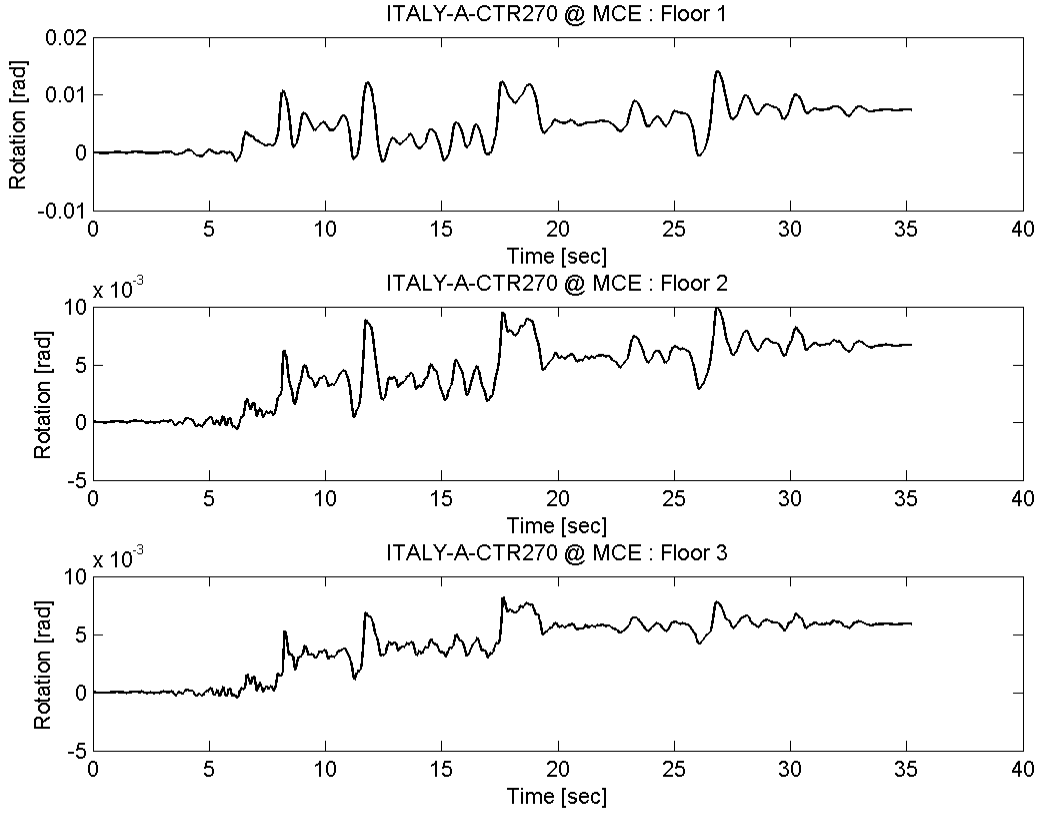
ITALY-A-CTR270 @ MCE : Floor 1
Rotation [rad]
Time [sec]
ITALY-A-CTR270 @ MCE : Floor 2
x 10^-3
Rotation [rad]
Time [sec]
ITALY-A-CTR270 @ MCE : Floor 3
x 10^-3
Rotation [rad]
Time [sec]

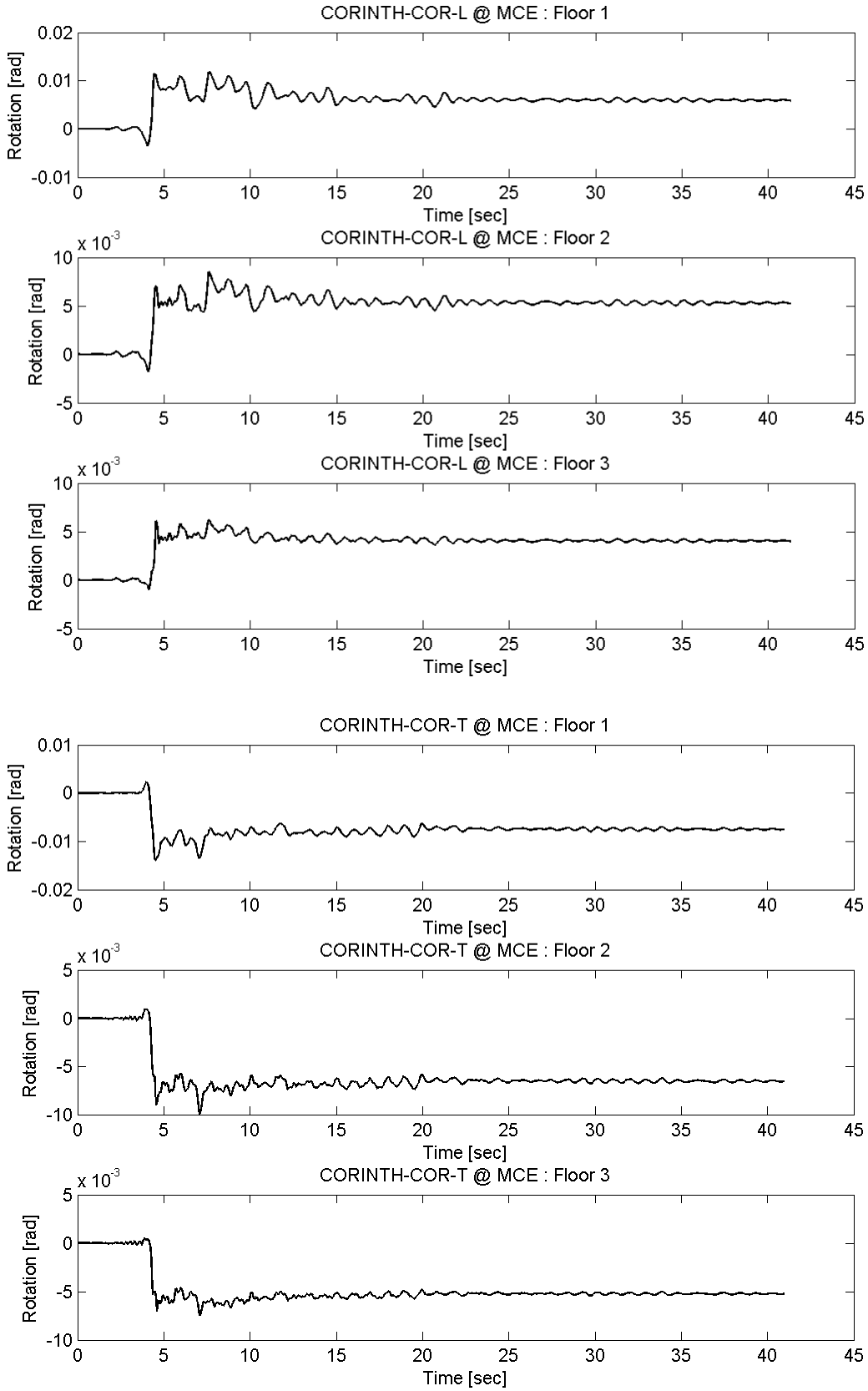
CORINTH-COR-L @ MCE : Floor 1
Rotation [rad]
Time [sec]
CORINTH-COR-L @ MCE : Floor 2
x 10^-3
Rotation [rad]
Time [sec]
CORINTH-COR-L @ MCE : Floor 3
x 10^-3
Rotation [rad]
Time [sec]
CORINTH-COR-T @ MCE : Floor 1
Rotation [rad]
Time [sec]
CORINTH-COR-T @ MCE : Floor 2
x 10^-3
Rotation [rad]
Time [sec]
CORINTH-COR-T @ MCE : Floor 3
x 10^-3
Rotation [rad]
Time [sec]

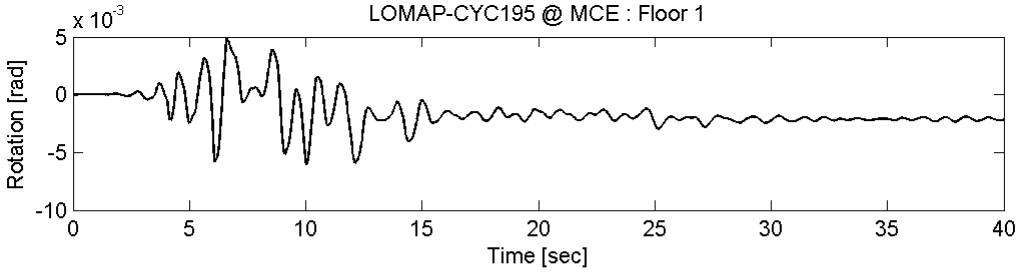
LOMAP-CYC195 @ MCE : Floor 1
x 10^-3
Rotation [rad]
Time [sec]

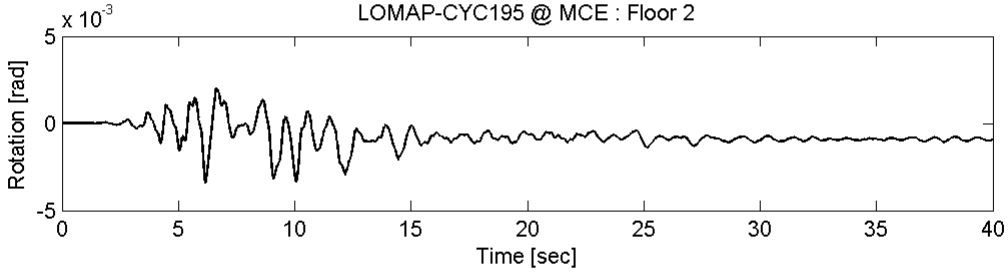
LOMAP-CYC195 @ MCE : Floor 2
x 10^-3
Rotation [rad]
Time [sec]

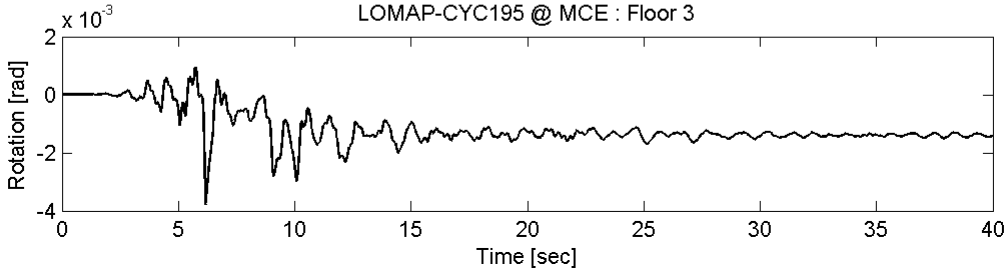
LOMAP-CYC195 @ MCE : Floor 3
x 10^-3
Rotation [rad]
Time [sec]

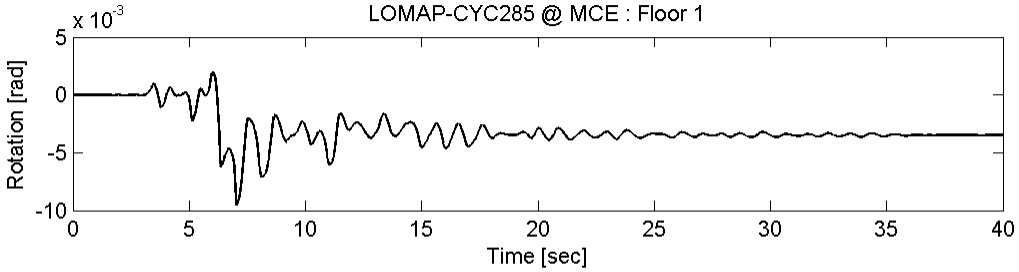
LOMAP-CYC285 @ MCE : Floor 1
x 10^-3
Rotation [rad]
Time [sec]

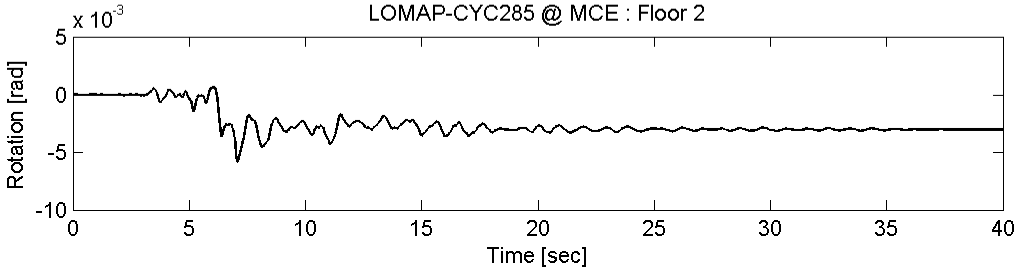
LOMAP-CYC285 @ MCE : Floor 2
x 10^-3
Rotation [rad]
Time [sec]

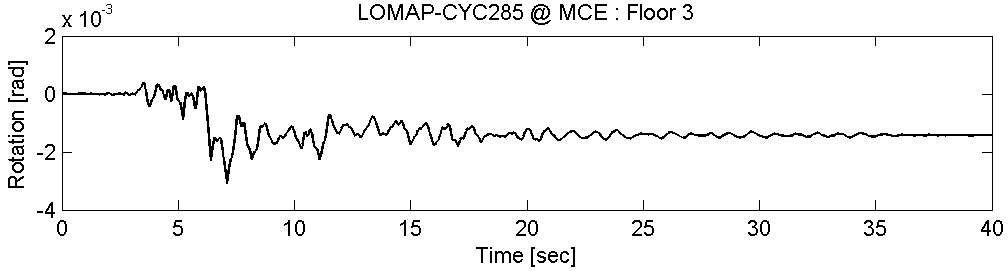
LOMAP-CYC285 @ MCE : Floor 3
x 10^-3
Rotation [rad]
Time [sec]

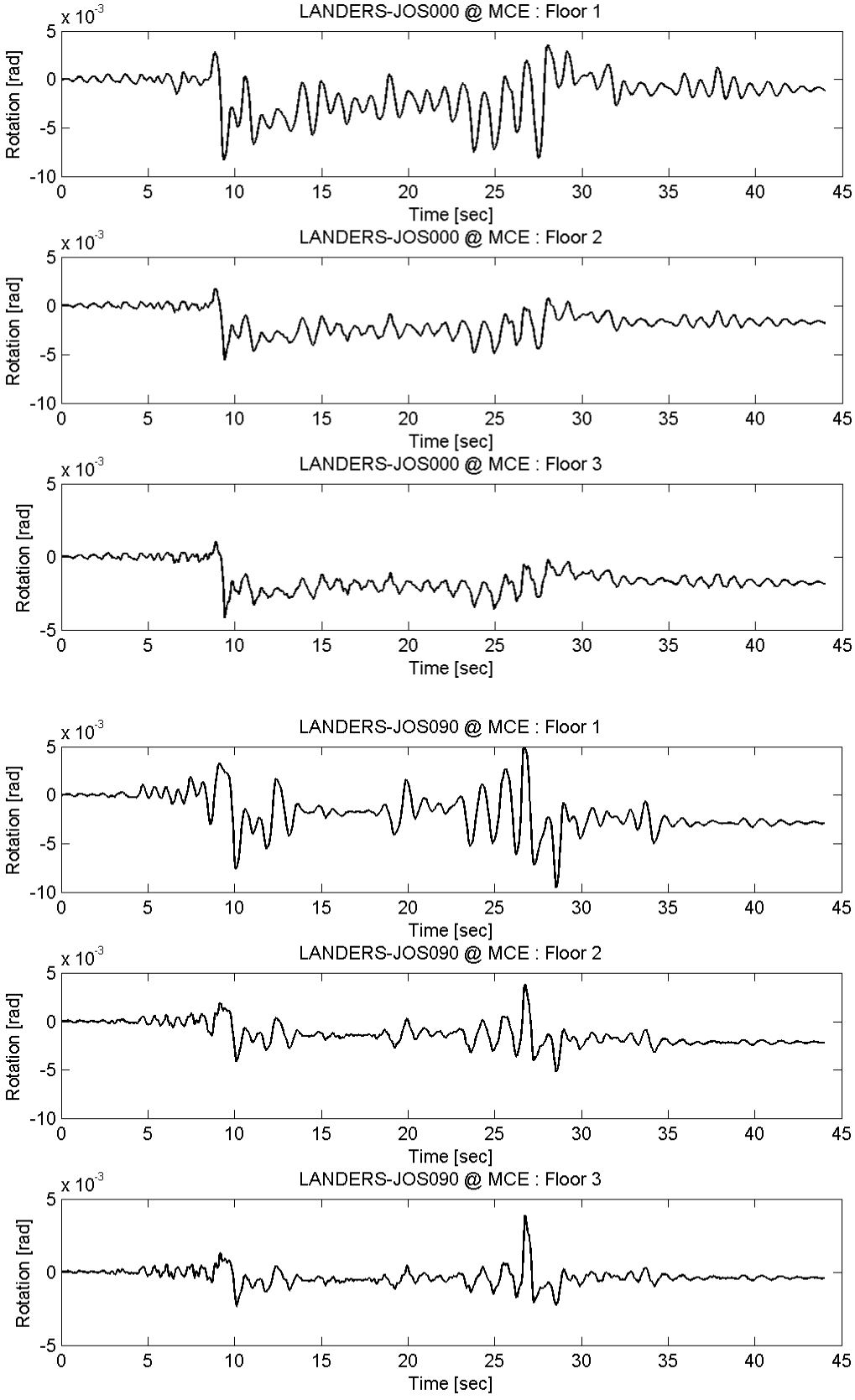
LANDERS-JOS000 @ MCE : Floor 1
LANDERS-JOS000 @ MCE : Floor 2
LANDERS-JOS000 @ MCE : Floor 3
LANDERS-JOS090 @ MCE : Floor 1
LANDERS-JOS090 @ MCE : Floor 2
LANDERS-JOS090 @ MCE : Floor 3
x 10-3
Rotation [rad]
Time [sec]

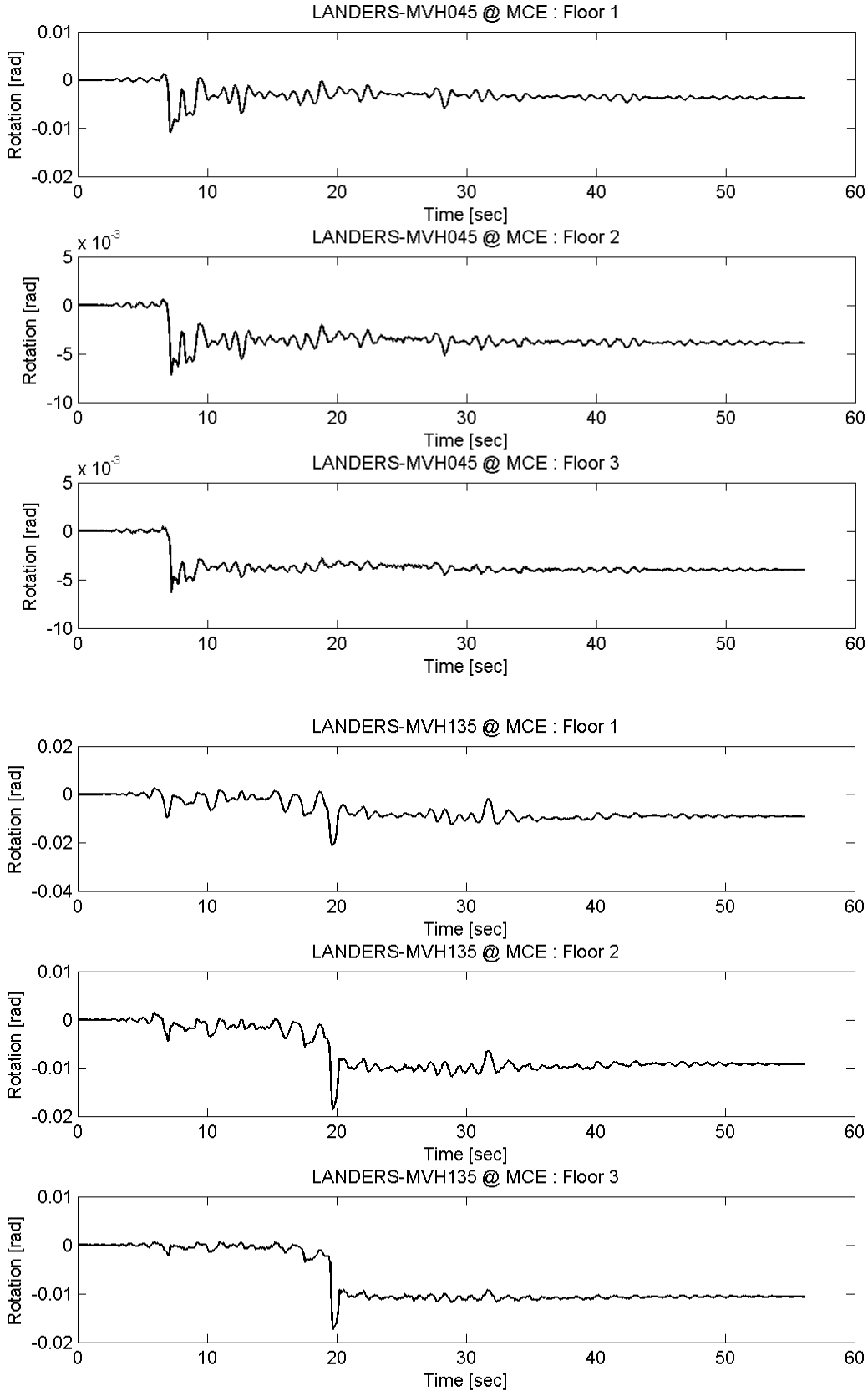
LANDERS-MVH045 @ MCE : Floor 1
Rotation [rad]
Time [sec]
LANDERS-MVH045 @ MCE : Floor 2
x 10^-3
Rotation [rad]
Time [sec]
LANDERS-MVH045 @ MCE : Floor 3
x 10^-3
Rotation [rad]
Time [sec]
LANDERS-MVH135 @ MCE : Floor 1
Rotation [rad]
Time [sec]
LANDERS-MVH135 @ MCE : Floor 2
Rotation [rad]
Time [sec]
LANDERS-MVH135 @ MCE : Floor 3
Rotation [rad]
Time [sec]

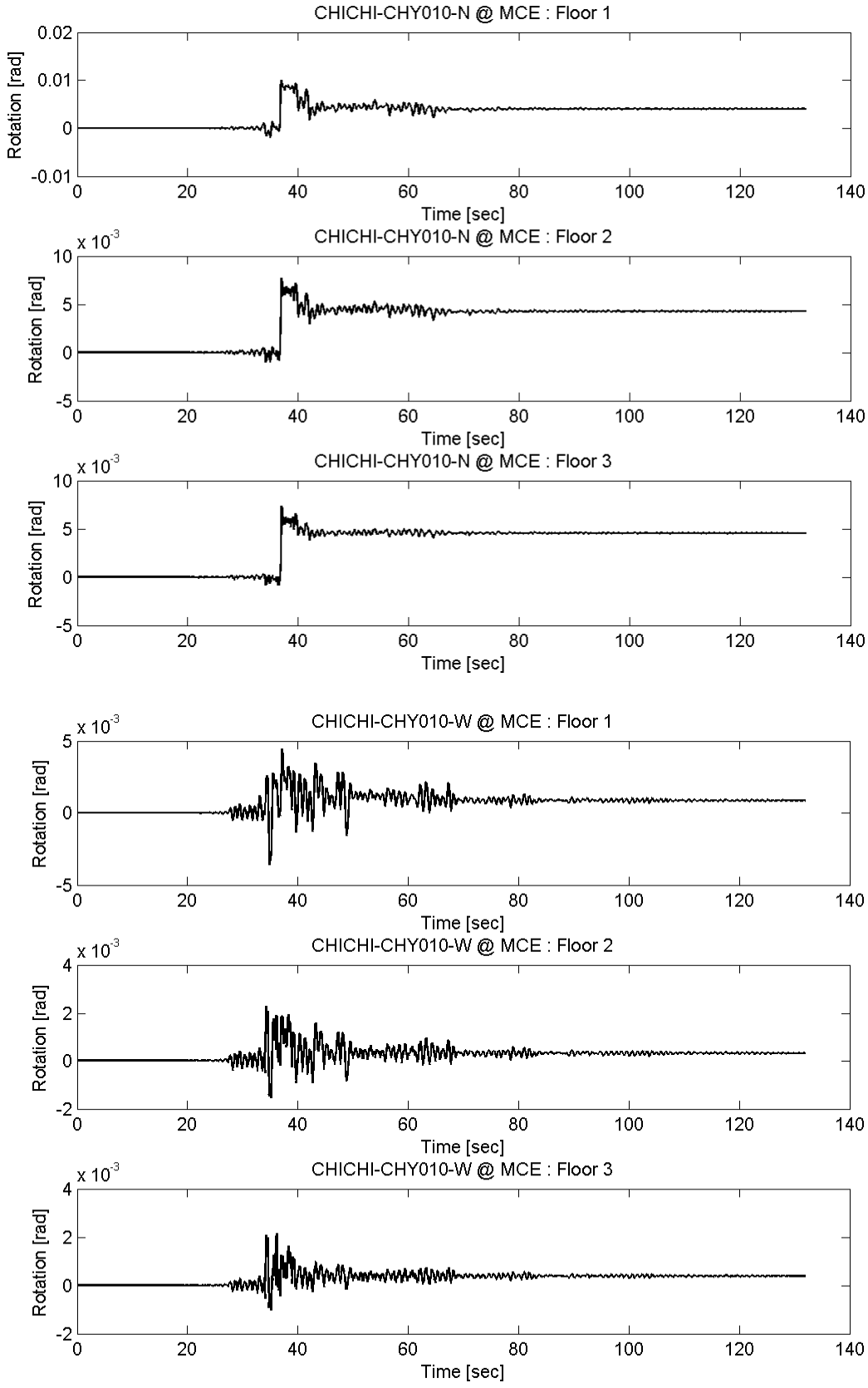
CHICHI-CHY010-N @ MCE : Floor 1
Rotation [rad]
Time [sec]
CHICHI-CHY010-N @ MCE : Floor 2
x 10^-3
Rotation [rad]
Time [sec]
CHICHI-CHY010-N @ MCE : Floor 3
x 10^-3
Rotation [rad]
Time [sec]
CHICHI-CHY010-W @ MCE : Floor 1
x 10^-3
Rotation [rad]
Time [sec]
CHICHI-CHY010-W @ MCE : Floor 2
x 10^-3
Rotation [rad]
Time [sec]
CHICHI-CHY010-W @ MCE : Floor 3
x 10^-3
Rotation [rad]
Time [sec]

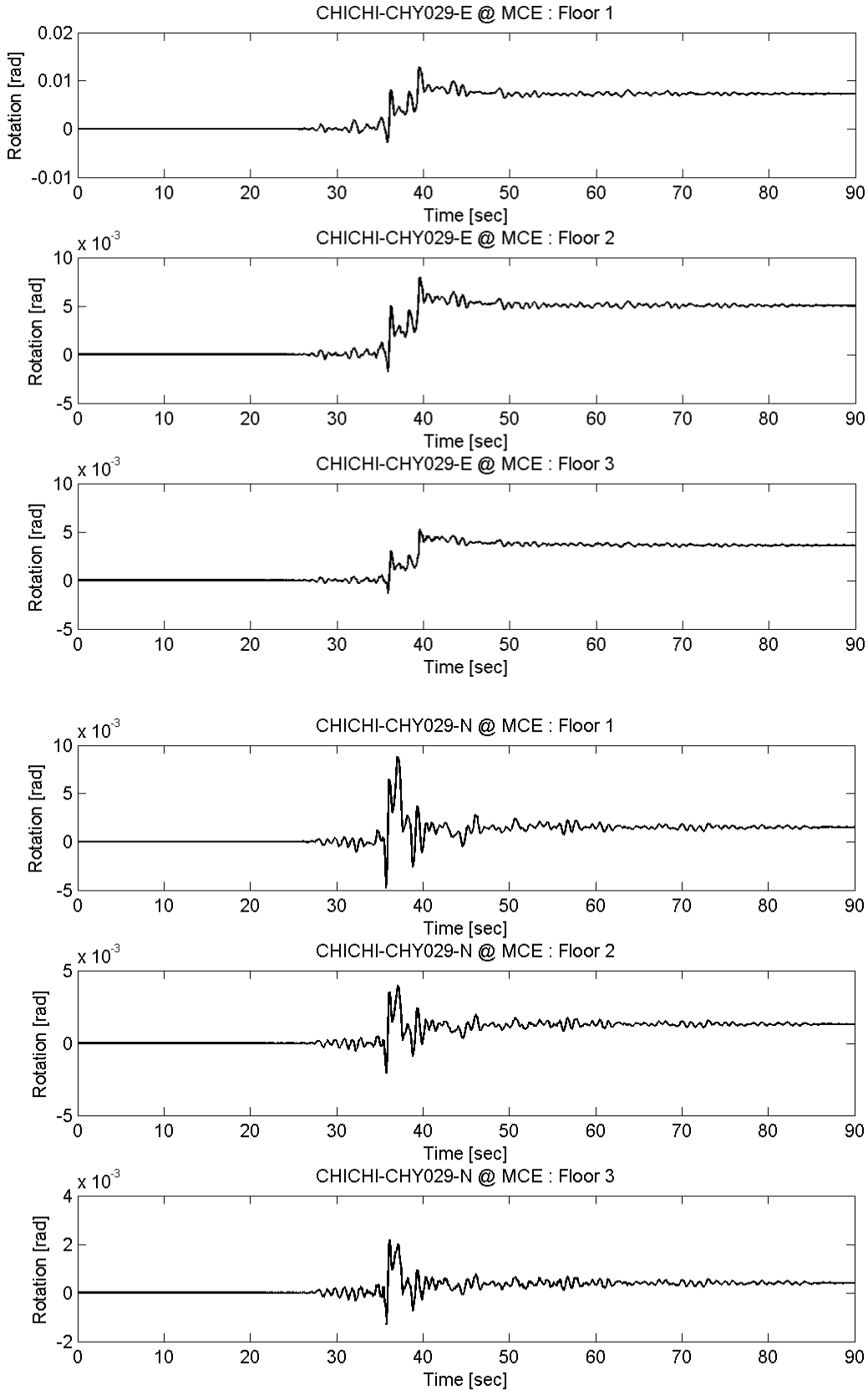
CHICHI-CHY029-E @ MCE : Floor 1
Rotation [rad]
Time [sec]
CHICHI-CHY029-E @ MCE : Floor 2
x 10^-3
Rotation [rad]
Time [sec]
CHICHI-CHY029-E @ MCE : Floor 3
x 10^-3
Rotation [rad]
Time [sec]
CHICHI-CHY029-N @ MCE : Floor 1
x 10^-3
Rotation [rad]
Time [sec]
CHICHI-CHY029-N @ MCE : Floor 2
x 10^-3
Rotation [rad]
Time [sec]
CHICHI-CHY029-N @ MCE : Floor 3
x 10^-3
Rotation [rad]
Time [sec]

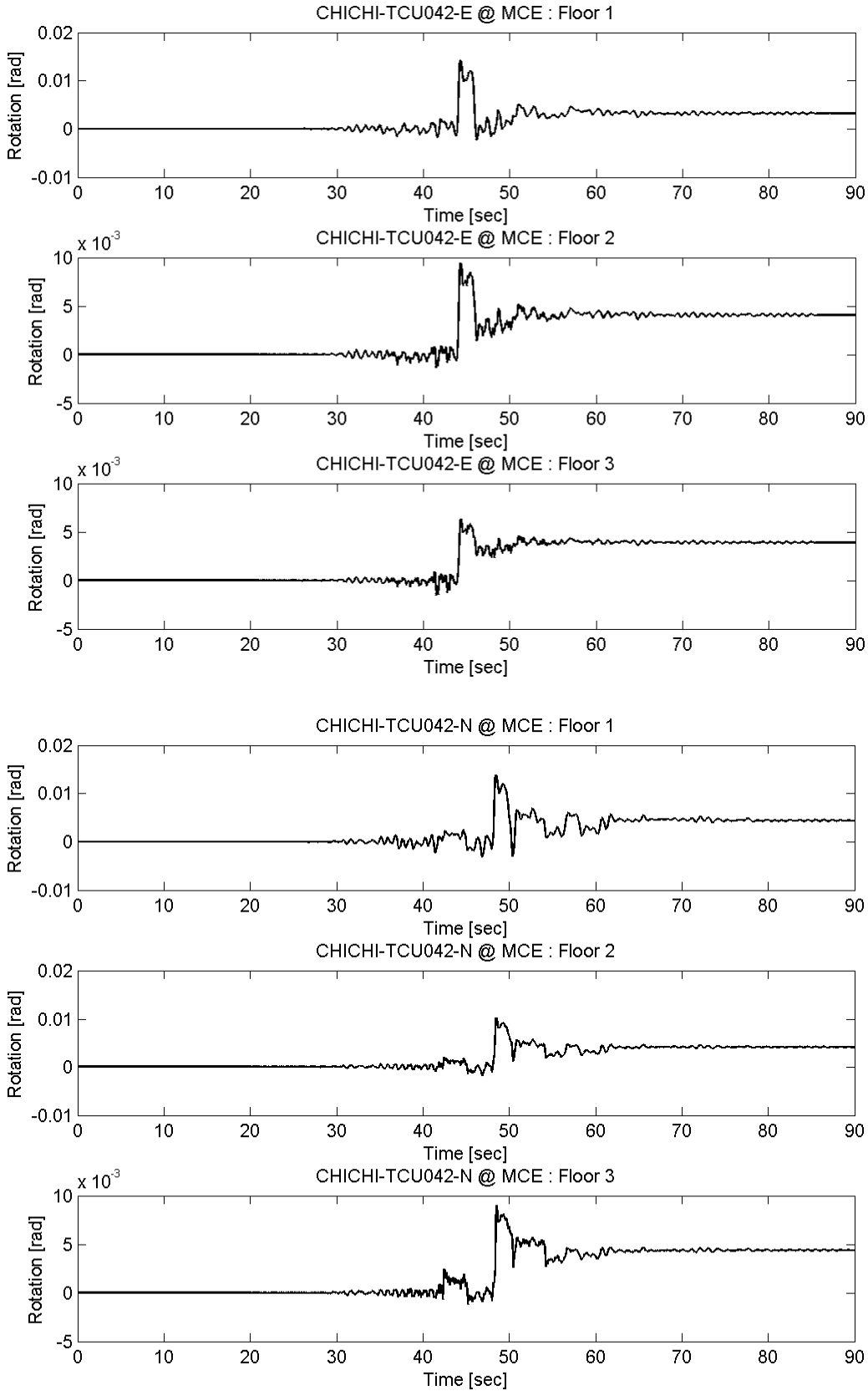
CHICHI-TCU042-E @ MCE : Floor 1
Rotation [rad]
Time [sec]
CHICHI-TCU042-E @ MCE : Floor 2
x 10^-3
Rotation [rad]
Time [sec]
CHICHI-TCU042-E @ MCE : Floor 3
x 10^-3
Rotation [rad]
Time [sec]
CHICHI-TCU042-N @ MCE : Floor 1
Rotation [rad]
Time [sec]
CHICHI-TCU042-N @ MCE : Floor 2
Rotation [rad]
Time [sec]
CHICHI-TCU042-N @ MCE : Floor 3
x 10^-3
Rotation [rad]
Time [sec]

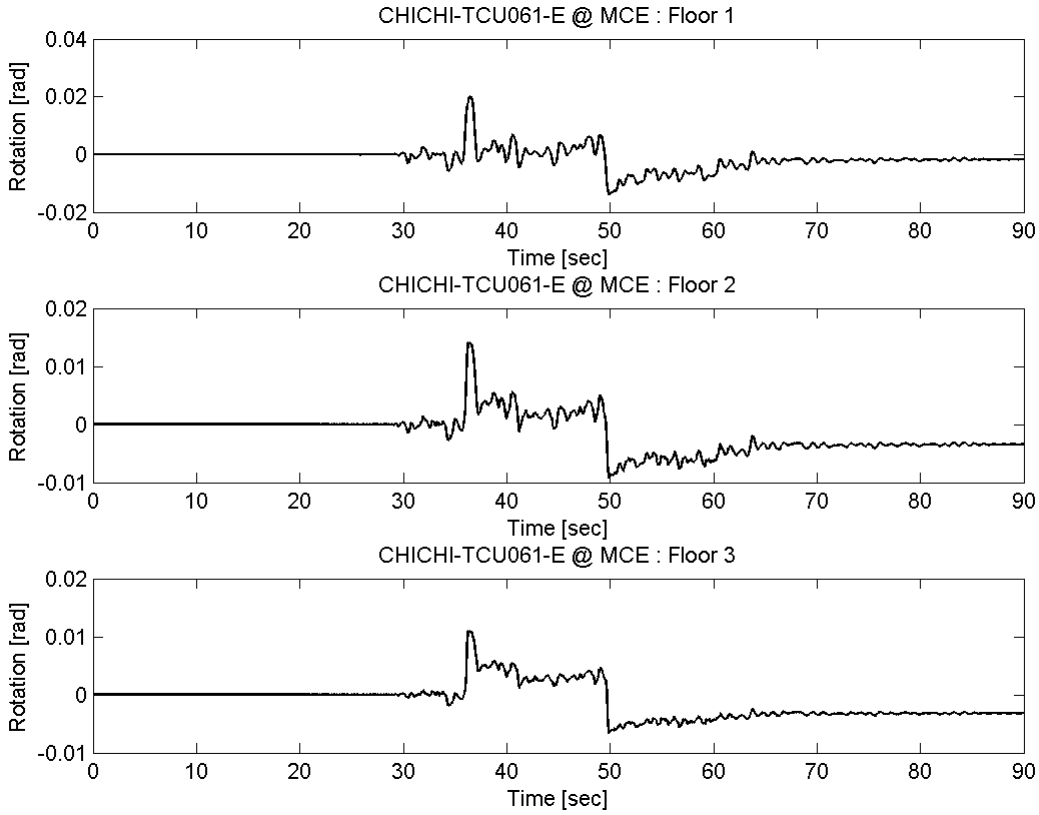
CHICHI-TCU061-E @ MCE : Floor 1
Rotation [rad]
Time [sec]
CHICHI-TCU061-E @ MCE : Floor 2
Rotation [rad]
Time [sec]
CHICHI-TCU061-E @ MCE : Floor 3
Rotation [rad]
Time [sec]

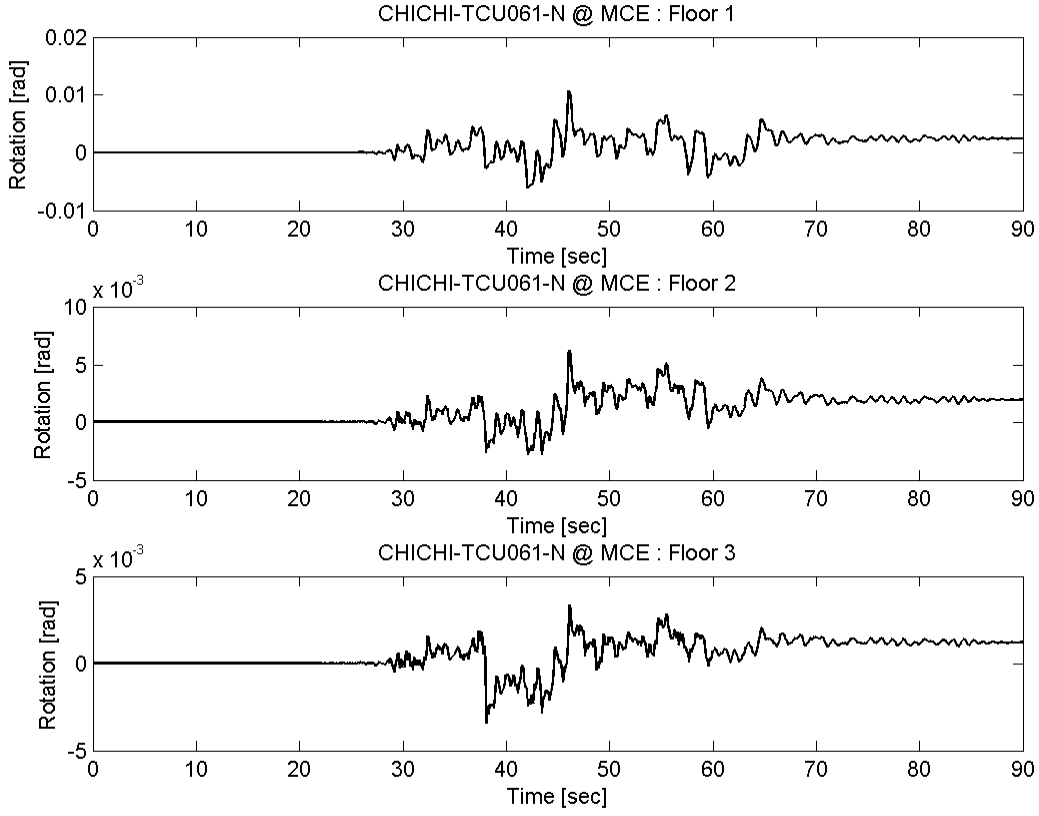
CHICHI-TCU061-N @ MCE : Floor 1
Rotation [rad]
Time [sec]
x 10-3
CHICHI-TCU061-N @ MCE : Floor 2
Rotation [rad]
Time [sec]
x 10-3
CHICHI-TCU061-N @ MCE : Floor 3
Rotation [rad]
Time [sec]

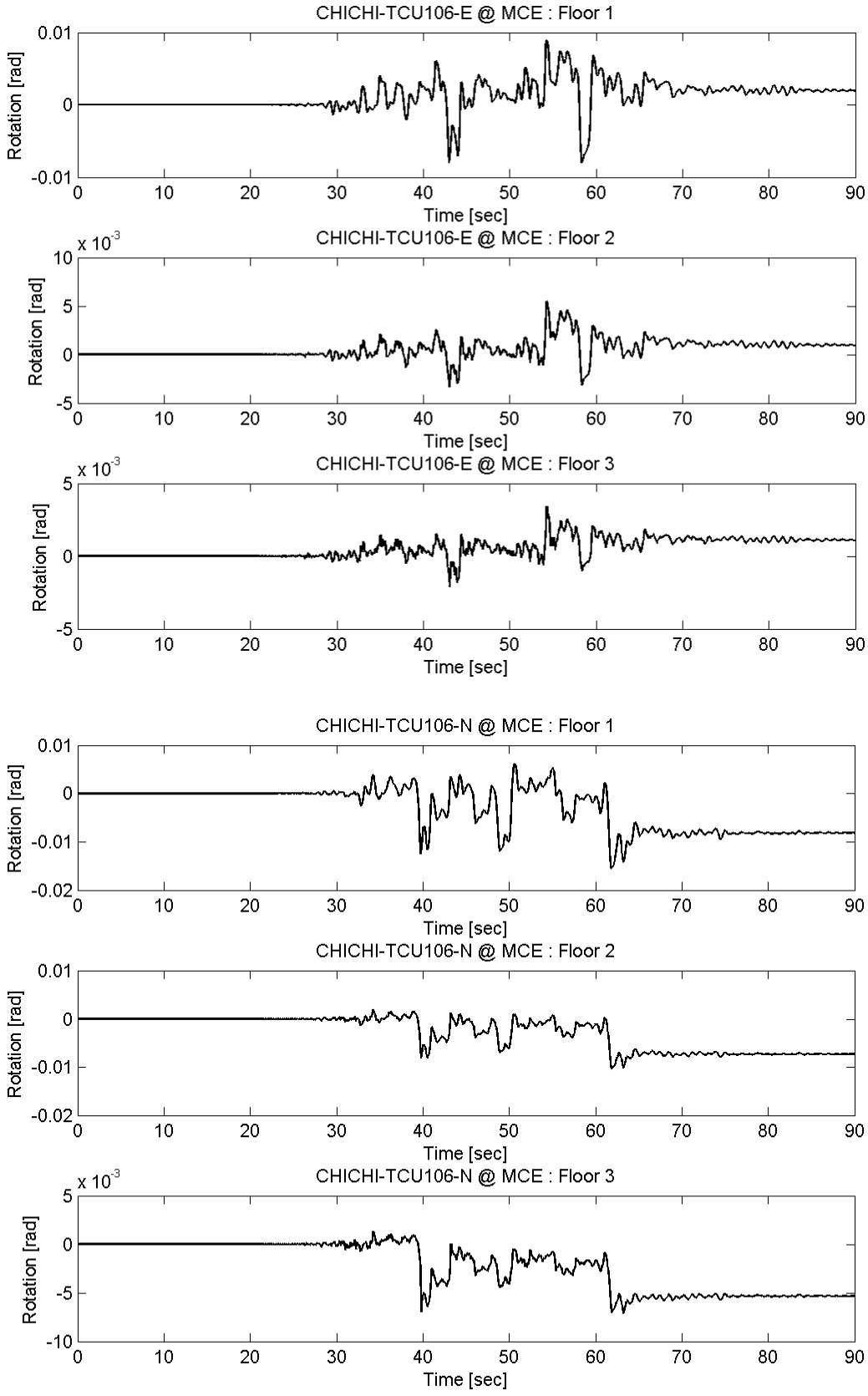
CHICHI-TCU106-E @ MCE : Floor 1
Rotation [rad]
Time [sec]
CHICHI-TCU106-E @ MCE : Floor 2
x 10^-3
Rotation [rad]
Time [sec]
CHICHI-TCU106-E @ MCE : Floor 3
x 10^-3
Rotation [rad]
Time [sec]
CHICHI-TCU106-N @ MCE : Floor 1
Rotation [rad]
Time [sec]
CHICHI-TCU106-N @ MCE : Floor 2
Rotation [rad]
Time [sec]
CHICHI-TCU106-N @ MCE : Floor 3
x 10^-3
Rotation [rad]
Time [sec]

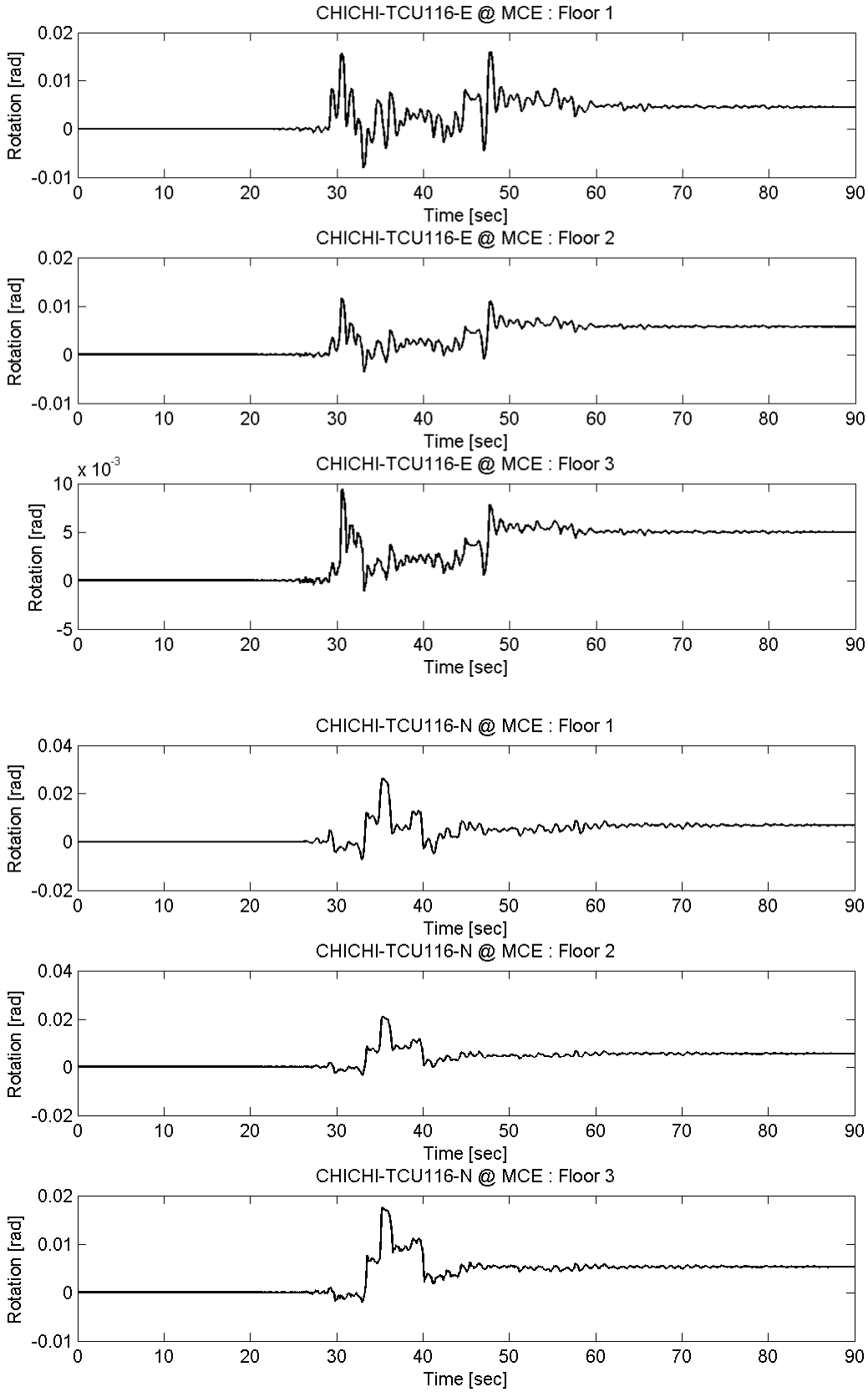
CHICHI-TCU116-E @ MCE : Floor 1
Rotation [rad]
Time [sec]
CHICHI-TCU116-E @ MCE : Floor 2
Rotation [rad]
Time [sec]
CHICHI-TCU116-E @ MCE : Floor 3
x 10-3
Rotation [rad]
Time [sec]
CHICHI-TCU116-N @ MCE : Floor 1
Rotation [rad]
Time [sec]
CHICHI-TCU116-N @ MCE : Floor 2
Rotation [rad]
Time [sec]
CHICHI-TCU116-N @ MCE : Floor 3
Rotation [rad]
Time [sec]

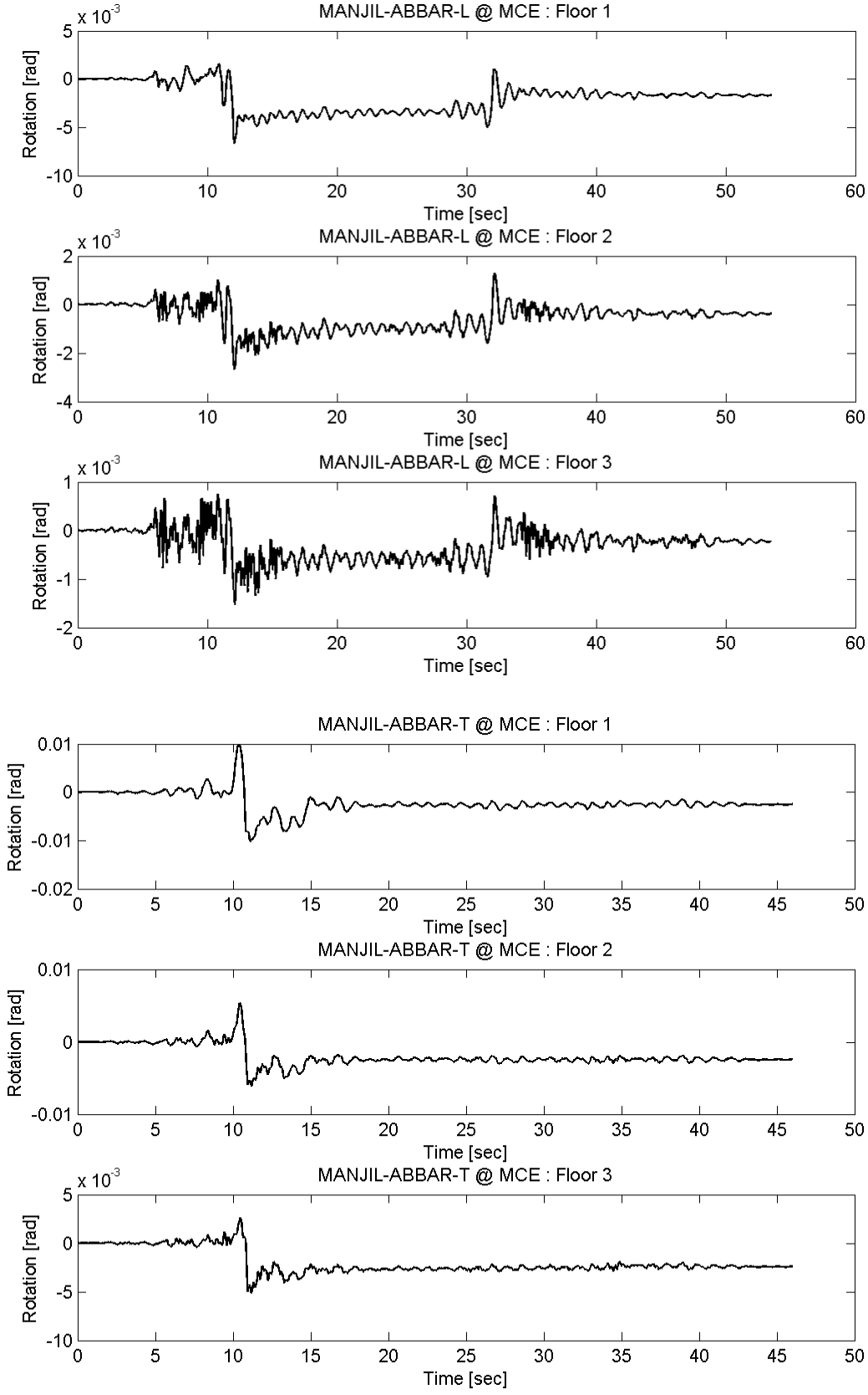
MANJIL-ABBAR-L @ MCE : Floor 1
x 10^-3
Rotation [rad]
Time [sec]
MANJIL-ABBAR-L @ MCE : Floor 2
x 10^-3
Rotation [rad]
Time [sec]
MANJIL-ABBAR-L @ MCE : Floor 3
x 10^-3
Rotation [rad]
Time [sec]
MANJIL-ABBAR-T @ MCE : Floor 1
Rotation [rad]
Time [sec]
MANJIL-ABBAR-T @ MCE : Floor 2
Rotation [rad]
Time [sec]
MANJIL-ABBAR-T @ MCE : Floor 3
x 10^-3
Rotation [rad]
Time [sec]

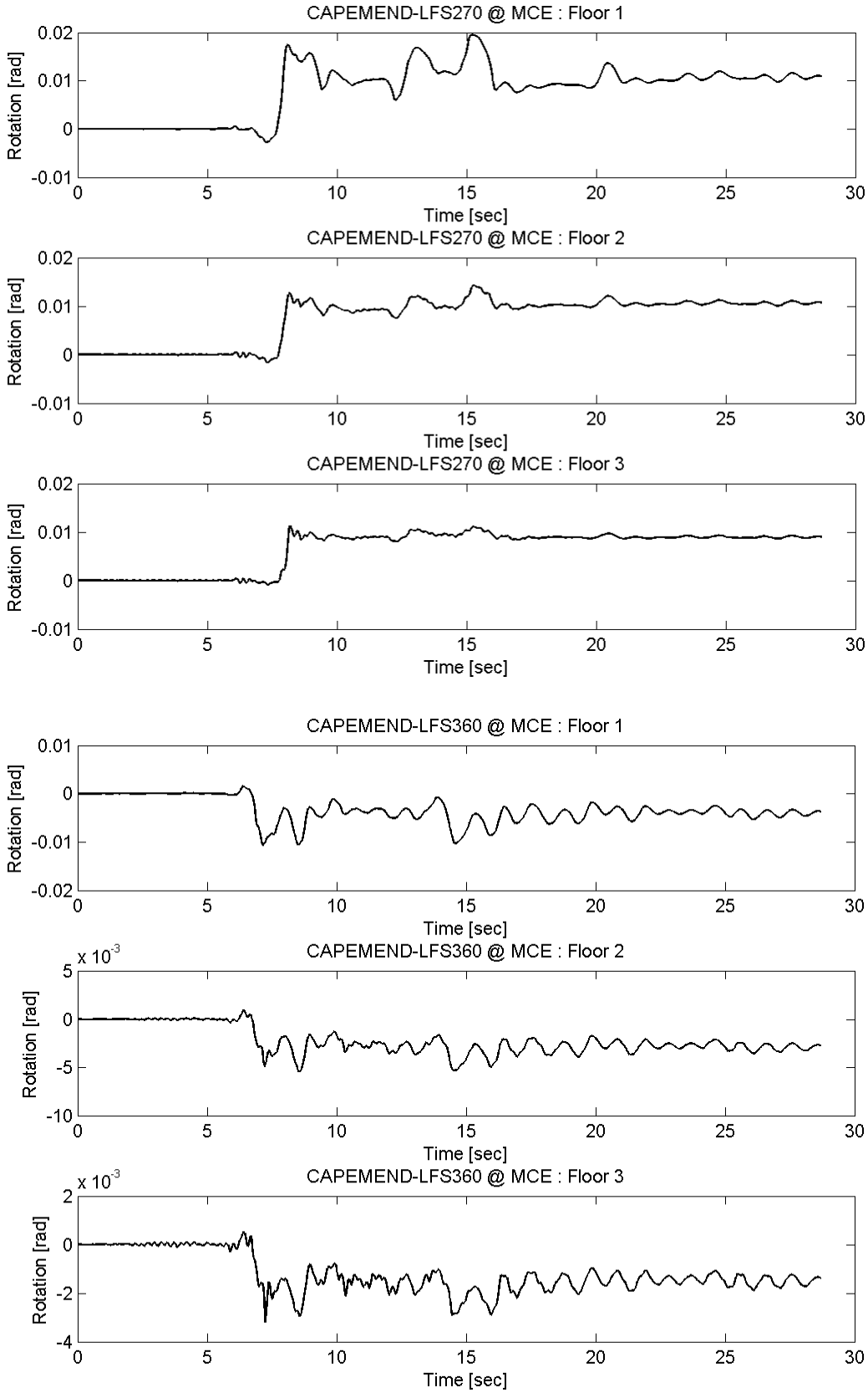
CAPEMEND-LFS270 @ MCE : Floor 1
Rotation [rad]
Time [sec]
CAPEMEND-LFS270 @ MCE : Floor 2
Rotation [rad]
Time [sec]
CAPEMEND-LFS270 @ MCE : Floor 3
Rotation [rad]
Time [sec]
CAPEMEND-LFS360 @ MCE : Floor 1
Rotation [rad]
Time [sec]
CAPEMEND-LFS360 @ MCE : Floor 2
x 10-3
Rotation [rad]
Time [sec]
CAPEMEND-LFS360 @ MCE : Floor 3
x 10-3
Rotation [rad]
Time [sec]

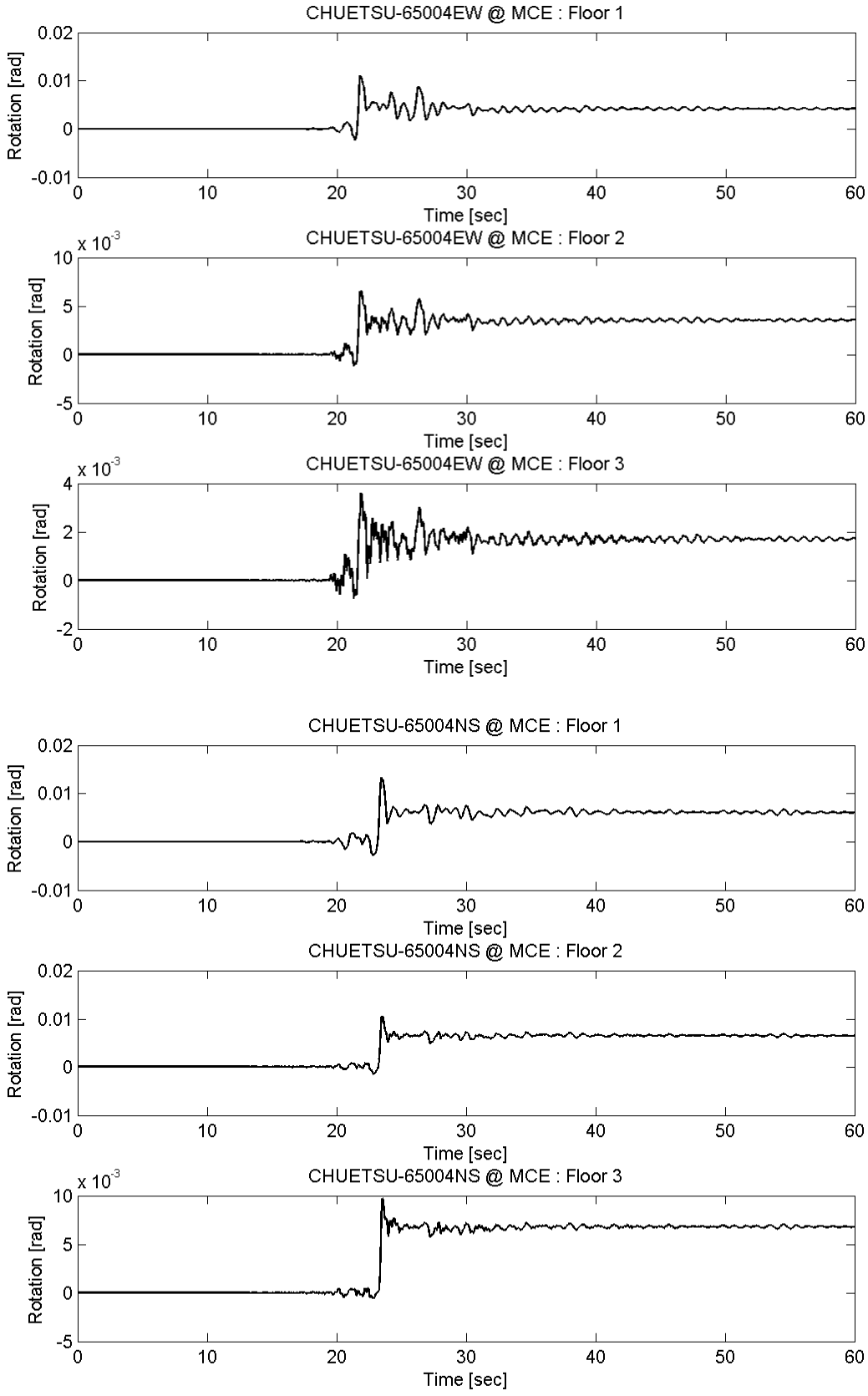
CHUETSU-65004EW @ MCE : Floor 1
Rotation [rad]
Time [sec]
CHUETSU-65004EW @ MCE : Floor 2
x 10-3
Rotation [rad]
Time [sec]
CHUETSU-65004EW @ MCE : Floor 3
x 10-3
Rotation [rad]
Time [sec]
CHUETSU-65004NS @ MCE : Floor 1
Rotation [rad]
Time [sec]
CHUETSU-65004NS @ MCE : Floor 2
Rotation [rad]
Time [sec]
CHUETSU-65004NS @ MCE : Floor 3
x 10-3
Rotation [rad]
Time [sec]

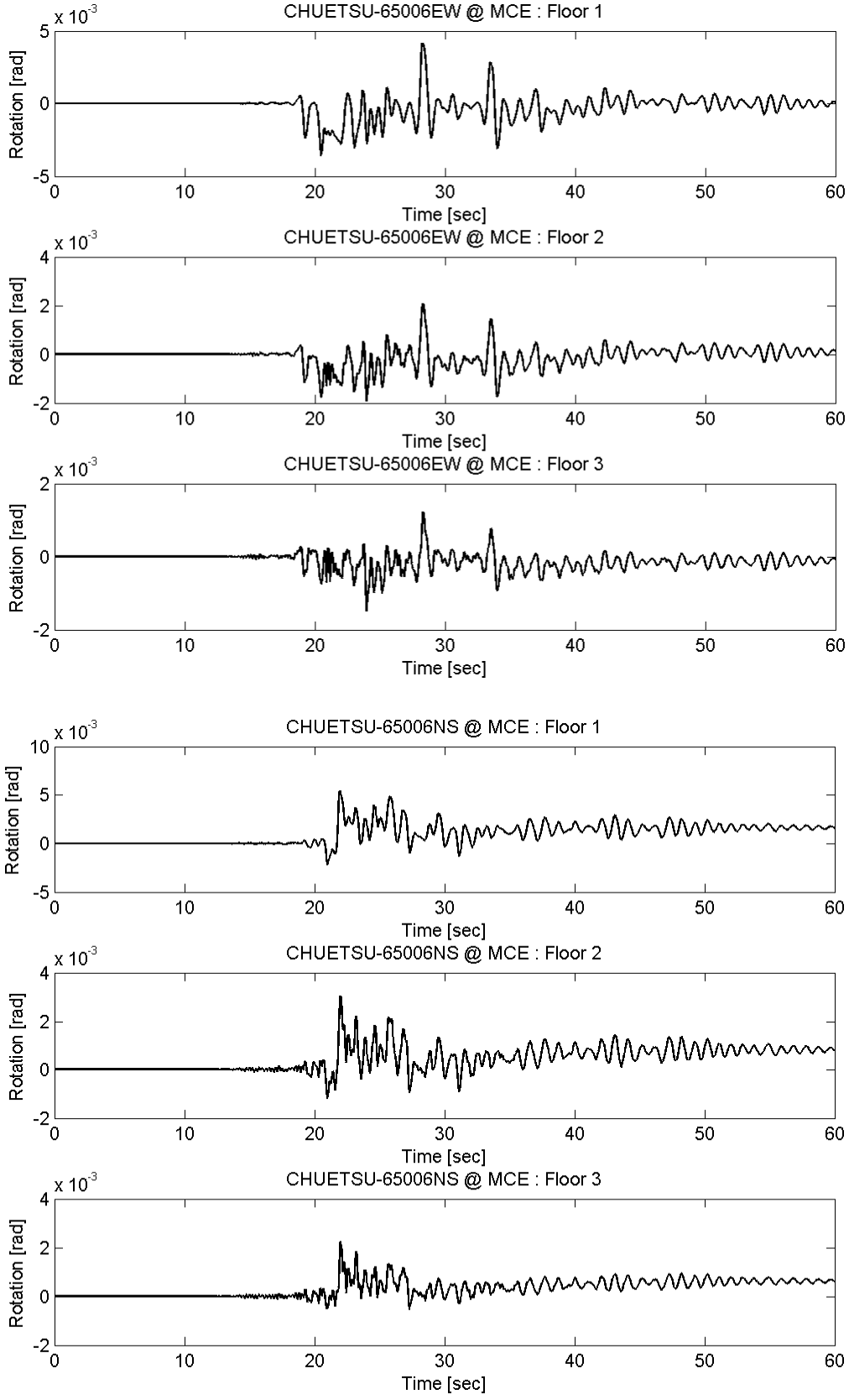
CHUETSU-65006EW @ MCE : Floor 1
CHUETSU-65006EW @ MCE : Floor 2
CHUETSU-65006EW @ MCE : Floor 3
CHUETSU-65006NS @ MCE : Floor 1
CHUETSU-65006NS @ MCE : Floor 2
CHUETSU-65006NS @ MCE : Floor 3
x 10^-3
Rotation [rad]
Time [sec]

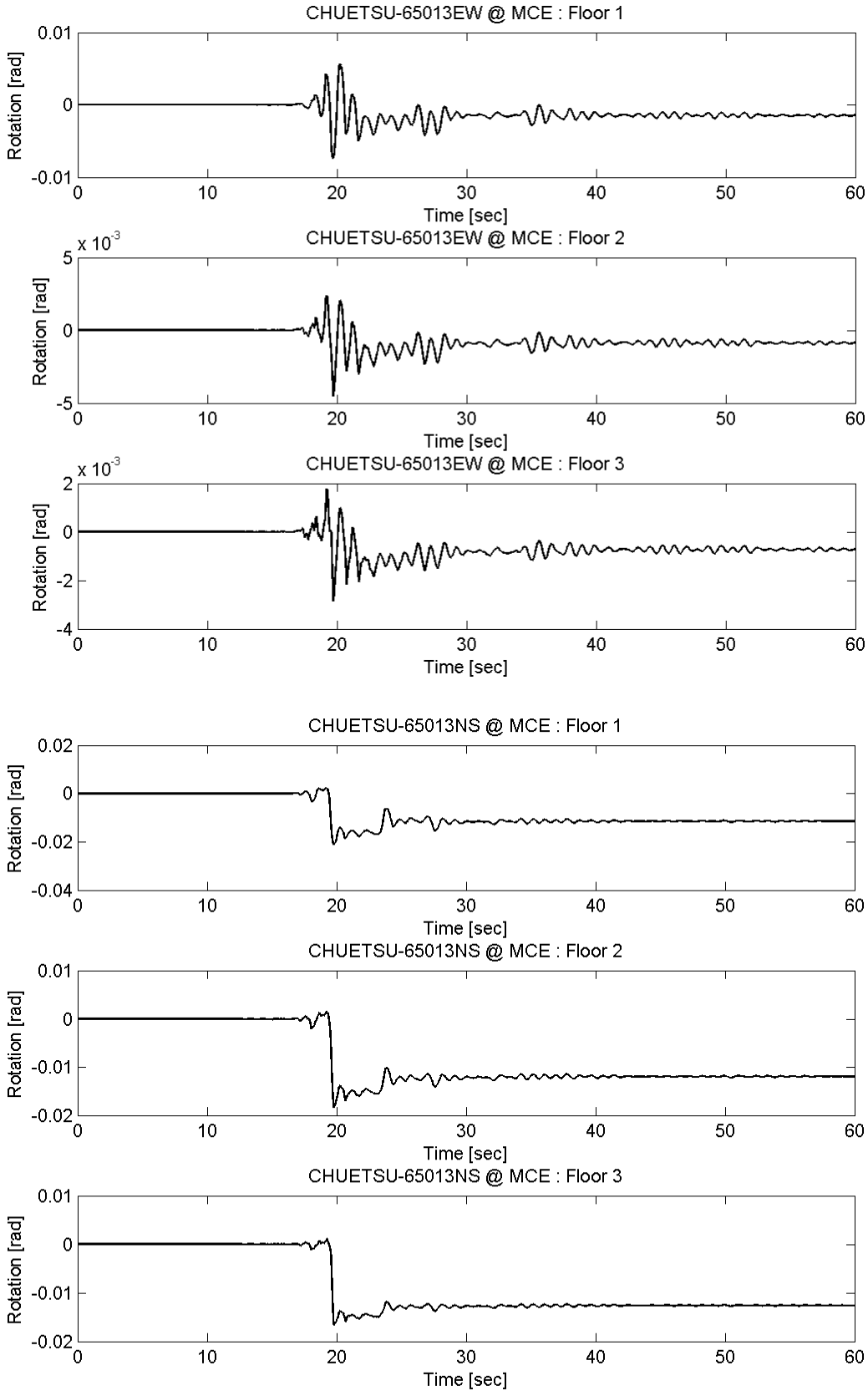
CHUETSU-65013EW @ MCE : Floor 1
Rotation [rad]
Time [sec]
CHUETSU-65013EW @ MCE : Floor 2
x 10-3
Rotation [rad]
Time [sec]
CHUETSU-65013EW @ MCE : Floor 3
x 10-3
Rotation [rad]
Time [sec]
CHUETSU-65013NS @ MCE : Floor 1
Rotation [rad]
Time [sec]
CHUETSU-65013NS @ MCE : Floor 2
Rotation [rad]
Time [sec]
CHUETSU-65013NS @ MCE : Floor 3
Rotation [rad]
Time [sec]

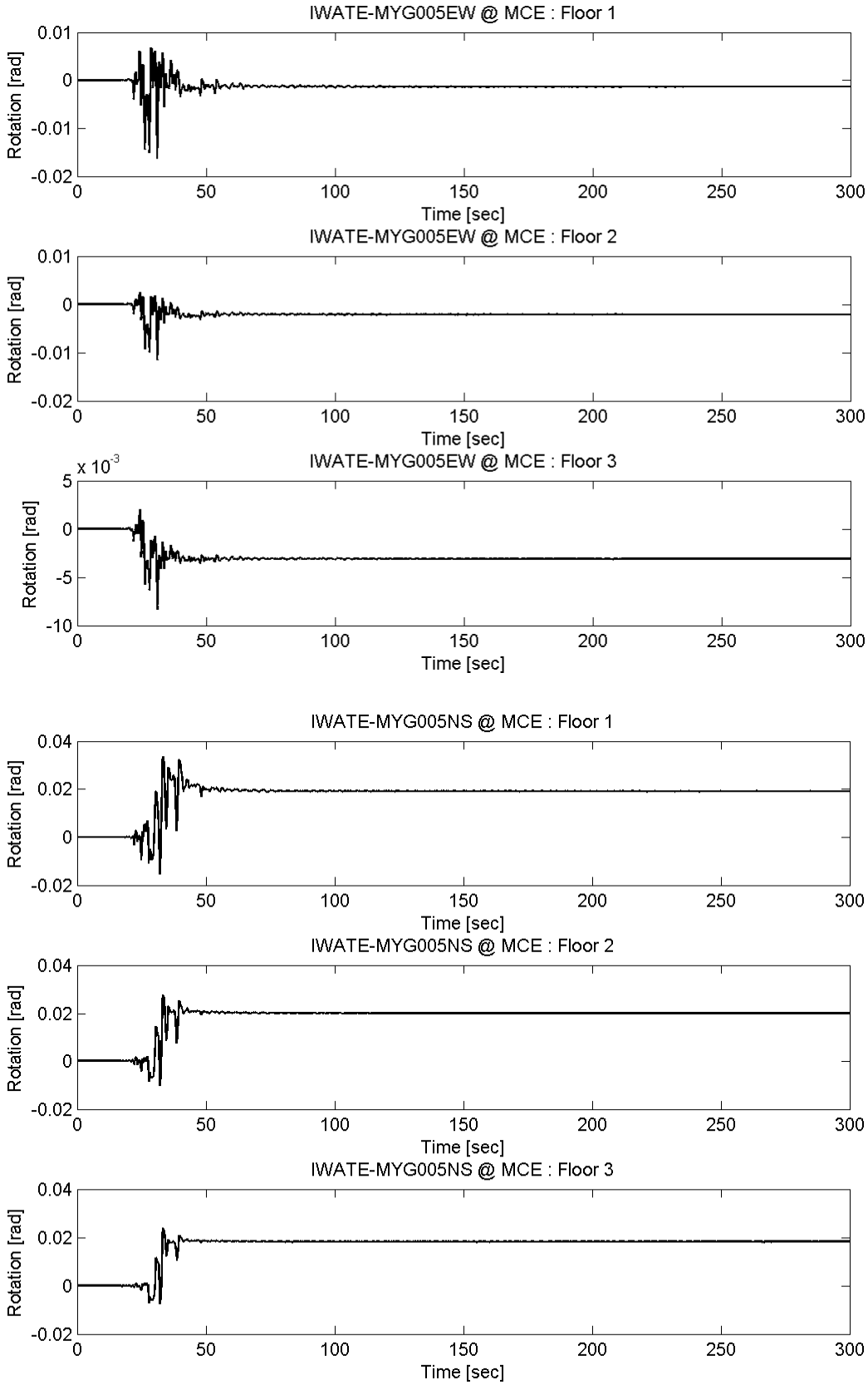
IWATE-MYG005EW @ MCE : Floor 1
Rotation [rad]
Time [sec]
IWATE-MYG005EW @ MCE : Floor 2
Rotation [rad]
Time [sec]
IWATE-MYG005EW @ MCE : Floor 3
x 10-3
Rotation [rad]
Time [sec]
IWATE-MYG005NS @ MCE : Floor 1
Rotation [rad]
Time [sec]
IWATE-MYG005NS @ MCE : Floor 2
Rotation [rad]
Time [sec]
IWATE-MYG005NS @ MCE : Floor 3
Rotation [rad]
Time [sec]

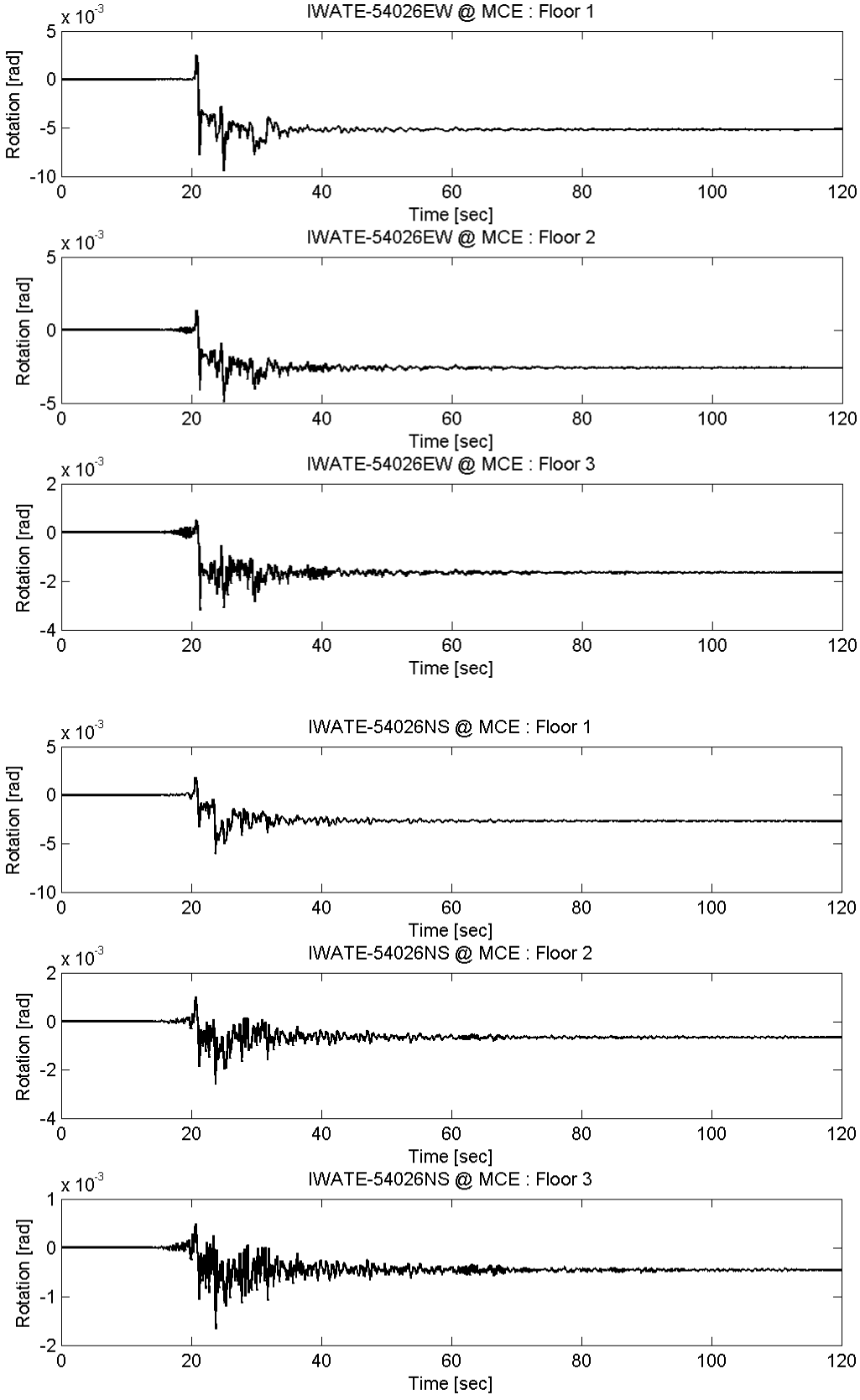
IWATE-54026EW @ MCE : Floor 1
x 10^-3
Rotation [rad]
Time [sec]
IWATE-54026EW @ MCE : Floor 2
x 10^-3
Rotation [rad]
Time [sec]
IWATE-54026EW @ MCE : Floor 3
x 10^-3
Rotation [rad]
Time [sec]
IWATE-54026NS @ MCE : Floor 1
x 10^-3
Rotation [rad]
Time [sec]
IWATE-54026NS @ MCE : Floor 2
x 10^-3
Rotation [rad]
Time [sec]
IWATE-54026NS @ MCE : Floor 3
x 10^-3
Rotation [rad]
Time [sec]

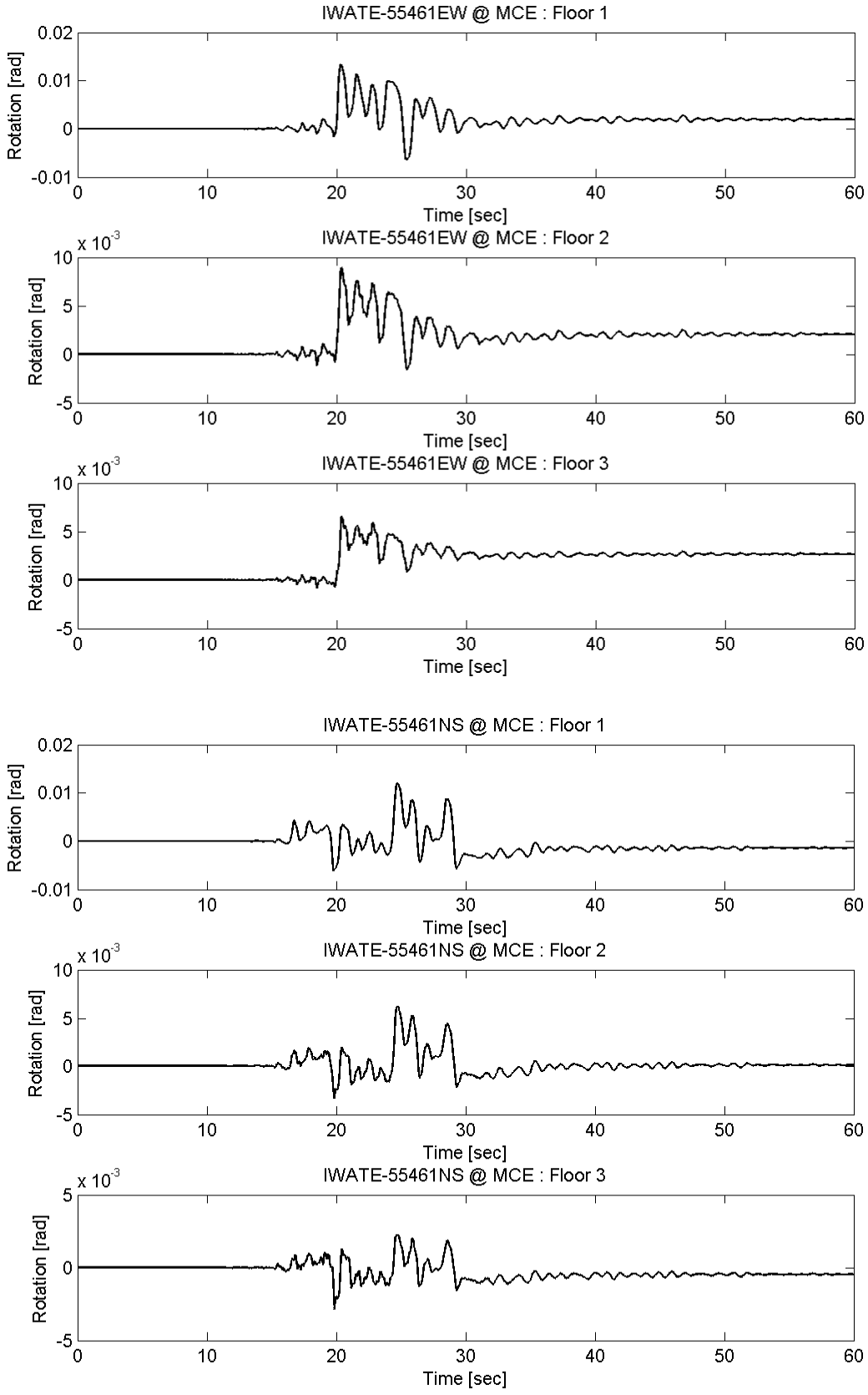
IWATE-55461EW @ MCE : Floor 1
Rotation [rad]
Time [sec]
IWATE-55461EW @ MCE : Floor 2
x 10^-3
Rotation [rad]
Time [sec]
IWATE-55461EW @ MCE : Floor 3
x 10^-3
Rotation [rad]
Time [sec]
IWATE-55461NS @ MCE : Floor 1
Rotation [rad]
Time [sec]
IWATE-55461NS @ MCE : Floor 2
x 10^-3
Rotation [rad]
Time [sec]
IWATE-55461NS @ MCE : Floor 3
x 10^-3
Rotation [rad]
Time [sec]

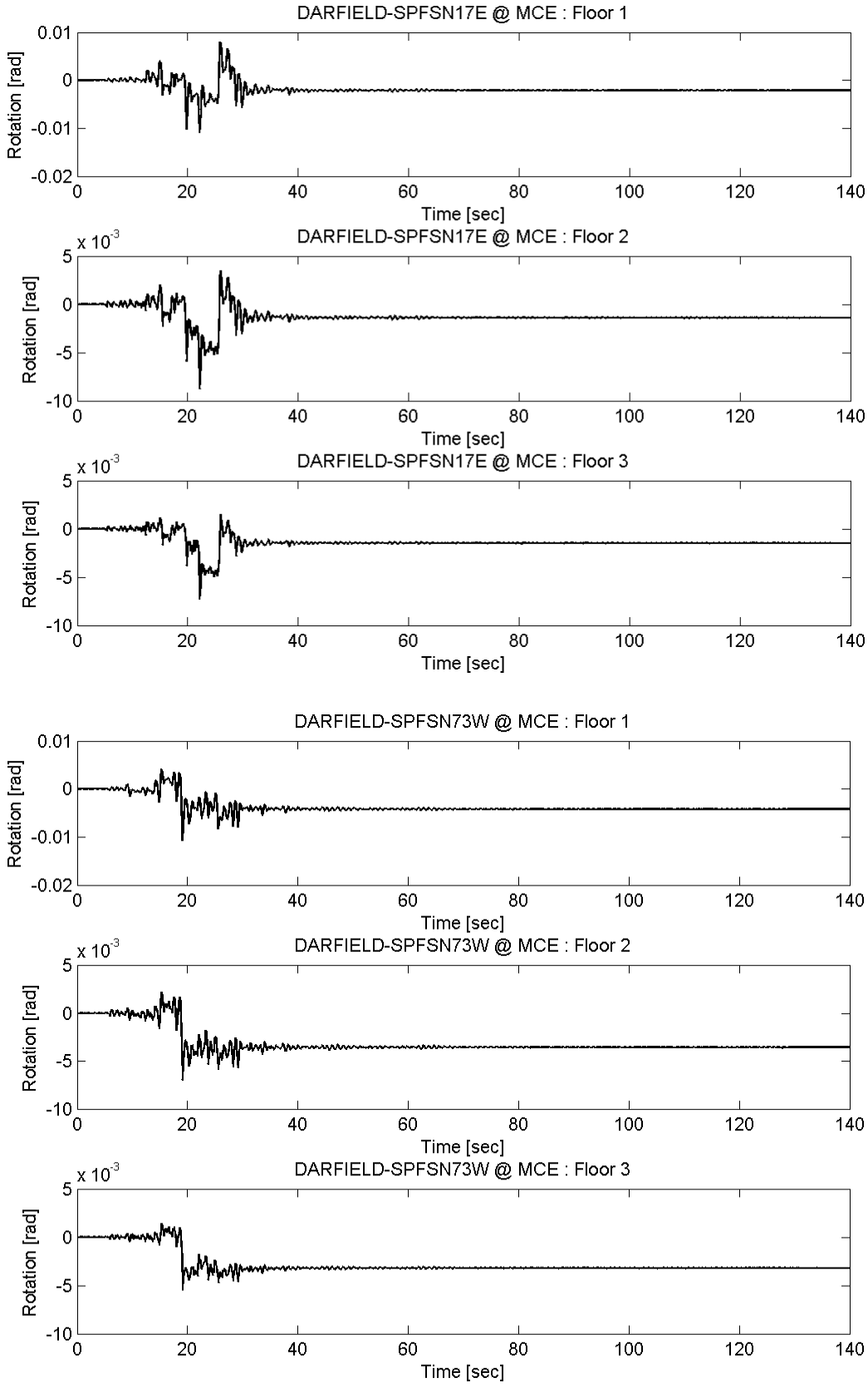
DARFIELD-SPFSN17E @ MCE : Floor 1
Rotation [rad]
Time [sec]
DARFIELD-SPFSN17E @ MCE : Floor 2
x 10^-3
Rotation [rad]
Time [sec]
DARFIELD-SPFSN17E @ MCE : Floor 3
x 10^-3
Rotation [rad]
Time [sec]
DARFIELD-SPFSN73W @ MCE : Floor 1
Rotation [rad]
Time [sec]
DARFIELD-SPFSN73W @ MCE : Floor 2
x 10^-3
Rotation [rad]
Time [sec]
DARFIELD-SPFSN73W @ MCE : Floor 3
x 10^-3
Rotation [rad]
Time [sec]

Appendix E

Smart Structure Testing Machine

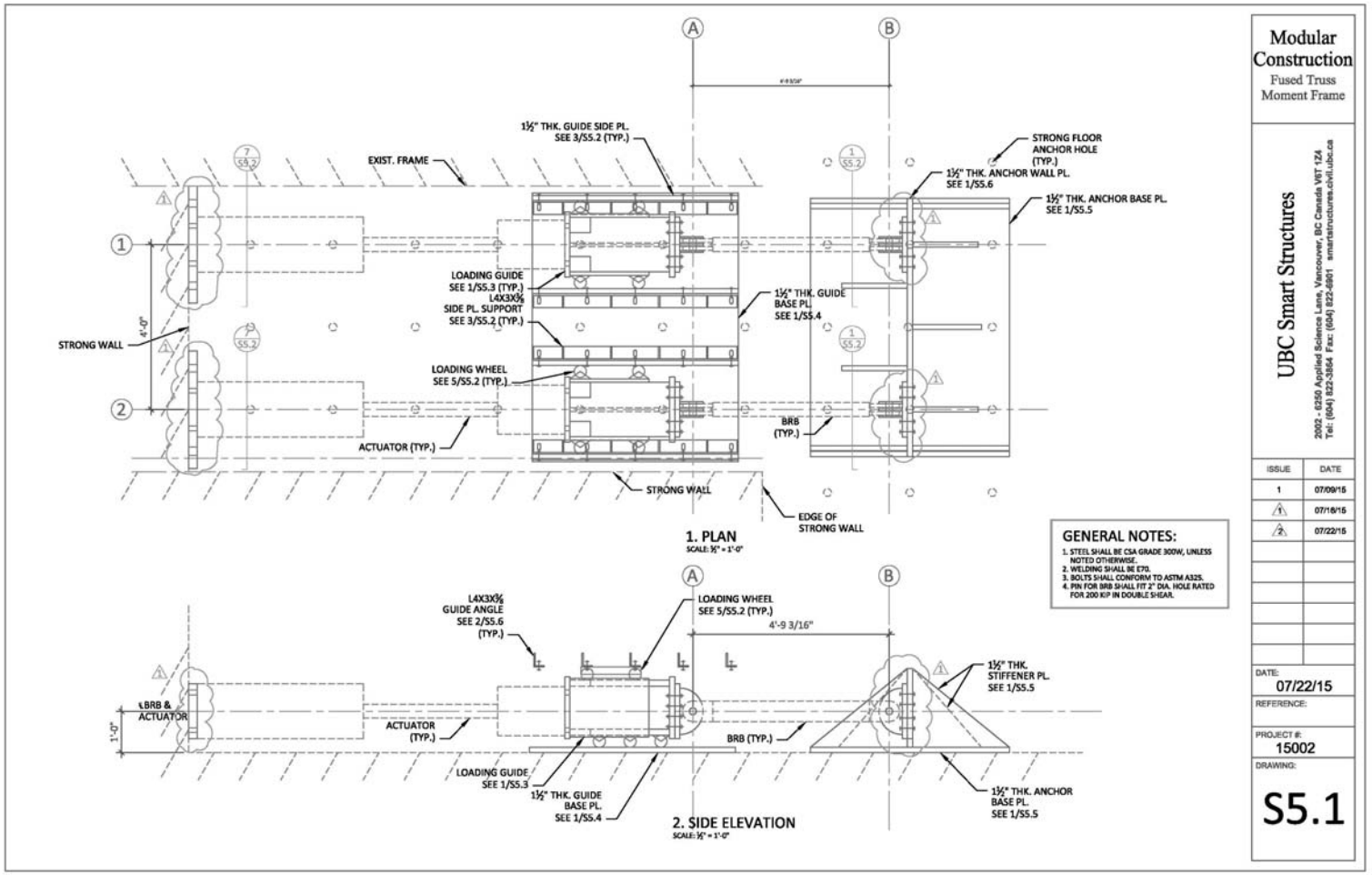

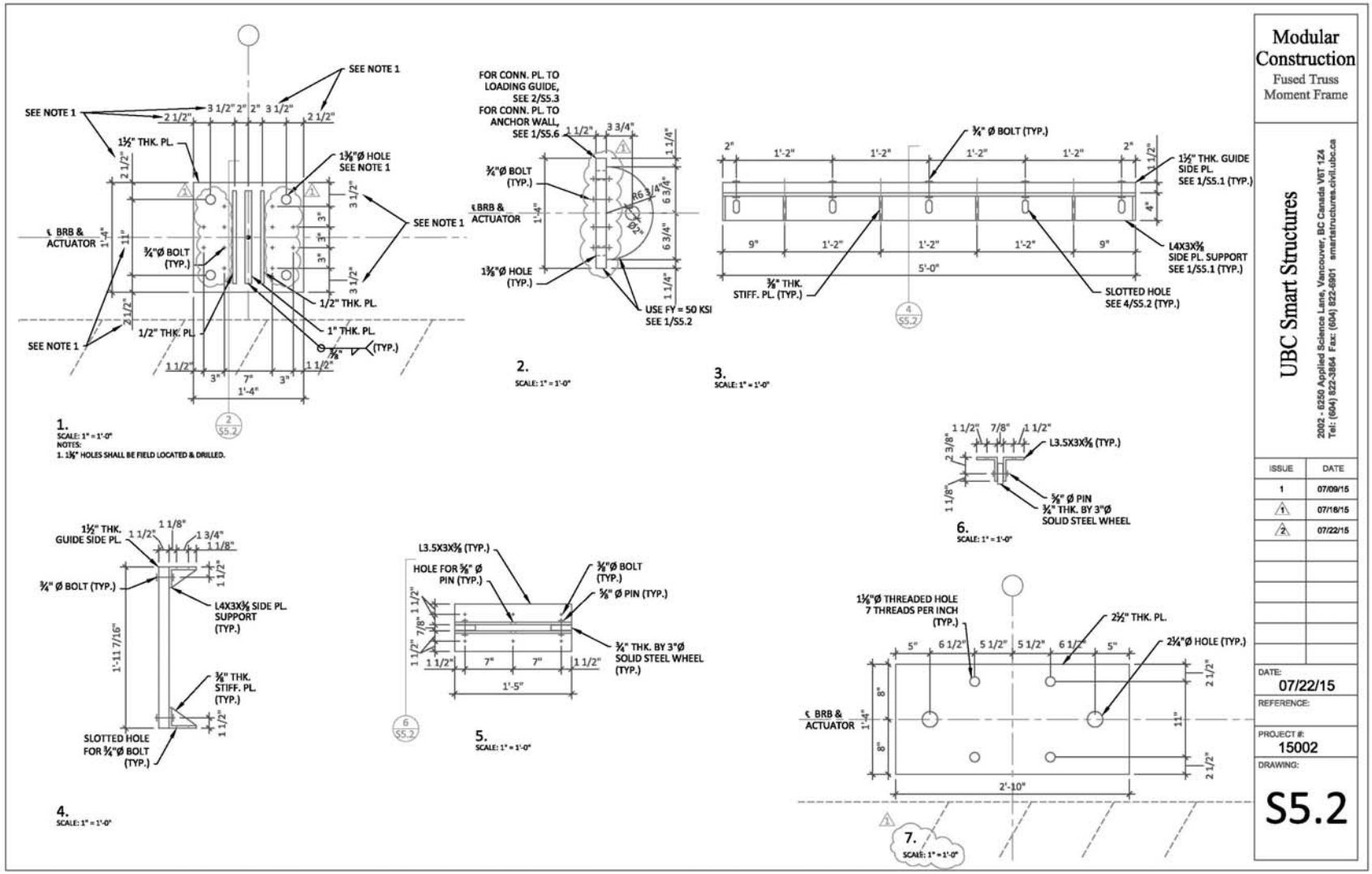
SEE NOTE 1
1½" THK. PL.
1⅜"Ø HOLE SEE NOTE 1
℄ BRB & ACTUATOR
¾"Ø BOLT (TYP.)
1/2" THK. PL.
1" THK. PL.
⅞" (TYP.)
1.
SCALE: 1" = 1'-0"
NOTES:
1. 1⅜" HOLES SHALL BE FIELD LOCATED & DRILLED.
FOR CONN. PL. TO LOADING GUIDE, SEE 2/S5.3
FOR CONN. PL. TO ANCHOR WALL, SEE 1/S5.6
¾"Ø BOLT (TYP.)
1⅜"Ø HOLE (TYP.)
USE FY = 50 KSI SEE 1/S5.2
2.
SCALE: 1" = 1'-0"
¾" Ø BOLT (TYP.)
1½" THK. GUIDE SIDE PL. SEE 1/S5.1 (TYP.)
L4X3X⅜ SIDE PL. SUPPORT SEE 1/S5.1 (TYP.)
⅜" THK. STIFF. PL. (TYP.)
SLOTTED HOLE SEE 4/S5.2 (TYP.)
3.
SCALE: 1" = 1'-0"
1½" THK. GUIDE SIDE PL.
¾" Ø BOLT (TYP.)
L4X3X⅜ SIDE PL. SUPPORT (TYP.)
⅜" THK. STIFF. PL. (TYP.)
SLOTTED HOLE FOR ¾"Ø BOLT (TYP.)
4.
SCALE: 1" = 1'-0"
L3.5X3X⅜ (TYP.)
HOLE FOR ⅜" Ø PIN (TYP.)
⅜"Ø BOLT (TYP.)
⅜" Ø PIN (TYP.)
¾" THK. BY 3"Ø SOLID STEEL WHEEL (TYP.)
5.
SCALE: 1" = 1'-0"
L3.5X3X⅜ (TYP.)
⅜" Ø PIN
¾" THK. BY 3"Ø SOLID STEEL WHEEL
6.
SCALE: 1" = 1'-0"
1¼"Ø THREADED HOLE 7 THREADS PER INCH (TYP.)
2½" THK. PL.
2¼"Ø HOLE (TYP.)
℄ BRB & ACTUATOR
7.
SCALE: 1" = 1'-0"
Modular Construction
Fused Truss Moment Frame
UBC Smart Structures
2002 - 6250 Applied Science Lane, Vancouver, BC Canada V6T 1Z4
Tel: (604) 822-3864 Fax: (604) 822-6901 smartstructures.civil.ubc.ca
ISSUE
DATE
1 07/09/15
1 07/16/15
2 07/22/15
DATE: 07/22/15
REFERENCE:
PROJECT #: 15002
DRAWING:
S5.2

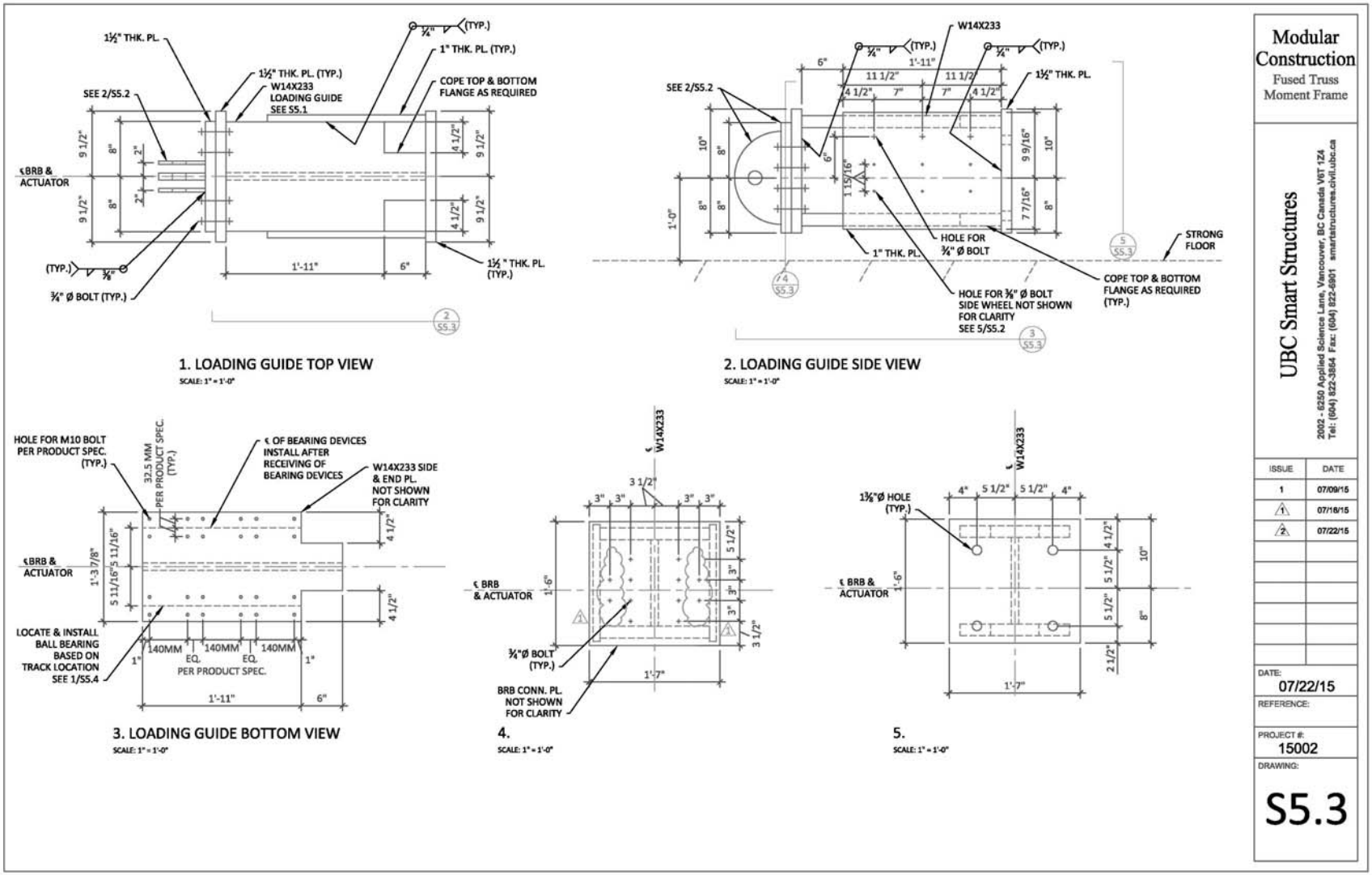

Modular Construction
Fused Truss Moment Frame

UBC Smart Structures
2002 - 6250 Applied Science Lane, Vancouver, BC Canada V6T 1Z4
Tel: (604) 822-3864 Fax: (604) 822-6901 smartstructures.civil.ubc.ca

ISSUE	DATE
1	07/09/15
1	07/16/15
2	07/22/15

DATE: 07/22/15
REFERENCE:
PROJECT #: 15002
DRAWING: S5.3

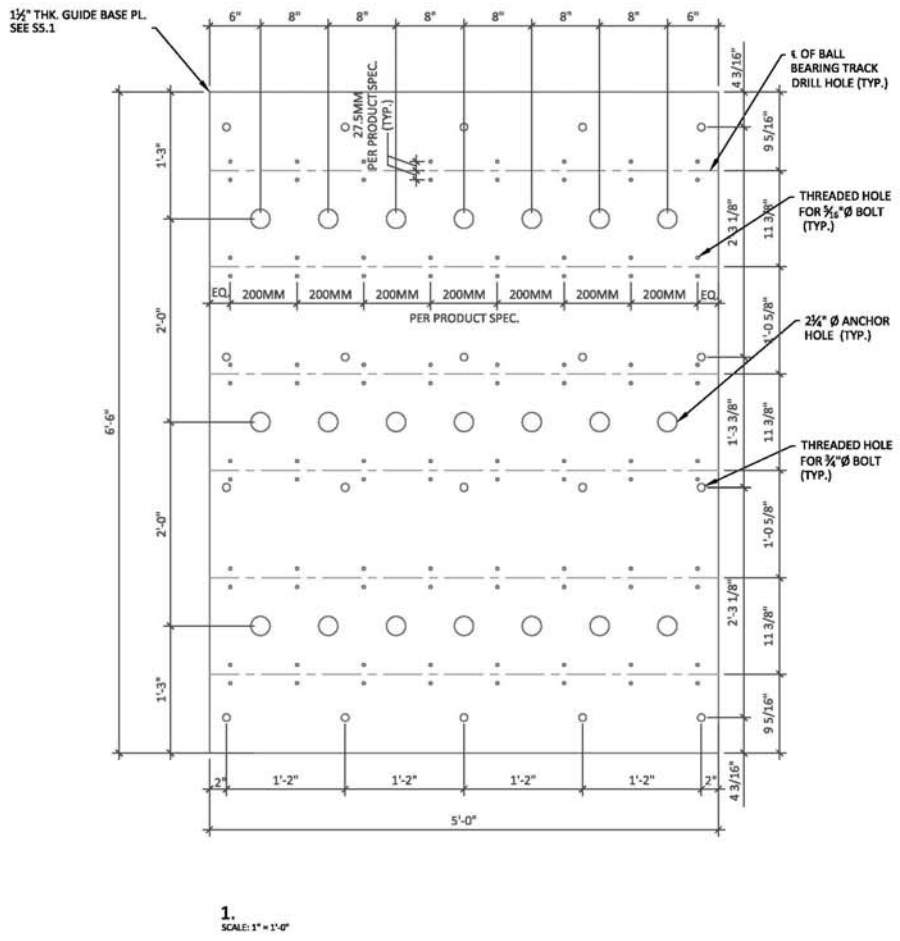

Modular Construction
Fused Truss Moment Frame

UBC Smart Structures
2002 - 6250 Applied Science Lane, Vancouver, BC Canada V6T 1Z4
Tel: (604) 822-3864 Fax: (604) 822-6901 smartstructures.civil.ubc.ca

ISSUE	DATE
1	07/09/15
1	07/16/15
2	07/22/15

DATE: 07/22/15
REFERENCE:
PROJECT #: 15002
DRAWING: S5.4

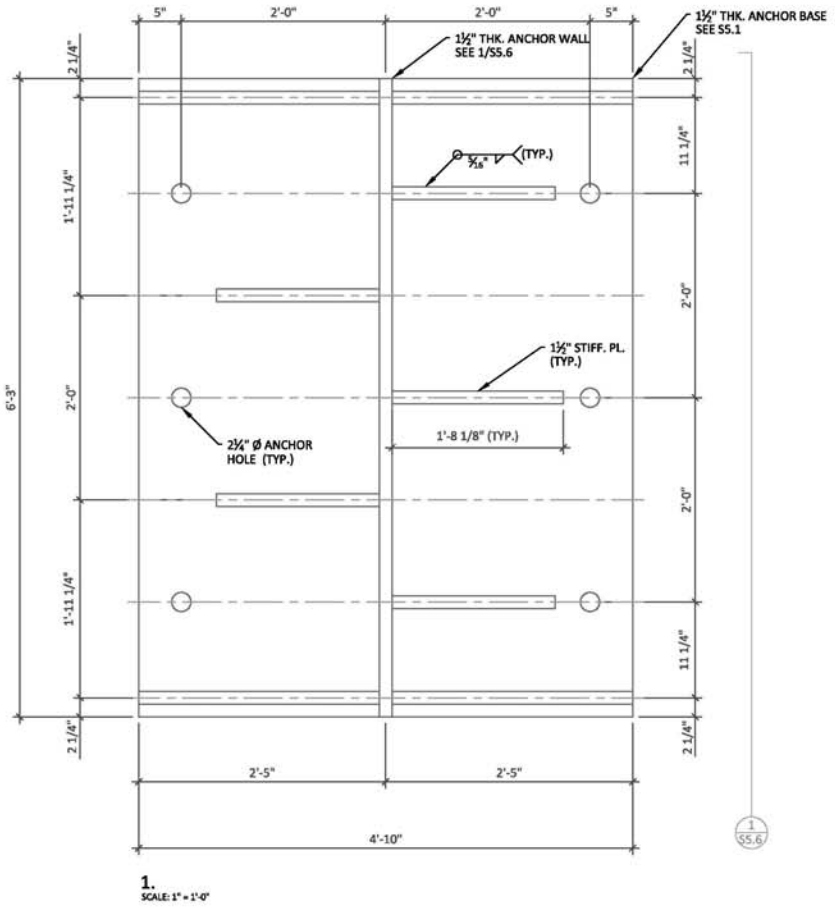

1.
SCALE: 1" = 1'-0"

Modular Construction
Fused Truss Moment Frame

UBC Smart Structures
2002 - 6250 Applied Science Lane, Vancouver, BC Canada V6T 1Z4
Tel: (604) 822-3864 Fax: (604) 822-6901 smartstructures.civil.ubc.ca

ISSUE	DATE
1	07/09/15
1	07/16/15
2	07/22/15

DATE: 07/22/15
REFERENCE:
PROJECT #: 15002
DRAWING: S5.5

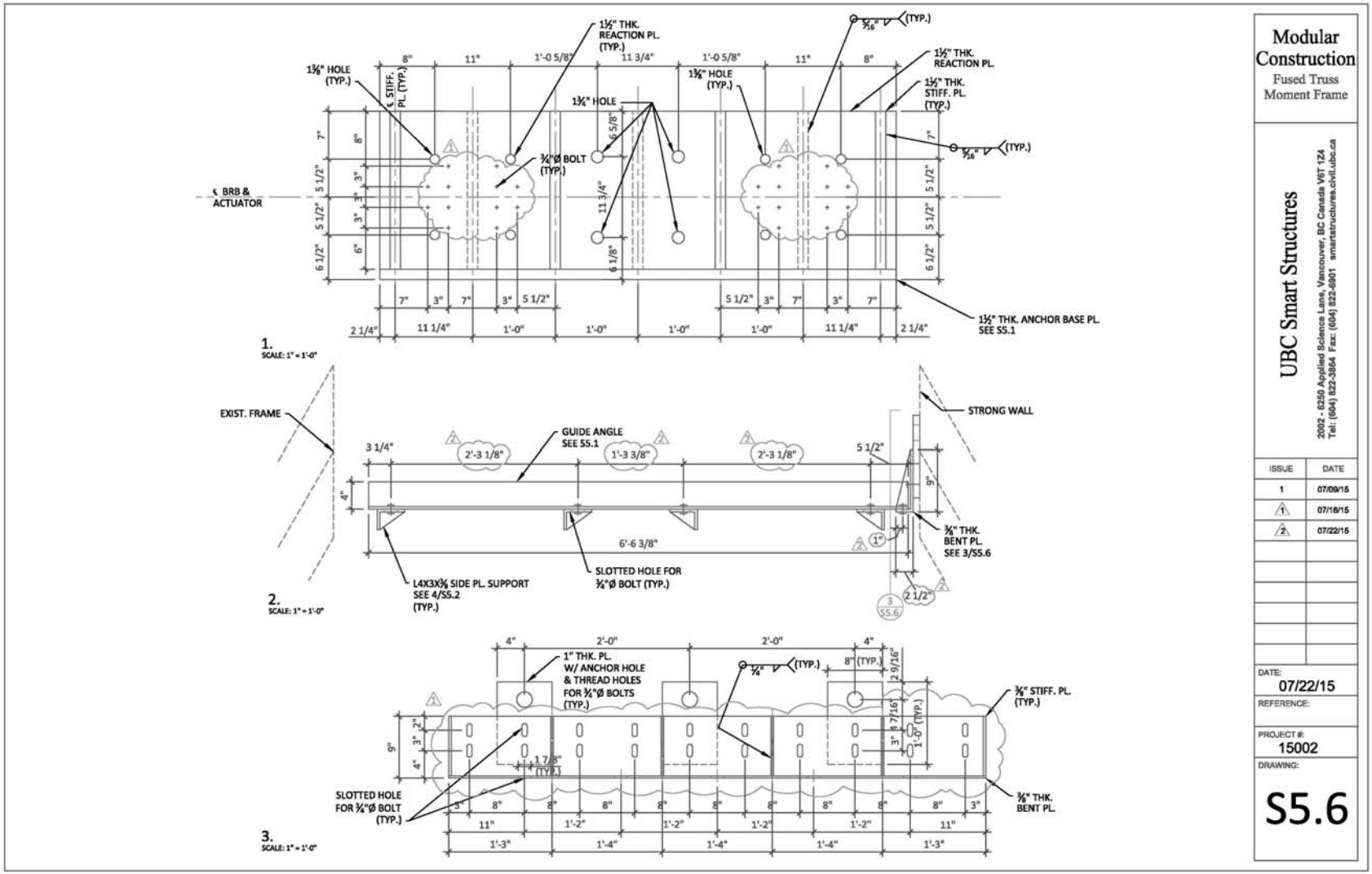

Modular Construction
Fused Truss Moment Frame

UBC Smart Structures
2002 - 6250 Applied Science Lane, Vancouver, BC Canada V6T 1Z4
Tel: (604) 822-3864 Fax: (604) 822-6901 smartstructures.civil.ubc.ca

ISSUE	DATE
1	07/09/15
1	07/16/15
2	07/22/15

DATE: 07/22/15
REFERENCE:
PROJECT #: 15002
DRAWING: S5.6

Appendix F
One-storey FTMF

In Chapter 3, an innovative earthquake resilient fused structure namely fused truss moment frame (FTMF) is developed. This system can be easily designed using the equivalent energy design procedure (EEDP) proposed in Chapter 2. In this appendix, the detailed EEDP design of a one-storey prototype building using FTMFs is presented. This building is used in Chapter 5 to conduct switch-based hybrid simulation (SHS) developed in Chapter 4.

The one-storey prototype building is adopted from the study by Goel *et al.* [1998]. Figure F.1 shows the structural layout. The roof assembly consists of 5-ply felt and gravel on top of poured-in-place insulation supported by corrugated steel deck. The roof joists span in the direction as shown in the figure and are supported by the girders along the long direction of the building. The columns are placed at the grid intersections. Seven FTMFs are utilized at the interior bays to provide the lateral resistance in the short direction of the building. This direction is the focus of the current study. The structural framing is strategically laid out to minimize gravity loadings on the FTMFs. As a result, the effects of gravity loadings on the trusses can be practically neglected. This simplifies the truss design and reserves truss capacity for earthquake loadings. It should be noted that the gravity loadings on the columns are included based on tributary area. The building is assumed to be in Berkeley, California, and situated on very dense soil and/or soft rock. The risk category of the building is assumed such that the importance factor is unity in accordance with ASCE/SEI 7-10 [2010]. The following steps summarize the design of the FTMFs using EEDP. The abbreviations, symbols, and equations used in EEDP have been explained in Chapter 2.

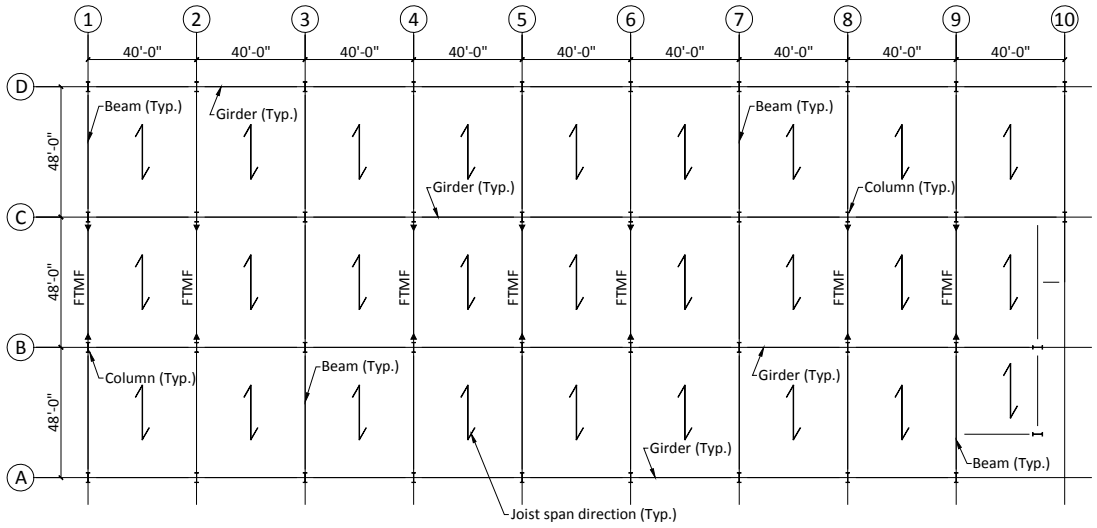

Figure F.1 Plan view of prototype building

Step 1: Select performance objectives under different earthquake shaking intensities

The first step of EEDP is to select the performance objectives for the building under different earthquake shaking intensities. For this building, the performance objectives are selected as follows: 1) immediate occupancy (IO) under the service level earthquake (SLE); 2) rapid return (RR) under the design based earthquake (DBE); 3) collapse prevention (CP) under the maximum considered earthquake (MCE). Figure F.2(a) shows the three shaking intensities calculated based on ASCE/SEI 7-10 [2010] at Berkeley.

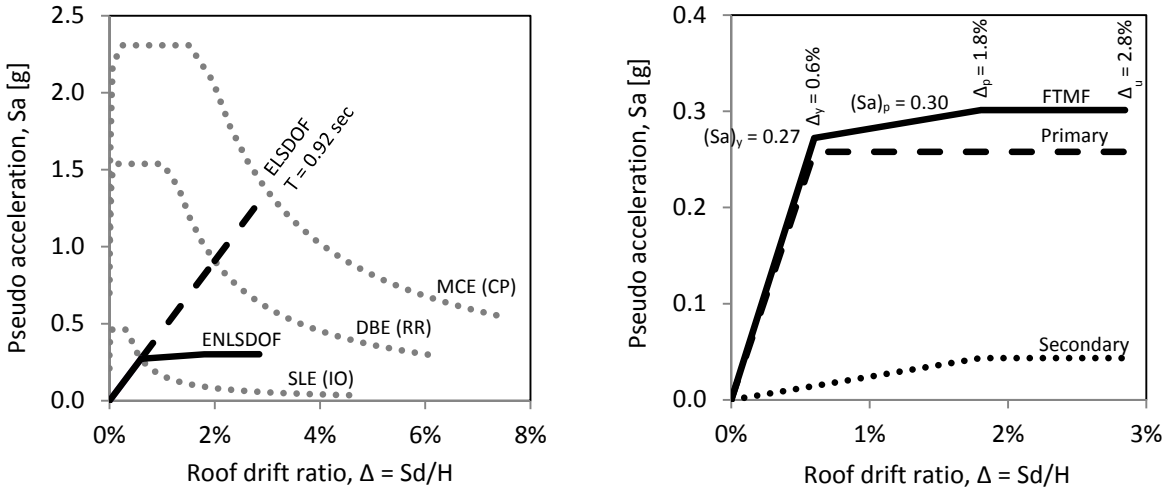

(a) Performance objectives and earthquake shaking intensities

(b) Design parameters

Figure F.2 EEDP design parameters

MCE and DBE correspond to earthquakes with a return period of 2475 years and 475 years, respectively. SLE is selected as one-fifth of MCE resulting in earthquakes with a return period of approximately 15 years. This selection is a realistic representation of frequent earthquakes that a typical Berkeley building could experience during its design lifetime.

Step 2: Select Δ_y to calculate F_y and T

Once the earthquake shaking intensities are selected, designers then select Δ_y which is 0.6% for this building. Δ_y defines the largest roof drift ratio where structural and non-structural components can sustain elastically. Because the system is designed to remain elastic under SLE, $(S_a)_y$ can be identified on Figure F.2(a) as the intersection of the SLE hazard curve and Δ_y. In this case, $(S_a)_y$ is found to be approximately 0.27 as better shown in Figure F.2(b). F_y is then $0.27W$ where W is the seismic weight. Finally, the structural period, T, can be calculated using Equation 2.4 as follow.

$$T = 2\pi\sqrt{\frac{(\Delta_y H)/C_o}{F_y/m}} = 0.92\ second$$

where Δ_y= 0.6%; $H = 372\ in$; $C_o = 1.0$; $F_y/m = (S_a)_y = 0.27 \times 386.4\ in/sec^2$.

With T determined, the following can be read off Figure F.2(a): $(S_a)_{IO} = 0.27$; $(S_a)_{RR} = 0.91$; $(S_a)_{CP} = 1.36$; $(S_d)_{IO} = 0.006H$; $(S_d)_{RR} = 0.020H$; $(S_d)_{CP} = 0.030H$. Equation 2.5 and Equation 2.9 can then be used to obtain the following incremental energies: $\Delta E_{E1} = 0.0083WH$ and $\Delta E_{E2} = 0.0113WH$.

Step 3: Select Δ_p to calculate F_p

The next step of EEDP is to select Δ_p. The selection of Δ_p decides the largest working range of the primary SFRS, which is the buckling restrained braces (BRBs) of the FTMFs. In other words, it defines the largest roof drift ratio within which the BRBs need to be functional before the secondary SFRS, which is the moment connections (MCs) of the FTMFs, starts to yield. For this building, Δ_p is selected to be 1.8% giving μ_p of 3. With the information

presented in Figure 2.12(c), γ_a for this building is identified to be 2.4. Using Equation 2.8, F_p is calculated as follow.

$$F_p = \frac{2\Delta E_{E1}}{\gamma_a H(\Delta_p - \Delta_y)} - F_y = 0.30W$$

where $\Delta E_{E1} = 0.0083WH$; $\gamma_a = 2.4$; $\Delta_y = 0.6\%$; $\Delta_p = 1.8\%$; $F_y = 0.27W$.

Step 4: Calculate Δ_u

With μ_p from the previous step and the information presented in Figure 2.13(c), γ_b for this building is 3.6. Δ_u is then calculated using Equation 2.12 as follow and shown in Figure F.2(b).

$$\Delta_u = \frac{\Delta E_{E2}}{\gamma_b F_p H} + \Delta_p = 2.8\%$$

where $\Delta E_{E2} = 0.0113WH$; $\gamma_b = 3.6$; $F_p = 0.30W$; $\Delta_p = 1.8\%$.

Step 5: Calculate F_{PR} *and* F_{SE}

The base shears calculated thus far are for the FTMFs and need to be distributed between the primary and secondary SFRSs as shown in Figure F.2(b). Equation 2.17 and Equation 2.18 are used to obtain F_{PR} and F_{SE}, respectively, as follow.

$$F_{PR} = F_y \frac{(\mu_p - \lambda)}{(\mu_p - 1)} = 0.26W$$

$$F_{SE} = \mu_p F_y \frac{(\lambda - 1)}{(\mu_p - 1)} = 0.045W$$

where $F_y = 0.27W$; $\mu_p = 3$; $\lambda = 0.30W/0.27W$.

Step 6: Select yielding mechanisms and plastic design yielding members

The yielding mechanism of the FTMF is selected and shown in Figure F.3(a). It has designated yielding members to achieve structural resilience. These members are the BRBs as the primary SFRS and MCs as the secondary SFRS. To plastic design the BRBs, the kinematic method is used. Equation F.1 shows the external work, W_{ext}, based on the selected

yielding mechanism. The external force of F, plastic rotation of θ_p, and structural height of H are illustrated in Figure F.3(a). It should be noted that for the design of the BRBs, the external force should be replaced by F_{PR} from the previous step of EEDP. Equation F.2 shows the internal work, W_{int}, done by the BRBs. The expression for BRB displacement assumes linear transformation as presented by Yang *et al.* [2016], and the parameters are defined in Figure F.3(b). Finally, the force demand in each BRB, F_{BRB}, can be calculated by equating W_{ext} to W_{int}. For the building, there are seven FTMFs and the seismic weight, W, per frame is approximately 136 kips.

$$W_{ext} = F\theta_p H \qquad \text{Equation F.1}$$

$$W_{int} = 2F_{BRB}(D\sin\alpha + L\cos\alpha)\theta_p \qquad \text{Equation F.2}$$

$$F_{BRB} = \frac{F_{PR}H}{2(D\sin\alpha + L\cos\alpha)} = 93\ kips \qquad \text{Equation F.3}$$

where $F_{PR} = 0.26W = 0.26 \times 136 = 35\ kips$; $H = 372\ in$; $D = 48\ in$; $L = 60\ in$; $\alpha = 63.43°$.

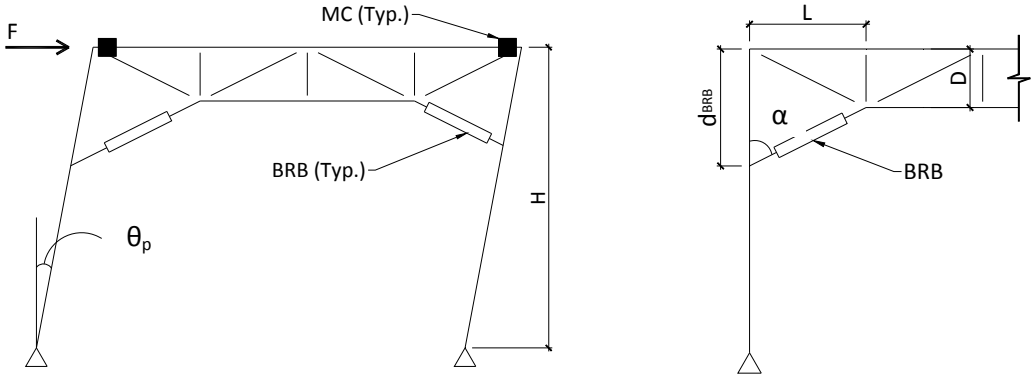

(a) Yielding mechanism (b) BRB geometry

Figure F.3 Plastic design of yielding members

To plastic design the MCs, the kinematic method is again used. The external force in Equation F.1 should be replaced by F_{SE} from the previous step of EEDP. Equation F.4 shows the internal work, W_{int}, done by the MCs. The moment demand in each MC, M_P, can be

calculated by equating W_{ext} to W_{int}. For the building, there are seven FTMFs and the seismic weight, W, per frame is approximately 136 kips.

$$W_{int} = 2M_p\theta_p \quad \text{Equation F.4}$$

$$M_p = \frac{F_{SE}H}{2} = 1116\ kip \cdot in \quad \text{Equation F.5}$$

where $F_{SE} = 0.045W = 0.045 \times 136 = 6\ kips$; $H = 372\ in$.

The capacity of each MC is provided by the coupled yielding plates. The area of each plate, A, can be determined by Equation F.6. The depth of the truss top chord, d, is assumed to be 10 inches, and the specified yielding strength of the steel plate, F_y, is selected to be 50ksi. It should be noted that the ratio of the expected to specified yielding strength is defined as R_y.

$$A = \frac{M_p}{(R_yF_y)d} = 2\ in^2 \quad \text{Equation F.6}$$

where $R_y = 1.1$ [ESR-2802 2013].

Step 7: Capacity design non-yielding members

After the yielding members are designed, the truss and columns of the FTMF need to be capacity designed to remain elastic under the probable forces created by the yielding members. For the BRBs, Equation F.7 and Equation F.8 give the probable BRB forces in tension and compression, respectively. The over-strength factors of 1.50 and 1.75 for tension and compression, respectively, are found during the material model calibration process and hence are used. For the MCs, Equation F.9 gives the probably moment based on the coupled yielding plates.

$$(F_{BRB})_T = 1.50F_{BRB} = 140\ kips \quad \text{Equation F.7}$$

$$(F_{BRB})_C = 1.75F_{BRB} = 163\ kips \quad \text{Equation F.8}$$

where $F_{BRB} = 93\ kips$.

$$M_{MC} = A(R_tF_u)d = 1560\ kip \cdot in \quad \text{Equation F.9}$$

where $A = 2\ in^2$; $R_t = 1.2$ [ESR-2802 2013]; $F_u = 65\ kip/in^2$; $d = 10\ in.$

Figure F.4 shows the free body diagram for the design of the truss. The directions of the probable forces and moments are based on the lateral direction indicated in the figure. It should be noted that the effects of gravity loading are negligible based on the span direction of the roof joists selected in Figure F.1.

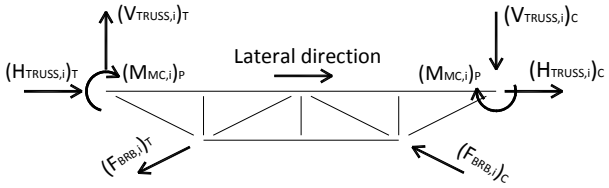

Figure F.4 Free body diagram of truss

Figure F.5 shows the free body diagram for the design of the columns. The gravity loadings are considered based on the column tributary area. With the truss reaction as well as the probable force and moment from the yielding elements, the column is not in equilibrium. Therefore, an equilibrium lateral force, F_L, is determined by taking moments about the column base. This column design approach has been proposed by Goel and Chao [2008].

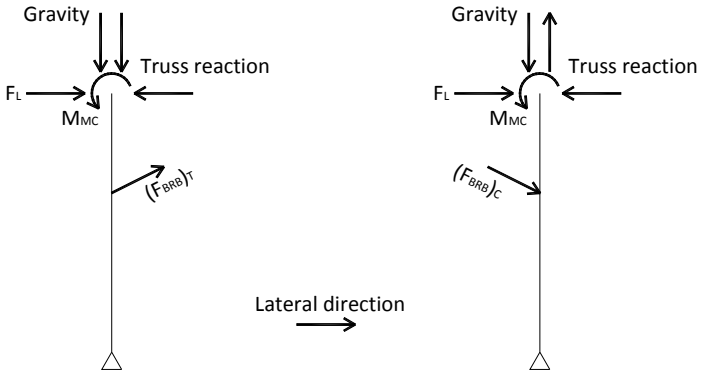

Figure F.5 Free body diagram of column

Figure F.6 presents the final design of the FTMF. The truss has a depth of 4’-0” and typical panel width of 6’-4”. The last panel width is adjusted to fit the overall column spacing. It should be noted that the truss diagonal web member at the last panel is moved 2 feet off the

grid along the top chord to accommodate the moment connection depicted in Figure F.6(b). A wide flange steel beam is selected as the top chord to provide adequate moment capacity and ease connection detailing. Double steel angles with short leg back-to-back (SLBB) are used as the bottom chord to be structurally economical. The design of the truss top and bottom chords as well as columns includes the interaction of moment with compression or tension. P-delta effects are considered in the column design. It is typical for structural engineers to specify BRB design based on BRB force since BRBs are proprietary and made to suit each specification. For the MCs, the yielding plates are detailed to provide proper spacing and edge distance for the high strength bolts. It should be noted that the FTMF designed using EEDP does not require iterations. The structural period calculated by EEDP is 0.92 second, while the period of the final design determined by Eigen analysis is 1.04 second.

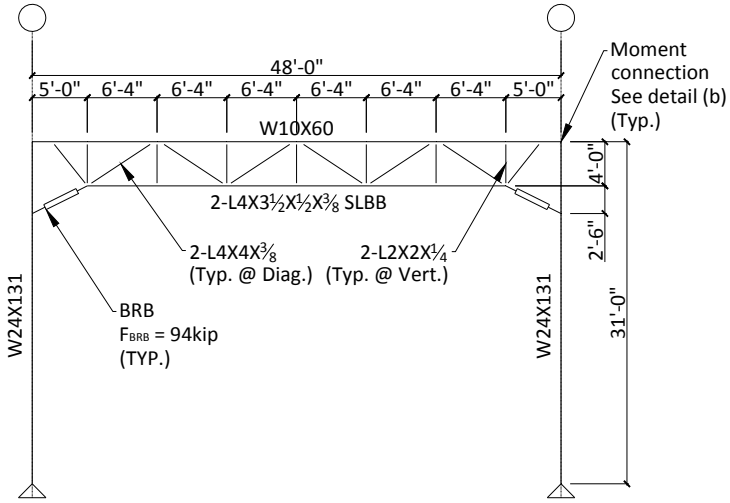

(a) Elevation view of FTMF

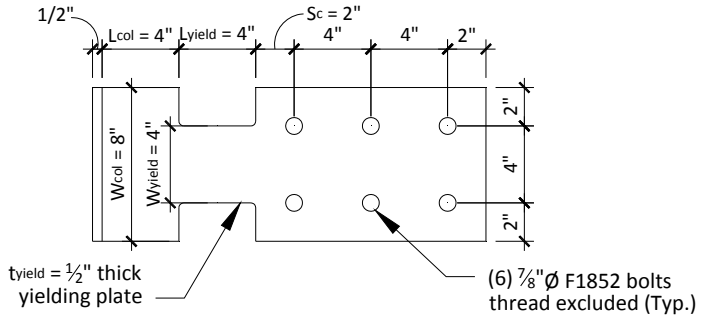

(b) Detail of coupled yielding plate

Figure F.6 FTMF designed by EEDP

Appendix G
Basic System

G.1 Element compatibility matrix

Figure G.1, Figure G.2, and Figure G.3 illustrate the coordinate transformation from the local to global degree-of-freedom (DOF) for a truss element, beam-column element, and zero-length element, respectively. The positive sign convention is shown in the sub-figure (a) for all the three types of elements. The global translational DOFs are $U1$ and $U2$ at one end of an element, and $U4$ and $U5$ at the other end. The global rotational DOFs are $U3$ and $U6$ at each end, respectively. A truss element only has one local axial DOF which is v_1. In addition to v_1, a beam-column element has local rotational DOFs, v_2 and v_3, at each end, respectively. A zero-length element has two local translational DOFs, v_1 and v_2, as well as one local rotational DOF, v_3. The sub-figure (b) gives the compatibility matrix for all the three types of elements. Each column vector of the matrix is obtained as the changes in local displacement due to a unit value of each global DOF. This is illustrated in the sub-figures (c) thru (h). For example, due to the global translational DOFs ($U1$, $U2$, $U4$, and $U5$), linear geometry transformation is assumed for truss and beam-column elements. Similar triangle between ABC and A'B'C' is utilized to determine ΔL as the column vector. In the case of a zero-length element in Figure G.3, the unit value of each global DOF is applied to the node shown as the open circle to determine the change in local displacement. A and B denote the original positions, while A' and B' indicate the new positions due to a global unit displacement.

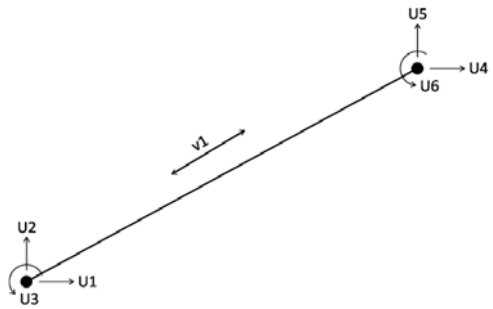

(a) Sign convention

$$[-\Delta x/L \quad -\Delta y/L \quad 0 \quad \Delta x/L \quad \Delta y/L \quad 0]$$

(b) Compatibility matrix

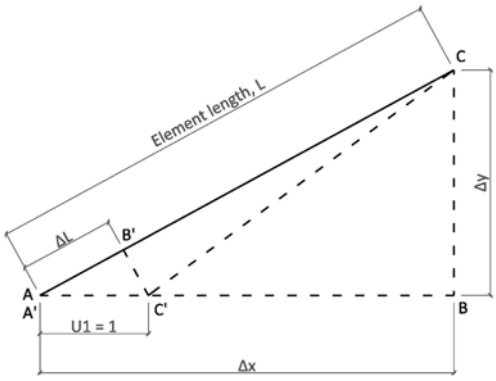

(c) U1 = 1

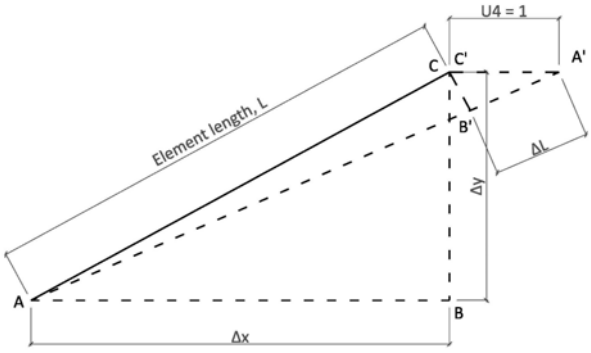

(d) U4 = 1

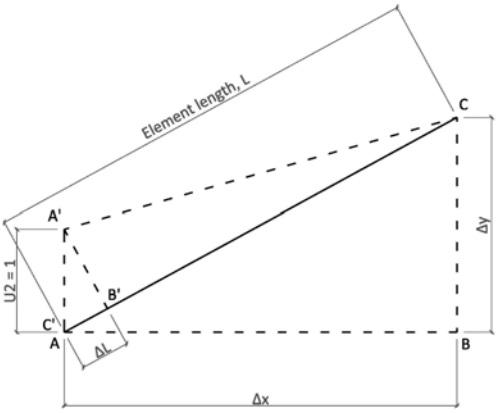

(e) U2 = 1

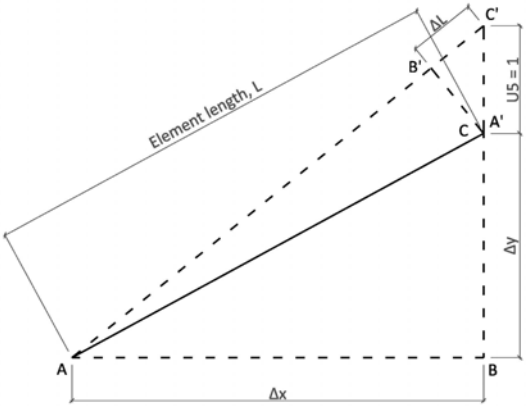

(f) U5 = 1

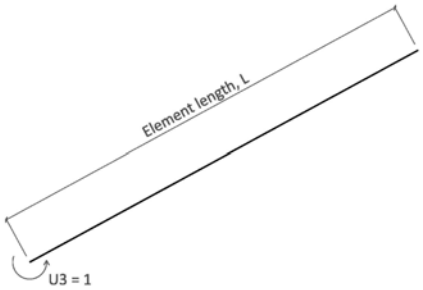

(g) U3 = 1

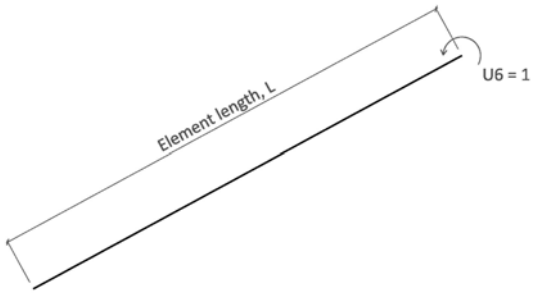

(h) U6 = 1

Figure G.1 Local-to-global coordinate transformation for truss element

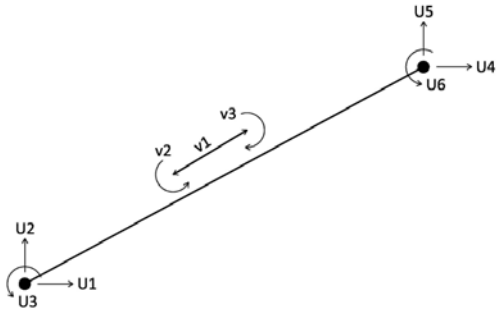

(a) Sign convention

$$\begin{bmatrix} -\Delta x/L & -\Delta y/L & 0 & \Delta x/L & \Delta y/L & 0 \\ -\Delta y/L^2 & \Delta x/L^2 & 1 & \Delta y/L^2 & -\Delta x/L^2 & 0 \\ \Delta y/L^2 & -\Delta x/L^2 & 0 & -\Delta y/L^2 & \Delta x/L^2 & -1 \end{bmatrix}$$

(b) Compatibility matrix

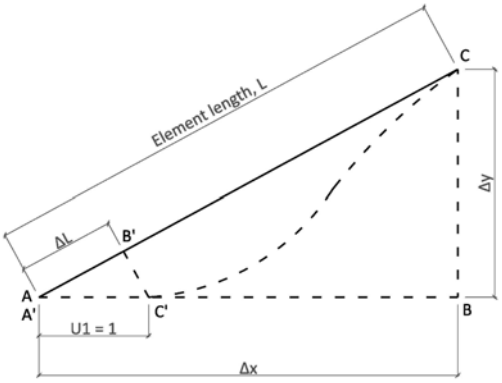

(c) U1 = 1

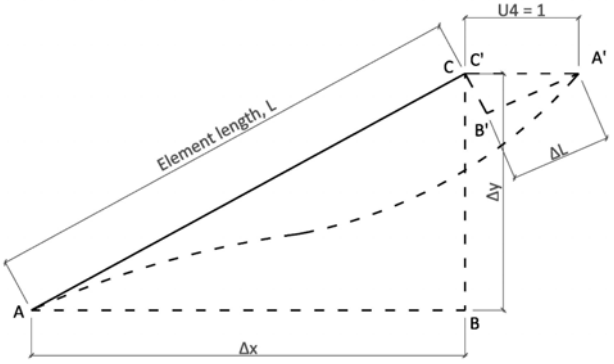

(d) U4 = 1

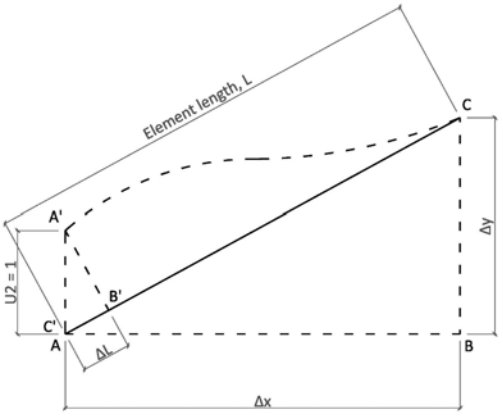

(e) U2 = 1

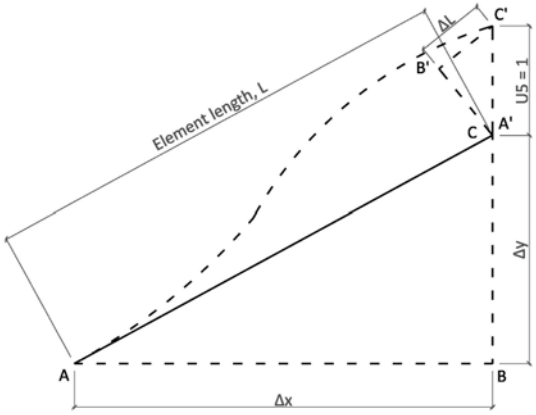

(f) U5 = 1

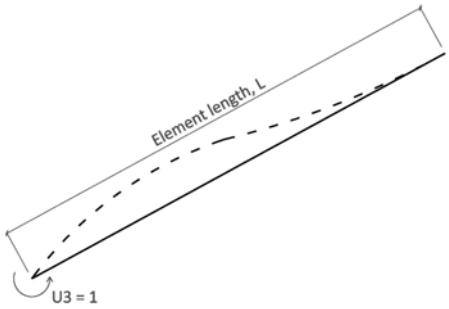

(g) U3 = 1

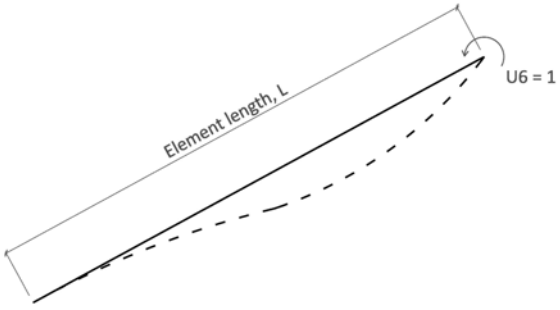

(h) U6 = 1

Figure G.2 Local-to-global coordinate transformation for beam-column element

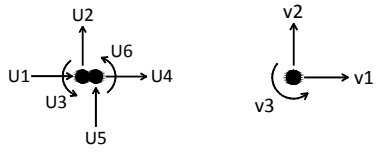

(a) Sign convention

$$\begin{bmatrix} -1 & 0 & 0 & 1 & 0 & 0 \\ 0 & -1 & 0 & 0 & 1 & 0 \\ 0 & 0 & 1 & 0 & 0 & -1 \end{bmatrix}$$

(b) Compatibility matrix

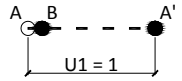

(c) U1 =1

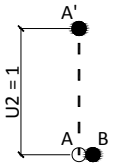

(d) U2 =1

(e) U3 =1

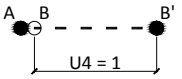

(f) U4 =1

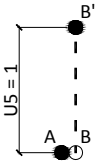

(g) U5 =1

(h) U6 =1

Figure G.3 Local-to-global coordinate transformation for zero-length element

G.2 Element basic stiffness matrix

Figure G.4 shows the basic stiffness matrix for each of the elements to relate between displacement and force in the local DOF. The inverse of each stiffness matrix is the basic flexibility matrix. A truss element only has one local DOF, and hence, the matrix is 1 by 1. Both beam-column and zero-length elements have three local DOFs, and hence, the matrix is 3 by 3.

$$[EA/L] \qquad \begin{bmatrix} EA/L & 0 & 0 \\ 0 & 4EI/L & -2EI/L \\ 0 & -2EI/L & 4EI/L \end{bmatrix} \qquad \begin{bmatrix} k_{axial} & 0 & 0 \\ 0 & k_{shear} & 0 \\ 0 & 0 & k_{moment} \end{bmatrix}$$

(a) Truss element (b) Beam-column element (c) Zero-length element

Legend:
E = modulus of elasticity
I = moment of inertia
A = area
L = length
k_{axial} = axial stiffness
k_{shear} = shear stiffness
k_{moment} = rotational stiffness

Figure G.4 Basic stiffness matrix

G.3 Element basic force

Depending on the element type, Figure G.5 shows the available basic force, q, that matches the available local DOF shown in Figure G.1(a), Figure G.2(a), and Figure G.3(a).

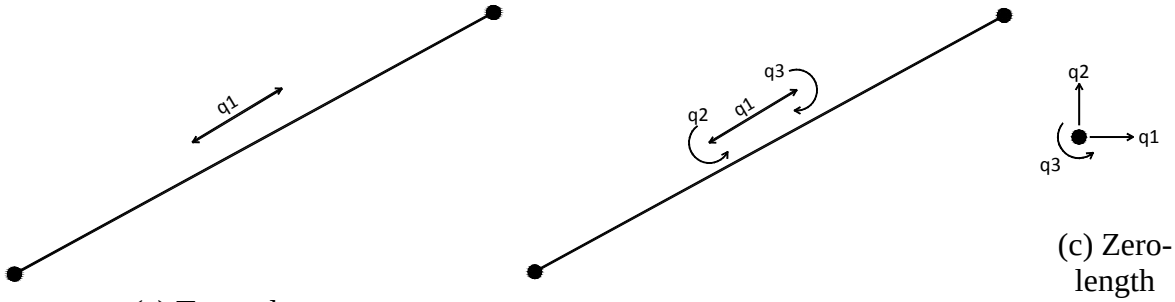

(a) Truss element (b) Beam-column element (c) Zero-length element

Figure G.5 Basic force